Laser Excitation and Infrared Absorption Spectroscopy of Rare-Earth Ion Centres in Fluorite Crystals

A THESIS
SUBMITTED IN PARTIAL FULFILMENT
OF THE REQUIREMENTS FOR THE DEGREE
OF
DOCTOR OF PHILOSOPHY IN PHYSICS
IN THE
UNIVERSITY OF CANTERBURY

BY

Nicholas M Strickland

University of Canterbury
1996

Abstract

Aspects of solid-state rare-earth and hydride-ion-vibrational spectroscopy have been studied, using the techniques of laser-selective excitation, infrared absorption and Zeeman spectroscopy. The calcium-fluoride family of host crystals form, in many respects, a model system with a well characterised cubic lattice and their ready acceptance of a variety of dopant ions.

A laser-selective excitation study of single-Tm^{3+} ion centres in CaF_2 has identified two main centres, having C_{4v} and C_{3v} symmetry respectively, while a third centre of cubic symmetry has been identified through infrared-absorption and Zeeman spectroscopy. In deuterated CaF_2:Tm^{3+} crystals, four Tm^{3+} centres involving D^- ions have been studied, with three of these centres exhibiting reversible polarised bleaching.

Several instances of upconversion fluorescence arising from single-ion centres in CaF_2:RE^{3+} have been observed for single-laser excitation. The upconversion mechanism has been shown to be a sequential-absorption process, with the laser tuned to resonance with one of the two sequential electronic transitions. A novel enhancement by two orders of magnitude of a particular red-to-blue upconversion fluorescence in CaF_2:Tm^{3+} has been observed upon warming the sample from 15 K to room temperature.

The doubly-degenerate transverse vibrational mode of the H^- ion in the C_{4v} site adjacent to a RE^{3+} ion can be split due to coupling of the vibrational modes with the RE^{3+} ion electronic states. The magnitude of these splittings is dependent on the specific rare-earth ion present; these splittings have been measured and compared with the results of calculations based on a point-charge model of the crystal-field potential.

Further splittings of these vibrational modes upon the application of external magnetic fields have been measured. These splittings are well accounted for by a first-order perturbation matrix involving the electronic Zeeman effect and measured zero-field splittings.

Acknowledgements

One might ask what it is that inspires a person to devote more than seven prime years of life to achieve goals which few will appreciate, whilst easier and more lucrative paths continuously beckon. For this (possibly unintended!) inspiration I thank my parents, Gerald and Christine Strickland. It can't always be easy to explain that your 26-year-old son is "still at school", but their support of my endeavours has been unfailing.

Many thanks go to Dr Glynn Jones whose insight and guidance have been invaluable in the struggles of the last few years. Dr Roger Reeves, as an unofficial second supervisor, has also had a huge influence on these studies. The knowledge and skills which have been passed on by Glynn and Roger are gratefully acknowledged.

The crystal-field calculations performed as part of this thesis have used the *F-Shell Empirical* routines written by Dr Mike Reid. Many thanks to Mike for making these programs available and for his continued interest in this work.

During the course of this work I have been fortunate to have available the wide variety of skills provided by all of the technical staff of this department. In particular, thanks go to: Wayne Smith and Ron Culley, instrument workshop; Ross Ritchie, electronics; and Bob Flygenring and Tom Walker, cryogenics.

My fellow research students of the laser-spectroscopy group have helped make my time here that much more enjoyable. Thanks especially to Jon Wells, Steve Jamison and Dr Keith Murdoch for the many discussions, arguments and joint discoveries of "fundamental flaws in physics". May these last not be repeated in public!

In January of 1995 I enjoyed a visit to the Australian National University for collaboration with Dr Neil Manson and Dr John Martin. This was a valuable learning experience, and I would like to thank Neil and John for making this visit possible.

Thanks to the Department of Physics and Astronomy for the financial support throughout this work provided in the form of a Teaching Assistantship.

Finally, I thank Mala for her love and patience through four years of excuses. It can be all too easy to take support and companionship for granted, but this has been constantly there and has been so important over the last few years.

Contents

Figures xxiii

Tables xxx

1 Introduction 1

1.1 The Rare Earths 1

1.2 The CaF_2 Host Crystal 3

1.3 This Thesis 5

2 Rare Earth Spectroscopy 8

2.1 The Free Ion 8

2.2 The Crystal Field 12

2.3 The Application of Group Theory 15

2.4 The Zeeman Effect 19

2.5 Transition Selection Rules and Polarisation Effects 21

3 Experimental 24

3.1 Crystal Growth 24

3.2 Hydrogenation of CaF_2 and SrF_2 Samples 26

3.3 Cryogenics and Superconducting Magnets 27

3.4 Infrared Absorption Spectroscopy 28

3.5 Optical Absorption Spectroscopy 29

3.6 Laser-Selective Excitation Spectroscopy 30

3.7 Fluorescence Lifetimes 36

4 Site-Selective Spectroscopy of Tm^{3+}-doped CaF_2 37

4.1 Previous Studies of CaF_2:Tm^{3+} and SrF_2:Tm^{3+} 37

4.2 Absorption Spectroscopy of CaF_2:Tm^{3+} 40

4.2.1 Zeeman Splittings of the Infrared-Absorption Spectra 46

4.3 Site-Selective Spectroscopy of the C_{4v} Centre in CaF_2:Tm^{3+} 49

4.3.1 Direct Excitation and Fluorescence Spectroscopy 49

4.3.2 Upconversion Fluorescence Spectroscopy 67

4.3.3 Crystal-Field Analysis for the C_{4v} Centre in CaF_2:Tm^{3+} 82

4.3.4 Fluorescence Lifetimes 88

4.4 Site-Selective Spectroscopy of the C_{3v} Centre in CaF_2:Tm^{3+} 93

4.4.1 Direct Excitation and Fluorescence Spectroscopy 93

4.4.2 Upconversion-Fluorescence Spectroscopy 108

4.4.3 Crystal-Field Analysis for the C_{3v} Centre in CaF_2:Tm^{3+} 122

4.4.4 Fluorescence Lifetimes 126

4.5 Analysis of the Cubic-Centre Line in CaF_2:Tm^{3+} 129

4.5.1 Cubic-Centre Wavefunctions 129

4.5.2 Relative Concentrations of the Cubic and Tetragonal Centres in CaF_2:0.01%Tm^{3+} 135

4.6 Deuteration of CaF_2:Tm^{3+} Crystals 139

4.6.1 Absorption Spectra of Deuterated CaF_2:Tm^{3+} Crystals 139

4.6.2 Laser-Selective Excitation and Fluorescence of D^- Centres 145

4.6.3 Bleaching Behaviour of D^- Centres 150

4.7 Summary of the Spectroscopy of CaF_2:Tm^{3+} 157

5 Sequential-Absorption Upconversion Processes in RE^{3+}-doped CaF_2 159

5.1 Upconversion Mechanisms 159

5.1.1 Upconversion in Single RE^{3+}-Ion Centres in CaF_2 166

5.2 Upconversion in CaF_2:Er^{3+} 167

5.2.1 Red-to-Green Upconversion of the C_{4v} Centre of CaF_2:Er^{3+} 167

5.2.2 Infrared-to-Green Upconversion of the C_{4v} Centre of CaF_2:Er^{3+} 174

5.3 Upconversion in CaF_2:Tm^{3+} 180

5.3.1 Red-to-Blue and Red-to-Violet Upconversion of the C_{4v} and C_{3v} Centres of CaF_2:Tm^{3+} 184

5.3.2 Red-to-Blue Upconversion of a Deuterium-Compensated Tm^{3+} Centre 192

5.3.3 Infrared-to-Blue Upconversion of the C_{3v} Centre of CaF_2:Tm^{3+} 195

5.4 Upconversion in CaF_2:Ho^{3+} 196

5.5 Upconversion in CaF_2:Nd^{3+} 201

5.6 Sequential-Absorption Processes for Other Rare-Earth Ions in CaF_2 204

5.7 Summary of Sequential-Absorption Upconversion Processes in CaF_2:RE^{3+} 207

6 H^- Local Modes in Hydrogenated RE^{3+}-doped CaF_2 and SrF_2 211

6.1 Local Modes of H^- in CaF_2 212

6.1.1 The Harmonic-Oscillator Approximation 214

6.1.2 Effect of Anharmonic Terms 216

6.2 Interaction with Electronic States of a Neighbouring RE^{3+} Ion 217

6.3 Estimating Derivatives of the Crystal-Field Potential 221

6.3.1 Derivatives of the Solid Harmonics 221

6.3.2 A Simple Model—The Point Charge Model 222

6.4 Splitting of the H^- x-y Vibronic Associated with Kramers Ions 226

6.4.1 $CaF_2:Ce^{3+}:H^-$ and $SrF_2:Ce^{3+}:H^-$ 230

6.4.2 $CaF_2:Nd^{3+}:H^-$ and $SrF_2:Nd^{3+}:H^-$ 235

6.4.3 $CaF_2:Sm^{3+}:H^-$ and $SrF_2:Sm^{3+}:H^-$ 240

6.4.4 $CaF_2:Dy^{3+}:H^-$ 247

6.4.5 $CaF_2:Yb^{3+}:H^-$ 251

6.4.6 $CaF_2:Er^{3+}:H^-$ 255

6.5 Splitting of the H^- x-y Vibronic Associated with Non-Kramers Ions 263

6.5.1 $CaF_2:Pr^{3+}:H^-$ and $SrF_2:Pr^{3+}:H^-$ 263

6.6 Summary of the x-y Vibronic Splittings in $CaF_2:RE^{3+}:H^-$ and $SrF_2:RE^{3+}:H^-$ 274

7 Zeeman Spectroscopy of H^- Local Modes in Hydrogenated RE^{3+}-doped CaF_2 and SrF_2 278

7.1 Calculating the Zeeman Splittings for H^- x-y Vibronics of Kramers Ions 279

7.1.1 Zeeman Splittings of the x-y Vibronics in $CaF_2:Ce^{3+}:H^-$ and $SrF_2:Ce^{3+}:H^-$ 280

7.1.2 Zeeman Splittings of the x-y Vibronics in $CaF_2:Sm^{3+}:H^-$ and $SrF_2:Sm^{3+}:H^-$ 294

7.1.3 Zeeman Splittings of the x-y Vibronics in $CaF_2:Yb^{3+}:H^-$ 305

7.1.4 Low Lying Excited States: $CaF_2:Er^{3+}:H^-$. 310

7.1.5 Zeeman Splittings of the x-y Vibronics in $CaF_2:Nd^{3+}:H^-$ and $SrF_2:Nd^{3+}:H^-$—Null Effect 316

7.1.6 Zeeman Splittings of the x-y Vibronics in $CaF_2:Gd^{3+}:H^-$—Null Effect 319

7.1.7 Zeeman Splittings of the x-y Vibronics in $CaF_2:Dy^{3+}:H^-$—Null Effect 319

7.2 Calculating the Zeeman Splittings for H^- x-y Vibronics of Non-Kramers Ions 322

7.2.1 Zeeman Splittings of the x-y Vibronics in CaF_2:Pr^{3+}:H^- and SrF_2:Pr^{3+}:H^- 323

7.3 Summary of the Zeeman Effect of the H^- x-y Vibronics 335

8 Conclusions and Suggestions for Further Work 339

References 345

A Differentiation of Solid Harmonics 353

Figures

1.1 The CaF_2 crystal structure. 3

1.2 The local environment of the rare earth ion in the F^- compensated C_{4v} and C_{3v} centres. 4

2.1 The splitting of Tm^{3+} ^{2S+1}L terms into $^{2S+1}L_J$ multiplets with increasing spin-orbit interaction. 11

3.1 Determination of the orientation of a CaF_2-type crystal by cleaving two inequivalent (111) planes. 25

3.2 Laboratory geometry for laser-selective excitation experiments. 31

4.1 Energy level multiplets of the Tm^{3+} ion. 38

4.2 Infrared-absorption spectrum of transitions to the $^3F_4$ multiplet of CaF_2:Tm^{3+}. 41

4.3 Infrared-absorption spectrum of transitions to the $^3H_5$ multiplet of CaF_2:Tm^{3+}. 41

4.4 Optical-absorption spectrum of transitions to the $^3H_4$ multiplet of CaF_2:Tm^{3+}. 42

4.5 Optical-absorption spectrum of transitions to the $^3F_3$ and $^3F_2$ multiplets of CaF_2Tm^{3+}. 43

4.6 Optical-absorption spectrum of transitions to the $^1G_4$ multiplet of CaF_2:Tm^{3+}. 44

4.7 Optical-absorption spectrum of transitions to the $^1D_2$ multiplet of CaF_2:Tm^{3+}. 44

4.8 Infrared-absorption spectrum of transitions to the $^3F_4$ multiplet of CaF_2:Tm^{3+} in $\langle 100 \rangle$ magnetic fields. 47

4.9 Infrared-absorption spectrum of transitions to the $^3H_5$ multiplet of CaF_2:Tm^{3+} in $\langle 100 \rangle$ magnetic fields. 48

4.10 15 K polarised excitation spectrum of the $^3F_3$ multiplet of the C_{4v} centre of CaF_2:Tm^{3+}. 50

4.11 Calculated $^3H_6$ multiplet energies plotted against increasing C_{4v} perturbation. 52

4.12 60 K polarised excitation spectrum of the $^3F_3$ multiplet of the C_{4v} centre of CaF_2:Tm^{3+}. 53

4.13 15 K polarised excitation spectrum of the $^3F_2$ multiplet of the C_{4v} centre of CaF_2:Tm^{3+}. 55

4.14 15 K and 60 K unpolarised excitation spectra of the $^3H_4$ multiplet of the C_{4v} centre of CaF_2:Tm^{3+}. 57

4.15 15 K polarised fluorescence spectrum of the $^3H_4 \rightarrow {}^3H_6$ transitions of the C_{4v} centre of CaF_2:Tm^{3+}. 59

4.16 15 K polarised fluorescence spectrum of the $^3F_3 \rightarrow {}^3H_6$ transitions of the C_{4v} centre of CaF_2:Tm^{3+}. 61

4.17 15 K polarised excitation spectrum of the $^1G_4$ multiplet of the C_{4v} centre of CaF_2:Tm^{3+}. 62

4.18 60 K polarised excitation spectrum of the $^1G_4$ multiplet of the C_{4v} centre of CaF_2:Tm^{3+}. 63

4.19 15 K polarised fluorescence spectrum of the $^1G_4 \rightarrow {}^3H_6$ transitions of the C_{4v} centre of CaF_2:Tm^{3+}. 65

4.20 15 K polarised fluorescence spectrum of the $^1G_4 \rightarrow {}^3F_4$ transitions of the C_{4v} centre of CaF_2:Tm^{3+}. 66

4.21 15 K polarised fluorescence spectrum of the $^1G_4 \rightarrow {}^3H_5$ and $^3H_4 \rightarrow {}^3H_6$ transitions of the C_{4v} centre of CaF_2:Tm^{3+}. 68

4.22 15 K broadband upconversion-excitation spectrum of CaF_2:0.02%Tm^{3+}. 69

4.23 15 K polarised excited-state excitation spectrum of the $^3F_4 \rightarrow {}^1G_4$ transitions of the C_{4v} centre of CaF_2:Tm^{3+}. 71

4.24 15 K polarised excited-state excitation spectrum of the $^3H_4 \rightarrow {}^1D_2$ transitions of the C_{4v} centre of CaF_2:Tm^{3+}. 73

4.25 45 K polarised upconversion fluorescence spectrum of the $^1D_2 \rightarrow {}^3H_6$ transitions of the C_{4v} centre of CaF_2:Tm^{3+}. 75

4.26 15 K polarised upconversion fluorescence spectrum of the $^1D_2 \rightarrow {}^3F_4$ transitions of the C_{4v} centre of CaF_2:Tm^{3+}. 76

4.27 15 K polarised upconversion fluorescence spectrum of the $^1D_2 \rightarrow {}^3H_5$ transitions of the C_{4v} centre of CaF_2:Tm^{3+}. 78

4.28 45 K unpolarised upconversion-fluorescence spectrum of the $^1D_2 \rightarrow {}^3H_4$ and $^1G_4 \rightarrow {}^3F_4$ transitions of the C_{4v} centre of CaF_2:Tm^{3+}. 80

4.29 45 K polarised upconversion fluorescence spectrum of the $^1D_2 \rightarrow {}^3F_3$ transitions of the C_{4v} centre of CaF_2:Tm^{3+}. 81

4.30 45 K polarised upconversion fluorescence spectrum of the $^1D_2 \rightarrow {}^3F_2$ transitions of the C_{4v} centre of CaF_2:Tm^{3+}. 83

4.31 15 K fluorescence decay transient of the $^1G_4$ multiplet of the C_{4v} centre of CaF_2:Tm^{3+}. 89

4.32 15 K fluorescence decay transient of the $^3H_4$ multiplet of the C_{4v} centre of CaF_2:Tm^{3+}. 89

4.33 15 K fluorescence decay transient of the $^3H_4$ multiplet upon pumping the $^1G_4$ multiplet of the C_{4v} centre of CaF_2:Tm^{3+}. 91

4.34 15 K two-laser upconversion-fluorescence decay transient of the $^1G_4$ multiplet of the C_{4v} centre of CaF_2:Tm^{3+}. 92

4.35 15 K two-laser upconversion-fluorescence decay transient of the $^1D_2$ multiplet of the C_{4v} centre of CaF_2:Tm^{3+}. 92

4.36 15 K and 60 K excitation spectrum of the $^3H_4$ multiplet of the C_{3v} centre in CaF_2:Tm^{3+}. 94

4.37 15 K $^3H_4 \rightarrow {}^3H_6$ fluorescence spectrum of the C_{3v} centre in CaF_2:Tm^{3+}. 95

4.38 15 K and 25 K excitation spectrum of the $^3F_3$ multiplet of the C_{3v} centre in CaF_2:Tm^{3+}. 97

4.39 15 K and 25 K excitation spectra of the $^3F_2$ multiplet of the C_{3v} centre in CaF_2:Tm^{3+}. 98

4.40 15 K and 30 K excitation spectrum of the $^1G_4$ multiplet of the C_{3v} centre in CaF_2:Tm^{3+}. 101

4.41 15 K $^1G_4 \rightarrow {}^3H_6$ fluorescence spectrum of the C_{3v} centre in CaF_2:Tm^{3+}. 103

4.42 15 K and 30 K $^1G_4 \rightarrow {}^3F_4$ fluorescence spectrum of the C_{3v} centre in CaF_2:Tm^{3+}. 104

4.43 15 K and 30 K $^1G_4 \rightarrow {}^3H_5$ fluorescence spectrum of the C_{3v} centre in CaF_2:Tm^{3+}. 107

4.44 15 K and 45 K $^3F_4 \rightarrow {}^1G_4$ excited-state absorption spectrum of the C_{3v} centre in CaF_2:Tm^{3+}. 109

4.45 15 K $^3H_4 \rightarrow {}^1D_2$ excited-state absorption spectrum of the C_{3v} centre in CaF_2:Tm^{3+}. 111

4.46 15 K and 45 K $^1D_2 \rightarrow {}^3H_6$ fluorescence spectra of the C_{3v} centre in CaF_2:Tm^{3+}. 112

4.47 15 K and 45 K $^1D_2 \rightarrow {}^3F_4$ fluorescence spectra of the C_{3v} centre in CaF_2:Tm^{3+}. 114

4.48 15 K and 45 K $^1D_2 \rightarrow {}^3H_5$ fluorescence spectra of the C_{3v} centre in CaF_2:Tm^{3+}. 116

4.49 15 K and 45 K $^1D_2 \rightarrow {}^3H_4$ fluorescence spectra of the C_{3v} centre in CaF_2:Tm^{3+}. 118

4.50 15 K and 45 K $^1D_2 \rightarrow {}^3F_3$ fluorescence spectra of the C_{3v} centre in CaF_2:Tm^{3+}. 119

4.51 15 K and 45 K $^1D_2 \rightarrow {}^3F_2$ fluorescence spectra of the C_{3v} centre in CaF_2:Tm^{3+}. 121

4.52 15 K fluorescence decay transient of the $^3H_4$ multiplet of the C_{3v} centre of CaF_2:Tm^{3+}. 126

4.53 15 K fluorescence decay transient of the $^1G_4$ multiplet of the C_{3v} centre of CaF_2:Tm^{3+}. 127

4.54 15 K fluorescence decay transient of the $^1D_2$ multiplet of the C_{3v} centre of CaF_2:Tm^{3+}. 128

4.55 Experimental splitting pattern of the 8429.6 cm^{-1} absorption transition of the cubic centre in CaF_2:Tm^{3+} for magnetic fields parallel to the $\langle 100 \rangle$ crystal axes. 130

4.56 Calculated energy levels of the $^3H_6$ multiplet of Tm^{3+} as a function of the crystal-field parameter, x. 132

4.57 Calculated energy levels of the $^3H_5$ multiplet of Tm^{3+} as a function of the crystal-field parameter, x. 133

4.58 Site configurations of the D^--compensated RE^{3+} centres proposed for CaF_2:Pr^{3+}:D^- and SrF_2:Pr^{3+}:D^-. 140

4.59 $^3H_4$ multiplet absorption spectra series for parent and deuterated CaF_2:Tm^{3+} crystals. 142

4.60 $^3F_3$ and $^3F_2$ multiplet absorption spectra series for parent and deuterated CaF_2:Tm^{3+} crystals. 143

4.61 Laser-absorption spectrum of the $^3F_3$ multiplet of CaF_2:Tm^{3+}:D^-. 145

4.62 Site-selective excitation spectra of the $^3F_3$ multiplet of the L_i D^--compensated centres in CaF_2:Tm^{3+}:D^-. 146

4.63 $^3H_4 \rightarrow {}^3H_6$ fluorescence spectra of the L_i D^--compensated centres in CaF_2:Tm^{3+}:D^-. 147

4.64 Proposed interstitialcy mechanism for bleaching of the CS(2) centre in CaF_2:Pr^{3+}:D^- and SrF_2:Pr^{3+}:D^-. 151

4.65 Bleaching curves for the L_1 centre of CaF_2:Tm^{3+}:D^-. 153

4.66 Bleaching curves for the L_2 centre of CaF_2:Tm^{3+}:D^-. 154

4.67 Bleaching curves for the L_3 centre of CaF_2:Tm^{3+}:D^-. 155

5.1 Production of upconversion fluorescence by the energy-transfer mechanism. 160

5.2 Production of upconversion fluorescence by the sequential absorption of photons. 162

5.3 Sequential-absorption processes which have demonstrated upconversion-laser action. 163

5.4 Population of a high-energy state by photon avalanche. 165

5.5 Red-to-green upconversion excitation spectrum of the C_{4v} centre of CaF_2:Er^{3+} 168

5.6 Sequential-absorption processes of CaF_2:Er^{3+} which produce red-to-green upconversion fluorescence. 170

5.7 Depiction of the phonon sidebands associated with the two electronic transitions of a sequential-absorption process at low temperatures. 171

5.8 Temperature dependence of the red-to-green upconversion excitation spectrum of the ESA lines of the CaF_2:Er^{3+} C_{4v} centre. 173

5.9 Temperature dependence of the integrated upconversion-excitation intensity of the CaF_2:Er^{3+} C_{4v} centre ESA transitions. 174

5.10 Infrared upconversion excitation spectra of CaF_2:Er^{3+}. 175

5.11 Possible infrared-to-green SAU mechanisms in Er^{3+}. 176

5.12 Absorption spectrum and infrared-to-green upconversion excitation spectrum of the C_{4v} centre in CaF_2:Er^{3+}. 178

5.13 Temperature dependence of the infrared-to-green upconversion-excitation spectrum of the C_{4v} centre in CaF_2:Er^{3+}. 181

5.14 Temperature dependence of the infrared-to-green upconversion-excitation of the C_{4v} centre in CaF_2:Er^{3+}. 182

5.15 SAU processes in CaF_2:Tm^{3+}. 183

5.16 Excitation spectra showing depletion of $^3H_4$ fluorescence at ESA wavelengths of the CaF_2:Tm^{3+} C_{4v} centre. 186

5.17 Excitation spectra showing depletion of $^3H_4$ fluorescence at ESA wavelengths of the CaF_2:Tm^{3+} C_{3v} centre. 186

5.18 Temperature dependence of red-to-blue upconversion intensity in CaF_2:Tm^{3+}. 189

5.19 Temperature dependence of the broadband excitation spectrum in the region of the red-to-blue ESA transitions of CaF_2:0.05%Tm^{3+}. 190

5.20 Temperature dependence of the $^3H_4 \rightarrow {}^3H_6$ fluorescence upon pumping at the frequency of the $Y_1 \rightarrow D_1$ ESA transition of the CaF_2:Tm^{3+} C_{4v} centre. 191

5.21 Temperature dependence of red-to-violet upconversion intensity of CaF_2:Tm^{3+}. 193

5.22 Broadband upconversion-excitation spectrum of CaF_2:Tm^{3+}:D^-. 194

5.23 Broadband infrared-to-blue upconversion-excitation spectrum of CaF_2:Tm^{3+}. 196

5.24 Temperature dependence of the broadband red-to-green upconversion-excitation spectrum of CaF_2:Ho^{3+}. 198

5.25 Excitation spectrum of CaF_2:Ho^{3+} at 15 K, monitoring upconversion and normal fluorescence. 199

5.26 Red-to-green SAU mechanism for CaF_2:Ho^{3+}. 200

5.27 Upconversion-excitation spectrum of the $^4F_{3/2} \rightarrow {}^4D_{3/2}$ ESA transition in CaF_2:Nd^{3+}. 201

5.28 SAU upconversion mechanisms observed for CaF_2:Nd^{3+}. 202

5.29 Temperature dependence of ESA upconversion in CaF_2:0.01%Nd^{3+}, pumping the $^4F_{3/2} \rightarrow {}^4D_{3/2}$ transition at 16659 cm^{-1} and monitoring broadband upconversion fluorescence. 203

5.30 Upconversion-excitation spectrum of the $^4I_{9/2} \rightarrow {}^4F_{9/2}$ GSA and proposed $^4F_{3/2} \rightarrow {}^2P_{3/2}$ ESA transitions of the C_{4v} centre of CaF_2:0.01%Nd^{3+} at 15 K, 50 K and 100 K. 205

6.1 The T_d symmetry substitutional H^- ion site in CaF_2 and SrF_2. 211

6.2 The C_{4v} symmetry H^- compensated RE^{3+} centre in CaF_2 and SrF_2. 212

6.3 Infrared-absorption spectrum of the H^- vibrational modes in CaF_2:Dy^{3+}:H^- 213

6.4 Coupling of vibrational and electronic states 218

6.5 Infrared-absorption spectrum of the x-y splitting in CaF_2:Ce^{3+}:H^-. 230

6.6 Infrared-absorption spectrum of the x-y splitting in SrF_2:Ce^{3+}:H^-. 233

6.7 Infrared-absorption spectrum of the x-y splitting in CaF_2:Nd^{3+}:H^-. 235

6.8 Infrared-absorption spectrum of the x-y splitting in SrF_2:Nd^{3+}:H^-. 237

6.9 Infrared-absorption spectrum of the x-y splitting in CaF_2:Sm^{3+}:H^-. 240

6.10 Infrared-absorption spectrum of the x-y splitting in SrF_2:Sm^{3+}:H^-. 244

6.11 Infrared-absorption spectrum of the x-y splitting in CaF_2:Dy^{3+}:H^-. 247

6.12 Infrared-absorption spectrum of CaF_2:Yb^{3+}:H^- 252

6.13 Infrared-absorption spectrum of the x-y splitting in CaF_2:Yb^{3+}:H^-. 253

6.14 Infrared-absorption spectrum of the x-y splitting in CaF_2:Er^{3+}:H^-. 256

6.15 Infrared-absorption spectrum of the x-y splitting in CaF_2:Pr^{3+}:H^-. 264

6.16 Infrared-absorption spectrum of the x-y splitting in SrF_2:Pr^{3+}:H^-. 264

6.17 Calculated first and second order contributions to the CaF_2:Pr^{3+}:H^- x-y splitting. 272

6.18 Calculated first and second order contributions to the SrF_2:Pr^{3+}:H^- x-y splitting. 272

7.1 Infrared-absorption spectra of the x-y vibronics in CaF_2:Ce^{3+}:H^- for $\langle 100 \rangle$ magnetic fields. 282

7.2 Infrared-absorption spectra of the x-y vibronics in CaF_2:Ce^{3+}:H^- for $\langle 111 \rangle$ magnetic fields. 283

7.3 Calculated ground-state and x-y-vibronic-state $\langle 100 \rangle$ Zeeman splittings of CaF_2:Ce^{3+}:H^-. 284

7.4 Calculated ground-state and x-y-vibronic-state $\langle 111 \rangle$ Zeeman splittings of CaF_2:Ce^{3+}:H^-. 285

7.5 Experimental and calculated $\langle 100 \rangle$ and $\langle 111 \rangle$ Zeeman splitting patterns of the x-y vibronics in CaF_2:Ce^{3+}:H^-. 286

7.6 Infrared-absorption spectra of the x-y vibronics in SrF_2:Ce^{3+}:H^- for $\langle 100 \rangle$ magnetic fields. 287

7.7 Infrared-absorption spectra of the x-y vibronics in SrF_2:Ce^{3+}:H^- for $\langle 111 \rangle$ magnetic fields. 288

7.8 Experimental and calculated $\langle 100 \rangle$ and $\langle 111 \rangle$ Zeeman splitting patterns of the x-y vibronics in SrF_2:Ce^{3+}:H^-. 290

7.9 Simulated spectra of the x-y vibronics in CaF_2:Ce^{3+}:H^- for $\langle 111 \rangle$ magnetic fields. 292

7.10 Simulated spectra of the x-y vibronics in SrF_2:Ce^{3+}:H^- for $\langle 111 \rangle$ magnetic fields. 293

7.11 Infrared-absorption spectra of the x-y vibronics in CaF_2:Sm^{3+}:H^- for $\langle 100 \rangle$ magnetic fields. 295

7.12 Infrared-absorption spectra of the x-y vibronics in CaF_2:Sm^{3+}:H^- for $\langle 111 \rangle$ magnetic fields. 296

7.13 Calculated ground-state and x-y-vibronic-state $\langle 100 \rangle$ Zeeman splittings of CaF_2:Sm^{3+}:H^-. 297

7.14 Experimental and calculated $\langle 100 \rangle$ and $\langle 111 \rangle$ Zeeman splitting patterns of the x-y vibronics in CaF_2:Sm^{3+}:H^-. 298

7.15 Infrared-absorption spectra of the x-y vibronics in SrF_2:Sm^{3+}:H^- for $\langle 100 \rangle$ magnetic fields. 300

7.16 Infrared-absorption spectra of the x-y vibronics in SrF_2:Sm^{3+}:H^- for $\langle 111 \rangle$ magnetic fields. 301

7.17 Experimental and calculated $\langle 100 \rangle$ and $\langle 111 \rangle$ Zeeman splitting patterns of the x-y vibronics in SrF_2:Sm^{3+}:H^-. 302

7.18 Simulated spectra of the x-y vibronics in CaF_2:Sm^{3+}:H^- for $\langle 111 \rangle$ magnetic fields. 303

7.19 Simulated spectra of the x-y vibronics in SrF_2:Sm^{3+}:H^- for $\langle 111 \rangle$ magnetic fields. 304

7.20 Infrared-absorption spectra of the x-y vibronics in CaF_2:Yb^{3+}:H^- for $\langle 100 \rangle$ magnetic fields. 306

7.21 Infrared-absorption spectra of the x-y vibronics in CaF_2:Yb^{3+}:H^- for $\langle 111 \rangle$ magnetic fields. 307

7.22 Experimental and calculated $\langle 100 \rangle$ and $\langle 111 \rangle$ Zeeman splitting patterns of the x-y vibronics in CaF_2:Yb^{3+}:H^-. 308

7.23 Simulated spectra of the x-y vibronics in CaF_2:Yb^{3+}:H^- for $\langle 111 \rangle$ magnetic fields. 309

7.24 Infrared-absorption spectra of the x-y vibronics in CaF_2:Er^{3+}:H^- for $\langle 111 \rangle$ magnetic fields. 311

7.25 Experimental and calculated $\langle 111 \rangle$ Zeeman splitting patterns of the x-y vibronics in CaF_2:Er^{3+}:H^-. 314

7.26 Infrared-absorption spectra of the x-y vibronics in CaF_2:Er^{3+}:H^- for $\langle 100 \rangle$ magnetic fields. 315

7.27 Experimental and calculated $\langle 100 \rangle$ Zeeman splitting patterns of the x-y vibronics in CaF_2:Ce^{3+}:H^-. 317

7.28 Experimental and simulated spectra of the x-y vibronics in CaF_2:Nd^{3+}:H^- for $\langle 111 \rangle$ magnetic fields. 318

7.29 Experimental and simulated spectra of the x-y vibronics in CaF_2:Ce^{3+}:H^- for $\langle 111 \rangle$ magnetic fields. 320

7.30 Infrared-absorption spectra of the x-y vibronics in CaF_2:Pr^{3+}:H^- for $\langle 100 \rangle$ magnetic fields. 324

7.31 Infrared-absorption spectra of the x-y vibronics in CaF_2:Pr^{3+}:H^- for $\langle 111 \rangle$ magnetic fields. 325

7.32 Calculated ground-state and x-y-vibronic-state $\langle 100 \rangle$ Zeeman splittings of CaF_2:Pr^{3+}:H^-. 326

7.33 Experimental and calculated $\langle 100 \rangle$ and $\langle 111 \rangle$ Zeeman splitting patterns of the x-y vibronics in CaF_2:Pr^{3+}:H^-. 327

7.34 Infrared-absorption spectra of the x-y vibronics in SrF_2:Pr^{3+}:H^- for $\langle 100 \rangle$ magnetic fields. 328

7.35 Infrared-absorption spectra of the x-y vibronics in SrF_2:Pr^{3+}:H^- for $\langle 111 \rangle$ magnetic fields. 330

7.36 Experimental and calculated $\langle 100 \rangle$ and $\langle 111 \rangle$ Zeeman splitting patterns of the x-y vibronics in SrF_2:Pr^{3+}:H^-. 331

7.37 Simulated spectra of the x-y vibronics in CaF_2:Pr^{3+}:H^- for $\langle 111 \rangle$ magnetic fields. 333

7.38 Simulated spectra of the x-y vibronics in SrF_2:Pr^{3+}:H^- for $\langle 111 \rangle$ magnetic fields. 334

Tables

2.1 Spin-orbit mixing between the J=4 multiplets in Tm^{3+}. 12

2.2 Decomposition of O_3 irreps (J-multiplets) into C_{4v} and C_{3v} irreps. 17

2.3 Decomposition of C_{4v} irreps into C_4 irreps. 19

2.4 Irreps of electric-dipole and magnetic-dipole operators 21

2.5 Polarisation selection rules for C_{4v} symmetry 22

2.6 Polarisation selection rules for C_{3v} symmetry 22

3.1 Laser dyes used to pump specific RE^{3+} multiplet transitions. 30

3.2 RE^{3+} multiplet transitions pumped with the Ti:sapphire laser using the mid-range optics. 31

3.3 Polarisation ratios for C_{4v} centres in $\langle 100 \rangle$ oriented CaF_2 crystals. 34

3.4 Polarisation ratios for C_{3v} centres in $\langle 111 \rangle$ oriented CaF_2 crystals. 35

4.1 Absorption transitions assigned to the C_{4v} and C_{3v} centres in CaF_2:Tm^{3+}. 45

4.2 4 T $\langle 100 \rangle$ Zeeman splitting of infrared-absorption lines in CaF_2:Tm^{3+}. 46

4.3 Crystal-field levels of the $^3F_3$ multiplet for the CaF_2:Tm^{3+} C_{4v} centre. 54

4.4 Crystal-field levels of the $^3F_2$ multiplet for the CaF_2:Tm^{3+} C_{4v} centre. 56

4.5 Assigned crystal-field levels of the $^3H_4$ multiplet for the CaF_2:Tm^{3+} C_{4v} centre. 58

4.6 Assigned crystal-field levels of the $^3H_6$ multiplet for the CaF_2:Tm^{3+} C_{4v} centre. 58

4.7 Crystal-field levels of the $^1G_4$ multiplet for the CaF_2:Tm^{3+} C_{4v} centre. 72

4.8 Crystal-field levels of the $^1D_2$ multiplet for the CaF_2:Tm^{3+} C_{4v} centre. 72

4.9 Crystal-field levels of the $^3F_4$ multiplet for the CaF_2:Tm^{3+} C_{4v} centre. 77

4.10 Crystal-field levels of the $^3H_5$ multiplet for the CaF_2:Tm^{3+} C_{4v} centre. 79

4.11 Crystal-field parameters determined for several of the RE^{3+} ions in the C_{4v} centres of CaF_2. 84

4.12 Minor free-ion interaction parameters, whose values were fixed at those found for LaF_3:Tm^{3+} [14] and were not varied in the crystal-field fit. 85

4.13 Best-fit values of the free-ion and crystal-field parameters which were varied in the fit for the C_{4v} centre of CaF_2:Tm^{3+} . 85

4.14 Tm^{3+} free-ion wavefunctions calculated from the CaF_2: Tm^{3+} C_{4v} centre data. 86

4.15 Measured and calculated crystal-field energy levels for the CaF_2:Tm^{3+} C_{4v} centre. 87

4.16 Polarisation ratios of $^3H_6 \rightarrow {}^3H_4$ excitation lines for the C_{3v} centre of CaF_2:Tm^{3+}. 94

4.17 Polarisation ratios of $^3H_6 \rightarrow {}^3H_4$ excitation lines for the C_{3v} centre of CaF_2:Tm^{3+}. 96

4.18 Polarisation ratios of $^3H_6 \rightarrow {}^3F_3$ excitation lines for the C_{3v} centre of CaF_2:Tm^{3+}. 99

4.19 Polarisation ratios of $^3H_6 \rightarrow {}^3F_2$ excitation lines for the C_{3v} centre of CaF_2:Tm^{3+}. 100

4.20 Transition energies of $^3H_6 \rightarrow {}^1G_4$ excitation lines for the C_{3v} centre of CaF_2:Tm^{3+}. 102

4.21 Transition energies of $^1G_4 \rightarrow {}^3H_6$ fluorescence lines for the C_{3v} centre of CaF_2:Tm^{3+}. 105

4.22 Transition energies of $^1G_4 \rightarrow {}^3F_4$ fluorescence lines for the C_{3v} centre of CaF_2:Tm^{3+}. 106

4.23 Transition energies of $^1G_4 \rightarrow {}^3H_5$ fluorescence lines for the C_{3v} centre of CaF_2:Tm^{3+}. 106

4.24 Transition energies of $^3F_4 \rightarrow {}^1G_4$ excitation lines for the C_{3v} centre of CaF_2:Tm^{3+}. 108

4.25 Transition energies of $^1D_2 \rightarrow {}^3H_6$ fluorescence lines for the C_{3v} centre of CaF_2:Tm^{3+}. 113

4.26 Transition energies of $^1D_2 \rightarrow {}^3F_4$ fluorescence lines for the C_{3v} centre of CaF_2:Tm^{3+}. 115

4.27 Transition energies of $^1D_2 \rightarrow {}^3H_5$ fluorescence lines for the C_{3v} centre of CaF_2:Tm^{3+}. 117

4.28 Transition energies of $^1D_2 \rightarrow {}^3F_3$ fluorescence lines for the C_{3v} centre of CaF_2:Tm^{3+}. 120

4.29 Transition energies of $^1D_2 \rightarrow {}^3F_2$ fluorescence lines for the C_{3v} centre of CaF_2:Tm^{3+}. 122

4.30 Best-fit values of the free-ion and crystal-field parameters which were varied in the fit for the C_{3v} centre of CaF_2:Tm^{3+}. 123

4.31 Measured and calculated energy levels for the CaF_2:Tm^{3+} C_{3v} centre. 124

4.32 Measured and calculated values of $g_{\langle 100 \rangle}$ for $^3F_4$ and $^3H_5$ multiplet absorption lines. 125

4.33 A comparison of the experimental lifetimes of the $^3H_4$, $^1G_4$ and $^1D_2$ lifetimes of the C_{4v} and C_{3v} centres of CaF_2:Tm^{3+}. 128

4.34 Transition energies of the L_i centre $^3F_3$ excitation lines and $^3H_4 \rightarrow {}^3H_6$ fluorescence lines. 148

5.1 Measured transition energies of $^4I_{13/2} \rightarrow {}^4F_{5/2}$ ESA lines for the C_{4v} centre of CaF_2:Er^{3+}. 169

5.2 Energies of the states and transitions which may contribute to infrared-to-green upconversion in the C_{4v} centre of CaF_2:Er^{3+}. 179

6.1 Values of α and β for CaF_2:RE^{3+}:H^- and SrF_2:RE^{3+}:H^- 215

6.2 C_{4v} harmonic oscillator wavefunctions 216

6.3 Values of $\langle r^2 \rangle$, $\langle r^4 \rangle$ and $\langle r^6 \rangle$, in Bohr radii. 225

6.4 Electronic state notation and bases for Kramers ions. 226

6.5 Vibrational state notation and bases. 226

6.6 Energy levels and wavefunctions of the Ce^{3+} ion in the CaF_2:Ce^{3+} C_{4v} centre. 231

6.7 Calculated energy shifts of the Φ_6^+ and Φ_7^+ states for CaF_2:Ce^{3+}:H^- 231

6.8 Energy levels and wavefunctions of the Ce^{3+} ion in the SrF_2:Ce^{3+} C_{4v} centre. 234

6.9 Calculated energy shifts of the Φ_6^+ and Φ_7^+ states for SrF_2:Ce^{3+}:H^- 234

6.10 Energy levels and wavefunctions of the Nd^{3+} ion in the CaF_2:Nd^{3+} D^- C_{4v} centre. 236

6.11 Calculated energy shifts of the Ψ_6^+ and Ψ_7^+ states for CaF_2:Nd^{3+}:H^- 236

6.12 Energy levels and wavefunctions of the Nd^{3+} ion in the SrF_2:Nd^{3+} T^- C_{4v} centre. 238

6.13 Calculated energy shifts of the Ψ_6^+ and Ψ_7^+ states for SrF_2:Nd^{3+}:H^- 239

6.14 Energies and wavefunctions of the Sm^{3+} ion in the CaF_2:Sm^{3+} C_{4v} centre. 241

6.15 Calculated energy shifts of the Ψ_6^+ and Ψ_7^+ states for CaF_2:Sm^{3+}:H^- 242

6.16 Energies and wavefunctions of the Sm^{3+} ion in the SrF_2:Sm^{3+} C_{4v} centre. 245

6.17 Calculated energy shifts of the Ψ_6^+ and Ψ_7^+ states for SrF_2:Sm^{3+}:H^- 246

6.18 Crystal-field parameters used to calculate CaF_2:Dy^{3+} C_{4v} centre energies and wavefunctions. 248

6.19 $^6H_{15/2}$-multiplet energies and wavefunctions of the Dy^{3+} ion in the CaF_2:Dy^{3+} C_{4v} centre. 249

6.20 Calculated energy shifts of the Φ_6^+ and Φ_7^+ states for CaF_2:Dy^{3+}:H^- 250

6.21 Calculated energies and wavefunctions of the Yb^{3+} ion in the CaF_2:Yb^{3+} C_{4v} centre. 254

6.22 Calculated energy shifts of the Φ_6^+ and Φ_7^+ states for CaF_2:Yb^{3+}:H^- 254

6.23 Energies and wavefunctions of the Er^{3+} ion in the CaF_2:Er^{3+}:H^- C_{4v} centre. 257

6.24 Calculated energy shifts of the Φ_6^+ and Φ_7^+ states for CaF_2:Er^{3+}:H^- 260

6.25 Calculated energy shifts of the Ψ_6^+ and Ψ_7^+ states for CaF_2:Er^{3+}:H^- 261

6.26 Measured and first and second order calculated shifts of the Ψ_6^+ and Ψ_7^+ states for CaF_2:Er^{3+}:H^-. 262

6.27 Energies and wavefunctions of the Pr^{3+} ion in the C_{4v} centres of CaF_2:Pr^{3+}:H^- and SrF_2:Pr^{3+}:H^-. 266

6.28 Electronic state notation and bases for non-Kramers ions. 266

6.29 Calculated x-y vibronic wavefunctions and first-order energies for CaF_2:Pr^{3+}:H^- and SrF_2:Pr^{3+}:H^- 268

6.30 Calculated second-order energy shifts of the x-y vibronic states for CaF_2:Pr^{3+}:H^-. 270

6.31 Calculated second-order energy shifts of the x-y vibronic states for SrF_2:Pr^{3+}:H^-. 271

6.32 Calculated and fitted values of the electron-phonon Hamiltonian for CaF_2:Pr^{3+}:H^- and SrF_2:Pr^{3+}:H^-. 273

6.33 Calculated and fitted shifts of the x-y vibronic states for CaF_2:Pr^{3+}:H^- and SrF_2:Pr^{3+}:H^-. 274

6.34 Measured splittings of the H^- x-y vibronic line of the RE^{3+}–H^- C_{4v} centres in CaF_2 and SrF_2. 275

6.35 Calculated and fitted values of the αD_1^2 electron-phonon interaction parameter for the C_{4v} centres of CaF_2:RE^{3+}:H^- and SrF_2:RE^{3+}:H^-. 276

7.1 Zero-field energy eigenvalues for the x-y vibronic states of CaF_2:Pr^{3+}:H^- and SrF_2:Pr^{3+}:H^-. 329

Chapter 1

Introduction

This thesis consists of the results of studies in rare-earth spectroscopy. Results are reported for

- The optical and infrared spectroscopy of Tm^{3+} ion centres in CaF_2:Tm^{3+} and CaF_2:Tm^{3+}:D^-, using laser-selective excitation and infrared and optical absorption spectroscopy.
- A study of sequential-absorption upconversion processes, pumped by a single tunable laser, for single-RE^{3+}-ion centres in CaF_2:RE^{3+}.
- Modelling of the splitting of the infrared-absorption lines of the transverse (x-y) vibrational-modes of H^- ions in the C_{4v}-symmetry RE^{3+}–H^- centres in CaF_2:RE^{3+}:H^-.
- The effect of applied magnetic fields on these H^- vibrational-mode absorption lines.

1.1 The Rare Earths

The rare earths comprise the elements of the lanthanide and actinide series, characterised by the partially filled $4f$ and $5f$ electron shells respectively. It is the trivalent ions of the lanthanide series (Ce^{3+} through Yb^{3+}) that are the focus of this thesis. The electronic structure of the neutral lanthanides consists of a xenon core ($1s^2 2s^2 2p^6 3s^2 3p^6 4s^2 3d^{10} 4p^6 5s^2 4d^{10} 5p^6$) plus the $6s^2$ shell and the partially filled $4f$ shell.

The eigenfunctions of the $4f$ electrons are remarkable in having their spatial maximum well within the the $5s^2 5p^6$ closed shells of the xenon core. This so-called lanthanide contraction, which does not occur for s, p or d electrons, increases along the lanthanide series as the effective charge of the core increases. Since the f electrons are shielded by the $5s^2 5p^6$ shells, the local environment of the ion has relatively little effect on the energies of the $4f^N$ states. This behaviour in the solid state is very different from the d^N configuration of the transition metal ions. The d electron eigenfunctions are affected more strongly by the environment; the energy-level splittings of these ions are dominated by the crystal-field interaction over the free-ion interactions, as illustrated by the Tanabe-Sugano diagrams [86] which plot the energies as a function of a cubic-crystal-field parameter, Dq. The energy levels of transition metal ions can therefore be changed by doping the transition metal ion into a different host crystal—for example Cr^{3+}-doped crystals appear different colours in transmission depending on the host, red for ruby but green for gadolinium gallium garnet. The energy levels of $4f^N$ configuration on the other hand are determined primarily by the free-ion interactions with relatively small perturbations, of the order of a few hundred cm^{-1}, from the crystal field. The small crystal field interaction with the lanthanide ions also means that the inhomogeneous broadening, the statistical broadening due to slight perturbations in the ion arrangements, is much smaller than that in the case of the transition metal ions and the spectra of rare-earth ions are characterised by having many sharp lines.

The most common oxidation state for most of the lanthanide elements is the trivalent (RE^{3+}) state in which the two $6s$ electrons and one of the $4f$ electrons are removed leaving the xenon core and the remaining $4f$ electrons. This behaviour, and the shielding of the remaining $4f$ electrons, dominates the chemistry of the lanthanide elements resulting in similar chemical properties across the series. In contrast the spectroscopic properties in the visible region are dominated by transitions between $4f^N$ states. A partially filled shell containing N electrons with 14 available single electron states yields $14!/N!(14-N)!$ possible states for the $4f^N$ configuration, spread in energy over typically many tens of thousands of cm^{-1}.

The sharpness of spectral lines and the wide spread of energy levels throughout the infrared, optical and ultraviolet regions of the electromagnetic spectrum makes the lanthanide ions versatile subjects for study and applications.

1.2 The CaF_2 Host Crystal

CaF_2 has a cubic symmetry with the F^- ions forming a simple cubic lattice with a Ca^{2+} ion occupying each alternate F^- cube (fig 1.1). It is well suited for use in

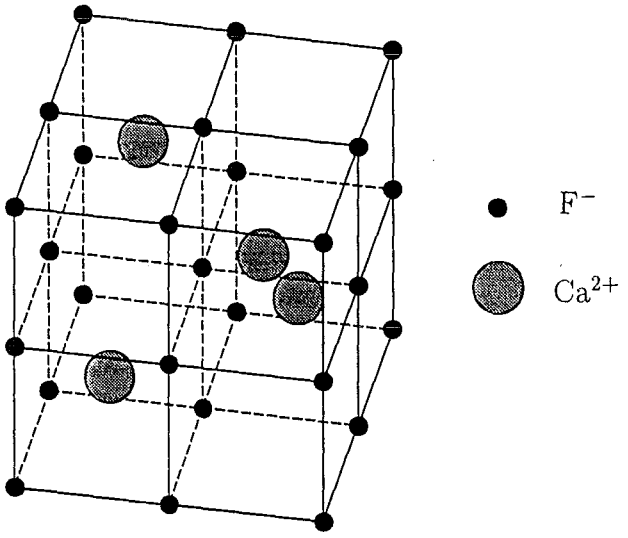

Figure 1.1 : The CaF_2 crystal structure. Atomic sizes are not represented to scale.

applications or research being robust, non-hygroscopic, transparent over a wide region of the spectrum, relatively easy to grow and accepting a wide range of impurity dopants. However, for trivalent dopant ions, lower-symmetry centres involving other interstitial or substitutional ions are often formed. These centres then have several equivalent directions in which they can be oriented in the cubic host lattice. Such orientational degeneracy can be a spectroscopic disadvantage, but also leads to such interesting phenomena as the reversible polarised bleaching of rare-earth centres involving multiple substitution of H^- for F^- ions [19].. CaF_2 cleaves along (111) planes (perpendicular to a cube body diagonal) and by cleaving two different (111) planes that intersect along a $\langle 110 \rangle$ axis, the crystal orientation can be determined readily.

Trivalent lanthanides, introduced in the melt, readily substitute for Ca^{2+} ions. Compensation for the charge discrepancy is required, and is generally achieved by an extra F^- ion entering in an interstitial position in an empty F^- cube. This charge compensation can either take place remotely, leaving the RE^{3+} ion in a nearly-cubic

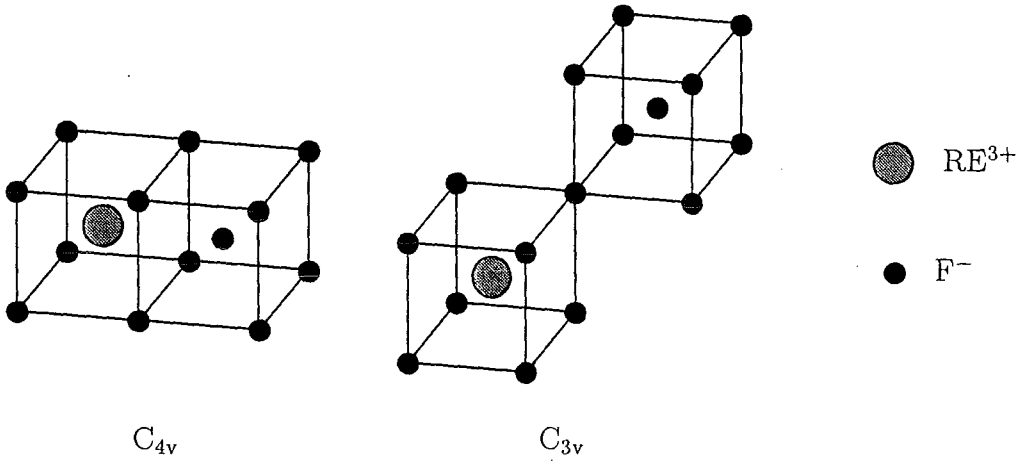

Figure 1.2 : The local environment of the rare earth ion in the F^- compensated C_{4v} and C_{3v} centres. Atomic sizes are not represented to scale.

centre, or locally, hence altering the immediate environment of the RE^{3+}. The requirement of charge compensation leads to a variety of possible RE^{3+} centres. The predominant charge-compensated centre for RE^{3+} molar concentrations of less than 0.1% , involves the interstitial F^- ion taking one of the immediately adjacent empty cubes along a $\langle 100 \rangle$ body axis giving a tetragonal, C_{4v}, symmetry. Another centre observed primarily for the heavier lanthanides involves the interstitial F^- in a next-nearest empty cube along a $\langle 111 \rangle$ body diagonal axis giving trigonal, C_{3v}, symmetry. These two RE^{3+}–F^- centres, depicted in fig 1.2, have respectively three-fold ($\langle 100 \rangle$-type axes) and four-fold ($\langle 111 \rangle$-type axes) orientational degeneracy. If oxygen is present in the crystal then an O^{2-} ion substituting for a lattice F^- immediately adjacent to the RE^{3+} can provide the charge compensation, giving another possible C_{3v} symmetry centre. More complex centres are also possible and may involve F^- vacancies or clusters of two or more RE^{3+} ions. At higher concentrations, such RE^{3+} clusters predominate.

SrF_2 crystals are isostructural with CaF_2 and have similar mechanical properties. The lattice constant is somewhat larger, resulting in an altered distribution of RE^{3+} centres from CaF_2. The lighter lanthanide ions form predominantly C_{4v} centres as in CaF_2, but the heavier lanthanide ions tend to form C_{3v} centres.

1.3 This Thesis

The work presented in this thesis falls into three main topics:

- Laser spectroscopy of lightly-doped (0.01%–0.1%) CaF_2:Tm^{3+} crystals. Two main single-ion centres were identified using laser selective excitation, and their symmetries established as being C_{4v} and C_{3v} using polarisation ratios. A crystal field analysis of the C_{4v} centre established that this centre has the same configuration as the C_{4v} centres previously observed for other CaF_2:RE^{3+} systems. Fluorescence lifetimes of the $^1D_2$, $^1G_4$ and $^3H_4$ multiplets of these Tm^{3+} centres were measured.

- Upconversion fluorescence of single RE^{3+} centres in CaF_2. Red-to-green upconversion fluorescence is observed in CaF_2:Ho^{3+} and CaF_2:Er^{3+} and red-to-blue/UV upconversion fluorescence is observed in CaF_2:Tm^{3+}. It is established that centres previously determined to be single ion centres exhibit upconversion fluorescence, in some cases upon pumping ground-state absorption transitions, and in some cases upon pumping excited-state absorption transitions. The upconversion mechanism appears to be a sequential excitation process.

- Zeeman-infrared absorption spectroscopy of the localised vibrational modes of H^- ions adjacent to RE^{3+} ions in CaF_2 and SrF_2. The doubly-degenerate x-y vibrational modes of H^- ions adjacent to RE^{3+} ions in CaF_2 are observed to split in some cases. Calculations of the electron–local-mode-phonon interaction splitting of these states compare reasonably well with the experimentally-determined values, providing a qualitative idea of which intermediate states are important to the splitting. The Zeeman splitting of these lines can be calculated without any further parametrisation and these calculations are very successful in matching the experimental data. This provides evidence that the electronic-vibrational coupled states resulting from the electron-phonon interaction can accurately account for the spectroscopic behaviour.

Chapter 2 gives an overview of the basic theory of rare-earth spectroscopy, crystal field theory and group theory which are used in the rest of this thesis.

Experimental details are described in chapter 3. The apparatus and procedures adopted for the growth, orientation and hydrogenation of CaF_2 crystal samples are outlined. The equipment and experimental arrangements used in performing optical, polarised laser-excited fluorescence and FTIR spectroscopy at cryogenic temperatures and with applied magnetic fields of up to 4 tesla are described.

Results and discussion of the site-selective laser spectroscopy of single Tm^{3+} ion centres in CaF_2:Tm^{3+} is presented in chapter 4. Energy levels up to $28000\,cm^{-1}$ of the two predominant centres are found by using upconversion fluorescence from the $^1D_2$ multiplet. A crystal field analysis of the C_{4v} symmetry centre is performed, demonstrating that this centre is structurally like that of other RE^{3+} C_{4v} centres in CaF_2. One line in the infrared-absorption spectrum of the $^3H_5$ multiplet is assigned to a cubic centre on the basis of the Zeeman splittings of that line, and the relative concentrations of the C_{4v} and cubic centres calculated from the relative linestrengths of two magnetic-dipole transitions.

Upconversion-fluorescence observed from single-ion centres in CaF_2:Tm^{3+}, CaF_2:Er^{3+}, CaF_2:Ho^{3+} and CaF_2:Nd^{3+} and the associated mechanisms are discussed in chapter 5. The mechanism for the single-ion centres is a sequential-excitation process, involving the laser being in resonance with one transition and simultaneously overlapping another broad phonon-assisted transition. A metastable state with a millisecond lifetime allows excited ions to absorb a second photon before decaying. A novel enhancement of upconversion fluorescence upon warming the sample to room temperature is described for red-to-blue upconversion in CaF_2:Tm^{3+}, and is explained in terms of a near energy mismatch of transitions becoming an overlap as the transitions broaden with increasing temperature.

The localised vibrational modes of the H^- ion in CaF_2 and SrF_2 are introduced in chapter 6. The coupling of these local modes to the electronic states of a neighbouring RE^{3+} ion is described making use of the group theory of section 2.3. The form of the electron–local-mode-phonon Hamiltonian is derived, and the radially-dependent parameters of the Hamiltonian estimated using the point-charge model, and equations derived in appendix A. These calculated values are compared with values obtained from the experimental splitting of the x-y local modes associated with each of the lanthanide ions for which a splitting is observed.

Chapter 7 extends the results of chapter 6 and tests the validity of the interpretation of the x-y splitting by applying a magnetic field. The effects of this field on the x-y splittings are compared with theoretical predictions. The Zeeman Hamiltonian is successful in producing, without any additional parameters, excellent theoretical comparisons to the experiment.

Finally, chapter 8 summarises the conclusions drawn from this thesis, and suggests further work which could build on the results presented here.

Chapter 2

Rare Earth Spectroscopy

The theory of rare earth spectra has been reviewed by several authors including Wybourne [91], Dieke [22] and Hüfner [38]. A summary of those parts of the theory used in the remainder of this thesis is included here.

The problem of determining the energy levels of rare earths in crystals is naturally divided into two parts, consideration of free ion effects and of the crystal field environment. The total Hamiltonian is the sum of these two parts:

$$\mathcal{H} = \mathcal{H}_f + \mathcal{H}_{cf}$$

As already stated in chapter 1, the free ion effects dominate the large-scale energy level splittings of lanthanide ions. However some degeneracy remains amongst the free-ion states. The splitting of the free-ion energy levels is due to crystal (or other perturbation) fields which can be regarded as perturbations on the free-ion interactions. Since the large-scale (free-ion) splittings are essentially independent of the perturbing field and have therefore been well characterised, it is in fact the smaller crystal-field splittings which are generally of interest.

2.1 The Free Ion

The Hamiltonian for an N-electron atom comprises the kinetic energy of the N electrons, the electrostatic interactions between these electrons and the nucleus and between individual electrons, and the spin-orbit interaction $\zeta \boldsymbol{l} \cdot \boldsymbol{s}$ for each elec-

tron [91]:

$$\mathcal{H} = -\frac{\hbar^2}{2m}\sum_i \nabla_i^2 - \sum_i \frac{Ze^2}{r_i} + \sum_{i<j}\frac{e^2}{r_{ij}} + \sum_i \zeta\, \boldsymbol{l}_i \cdot \boldsymbol{s}_i.$$

Schrödinger's equation for such a Hamiltonian for more than a single electron cannot be solved exactly and so the central field approximation is usually adopted. The distorting effect of the unfilled $4f$-shell itself is assumed small, so that as a first approximation for the first two terms in the above Hamiltonian, each electron can be considered to move independently in a central field provided by the xenon core and the other $4f$ electrons. The atomic eigenfunctions of this central-field part of the Hamiltonian are antisymmetrised product states of the one-electron eigenfunctions, which have an angular dependence identical to that of the hydrogenic wavefunctions, and the eigenvalues are the energies of the configurations which are labelled by the quantum numbers $(n_1 l_1)(n_2 l_2)\ldots(n_N l_N)$.

Normally one is only studying the states of one particular configuration (in this case $4f^N$) and the energy separation between configurations is sufficiently large that only the states of this particular configuration need be considered. The central-field part of the Hamiltonian, which separated the configurations, need not be considered further and the remaining part of the free-ion Hamiltonian $\mathcal{H}_f$ which is used in the calculations in this thesis then has the form:

$$\begin{aligned}\mathcal{H}_f \;=\; & \sum_{k=2,4,6} F^k f_k + \sum_i \zeta\, \boldsymbol{l}_i \cdot \boldsymbol{s}_i + \alpha L(L+1) + \beta G(G_2) + \gamma G(R_7) \\ & + \sum_{k=0,2,4} M^k m_k + \sum_{k=2,4,6} P^k p_k + \sum_i T^i t_i \end{aligned} \tag{2.1}$$

The $F^k f_k$ component is the remaining (non-central) electrostatic interaction (electron-nucleus and electron-electron) which splits the configuration into *terms* characterised by the total spin and orbital angular momenta, S and L, of the N electrons.

The second component in equation 2.1, $\sum_i \zeta\, \boldsymbol{l}_i \cdot \boldsymbol{s}_i$, is the spin-orbit interaction. This couples the spin and orbital angular momenta to give the total angular momentum J, which can take values from $|L-S|$ to $L+S$ in integer increments, and splits the term into *multiplets* of different J values. As an example, figure 2.1 shows the electrostatic-interaction split terms of the Tm^{3+} ion at the left hand end ($\zeta = 0$) splitting into multiplets as the spin-orbit interaction is increased.

Whereas the electrostatic interaction is diagonal in S and L, and independent of J,

the spin-orbit interaction is diagonal in J but not in S and L. This has the effect of mixing all the multiplets of a given J, each originating from a different term. The extent of this mixing varies with the elements. In the transition metals the spin-orbit interaction is much weaker than the electrostatic interactions and can be considered a perturbation. In such a case it is a reasonable approximation to assume the J-multiplets remain pure ("LS coupling") and are well characterised by their SLJ quantum numbers. However, in the case of the rare earths, some multiplets have a high degree of mixing and this approach is no longer valid. With modern computing methods it has become possible, and usual, to diagonalise the electrostatic and spin-orbit interactions together for the entire configuration ("intermediate coupling"). The usual multiplet notation follows the format $^{2S+1}L_J$ where the L component is written in spectroscopic notation (S,P,D,F,G,H... for 0,1,2,3,4,5...). Thus the ground multiplet of Tm^{3+}, with $S = 1$, $L = 5$ and $J = 6$ is denoted $^3H_6$.

While it is not strictly correct to attribute any one set of SL quantum numbers to a particular intermediate-coupled multiplet, this is often still done for the purposes of labelling. However, two schools of thought exist on choosing the SL label: the SL quantum numbers of either the largest component of the wavefunction, or of the "parent" state (the state as it was before spin-orbit mixing). For most RE^{3+} multiplets these will be the same, however some exceptions do occur. One such instance is in the f^{12} configuration of trivalent thulium, Tm^{3+}, and is worth clarifying as this ion is one of the subjects of this thesis. In this configuration there is heavy mixing between the three $J = 4$ multiplets, resulting in the $^3H_4$ and $^3F_4$ swapping their leading terms. The notation of the largest wavefunction component is adopted in this thesis; however it should be noted that some authors, by adopting the alternative notation, will have the labels of these two multiplets reversed.

Figure 2.1 illustrates the effect of the spin-orbit interaction on the f^{12} configuration. The strong repulsion ("anticrossing") between the $^3H_4$ and $^3F_4$ multiplets is characteristic of states that are being mixed. $^3F_4$ actually originates from the ^3H term, but once the spin-orbit interaction is included to its full physical value (indicated by the dotted line), the eigenfunction decomposition is that listed in table 2.1, with $^3F_4$ having become the largest component.

The remaining interactions in the free-ion Hamiltonian have a much smaller effect

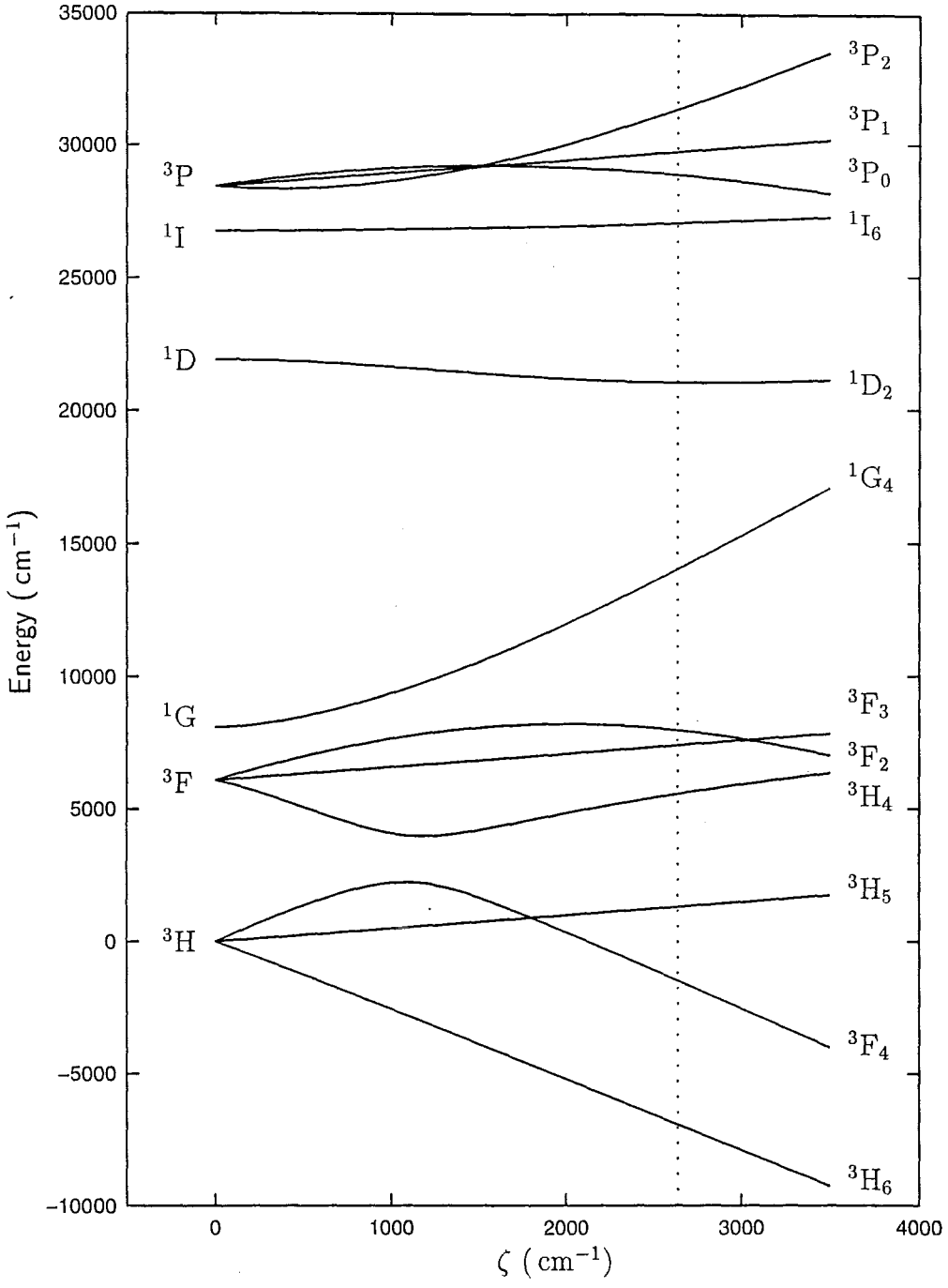

Figure 2.1 : The splitting of Tm^{3+} ^{2S+1}L terms into $^{2S+1}L_J$ multiplets with increasing spin-orbit interaction. The electrostatic interaction parameters used were those obtained by least-squares fit to the experimental C_{4v}-centre crystal-field levels (chapter 4). The value of the spin-orbit parameter obtained in the same fit is indicated by the dotted line.

Parent LS state	SLJ label	Intermediate-coupled wavefunction
^{3}H	$^3F_4$	$0.7954\,\|^3F_4\rangle + 0.5374\,\|^1G_4\rangle - 0.2804\,\|^3H_4\rangle$
^{3}F	$^3H_4$	$0.7739\,\|^3H_4\rangle + 0.5185\,\|^3F_4\rangle - 0.3636\,\|^1G_4\rangle$
^{1}G	$^1G_4$	$0.7609\,\|^1G_4\rangle + 0.5678\,\|^3H_4\rangle - 0.3140\,\|^3F_4\rangle$

Table 2.1 : Spin-orbit mixing between the J=4 multiplets in Tm^{3+}, for the free-ion parameters obtained by least-squares fit to the experimental C_{4v}-centre crystal-field levels (chapter 4).

than the electrostatic and spin-orbit terms. The $\alpha L(L+1)+\beta G(G_2)+\gamma G(R_7)$ terms represent an inter-configuration interaction, that is a correction for the fact that we have ignored all but the $4f^N$ configuration. The $M^k m_k$ terms contain spin-spin and spin-other-orbit interactions. The $P^k p_k$ terms are two-body electrostatically correlated magnetic interactions and the $T^i t_i$ terms are three-body electrostatic corrections, required for the f^3 through f^{11} configurations [91].

Each of the operators has been separated into radial and angular parts. The form of the angular parts can be determined using symmetry and other arguments, but the radial parts generally cannot be determined accurately. Thus the usual approach to fitting rare earth energy levels is to treat the radial parts as parameters, and vary them to obtain a best fit to the experimental data. This is illustrated in figure 2.1 where the radial part, ζ, of the spin orbit interaction is varied.

The free ion and crystal field calculations presented in this thesis followed this formalism, and used the *F-Shell Empirical* routines written by Dr Mike Reid of this department to perform least squares fits to experimental data. Where only a small number of experimental levels was available for a particular rare-earth-ion centre, the free ion parameters obtained for that rare-earth ion in LaF_3 by Carnall *et al* [14] were either used as starting parameters or set as fixed values.

2.2 The Crystal Field

Since the free-ion effects are almost wholly independent of the environment, the major interest in determining rare earth energy levels is in the small perturba-

tions introduced by this environment, in this case the crystal field. The free ion J-multiplets have a degeneracy of $2J+1$, with constituent states labelled by the projection, M (running from $-J$ to J in integer increments), of the total angular momentum. Any external, non-spherical field will lift some, or all, of this degeneracy. The degree to which the degeneracy is lifted depends on the symmetry of the external field, hence the relevance of group theory (section 2.3) to crystal-field theory.

The terms in the crystal-field Hamiltonian can again be separated into radial and angular parts, with the radial part treated as a parameter. Since the free ion has spherical symmetry, the angular parts of the Hamiltonian are conveniently expressed in terms of spherical harmonics Y_{kq}, or the Racah spherical tensors $\mathrm{C}_q^{(k)}$ related to these by

$$\mathrm{C}_q^{(k)} = \sqrt{\frac{4\pi}{2k+1}}\,\mathrm{Y}_{kq}.$$

The crystal-field Hamiltonian thus takes the parametrised form

$$\mathcal{H}_{cf} = \sum_{k,q} \mathrm{B}_q^k\,\mathrm{C}_q^{(k)}.$$

In calculating matrix elements between $4f^N$ states, k is restricted by parity considerations to be even and by the angular momentum triangle condition to be no greater than 6. Further, the $k=0$ term (which is by far the largest term and is responsible for the greater part of the lattice energy of the ion) produces only a uniform energy shift to levels of the entire configuration, so for our purposes can be ignored. The sum over q runs from $-k$ to k, however if the symmetry of the crystal field is high then some restrictions and relationships between the B_q^k parameters will be imposed.

The principal symmetries met in this thesis are $\mathrm{C_{4v}}$ and $\mathrm{C_{3v}}$. For $\mathrm{C_{4v}}$ symmetry, q is restricted to 0, ±4 and for $\mathrm{C_{3v}}$ symmetry, q is restricted to 0, ±3, ±6. Because, in both cases, the symmetry is derived from cubic, it is appropriate to group the terms in linear combinations having well-defined transformation properties in cubic symmetry. The respective crystal-field Hamiltonians are then:

$$\begin{aligned}\mathcal{H}_{\mathrm{C_{4v}}} &= \mathrm{B}_C^4\left[\mathrm{C}_0^{(4)} + \sqrt{\tfrac{5}{14}}(\mathrm{C}_4^{(4)} + \mathrm{C}_{-4}^{(4)})\right] \\ &\quad + \mathrm{B}_C^6\left[\mathrm{C}_0^{(6)} - \sqrt{\tfrac{7}{2}}(\mathrm{C}_4^{(6)} + \mathrm{C}_{-4}^{(6)})\right]\end{aligned}$$

$$
\begin{aligned}
&+ \mathrm{B}_A^2\,\mathrm{C}_0^{(2)} \\
&+ \mathrm{B}_A^4\left[\mathrm{C}_0^{(4)} - \sqrt{\tfrac{7}{10}}(\mathrm{C}_4^{(4)} + \mathrm{C}_{-4}^{(4)})\right] \\
&+ \mathrm{B}_A^6\left[\mathrm{C}_0^{(6)} + \sqrt{\tfrac{1}{14}}(\mathrm{C}_4^{(6)} + \mathrm{C}_{-4}^{(6)})\right]
\end{aligned} \tag{2.2}
$$

$$
\begin{aligned}
\mathcal{H}_{\mathrm{C_{3v}}} \;=\; & \mathrm{B}_C^4\left[\mathrm{C}_0^{(4)} + \sqrt{\tfrac{10}{7}}(\mathrm{C}_3^{(4)} - \mathrm{C}_{-3}^{(4)})\right] \\
&+ \mathrm{B}_C^6\left[\mathrm{C}_0^{(6)} - \sqrt{\tfrac{35}{96}}(\mathrm{C}_3^{(6)} - \mathrm{C}_{-3}^{(6)}) + \sqrt{\tfrac{77}{192}}(\mathrm{C}_6^{(6)} + \mathrm{C}_{-6}^{(6)})\right] \\
&+ \mathrm{B}_A^2\,\mathrm{C}_0^{(2)} \\
&+ \mathrm{B}_A^4\left[\mathrm{C}_0^{(4)} - \sqrt{\tfrac{7}{40}}(\mathrm{C}_3^{(4)} - \mathrm{C}_{-3}^{(4)})\right] \\
&+ \mathrm{B}_A^6\left[\sqrt{\tfrac{11}{42}}(\mathrm{C}_3^{(6)} - \mathrm{C}_{-3}^{(6)}) + \sqrt{\tfrac{5}{21}}(\mathrm{C}_6^{(6)} + \mathrm{C}_{-6}^{(6)})\right] \\
&+ \hat{\mathrm{B}}_A^6\left[\mathrm{C}_0^{(6)} + \sqrt{\tfrac{160}{1029}}(\mathrm{C}_3^{(6)} - \mathrm{C}_{-3}^{(6)}) - \sqrt{\tfrac{176}{1029}}(\mathrm{C}_6^{(6)} + \mathrm{C}_{-6}^{(6)})\right]
\end{aligned} \tag{2.3}
$$

where, in each case, the B_C^k terms alone form a cubic-symmetry Hamiltonian and the B_A^k terms represent the non-cubic distortions appropriate to the true $\mathrm{C_{4v}}$ or $\mathrm{C_{3v}}$ symmetry. The angular expressions of the cubic operators are in fact the same for both $\mathrm{C_{4v}}$ and $\mathrm{C_{3v}}$, but appear to be different because of the different axes of quantisation chosen ($\langle 100\rangle$ for $\mathrm{C_{4v}}$ and $\langle 111\rangle$ for $\mathrm{C_{3v}}$). An appropriate coordinate rotation transforms the two expressions into one another.

The Racah tensor operators $\mathrm{C}_q^{(k)}$ operate on the $\left|4f^N\alpha LSJM\right\rangle$ basis states with matrix elements given by:

$$
\begin{aligned}
&\left\langle 4f^N\alpha SLJM\middle|\mathrm{C}_q^{(k)}\middle|4f^N\alpha' SL'J'M'\right\rangle \\
&\quad= \langle f||\mathrm{C}^{(k)}||f\rangle\left\langle 4f^N\alpha SLJM\middle|\mathrm{U}_q^{(k)}\middle|4f^N\alpha' SL'J'M'\right\rangle \\
&\quad= -7\begin{pmatrix} 3 & k & 3 \\ 0 & 0 & 0\end{pmatrix}(-1)^{2J-M+S+L'+k}\sqrt{(2J+1)(2J'+1)} \\
&\qquad\times\begin{Bmatrix} J & J' & k \\ L' & L & S\end{Bmatrix}\begin{pmatrix} J & k & J' \\ -M & q & M'\end{pmatrix}\left\langle f^N\alpha SL\middle\|\mathrm{U}^{(k)}\middle\|f^N\alpha' SL'\right\rangle
\end{aligned} \tag{2.4}
$$

Here the three-j $\begin{pmatrix} j_1 & j_2 & j_3 \\ m_1 & m_2 & m_3\end{pmatrix}$ and six-j $\begin{Bmatrix} l_1 & l_2 & l_3 \\ j_1 & j_2 & j_3\end{Bmatrix}$ symbols can be computed from formulas derived, for example, by Edmonds [26] or by using the tables of Rotenberg *et al* [79], while the doubly-reduced matrix elements $\left\langle f^N\alpha SL\middle\|\mathrm{U}^{(k)}\middle\|f^N\alpha' SL'\right\rangle$

have been tabulated by Nielson and Koster [72]. The symbols α and α' represent other quantum numbers which may be required to distinguish states from repeated SL terms [91].

In performing crystal field calculations it is sometimes necessary to choose a restricted basis of states (the entire f^6 configuration, for example, contains 3003 states!). In doing so, care must be taken to include all nearby states that may perturb those states of interest. For the $4f^{12}$ configuration of Tm^{3+}, the complete basis of 91 states is sufficiently small that no truncation of the basis is necessary.

2.3 The Application of Group Theory

Group theory plays a vital role in spectroscopy, especially in systems exhibiting a high degree of symmetry, by allowing one to (at least partially) determine the form of the Hamiltonian, the decomposition of J-multiplets into energy levels, the form of the wavefunctions and hence properties under certain perturbations.

The expectation values $\mathcal{E}$ and normalised eigenstates ψ of a physical observable such as the Hamiltonian are defined by the equation

$$\langle\psi|\mathcal{H}|\psi\rangle = \mathcal{E}\langle\psi|\mathbf{1}|\psi\rangle = \mathcal{E}$$

where $\mathbf{1}$ is the identity operator. Since such an equation (with appropriate expectation values) holds for any normalised eigenstate ψ of the system, it is clear that the Hamiltonian must transform like the identity operator; i.e. as the totally symmetric irrep of the point group of the centre. This important result allows us to determine the form of the crystal-field Hamiltonian, as in section 2.2, without even knowing the nature of the interactions involved.

The states of the system must have well defined transformation properties under the operations of the group. Let R, S and T be transformations belonging to the point group G such that $T = RS$ and let $\mathcal{E}$ be a degenerate energy eigenvalue of the Hamiltonian with eigenstates ψ_k. The operation of T upon one of these eigenstates ψ_i cannot affect the result of the measurement of an observable, since the environment looks identical under a transformation which is a member of the group. The new state $T\psi_i$ therefore has the same eigenvalue as ψ_i and hence must

be a linear combination of the ψ_k's. Let the coefficients of this linear combination form the matrix $D^{(T)}$:

$$T\psi_i = \sum_k \psi_k D^{(T)}_{ki}$$

(note $D^{(T)}_{ki}$ with indices is simply a number so commutes with any state or operator). The R and S transformations similarly produce matrices $D^{(R)}$ and $D^{(S)}$. The combination RS has the effect:

$$\begin{aligned} RS\psi_i &= R\sum_j \psi_j D^{(S)}_{ji} \\ &= \sum_{j,k} \psi_k D^{(R)}_{kj} D^{(S)}_{ji} \end{aligned}$$

which must be equivalent to the single operation, T. We can therefore form the matrix equation

$$D^{(R)}_{kj} D^{(S)}_{ji} = D^{(T)}_{ki}$$

and hence have produced a set of matrices which is homomorphic to the group, i.e. a representation. Barring "accidental" degeneracies, the set of states ψ_k are interdependent, and the representation is irreducible. We can therefore associate with any energy level of the system, an irreducible representation (irrep) of the point group, the dimension of the irrep matching the degeneracy of the level. Since the operation of the Hamiltonian cannot change the irrep of a wavefunction, the irreps can be considered as good quantum numbers for the crystal field calculation. The Hamiltonian matrix can therefore be block-diagonalised immediately, breaking down the problem of full diagonalisation into the diagonalisation of a series of smaller matrices. Each point-group irrep with dimension d has d (identical) sub-matrices, formed from the states transforming as a particular partner of that irrep.

The free-ion multiplets can themselves be associated with irreps of the full rotation group, O_3 (being the symmetry group of the free ion). For each integer or half-integer J, O_3 has two irreps of dimension $2J+1$, denoted $\mathcal{D}^+_J$ and $\mathcal{D}^-_J$ of even and odd parity respectively. Since f electrons have odd parity the f^N configuration as a whole will have even parity for even N (non-Kramers ions) and odd parity for odd N (Kramers ions). Each multiplet of a given J is associated with the $\mathcal{D}_J$ irrep (of the appropriate parity for the number of electrons), hence the mixing of LS states but retention of J as a quantum number. By considering the group chain O_3–G, the decomposition

of J-multiplets into irreps of G can be deduced. Such decompositions to each of the 32 point groups have been tabulated in the group tables of Koster *et al* [51] and are reproduced in table 2.2 for the C_{4v} and C_{3v} groups. For example, for C_{4v} symmetry a $J = 4$ multiplet of a non-Kramers ion decomposes into seven levels with irreps $2\gamma_1 + \gamma_2 + \gamma_3 + \gamma_4 + 2\gamma_5$, using Koster's subscript notation. Of these levels, only the γ_5 levels are doubly degenerate and the remainder non-degenerate.

O_3 (J)	C_{4v}	C_{3v}
0	γ_1	γ_1
1	$\gamma_2 + \gamma_5$	$\gamma_2 + \gamma_3$
2	$\gamma_1 + \gamma_3 + \gamma_4 + \gamma_5$	$\gamma_1 + 2\gamma_3$
3	$\gamma_2 + \gamma_3 + \gamma_4 + 2\gamma_5$	$\gamma_1 + 2\gamma_2 + 2\gamma_3$
4	$2\gamma_1 + \gamma_2 + \gamma_3 + \gamma_4 + 2\gamma_5$	$2\gamma_1 + \gamma_2 + 3\gamma_3$
5	$\gamma_1 + 2\gamma_2 + \gamma_3 + \gamma_4 + 3\gamma_5$	$\gamma_1 + 2\gamma_2 + 4\gamma_3$
6	$2\gamma_1 + \gamma_2 + 2\gamma_3 + 2\gamma_4 + 3\gamma_5$	$3\gamma_1 + 2\gamma_2 + 4\gamma_3$
$\frac{1}{2}$	γ_6	γ_4
$\frac{3}{2}$	$\gamma_6 + \gamma_7$	$\gamma_4 + (\gamma_5 + \gamma_6)$
$\frac{5}{2}$	$\gamma_6 + 2\gamma_7$	$2\gamma_4 + (\gamma_5 + \gamma_6)$
$\frac{7}{2}$	$2\gamma_6 + 2\gamma_7$	$3\gamma_4 + (\gamma_5 + \gamma_6)$
$\frac{9}{2}$	$3\gamma_6 + 2\gamma_7$	$3\gamma_4 + 2(\gamma_5 + \gamma_6)$
$\frac{11}{2}$	$3\gamma_6 + 3\gamma_7$	$4\gamma_4 + 2(\gamma_5 + \gamma_6)$
$\frac{13}{2}$	$3\gamma_6 + 4\gamma_7$	$5\gamma_4 + 2(\gamma_5 + \gamma_6)$
$\frac{15}{2}$	$4\gamma_6 + 4\gamma_7$	$5\gamma_4 + 3(\gamma_5 + \gamma_6)$

Table 2.2 : Decomposition of O_3 irreps (J-multiplets) into C_{4v} and C_{3v} irreps.

Since the symmetry of the RE^{3+} site in the crystal field is no longer spherical, J is no longer strictly a good quantum number. However since the crystal-field interaction is very much weaker than the free-ion interactions, interaction between levels of separate multiplets is negligibly small and to a good approximation J-mixing can be neglected. In this approximation, in the example for $J = 4$ above, those levels which have unique C_{4v} irreps (i.e. the γ_2, γ_3 and γ_4 levels) will remain pure and therefore their wavefunctions can be determined without further knowledge of the crystal

field parameters. The two γ_1 irrep states will have crystal field matrix elements between them and therefore the two γ_1 eigenfunctions of the Hamiltonian will be crystal-field-dependent orthogonal linear combinations of the two zero-order states. Similarly for the two γ_5 levels. The choice of appropriate combinations of JM-basis states to form irreps of the symmetry group therefore gives much information on the states of the system. Butler [13] has listed tables of such combinations for the pure rotation groups only, however the combinations for C_{4v} and C_{3v} are identical to those for their isomorphic pure-rotation groups D_4 and D_3.

In addition to the crystal-field symmetry, the system has another symmetry: time-reversal symmetry. This is particularly significant for ions with an odd number of electrons, since it is a consequence of Kramers' theorem that a time-even Hamiltonian must leave all energy eigenvalues of an odd-electron system at least two-fold degenerate [1]. All terms in the Hamiltonian thus far considered are time-even (are invariant under time-reversal), so the crystal field states of Kramers ions are all at least doubly degenerate. This degeneracy can only be broken by a time-odd interaction, such as the Zeeman (magnetic-field) interaction.

The decomposition of C_{4v} irreps into the irreps of its C_4 subgroup is also used in this thesis. Clearly the group theoretical considerations apply equally well to any subgroup of the RE^{3+} site symmetry, so this is a valid procedure. Its advantage is that under a C_4 perturbation (which in practice would be achieved by application of a magnetic field along the 4-fold symmetry axis), all remaining C_{4v} degeneracies (including Kramers' degeneracy) are lifted. The use of C_4 irreps then serves as a way of labelling the partner states of doubly degenerate levels in such a way that the C_{4v} irreps of direct product states (such as those encountered in electron-phonon coupling, section 6.2) can easily be determined. The decomposition of C_{4v} to C_4 irreps is given in table 2.3. The notation μ_k for C_4 irreps is adopted in this thesis to distinguish these from C_{4v} irreps.

The use of irrep bases can be used in many cases to determine when matrix elements of other operators will be identically zero. The matrix element $\langle\psi_f|O_{op}|\psi_i\rangle$ of an operator transforming as γ_{op} between states transforming as irreps γ_f and γ_i is non zero only if the condition

$$\gamma_f{}^* \times \gamma_{op} \times \gamma_i \supset \gamma_1$$

C_{4v} irrep	C_4 irrep	Basis
γ_1	μ_1	z
γ_2	μ_1	S_z
γ_3	μ_2	$x^2 - y^2$
γ_4	μ_2	xy
γ_5	μ_3	$x + iy$
	μ_4	$x - iy$
γ_6	μ_5	$\left\|+\frac{1}{2}\right\rangle$
	μ_6	$\left\|-\frac{1}{2}\right\rangle$
γ_7	μ_7	$\left\|-\frac{3}{2}\right\rangle$
	μ_8	$\left\|+\frac{3}{2}\right\rangle$

Table 2.3 : Decomposition of C_{4v} irreps into C_4 irreps.

holds. That is the decomposition of the direct product of the irreps ($\gamma_f{}^*$ being the conjugate irrep of γ_f) contains the totally symmetric irrep. By premultiplying both sides by γ_f, this can be re-expressed as

$$\gamma_{op} \times \gamma_i \supset \gamma_f. \tag{2.5}$$

This is vital in determining selection rules and polarisation dependences (section 2.5) and in determining the mixing of levels under a perturbing Hamiltonian such as a magnetic field (section 2.4) or the electron-phonon interaction (section 6.2).

2.4 The Zeeman Effect

The effect of laboratory-sized magnetic fields can generally be treated as a perturbation on the crystal field states. The Zeeman Hamiltonian is

$$\mathcal{H}_z = \mu_B \mathbf{B} \cdot (\mathbf{L} + 2\mathbf{S})$$

where μ_B is the Bohr magneton, $\frac{e\hbar}{2m_e}$. The Zeeman interaction is of importance to spectroscopy because it provides a mechanism to split or shift many spectral line components beyond their overall line profile. As a time-odd interaction, it will

lift the residual Kramers' degeneracy of odd-electron systems. It is dependent upon the magnitude and direction of an experimentally-controllable continuously-variable external field, while introducing no new parameters to the Hamiltonian. This last point is relevant; once the crystal field states have been determined, it is possible to calculate their magnetic field-induced shifts and splittings.

Since the angular part of the Zeeman Hamiltonian, $\mathbf{L} + 2\mathbf{S}$ transforms the same way as the total angular momentum operator J, it follows from the Wigner-Eckart theorem [91] that all the matrix elements of the two operators are proportional within a multiplet (this being the basis of Stevens' "Operator Equivalents" formalism for simplifying the calculation of crystal-field matrix elements [83]).

$$\mathcal{H}_z = \mu_B g_L \mathbf{B} \cdot \mathbf{J}.$$

The proportionality constant is the Landé g-factor given by

$$g_L = 1 + \frac{S(S+1) + J(J+1) - L(L+1)}{2J(J+1)}.$$

This form makes the calculation in the JM basis very simple, but is appropriate only when crystal-field and magnetic-field mixing between multiplets can be neglected.

The Zeeman Hamiltonian has well defined transformation properties in the higher-symmetry crystal-field point groups, which enables the determination of which matrix elements are identically zero. In C_{4v} symmetry, the J_z component transforms as the γ_2 irrep and for a non-Kramers ion can therefore connect γ_1 and γ_2 or γ_3 and γ_4 states and split the doubly-degenerate γ_5 states. The J_x and J_y components transform as partners of the γ_5 irrep and will connect γ_5 states to all the other singlet states. For Kramers ions, either J_z or (J_x,J_y) will split both γ_6 and γ_7 states.

The symmetry of a magnetic field alone is $C_{\infty h}$, that is all rotations about the symmetry axis and a reflection plane perpendicular to that axis. When applied in addition to the crystal field, the new symmetry must be a subgroup of both the crystal and magnetic field groups and will depend on the relative orientations of the symmetry axes of each.

2.5 Transition Selection Rules and Polarisation Effects

While we now have a formalism for obtaining the energy levels of the ion, it is the transitions between these levels that are observed. The leading terms in the radiation-matter interaction Hamiltonian are the electric dipole and magnetic dipole terms:

$$\mathcal{H} = e\mathbf{E} \cdot \mathbf{D} + \mu_B \mathbf{B} \cdot \mathbf{M}$$

where $\mathbf{E}$ and $\mathbf{B}$ are the electric- and magnetic-field vectors of the radiation, $-e\mathbf{D} = -e\sum_i \boldsymbol{r}_i$ is the electric-dipole transition moment and $\mu_B \mathbf{M} = \mu_B \sum_i (\mathbf{L}_i + 2\mathbf{S}_i)$ the magnetic-dipole transition moment of the electronic states.

In spherical (free ion) symmetry, these transition-moment operators transform as the $\mathcal{D}_1^-$ and $\mathcal{D}_1^+$ irreps of O_3 respectively. Their irreps in C_{4v} and C_{3v} symmetry are given in table 2.4. The transition selection rules arise by considering equation 2.5

Polarisation	Dipole component	C_{4v} irrep	C_{3v} irrep
π	D_z	γ_1	γ_1
σ	D_x, D_y	γ_5	γ_3
π_{md}	M_z	γ_2	γ_2
σ_{md}	M_x, M_y	γ_5	γ_3

Table 2.4 : Irreps of electric-dipole and magnetic-dipole operators

for the appropriate dipole operator; it is clear from table 2.4 that these rules are polarisation-dependent. π polarisation refers to the $\mathbf{E}$ vector of the light being parallel to the symmetry axis of the centre, and σ perpendicular to this direction. π_{md} and σ_{md} are the analogous magnetic-dipole polarisations, referred to the $\mathbf{B}$ vector of the light. The selection rules for C_{4v} and C_{3v} symmetry centres, obtained by using equation 2.5 and the irrep multiplication tables of Koster [51], are given in tables 2.5 and 2.6. All transitions labelled σ in these tables are simultaneously σ_{md} allowed.

While the electric dipole operator is the leading term in the interaction Hamiltonian, it is an odd parity operator and therefore cannot have matrix elements between states of the same parity—i.e. between two pure $4f^N$ states. Electric dipole transitions can only gain intensity if the $4f^N$ states have some admixture of states θ from

	γ_1	γ_2	γ_3	γ_4	γ_5
γ_1	π	π_{md}			σ
γ_2	π_{md}	π			σ
γ_3			π	π_{md}	σ
γ_4			π_{md}	π	σ
γ_5	σ	σ	σ	σ	π, π_{md}

	γ_6	γ_7
γ_6	π, π_{md}, σ	σ
γ_7	σ	π, π_{md}, σ

Table 2.5 : Polarisation selection rules for C_{4v} symmetry

	γ_1	γ_2	γ_3
γ_1	π	π_{md}	σ
γ_2	π_{md}	π	σ
γ_3	σ	σ	π, π_{md}, σ

	γ_4	$\gamma_{5,6}$
γ_4	π, π_{md}, σ	σ
$\gamma_{5,6}$	σ	π, π_{md}, σ

Table 2.6 : Polarisation selection rules for C_{3v} symmetry

higher configurations of the opposite parity (eg $4f^{N-1}5d^1$). If the symmetry of the crystal field is non-centrosymmetric then odd crystal field terms, V_{odd}, can provide this admixture:

$$|\psi'\rangle = |\psi\rangle + \sum_{\theta} \frac{|\theta\rangle\langle\theta|V_{odd}|\psi\rangle}{\mathcal{E}_\psi - \mathcal{E}_\theta}$$

Since little is generally known about the higher configurations, the summation cannot be evaluated explicitly. However, Judd [48] and Ofelt [73] have obtained an approximation by replacing the energy denominators in the summation with an average energy, hence enabling the use of closure to sum over the perturbing states of each higher configuration.

In a centrosymmetric crystal field, the odd crystal field terms vanish. Admixtures can still be induced by crystal vibrational modes, but generally in such cases magnetic-dipole transitions dominate. It is for this reason that the cubic-symmetry centres in CaF_2 are in most cases not observed in optical spectra (notable exceptions being Eu^{3+} and Sm^{3+} which have strong magnetic-dipole transitions [88]).

Although the magnetic-dipole term in the radiation-matter Hamiltonian would be

very much smaller than the electric-dipole term, it has even parity so that transitions between $4f^N$ states are allowed in first order. However, the selection rules of $\Delta J = 0, \pm 1$ (but not $0 \leftrightarrow 0$) and $\Delta L = \Delta S = 0$ (which may be relaxed by spin-orbit coupling) limits cases where magnetic-dipole transitions might be important. In EPR spectroscopy, magnetic-dipole transitions are observed, demonstrating that the cubic RE^{3+} centres do exist even though they are optically inactive.

Chapter 3

Experimental

3.1 Crystal Growth

All of the CaF_2:RE^{3+} and SrF_2:RE^{3+} crystals used in this study were grown using the Bridgeman-Stockbarger method of lowering the molten material through a temperature gradient. Starting materials were pure CaF_2 or SrF_2 crystal offcuts supplied by Optovac, Inc and 99.9% $(RE)F_3$ powder supplied by either Alfa Inorganics Inc or Johnson Matthey. The crystal offcuts were crushed to a coarse powder, mixed with the $(RE)F_3$ powder and placed in a carbon crucible with a tight-fitting lid. The crucible was placed in the growth chamber of a Arthur D Little model MP crystal growth furnace which was then evacuated to a pressure of 10^{-5} torr. The crucible was centred in an rf-induction coil powered by a 38kW Radyne rf generator which was brought up to the required power over the course of 2–4 hours. The crucible was left in the hot zone of the furnace for one hour to ensure it was uniformly heated, then lowered at a rate of approximately 8–10 mm/h over a 50 mm range. Upon completion of lowering, the rf power was automatically wound down over about 4 hours. At these growth/annealing rates, a crystal could be grown in 24 hours. While slower growing rates might ultimately produce better crystals, the crystals produced using these parameters cleaved well enough for reliable orientation and were suitable for the Zeeman and polarised laser-excitation studies performed here. A vacuum of 10^{-5} torr was needed to avoid oxygen impurities in the crystals. To further prevent incorporation of oxygen for some samples a small amount (around 0.02% by mass) of PbF_2 was added to the starting material. PbO evaporates from the melt before the PbF_2, thus acting as an oxygen scavenger [37]. The addition of this PbF_2 had

no observable effect on the physical or spectroscopic properties of the crystals, other than reducing the amount of oxygen (O^{2-}) impurity.

The samples produced were cylindrical boules of 10 mm diameter and typically 30 mm length. These could be cut into slices using a diamond saw if oriented samples were not required. ⟨111⟩ oriented samples could be obtained by cleaving the crystal boules along the (111) planes by using a sharp scalpel and a small hammer. If another specific orientation (usually ⟨100⟩) was required, the orientation of the crystal axes was determined by cleaving two inequivalent (111) planes. If chosen appropriately, these planes would intersect at an angle of $\cos^{-1}\left(\frac{1}{3}\right) = 109.5°$, and their intersection would be along a ⟨110⟩ axis (figure 3.1). Samples which had been

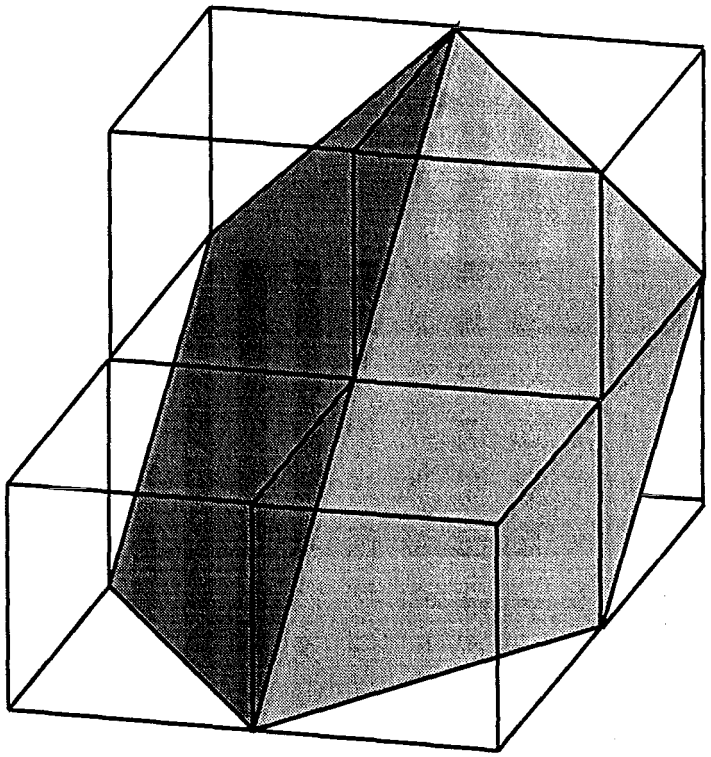

Figure 3.1 : Determination of the orientation of a CaF_2-type crystal by cleaving two inequivalent (111) planes. The intersection of the two planes is along a ⟨110⟩ axis.

cleaved in this way were glued, using araldite or superglue, onto a brass chuck which had had a wedge of the correct angle cut into one end. By clamping the chuck such that the intersection axis was horizontal and at an angle of 45° to the saw blade,

(100) planes could be cut using a diamond saw. ⟨100⟩ oriented samples for polarised laser-excitation studies were cut with a ⟨100⟩ laser-entry face perpendicular to the large (100) flats so that the complete orientation was known, rather than just one axis. The faces of the sample slices were polished using successively finer grades of emery paper, with a final finish produced by tin-oxide powder mixed to a smooth paste in water. A smooth, but not too hard, polishing surface is required for this last stage; the back surface of a piece of photographic paper was found to be ideal.

3.2 Hydrogenation of CaF_2 and SrF_2 Samples

Negative hydride (H^-) ions can be diffused into CaF_2 or SrF_2 crystals using the method of Hall and Schumacher [31]. The crystal samples, prepared as above, were sandwiched between two small coils of aluminium wire and placed in an alumina crucible in a quartz tube. The quartz tube was evacuated to a vacuum of better than 10^{-3} torr using a mercury diffusion pump and heated to 250°C for one or more hours to remove traces of moisture, which could otherwise produce unwanted oxygen-compensated centres. The system was then flushed twice with dry hydrogen gas, before being filled with hydrogen gas to an absolute pressure of approximately $\frac{2}{3}$ of an atmosphere. The temperature was then raised to 850°C, by which point the aluminium had melted and the pressure of hydrogen gas had increased to approximately 0.85 atmospheres, and maintained at that level for periods of between 1–40 hours. At the end of this period, the sample was then cooled back to room temperature either rapidly, over a few minutes, by simply withdrawing the furnace from the quartz tube, or over several hours by turning off the furnace and allowing to cool with all insulation in place. Rapid quenching has been shown to produce a higher yield of simpler centres, such as the hydrogenic C_{4v} centre, while slower annealing promotes more complex clusters, such as the bleachable centres [17]. Any aluminium which had attached to the crystal could be etched off by immersion of the sample in a solution of hydrochloric acid.

Hydrogenation periods of 1–8 hours were generally sufficient to produce strong infrared absorption from the x-y vibrational modes of H^- ions in the RE^{3+}-H^- C_{4v} centres. Exceptions were for samples doped with Eu^{3+} and Yb^{3+}, both of which were

easily reduced to the divalent state by the aluminium metal. Longer hydrogenation periods of up to 40 hours were required to obtain sufficiently strong absorption lines of the Yb^{3+}-H^- C_{4v} centre for Zeeman studies, while longer hydrogenation periods were not pursued for the Eu^{3+} system, since no x-y splittings or Zeeman effects are expected.

Ions of the heavier hydrogen isotope, deuterium (D^-), were introduced into samples in a similar way. These were preferred for laser-excitation studies as the D^--compensated centres produce stronger fluorescence than the corresponding H^- centres. Treatment periods for these samples varied from 8–72 hours, depending on the desired complexity of the distribution of centres.

3.3 Cryogenics and Superconducting Magnets

Most of the experiments described in this thesis need to be performed at cryogenic temperatures. For the bulk of the optical and laser experiments, and for FTIR infrared-transmission spectroscopy, two CTI Cryogenics Cryodyne 22C closed cycle helium refrigerator units were used. The water-cooled unit used for optical spectroscopy attained temperatures of 10–16K at the base of the cold finger, while the newer, air-cooled unit used for FTIR spectroscopy attained temperatures down to 8K. Both reached these temperatures in a time of about one hour. For both units, copper sample holders were bolted directly on to the base of the cold finger, with a layer of indium foil sandwiched between to improve thermal contact. The crystal samples were clamped to the copper holder, again using indium foil to improve thermal contact.

The temperature of the block could be increased up to room temperature by passing current through a set of heater resistors attached to the base of the cold finger. Department-built temperature controllers were used to control the temperature at the cold-finger base.

A department-built liquid-helium immersion glass dewar was used occasionally for laser excitation experiments when temperatures down to 2K were required. Once filled with liquid helium the dewar was evacuated by a 1100 litre/min rotary pump, reducing the temperature of the liquid helium to below the transition to the super-

fluid state at 2.2 K. Over eight hours of operating time could be achieved on one fill of 4–5 litres of liquid helium.

For the infrared Zeeman experiments, an Oxford Instruments superconducting magnet, built into the can of a metal helium cryostat, was used to provide magnetic fields of up to 4T. A British Oxygen Company DPS 60-72/2A power supply was used to provide a current to the superconducting solenoid which was operated in persistent-current mode. A current of 50A was required to produce a 4T field at the sample. The solenoid was immersed in liquid helium, which was transferred continuously throughout the run. The sample itself was not immersed, but mounted in a stainless-steel tube in the centre of the magnet bore, and cooled by thermal contact to an estimated temperature of 10K. This arrangement eliminated the need for low temperature infrared windows. The samples were clamped to a copper block which then screwed into a copper ring at the centre of the stainless-steel tube.

As the solenoid is not a split-solenoid type, the light propagation direction is always parallel to the magnetic field. Some transitions may not be observed in this polarisation geometry; for example, for a C_4 magnetic sub-site (C_{4v} centre with the magnetic field along the four-fold symmetry axis), no π transitions can be observed since the $\boldsymbol{E}$ vector of the light is necessarily perpendicular to the symmetry axis of the centre.

3.4 Infrared Absorption Spectroscopy

The infrared absorption measurements were carried out using a Bio-Rad FTS-40 Fourier-transform infrared spectrometer, with a maximum resolution of $0.1\,\mathrm{cm}^{-1}$. The combination of globar source, KBr beam splitter and mercury-cadmium-telluride detector provide a useful scanning range of $700–4500\,\mathrm{cm}^{-1}$. The H^- local modes in CaF_2 and SrF_2 lie in the region 900-1020 cm^{-1} for which this combination is optimum. Recently, a new combination of tungsten-halogen lamp, quartz beam splitter and indium-antimonide detector has extended the range into the near-infrared from $3000–11000\,\mathrm{cm}^{-1}$. Absorption spectra of the $^3F_4$ and $^3H_5$ multiplets of Tm^{3+} were accessible with this combination.

To reduce the signal-noise ratio, many interferograms need to be added. Typically

64 to 256 scans were averaged. Because of helium hold-time constraints, Zeeman spectra were generally averaged over only 64 scans, and it then took about 15 minutes to record the spectrum for each value of the applied magnetic field.

It was found that at the maximum resolution of $0.1\,\mathrm{cm}^{-1}$, a background ripple with an amplitude of around 1% of the signal and a period of $0.25\,\mathrm{cm}^{-1}$ was often present, depending on the wavelength region of interest. This is due to interference fringing from the beam splitter itself and could be minimised by taking a background scan with the sample warmed up, then ratioing the spectrum to this background scan. However, this method was not always reliable for the Zeeman measurements since the sample would move slightly as the cryostat changed temperature, shifting the interference fringes. In many cases, the background ripple could be minimised by removing a single peak from the interferogram (Fourier transform of the spectrum). Often, other fringes with longer periods were also present and these could not be removed by the same methods without interfering with the absorption features of the spectrum. If only a small frequency range (less than about $50\,\mathrm{cm}^{-1}$) was required, this component of the background could be compensated for by fitting a sine function to the ripple and ratioing this out. These two methods have the added advantage over the method of recording a background spectrum of not introducing further significant noise into the spectrum.

3.5 Optical Absorption Spectroscopy

Optical absorption spectra were obtained using a 100W tungsten-halogen lamp, stabilised by a department-built 12V regulated power supply. The light from this lamp was filtered through appropriate Corning Glass filters to remove unwanted grating orders, passed through the sample and focussed onto the entrance slit of a Spex 1701 0.75 m single-grating spectrometer, set to measure in either first or second order. The light was detected using either a red-sensitive EMI 9558 photomultiplier tube (450–850 nm) or a blue-sensitive EMI 6255 photomultiplier tube (350–550 nm), both thermoelectrically cooled to −25°C. The signal from the appropriate photomultiplier tube was measured on a Keithley 610B electrometer and then either plotted on a chart recorder or digitised using a department-built voltage-to-frequency converter.

3.6 Laser-Selective Excitation Spectroscopy

Laser-selective excitation experiments were performed with either of two tunable continuous-wave (cw) lasers or a tunable pulsed laser. Most of the experiments used a Spectra-Physics 375 tunable dye laser pumped with a Spectra-Physics 2045E 30W argon-ion laser. The dye laser was fitted with a Spectra-Physics 573 three-plate birefringent filter, which allowed the laser to be tuned continuously throughout the full range of the dye. The dyes used were Rhodamine 6G, Rhodamine 640 and Coumarin 460. Table 3.1 lists the rare-earth transitions pumped with these dyes.

Dye	RE^{3+}	Transition
Rhodamine 6G	Pr^{3+}	$^3H_4 \rightarrow {}^1D_2$
	Nd^{3+}	$^4I_{9/2} \rightarrow {}^4G_{5/2}$
		$^4F_{3/2} \rightarrow {}^4D_{3/2}$
Rhodamine 640	Tm^{3+}	$^3H_6 \rightarrow {}^3F_3$
		$^3H_6 \rightarrow {}^3F_2$
		$^3F_4 \rightarrow {}^1G_4$
		$^3H_4 \rightarrow {}^1D_2$
	Er^{3+}	$^4I_{15/2} \rightarrow {}^4F_{9/2}$
		$^4I_{13/2} \rightarrow {}^4F_{5/2}$
	Ho^{3+}	$^5I_8 \rightarrow {}^5F_5$
Coumarin 460	Tm^{3+}	$^3H_6 \rightarrow {}^1G_4$

Table 3.1 : Laser dyes used to pump specific RE^{3+} multiplet transitions.

More recently, a Coherent 899 tunable Ti:sapphire ring laser was installed and was used for part of the work of this thesis. Also argon-laser pumped, the Ti:sapphire laser has three sets of optics providing three tuning ranges from 700–1050 nm. The mid-wave or short-wave set of optics were used to give laser emission around 800 nm to pump the rare-earth multiplet transitions listed in table 3.2.

The polarisation of the emission from both lasers was vertical and could be altered by use of a Spectra-Physics 310 polarisation rotator. A lens was used to bring the laser beam to focus inside the sample. For upconversion experiments in par-

RE^{3+}	Transition
Tm^{3+}	$^3H_6 \rightarrow {}^3H_4$
	$^3H_5 \rightarrow {}^1G_4$
Er^{3+}	$^4I_{15/2} \rightarrow {}^4I_{9/2}$
	$^4I_{13/2} \rightarrow {}^4S_{3/2}$

Table 3.2 : RE^{3+} multiplet transitions pumped with the Ti:sapphire laser using the mid-range optics.

ticular, focusing of the beam is critical since the upconversion intensity varies as the square of the laser intensity. It is desirable to use a short focal length lens to obtain the tightest possible focusing, bearing in mind the physical dimensions of the cryostat. A 6 cm focal-length lens was used for the upconversion experiments here. When the closed-cycle helium refrigerator was being used, the laser was directed vertically up through the crystal (figure 3.2). This gave a vertical fluorescence image which could then be projected directly onto the entrance slit of a spectrometer. Two spectrometers were set up on either side of the cold head. On

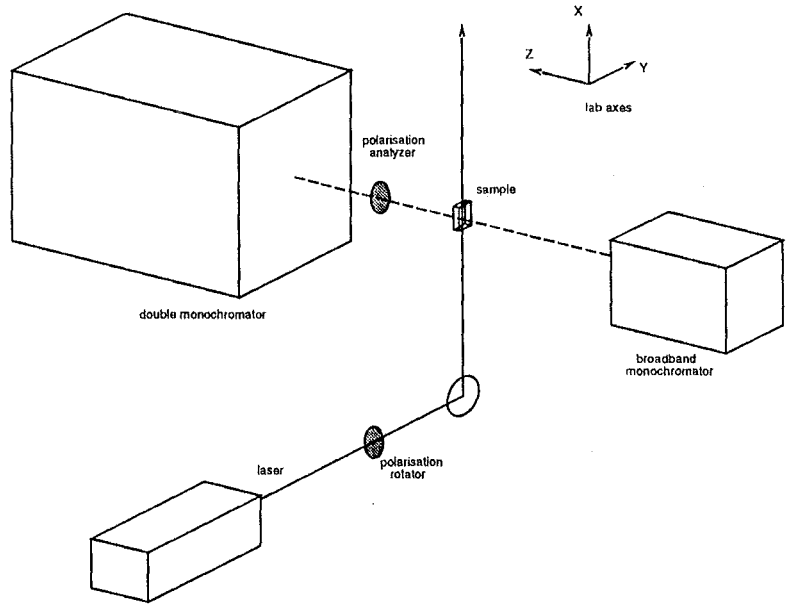

Figure 3.2 : Laboratory geometry for laser-selective excitation experiments.

one side a Spex 1403 double-grating spectrometer with a thermoelectrically-cooled RCA C31034 photomultiplier tube was used for site-selective spectroscopy, while on the other a low-resolution Bausch and Lomb 0.25 m single-grating spectrometer with a thermoelectrically-cooled EMI 9558 photomultiplier tube was used for broadband (non-selective) spectroscopy. The signal from the photomultiplier tubes was then processed by a Princeton Applied Research model 1121 preamplifier/discriminator and model 1112 photon counter/processor.

Laser excitation spectroscopy involved three types of spectra:

- **Broadband excitation spectra.** The slits of the Bausch and Lomb spectrometer were fully opened, maximising its bandpass to approximately 50 nm. As crystal-field splittings of RE^{3+} multiplets are usually much less than this bandpass, this did not discriminate between centres producing fluorescence from the same RE^{3+} inter-multiplet transitions. It could however discriminate fluorescence from other impurity ions, and any scattered laser light.

  The laser frequency was scanned across the absorption transitions of interest. Any fluorescing species which absorbed a particular laser frequency then recorded a fluorescence peak through the Bausch and Lomb spectrometer. A broadband excitation spectrum is essentially equivalent to an absorption spectrum, but with the fluorescence signals from different centres scaled by their relative fluorescence efficiencies. However, the signal-to-noise ratio of a broadband excitation spectrum is greatly improved over that of an absorption spectrum, since the background signal corresponds to a low rather than high signal and fluorescence peaks can be recorded at much higher gain.

  As an alternative to using the Bausch and Lomb spectrometer, if a greater bandpass was required, the Spex 1701 single monochromator could be used in zero order. Corning glass filters were used to cut out scattered laser light and provide any further wavelength discrimination required.

- **Fluorescence spectrum.** The laser was then tuned to match each excitation transition from the broadband excitation spectrum in turn (the signal from the broadband spectrometer was displayed on a Keithley 610B electrometer to assist with manual tuning), and the fluorescence images focussed onto the Spex

1403 double monochromator. This spectrometer has a resolution of $0.1\,\mathrm{cm}^{-1}$ for 10μm slits; however such resolution was not generally required and slits of 20–100μm were used, depending on the signal strength. The spectrometer was scanned through the fluorescence transitions to obtain a fluorescence spectrum of just the particular RE^{3+} centre being excited.

The fluorescence spectrum forms a signature of the centre. By tuning the laser to other excitation transitions corresponding to the same centre, the same fluorescence transitions will be observed. However the relative transition intensities may be affected by polarisation effects (section 2.5).

- **Selective excitation spectra.** The Spex 1403 double monochromator was tuned onto a strong transition of the fluorescence spectrum. The laser frequency was then scanned again as in the broadband excitation spectrum, but this time the only excitation lines which appeared were those corresponding to the particular centre which fluoresces at the chosen wavelength. For samples with a complex distribution of centres, care had to be taken to choose a fluorescence line which was well resolved from fluorescence lines of other centres. Provided this was done, a selective excitation spectrum of one particular centre could be obtained.

The site-selected fluorescence and spectra give spectral information about the one particular centre selected. It is from the transitions measured in this way that an energy level scheme for the rare-earth ion in that particular centre can be constructed.

By altering the laser polarisation between horizontal and vertical and using a polaroid analyser in front of the spectrometer, polarisation ratios for pairs of excitation and fluorescence transitions were measured. For the orientational degeneracy of rare-earth centres in CaF_2, differently oriented centres absorb the laser light with different intensities for different polarisations and hence polarised emission is produced. Referring to the lab axes of figure 3.2, the notation X(a b)Z indicates that a (= Y or Z) is the polarisation of the incident laser beam, propagating in the X-direction, and b (= X or Y) is the polarisation selected by the analyser for the detected fluorescence, propagating in the Z-direction. In all of this work, the pump-beam and fluorescence propagation directions remain X and Z respectively, and the notation is shortened to (a b). For the C_{4v} symmetry centres, if the crystal is oriented with its

⟨100⟩ body axes aligned with the lab axes, then the well-defined polarisation ratios of table 3.3 are obtained. From the group theory of section 2.3, these ratios give information on the irreps of the states involved in the observed transitions.

transition polarisations		polarisation geometry			
absorption	emission	YX	YY	ZX	ZY
π	π	0	1	0	0
	σ	1	0	1	1
	π_{md}	1	0	0	0
	σ_{md}	0	1	1	1
π_{md}	π	0	0	0	1
	σ	1	1	1	0
	π_{md}	0	0	1	0
	σ_{md}	1	1	0	1
σ	π	1	0	1	1
	σ	1	2	1	1
	π_{md}	0	1	1	1
	σ_{md}	2	1	1	1
σ_{md}	π	1	1	1	0
	σ	1	1	1	2
	π_{md}	1	1	0	1
	σ_{md}	1	1	2	1

Table 3.3 : Polarisation ratios for C_{4v} centres in ⟨100⟩ oriented CaF_2 crystals. The polarisation of transitions between states transforming as particular C_{4v} irreps is given in table 2.5.

For C_{3v} symmetry centres, no polarisation dependence would be expected for ⟨100⟩ oriented crystals in the above geometry, since all possible orientations of the centre are inclined at the same angle (54.7°) to both the incident laser and the fluorescence-detection direction. However if a sample is oriented with one of its ⟨111⟩ axes parallel to the lab Z axis, then the polarisation ratios of table 3.4 are obtained. These ratios are independent of the orientation of the laser beam in the plane perpendicular to

the chosen ⟨111⟩ axis, eliminating the need for extra cleaves to be made [17]. These C_{3v} centre ratios are less clearly defined than those for the C_{4v} and, in addition, $\gamma_3 \rightarrow \gamma_3$ transitions in C_{3v} symmetry are allowed for both polarisations for both electric-dipole and magnetic-dipole operators, leading to essentially arbitrary ratios whenever either the excitation or fluorescence transition is a $\gamma_3 \rightarrow \gamma_3$ transition.

transition polarisations		polarisation geometry			
absorption	emission	YX	YY	ZX	ZY
π	π	2	6	1	1
	σ	7	3	8	8
	π_{md}	6	2	1	1
	σ_{md}	3	7	8	8
π_{md}	π	1	1	2	6
	σ	8	8	7	3
	π_{md}	1	1	6	2
	σ_{md}	8	8	3	7
σ	π	7	3	8	8
	σ	11	15	10	10
	π_{md}	3	7	8	8
	σ_{md}	15	11	10	10
σ_{md}	π	8	8	7	3
	σ	10	10	11	15
	π_{md}	8	8	3	7
	σ_{md}	10	10	15	11

Table 3.4 : Polarisation ratios for C_{3v} centres in ⟨111⟩ oriented CaF_2 crystals. The polarisation of transitions between states transforming as particular C_{3v} irreps is given in table 2.6.

3.7 Fluorescence Lifetimes

Fluorescence decay transients were measured using a Photochemical Research Associates LN1000 pulsed nitrogen laser pumping a model LN107 dye laser.

Lifetimes of the $^1G_4$ and $^3H_4$ multiplets of Tm^{3+} could be measured using Coumarin 460 and LDS 820 dyes, respectively. The lifetime of the $^1D_2$ was measured using Rhodamine 640 dye to pump the $^3H_4 \rightarrow {}^1D_2$ excited-state absorption transition with the cw dye laser simultaneously pumping the $^3F_3$ absorption transitions.

Chapter 4

Site-Selective Spectroscopy of Tm^{3+}-doped CaF_2

Notation

Many of the trivalent lanthanide ions have had their multiplets labelled by letters as well as by their $^{2S+1}L_J$ labels. This notation has historically followed the convention of multiplets first observed by optical absorption being labelled A,B,C... from lowest energy up. The multiplets below these energies were identified later as experimental techniques for measuring fluorescence-transition energies developed, and were then labelled Z,Y,X... from the lowest-energy multiplet up. Having developed historically, the notation has at times become somewhat ad-hoc and the many gaps and "missing" letters are due to original mis-assignments of multiplets to ions. However, this notation is compact (with crystal field components being denoted by numeral subscripts) and often easier to remember than the formal spectroscopic notation. Hence, even though the Tm^{3+} ion has not historically been so labelled, a single-letter notation scheme is introduced in the energy-level diagram of figure 4.1 to assist in the energy-level labelling for this chapter. Both styles of notation will be used here.

4.1 Previous Studies of CaF_2:Tm^{3+} and SrF_2:Tm^{3+}

CaF_2:Tm^{3+} seems to have been one of the least studied of the lanthanide-doped calcium fluoride systems. Muto [67] reported optical-absorption spectra and Zeeman effects of CaF_2:Tm^{3+} for Tm^{3+} concentrations of 0.1%, 0.3% and 1.0%, and proposed a classification of absorption transitions into four types of sites on the basis of the

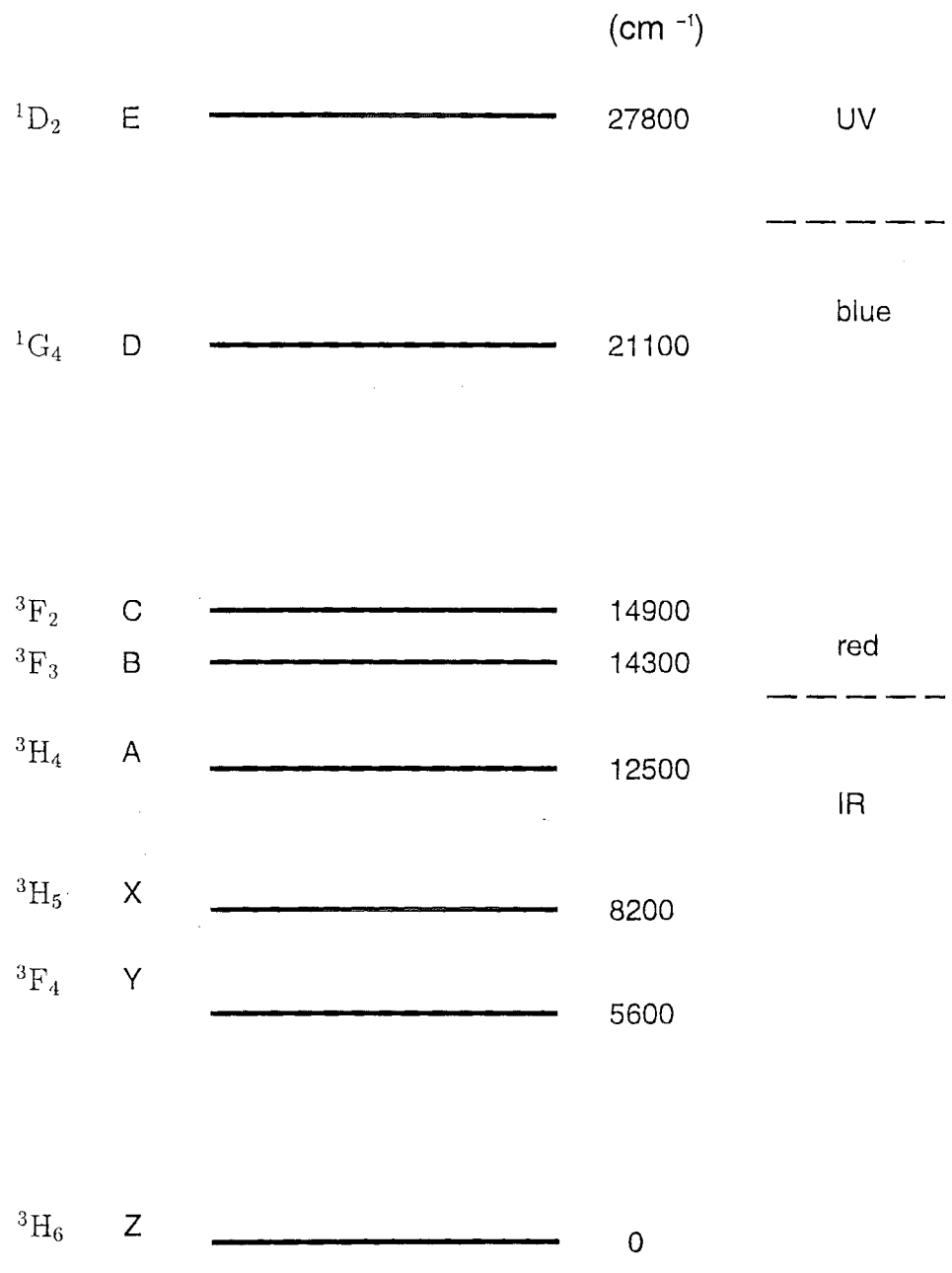

Figure 4.1 : Energy level scheme of all multiplets up to $^1D_2$ for the Tm^{3+} ion, with their approximate free-ion energies and the two alternative labelling schemes.

dependence on concentration and growth conditions. Zeeman splittings of two of the lines demonstrated that a tetragonal centre and a trigonal centre (determined to have O^{2-} charge compensation) were present. From the absence of any temperature dependence of the Zeeman components, it was determined that the splitting of the line assigned to the tetragonal centre was due to splitting of the excited state rather than the ground state. This result is consistent with the EPR observation of Hayes and Twidell [34] that CaF_2:0.05%Tm^{3+} showed no ground-state resonances before being X-irradiated.

Macfarlane [56] has reported spectral-holeburning experiments on two centres in CaF_2:0.01%Tm^{3+}, pumping the lowest crystal-field level of the $^3H_4$ multiplet in each case. The holeburning mechanism of population storage in the intermediate $^3F_4$ multiplet produced holes with a short lifetime of around 10 ms. The polarisation behaviour of these spectral holes led to the assignment of the two centres to C_{4v} and C_{3v} centres. Low-field Zeeman experiments showed that the C_{4v} centre transition at 12568.6 cm^{-1} did not split and hence was due to a transition between two singlets of the same C_{4v} irrep, while the C_{3v} centre transition at 12497.8 cm^{-1} did split in a magnetic field. It was not determined whether this magnetic field splitting was due to the ground or excited state. Because of their short lifetimes, the spectral holes were scanned by applying an electric-field ramp directly to the sample. Stark coefficients for the electric field parallel to the $\langle 100 \rangle$ crystal axis were found to be 25 kHz/V cm^{-1} for the C_{4v} centre and 4.6 kHz/V cm^{-1} for the C_{3v} centre.

Red-to-blue upconversion fluorescence at 77 K has been reported by Jouart *et al* [46] for 0.1–2.0% Tm^{3+}-doped CaF_2, SrF_2, BaF_2 and CdF_2. Blue fluorescence from the $^1G_4$ multiplet and ultraviolet and violet fluorescence from the $^1D_2$ multiplet was reported upon pumping the $^3F_4 \rightarrow {}^1G_4$ and $^3H_4 \rightarrow {}^1D_2$ excited-state transitions respectively, with red (650nm) laser light. For the concentrations investigated of 0.1–2%, a cubic centre and a tentatively-assigned tetragonal centre were reported for CaF_2, while a trigonal and a cubic centre were reported for SrF_2. A few fluorescence transitions were reported for SrF_2, while only the main excitation transitions of each site were reported for each of the other three systems. No attempt was made to produce an energy level scheme for any of these centres, and no justification was given for the assignment of the various centre symmetries. Further discussion of the upconversion mechanisms is given in chapter 5.

4.2 Absorption Spectroscopy of CaF_2:Tm^{3+}

Infrared-absorption spectra of a 30 mm boule of CaF_2:0.01%Tm^{3+} were measured using the near-infrared source-beamsplitter-detector combination of the Bio-Rad FTIR spectrometer. The spectra of the $^3F_4$ and $^3H_5$ multiplets are shown in figures 4.2 and 4.3 respectively. Most of the strong absorption lines have been assigned to either the C_{4v} or C_{3v} symmetry centre from the results of the site-selective spectroscopy of sections 4.3 and 4.4, and have been so labelled on these spectra. The absorption line at 8429.6 cm^{-1} in the spectrum of the $^3H_5$ multiplet, labelled "O" is unique in all of the absorption spectra measured in this work in being the only major absorption line which has not been assigned to either of these two centres. The question arises of what other Tm^{3+} centre might produce a single strong absorption line for transitions to only one multiplet. Clustering would not be expected to be significant at the concentration of 0.01%, and further would be expected to produce a complex set of absorption lines to every multiplet rather than the simple feature observed.

The explanation offered in section 4.5 is that this line is associated with the cubic symmetry centre of an isolated Tm^{3+} ion produced by remote charge compensation. Because of the centro-symmetry of this centre, electric-dipole transitions are forbidden, leaving only magnetic-dipole transitions observable. The magnetic-dipole selection rules (section 2.5) of $\Delta J = 0, \pm 1$ and $\Delta L = \Delta S = 0$ imply that the $^3H_5$ multiplet would be the only excited multiplet to have strong magnetic-dipole allowed transitions from the $^3H_6$ ground state. The $^1I_6$ multiplet is the only other excited multiplet which could have weakly-allowed magnetic-dipole transitions due to the small intermediate coupling with the $^3H_6$ multiplet.

The strength of magnetic-dipole absorption transitions to $^3H_5$ is illustrated by the strong C_{4v} centre absorption at 8340 cm^{-1} which corresponds to a $\gamma_3 \rightarrow \gamma_4$ transition (section 4.3) which is only magnetic-dipole allowed.

The optical absorption spectra of figures 4.4–4.7 were measured on a 2 mm thick slice of CaF_2:0.05%Tm^{3+}, using the optical absorption apparatus described in section 3.5. The absorption spectra of the $^3H_4$, $^3F_3$ and $^3F_2$ multiplets were measured using the spectrometer in first order, while the spectra of the $^1G_4$ and $^1D_2$ multiplets

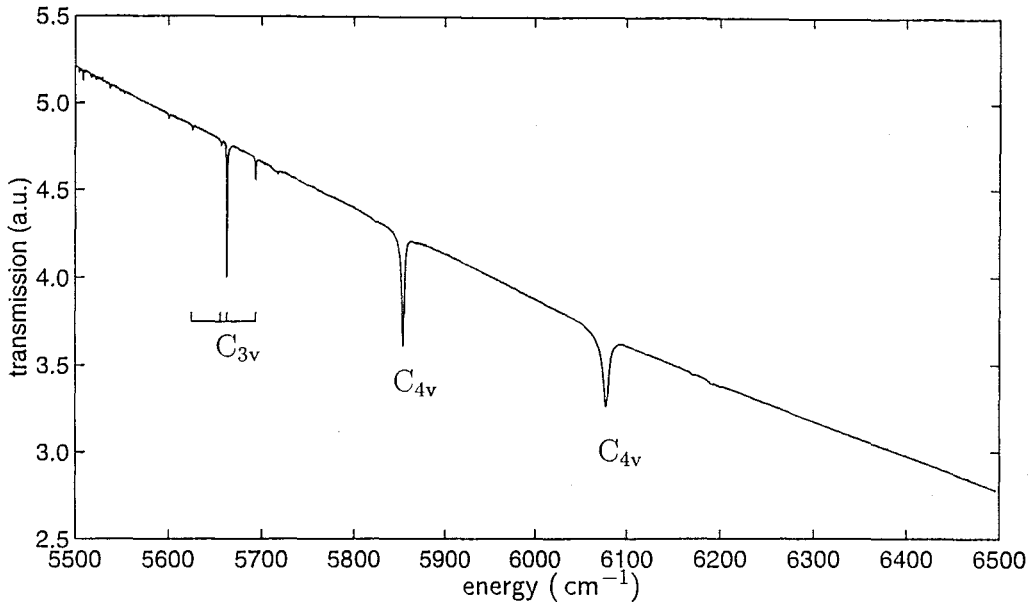

Figure 4.2 : Infrared-absorption spectrum of transitions to the $^3F_4$ multiplet for CaF_2:0.01%Tm^{3+}. Absorption lines assigned to the C_{4v} and C_{3v} centres are indicated.

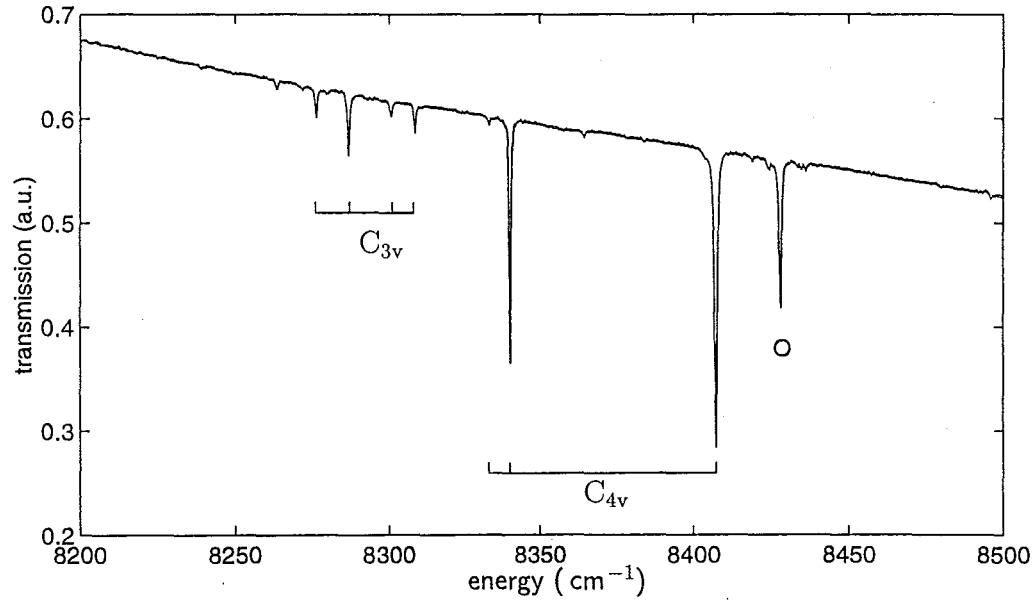

Figure 4.3 : Infrared-absorption spectrum of transitions to the $^3H_5$ multiplet for CaF_2:0.01%Tm^{3+}. Absorption lines assigned to the C_{4v} and C_{3v} centres are indicated. The absorption line labelled "O" is assigned to the cubic Tm^{3+} centre.

were measured in second-order. The absorption transitions to the $^3H_4$ multiplet (figure 4.4) are in the region accessible to the tunable Ti:sapphire laser, with the two sharp lines near 795 nm and 800 nm being the two transitions which were investigated by Macfarlane [56].

The $^3F_3$ and $^3F_2$ multiplets (figure 4.5) could be pumped by the rhodamine 640 dye laser. The $^3F_3$ multiplet has two particularly strong absorption lines for the C_{4v} centre. The lower-energy line of these two was observed by Muto [67] to split in a magnetic field and was assigned by him to a tetragonal centre. The weak $^3F_2$ multiplet absorption lines of the C_{4v} centre are too weak to appear in this spectrum, but were observed using laser excitation and appear in the 650–660 nm region. The several additional weak lines in this spectrum belong to minority sites and remain unassigned.

The $^1G_4$ multiplet, figure 4.6, has the weakest absorption transitions of the multiplets studied here. The transitions are accessible by a coumarin 460 dye laser. Excited state absorption transitions from $^3F_4$ were also observed using a rhodamine 640

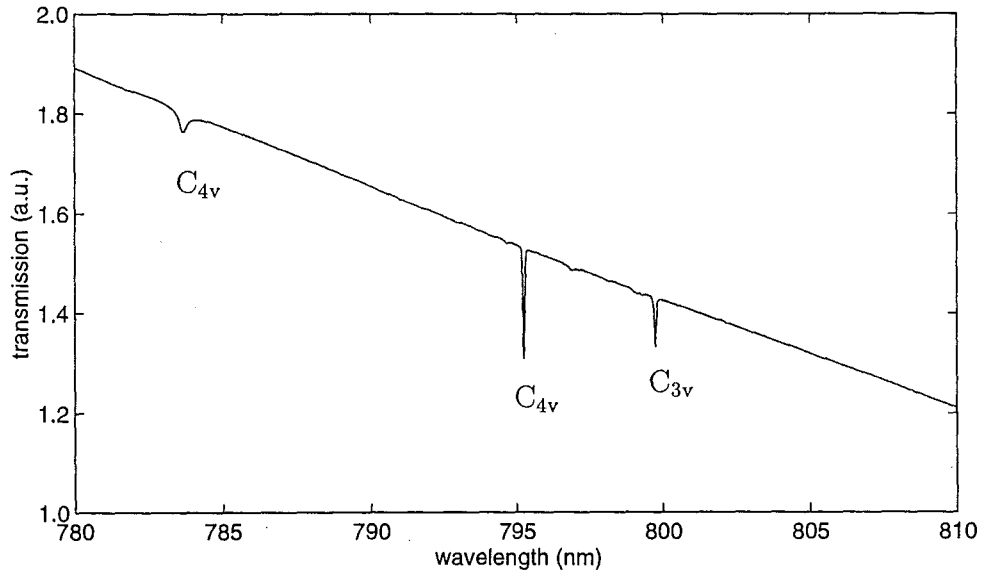

Figure 4.4 : Optical-absorption spectrum of transitions to the $^3H_4$ multiplet of CaF_2:0.05%Tm^{3+}. Absorption lines assigned to the C_{4v} and C_{3v} centres are indicated.

dye laser. The $^1D_2$ multiplet could not be pumped directly from the ground state by using the dye laser, however excited state absorption transitions from the $^3H_4$ multiplet were observed, again using the rhodamine 640 dye laser.

Table 4.1 lists the energies or wavelengths of all of the absorption transitions in CaF_2:0.01%Tm^{3+} and CaF_2:0.05%Tm^{3+} which have been assigned to the C_{4v} and C_{3v} centres. The assignments were made on the basis of the laser-selective excitation results of sections 4.3 and 4.4. The FTIR spectrometer gives energies in vacuum wavenumbers, while the optical-absorption data is for wavelengths in air. These results have not been adjusted for these corrections, and have not been calibrated against a standard source. However, the corrections are sufficiently small that the assignments to the calibrated energies (in air) of sections 4.3 and 4.4 can be made unambiguously.

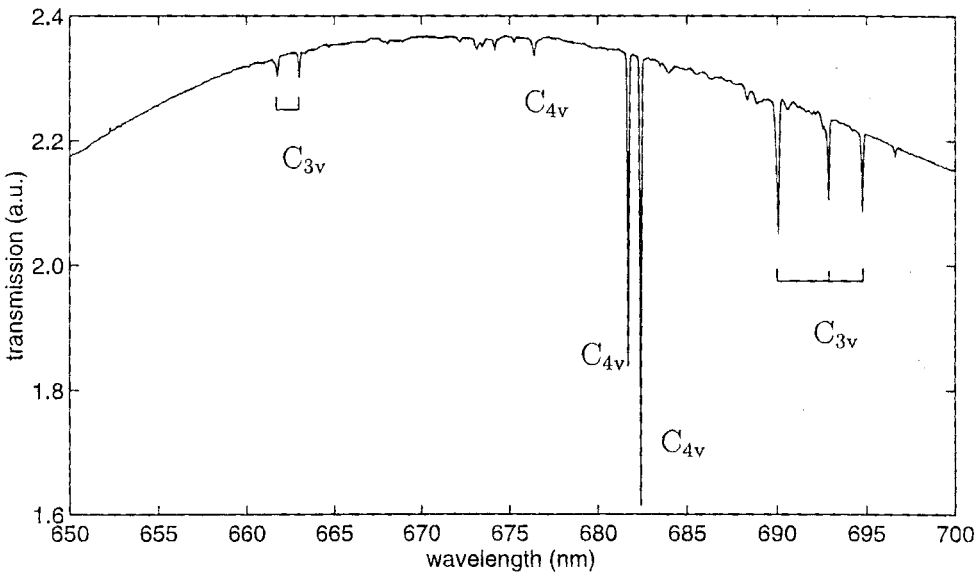

Figure 4.5 : Optical-absorption spectrum of transitions in the region of the $^3F_3$ and $^3F_2$ multiplets of CaF_2:0.05%Tm^{3+}. Absorption lines assigned to the C_{4v} and C_{3v} centres are indicated.

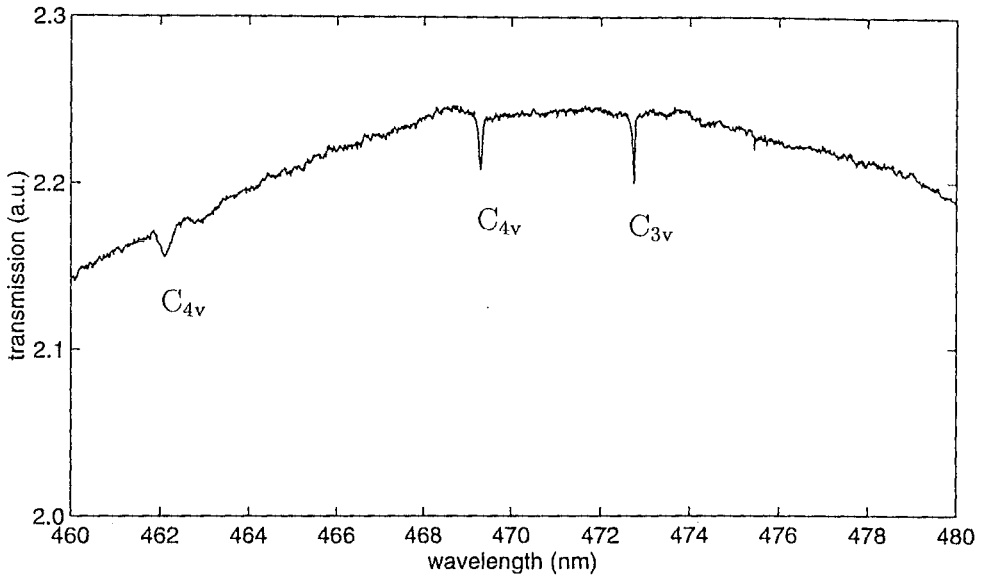

Figure 4.6 : Optical-absorption spectrum of transitions to the $^1G_4$ multiplet of CaF_2:0.05%Tm^{3+}. Absorption lines assigned to the C_{4v} and C_{3v} centres are indicated.

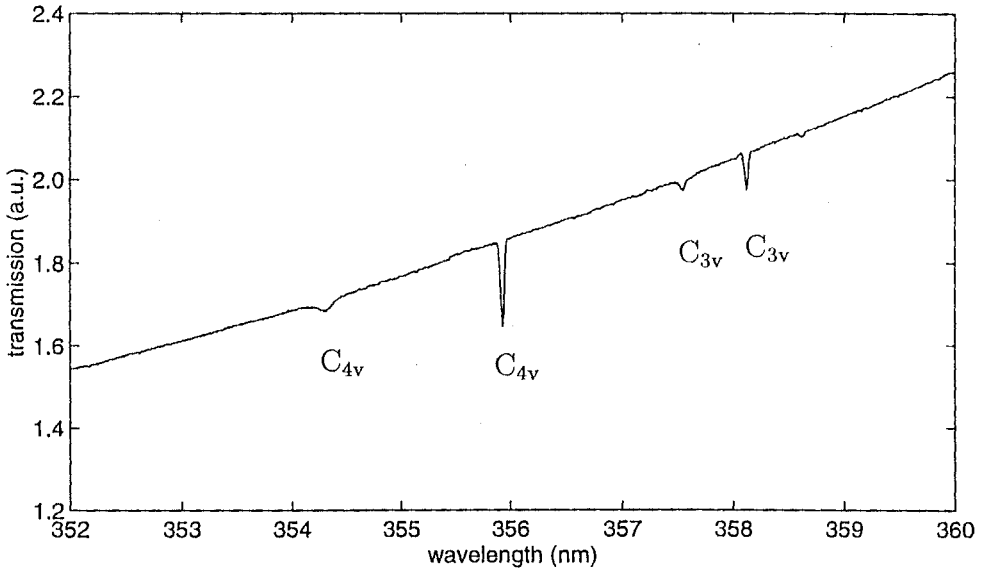

Figure 4.7 : Optical-absorption spectrum of transitions to the $^1D_2$ multiplet of CaF_2:0.05%Tm^{3+}. Absorption lines assigned to the C_{4v} and C_{3v} centres are indicated.

Multiplet	absorption energies (cm^{-1})			
	C_{4v} centre		C_{3v} centre	
$^3F_4$	Y_2	5854.9	Y_2^*	5626.1
	Y_5	6079.7	Y_3^*	5657.0
			Y_2	5663.4
			Y_3	5694.3
$^3H_5$	X_2^*	8334.4	X_1	8277.2
	X_1	8341.5	X_2	8287.8
	X_2	8408.8	X_3	8301.7
			X_4	8309.6
	absorption wavelengths (nm)			
	C_{4v} centre		C_{3v} centre	
$^3H_4$	A_1	795.24	A_1	799.75
	A_2	783.68		
$^3F_3$	B_1	682.41	B_1	694.77
	B_2	681.70	B_2	692.88
	B_5	676.38	B_3	690.07
$^3F_2$			C_1	663.01
			C_2	661.76
$^1G_4$	D_2	469.30	D_2	472.74
	D_5	462.10		
$^1D_2$	E_1	355.93	E_1	358.12
	E_3	354.32	E_2	357.55

Table 4.1 : Absorption lines assigned to transitions to crystal-field levels of the C_{4v} and C_{3v} centres in CaF_2:Tm^{3+}. * denotes a transition from the thermally-populated Z_2 state.

4.2.1 Zeeman Splittings of the Infrared-Absorption Spectra

The splitting in magnetic fields of the lines observed in the infrared-absorption spectra, figures 4.2 and 4.3, were measured for magnetic fields applied parallel to the $\langle 100 \rangle$ crystal axes of CaF_2:0.02%Tm^{3+}. In the series of spectra for increasing applied magnetic fields, figures 4.8 and 4.9, several of the lines are clearly split into two or three components, while the broad line at 5854.9 cm^{-1} appears to have a small, unresolved splitting. The spectra in these two figures have had a linear background ratioed out.

The g-values for the $\langle 100 \rangle$ field are calculated from the experimental splitting ΔE in a field of $B = 4\,T$ from

$$g_{\langle 100 \rangle} = \frac{\Delta E}{\mu_B B}$$

where $\mu_B = e\hbar/2m$ is the Bohr magneton. The 4 T splittings and $g_{\langle 100 \rangle}$ values of the C_{4v}, C_{3v} and cubic centre lines, listed in table 4.2, are further discussed in sections 4.3, 4.4 and 4.5, respectively.

Centre	zero-field position (cm^{-1})	4 T splitting	$g_{\langle 100 \rangle}$ value
C_{4v}	5854.9	2 ± 1	1.1 ± 0.5
	6079.7	0	0
	8341.5	0	0
	8408.8	1.1	0.59
C_{3v}	5663.4	6.7	3.59
	5694.3	1.7	0.91
	8277.2	0	0
	8287.8	1.0	0.54
	8301.7	2.2	1.18
	8309.6	0	0
cubic	8429.6	9.5	5.09

Table 4.2 : 4 T $\langle 100 \rangle$ Zeeman splitting of infrared-absorption lines in CaF_2:0.02%Tm^{3+}.

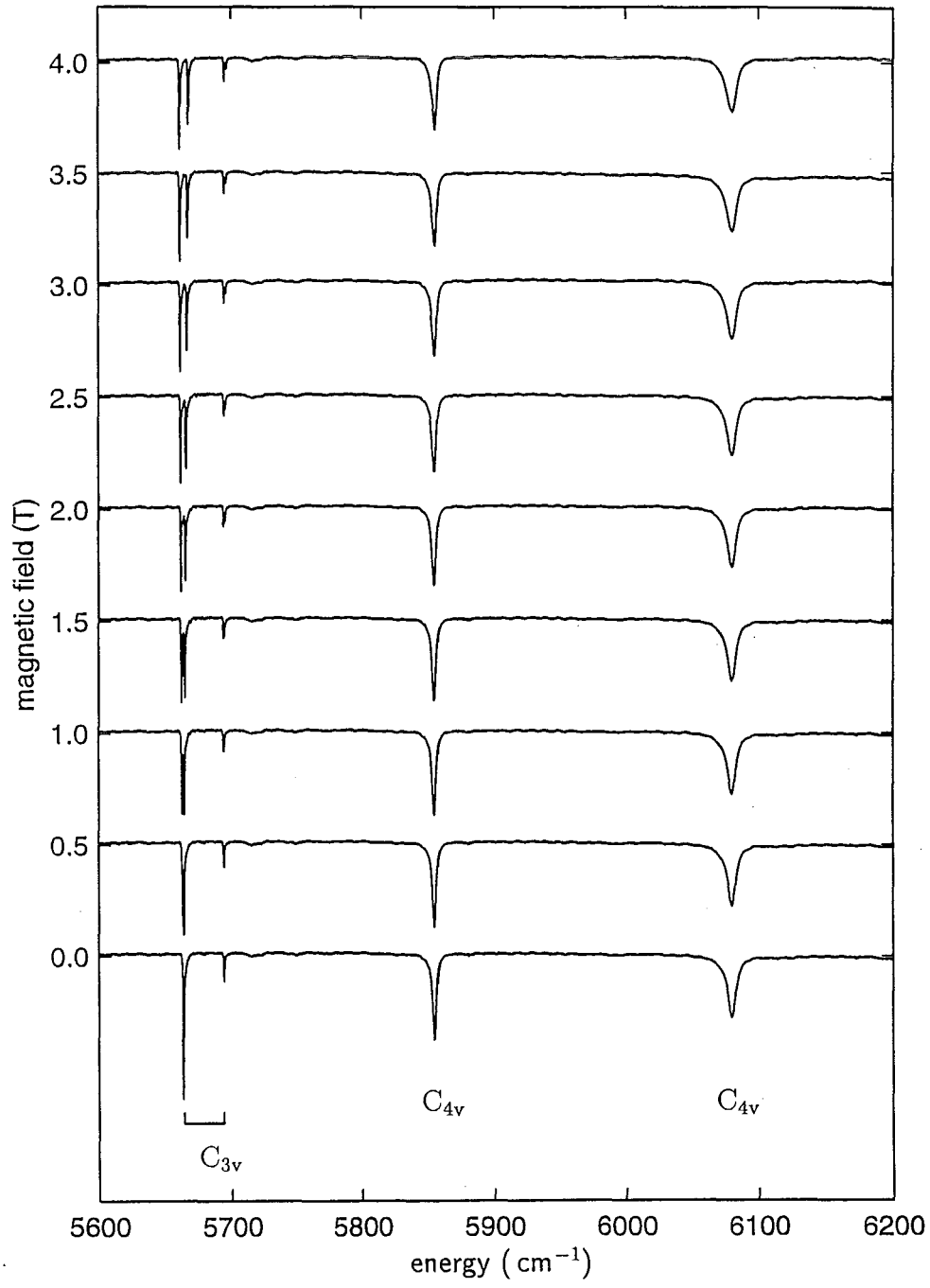

Figure 4.8 : Infrared-absorption spectrum of transitions to the $^3F_4$ multiplet of CaF_2:0.02%Tm^{3+} in applied magnetic fields parallel to the ⟨100⟩ crystal axes. Absorption lines assigned to the C_{4v} and C_{3v} centres are indicated.

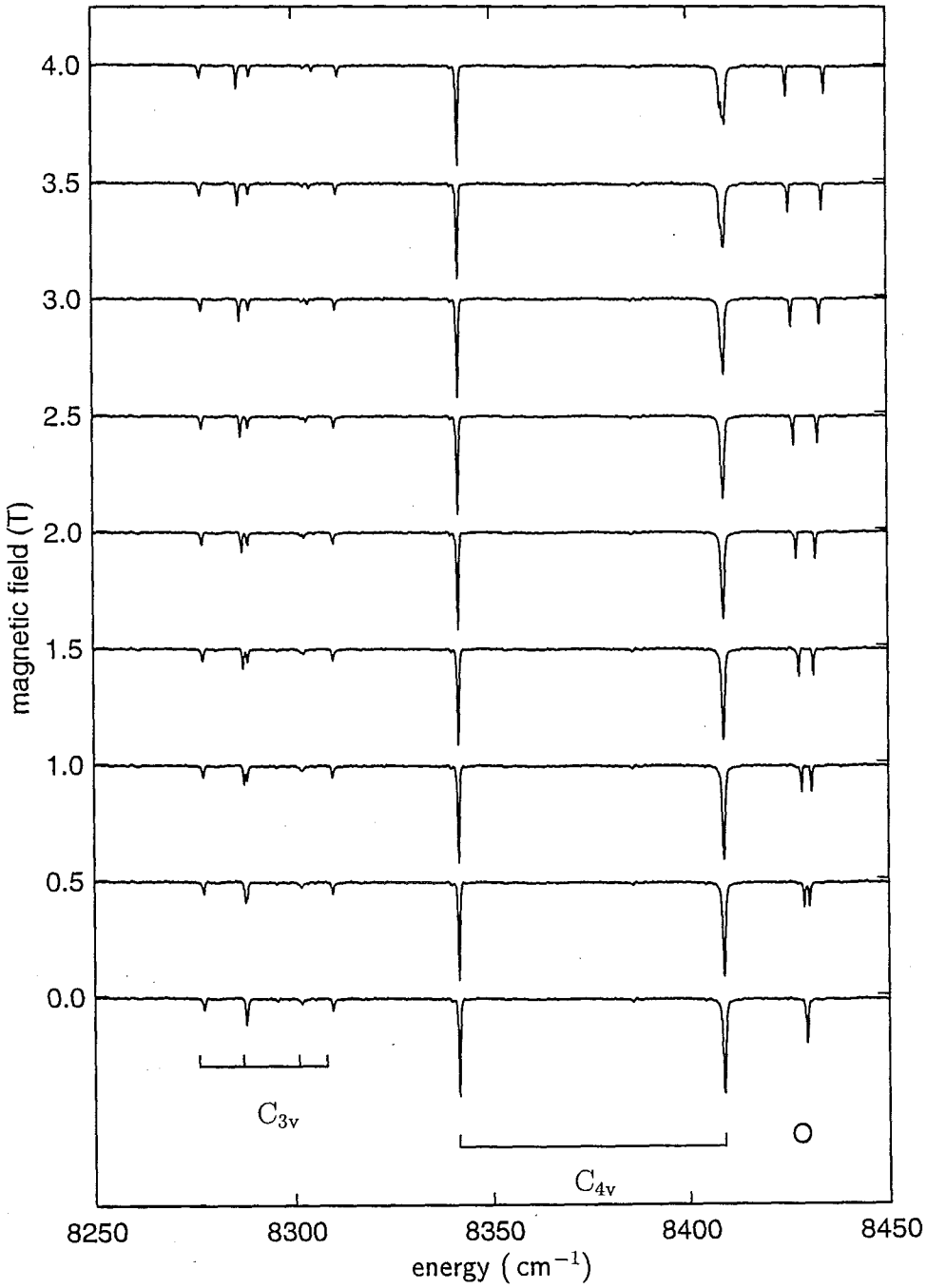

Figure 4.9 : Infrared-absorption spectrum of transitions to the $^3H_5$ multiplet of CaF_2:0.02%Tm^{3+} in applied magnetic fields parallel to the ⟨100⟩ crystal axes. Absorption lines assigned to the C_{4v} and C_{3v} centres are indicated. The absorption line labelled "O" is assigned to the cubic Tm^{3+} centre.

4.3 Site-Selective Spectroscopy of the C_{4v} Centre in CaF_2:Tm^{3+}

4.3.1 Direct Excitation and Fluorescence Spectroscopy

The $^3F_3$ and $^3F_2$ multiplet energies lie within the lasing range of the rhodamine 640 dye laser, and were pumped using this dye.

Direct excitation of the $^3F_3$ multiplet

The polarised site-selective excitation spectrum of the $^3F_3$ multiplet, monitoring the fluorescence line at 12572 cm^{-1}, is shown in figure 4.10. As the fluorescence transition being monitored is also seen in the absorption spectrum at 15 K (figure 4.4) it is identified as the $A_1 \rightarrow Z_1$ transition. Three polarisation combinations are sufficient to identify the polarisation character of each excitation line. Table 3.3 shows that the (YX):(YY):(ZY) ratio of 0:1:0 observed for the $Z_1 \rightarrow B_2$ line at 14675 cm^{-1} is only possible for a π excitation/π fluorescence transition pair. Knowing that the fluorescence transition being monitored is a π-polarised transition, the (YX):(YY):(ZY) ratios determine the polarisations of the four excitation lines to be σ, π, π_{md} and σ respectively.

From the O_3–C_{4v} irrep decomposition (table 2.2, section 2.3) a $J = 3$ multiplet decomposes to the C_{4v} irreps $\gamma_2 + \gamma_3 + \gamma_4 + 2\gamma_5$. The polarisations determined for the $^3F_3$ multiplet excitation spectrum can only be accounted for by the ground state being either a γ_3 or γ_4 singlet state. The crystal-field wavefunctions corresponding to these two irreps are closely related; for even J a γ_3 state is spanned by $[(|2\rangle + |-2\rangle), (|6\rangle + |-6\rangle)]$ and a γ_4 state by $[(|2\rangle - |-2\rangle), (|6\rangle - |-6\rangle)]$, while for odd J the reverse holds. Since any multiplet necessarily contains equal numbers of γ_3 and γ_4 states, laser excitation and fluorescence experiments (or indeed Zeeman or Stark effect measurements) alone cannot distinguish which of these two, γ_3 or γ_4, is appropriate for the ground state.

In order to determine the ground-state irrep, comparison can be made with a crystal-field analysis such as that performed by Reid and Butler [78]. In such an analysis, cubic crystal-field parameters are determined by extrapolation from crystal-field fits

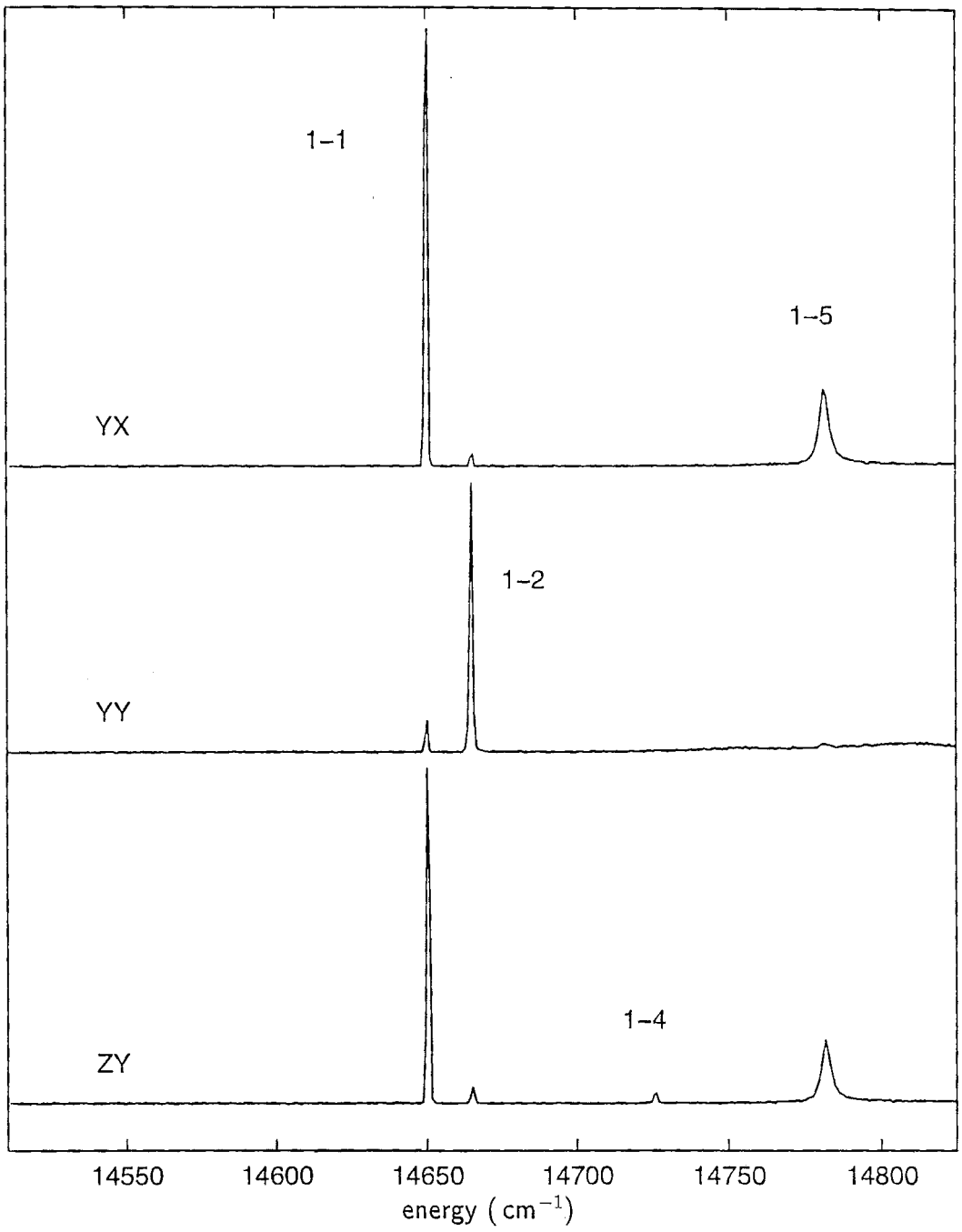

Figure 4.10 : 15 K polarised excitation spectrum of the $^3F_3$ multiplet of the C_{4v} centre of CaF_2:0.05%Tm^{3+}, monitoring the $A_1 \rightarrow Z_1$ fluorescence transition at 12572 cm^{-1}, for (YX), (YY) and (ZY) polarisation geometries (section 3.6). Transitions are identified by their lower and upper crystal-field level labels.

for other members of the lanthanide series, and the calculated crystal-field energies are plotted against a single C_{4v} distortion parameter. Such a plot for the $^3H_6$ multiplet is shown in figure 4.11. The crystal-field parameters used are those determined by least-squares fit for the C_{4v} centre of CaF_2:Er^{3+} [30] and the non-cubic part of the crystal-field Hamiltonian is scaled by the perturbation parameter, λ, such that $\lambda = 1$ represents the best-fit value:

$$\mathcal{H}_{cf} = \mathcal{H}_{cubic} + \lambda\, \mathcal{H}_{tetragonal} \,.$$

It is clear from figure 4.11 that, unless the parameters change dramatically in going from Er^{3+} to Tm^{3+} (including reversal in some signs), the ground state for the CaF_2:Tm^{3+} C_{4v} centre can only be a γ_3 irrep state. This is in agreement with the polarisation behaviour already discussed. The four observed $^3F_3$ excitation lines are therefore identified as transitions from the γ_3 ground state to γ_5, γ_3, γ_4 and γ_5 levels respectively.

Heating the sample to 60 K yields new transitions which appear at 84 cm^{-1} intervals below each of the four seen at 15 K, indicating the presence of a thermally populated Z_2 level at 84 cm^{-1}. The 60 K $^3F_3$ multiplet excitation spectrum is shown in figure 4.12, with these new so-called "hot" lines marked *. The polarisations of these lines unequivocally indicate that the Z_2 level is a γ_5 state. One additional new line appears (marked +) and is assigned to the transition from Z_2 to the $^3F_3$ multiplet γ_2 state, which was unobserved from the ground state (as expected from the C_{4v} transition selection rules, table 2.5).

Thus the Z_1 and Z_2 $^3H_6$ multiplet levels are assigned as γ_3 and γ_5 states respectively, with a splitting of 84.0 cm^{-1} between them, and all of the $^3F_3$ multiplet levels are assigned as in table 4.3.

Direct excitation of the $^3F_2$ multiplet

The absorption transitions of the $^3F_2$ multiplet are at significantly weaker intensity than those of the $^3F_3$ multiplet, to the extent that they were not observed in the absorption spectrum of 2 mm thick CaF_2:0.01%Tm^{3+}, figure 4.5. For monitoring the $A_1 \rightarrow Z_1$ π-allowed fluorescence line, the excitation spectrum reveals five absorption

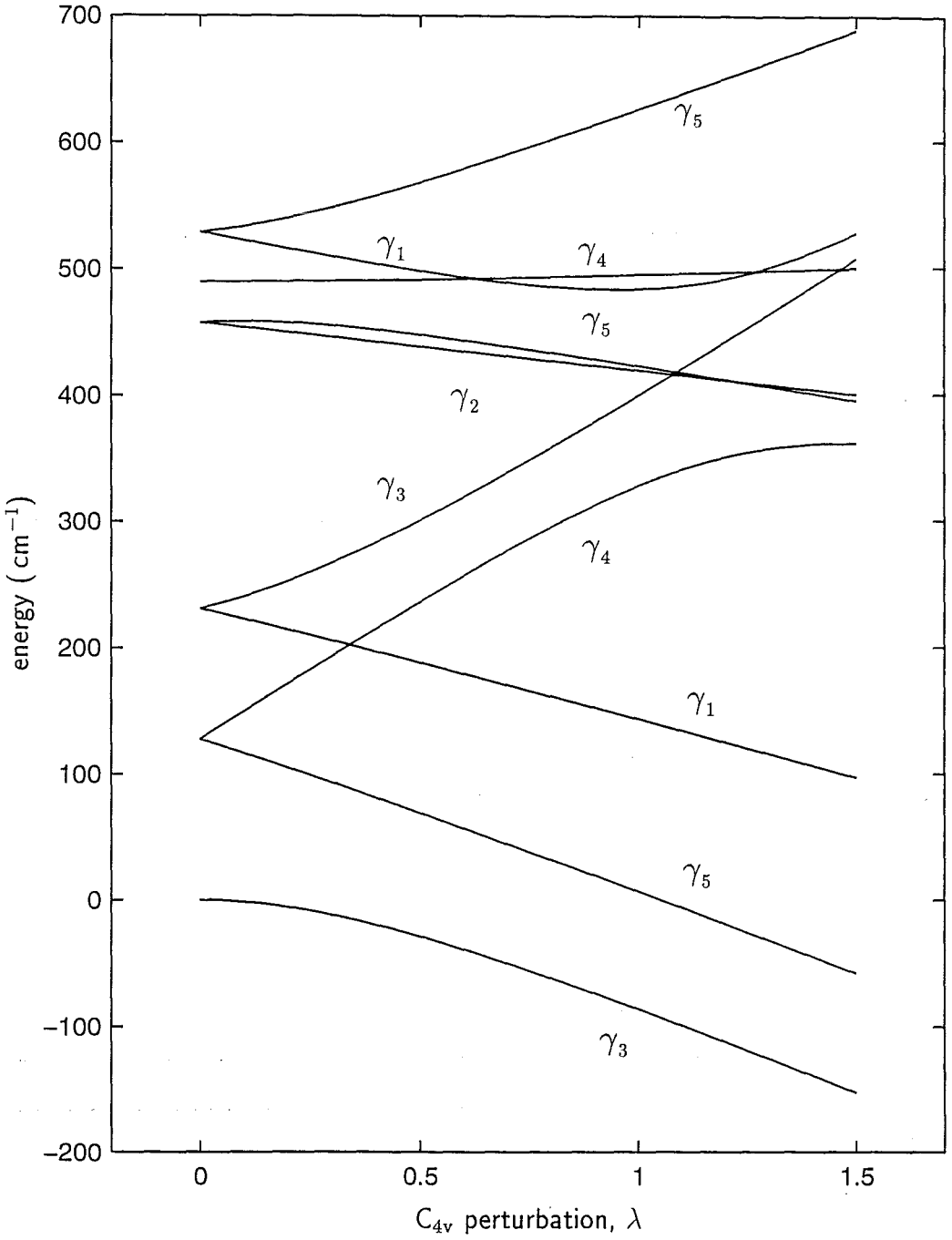

Figure 4.11 : Calculated $^3H_6$ multiplet energy levels, labelled by their C_{4v} irreps, plotted against increasing C_{4v} perturbation, characterised by the parameter λ. The crystal-field parameters used are those obtained for the C_{4v} centre in CaF_2:Er^{3+} [30].

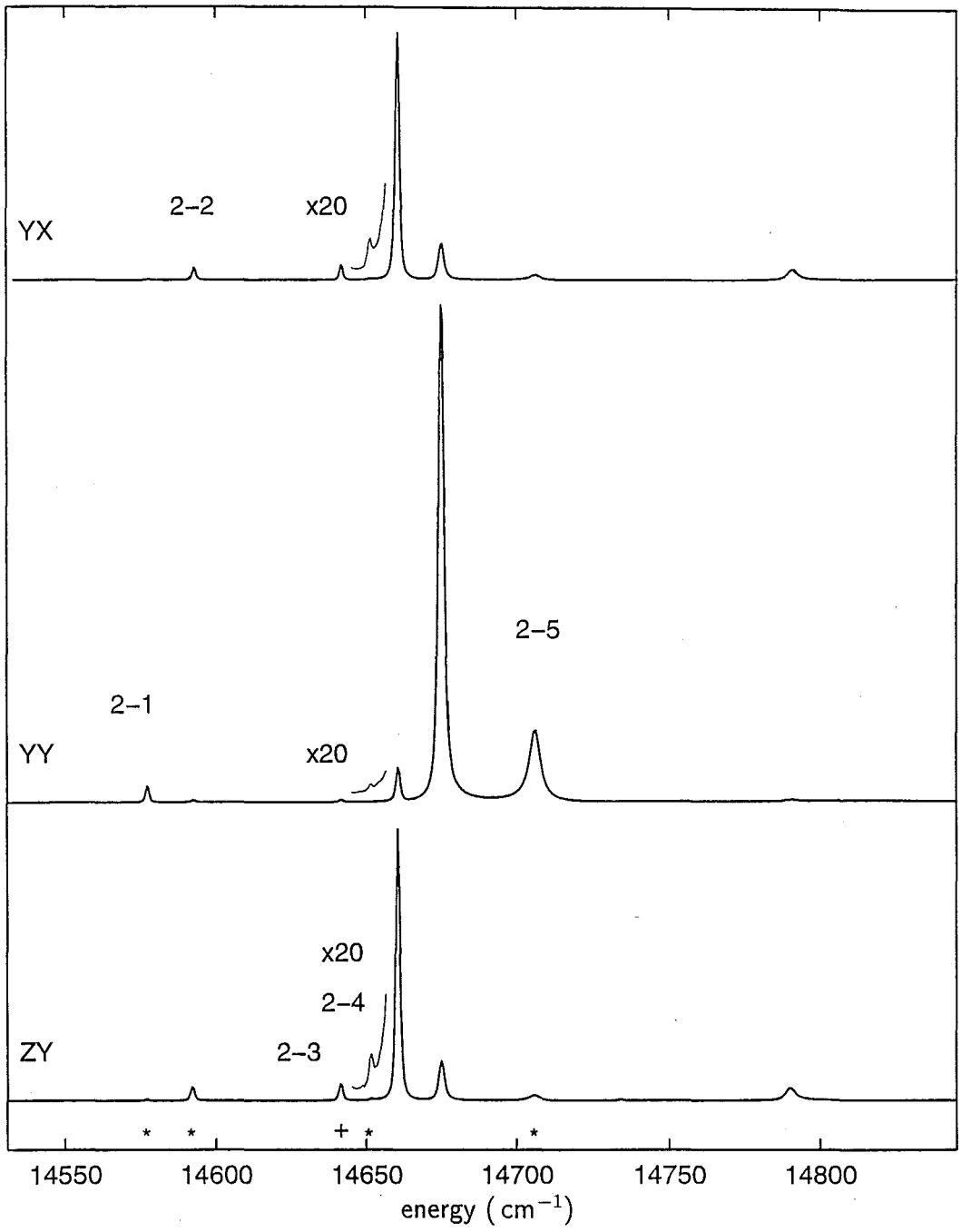

Figure 4.12 : 60 K polarised excitation spectrum of the $^3F_3$ multiplet of the C_{4v} centre of CaF_2:0.05%Tm^{3+}, monitoring the $A_1 \rightarrow Z_1$ fluorescence transition at 12572 cm^{-1}, for (YX), (YY) and (ZY) polarisation geometries. Transitions are identified by their lower and upper crystal-field level labels.

State	Energy (cm^{-1})	Irrep	Polarisation	
			$Z_1\gamma_3 \rightarrow B_i$	$Z_2\gamma_5 \rightarrow B_i$
B_1	14659.4	γ_5	σ	π
B_2	14674.7	γ_3	π	σ
B_3	14720.9	γ_2	-	σ
B_4	14732.7	γ_4	π_{md}	σ
B_5	14789.3	γ_5	σ	π

Table 4.3 : Crystal-field levels of the $^3F_3$ multiplet for the CaF_2:Tm^{3+} C_{4v} centre.

lines (figure 4.13) over this region. The two broad features at the lower energy end of the spectrum are attributed to lattice-phonon sidebands associated with the electronic transitions of the $^3F_3$ multiplet. These appear to be strong because of the large intensity of the absorption lines of the $^3F_3$ multiplet compared to those of the $^3F_2$ multiplet. The three lines associated with electronic transitions to the $^3F_2$ multiplet have π_{md}, π and σ_{md} polarisation characters. A $J = 2$ multiplet decomposes to the C_{4v} irreps $\gamma_1 + \gamma_3 + \gamma_4 + \gamma_5$. The π_{md} and π polarised lines are necessarily transitions from the γ_3 ground state to the γ_4 and γ_3 states respectively. While the σ_{md} polarised line is a $\gamma_3 \rightarrow \gamma_5$ transition, the absence of the expected electric-dipole component is anomalous. This transition at 15365 cm^{-1} is barely resolved from the stronger π transition at 15370 cm^{-1}. Assignment of these levels is confirmed by analysis of the $^1D_2 \rightarrow {}^3F_2$ fluorescence spectrum.

When the sample is heated to 60 K, the expected hot-band transitions 84 cm^{-1} below each of these three levels are observed, and are considerably stronger than those from the ground state. The other expected transition from the Z_2 state to the $^3F_2$ γ_2 state is not observed. However, the crystal-field analysis of section 4.3.3 suggests that the energy of this transition is nearly coincident with the pair at 15365 cm^{-1} and 15370 cm^{-1}, and thus may be overlapped by these. The $^3F_2$ multiplet state assignments are listed in table 4.4.

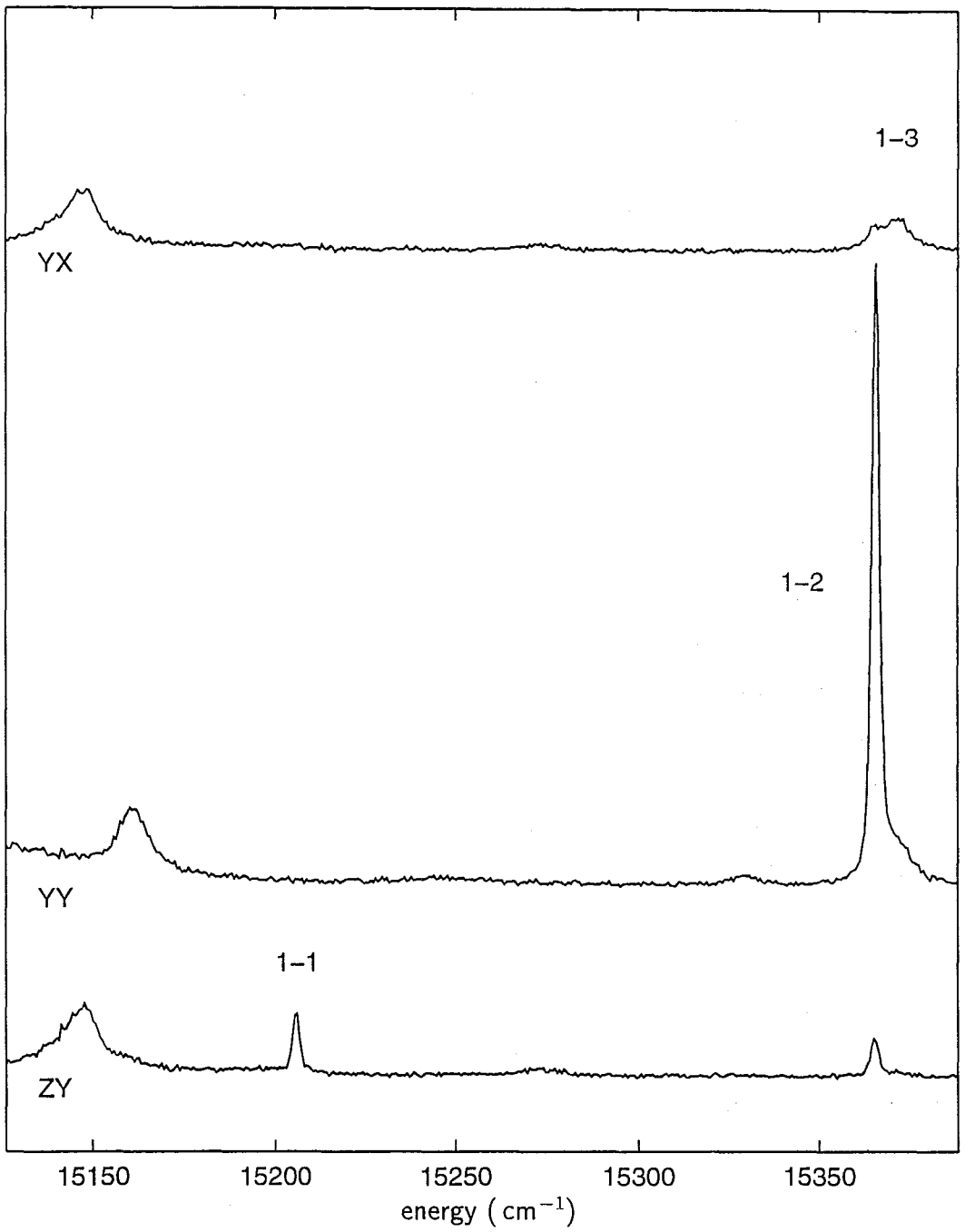

Figure 4.13 : 15 K polarised excitation spectrum of the $^3F_2$ multiplet of the C_{4v} centre of CaF_2:0.05%Tm^{3+}, monitoring the $A_1 \rightarrow Z_1$ fluorescence transition at 12572 cm^{-1}, for (YX), (YY) and (ZY) polarisation geometries. Transitions are identified by their lower and upper crystal-field level labels.

State	Energy (cm^{-1})	Irrep	Polarisation			
			$Z_1\gamma_3 \rightarrow C_i$	$Z_2\gamma_5 \rightarrow C_i$	$E_1\gamma_3 \rightarrow C_i$	$E_2\gamma_4 \rightarrow C_i$
C_1	15206	γ_4	π_{md}	σ	π_{md}	π
C_2	15365	γ_3	π	σ	π	π_{md}
C_3	15370	γ_5	σ_{md}	π	(σ)	σ
C_4	-	(γ_2)	-	-	-	-

Table 4.4 : Crystal-field levels of the $^3F_2$ multiplet for the CaF_2:Tm^{3+} C_{4v} centre.

Direct excitation of the $^3H_4$ multiplet

The absorption lines of the $^3H_4$ multiplet lie within the lasing range of the Ti:sapphire laser equipped with either short-wave or medium-wave optics sets. The 15 K and 60 K excitation spectra of the CaF_2:Tm^{3+} C_{4v} centre are shown in figure 4.14. The fluorescence transition monitored is the $A_1 \rightarrow Z_2$ transition at 12488 cm^{-1}. Scattered laser light from the crystal was masked so that the laser could be scanned over the detection frequency without requiring the spectrometer shutter to be closed. The corresponding $Z_2 \rightarrow A_1$ excitation transition can thus be seen in the 60 K spectrum, while only a very small peak due to scattered laser light is apparent at the same frequency in the 15 K spectrum. In the 15 K spectrum, absorption transitions to two $^3H_4$ multiplet levels are observed. As the $Z_1 \rightarrow A_1$ (12572 cm^{-1}) transition is a π allowed transition, the A_1 level must be a γ_3 irrep state. Polarisation ratios show that the $Z_1 \rightarrow A_2$ excitation transition is a σ polarised line and therefore associated with a γ_5 final state. From the 60 K spectrum, this is the A_2 state. In the 60 K spectrum, transitions from the Z_2 level to the A_1 and A_2 states is observed, and in addition another transition is seen at 12702.7 cm^{-1} to a third $^3H_4$ state, A_3. The A_3 state must be a singlet state other than a γ_3 state, otherwise it would have been observed in absorption from the ground state. In any case the $^3H_4$ multiplet should have only one γ_3 state, which has already been assigned to A_1. An assignment of this state to a γ_1 irrep is made purely on the basis of the crystal-field calculation performed in section 4.3.3. Another broad peak at 12993 cm^{-1} is observed at 60 K. This could be a hot-line transition from the Z_2 level, but this assignment must remain tentative considering the broadness of the transition. The $^3H_4$ multiplet assignments are thus

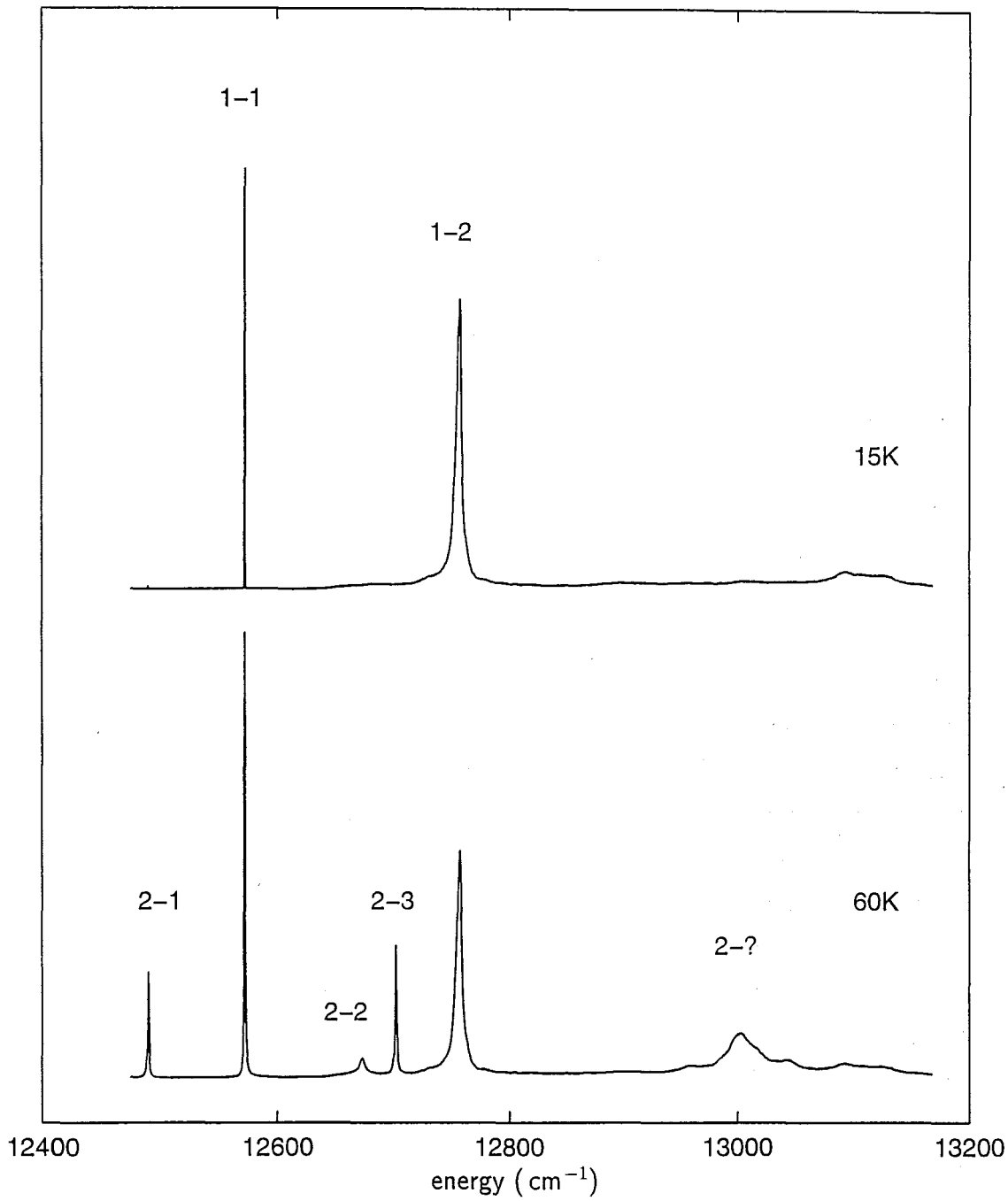

Figure 4.14 : 15 K and 60 K unpolarised excitation spectra of the $^3H_4$ multiplet of the C_{4v} centre of CaF_2:0.02%Tm^{3+}, monitoring the $A_1 \rightarrow Z_2$ fluorescence transition at 12488 cm^{-1}. Transitions are identified by their lower and upper crystal-field level labels; ? indicates an unassigned level.

summarised in table 4.5.

State	Energy (cm^{-1})	Irrep
A_1	12571.9	γ_3
A_2	12757.2	γ_5
A_3	12786.7	γ_1

Table 4.5 : Assigned crystal-field levels of the $^3H_4$ multiplet for the CaF_2:Tm^{3+} C_{4v} centre.

Fluorescence spectrum of the $^3H_4 \rightarrow {}^3H_6$ transitions

The polarised fluorescence spectrum of the $^3H_4 \rightarrow {}^3H_6$ transitions, obtained by pumping the $Z_1 \rightarrow B_2$ π-allowed transition is shown in figure 4.15. The $A_1 \rightarrow Z_1$ and $A_1 \rightarrow Z_2$ transitions are seen with their expected polarisation behaviour. Only one further transition is seen at 12121 cm^{-1}. This transition also has a clear π polarisation so could be to the second γ_3 level of the $^3H_6$ multiplet at 451 cm^{-1}. Alternatively it could be a phonon sideband associated with the $^3H_6$ ground multiplet. The fact that other phonon bands are not seen suggests that this is more probably an electronic level. Here it is labelled tentatively as the Z_5 level, on the basis that the crystal-field calculation has two other unobserved singlet states, of γ_1 and γ_4 symmetry, below it for the $^3H_6$ ground multiplet. The three assigned levels are summarised in table 4.6.

State	Energy (cm^{-1})	Irrep
Z_1	0.0	γ_3
Z_2	84.0	γ_5
Z_5	451	γ_3

Table 4.6 : Assigned crystal-field levels of the $^3H_6$ multiplet for the CaF_2:Tm^{3+} C_{4v} centre.

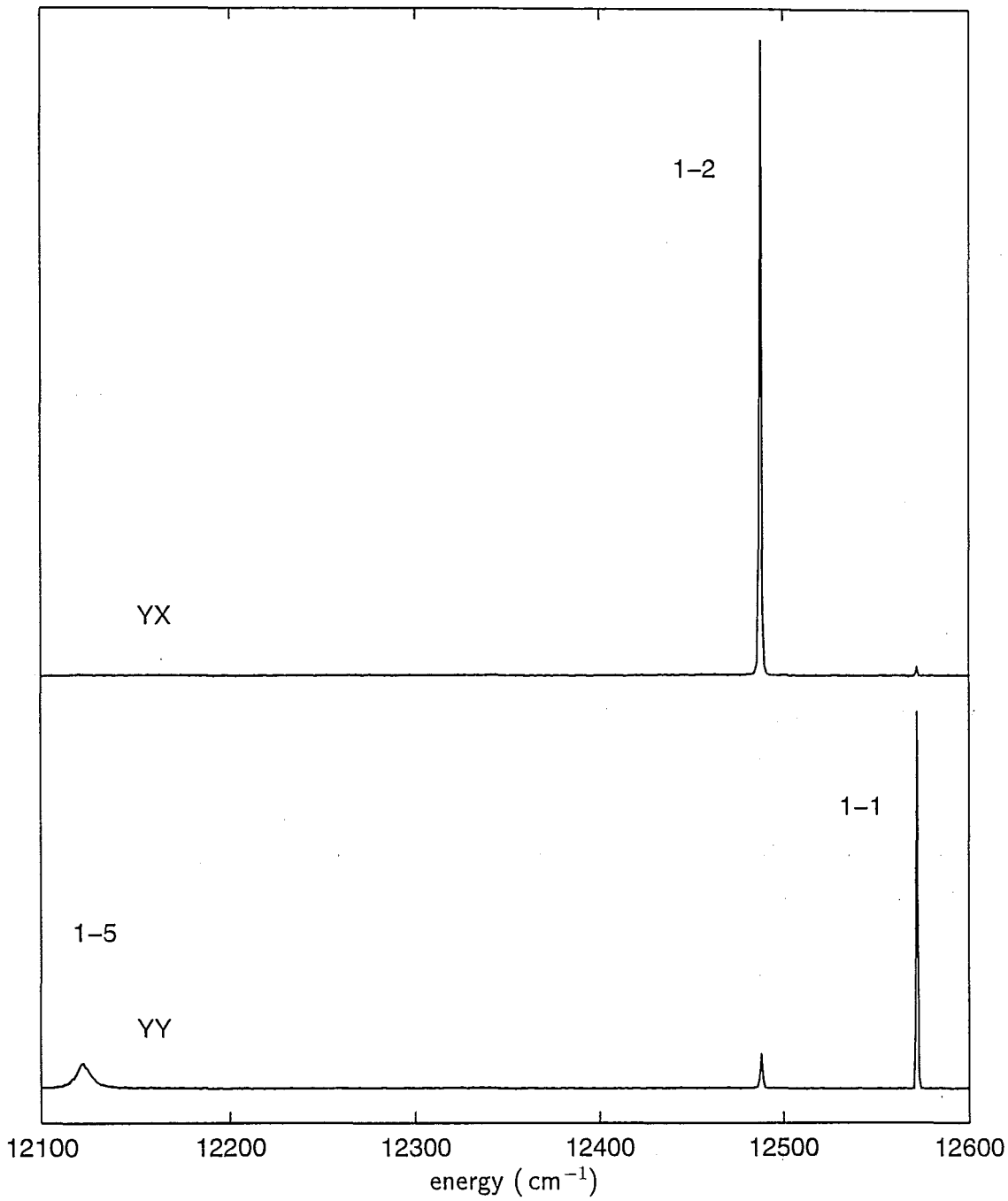

Figure 4.15 : 15 K polarised fluorescence spectrum of the $^3H_4 \rightarrow {}^3H_6$ transitions of the C_{4v} centre of CaF_2:0.05%Tm^{3+}, for pumping the $Z_1 \rightarrow B_2$ excitation transition at 14675 cm^{-1}, for (YX) and (YY) polarisation geometries. Transitions are identified by their upper and lower crystal-field level labels.

Fluorescence spectrum of the $^3F_3 \rightarrow {}^3H_6$ transitions

The fluorescence from the $^3F_3$ multiplet is partially quenched by non-radiative decay to the $^3H_4$ multiplet. However the $^3F_3$ multiplet has a γ_5 lowest level, so that all transitions from that level should be electric-dipole allowed. The fluorescence spectrum of the $^3F_3 \rightarrow {}^3H_6$ transitions, for pumping of the $Z_1 \rightarrow B_2$ π-allowed transition at 14675 cm^{-1}, is shown in figure 4.16. The $B_{1,2} \rightarrow Z_{1,2}$ transitions are all electric-dipole allowed. As the $B_2 \rightarrow Z_1$ is the pump transition it is not shown and would lie just off the right-hand edge of the spectrum; the other three have their expected polarisation behaviour. At least three broad σ-polarised transitions are also seen and would correspond to transitions to singlet electronic states or to phonon sidebands of the $^3H_6$ multiplet. The level at 451 cm^{-1} determined from the $^3H_4 \rightarrow {}^3H_6$ fluorescence spectrum is not seen here, which makes its assignment tentative. The $^3H_6$ multiplet has two further γ_5 levels which have not yet been assigned, which should show up as π-polarised transitions. The absence of any π-polarised transitions or a transition to a state at 451 cm^{-1} suggests the observed broad lines are not purely electronic transitions.

Direct excitation of the $^1G_4$ multiplet

The $^1G_4$ multiplet of Tm^{3+} lies within the tuning range of the coumarin 460 dye laser. The site-selective excitation spectrum of this multiplet for the C_{4v} centre is shown in figure 4.17. The fluorescence transition monitored is the π-allowed transition at 15345 cm^{-1}, which will be identified from the fluorescence and upconversion spectra as the $D_1 \rightarrow Y_1$ transition. The three excitation lines seen are polarised σ, π and σ respectively and the corresponding $^1G_4$ multiplet states can therefore be assigned as γ_5(21302.4 cm^{-1}), γ_3(21549.4 cm^{-1}) and γ_5(21633.6 cm^{-1}) irreps. The lowest transition at 21302.4 cm^{-1} is not seen in the fluorescence spectrum, hence there must be at least one lower level in the $^1G_4$ multiplet whose absorption transition from the γ_3 ground state is forbidden. The excitation spectrum at 60 K is shown in figure 4.18. Several new lines appear, corresponding to transitions from the $Z_2\gamma_5$ state. We see new transitions at 21218 cm^{-1} and 21465 cm^{-1} to the previously seen γ_5 and γ_3 levels (the transition from Z_2 to the second γ_5 state overlaps the $Z_1 \rightarrow D_4\gamma_3$ transition at 21549 cm^{-1}).

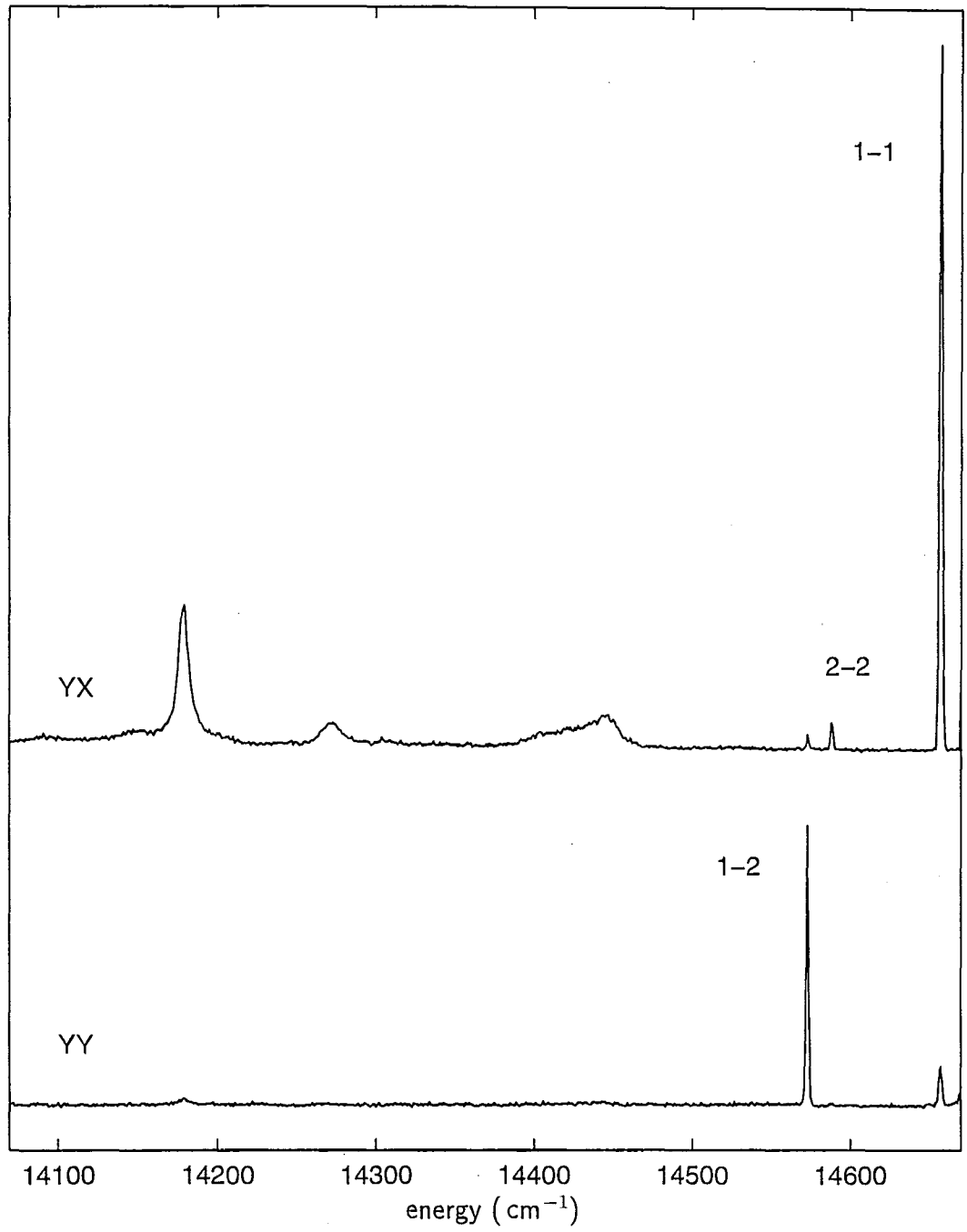

Figure 4.16 : 15 K polarised fluorescence spectrum of the $^3F_3 \rightarrow {}^3H_6$ transitions of the C_{4v} centre of CaF_2:0.05%Tm^{3+}, pumping the $Z_1 \rightarrow B_2$ transition at 14675 cm^{-1}, for (YX) and (YY) polarisation geometries. Transitions are identified by their upper and lower crystal-field level labels.

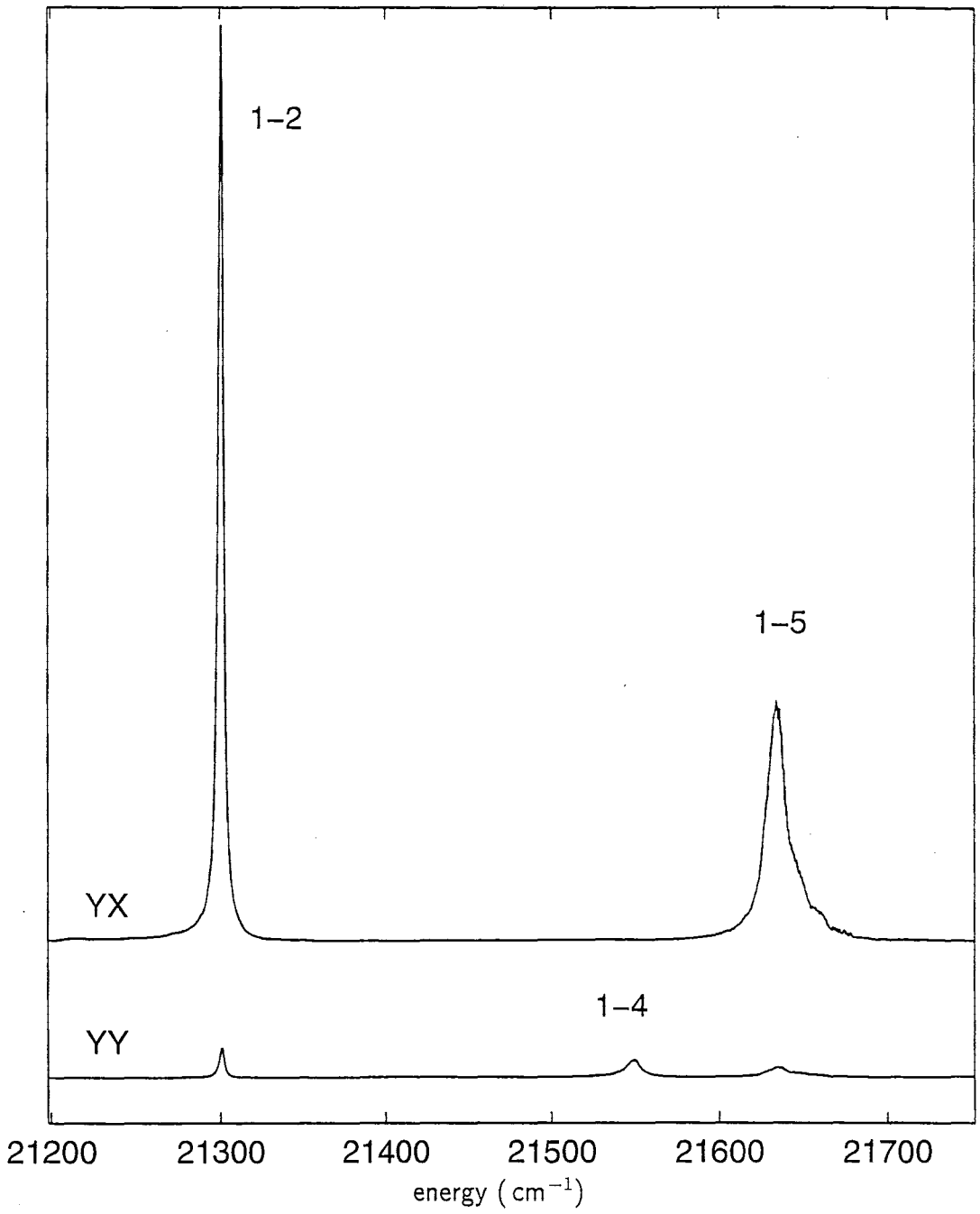

Figure 4.17 : 15 K polarised excitation spectrum of the $^1G_4$ multiplet of the C_{4v} centre of CaF_2:0.05%Tm^{3+}, monitoring the $D_1 \rightarrow Y_1$ transition at 15345 cm^{-1}, for (YX) and (YY) polarisation geometries. Transitions are identified by their lower and upper crystal-field level labels.

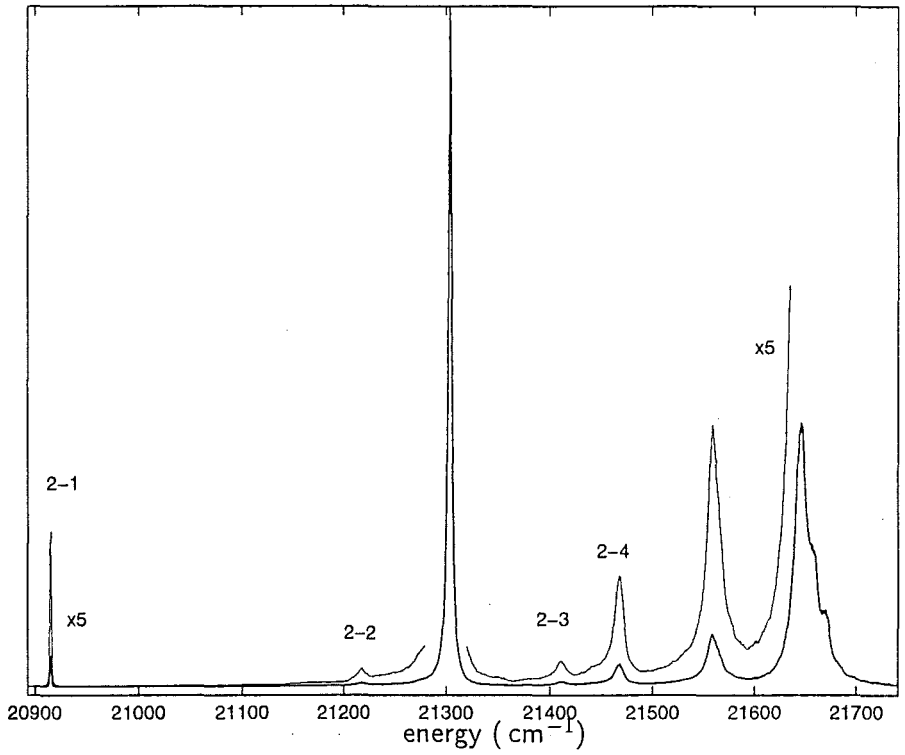

Figure 4.18 : 60 K excitation spectrum of the $^1G_4$ multiplet of the C_{4v} centre of CaF_2:0.05%Tm^{3+}, monitoring the $D_1 \rightarrow Y_1$ transition at 15345 cm^{-1}. "Hot-line" transitions only are identified by lower and upper crystal-field level labels.

In addition we see two other new lines. The lowest line is at 20918 cm^{-1}, indicating a $^1G_4$ multiplet level at 21002 cm^{-1} and the second new line is at 21408 cm^{-1}, indicating a $^1G_4$ multiplet level at 21492 cm^{-1}. Both of these states must be singlets other than γ_3 to have no absorption transitions from the γ_3 ground state.

Fluorescence spectrum of the $^1G_4 \rightarrow {}^3H_6$ transitions

The 15 K $^1G_4 \rightarrow {}^3H_6$ fluorescence spectrum for pumping the 21302.4 cm^{-1} σ transition, figure 4.19, has only one sharp transition. This transition at 20918 cm^{-1} is the same one seen in the 60 K excitation spectrum which indicates that this is the $D_1 \rightarrow Z_2$ transition, with the D_1 level at 21002 cm^{-1}. Again, there are several broad transitions which cannot be unambiguously assigned to electronic levels of the $^3H_6$ multiplet.

Fluorescence spectrum of the $^1G_4 \rightarrow {}^3F_4$ transitions

The 15 K $^1G_4 \rightarrow {}^3F_4$ fluorescence spectrum is given in figure 4.20. The pump transition is again the σ-allowed $Z_1 \rightarrow D_2$ transition at 21302.4 cm^{-1}. Five $^1G_4 \rightarrow {}^3F_4$ transitions are observed, polarised π, σ, π_{md}, σ and π respectively. This allows the determination of the irrep label of the D_1 state. The $^3F_4$ free-ion multiplet decomposes into the C_{4v} irreps $2\gamma_1 + \gamma_2 + \gamma_3 + \gamma_4 + 2\gamma_5$. The C_{4v} selection rules of table 2.5 therefore show that the polarisations of the observed transitions can only be accounted for by the D_1 emitting level being a γ_1 state. This then determines four of the $^3F_4$ multiplet states as γ_1(5658.0 cm^{-1}), γ_5(5857.4 cm^{-1}), γ_2(5893.9 cm^{-1}) and γ_5(6082.1 cm^{-1}).

The remaining γ_3 and γ_4 levels of $^3F_4$ multiplet are identified from the $^1D_2 \rightarrow {}^3F_4$ upconversion-fluorescence spectrum given later and all the $^3F_4$ state assignments are listed in table 4.9.

Fluorescence spectrum of the $^1G_4 \rightarrow {}^3H_5$ transitions

The $^1G_4 \rightarrow {}^3H_5$ fluorescence spectrum overlaps the $^3H_4 \rightarrow {}^3H_6$ fluorescence spectrum region. Upon pumping the $^1G_4$ multiplet, one of the possible decay paths is via the

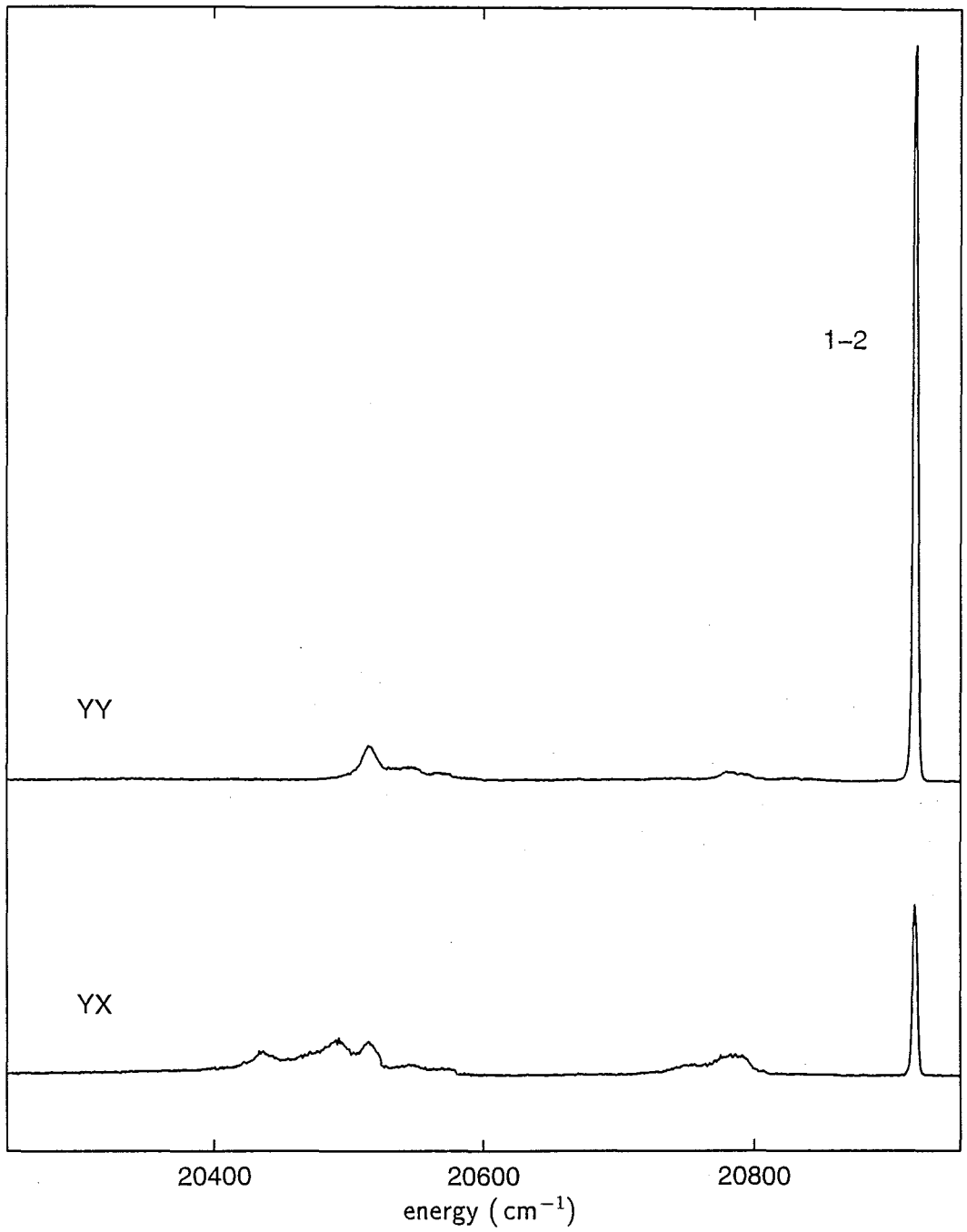

Figure 4.19 : 15 K polarised fluorescence spectrum of the $^1G_4 \rightarrow {}^3H_6$ transitions of the C_{4v} centre of CaF_2:0.05%Tm^{3+} for pumping the $Z_1 \rightarrow D_2$ excitation transition at 21302.4 cm^{-1}, for (YX) and (YY) polarisation geometries. The $D_1 \rightarrow Z_2$ transition is identified.

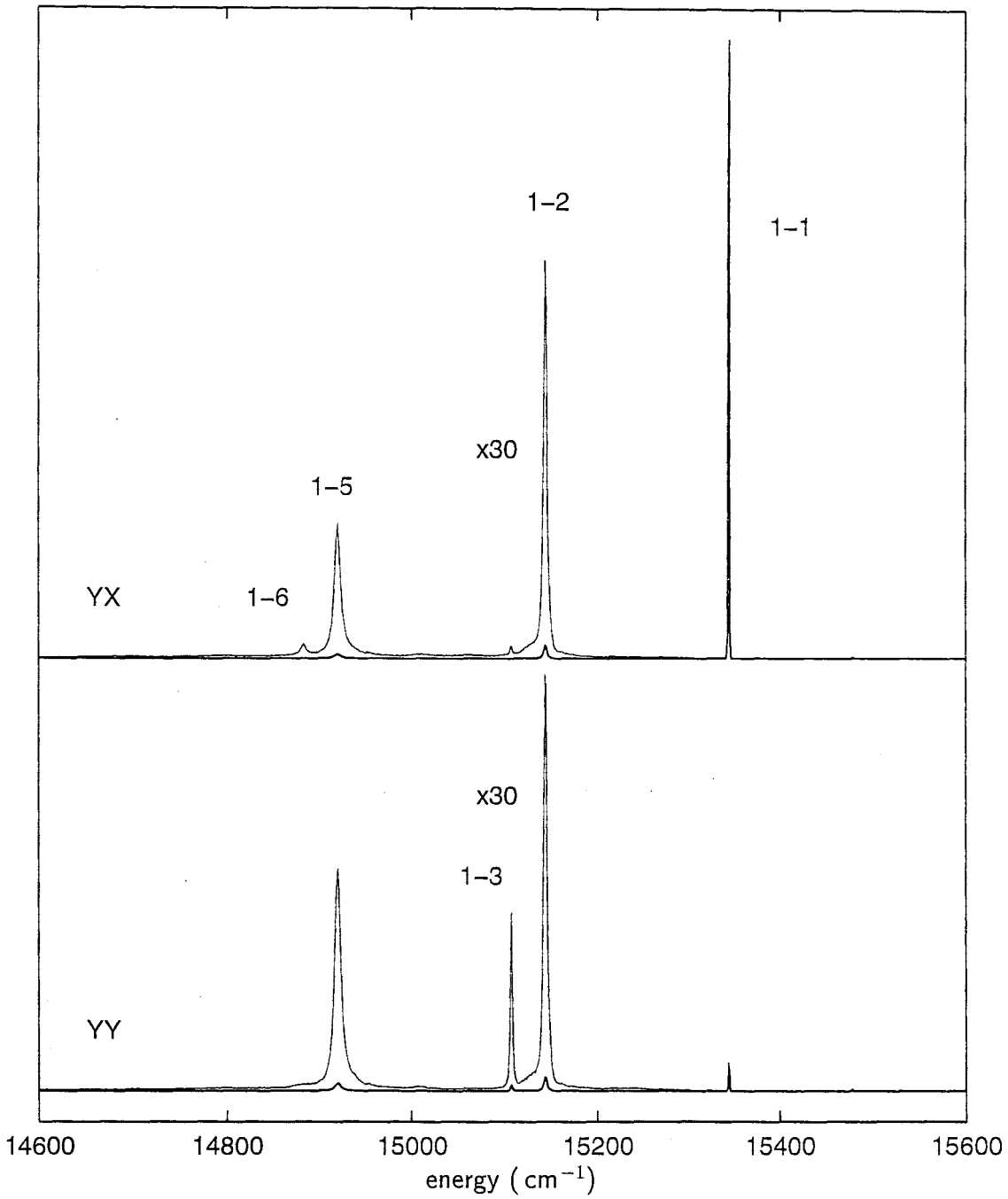

Figure 4.20 : 15 K polarised fluorescence spectrum of the $^1G_4 \rightarrow {}^3F_4$ transitions of the C_{4v} centre of CaF_2:0.05%Tm^{3+} for pumping the $Z_1 \rightarrow D_2$ excitation transition at 21302.4 cm^{-1}, for (YX) and (YY) polarisation geometries. Transitions are identified by their upper and lower crystal-field level labels.

$^3H_4$ multiplet, so that the lines of both sets of transitions appear in the spectrum of figure 4.21.

The lines associated with the $^3H_4 \rightarrow {}^3H_6$ transitions have already been identified from the spectrum of figure 4.15 and are marked with a * in figure 4.21, while the $^1G_4 \rightarrow {}^3H_5$ transitions are identified by their numerical labels. The two sets of transitions could also be distinguished by examining the fluorescence-decay transients of each line (section 4.3.4).

The three remaining lines corresponding to $^1G_4 \rightarrow {}^3H_5$ transitions all have polarisation ratios indicative of at least partial magnetic-dipole character. This is understandable since the $^1G_4$ multiplet has a significant admixture of the $^3H_4$ wavefunction through the spin-orbit interaction (table 2.1), which makes the $^1G_4 \rightarrow {}^3H_5$ inter-multiplet transition magnetic-dipole allowed. The three transitions have respective polarisations σ_{md}, π_{md} and σ_{md}, indicating transitions from the $D_1\gamma_1$ state to γ_5, γ_2 and γ_5 states of the $^3H_5$ multiplet at 8411.7 cm^{-1}, 8472.1 cm^{-1} and 8694.1 cm^{-1}, respectively. One further level can be identified from the $^1D_2 \rightarrow {}^3H_5$ upconversion-fluorescence spectrum; the assignments are summarised in table 4.10.

4.3.2 Upconversion Fluorescence Spectroscopy

Upconversion fluorescence from both C_{4v} and C_{3v} single ion centres has been observed from both the $^1G_4$ and $^1D_2$ multiplets upon pumping excited-state absorption transitions in the region of 650 nm with rhodamine 640 dye laser. The broadband upconversion-excitation spectrum of CaF_2:0.02%Tm^{3+} (figure 4.22) was obtained by monitoring both blue ($^1G_4 \rightarrow {}^3H_6$) and violet ($^1D_2 \rightarrow {}^3F_4$) upconversion fluorescence together by using broadband glass filters and setting the spectrometer to zero-order. Lines associated with upconversion to the $^1G_4$ and $^1D_2$ multiplets of the C_{4v} and C_{3v} centres, identified by their fluorescence spectra, are labelled in the figure. Several other centres are apparent, including two with an order of magnitude greater upconversion efficiency than the identified centres. Such centres are likely to involve clusters of Tm^{3+} ions which would show enhanced upconversion efficiencies through energy transfer processes.

A discussion of the upconversion mechanism is included in chapter 5. It was found

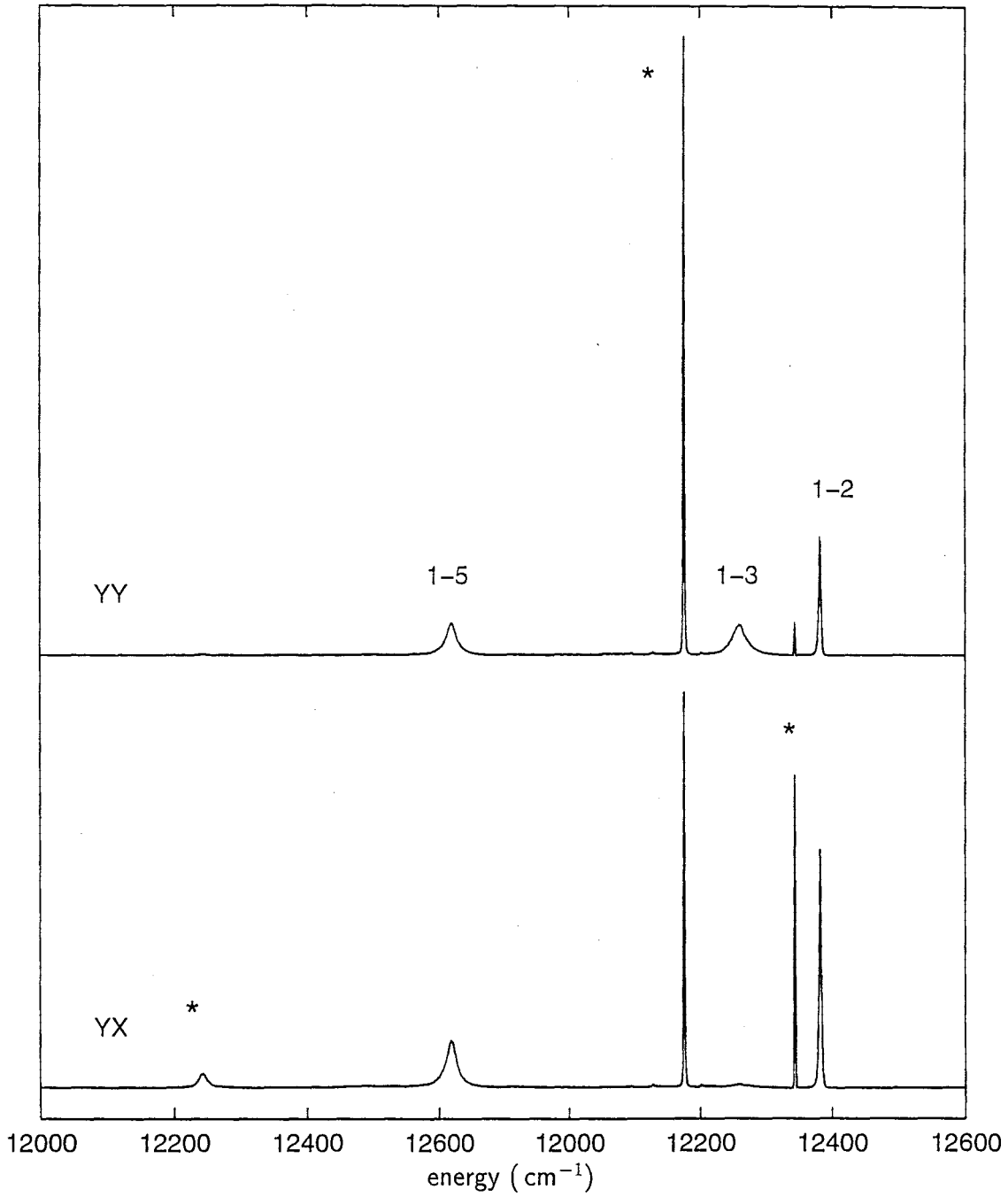

Figure 4.21 : 15 K polarised fluorescence spectrum of the $^1G_4 \rightarrow {}^3H_5$ and $^3H_4 \rightarrow {}^3H_6$ transitions of the C_{4v} centre of CaF_2:0.05%Tm^{3+}, for (YX) and (YY) polarisation geometries. The $^3H_4 \rightarrow {}^3H_6$ transitions are labelled * and the $^1G_4 \rightarrow {}^3H_5$ transitions are identified by upper and lower crystal-field level labels. The pump transition is the $Z_1 \rightarrow D_2$ excitation transition at 21302.4 cm^{-1}.

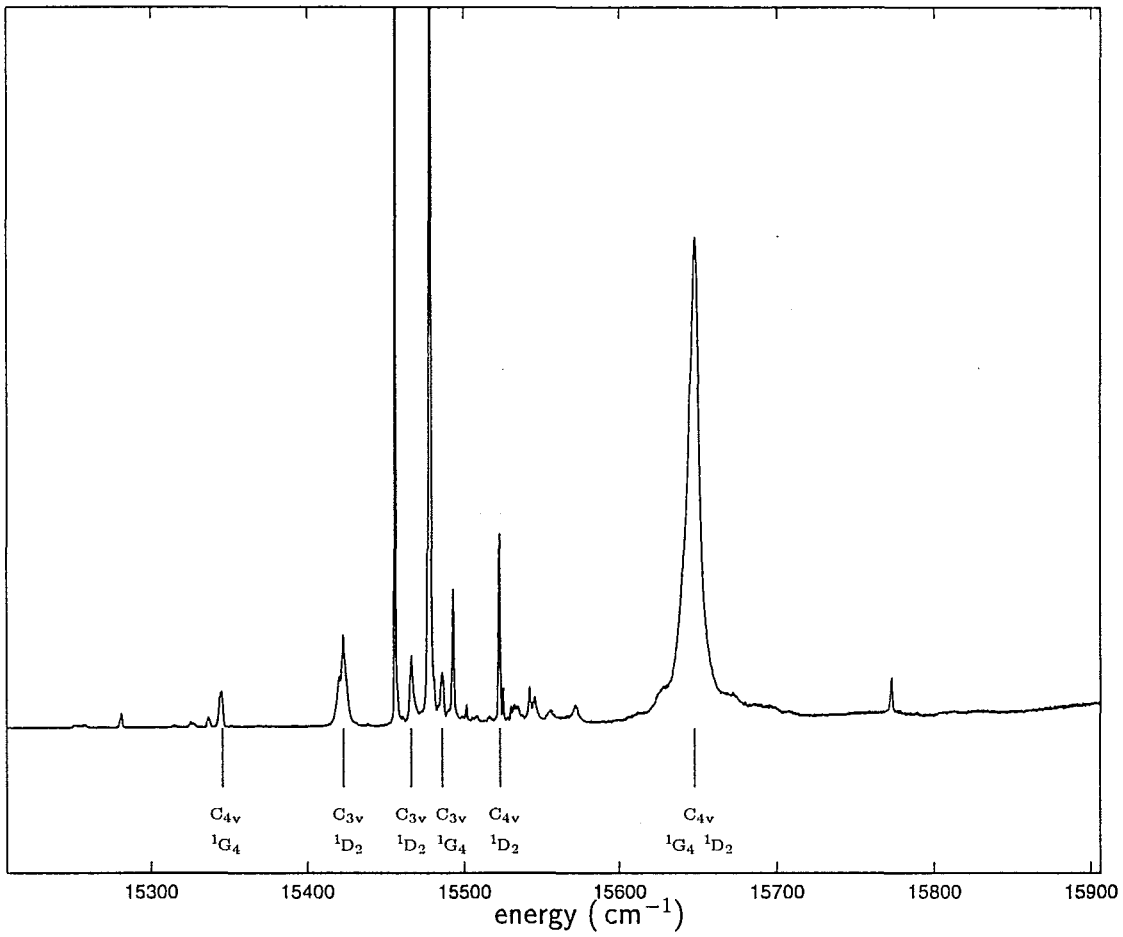

Figure 4.22 : 15 K broadband upconversion-excitation spectrum of CaF_2:0.02%Tm^{3+}, monitoring all upconversion fluorescence from the $^1G_4$ and $^1D_2$ multiplets. Transitions assigned to the C_{4v} and C_{3v} centres are identified.

that the C_{4v}-centre upconversion fluorescence intensity increased with increasing temperature. For some of the weak inter-multiplet transitions, 45 K polarised spectra are presented here instead of the usual 15 K, in order to provide a better signal-to-noise ratio. For these, some of the sharper lines will be a little broader, and there will be enhanced emission from the thermally populated E_2 state.

Excitation of the $^1G_4$ multiplet by Excited State Absorption

The excited-state $^3F_4 \rightarrow {}^1G_4$ excitation spectrum is shown in figure 4.23. The fluorescence transition monitored is the $D_1 \rightarrow Z_2$ transition at 20918 cm^{-1} seen in figure 4.19. Several excitation transitions between 15450–15620 cm^{-1} are not associated with the C_{4v} centre. The background spectrum, obtained by detuning the spectrometer slightly from the $D_1 \rightarrow Z_2$ transition, depicts those lines associated with other centres. The $^1G_4 \rightarrow {}^3H_6$ fluorescence spectrum obtained upon exciting one of the C_{4v} upconversion lines is identical to that obtained for direct pumping of the $^1G_4$ multiplet (figure 4.19), but at much lower intensity. Good $^1G_4 \rightarrow {}^3F_4$ and $^1G_4 \rightarrow {}^3H_5$ fluorescence spectra could not be obtained at low temperature, due to their much lower intensity.

Four $^3F_4 \rightarrow {}^1G_4$ excitation transitions are observed, polarised π, σ, π_{md} and σ respectively. The lowest (π) transition at 15345 cm^{-1} corresponds to the transition seen in the $^1G_4 \rightarrow {}^3F_4$ fluorescence spectrum, so must be the $Y_1 \rightarrow D_1$ transition. Having established the Y_1 state and energy as $\gamma_1(5658.0\,cm^{-1})$, the two σ excitation transitions are determined to be transitions to the γ_5 states previously observed in excitation from the $^3H_6$ multiplet (figure 4.17). The π_{md} transition is determined to be to a γ_2 state at 21491.5 cm^{-1}, also seen in excitation from the Z_2 level, but not previously assigned as an irrep. The assigned states of the $^1G_4$ multiplet are summarised in table 4.7.

Two weak transitions appear which populate the $^1G_4$ multiplet of the C_{4v} centre, but do not correspond to any $^3F_4 \rightarrow {}^1G_4$ transitions. The line marked † at 15520 cm^{-1} corresponds to the $A_1 \rightarrow E_1$ transition which produces fluorescence from the $^1D_2$ multiplet. The low strength of this line indicates that the $^1D_2 \rightarrow {}^1G_4$ decay path is inefficient. The line marked * at 15365 cm^{-1} corresponds to the $Z_1 \rightarrow C_2$ ground-state absorption of the $^3F_2$ multiplet. This is the only ground-state absorption transition

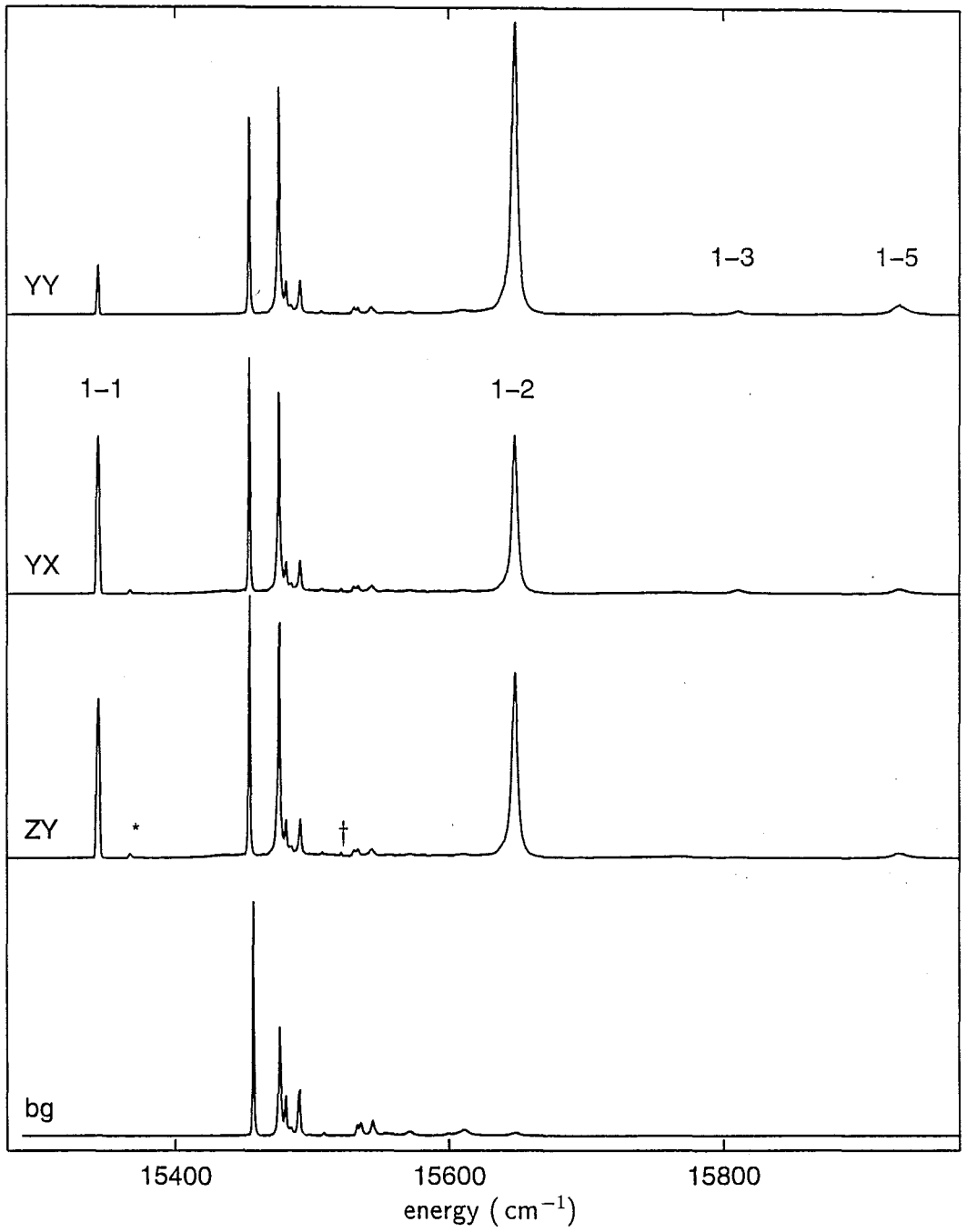

Figure 4.23 : 15 K polarised excited-state excitation spectrum of the $^3F_4 \rightarrow {}^1G_4$ transitions of the C_{4v} centre of CaF_2:0.05%Tm^{3+}, monitoring the $D_1 \rightarrow Z_2$ fluorescence transition at 20918 cm^{-1}, for (YY), (YX) and (ZY) polarisation geometries. The fourth spectrum is a background spectrum (bg) with the spectrometer detuned from the C_{4v}-centre fluorescence line. C_{4v}-centre transitions are identified by lower and upper crystal-field level labels. * is the $Z_1 \rightarrow C_2$ GSA and † the $A_1 \rightarrow E_1$ ESA excitation transition.

State	Energy (cm^{-1})	Irrep	Polarisation	
			$Z_1\gamma_3 \rightarrow D_i$	$Y_1\gamma_1 \rightarrow B_i$
D_1	21002.1	γ_1	-	π
D_2	21302.4	γ_5	σ	σ
D_3	21491.5	γ_2	-	π_{md}
D_4	21549.4	γ_3	π	-
D_5	21633.6	γ_5	σ	σ
D_6	-	(γ_4)	-	-
D_7	-	(γ_1)	-	-

Table 4.7 : Crystal-field levels of the $^1G_4$ multiplet for the CaF_2:Tm^{3+} C_{4v} centre.

which has been observed to produce upconversion fluorescence in CaF_2:Tm^{3+}.

Excitation of the $^1D_2$ multiplet by Excited State Absorption

The excited-state $^3H_4 \rightarrow {}^1D_2$ excitation spectrum is shown in figure 4.24. The fluorescence transition monitored is the π allowed $E_1 \rightarrow B_2$ transition at 13415 cm^{-1}. The three excitation transitions are polarised π, π_{md} and σ respectively. As the A_1 state is a γ_3 state at 12571.9 cm^{-1}, this yields the assignment of the γ_3, γ_4 and γ_5 states of $^1D_2$ as in table 4.8.

State	Energy (cm^{-1})	Irrep	Polarisation
			$A_1\gamma_3 \rightarrow E_i$
E_1	28089.8	γ_3	π
E_2	28105.7	γ_4	π_{md}
E_3	28218.1	γ_5	σ
E_4	-	(γ_2)	-

Table 4.8 : Crystal-field levels of the $^1D_2$ multiplet for the CaF_2:Tm^{3+} C_{4v} centre.

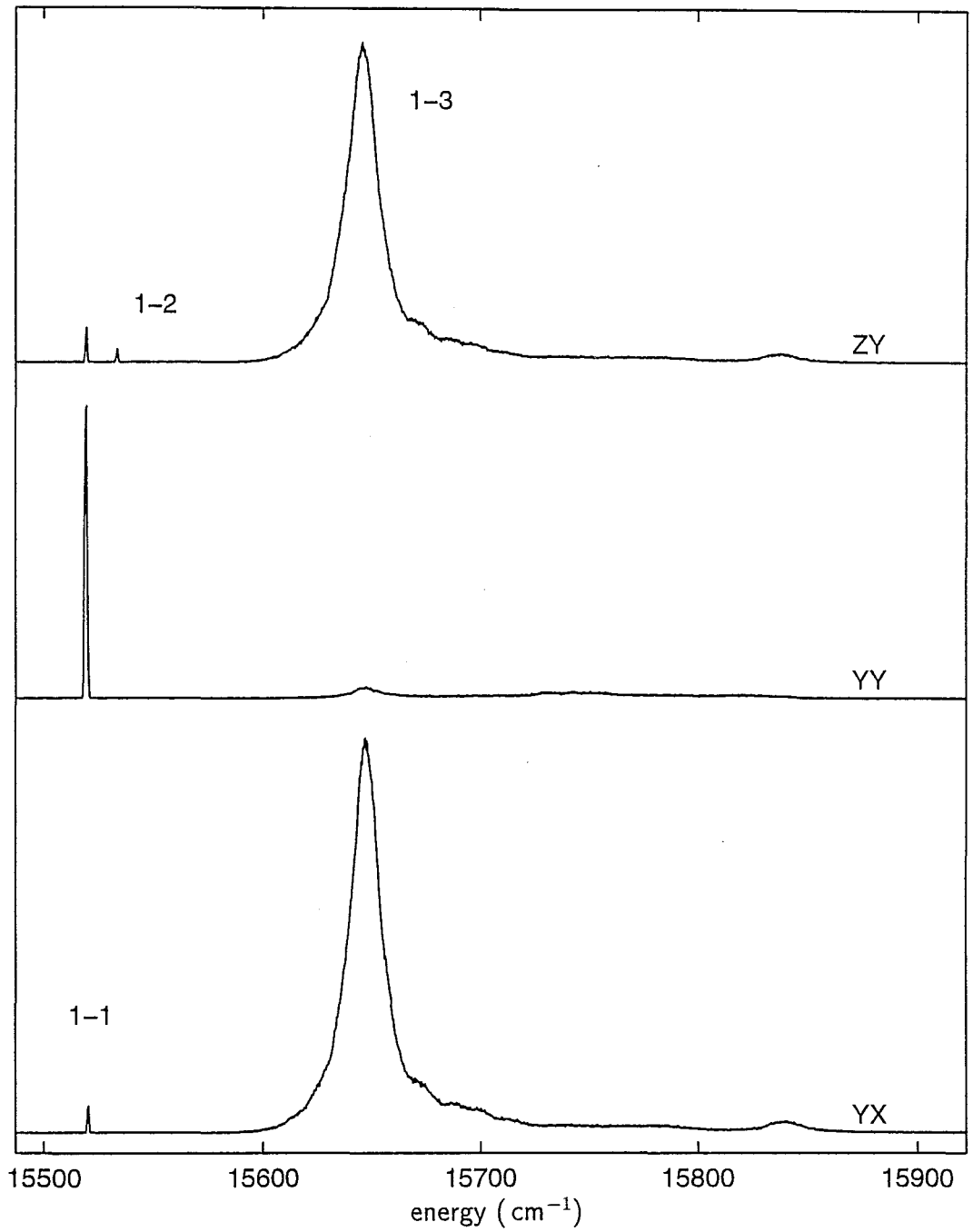

Figure 4.24 : 15 K polarised excited-state excitation spectrum of the $^3H_4 \rightarrow {}^1D_2$ transitions of the C_{4v} centre of CaF_2:0.05%Tm^{3+}, for (ZY), (YY) and (YX) polarisation geometries, monitoring the $E_1 \rightarrow B_2$ transition at 13415 cm^{-1}.Transitions are identified by their lower and upper crystal-field level labels.

Upconversion fluorescence spectrum of the $^1D_2 \rightarrow {}^3H_6$ transitions

In the 45 K fluorescence from the $^1D_2$ multiplet, both the E_1 and E_2 levels are thermally populated. The $^1D_2 \rightarrow {}^3H_6$ fluorescence spectrum is shown in figure 4.25. The excitation transition for this and all the following $^1D_2$ multiplet fluorescence spectra is the $A_1 \rightarrow E_1$ π-allowed transition at 15518 cm^{-1}. The three sharp transitions are the expected $E_1 \rightarrow Z_1(\pi)$, $E_2 \rightarrow Z_2(\sigma)$ and $E_1 \rightarrow Z_2(\sigma)$ transitions. The additional broad π-polarised transition at 27633 cm^{-1} matches the transition from E_1 to the previously tentatively assigned Z_5 level. A broad σ-polarised transition at 27614 cm^{-1} could be a transition to a γ_5 state of the $^3H_6$ multiplet, but would be expected to appear in transitions from both E_1 and E_2 levels. As this state is not seen in the $^3H_4 \rightarrow {}^3H_6$ spectrum, its origin remains uncertain.

Upconversion fluorescence spectrum of the $^1D_2 \rightarrow {}^3F_4$ transitions

The polarised $^1D_2 \rightarrow {}^3F_4$ fluorescence spectrum at 15 K is shown in figure 4.26. As with the $^1G_4$ multiplet upconversion-fluorescence spectra, cross pumping to other centres was inevitable, and the bottom spectrum of figure 4.26 is a background spectrum obtained by slightly detuning the laser from the excited-state absorption line. Any lines appearing as strongly in this background spectrum as in the on-resonance spectrum are not associated with the C_{4v} centre.

The three σ-polarised transitions correspond to transitions from the E_1 or E_2 states to the two known γ_5 states of the $^3F_4$ multiplet. We would expect in addition two π transitions corresponding to the $E_1(\gamma_3) \rightarrow Y(\gamma_3)$ and $E_2(\gamma_4) \rightarrow Y(\gamma_4)$ transitions. The fact that we see three π polarised lines is anomalous; the weakest and broadest of these three lines (at 22060 cm^{-1}, labelled * in figure 4.26) is attributed to a phonon sideband associated with the forbidden $E_1 \rightarrow Y_1$ transition. This would correspond to a 373 cm^{-1} phonon energy, which has been reported as a vibronic-sideband energy for CaF_2:Er^{3+} [87]. Vibronic-sideband peaks were not reported at energies which would correspond to either of the other two π-polarised lines.

The assignment of the two strong π-polarised lines at 21933 cm^{-1} and 22018 cm^{-1} can be determined from the temperature dependence of the transition intensities, since the emitting levels are expected to be different crystal-field levels of the $^1D_2$

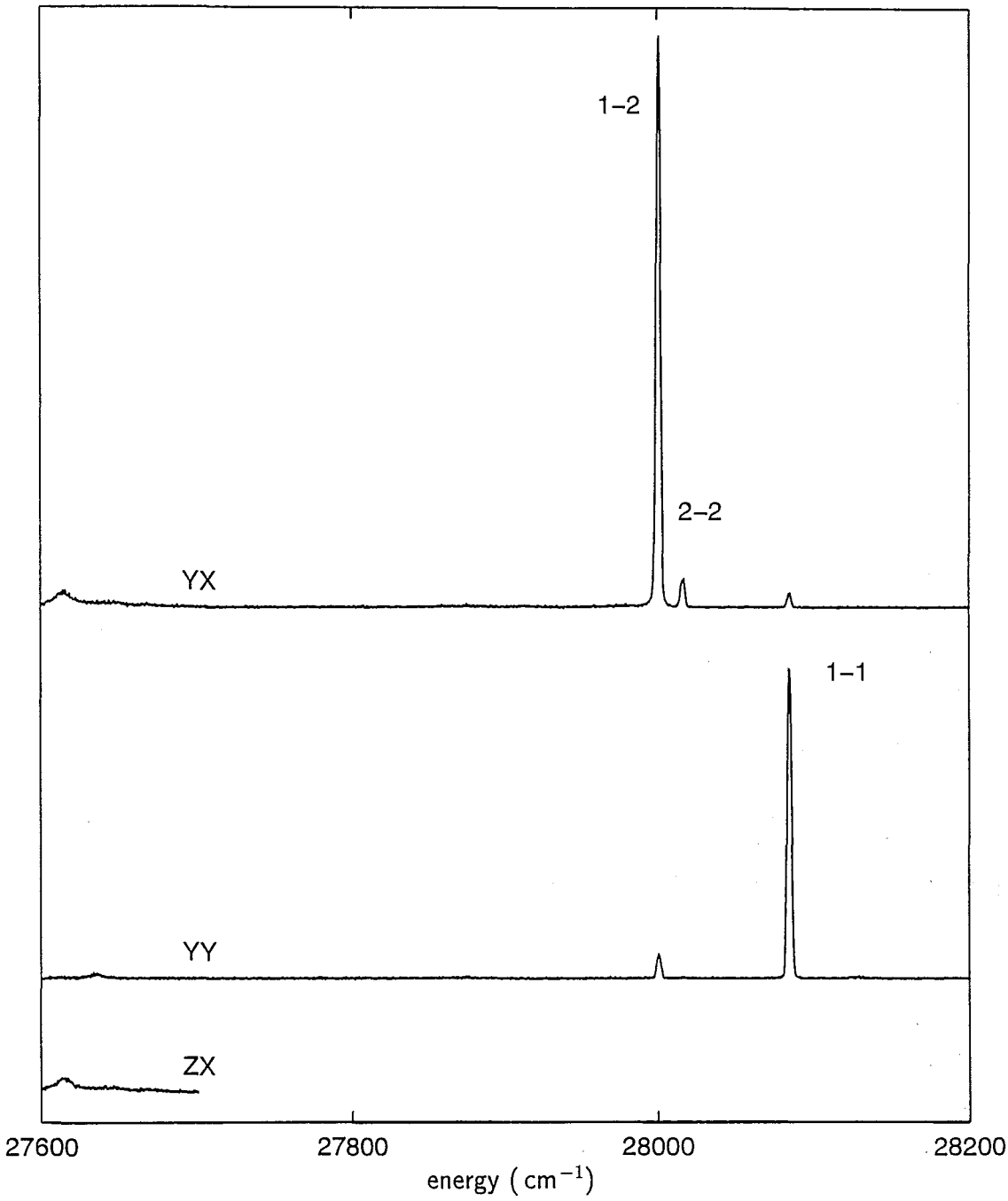

Figure 4.25 : 45 K polarised upconversion fluorescence spectrum of the $^1D_2 \rightarrow {}^3H_6$ transitions of the C_{4v} centre of CaF_2:0.05%Tm^{3+}, for (YX), (YY) and (ZX) polarisation geometries, for pumping the $A_1 \rightarrow E_1$ π-allowed transition at 15518 cm^{-1}. Transitions are identified by their upper and lower crystal-field level labels.

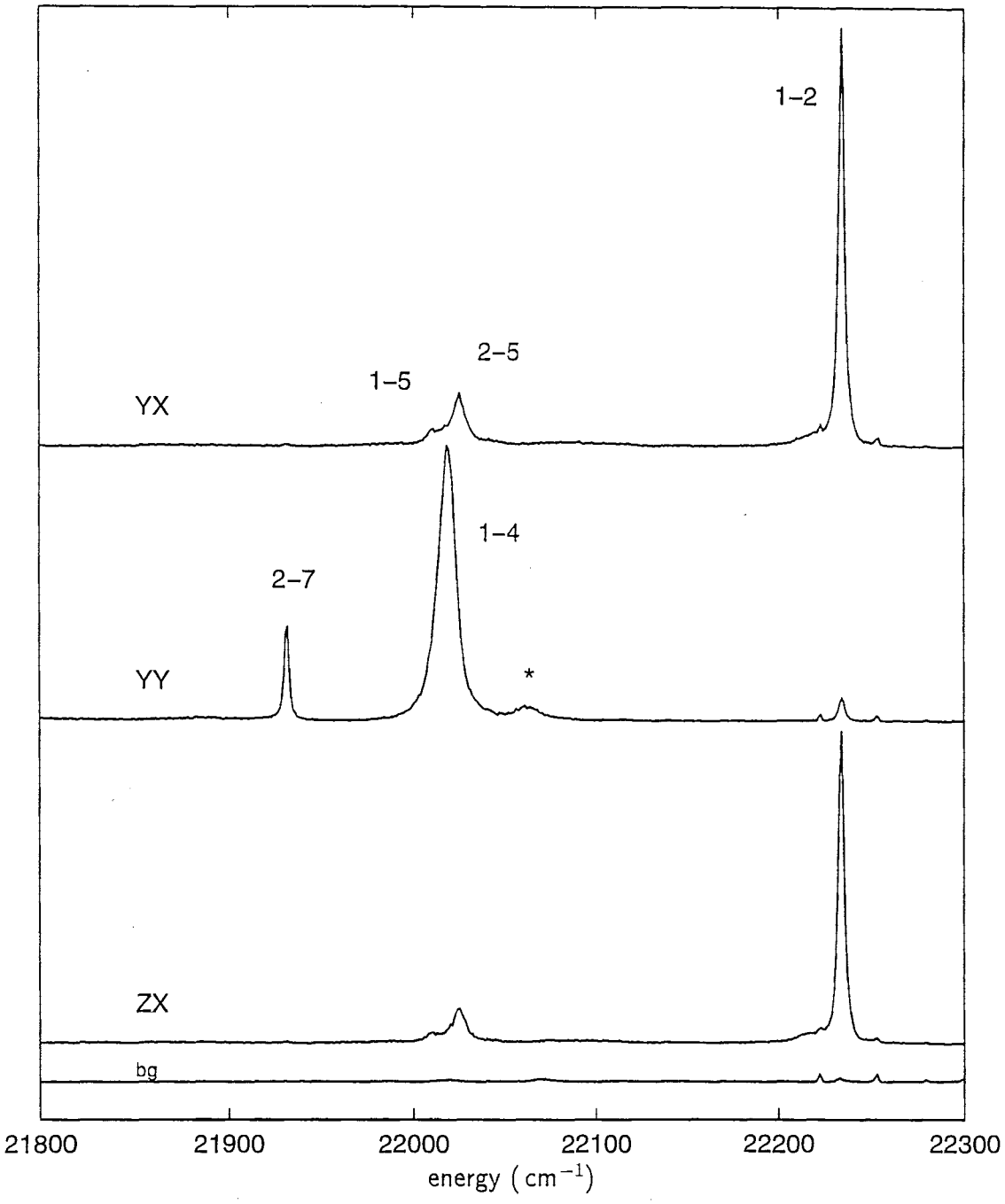

Figure 4.26 : 15 K polarised upconversion fluorescence spectrum of the $^1D_2 \rightarrow {}^3F_4$ transitions of the C_{4v} centre of CaF_2:0.05%Tm^{3+}, for (YX), (YY) and (ZX) polarisation geometries, for pumping the $A_1 \rightarrow E_1$ π-allowed transition at 15518 cm^{-1}. The fourth spectrum is a background spectrum (bg) with the laser detuned from the C_{4v}-centre excitation line. Transitions are identified by their upper and lower crystal-field level labels.

multiplet. When the temperature is increased to 45 K, the line at 21933 cm^{-1} increases in intensity relative to the line at 22018 cm^{-1}. The assignment therefore is to $E_1(\gamma_3) \rightarrow Y(\gamma_3)$ for the 22018 cm^{-1} transition and to $E_2(\gamma_4) \rightarrow Y(\gamma_4)$ for the 21933 cm^{-1} transition. The crystal-field levels of the $^3F_4$ multiplet have now been fully assigned, as in table 4.9.

State	Energy (cm^{-1})	Irrep	Polarisation		
			$D_1\gamma_1 \rightarrow Y_i$	$E_1\gamma_3 \rightarrow Y_i$	$E_2\gamma_4 \rightarrow Y_i$
Y_1	5658.0	γ_1	π	-	-
Y_2	5857.4	γ_5	σ	σ	σ
Y_3	5893.9	γ_2	π_{md}	-	-
Y_4	6069.7	γ_3	-	π	-
Y_5	6082.1	γ_5	σ	σ	σ
Y_6	6118.1	(γ_1)	π	-	-
Y_7	6173.1	(γ_4)	-	-	π

Table 4.9 : Crystal-field levels of the $^3F_4$ multiplet for the CaF_2:Tm^{3+} C_{4v} centre.

Upconversion fluorescence spectrum of the $^1D_2 \rightarrow {}^3H_5$ transitions

The 15 K polarised $^1D_2 \rightarrow {}^3H_5$ fluorescence spectrum is shown in figure 4.27. One π and two σ transitions are seen. The two σ transitions at 19678 cm^{-1} and 19698 cm^{-1} correspond to transitions from the E_1 and E_2 levels to the $^3H_5$ γ_5 level at 8411.7 cm^{-1}, previously identified from the $^1G_4 \rightarrow {}^3H_5$ fluorescence spectrum.

The π transition at 19763.5 cm^{-1} could correspond either to the $E_1(\gamma_3) \rightarrow X_i(\gamma_3)$ or to the $E_2(\gamma_4) \rightarrow X_i(\gamma_4)$ transition, which would put the terminating level either at 8326.3 $cm^{-1}(\gamma_3)$ or at 8342.2 $cm^{-1}(\gamma_4)$. The $^3H_5$ absorption spectrum (figure 4.3) has a strong absorption line at 8340 cm^{-1} but nothing near 8326 cm^{-1} which suggests that the X_1 state is a γ_4 at 8342.2 cm^{-1}. This is also consistent with crystal-field calculations. This assignment implies that the observed strong absorption line is purely magnetic-dipole in character, which is consistent with $^3H_6 \rightarrow {}^3H_5$ inter-multiplet transition being the only magnetic-dipole allowed absorption transition (section 2.5).

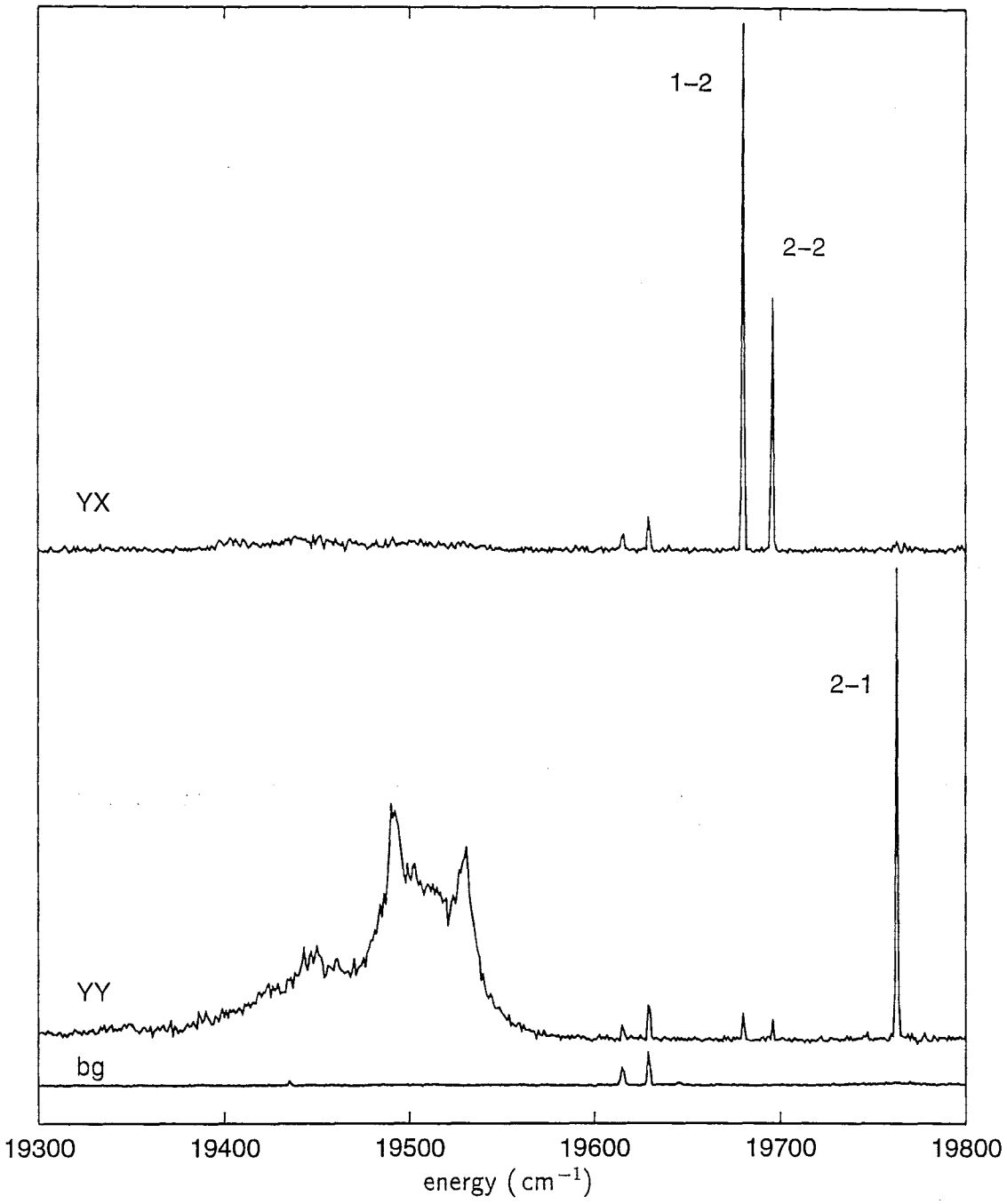

Figure 4.27 : 15 K polarised upconversion fluorescence spectrum of the $^1D_2 \rightarrow {}^3H_5$ transitions of the C_{4v} centre of CaF_2:0.05%Tm^{3+}, for (YX) and (YY) polarisation geometries, for pumping the $A_1 \rightarrow E_1$ π-allowed transition at 15518 cm^{-1}. The third spectrum is a background spectrum (bg) with the laser detuned from the C_{4v}-centre excitation line. Transitions are identified by their upper and lower crystal-field level labels.

A second π-polarised transition would be expected, corresponding to the $E_1\gamma_3 \rightarrow X\gamma_3$ transition; this may form part of the strong broad feature observed near 19500 cm^{-1}. The resulting $^3H_5$ crystal-field state assignments are given in table 4.10.

State	Energy (cm^{-1})	Irrep	Polarisation		
			$D_1\gamma_1 \rightarrow X_i$	$E_1\gamma_3 \rightarrow X_i$	$E_2\gamma_4 \rightarrow X_i$
X_1	8342.2	γ_4	-	-	π
X_2	8411.7	γ_5	σ_{md}	σ	σ
X_3	8472.1	γ_2	π_{md}	-	-
X_4	-	γ_3	-	-	-
X_5	8694.1	γ_5	σ_{md}	-	-
X_6	-	(γ_4)	-	-	-
X_7	-	(γ_1)	-	-	-
X_8	-	(γ_2)	-	-	-

Table 4.10 : Crystal-field levels of the $^3H_5$ multiplet for the CaF_2:Tm^{3+} C_{4v} centre.

Upconversion fluorescence spectrum of the $^1D_2 \rightarrow {}^3H_4$ transitions

The 45 K $^1D_2 \rightarrow {}^3H_4$ fluorescence spectrum is shown in figure 4.28. The pump transition in this case is the broad $A_1 \rightarrow E_3$ excited-state absorption (ESA) line at 15650 cm^{-1}. Because this line overlaps the $Y_1 \rightarrow D_2$ ESA line of the same centre, the $^1G_4 \rightarrow {}^3F_4$ spectrum (labelled *, see figure 4.20) is superimposed on the $^1D_2 \rightarrow {}^3H_4$ spectrum. Three expected transitions, $E_1 \rightarrow A_1$, $E_2 \rightarrow A_2$ and $E_1 \rightarrow A_2$ are identified. Several lines due to cross pumping other centres are also present.

Upconversion fluorescence spectrum of the $^1D_2 \rightarrow {}^3F_3$ transitions

The 45 K $^1D_2 \rightarrow {}^3F_3$ upconversion fluorescence spectrum, shown in figure 4.29, has seven lines. All the states involved in this set of transitions have already been determined (tables 4.3 and 4.8), however the two highest energy lines, at 13447 cm^{-1} and 13431 cm^{-1}, have anomalous polarisation ratios.

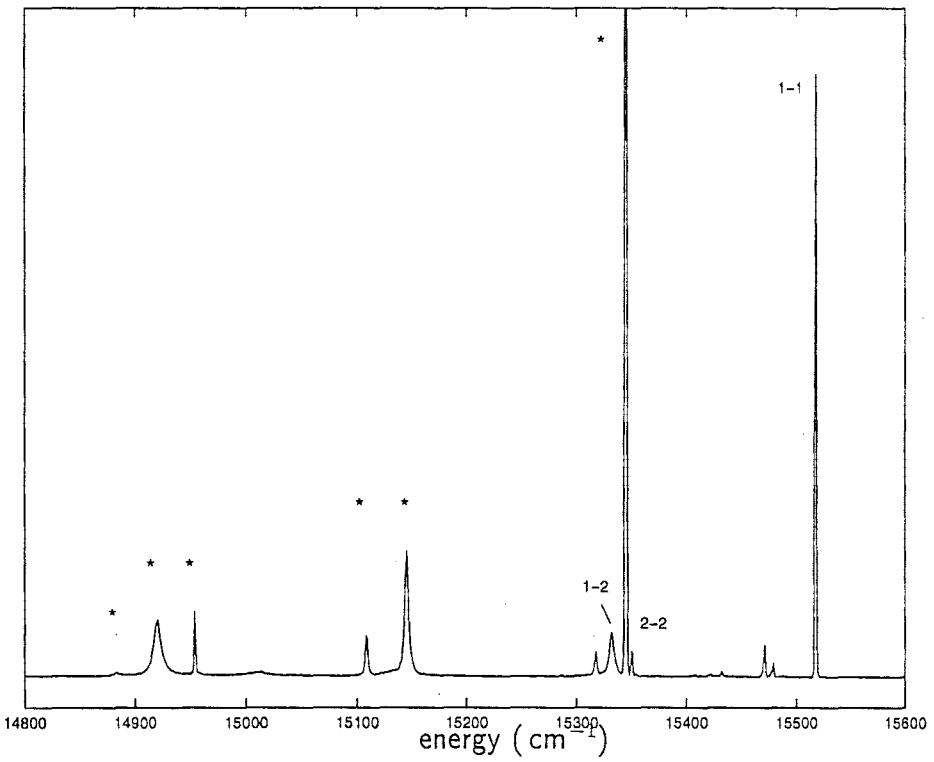

Figure 4.28 : 45 K unpolarised upconversion-fluorescence spectrum of the $^1D_2 \rightarrow {}^3H_4$ (numbered) and $^1G_4 \rightarrow {}^3F_4$ (labelled *) transitions of the C_{4v} centre of CaF_2:0.05%Tm^{3+} for pumping the $A_1 \rightarrow E_1$ π-allowed transition at 15518 cm^{-1}.

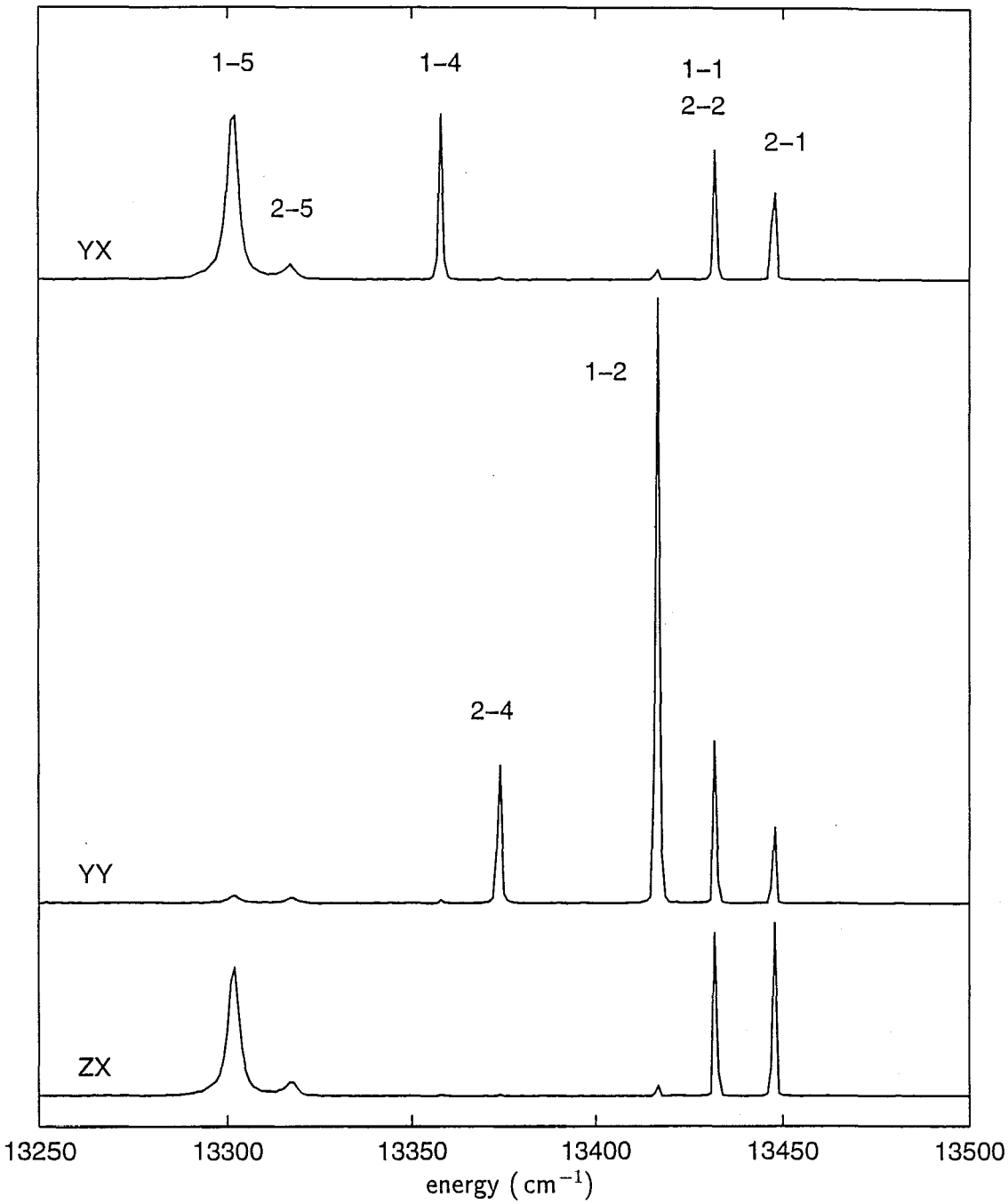

Figure 4.29 : 45 K polarised upconversion fluorescence spectrum of the $^1D_2 \rightarrow {}^3F_3$ transitions of the C_{4v} centre of CaF_2:0.05%Tm^{3+}, for (YX), (YY) and (ZX) polarisation geometries, for pumping the $A_1 \rightarrow E_1$ π-allowed transition at 15518 cm^{-1}. Transitions are identified by their upper and lower crystal-field level labels.

The 13447 cm^{-1} line is assigned to the $E_2\gamma_4 \rightarrow B_1\gamma_5$ transition which is expected to be σ allowed, giving YX:YY:ZX polarisation ratios of 1:0:1. The deviation from this could be explained by considering that σ_{md} allowed transitions have expected polarisation ratios of 0:1:1. Since this transition is both σ and σ_{md} allowed, similar contributions from both would yield polarisation ratios of 1:1:2, as observed. As the $^1D_2 \rightarrow {}^3F_3$ transition is magnetic-dipole allowed through spin-orbit mixing of the $^1D_2$ and $^3F_2$ multiplets (as illustrated by the strong π_{md} $E_1\gamma_3 \rightarrow B_4\gamma_4$ transition at 13357 cm^{-1}), this is reasonable.

The 13431 cm^{-1} transition is expected to be a superposition of two transitions, $E_1\gamma_3 \rightarrow B_1\gamma_5$ and $E_2\gamma_4 \rightarrow B_2\gamma_3$. These are expected to be σ and π_{md} allowed respectively, however any combination of these two transition polarisations should still have zero intensity in the YY configuration. Again, a σ_{md} component of the $E_1\gamma_3 \rightarrow B_1\gamma_5$ transition would be needed to explain the observed polarisation dependence.

The remaining lines have polarisation ratios corresponding to (from highest energy) π, π, π_{md}, σ and σ allowed transitions, as expected.

Upconversion fluorescence spectrum of the $^1D_2 \rightarrow {}^3F_2$ transitions

The 45 K $^1D_2 \rightarrow {}^3F_2$ upconversion fluorescence spectrum is shown in figure 4.30. As with the previous spectrum, the $^1D_2 \rightarrow {}^3F_2$ transition is magnetic-dipole allowed because of the spin-orbit admixing of the $^3F_2$ and $^1D_2$ multiplets. Again, all the states involved in this set of transitions have already been determined (tables 4.4 and 4.8). The $C_4\gamma_1$ state remains unassigned as it is not expected to appear in this spectrum, as the transitions from both the $E_1\gamma_3$ and $E_2\gamma_4$ levels to a γ_1 level are electric-dipole and magnetic-dipole forbidden. The remaining transitions have their expected polarisation dependences, included in table 4.4.

The C_2–C_3 level splitting is clearer in this spectrum than in the $^3F_2$ excitation spectrum of figure 4.13.

4.3.3 Crystal-Field Analysis for the C_{4v} Centre in CaF_2:Tm^{3+}

No crystal-field parametrisations of any single-Tm^{3+}-ion centres in CaF_2 or SrF_2 have been reported to date. It is of interest to compare the crystal-field parameters

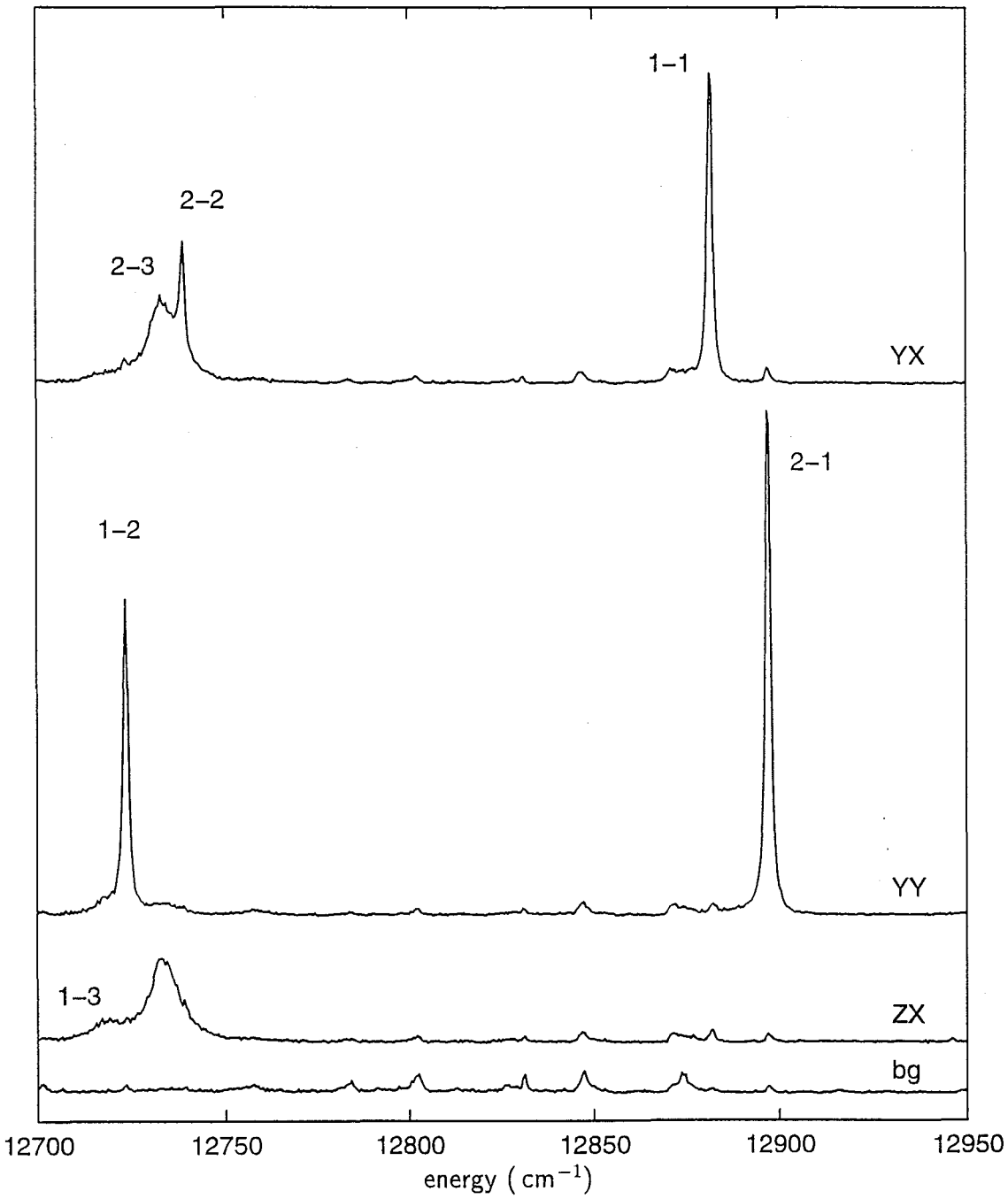

Figure 4.30 : 45 K polarised upconversion fluorescence spectrum of the $^1D_2 \rightarrow {}^3F_2$ transitions of the C_{4v} centre of CaF_2:0.05%Tm^{3+}, for (YX), (YY) and (ZX) polarisation geometries, for pumping the $A_1 \rightarrow E_1$ π-allowed transition at 15518 cm^{-1}. The fourth spectrum is a background spectrum (bg) with the laser detuned from the C_{4v}-centre excitation line. Transitions are identified by their upper and lower crystal-field level labels.

RE^{3+}	B^4_C	B^6_C	B^2_A	B^4_A	B^6_A	reference
Ce^{3+}	-2082	1127	906	692	569	[29, 89]
Pr^{3+}	-1841	904	838	586	411	[75, 89]
Nd^{3+}	-1602	837	813	585	613	[29, 33, 89]
Sm^{3+}	-1208	669	749	616	617	[88]
Eu^{3+}	-1217	682	703	437	564	[88]
Tb^{3+}	-1330	624	807	504	445	[66]
Ho^{3+}	-1075	559	678	345	420	[64]
Er^{3+}	-1172	505	608	409	403	[30]
Tm^{3+}	-1101	489	567	393	386	this work
Yb^{3+}	-682	523	378	306	230	[8]

Table 4.11 : Crystal-field parameters determined for several of the RE^{3+} ions in the C_{4v} centres of CaF_2.

for the C_{4v} centre with the parameters reported for other RE^{3+} ions. Such parameters have previously been reported for all of the trivalent lanthanide ions in the C_{4v} centre in CaF_2, with the exceptions of Pm^{3+} (radioactive), Gd^{3+} (half-filled shell, thus no first-order crystal-field splitting) and Tm^{3+}, while there is disagreement on crystal-field level assignments for Dy^{3+}. The most up-to-date parametrisations, converted to the parameters used here, are tabulated in table 4.11 with the CaF_2:Tm^{3+} parameters calculated here included. The data shows fairly systematic trends across the series.

The energy levels and irrep assignments found in sections 4.3 were fitted to the combined free-ion Hamiltonian (equation 2.1 of section 2.1) and crystal-field Hamiltonian (equation 2.2 of section 2.2), using the F-shell Empirical fitting package written by Dr Mike Reid of this department.

The minor free-ion interaction parameters (see section 2.1) were fixed at the values found for LaF_3:Tm^{3+} [14], listed in table 4.12. The free-ion parameters which have a greater effect—the electrostatic and spin-orbit parameters—and the five crystal-field parameters were varied simultaneously for the entire $4f^n$ configuration of Tm^{3+}, thus fully incorporating all intermediate-coupling and crystal-field J-mixing effects.

Parameter	Value (cm^{-1})	Parameter	Value (cm^{-1})
α	17.26	M^4	1.45
β	-624.5	P^2	695.0
γ	1820	P^4	521.3
M^0	3.81	P^6	347.5
M^2	2.13		

Table 4.12 : Minor free-ion interaction parameters, whose values were fixed at those found for LaF_3:Tm^{3+} [14] and were not varied in the crystal-field fit.

Parameter	Value (cm^{-1})	Parameter	Value (cm^{-1})
F^2	102249.9	B^2_A	567.0
F^4	71603.9	B^4_A	392.8
F^6	51401.8	B^6_A	385.5
ζ	2633.8	B^4_C	-1100.7
		B^6_C	489.0

Table 4.13 : Best-fit values of the free-ion and crystal-field parameters which were varied in the fit for the C_{4v} centre of CaF_2:Tm^{3+} .

The resulting best-fit values of these parameters are listed in table 4.13. The free-ion wavefunctions are given in table 4.14 and the measured and calculated crystal-field energies are given in table 4.15. With the 31 experimental energies and ten varied parameters (including a uniform-shift of the entire configuration), a standard deviation of 8.3 cm^{-1} was obtained.

Of the four infrared-absorption lines assigned to the C_{4v} centre in section 4.2, two of these did not split, and the other two had only partially resolvable structure when a 4 T magnetic field was applied parallel to the $\langle 100 \rangle$ crystal axis. The broad transition at 5854.9 cm^{-1}, assigned to the $Z_1 \rightarrow Y_2$ transition, showed further asymmetric broadening and its $g_{\|}$-value was estimated at 1.1 ± 0.5. The crystal-field fit here gives a calculated $g_{\|}$-value of 1.5, within the stated range.

The line at 6079.7 cm^{-1} was too broad to measure a splitting. The results of the

SLJ multiplet label	Calculated barycentre (cm^{-1})	Intermediate-coupled wavefunction
$^3H_6$	400	$0.9957\,\|^3H_6\rangle + 0.0921\,\|^1I_6\rangle$
$^3F_4$	6000	$0.7954\,\|^3F_4\rangle + 0.5374\,\|^1G_4\rangle - 0.2804\,\|^3H_4\rangle$
$^3H_5$	8600	$1.0000\,\|^3H_5\rangle$
$^3H_4$	12900	$0.7739\,\|^3H_4\rangle + 0.5185\,\|^3F_4\rangle - 0.3636\,\|^1G_4\rangle$
$^3F_3$	14700	$1.0000\,\|^3F_3\rangle$
$^3F_2$	15300	$0.8780\,\|^3F_2\rangle - 0.4579\,\|^1D_2\rangle - 0.1395\,\|^3P_2\rangle$
$^1G_4$	21500	$0.7609\,\|^1G_4\rangle + 0.5678\,\|^3H_4\rangle - 0.3140\,\|^3F_4\rangle$
$^1D_2$	28200	$0.6381\,\|^1D_2\rangle + 0.6361\,\|^3P_2\rangle + 0.4338\,\|^3F_2\rangle$
$^1I_6$	35200	$0.9957\,\|^1I_6\rangle - 0.0921\,\|^3H_6\rangle$
$^3P_0$	35700	$0.9692\,\|^3P_0\rangle - 0.2462\,\|^1S_0\rangle$
$^3P_1$	36600	$1.0000\,\|^3P_1\rangle$
$^3P_2$	38400	$0.7589\,\|^3P_2\rangle - 0.6190\,\|^1D_2\rangle - 0.2023\|^3F_2\rangle$
$^1S_0$	75000	$0.9692\,\|^1S_0\rangle + 0.2462\,\|^3P_0\rangle$

Table 4.14 : Tm^{3+} free-ion wavefunctions calculated from the CaF_2: Tm^{3+} C_{4v} centre data.

Multiplet/ C_{4v} irrep		Energies (cm^{-1}) measured	calculated
$^3H_6$	γ_3	0	5.6
	γ_5	84.0	94.3
	γ_1	-	236.9
	γ_4	-	402.2
	γ_3	-	465.9
	γ_2	-	488.9
	γ_5	-	496.7
	γ_4	-	555.9
	γ_1	-	562.7
	γ_5	-	690.0
$^3F_4$	γ_1	5658.0	5646.5
	γ_5	5857.4	5853.4
	γ_2	5893.9	5901.9
	γ_3	6069.7	6070.5
	γ_5	6082.1	6077.5
	γ_1	6118.1	6119.7
	γ_4	6173.1	6171.9
$^3H_5$	γ_4	8342.2	8337.9
	γ_5	8411.7	8408.1
	γ_2	8472.1	8472.0
	γ_3	-	8636.8
	γ_5	8694.1	8673.6
	γ_5	-	8697.4
	γ_1	-	8762.7
	γ_2	-	8780.9

Multiplet/ C_{4v} irrep		Energies (cm^{-1}) measured	calculated
$^3H_4$	γ_3	12571.9	12577.9
	γ_5	12757.2	12763.9
	γ_1	-	12804.7
	γ_2	-	12903.3
	γ_4	-	12984.8
	γ_1	-	13035.1
	γ_5	-	13095.8
$^3F_3$	γ_5	14659.4	14663.2
	γ_3	14674.7	14677.1
	γ_2	14720.9	14725.3
	γ_4	14732.7	14726.3
	γ_5	14789.3	14790.6
$^3F_2$	γ_4	15206	15213.5
	γ_3	15365	15364.4
	γ_5	15370	15368.6
	γ_1	-	15448.8
$^1G_4$	γ_1	21002.1	20995.0
	γ_5	21302.4	21300.3
	γ_2	21491.5	21498.9
	γ_3	21549.4	21549.3
	γ_5	21633.6	21638.4
	γ_4	-	21722.3
	γ_1	-	21730.8
$^1D_2$	γ_3	28089.8	28075.9
	γ_4	28105.7	28112.4
	γ_5	28218.1	28222.3
	γ_1	-	28253.4

Table 4.15 : Measured and calculated crystal-field energy levels for the CaF_2:Tm^{3+} C_{4v} centre.

laser-selective excitation study has two levels, a γ_3 singlet and a γ_5 doublet, both of which would have allowed transitions from the ground state which could correspond to this line. The absence of a splitting suggests that the γ_3 state has the stronger transition intensity.

In the $^3H_5$ multiplet absorption spectrum, the sharp line at 8341.5 cm^{-1} did not split, consistent with its assignment as the π_{md}-allowed $Z_1 \rightarrow X_1$ transition. The line at 8408.8 cm^{-1} split into three partially-resolved components at 4 T. This is consistent with the X_2 being a γ_5 doublet splitting into two for the C_4 subsite and remaining unsplit for the C_s subsite. Magnetic-field calculations suggests that the line corresponding to the C_s subsite is the highest energy of these three lines, so that the $g_{\|}$-value is somewhat smaller than that calculated in section 4.2.1 from the total splitting. The $g_{\|}$-value calculated from the lower two components is 0.34, however this is difficult to measure with the more intense transition of the C_s subsite distorting the position of the middle line, and is considerably larger than the calculated $g_{\|}$-value of 0.18. Given that the nominal resolution for these spectra is 0.25 cm^{-1} compared to the experimental splitting at 4 T of 0.6 cm^{-1}, such small g-values are difficult to measure reliably, especially when a third component is present.

The γ_5 B_1 level at 14659.4 cm^{-1} was observed in optical-absorption by Muto [67] and split in a magnetic field with a $g_{\|}$-value of 6.1. The calculated value obtained from this fit is $g_{\|} = 5.9$, in reasonable agreement with the measured value.

4.3.4 Fluorescence Lifetimes

Fluorescence lifetimes have not previously been reported for any single-ion centres in CaF_2:Tm^{3+}. All the transients displayed here are for sample concentrations of 0.05% (molar) of Tm^{3+}. No significant changes in the lifetimes were found for a sample of 0.02% Tm^{3+}.

The simple decay transients, where the emitting level is in the same multiplet as that being pumped, were fitted to single exponential decay curves of the form:

$$y = S + A\,e^{-t/\tau}$$

with τ the lifetime of the emitting state and S being the background signal level. In all cases, 256 scans were averaged to improve the signal-to-noise ratio. Decay

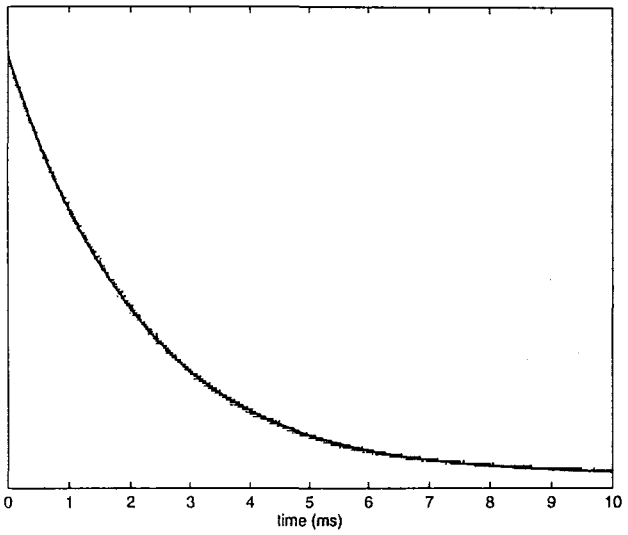

Figure 4.31 : 15 K fluorescence decay transient of the $^1G_4$ multiplet of the C_{4v} centre of CaF_2:0.05%Tm^{3+}, pumping the $Z_1 \rightarrow D_2$ excitation transition at 21302 cm^{-1} and monitoring the $D_1 \rightarrow Y_1$ fluorescence transition at 15345 cm^{-1}. The fitted curve gives a lifetime of 2.1 ms.

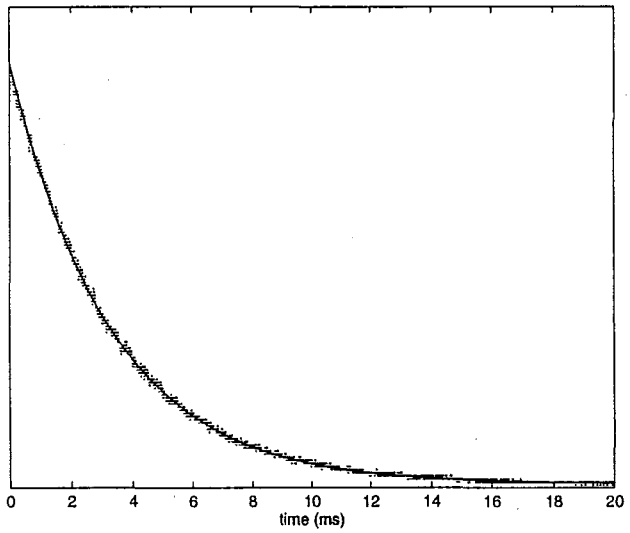

Figure 4.32 : 15 K fluorescence decay transient of the $^3H_4$ multiplet of the C_{4v} centre of CaF_2:0.05%Tm^{3+}, pumping the $Z_1 \rightarrow A_1$ excitation transition at 12572 cm^{-1} and monitoring the $A_1 \rightarrow Z_2$ fluorescence transition at 12488 cm^{-1}. The fitted curve gives a lifetime of 3.3 ms.

transients for the $^1G_4$ and $^3H_4$ multiplets are displayed in figures 4.31 and 4.32 respectively. The fitted curves represent lifetimes of 2.1 ms for the $^1G_4$ multiplet and 3.3 ms for the $^3H_4$ multiplet. Lifetimes are generally expected to decrease with increasing temperature, as non-radiative decay rates increase. Unexpectedly, the $^3H_4$ lifetime was observed to increase slightly to 3.6 ms at room temperature. However, the reduced signal obtained at elevated temperatures produced noisier data and the fitted curves do appear to deviate slightly from the experimental data. In addition, the weak signal required that no terminating resistor be used, thus adding a short rise-time to the transient and further affecting the fit. However, it is significant for the upconversion results presented in chapter 5 that the $^3H_4$ multiplet lifetime does not change greatly. The $^1G_4$ multiplet lifetime, on the other hand does decrease with increased temperature, to 1.6 ms at room temperature.

In cases where the emitting state is populated by decay from an intermediate metastable state, an exponential rise time must be included:

$$y = S + A(e^{-t/\tau_1} - e^{-t/\tau_2})$$

where τ_1 is the lifetime of the emitting state and τ_2 is the rise-time of the population. In cases where there is a simple decay pathway from the pumped state to the emitting state, the rise-time is the lifetime of the pumped metastable state. This occurs, for example, when observing emission from the $^3H_4$ multiplet of Tm^{3+} after pumping the levels of the $^1G_4$ multiplet, as in figure 4.33. The fitted curve represents a rise-time of 1.9 ms and decay time of 3.6 ms. While this curve fits the data well, the rise and decay times do not quite match the $^1G_4$ and $^3H_4$ multiplet lifetimes measured from figures 4.31 and 4.32, with discrepancies of 10%. The fit in figure 4.33 is less reliable since an extra lifetime parameter is involved.

The lifetime of the $^1D_2$ multiplet could be measured by using two lasers, combined by use of a beam splitter before the sample. The cw laser, with rhodamine 640 dye, was tuned to pump the $^3F_3$ multiplet excitation lines, while the pulsed laser, also with rhodamine 640 dye, was tuned to the $^3H_4 \rightarrow {}^1D_2$ excited-state absorption transition. As a comparison with direct-excitation lifetime measurements, the $^1G_4$ lifetime was measured in a similar way, with the pulsed laser tuned to $^3F_4 \rightarrow {}^1G_4$ excited-state absorption transitions. As expected with a sequential-excitation as opposed to energy-transfer mechanism, no upconversion was observed when the cw

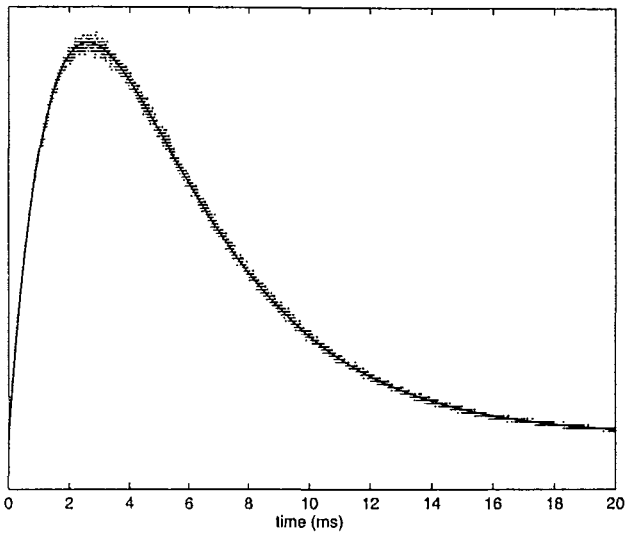

Figure 4.33 : 15 K fluorescence decay transient of the $^3H_4$ multiplet, upon pumping the $^1G_4$ multiplet, of the C_{4v} centre of CaF_2:0.05%Tm^{3+}. The pump transition was the $Z_1 \rightarrow D_2$ excitation transition at 21302 cm^{-1} and the fluorescence monitored was the $A_1 \rightarrow Z_2$ transition at 12488 cm^{-1}.

laser beam was removed.

The decay transient for the $^1G_4$ multiplet upconverted emission is shown in figure 4.34, with a fitted lifetime of 2.0 ms, slightly less than that measured for direct excitation, while that for $^1D_2$ is shown in figure 4.35 with fitted lifetime of 0.18 ms.

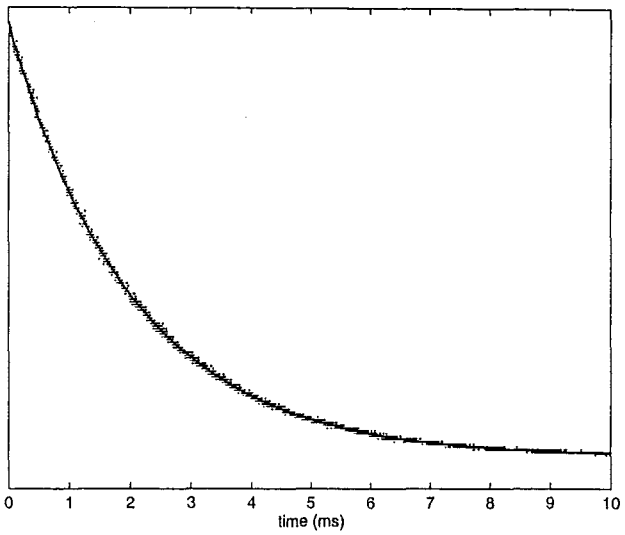

Figure 4.34 : 15 K upconversion fluorescence decay transient of the $^1G_4$ multiplet of the C_{4v} centre of CaF_2:0.05%Tm^{3+}, upon pumping the $Z_1 \rightarrow B_1$ transition at 14659 cm^{-1} with the cw laser and the $Y_1 \rightarrow D_1$ transition at 15345 cm^{-1} with the pulsed laser, monitoring the $D_1 \rightarrow Z_2$ fluorescence transition at 20918 cm^{-1}. The fitted lifetime is 2.0 ms.

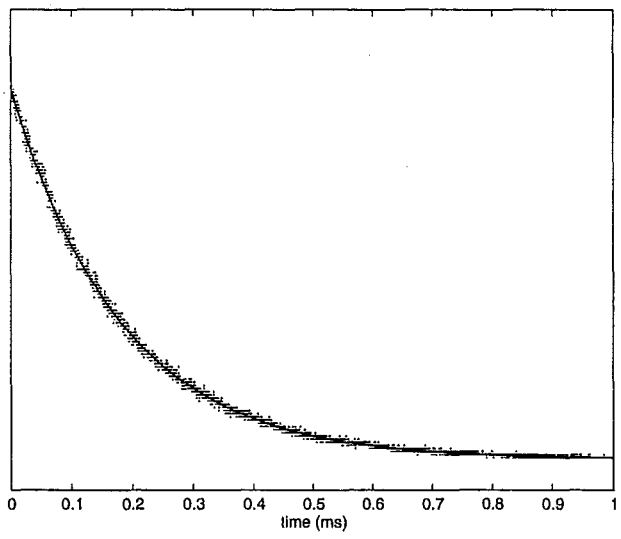

Figure 4.35 : 15 K upconversion fluorescence decay transient of the $^1D_2$ multiplet of the C_{4v} centre of CaF_2:0.05%Tm^{3+}, upon pumping the $Z_1 \rightarrow B_1$ transition at 14659 cm^{-1} with the cw laser and the $A_1 \rightarrow E_1$ transition at 15518 cm^{-1} with the pulsed laser, monitoring the $E_1 \rightarrow Y_2$ fluorescence transition at 22232 cm^{-1}. The fitted lifetime is 0.18 ms.

4.4 Site-Selective Spectroscopy of the C_{3v} Centre in CaF_2:Tm^{3+}

While many energy levels of the trigonal-symmetry C_{3v} centre have been determined, the polarisation ratios are not as clearly interpretable as those of the C_{4v} centres. The complexity of the predicted polarisation ratios (table 3.4) arises from having four possible non-orthogonal orientations of the centre. In addition, $\gamma_3 \rightarrow \gamma_3$ transitions are allowed for both electric-dipole and magnetic-dipole polarisations, so that any excitation-emission pair of transitions which involves such a transition will have arbitrary polarisation ratios. C_{3v} irreps have therefore not been able to be unambiguously assigned, nor has a rigorous crystal-field calculation been possible. A tentative crystal-field fit in which the experimental and theoretical energies are matched without any regard to irrep assignments is presented in section 4.4.3.

When performing crystal-field calculations, the Hamiltonian matrix is reduced to sub-matrices according to the distinct "crystal quantum numbers", $\mu = (M_J)_{\text{mod } 3}$, since the C_{3v} crystal-field Hamiltonian can only have matrix elements between within such pairs of states. However, this does not fully reduce the matrix, since both γ_1 and γ_2 states have the $\mu = 1$ crystal quantum number. Therefore, when classifying states for input into a crystal-field fitting routine, it is necessary only to distinguish between singlet and doublet states.

One possible solution to the problem of classifying states for crystal-field fitting, then, would be to use the Zeeman effect qualitatively to determine which levels are doublets. By measuring the g-values of these states we would also obtain a quantitative test of the wavefunctions produced in the calculation.

4.4.1 Direct Excitation and Fluorescence Spectroscopy

Direct excitation of the $^3H_4$ multiplet

The 15 K and 60 K $^3H_4$ excitation spectra, recorded using the Ti:sapphire laser with short-wave optics, are shown in figure 4.36. The fluorescence transition monitored was the $A_1 \rightarrow Z_3$ transition at 12448.3 cm^{-1}, which is also seen as an excitation line. Direct laser scatter from the crystal was minimal, as evidenced by the large increase

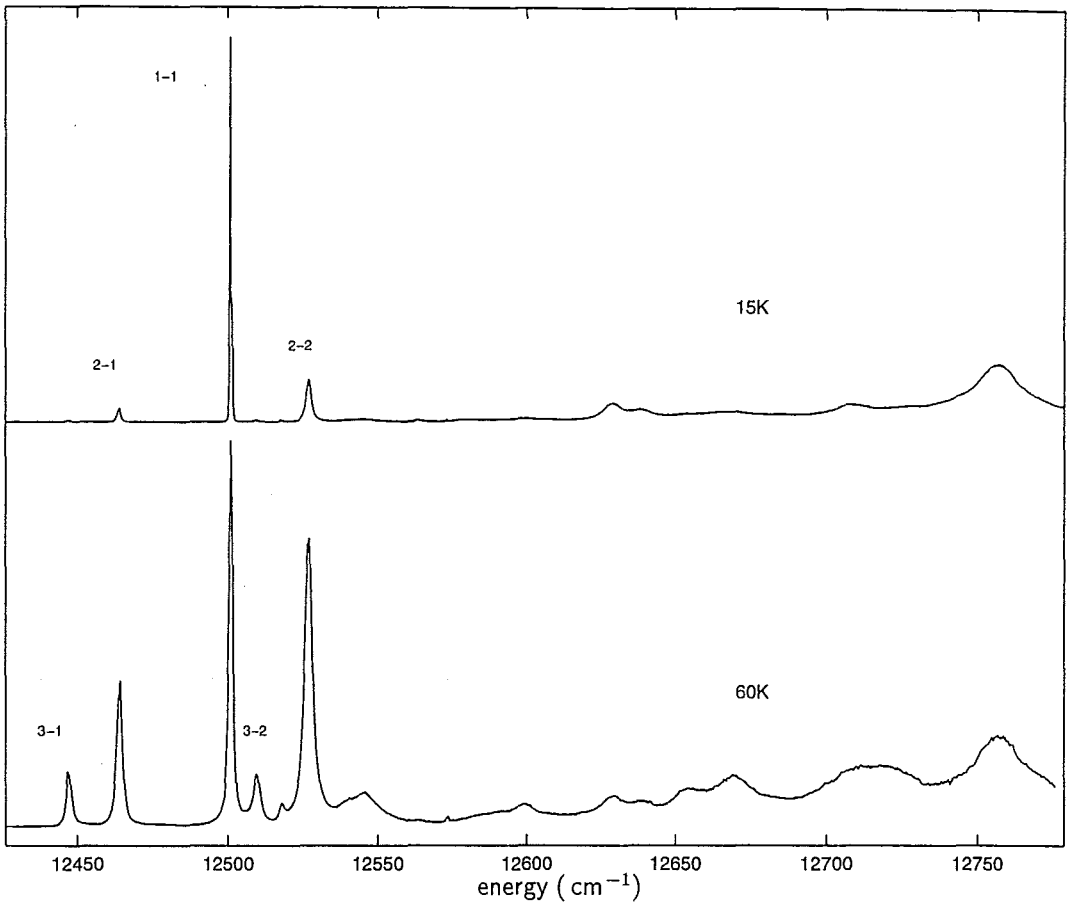

Figure 4.36 : 15 K and 60 K excitation spectrum of the $^3H_4$ multiplet of the C_{3v} centre in CaF_2:0.02%Tm^{3+}, monitoring the $A_1 \rightarrow Z_3$ transition at 12448.3 cm^{-1}. Transitions are identified by their lower and upper crystal-field level labels.

Pump transition		Emission transition		YX : YY : ZY	Polarisation (pump,decay)
$Z_1 \rightarrow A_1$	12501.7 cm^{-1}	$A_1 \rightarrow Z_3$	12448.3 cm^{-1}	69 : 42 : 64	$(\pi\sigma)$ or $(\sigma\pi)$
$Z_2 \rightarrow A_1$	12464.3 cm^{-1}	"	"	17 : 21 :12.5	$(\sigma\sigma)$
$Z_2 \rightarrow A_2$	12527.2 cm^{-1}	"	"	72 : 107 : 52	$(\sigma\sigma)$
$Z_3 \rightarrow A_2$	12510.4 cm^{-1}	"	"	23 : 11 : 23	$(\sigma\sigma)$

Table 4.16 : Polarisation ratios of $^3H_6 \rightarrow {}^3H_4$ excitation lines for the C_{3v} centre of CaF_2:Tm^{3+}.

in this excitation line at 60K. The recorded energies and polarisation ratios are given in table 4.16.

The $Z_1 \rightarrow A_1$, $Z_2 \rightarrow A_1$ and $Z_3 \rightarrow A_1$ transitions are identified by their presence in both the 60 K excitation spectrum and in the fluorescence spectrum (figure 4.37). The transitions at 12510.4 cm^{-1} and 12527.2 cm^{-1} have the appropriate Z_2–Z_3 separation and are therefore assigned to the $Z_3 \rightarrow A_2$ and $Z_2 \rightarrow A_2$ transitions, respectively. The $Z_1 \rightarrow A_2$ transition is absent and appears to be forbidden, which suggests it is a $\gamma_1 \rightarrow \gamma_2$ or $\gamma_2 \rightarrow \gamma_1$ transition. In either case, the ground state would be a singlet state.

Fluorescence Spectrum of the $^3H_4 \rightarrow {}^3H_6$ transitions

The 15 K $^3H_4 \rightarrow {}^3H_6$ fluorescence spectrum is shown in figure 4.37. The laser pump

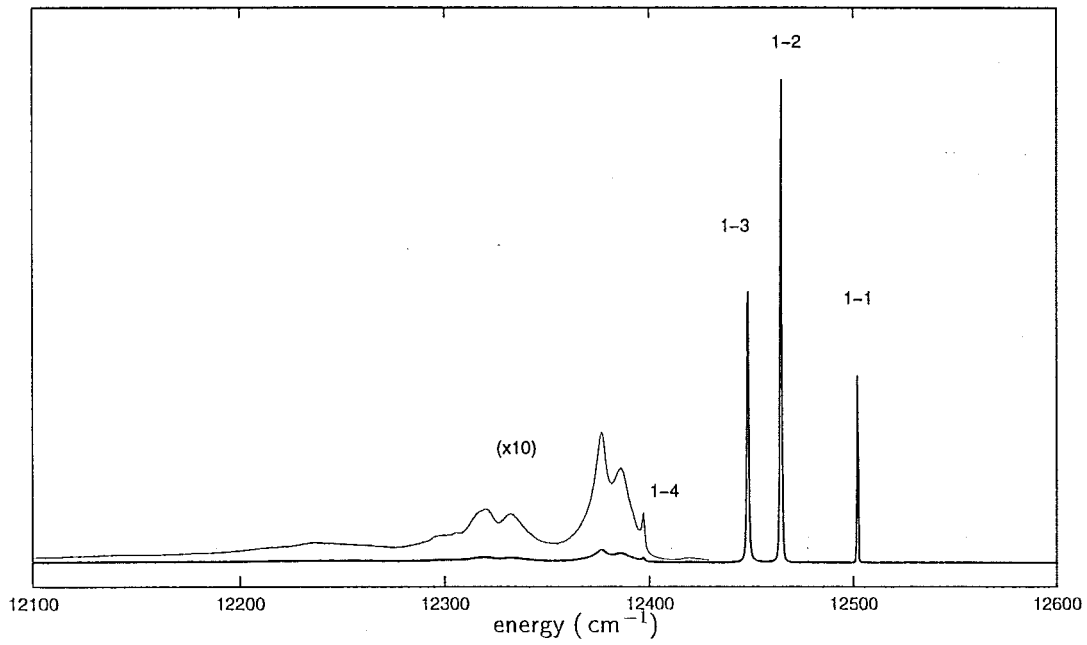

Figure 4.37 : 15 K $^3H_4 \rightarrow {}^3H_6$ fluorescence spectrum of the C_{3v} centre in CaF_2:0.02%Tm^{3+}, pumping the $Z_1 \rightarrow B_3$ transition at 14497.2 cm^{-1}. Transitions are identified by their upper and lower crystal-field level labels.

transition was the $Z_1 \rightarrow B_3$ transition at 14497.2 cm^{-1}. The $A_1 \rightarrow Z_{1,2,3}$ transitions

are seen, corresponding to the excitation lines of figure 4.36. Transition energies and polarisation ratios for these three strong fluorescence transitions are given in table 4.17. The other sharp transition at 12398 cm^{-1}, assigned to the $A_1 \rightarrow Z_4$ electronic transition, lies at the edge of a set of broad (presumably phonon-assisted) transitions making the measurement of polarisation ratios for that line unreliable.

Pump transition		Emission transition		YX : YY : ZY	Polarisation (pump,decay)
$Z_1 \rightarrow B_3$	14497.2 cm^{-1}	$A_1 \rightarrow Z_1$	12501.7 cm^{-1}	20.8: 10.4 :23.3	$(\pi\sigma)$ or $(\sigma\pi)$
"	"	$A_1 \rightarrow Z_2$	12464.3 cm^{-1}	43.0: 88.5 :31.2	$(\pi\pi)/(\sigma\sigma)$
"	"	$A_1 \rightarrow Z_3$	12448.3 cm^{-1}	29.0: 65.2 :20.6	$(\pi\pi)/(\sigma\sigma)$
"	"	$A_1 \rightarrow Z_4$	12396.5 cm^{-1}		

Table 4.17 : Polarisation ratios of $^3H_6 \rightarrow {}^3H_4$ excitation lines for the C_{3v} centre of CaF_2:Tm^{3+}.

Direct excitation of the $^3F_3$ multiplet

The $^3F_3$ multiplet excitation spectrum, recorded with the rhodamine 640 dye laser for sample temperatures of 15 K and 25 K, is given in figure 4.38. The fluorescence transition monitored is the $A_1 \rightarrow Z_1$ transition at 12501.7 cm^{-1}. With $J = 3$, the $^3F_3$ multiplet should decompose into C_{3v} irreps $\gamma_1 + 2\gamma_2 + 2\gamma_3$ giving five levels (see table 2.2, section 2.3). The 15 K $^3F_3$ excitation spectrum has four lines, which would be consistent with the ground state being a γ_2 irrep state. The missing level from this spectrum would then be the $^3F_3$ γ_1 state. The recorded transition energies and polarisation ratios are in table 4.18.

Direct excitation of the $^3F_2$ multiplet

The $^3F_2$ excitation spectrum, also recorded with the rhodamine 640 dye laser for sample temperatures of 15 K and 25 K and for monitoring the $A_1 \rightarrow Z_1$ fluorescence transition, is given in figure 4.39. For a $J = 2$ multiplet, the C_{3v} irrep decomposition is $\gamma_1 + 2\gamma_3$. Only two transitions are seen at 15 K, which is again consistent with

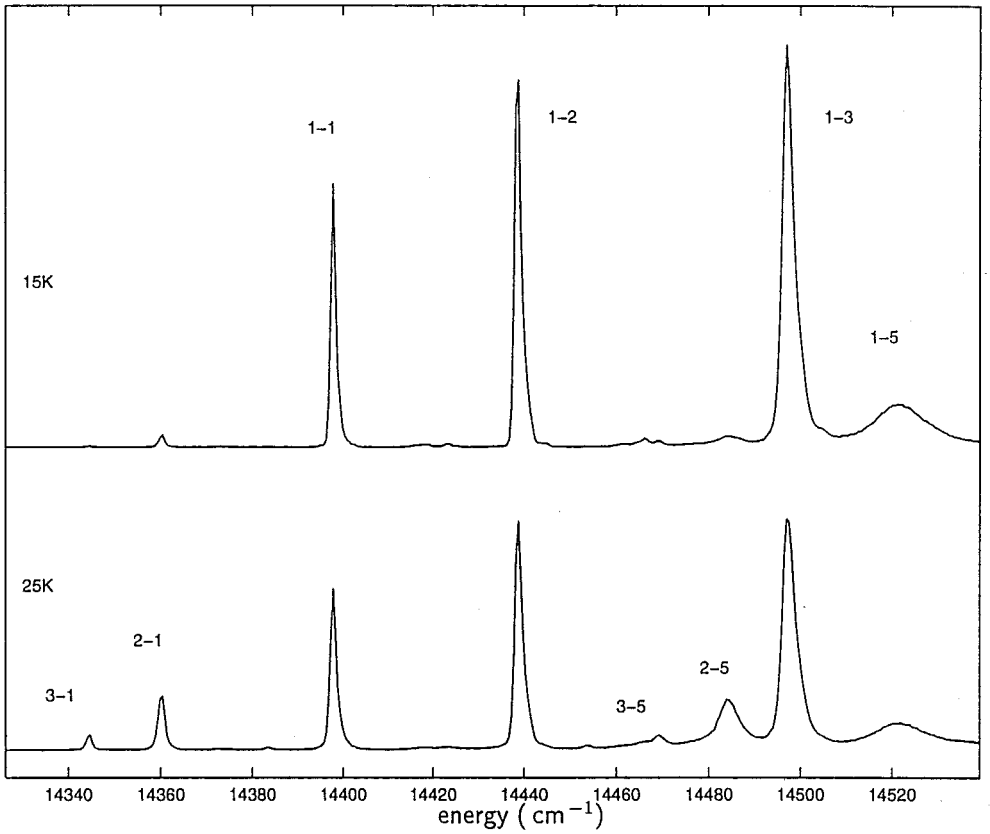

Figure 4.38 : 15 K and 25 K excitation spectrum of the $^3F_3$ multiplet of the C_{3v} centre in CaF_2:0.1%Tm^{3+}, monitoring the $A_1 \rightarrow Z_1$ fluorescence transition at 12501.7 cm^{-1}. Transitions are identified by their lower and upper crystal-field level labels.

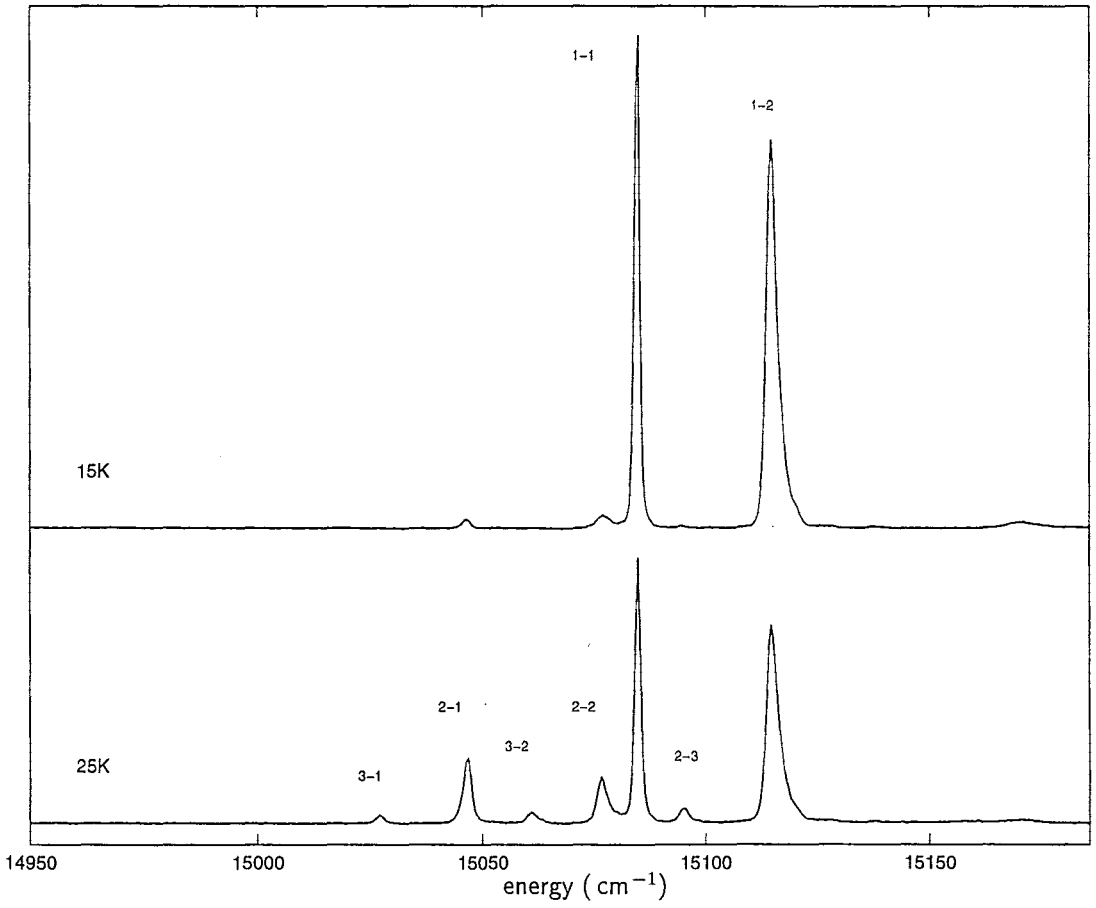

Figure 4.39 : 15 K and 25 K excitation spectra of the $^3F_2$ multiplet of the C_{3v} centre in CaF_2:0.1%Tm^{3+}, monitoring the $A_1 \rightarrow Z_1$ transition at 12501.7 cm^{-1}. Transitions are identified by their lower and upper crystal-field level labels.

Pump transition		Emission transition		YX : YY : ZY	Polarisation (pump,decay)
$Z_1 \rightarrow B_1$	$14398.8\,cm^{-1}$	$A_1 \rightarrow Z_1$	$12501.7\,cm^{-1}$	12.0: 6.0 :13.4	$(\pi\sigma)$ or $(\sigma\pi)$
$Z_1 \rightarrow B_2$	$14438.2\,cm^{-1}$	"	"	14.2: 18.9 :13.4	$(\sigma\sigma)$
$Z_1 \rightarrow B_3$	$14497.2\,cm^{-1}$	"	"	20.8: 10.4 :23.3	$(\pi\sigma)$ or $(\sigma\pi)$
$Z_1 \rightarrow B_5$	$14520.8\,cm^{-1}$	"	"	3.3 : 1.7 : 3.4	$(\pi\sigma)$ or $(\sigma\pi)$
$Z_2 \rightarrow B_1$	$14361.1\,cm^{-1}$	"	"	4.4 : 5.9 : 3.8	$(\sigma\sigma)$
$Z_2 \rightarrow B_5$	$14485.0\,cm^{-1}$	"	"	2.6 : 1.5 : 2.5	$(\pi\sigma)$ or $(\sigma\pi)$
$Z_3 \rightarrow B_1$	$14345.3\,cm^{-1}$	"	"	4.4 : 5.7 : 4.0	$(\sigma\sigma)$
$Z_3 \rightarrow B_5$	$14469.3\,cm^{-1}$	"	"	8.5 : 5.3 : 8.6	$(\pi\sigma)$ or $(\sigma\pi)$

Table 4.18 : Polarisation ratios of $^3H_6 \rightarrow {}^3F_3$ excitation lines for the C_{3v} centre of CaF_2:Tm^{3+}.

the ground state being a γ_2 state, such that the transition to the $^3F_2$ γ_1 state would be forbidden. The extra line is seen as a "hot-line" transition from the Z_2 state at elevated temperatures, and is at higher energy than the two known levels. The C_1 and C_2 states would thus both transform as the γ_3 irrep and the C_3 state as the γ_1 irrep. The measured energies and polarisation ratios of these transitions are given in table 4.19.

Discussion of Measured Polarisation Ratios

Many of the polarisation ratios presented in tables 4.16, 4.17, 4.18 and 4.19 are ambiguous, since the $(\pi\sigma)$ and $(\sigma\pi)$ transition pairs give the same ratios. In most cases where the ratios indicate one of these two cases, it should be possible to choose one by comparing with another set of ratios which have a common pump or emission transition. Even so, the ratios cannot be reconciled with a single set of irrep assignments. For example, the $A_1 \rightarrow Z_1$ fluorescence transition appears to be σ allowed. This means that the $Z_1 \rightarrow B_{1,2,3,5}$ set of excitation transitions comprises three π and one σ polarised transition. This is not consistent with the C_{3v} irrep decomposition of the $^3F_3$ multiplet being $\gamma_1 + 2\gamma_2 + 2\gamma_3$, for any ground-state irrep. The origin of these anomalous ratios may lie in some $\gamma_3 \rightarrow \gamma_3$ transitions being involved, intro-

Pump transition		Emission transition		YX : YY : ZY	Polarisation (pump,decay)
$Z_1 \rightarrow C_1$	$15086.2\,cm^{-1}$	$A_1 \rightarrow Z_1$	$12501.7\,cm^{-1}$	43.6: 57.8 :38.9	$(\sigma\sigma)$
$Z_1 \rightarrow C_2$	$15115.7\,cm^{-1}$	"	"	27.0: 37.1 :24.3	$(\sigma\sigma)$
$Z_2 \rightarrow C_1$	$15049.0\,cm^{-1}$	"	"	4.7 : 6.1 : 4.1	$(\sigma\sigma)$
$Z_2 \rightarrow C_2$	$15077.9\,cm^{-1}$	"	"	4.3 : 3.9 : 4.4	$(\pi\sigma)$ or $(\sigma\pi)$
$Z_2 \rightarrow C_3$	$15096.6\,cm^{-1}$	"	"	11.5: 15.8 :10.2	$(\sigma\sigma)$
$Z_3 \rightarrow C_1$	$15033.0\,cm^{-1}$	"	"	10.5: 5.5 :11.0	$(\pi\sigma)$ or $(\sigma\pi)$
$Z_3 \rightarrow C_2$	$15062.0\,cm^{-1}$	"	"	12.6: 6.6 :13.3	$(\pi\sigma)$ or $(\sigma\pi)$

Table 4.19 : Polarisation ratios of $^3H_6 \rightarrow {}^3F_2$ excitation lines for the C_{3v} centre of CaF_2:Tm^{3+}.

ducing arbitrary ratios, or some magnetic-dipole contributions becoming significant. Further discussion on resolving this issue is contained in section 4.4.3.

Direct excitation of the $^1G_4$ multiplet

The excitation spectrum of the $^1G_4$ multiplet, pumped with the coumarin 460 dye laser, is shown in figure 4.40 for sample temperatures of 15 K and 30 K. The monitored fluorescence transition is the $D_1 \rightarrow Y_1$ fluorescence transition at $15479.0\,cm^{-1}$. The transitions originating from the Z_1 ground state can be identified from their temperature dependence (decreasing in intensity as temperature is increased). The lowest in energy of these transitions is at $21149.8\,cm^{-1}$. This transition is seen also as a fluorescence transition (figure 4.41), but the temperature dependence in that case shows that it does not originate from the D_1 level. Thus the $Z_1 \rightarrow D_1$ transition is forbidden, and the D_1 level is likely to be a γ_1 state, which is electric-dipole forbidden from the γ_2 ground state.

Transitions from the Z_2 and Z_3 states can be seen, increasing with increasing temperature, identified by the known energy spacings between these states.

The transition energies are listed in table 4.20.

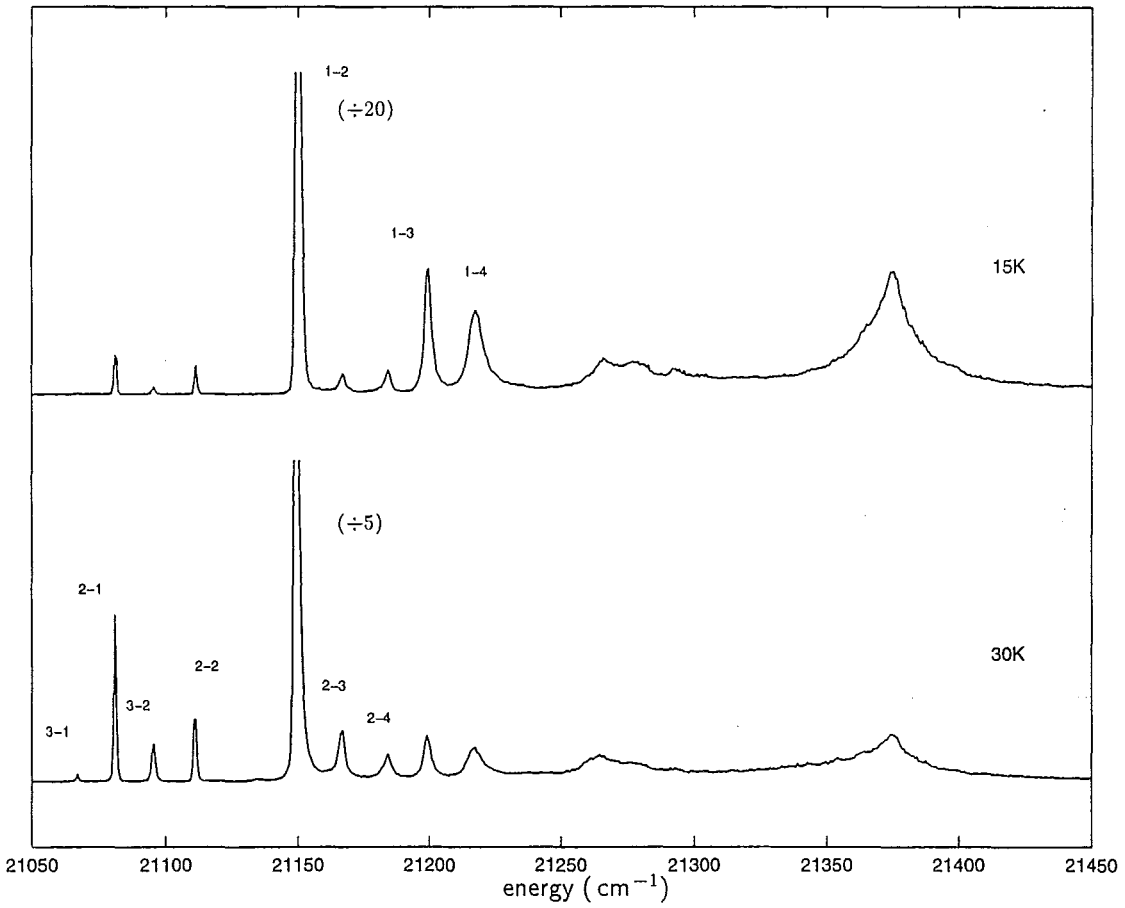

Figure 4.40 : 15 K and 30 K excitation spectrum of the $^1G_4$ multiplet of the C_{3v} centre in CaF_2:0.05%Tm^{3+}, monitoring the $D_1 \rightarrow Y_1$ fluorescence line at 15479.0 cm^{-1}. Transitions are identified by their lower and upper crystal-field level labels. The strong 1-2 transition has been truncated at 1/20 and 1/5 of its peak intensity, for the 15 K and 30 K spectra respectively.

Transition	Energy (cm^{-1})
$Z_1 \rightarrow D_2$	21149.8
$Z_1 \rightarrow D_3$	21205.3
$Z_1 \rightarrow D_4$	21225.2
$Z_2 \rightarrow D_1$	21081.1
$Z_2 \rightarrow D_2$	21112.0
$Z_2 \rightarrow D_3$	21167.3
$Z_2 \rightarrow D_4$	21187.7
$Z_3 \rightarrow D_1$	21065.3
$Z_3 \rightarrow D_2$	21096.2

Table 4.20 : Transition energies of $^3H_6 \rightarrow {}^1G_4$ excitation lines for the C_{3v} centre of CaF_2:Tm^{3+}.

Fluorescence Spectrum of the $^1G_4 \rightarrow {}^3H_6$ Transitions

The 15 K $^1G_4 \rightarrow {}^3H_6$ fluorescence spectrum is shown in figure 4.41. The excitation transition pumped here is the $Z_1 \rightarrow D_2$ transition at 21149.8 cm^{-1}. The laser line is included in the spectrum (labelled "laser") as it is pumping a resonant fluorescence transition. With the exception of the apparently forbidden $D_1 \rightarrow Z_1$ transition, all of the other transitions from the two lowest states of the $^1G_4$ multiplet to the four lowest states of the $^3H_6$ multiplet are identified in this spectrum. Their transition energies are listed in table 4.21.

Fluorescence Spectrum of the $^1G_4 \rightarrow {}^3F_4$ Transitions

The $^1G_4 \rightarrow {}^3F_4$ inter-multiplet transitions are magnetic-dipole allowed, due to the strong spin-orbit mixing of the $^1G_4$, $^3F_4$ and $^3H_4$ multiplets. Thus the electric-dipole forbidden $\gamma_1 \leftrightarrow \gamma_2$ transitions are now expected to be seen as well.

The $^1G_4 \rightarrow {}^3F_4$ fluorescence spectrum at 15 K and 30 K is shown in figure 4.42, again for pumping the $Z_1 \rightarrow D_2$ transition at 21149.8 cm^{-1}. The spectrum is dominated by the intense $D_1 \rightarrow Y_1$ feature, which has been truncated for both 15 K and 30 K spectra in figure 4.42. Several very weak features in the spectrum are identified

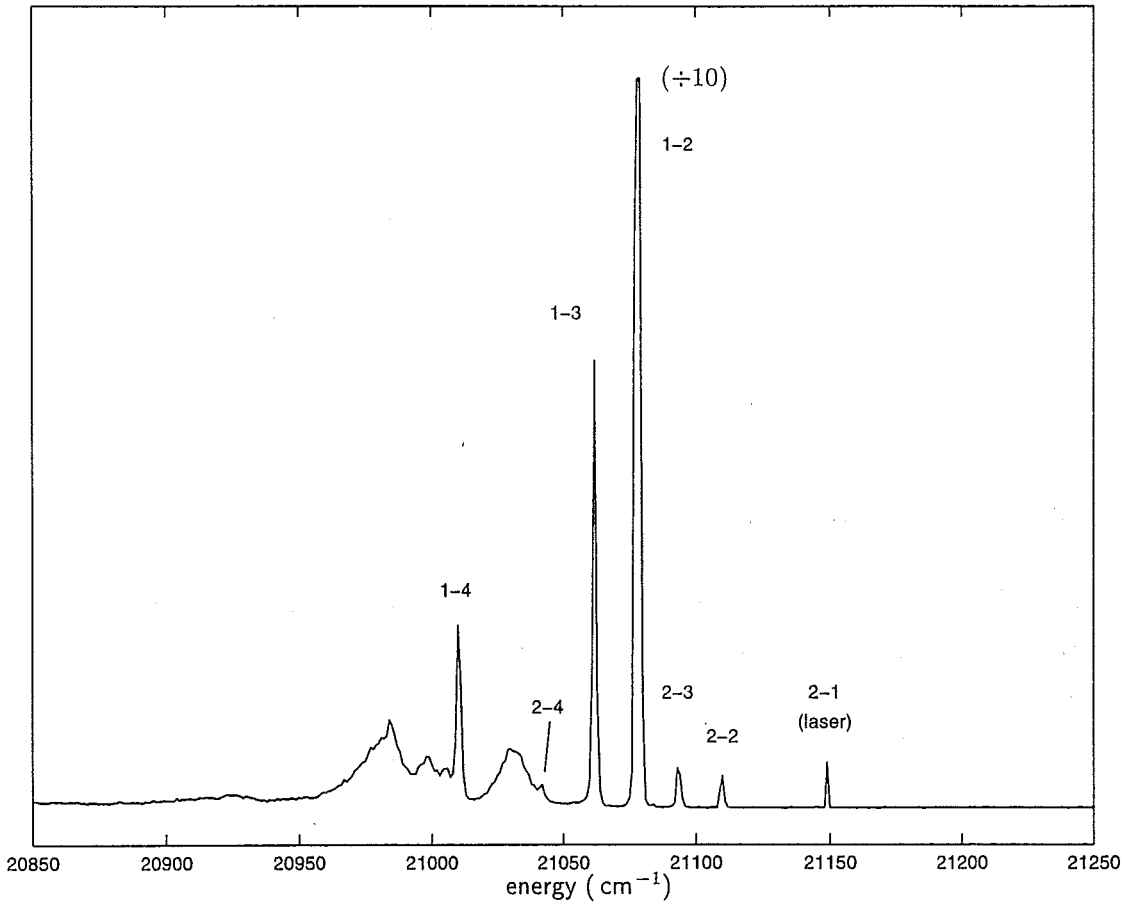

Figure 4.41 : 15 K $^1G_4 \rightarrow {}^3H_6$ fluorescence spectrum of the C_{3v} centre in CaF_2:0.05%Tm^{3+}. The $D_2 \rightarrow Z_1$ fluorescence transition at 21149.8 cm^{-1} also corresponds to the excitation transition and is identified as (laser). Transitions are identified by their upper and lower crystal-field level labels. The strong 1-2 transition has been truncated at 1/10 of its peak intensity.

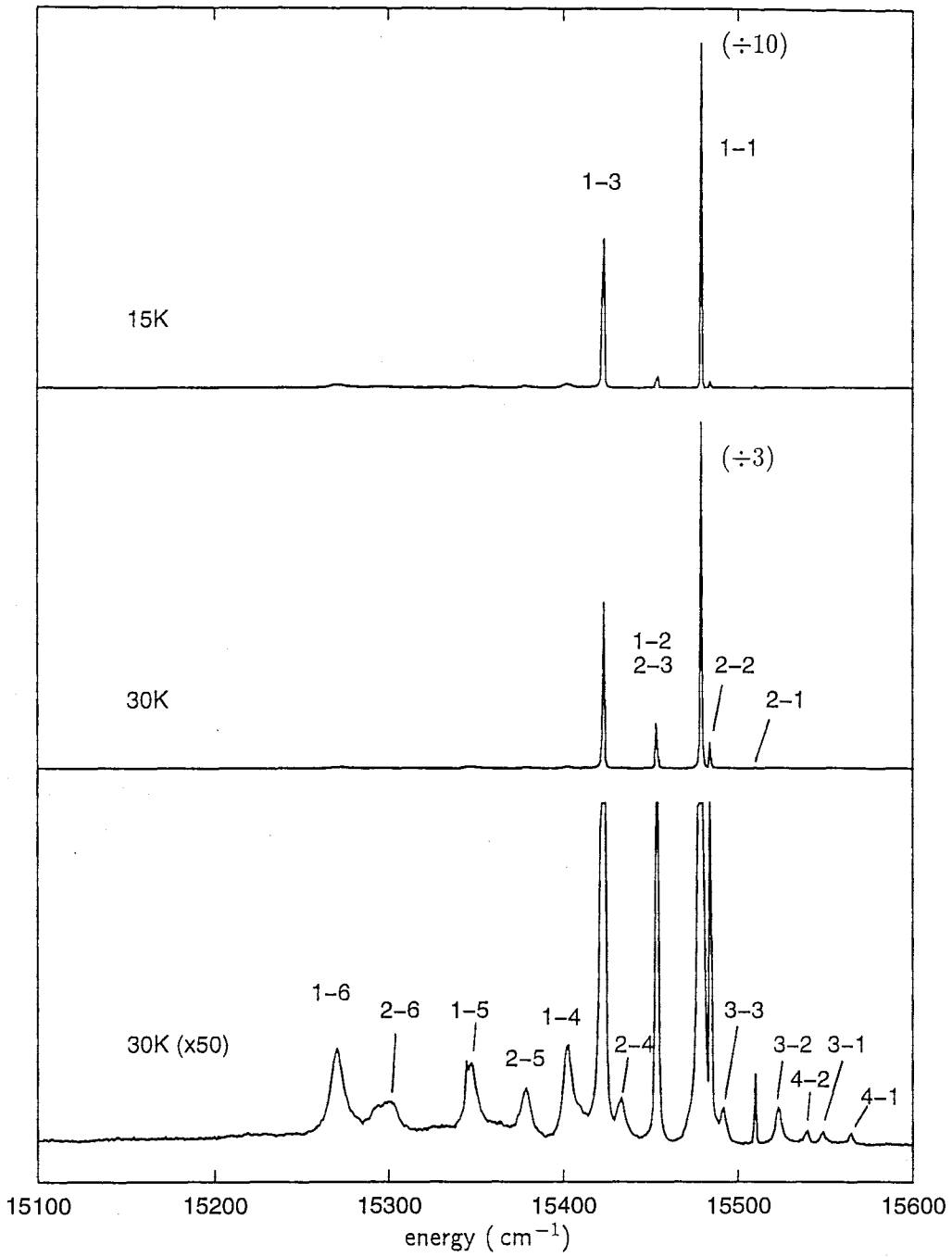

Figure 4.42 : 15 K and 30 K $^1G_4 \rightarrow {}^3F_4$ fluorescence spectrum of the C_{3v} centre in CaF_2:0.05%Tm^{3+}, pumping the $Z_1 \rightarrow D_2$ transition at 21149.8 cm^{-1}. Transitions are identified by their upper and lower crystal-field level labels. The strong 1-1 transition has been truncated at 1/10 and 1/3 of its peak intensity, for the 15 K and 30 K spectra respectively, while the third spectrum is the 30 K spectrum with 50-fold expansion to show weak transitions.

Transition	Energy (cm^{-1})
$D_1 \rightarrow Z_2$	21081.5
$D_1 \rightarrow Z_3$	21065.4
$D_1 \rightarrow Z_4$	21013.8
$D_2 \rightarrow Z_1$	21149.9
$D_2 \rightarrow Z_2$	21112.5
$D_2 \rightarrow Z_3$	21096.2
$D_2 \rightarrow Z_4$	21045.3

Table 4.21 : Transition energies of $^1G_4 \rightarrow {}^3H_6$ fluorescence lines for the C_{3v} centre of CaF_2:Tm^{3+}.

at a gain of about two orders of magnitude greater than that required to record the $D_1 \rightarrow Y_1$ line. Transitions from the D_1 and D_2 levels to all six levels of the $^3H_5$ multiplet are assigned, with the exception that the $D_1 \rightarrow Y_2$ and $D_2 \rightarrow Y_3$ transitions overlap and cannot be resolved into two lines. The $D_2 \rightarrow Y_3$ transition appears to dominate this line at 30 K since the line increases at a similar rate to the $D_2 \rightarrow Y_2$ line. Some transitions from the D_3 and D_4 levels are also observed at 30 K.

The transition energies are listed in table 4.22.

Fluorescence Spectrum of the $^1G_4 \rightarrow {}^3H_5$ Transitions

The $^1G_4 \rightarrow {}^3H_5$ transitions are also magnetic-dipole allowed. The $^1G_4 \rightarrow {}^3H_5$ fluorescence spectrum at 15 K and 30 K is shown in figure 4.43, again for pumping the $Z_1 \rightarrow D_2$ transition at 21149.8 cm^{-1}, with the transition energies listed in table 4.23. The energies are such that the $D_1 \rightarrow X_1$ and $D_2 \rightarrow X_4$ transitions overlap, and the assignment of the line to either or both of these transitions is uncertain. It is likely that the $D_1 \rightarrow X_1$ transition dominates, since the strength of this fluorescence line does not increase significantly at 30 K.

Transition	Energy (cm^{-1})
$D_1 \rightarrow Y_1$	15479.0
$D_1 \rightarrow Y_2$	15454.2†
$D_1 \rightarrow Y_3$	15422.3
$D_1 \rightarrow Y_4$	15348.2
$D_1 \rightarrow Y_5$	15269.9
$D_2 \rightarrow Y_1$	15510.8
$D_2 \rightarrow Y_2$	15484.9
$D_2 \rightarrow Y_3$	15453.1†
$D_2 \rightarrow Y_4$	15432.5
$D_2 \rightarrow Y_5$	15378.1
$D_2 \rightarrow Y_6$	15301.1

Table 4.22 : Transition energies of $^1G_4 \rightarrow {}^3F_4$ fluorescence lines for the C_{3v} centre of CaF_2:Tm^{3+}. The † assignment here is tentative since these two transitions appear to overlap.

Transition	Energy (cm^{-1})
$D_1 \rightarrow X_1$	12839.3†
$D_1 \rightarrow X_2$	12828.7
$D_1 \rightarrow X_3$	12814.9
$D_1 \rightarrow X_4$	12806.7
$D_2 \rightarrow X_1$	12871.7
$D_2 \rightarrow X_2$	12861.2
$D_2 \rightarrow X_3$	12847.1
$D_2 \rightarrow X_4$	12839.3†

Table 4.23 : Transition energies of $^1G_4 \rightarrow {}^3H_5$ fluorescence lines for the C_{3v} centre of CaF_2:Tm^{3+}. The † assignment here is tentative since these two transitions appear to overlap.

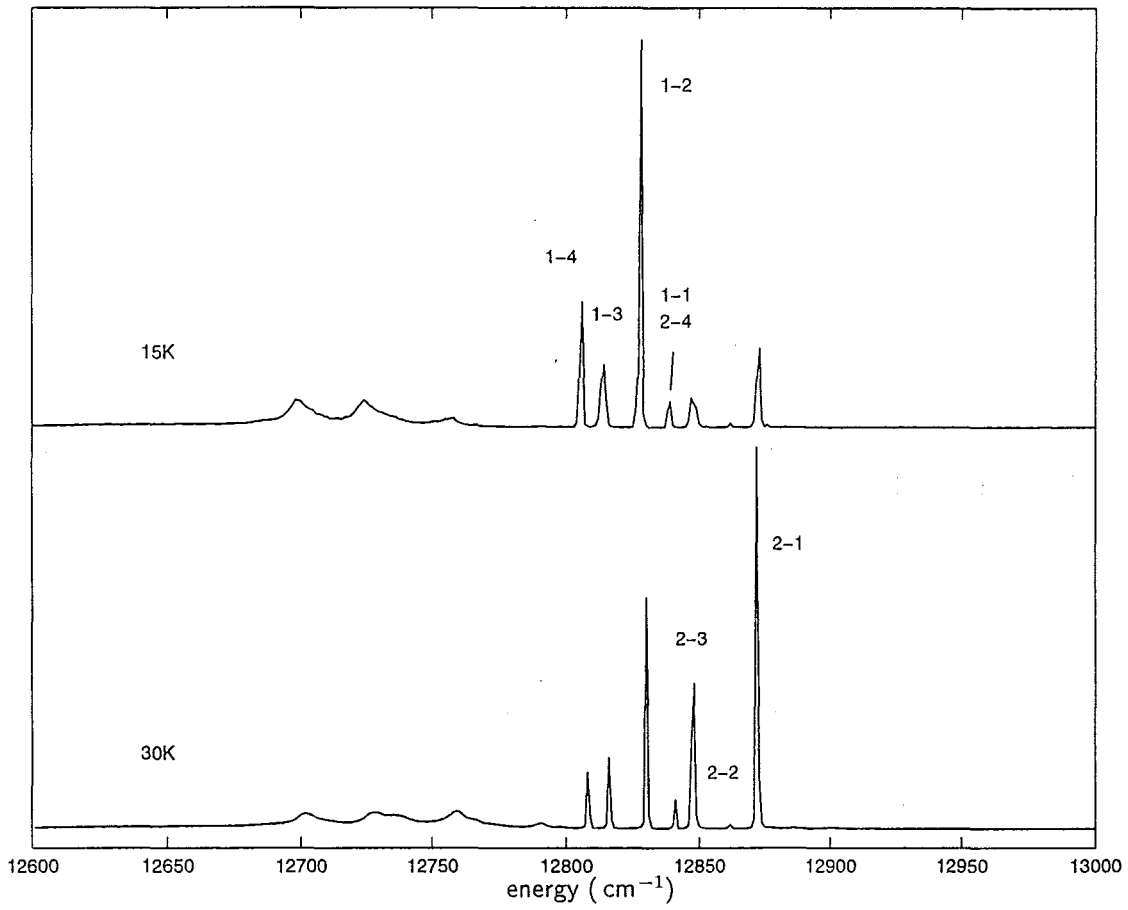

Figure 4.43 : 15 K and 30 K $^1G_4 \rightarrow {}^3H_5$ fluorescence spectrum of the C_{3v} centre in CaF_2:0.05%Tm^{3+}, pumping the $Z_1 \rightarrow D_2$ transition at 21149.8 cm^{-1}. Transitions are identified by their upper and lower crystal-field level labels.

4.4.2 Upconversion-Fluorescence Spectroscopy

The non-site selective upconversion excitation spectrum is shown in figure 4.22. Three lines are associated with the C_{3v} centre. One of these, at 15480 cm^{-1} yields emission from the $^1G_4$ multiplet and is associated with a $^3F_4 \rightarrow {}^1G_4$ excited-state absorption. The reverse transition has already been identified as the $D_1 \rightarrow Y_1$ fluorescence transition in the spectrum of figure 4.42. Two other lines, at 15417 cm^{-1} and 15462 cm^{-1} produce $^1D_2$ multiplet emission and are associated with $^3H_4 \rightarrow {}^1D_2$ excited-state absorption transitions.

Excitation of the $^1G_4$ multiplet by Excited-State Absorption

The $^3F_4 \rightarrow {}^1G_4$ transitions are magnetic-dipole allowed. The spectra at 15 K and 45 K are shown in figure 4.44, with monitoring the $D_1 \rightarrow Z_2$ transition at 21081.5 cm^{-1}. Transitions from the Y_1 and Y_2 levels to each of $D_{1,2,3,4}$ levels are present, and their energies listed in table 4.24.

Transition	Energy (cm^{-1})
$Y_1 \rightarrow D_1$	15480.2
$Y_1 \rightarrow D_2$	15510.7
$Y_1 \rightarrow D_3$	15549.8
$Y_1 \rightarrow D_4$	15566.6
$Y_2 \rightarrow D_1$	15454.9
$Y_2 \rightarrow D_2$	15486.1
$Y_2 \rightarrow D_3$	15524.0
$Y_2 \rightarrow D_4$	15540.1
$Y_3 \rightarrow D_1$	15423.7

Table 4.24 : Transition energies of $^3F_4 \rightarrow {}^1G_4$ excitation lines for the C_{3v} centre of CaF_2:Tm^{3+}.

As expected, the fluorescence spectra from the $^1G_4$ multiplet are the same as for the direct blue excitation case.

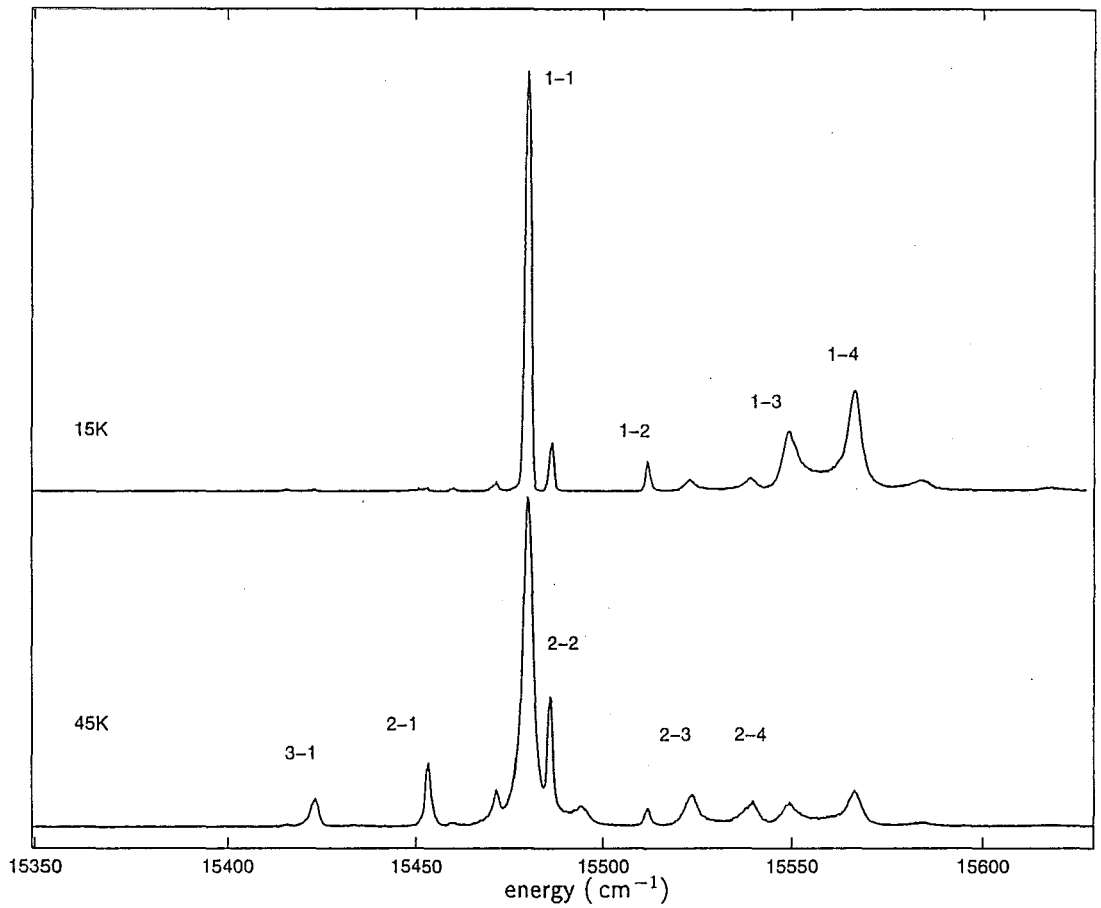

Figure 4.44 : 15 K and 45 K $^3F_4 \rightarrow {}^1G_4$ excited-state absorption spectrum of the C_{3v} centre in CaF_2:0.02%Tm^{3+}, monitoring the $D_1 \rightarrow Z_2$ transition at 21081.5 cm^{-1}. Transitions are identified by their lower and upper crystal-field level labels.

Excitation of the $^1D_2$ multiplet by Excited-State Absorption

For both the C_{4v} and C_{3v} centres, only weak $^1G_4$ multiplet emission is seen for $^1D_2$ multiplet excitation. If decay via $^1G_4$ had been a principal pathway for $^1D_2$ multiplet populated ions, then the two strong $^3H_4 \rightarrow {}^1D_2$ excitation lines seen in figure 4.45 should also appear in the $^3F_4 \rightarrow {}^1G_4$ excitation spectrum. As it is, these lines can only just be discerned in figure 4.44. The identification of the $^3H_4 \rightarrow {}^1D_2$ excitation lines for the C_{3v} centre from the broadband spectrum (figure 4.22) was not a trivial problem, since the $^1D_2$ multiplet energies were not known.

This problem was resolved with a two-laser experiment, using the cw laser and pulsed nitrogen-pumped dye laser together. The cw laser was tuned to the known $^3F_2$ absorption lines, and the pulsed laser tuned initially to the known $^3F_4 \rightarrow {}^1G_4$ transitions to align the two lasers. The pulsed laser was then swept through the excited-state absorption region, while the spectrometer was set to zero-order to detect all upconversion emission. Two other lines appeared, with a different decay lifetime from the $^1G_4$ multiplet lifetime. Since the presence of these lines depended strictly on the cw laser frequency, it followed that they must belong to the same, C_{3v} centre. Lower-multiplet energy levels inferred from the fluorescence spectra obtained upon pumping these lines with the cw laser confirmed this result.

The 15 K excitation spectrum of the $^3H_4 \rightarrow {}^1D_2$ transitions is shown in figure 4.45. The fluorescence transition monitored was the 22253.6 cm^{-1} $E_1 \rightarrow Y_2$ transition. The transitions at 15416.8 cm^{-1} and 15462.2 cm^{-1} are the $A_1 \rightarrow E_1$ and $A_1 \rightarrow E_2$ transitions, respectively. The smaller peak at 15474 cm^{-1} is the higher energy of the two strong upconversion lines in the broadband excitation spectrum, figure 4.22, and belongs to a different centre. The $A_1 \rightarrow E_2$ transition was pumped to obtain all of the following fluorescence spectra, as it gave better site discrimination than the $A_1 \rightarrow E_1$ transition.

Fluorescence Spectrum of the $^1D_2 \rightarrow {}^3H_6$ Transitions

The $^1D_2 \rightarrow {}^3H_6$ fluorescence spectrum is shown in figure 4.46 for sample temperatures of 15 K and 45 K. From the temperature dependence, it is confirmed that the two levels observed in the excitation spectrum, figure 4.45, are the lowest two states of

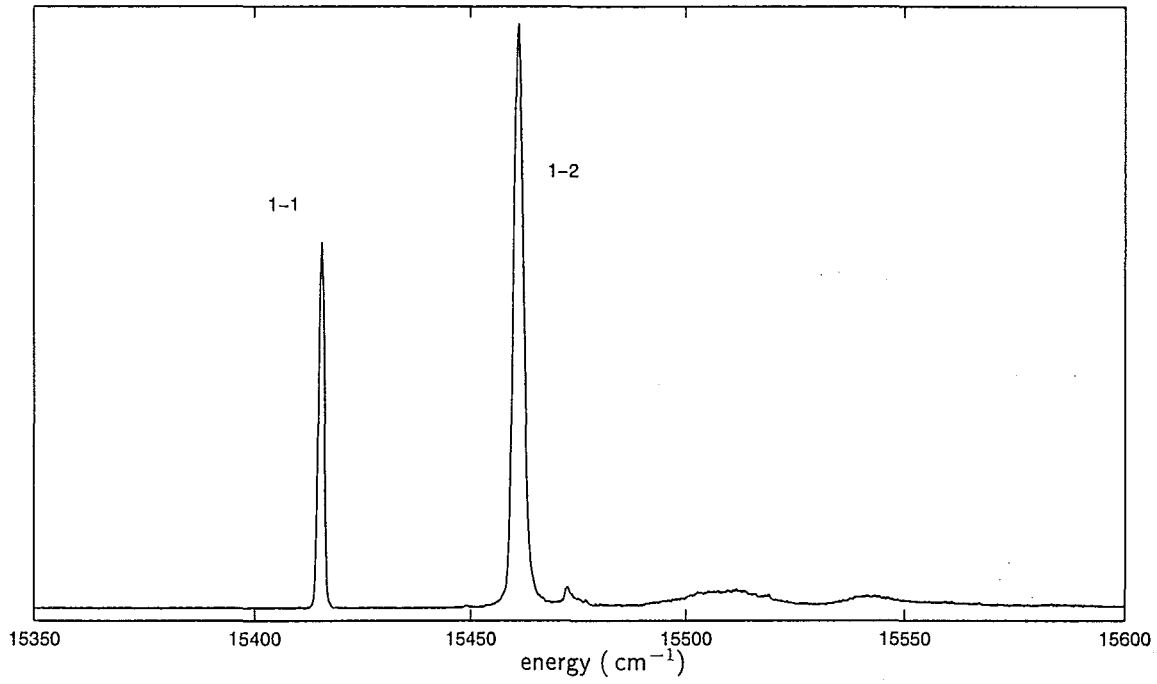

Figure 4.45 : 15 K $^3H_4 \rightarrow {}^1D_2$ excited-state absorption spectrum of the C_{3v} centre in CaF_2:0.05%Tm^{3+}, monitoring the $E_1 \rightarrow Y_2$ fluorescence transition at 22253.6 cm^{-1}. Transitions are identified by their lower and upper crystal-field level labels.

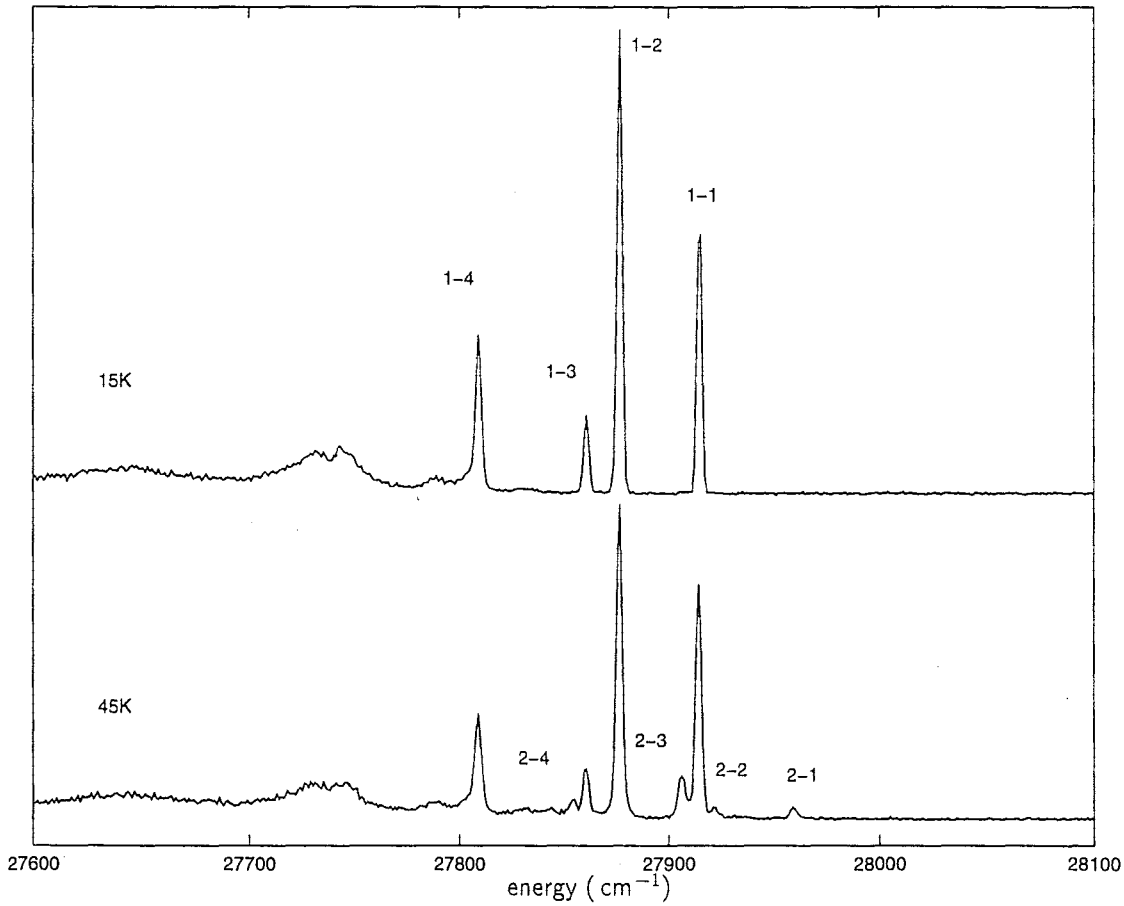

Figure 4.46 : 15 K and 45 K $^1D_2 \rightarrow {}^3H_6$ fluorescence spectra of the C_{3v} centre in CaF_2:0.05%Tm^{3+}, pumping the $A_1 \rightarrow E_2$ excited-state absorption transition at 15462.2 cm^{-1}. Transitions are identified by their upper and lower crystal-field level labels.

the $^1D_2$ multiplet. Only three states are expected for a $J = 2$ multiplet; the third must be at too high an energy to be significantly populated at 45 K. Because of the weak response of the photomultiplier tube at the shorter wavelengths, slit widths of 100, μm were used, resulting in some instrumental broadening of the spectrum. The eight expected transitions are seen, with energies listed in table 4.25.

Transition	Energy (cm^{-1})
$E_1 \rightarrow Z_1$	27918.4
$E_1 \rightarrow Z_2$	27880.9
$E_1 \rightarrow Z_3$	27864.7
$E_1 \rightarrow Z_4$	27812.8
$E_2 \rightarrow Z_1$	27963.1
$E_2 \rightarrow Z_2$	27925.3
$E_2 \rightarrow Z_3$	27910.0
$E_2 \rightarrow Z_4$	27858.6

Table 4.25 : Transition energies of $^1D_2 \rightarrow {}^3H_6$ fluorescence lines for the C_{3v} centre of CaF_2:Tm^{3+}.

Fluorescence Spectrum of the $^1D_2 \rightarrow {}^3F_4$ Transitions

The $^1D_2 \rightarrow {}^3F_4$ fluorescence spectrum is shown in figure 4.47 for sample temperatures of 15 K and 45 K. With $J = 4$, the $^3F_4$ multiplet should split into six crystal-field levels. However, seven transitions appear to originate from the E_1 emitting state. The assignments in figure 4.47 have been made in conjunction with those of the $^1G_4 \rightarrow {}^3F_4$ fluorescence spectrum (figure 4.42) with the origin of the unassigned line at 22117 cm^{-1} uncertain.

The decreased intensity of the $E_1 \rightarrow Y_5$ line at 45 K is also anomalous. This line tunes with the C_{3v} excitation line so does belong with this centre. In addition, both the $D_1 \rightarrow Y_5$ and $D_2 \rightarrow Y_5$ transitions are seen at the appropriate energy in the $^1G_4 \rightarrow {}^3F_4$ fluorescence spectrum (figure 4.42), which confirms this assignment. The transition energies of the $^1D_2 \rightarrow {}^3F_4$ fluorescence spectrum are given in table 4.26.

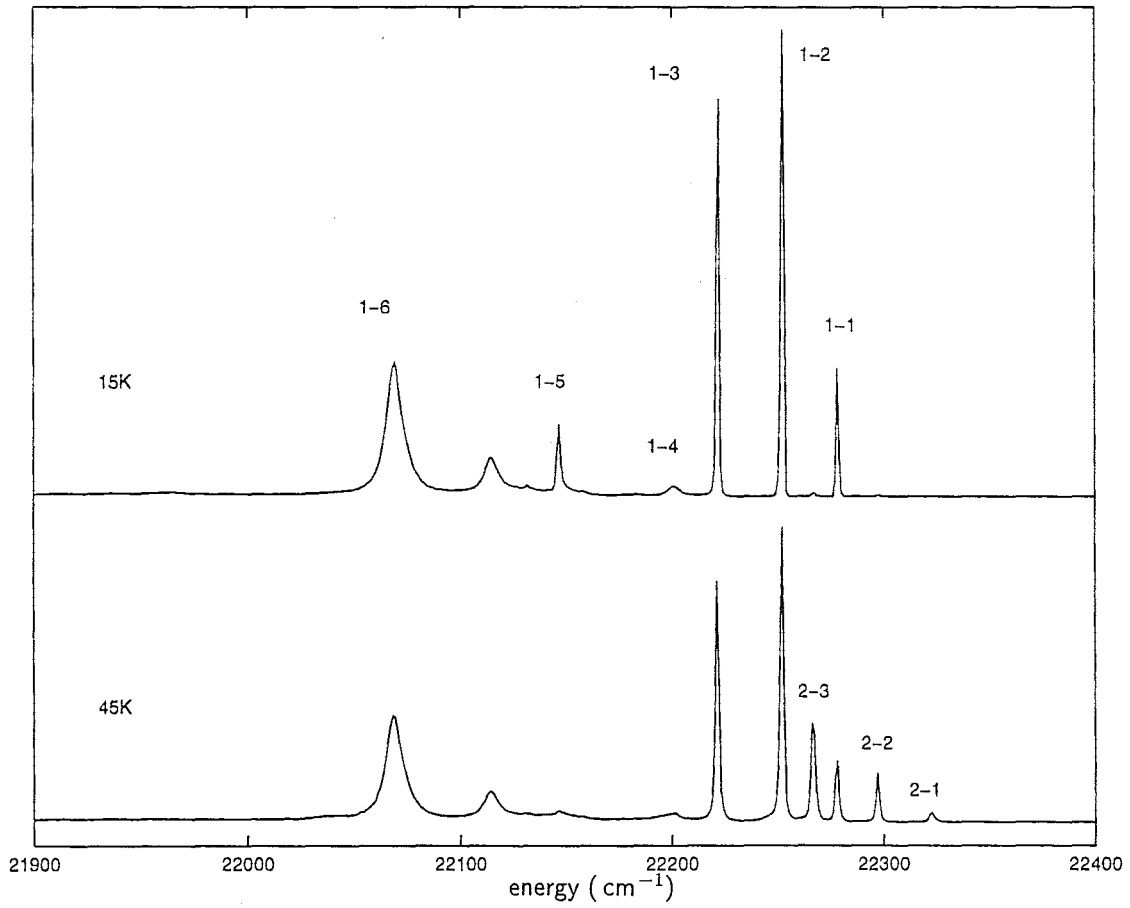

Figure 4.47 : 15 K and 45 K $^1D_2 \rightarrow {}^3F_4$ fluorescence spectra of the C_{3v} centre in CaF_2:0.05%Tm^{3+}, pumping the $A_1 \rightarrow E_2$ excited-state absorption transition at 15462.2 cm^{-1}. Transitions are identified by their upper and lower crystal-field level labels.

Transition	Energy (cm^{-1})
$E_1 \rightarrow Y_1$	22279.0
$E_1 \rightarrow Y_2$	22253.6
$E_1 \rightarrow Y_3$	22222.6
$E_1 \rightarrow Y_4$	22201.5
$E_1 \rightarrow Y_5$	22147.7
$E_1 \rightarrow Y_6$	22070.2
$E_2 \rightarrow Y_1$	22323.6
$E_2 \rightarrow Y_2$	22298.3
$E_2 \rightarrow Y_3$	22267.3
unassigned	22115.2

Table 4.26 : Transition energies of $^1D_2 \rightarrow {}^3F_4$ fluorescence lines for the C_{3v} centre of CaF_2:Tm^{3+}.

Fluorescence Spectrum of the $^1D_2 \rightarrow {}^3H_5$ Transitions

The 15 K and 45 K $^1D_2 \rightarrow {}^3H_5$ fluorescence spectra are shown in figure 4.48. At 15 K, four transitions are seen corresponding to $E_1 \rightarrow X_1$, X_2, X_3, X_4 as derived from the $^1G_4 \rightarrow {}^3H_5$ spectrum. However, an extra line is seen at 19801 cm^{-1}. At 45 K, this line almost disappears, and a corresponding E_2 hot line does not appear. However the $E_1 \rightarrow Y_5$ transition had a similar behaviour, so this alone does not rule out the 19801 cm^{-1} line as belonging to the C_{3v} centre.

The transition from the D_1 level to this $^3H_5$ level should be present at the right hand edge of the $^1G_4 \rightarrow {}^3H_5$ spectrum (figure 4.43), but is not observed. In addition, the crystal-field splitting between this level and the other $^3H_5$ levels would be anomalously large in comparison to the other multiplets of this centre, and also to the calculated splitting. The crystal-field fit of section 4.4.3 was repeated without the experimental $^3H_5$ energies, and gave no indication that such a large splitting would be expected. Hence, the line at 19801 cm^{-1} is thought to be spurious. The energies of this line and the assigned lines are tabulated in table 4.27.

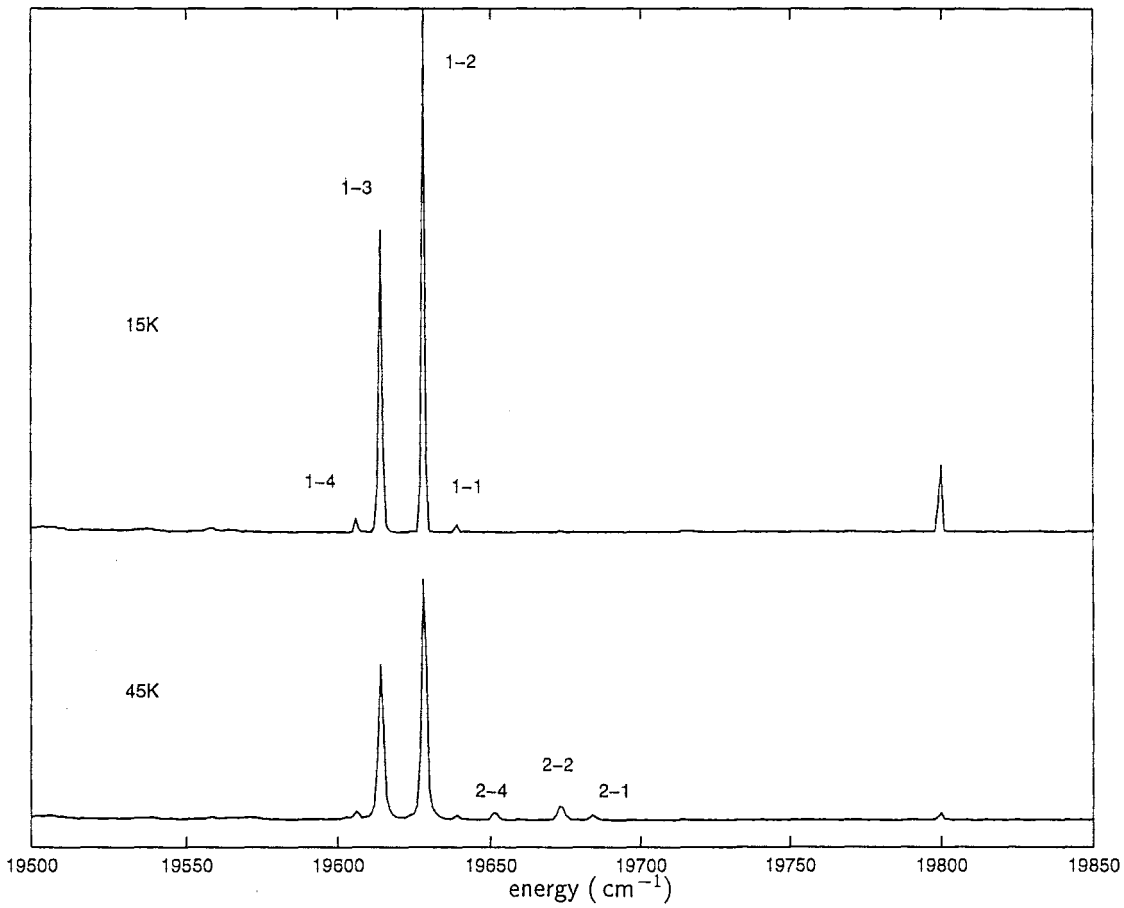

Figure 4.48 : 15 K and 45 K $^1D_2 \rightarrow {}^3H_5$ fluorescence spectra of the C_{3v} centre in CaF_2:0.05%Tm^{3+}, pumping the $A_1 \rightarrow E_2$ excited-state absorption transition at 15462.2 cm^{-1}. Assigned transitions are identified by their upper and lower crystal-field level labels, while the line labelled † is not assigned to the C_{3v} centre.

Transition	Energy (cm^{-1})
$E_1 \rightarrow X_1$	19640.2
$E_1 \rightarrow X_2$	19629.5
$E_1 \rightarrow X_3$	19615.6
$E_1 \rightarrow X_4$	19607.5
$E_2 \rightarrow X_1$	19684.7
$E_2 \rightarrow X_2$	19674.0
$E_2 \rightarrow X_4$	19652.2
unassigned	19800.9

Table 4.27 : Transition energies of $^1D_2 \rightarrow {}^3H_5$ fluorescence lines for the C_{3v} centre of CaF_2:Tm^{3+}.

Fluorescence Spectrum of the $^1D_2 \rightarrow {}^3H_4$ Transitions

The 15 K and 45 K $^1D_2 \rightarrow {}^3H_4$ fluorescence spectra are shown in figure 4.49. The laser line corresponding to the $E_2 \leftrightarrow A_1$ transition at 15462 cm^{-1} has been shuttered out. The $E_1 \rightarrow A_1$ transition is seen at 15416.9 cm^{-1}, and the $E_1 \rightarrow A_2$ transition at 15355.1 cm^{-1}. The remaining sharp lines near 15370 cm^{-1} become weak at 45 K and, further, no corresponding levels are seen in the $^3H_4$ excitation spectrum at either 15 K or 60 K (figure 4.36). These lines have therefore not been assigned as $^1D_2 \rightarrow {}^3H_4$ transitions. As the strong transition at 15345 cm^{-1} corresponds to the strong $D_1 \rightarrow Y_1$ transition of the C_{4v} centre, it is likely to be due to cross pumping. There are several features in this spectrum, clearly not all of which are $^1D_2 \rightarrow {}^3H_4$ transitions of the C_{3v} centre. It would seem unlikely that cross-pumping of other centres would be responsible for more than a few of these lines, since not much cross-pumping is observed in other fluorescence spectra. Some of the features in this spectrum could be due to Raman scattering, since this is in the proximity of the laser line and relatively high powers (300 mW) are being used.

Fluorescence Spectrum of the $^1D_2 \rightarrow {}^3F_3$ Transitions

The $^1D_2 \rightarrow {}^3F_3$ fluorescence spectrum at 15 K and 45 K is shown in figure 4.50. The

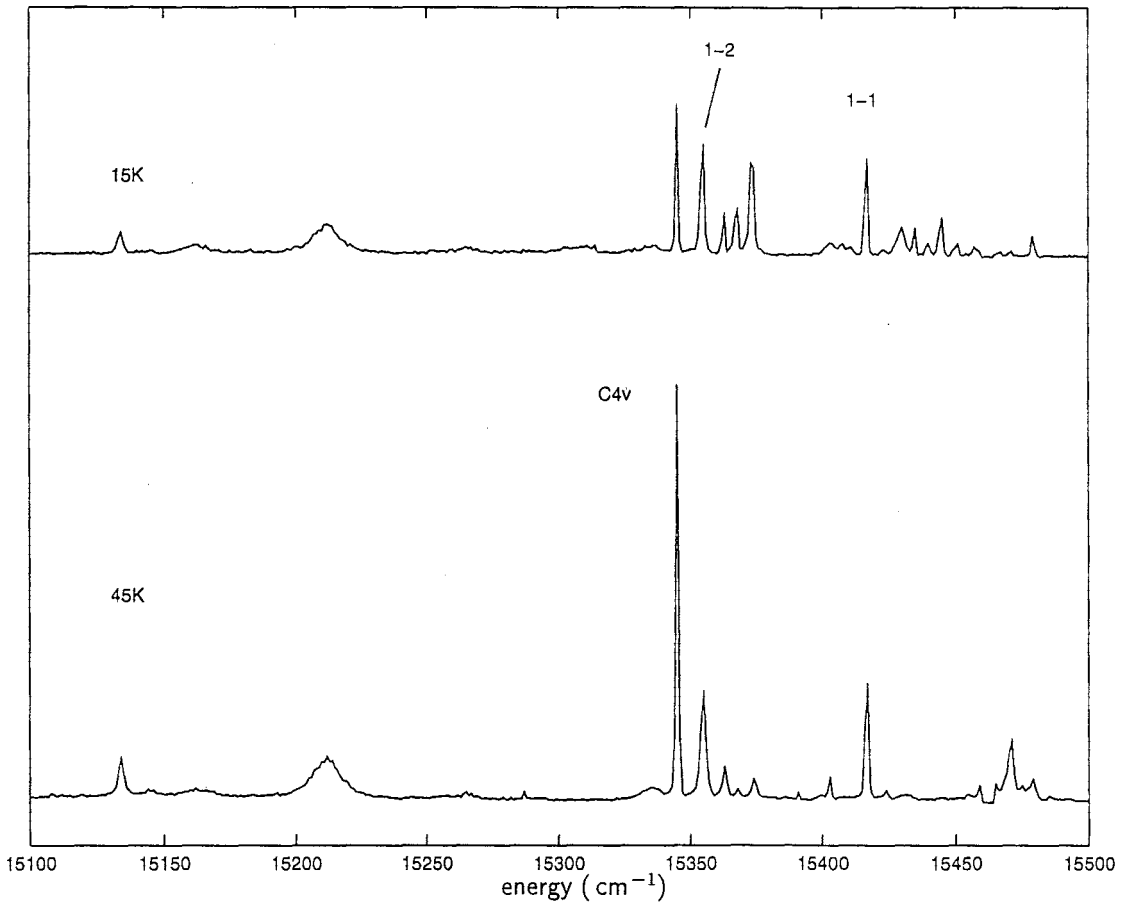

Figure 4.49 : 15 K and 45 K $^1D_2 \rightarrow {}^3H_4$ fluorescence spectra of the C_{3v} centre in CaF_2:0.05%Tm^{3+}, pumping the $A_1 \rightarrow E_2$ excited-state absorption transition at 15462.2 cm^{-1}. Assigned transitions are identified by their upper and lower crystal-field level labels, with one strong line assigned with a C_{4v} centre transition and so labelled.

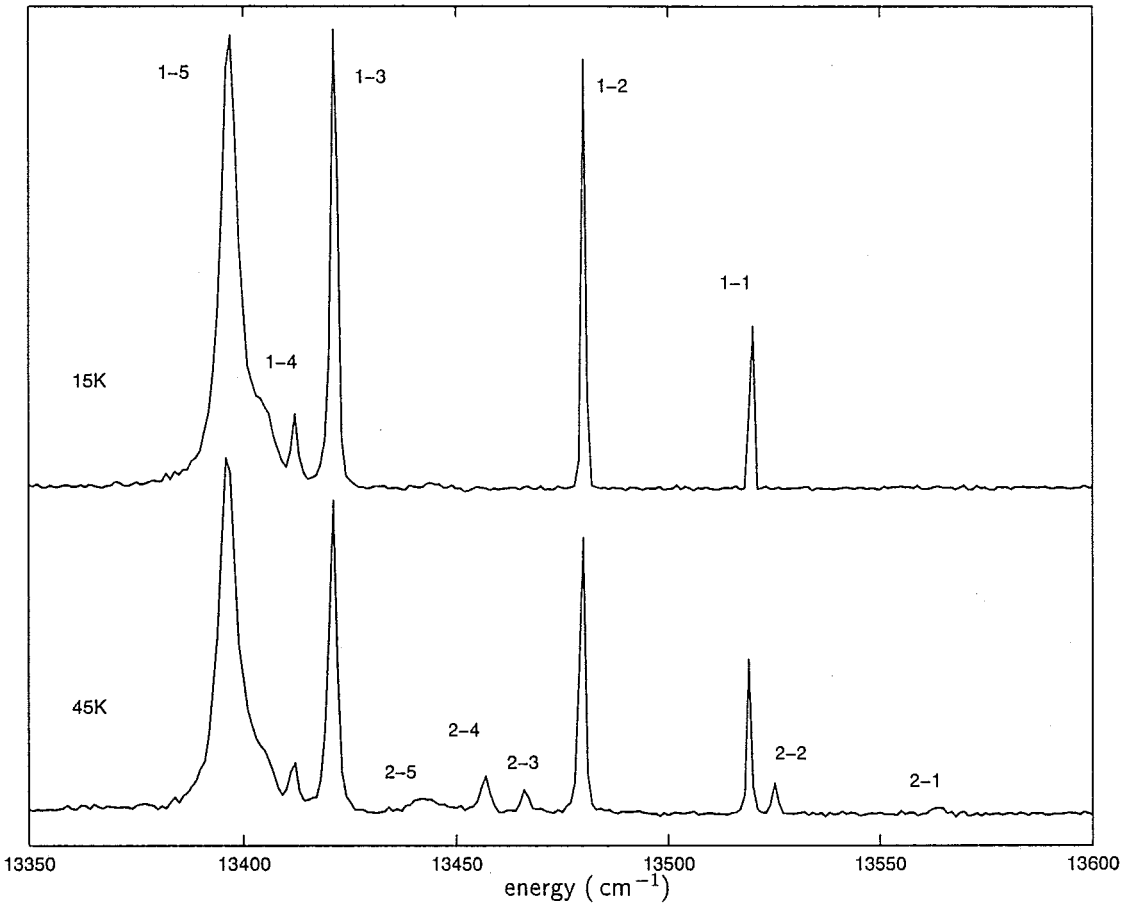

Figure 4.50 : 15 K and 45 K $^1D_2 \rightarrow {}^3F_3$ fluorescence spectra of the C_{3v} centre in CaF_2:0.05%Tm^{3+}, pumping the $A_1 \rightarrow E_2$ excited-state absorption transition at 15462.2 cm^{-1}. Transitions are identified by their upper and lower crystal-field level labels.

$^1D_2 \rightarrow {}^3F_3$ transition is magnetic-dipole allowed, and all five levels of $^3F_3$ are seen from both the E_1 and E_2 levels. The B_4 level, which was not seen in the $^3F_3$ excitation spectrum, is observed here. Its assignment is confirmed by the appearance of the $E_2 \rightarrow B_4$ transition at 45 K.

The $E_1 \rightarrow B_5$ transition lineshape appears to be obscuring another line. However, because all the other lines have corresponding transitions from the E_2 level, the assignments are clear. The transition energies are listed in table 4.28.

Transition	Energy (cm^{-1})
$E_1 \rightarrow B_1$	13519.1
$E_1 \rightarrow B_2$	13479.7
$E_1 \rightarrow B_3$	13421.0
$E_1 \rightarrow B_4$	13411.5
$E_1 \rightarrow B_5$	13396.3
$E_2 \rightarrow B_1$	13563.2
$E_2 \rightarrow B_2$	13525.1
$E_2 \rightarrow B_3$	13466.0
$E_2 \rightarrow B_4$	13456.9
$E_2 \rightarrow B_5$	13442.0

Table 4.28 : Transition energies of $^1D_2 \rightarrow {}^3F_3$ fluorescence lines for the C_{3v} centre of CaF_2:Tm^{3+}.

Fluorescence Spectrum of the $^1D_2 \rightarrow {}^3F_2$ Transitions

The $^1D_2 \rightarrow {}^3F_2$ fluorescence spectrum at 15 K and 45 K is shown in figure 4.51. The $^1D_2 \rightarrow {}^3F_2$ transition is also magnetic-dipole allowed, and all three levels of the $^3F_2$ multiplet, previously determined from the excitation spectrum (figure 4.39), are seen as fluorescence transitions from both the E_1 and E_2 levels.

The transition energies are listed in table 4.29.

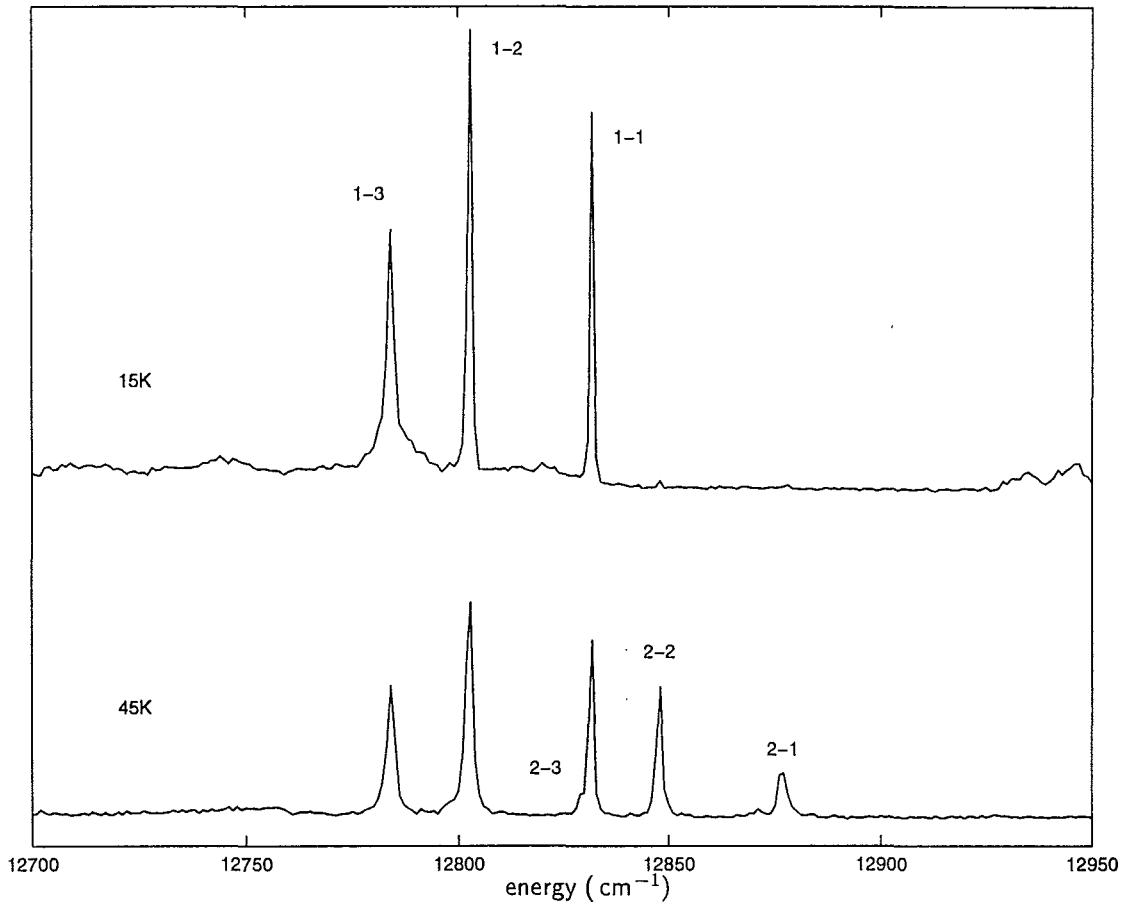

Figure 4.51 : 15 K and 45 K $^1D_2 \rightarrow {}^3F_2$ fluorescence spectra of the C_{3v} centre in CaF_2:0.05%Tm^{3+}, pumping the $A_1 \rightarrow E_2$ excited-state absorption transition at 15462.2 cm^{-1}. Transitions are identified by their upper and lower crystal-field level labels.

Transition	Energy (cm^{-1})
$E_1 \rightarrow C_1$	12831.6
$E_1 \rightarrow C_2$	12802.8
$E_1 \rightarrow C_3$	12784.1
$E_2 \rightarrow C_1$	12876.4
$E_2 \rightarrow C_2$	12848.1
$E_2 \rightarrow C_3$	12829

Table 4.29 : Transition energies of $^1D_2 \rightarrow {}^3F_2$ fluorescence lines for the C_{3v} centre of CaF_2:Tm^{3+}.

4.4.3 Crystal-Field Analysis for the C_{3v} Centre in CaF_2:Tm^{3+}

In the absence of any experimental irrep assignments, the assignments in this fit were made in two steps. A preliminary calculation was performed without fitting, using the best-fit parameters obtained from the crystal-field analysis for the C_{3v} centre in CaF_2:Er^{3+} [17]. The experimental energy levels were then matched to the resulting calculated levels simply in the order in which they appeared. Upon performing a fit with these assignments, two pairs of levels (Y_1/Y_2 and C_2/C_3) were found to reverse their ordering. These assignments were reversed to produce the final fit.

As a rudimentary check of the ordering, all of the levels of each multiplet in turn were left out of the fit. In each case the calculated order remained the same as that assigned. This gives some confidence in the fit, but it may still be that several mis-assignments are collectively forcing an incorrect minimum. Where the number of levels is short of the expected number for a particular multiplet, it has been assumed that the observed levels are the lower energy ones. This may be an inappropriate assumption which would lead to an incorrect fit, but again the checking procedure just outlined did not indicate this to be the case.

As with the crystal-field fit of the C_{4v} centre (section 4.3.3), the electrostatic (F_i), spin-orbit (ζ) and crystal-field ($C_q^{(k)}$) parameters were varied, while the minor free-ion parameters were held fixed at the LaF_3:Tm^{3+} values [14] as given in table 4.12.

The best-fit values of those parameters which were varied are listed in table 4.30.

Parameter	Value (cm^{-1})	Parameter	Value (cm^{-1})
F^2	102372.0	B_A^2	231.4
F^4	71469.8	B_A^4	374.4
F^6	51497.8	$\hat{B}_A^6$	-480.9
ζ	2635.6	B_A^6	-411.3
		B_C^4	-40.7
		B_C^6	556.5

Table 4.30 : Best-fit values of the free-ion and crystal-field parameters which were varied in the fit for the C_{3v} centre of CaF_2:Tm^{3+}.

These eleven parameters (including a uniform shift of the entire configuration) gave a standard deviation from the measured levels of 10.2 cm^{-1} for the 30 energy levels fitted.

The results of the crystal-field fit presented here are not as stringent as those presented for the C_{4v} centre, in that the C_{3v} irreps of the states have not been determined experimentally. Indeed, some of the irrep assignments from the fit, are contrary to the few proposed experimental assignments in section 4.4.1, and in fact, to Zeeman splittings measured in section 4.2.1. For example, the ground state was proposed to be a γ_2 irrep on the basis of observing four allowed transitions to the $^3F_3$ multiplet. Here it has been fitted to a γ_1 state. Further, the D_1 state has also been assigned to a γ_1 state, which implies that the $Z_1 \rightarrow D_1$ transition should be allowed. This transition was not seen in either the excitation or fluorescence spectrum, which indicated that the two states should be singlet states of different irreps.

In the Zeeman measurements of section 4.2.1, four of the six absorption transitions assigned to the C_{3v} centre were observed to split in magnetic fields applied parallel to the $\langle 100 \rangle$ crystal axis. However the g-values as listed in table 4.32 are not in good agreement with the calculated values, and the X_3 and X_4 levels appear to be mis-assigned.

Because attempts to force the fit to accommodate such assignments were ultimately unsuccessful, the fit of table 4.31 is presented as a best attempt without regard to the experimental polarisation ratios or relative intensities.

Multiplet/ C_{3v} irrep		Energies (cm^{-1}) calculated	measured
$^3H_6$	γ_1	7.9	0.0
	γ_2	29.3	37.4
	γ_3	60.8	53.4
	γ_3	100.9	105.1
	γ_3	195.1	-
	γ_1	211.2	-
	γ_3	266.1	-
	γ_3	317.3	-
	γ_1	385.0	-
$^3F_4$	γ_1	5634.7	5639.9
	γ_3	5658.1	5664.7
	γ_3	5700.5	5696.6
	γ_2	5717.4	5716.9
	γ_1	5770.9	5770.7
	γ_3	5855.6	5848.2
$^3H_5$	γ_2	8266.0	8279.6
	γ_3	8299.2	8290.2
	γ_1	8301.1	8304.0
	γ_3	8322.9	8312.2
	γ_3	8394.1	-
	γ_2	8417.4	-
	γ_3	8460.2	-

Multiplet/ C_{3v} irrep		Energies (cm^{-1}) calculated	measured
$^3H_4$	γ_3	12521.0	12501.5
	γ_1	12555.9	12564.6
	γ_2	12604.7	-
	γ_3	12683.8	-
	γ_3	12768.9	-
	γ_1	12820.4	-
$^3F_3$	γ_2	14411.7	14398.8
	γ_3	14432.6	14438.2
	γ_1	14487.2	14497.2
	γ_2	14500.6	14506.9
	γ_3	14523.0	14520.8
$^3F_2$	γ_3	15071.8	15086.2
	γ_1	15113.8	15115.7
	γ_3	15132.2	15134.0
$^1G_4$	γ_1	21108.8	21118.9
	γ_3	21145.7	21149.8
	γ_3	21210.0	21205.3
	γ_2	21231.4	21225.2
	γ_1	21276.0	-
	γ_3	21428.8	-
$^1D_2$	γ_3	27923.8	27918.4
	γ_3	27967.0	27963.1
	γ_1	27996.4	-

Table 4.31 : Measured and calculated energy levels for the CaF_2:Tm^{3+} C_{3v} centre. Irrep assignments were made arbitrarily, purely to obtain the best possible fit to the experimental data.

Transition	energy (cm^{-1})	Measured $g_{\langle 100\rangle}$	Calculated $g_{\langle 100\rangle}$
$Z_1 \rightarrow Y_2$	5663.4	3.6	3.1
$Z_1 \rightarrow Y_3$	5694.3	0.9	1.7
$Z_1 \rightarrow X_1$	8277.2	0	0
$Z_1 \rightarrow X_2$	8287.8	0.5	1.8
$Z_1 \rightarrow X_3$	8301.7	1.2	0
$Z_1 \rightarrow X_4$	8309.6	0	2.3

Table 4.32 : Measured and calculated values of $g_{\langle 100\rangle}$ for $^3F_4$ and $^3H_5$ multiplet absorption lines.

The situation could be remedied by further Zeeman-splitting experiments. If a sizeable number of the doublets could be identified, with their g-values, the fit presented above could be rigorously tested. Definite assignments on the basis of such data would give greater confidence in the fit. As an additional point, Zeeman experiments on $\langle 111\rangle$ oriented samples might allow one particular subsite oriented parallel to the field to be pumped selectively. Polarisation ratios measured with such an arrangement should be much less ambiguous and would discriminate magnetic-dipole from electric-dipole transitions as well as unresolved doublets. An attempt to measure Zeeman splittings of several upconversion-fluorescence transitions was unsuccessful due to their low signal intensity. The physical dimensions of the magnet dewar are such that a lens cannot be placed closer than about 20 cm from the sample, resulting in a weakly focussed laser beam at the sample, and therefore low upconversion-fluorescence intensities. A similar problem occurred with the fluorescence-signal collection lens, and the mapping of the horizontal image onto vertical slits compounded this problem. This problem might be overcome with a double-laser experiment. If two cw tunable lasers could be overlapped at the sample, far more efficient upconversion should be achievable. Such an experiment could be performed using the Ti:sapphire laser to pump the $^3H_4$ multiplet and the Rhodamine 640 dye laser for the excited-state absorption transitions. However, both of these lasers require argon-laser pumping, so this would be possible only with the availability of a single sufficiently high-power argon laser, or two argon lasers.

4.4.4 Fluorescence Lifetimes

The measurement of the fluorescence lifetimes of the C_{4v} centre of CaF_2:Tm^{3+} was described in section 4.3.4. The same methods were employed for the C_{3v} centre, including the two-laser method used to measure the $^1D_2$ multiplet lifetime. A sample with a Tm^{3+} concentration of 0.05% (molar) was used for the transients displayed here. No significant change in lifetimes was observed for a lower concentration of 0.02%.

Rhodamine 640 dye could be used to pump the $^3F_2$ multiplet for this C_{3v} centre. This was not possible with the C_{4v} centre because of the weak absorption strengths of the transitions for that centre. Figure 4.52 shows the fluorescence-decay transient of emission from the $^3H_4$ multiplet, with pumping of the $^3F_2$ multiplet levels. No significant rise time is observed, indicating that the (largely non-radiative) decay of the $^3F_2$ and $^3F_3$ multiplets is very much faster than the lifetime of the $^3H_4$ multiplet itself. The fitted decay time for the $^3H_4$ multiplet is 3.1 ms.

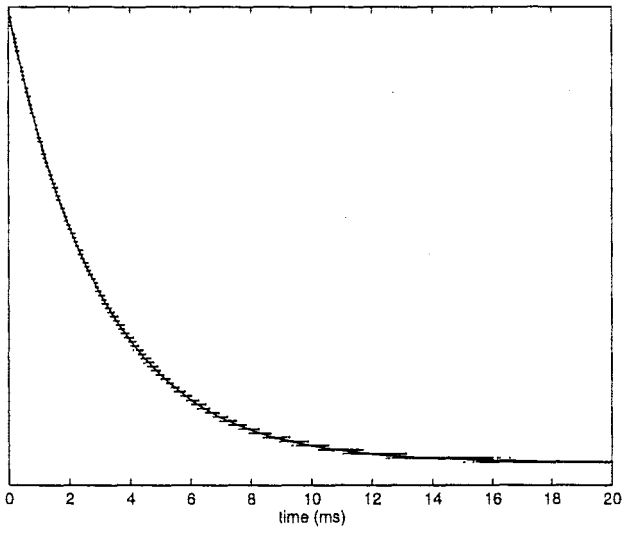

Figure 4.52 : 15 K fluorescence decay transient of the $^3H_4$ multiplet of the C_{3v} centre of CaF_2:0.05%Tm^{3+}, upon pumping the $Z_1 \rightarrow C_1$ excitation transition at 15086 cm^{-1} and monitoring the $A_1 \rightarrow Z_1$ fluorescence transition at 12502 cm^{-1}. The solid curve represents a decay time of 3.1 ms.

The $^1G_4$ multiplet was pumped directly with Coumarin 460 dye, or via excited-state absorption with two Rhodamine 640 dye lasers. Figure 4.53 shows the $^1G_4$ multiplet decay transient upon direct pumping of the $Z_1 \rightarrow D_2$ absorption line. The fitted decay time is 1.1 ms.

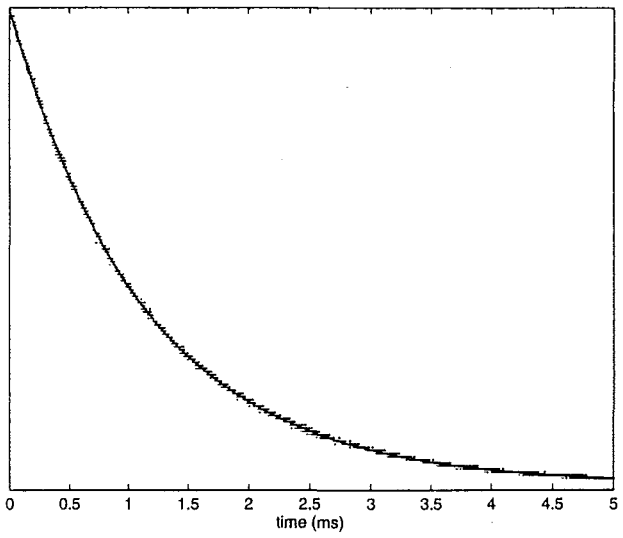

Figure 4.53 : 15 K fluorescence decay transient of the $^1G_4$ multiplet of the C_{3v} centre of CaF_2:0.05%Tm^{3+}, pumping the $Z_1 \rightarrow D_2$ excitation transition at 21150 cm^{-1} and monitoring the $D_1 \rightarrow Z_2$ fluorescence transition at 21082 cm^{-1}. The solid curve represents a decay time of 1.1 ms.

The $^1D_2$ multiplet could not be pumped directly, but was pumped by the two-laser excited-state absorption method. For the transient in figure 4.54, the cw laser was tuned to pump the $Z_1 \rightarrow C_1$ transition at 15086 cm^{-1} and the pulsed laser to the $A_1 \rightarrow E_1$ transition at 15417 cm^{-1}. No upconversion was observed with only the cw laser running. The fitted lifetime of $^1D_2$ is 0.10 ms.

The measured lifetimes of the $^3H_4$, $^1G_4$ and $^1D_2$ multiplets of the Tm^{3+} ion in the C_{4v} and C_{3v} centres in CaF_2 are summarised in table 4.33.

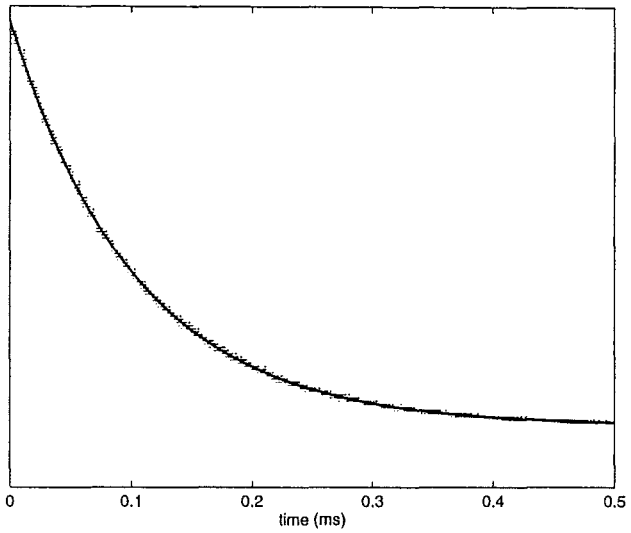

Figure 4.54 : 15 K fluorescence decay transient of the $^1D_2$ multiplet of the C_{3v} centre of CaF_2:0.05%Tm^{3+}, upon pumping the $Z_1 \rightarrow C_1$ transition at 15086 cm^{-1} with the cw laser and the $A_1 \rightarrow E_1$ transition at 15417 cm^{-1} with the pulsed laser and monitoring broadband blue/violet upconversion fluorescence. The solid curve represents a decay time of 0.10 ms.

Multiplet	CaF_2:Tm^{3+} lifetime (ms ±5%)	
	C_{4v} centre	C_{3v} centre
$^3H_4$	3.3	3.1
$^1G_4$	2.1	1.1
$^1D_2$	0.18	0.10

Table 4.33 : A comparison of the experimental lifetimes of the $^3H_4$, $^1G_4$ and $^1D_2$ lifetimes of the C_{4v} and C_{3v} centres of CaF_2:Tm^{3+}.

4.5 Analysis of the Cubic-Centre Line in CaF_2:Tm^{3+}

In the infrared-absorption spectrum of the $^3H_5$ multiplet, section 4.2, a strong absorption line was found at $8429.6\,cm^{-1}$ which could not be associated with either of the C_{4v} or C_{3v} centres. As this line is the only strong absorption line for all of the excited multiplets up to $^1D_2$ at $30000\,cm^{-1}$ which could not be so assigned, the possibility of it being associated with a cluster centre can be rejected, and it is assigned to the remotely charge-compensated essentially-cubic Tm^{3+} centre.

Because it has a centre of inversion, electric-dipole transitions are strictly forbidden for the cubic centre (section 2.5). Therefore, any purely-electronic transition can only take place if it is magnetic-dipole allowed. The ($\Delta J = 0, \pm 1,\ \Delta L = \Delta S = 0$) selection rules for magnetic-dipole transitions are such that the most absorption transitions in the optical regime, being between different LS terms, are magnetic-dipole forbidden.

Neglecting crystal-field mixing between multiplets, for the Tm^{3+} ion the $^3H_6 \rightarrow {}^3H_5$ transitions are the only absorption transitions which are strongly magnetic-dipole allowed, with the absorption transitions to the $^1I_6$ multiplet being the only others to gain some magnetic-dipole intensity through the small spin-orbit coupling with the $^3H_6$ multiplet. Therefore absorption transitions of the cubic centre are not expected to be observed in the absorption spectra to multiplets other than the $^3H_5$ multiplet, which is consistent with the results of section 4.2.

The Zeeman splittings of the absorption lines of the $^3H_5$ multiplet were shown in figure 4.9 in section 4.2.1. The line assigned to the cubic centre split into two components; the energies of these Zeeman sub-transitions are plotted in figure 4.55. The solid lines through the experimental points represent the best-fit linear splitting, giving a g-value of 5.09.

4.5.1 Cubic-Centre Wavefunctions

The cubic crystal-field Hamiltonian for the $4f^n$ configuration is parametrised by two parameters, B^4_C and B^6_C:

$$\mathcal{H} = B^4_C\, C^{(4)}_C + B^6_C\, C^{(6)}_C\ .$$

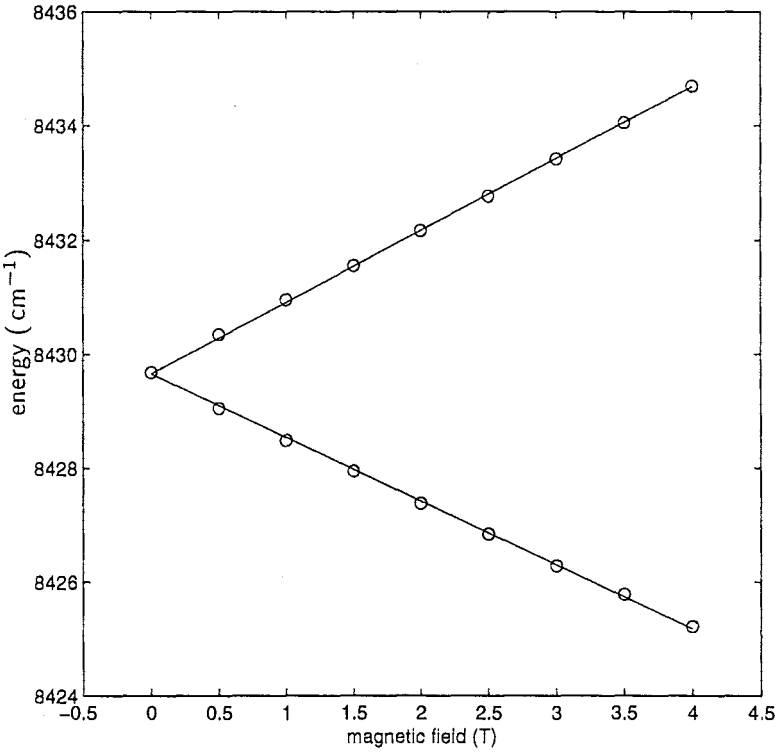

Figure 4.55 : Experimental splitting pattern of the 8429.6 cm^{-1} absorption transition of the cubic centre in CaF_2:0.02%Tm^{3+} for magnetic fields parallel to the ⟨100⟩ crystal axes.

The form of the angular operators of the fourth and sixth degree cubic terms, $C_C^{(4)}$ and $C_C^{(6)}$, are given by the leading two terms of equation 2.2 or equation 2.3, depending on whether a tetragonal or trigonal quantisation is chosen. We use the tetragonal quantisation of equation 2.2 to be consistent with Lea *et al* [52].

In order to deduce the wavefunction of the ground state in the cubic centre of CaF_2:Tm^{3+}, it is necessary only to know the order of the levels, not their absolute energies. Following Lea *et al* [52], we re-parametrise the Hamiltonian as:

$$\mathcal{H} = W[\, x\, C_C^{(4)} + (1 - |x|)\, C_C^{(6)}\,]$$

so that the order of the levels is determined by the single parameter x, provided only that the sign of W is known. The cubic-field splitting diagrams of the $^3H_6$ and $^3H_5$ multiplets of Tm^{3+} as a function of the x parameter are plotted in figures 4.56 and 4.57, respectively, with the energy in units of W and levels labelled by their cubic irreps, Γ_i. Note that we use here the Racah spherical-tensor formalism, rather than the operator equivalents used by Lea *et al*. The resulting splitting diagrams are qualitatively similar, but different values of x and W may arise. The advantage of using the spherical tensors is that the same values of x and W apply to all multiplets, whereas operator equivalents require different parameters for each multiplet.

The crystal-field parameters for the CaF_2:Tm^{3+} cubic centre can be estimated by using the cubic terms of the C_{4v} Hamiltonian determined from the experimental fit to the CaF_2:Tm^{3+} data in section 4.3.3, or by using the cubic-field parameters reported for the cubic centre in CaF_2: Er^{3+} [2]. In the parametrisation described here, these two sets of parameters give $x = -0.69$ and $x = -0.76$ respectively, both with $W > 0$. In either case, the $^3H_6$ splitting diagram, figure 4.56, predicts that the ground state is unambiguously a Γ_2 singlet. As this becomes a γ_3 singlet in a descent to C_{4v} symmetry, this is consistent with the C_{4v} centre having a well isolated γ_3 ground state as determined in section 4.3.

Since the magnetic-dipole operator transforms as Γ_4, the final state in an absorption transition from the Γ_2 ground state must transform as $\Gamma_4 \times \Gamma_2 = \Gamma_5$. Crystal-field calculations using either set of parameters above show that the Γ_5 state is the lowest crystal-field component of the $^3H_5$ multiplet and is therefore expected to be a sharp absorption line. Further, this is the only Γ_5 state on the $^3H_5$ multiplet and therefore is the only transition expected to be observed. This is in agreement with

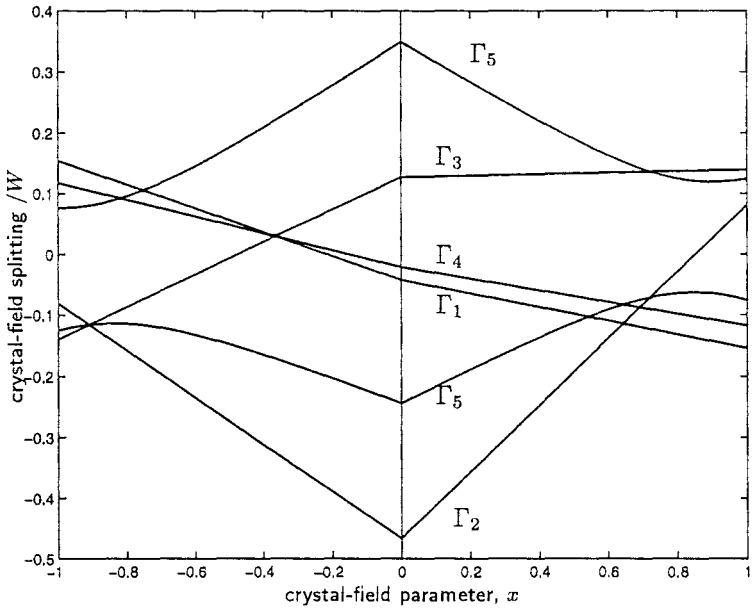

Figure 4.56 : Calculated energy levels of the $^3H_6$ multiplet of Tm^{3+}, in units of W, as a function of the crystal-field parameter, x (after [52]). The levels are labelled by their cubic irreps.

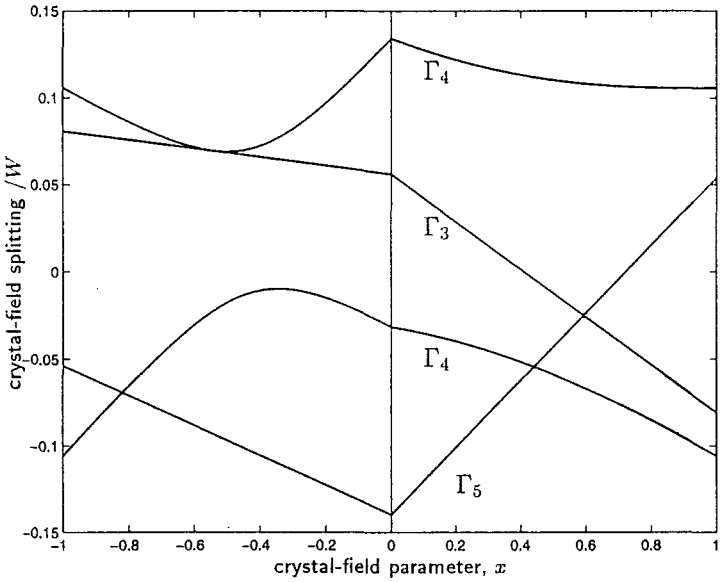

Figure 4.57 : Calculated energy levels of the $^3H_5$ multiplet of Tm^{3+}, in units of W, as a function of the crystal-field parameter, x (after [52]). The levels are labelled by their cubic irreps.

the experimental result that only one line was measured which might belong to this centre.

Because both of the states involved in this transition are the only state of their appropriate irrep in their multiplets, there is no significant crystal-field mixing of the wavefunctions. Therefore we need no more information to be able to write the form of the ground state wavefunction as:

$$Z_1 = |^3H_6, \Gamma_2\gamma_3\mu_2\rangle = \sqrt{\tfrac{11}{32}}\,(|2\rangle + |-2\rangle) - \sqrt{\tfrac{5}{32}}\,(|6\rangle + |-6\rangle)$$

and the Γ_5 triplet, lowest level of the $^3H_5$ multiplet as:

$$\begin{aligned} X_1^+ = |^3H_5, \Gamma_5\gamma_5\mu_3\rangle &= \sqrt{\tfrac{15}{32}}\,|5\rangle - \sqrt{\tfrac{14}{32}}\,|1\rangle - \sqrt{\tfrac{3}{32}}\,|-3\rangle \\ X_1^- = |^3H_5, \Gamma_5\gamma_5\mu_4\rangle &= \sqrt{\tfrac{15}{32}}\,|-5\rangle - \sqrt{\tfrac{14}{32}}\,|-1\rangle - \sqrt{\tfrac{3}{32}}\,|3\rangle \\ X_1^0 = |^3H_5, \Gamma_5\gamma_4\mu_2\rangle &= \tfrac{1}{\sqrt{2}}\,(|2\rangle + |-2\rangle) \end{aligned}$$

where the O_h–C_{4v}–C_4 group-chain decomposition (section 2.3) is used to distinguish components of the degenerate state.

In a magnetic field, the X_1 level will split into three components, with each component of the Γ_4 magnetic-dipole operator connecting the ground state to one of these. For a magnetic field along the $\langle 100\rangle$ axis, the O_h–C_{4v}–C_4 group-chain decomposition is appropriate and gives the transitions:

	O_{md}	$\times$	$^3H_6(Z_1)$	$\rightarrow$	$^3H_5(X_1)$
π :	$\Gamma_4\gamma_2\mu_1$	$\times$	$\Gamma_2\gamma_3\mu_2$	$\rightarrow$	$\Gamma_5\gamma_4\mu_2$
σ_R :	$\Gamma_4\gamma_5\mu_3$	$\times$	$\Gamma_2\gamma_3\mu_2$	$\rightarrow$	$\Gamma_5\gamma_5\mu_4$
σ_L :	$\Gamma_4\gamma_5\mu_4$	$\times$	$\Gamma_2\gamma_3\mu_2$	$\rightarrow$	$\Gamma_5\gamma_5\mu_3$

For the infrared-absorption measurements with the 4 T magnet in the FTIR spectrometer (section 3.3) the magnetic-field direction is always parallel to the optical axis, so that no π transitions (neither magnetic-dipole nor electric-dipole) can be observed. Thus, while the X_1 state splits into three, only the outer two of the three transitions from the ground-state singlet can be observed.

With the wavefunctions determined above, the calculated isotropic g-value for this Γ_5 X_1 state is

$$g_{(X_1)} = 5.17 \text{ (calculated)}.$$

This calculation is in excellent qualitative and quantitative agreement with the two-component splitting in a ⟨100⟩ magnetic field of the line assigned to this cubic-centre transition observed in section 4.2, which gave a measured g-value of

$$g_{(X_1)} = 5.09 \text{ (measured)}.$$

This agreement provides compelling evidence supporting the assignment of the infrared-absorption line at 8429.6 cm^{-1} in CaF_2:Tm^{3+} to a cubic centre. Full confirmation could be attained by demonstrating that the Zeeman splittings are strictly isotropic, as required for a cubic-symmetry centre, by measuring these for magnetic fields applied along a ⟨111⟩ or ⟨110⟩ crystal axis.

4.5.2 Relative Concentrations of the Cubic and Tetragonal Centres in CaF_2:0.01%Tm^{3+}

In principle, the concentration N of a particular centre in a crystal can be found from the integrated absorption coefficient L of an absorption line and the transition oscillator strength I of that transition. However, such analyses are usually prevented by an inability to calculate the transition oscillator strength, either for lack of knowledge of the wavefunctions or because of the fact that electric-dipole transitions require knowledge of the higher-configuration admixtures in the wavefunctions (section 2.5). However, in the absorption spectrum of the $^3H_5$ multiplet for CaF_2:Tm^{3+} we have one transition for each of two centres, 8429.6 cm^{-1} for the cubic centre and 8341.5 cm^{-1} for the C_{4v} centre (section 4.3), which are purely magnetic-dipole in character and for which we have well-documented wavefunctions. Therefore, by measuring the linestrengths and calculating the transition magnetic-dipole moments of these two transitions we can calculate the relative concentrations of these two centres.

Transition linestrengths

The absorption coefficient at maximum absorption, α_m, for a crystal of thickness t, is given by

$$\alpha_m = \ln\left(\frac{I_0}{I_m}\right) / t$$

where I_0 is the estimated transmission intensity in the absence of the absorption line and I_m is the transmission intensity at the peak of the absorption line.

If the line-shapes are assumed to be Lorentzian, the the integrated absorption coefficient is given by

$$L = \frac{\pi \alpha_m w}{2}$$

where w is the full linewidth at $I_{1/2} = \sqrt{I_0 I_m}$.

For the absorption spectrum of CaF_2:0.01%Tm^{3+} in figure 4.3 the line-strengths of the 8429.6 cm^{-1} transition of the cubic centre and the 8341.5 cm^{-1} transition of the C_{4v} centre are:

$$\begin{aligned} L(8429.6\,\mathrm{cm}^{-1}) &= 13.3\,\mathrm{cm}^{-1}\mathrm{m}^{-1} \\ L(8341.5\,\mathrm{cm}^{-1}) &= 17.3\,\mathrm{cm}^{-1}\mathrm{m}^{-1} \end{aligned}$$

For other line profiles, modified proportionality constants would be appropriate for the integrated absorption coefficient. However, if it is assumed that the form of the line profile is the same for the two transitions in question then the ratio between the two line-strengths will remain the same.

Transition magnetic-dipole moments

The magnetic-dipole-moment operator is $\mu_B \boldsymbol{M}$ where $\boldsymbol{M} = \boldsymbol{L} + 2\boldsymbol{S}$, so that the magnetic-dipole term in the matter-radiation interaction Hamiltonian can be written in terms of the standard tensor-operator components $\mathrm{M}_q^{(1)}$ [26]:

$$\begin{aligned} \mathcal{H} &= \mu_B \boldsymbol{B} \cdot \boldsymbol{M} \\ &= \mu_B B_z \mathrm{M}_0^{(1)} + \mu_B \frac{-B_x + iB_y}{\sqrt{2}} \mathrm{M}_1^{(1)} + \mu_B \frac{B_x + iB_y}{\sqrt{2}} \mathrm{M}_{-1}^{(1)} \end{aligned}$$

For the cubic centre, each of the three components in this Hamiltonian couples one of the three sub-transitions from the ground-state singlet to the excited-state triplet, the three matrix elements necessarily having the same value. For example, the matrix element for the π component is given by:

$$\begin{aligned} \mathrm{M}_\pi &= \langle {}^3\mathrm{H}_5, \Gamma_5 \gamma_4 \mu_2 | \Gamma_4 \gamma_2 \mu_1 | {}^3\mathrm{H}_6, \Gamma_2 \gamma_3 \mu_2 \rangle \\ &= \tfrac{1}{\sqrt{2}} \sqrt{\tfrac{11}{32}} \left(\langle {}^3\mathrm{H}_5, 2 | \mathrm{M}_0^{(1)} | {}^3\mathrm{H}_6, 2 \rangle + \langle {}^3\mathrm{H}_5, -2 | \mathrm{M}_0^{(1)} | {}^3\mathrm{H}_6, -2 \rangle \right) \end{aligned}$$

$$
\begin{aligned}
&= \frac{\sqrt{11}}{8} \times 2 \times 0.634419 \\
&= 0.526032
\end{aligned}
$$

For an arbitrary incident radiation $\boldsymbol{B}$-vector direction, we have magnetic-dipole transitions to each of the three degenerate Γ_5 states, through the three components of $\boldsymbol{M}$. The intensity of the absorption line is proportional to the sum of the squared matrix elements, yielding:

$$
\begin{aligned}
I(8429.6\,\mathrm{cm}^{-1}) &= I_\pi + I_{\sigma_R} + I_{\sigma_L} \\
&= {\mu_B}^2 \left(B_z^2 + \left| \frac{-B_x + iB_y}{\sqrt{2}} \right|^2 + \left| \frac{B_x + iB_y}{\sqrt{2}} \right|^2 \right) |M|^2 \\
&= {\mu_B}^2 B^2 |M|^2 \\
&= 0.277\, {\mu_B}^2 B^2
\end{aligned}
$$

The $8340\,\mathrm{cm}^{-1}$ absorption transition has been identified as the $Z_1\gamma_3 \rightarrow X_1\gamma_4$ transition of the C_{4v} centre. For the C_{4v} centre, the wavefunctions have been found in the crystal-field fit of section 4.3.3 and for the two states of this transition are:

$$
\begin{aligned}
|\mathrm{Z}_1, {}^3\mathrm{H}_6, \gamma_3\rangle &= 0.6991(\,|{}^3\mathrm{H}_6, 2\rangle + |{}^3\mathrm{H}_6, -2\rangle) - 0.1005(\,|6\rangle + |-6\rangle) \\
|\mathrm{X}_1, {}^3\mathrm{H}_5, \gamma_4\rangle &= 0.7063(\,|{}^3\mathrm{H}_5, 2\rangle + |{}^3\mathrm{H}_5, -2\rangle)
\end{aligned}
$$

This transition is only π_{md} allowed, with matrix element:

$$
\begin{aligned}
M_\pi &= \langle {}^3\mathrm{H}_5, \gamma_4 | \gamma_2 | {}^3\mathrm{H}_6, \gamma_3 \rangle \\
&= 0.7063 \times 0.6991 \times (\langle {}^3\mathrm{H}_5, 2 | \mathrm{M}_0^{(1)} | {}^3\mathrm{H}_6, 2\rangle + \langle {}^3\mathrm{H}_5, -2 | \mathrm{M}_0^{(1)} | {}^3\mathrm{H}_6, -2\rangle) \\
&= 0.7063 \times 0.6991 \times 2 \times 0.634419 \\
&= 0.626520
\end{aligned}
$$

For an arbitrary incident radiation $\boldsymbol{B}$-vector direction we need to consider the three orientations, X, Y, Z of the C_{4v} centre. The intensity of the transition per absorbing C_{4v} centre is the average of these:

$$
\begin{aligned}
I(8341.5\,\mathrm{cm}^{-1}) &= \tfrac{1}{3}(I_X + I_Y + I_Z) \\
&= \tfrac{1}{3}({\mu_B}^2 B_X^2 |M_\pi|^2 + {\mu_B}^2 B_Y^2 |M_\pi|^2 + {\mu_B}^2 B_Z^2 |M_\pi|^2) \\
&= \tfrac{1}{3} {\mu_B}^2 B^2 |M_\pi|^2 \\
&= 0.134\, {\mu_B}^2 B^2
\end{aligned}
$$

Relative concentrations of the cubic and tetragonal centres in CaF_2:0.01%Tm^{3+}

For a fixed sample length and concentration, the linestrength L of a transition is proportional to the concentration of the absorbing centre and to the intensity per centre of that transition. The relative concentrations of the cubic and tetragonal centres can thus be determined from the preceding calculations:

$$\begin{aligned} \frac{N_{tetragonal}}{N_{cubic}} &= \frac{L_{tetragonal}/I_{tetragonal}}{L_{cubic}/I_{cubic}} \\ &= \frac{17.3/0.134}{13.3/0.277} \\ &= 2.69 \end{aligned}$$

These calculations estimate that there are 2.7 times as many C_{4v} centres as cubic centres, which is in qualitative agreement with results described by Moore [62] for CaF_2:Er^{3+}. Moore reported that at 0.1% Er^{3+} the concentration of cubic centres is almost twice that of tetragonal centres, but that at the lower concentration of 0.015% Er^{3+} the situation is reversed and the tetragonal-centre concentration is about 1.5 times the cubic-centre concentration. These results rely either on theoretical predictions or on indirect estimates of the cubic-centre concentration from the total Er^{3+} concentration.

As the Tm^{3+} concentration used in our crystal is nominally 0.01% and may be somewhat lower than that in the grown crystal, our results qualitatively support those of Moore. Further, the results obtained here do not rely on any form of model of defect aggregation in the CaF_2 crystal, but rather follow directly from measurement of line-strengths and wavefunctions derived from crystal-field analyses.

4.6 Deuteration of CaF_2:Tm^{3+} Crystals

The diffusion of deuterium into rare-earth-doped CaF_2 crystals produces essentially the same centres as for diffusion of the normal isotope of hydrogen. The deuterium enters the crystal in the form of negative deuteride ions (D^-), substituting for F^- ions. The fluorescence of the RE^{3+} ions in these centres is strongly quenched by non-radiative relaxation pathways involving the high-energy local-mode vibrations of the H^- and D^- ions. With these local-modes having lower energy for the D^- isotope than for the lighter H^- isotope, this quenching is less pronounced for the D^- compensated centres which were therefore studied here.

Laser selective excitation studies have previously been performed on deuterated CaF_2 and SrF_2 crystals doped with Pr^{3+} [75, 77], Er^{3+} [17, 21], Nd^{3+} [32, 33] and Tb^{3+} [66, 43]. For each of these systems, several centres involving deuteride ions have been observed to undergo reversible or non-reversible polarised bleaching. The most detailed studies have been undertaken on the Pr^{3+} doped systems [75, 77, 66], yielding the proposed series of centres depicted in figure 4.58. These centres comprised the D^- C_{4v} centre, and five other centres involving multiple D^- ions, labelled as the CS(1)...CS(5) centres. The proposed site configurations were based on their spectroscopy, in particular the number of local-mode vibronics present, and bleaching behaviour. The bleaching properties of these centres is outlined in section 4.6.3.

It appears from these configurations that the trend is for the D^- ion to take first the interstitial position, and then to substitute sequentially for the four lattice F^- ions which lie between the RE^{3+} ion and the interstitial D^- ion. Centres involving D^- ions substituting for F^- ions on the other side of the RE^{3+} ion are thought not to exist in non-irradiated samples, but rather only as possible photoproduct centres of the centres proposed in figure 4.58 (see section 4.6.3).

4.6.1 Absorption Spectra of Deuterated CaF_2:Tm^{3+} Crystals

The deuterium treatment process, described in section 3.2, was found to give quite variable concentrations of deuterium in the crystals. The success of the treatment seems to hinge largely on the effect of wetting of the crystal surface by the molten

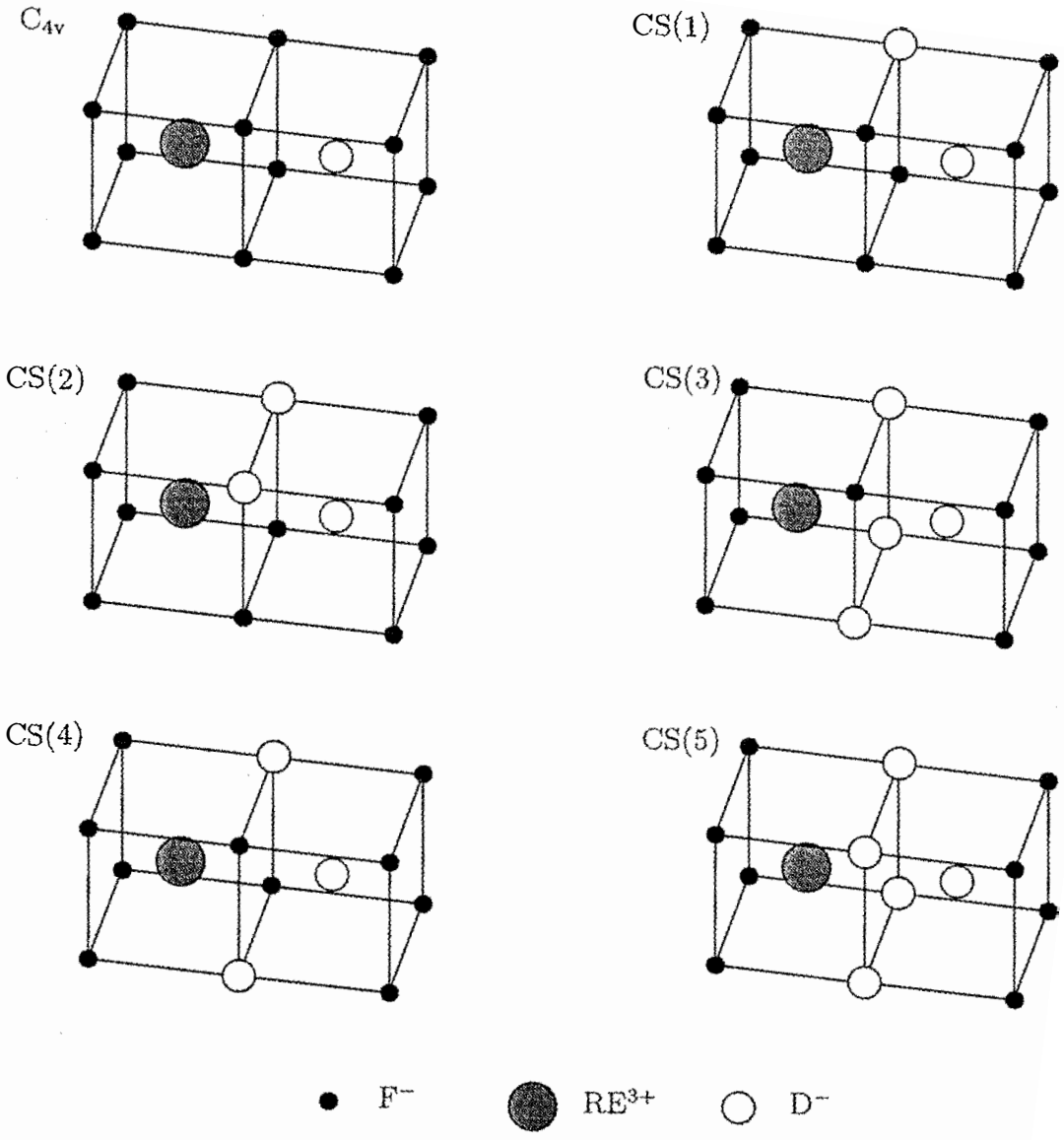

Figure 4.58 : Site configurations of the D^--compensated RE^{3+} centres proposed for CaF_2:Pr^{3+}:D^- and SrF_2:Pr^{3+}:D^- [76, 66]. Atomic sizes are not represented to scale.

aluminium. The deuterium concentration series depicted in figures 4.59 and 4.60 shows the $^3H_4$ and $^3F_3$+$^3F_2$ absorption spectra for the parent CaF_2:Tm^{3+} crystal and representative samples which had been deuterated for periods of 8, 43, and 16 hours. As an example of the variable nature of the success of the treatment, the sample which had been deuterated for 43 hours has considerably less absorption due to deuterium compensated centres than the 16 hour sample.

In the parent-crystal spectra, the absorption lines of the F^- C_{4v} and C_{3v} centres have been labelled. In addition, in the $^3H_4$ spectra, there appears a line near 793 nm which does not correlate with the apparent concentration of D^- ions, as gauged by the other lines. This line is in fact associated with an oxygen compensated centre and is labelled "O^{2-}". The assignment of this line was confirmed by its presence in samples which had been treated in a manner similar to deuteration, but in the presence of pure oxygen only. Oxygen centres can arise from the deuteration process if the apparatus is not sufficiently well flushed of air and water vapour before the treatment.

At low D^- concentrations, a series of lines appears in the proximity of the C_{4v} lines of the $^3F_3$ spectra at 675–685 nm. As the concentration increases, more lines appear in this region. It appears likely that these centres are the Tm^{3+} analogues of the D^- C_{4v} and lower-symmetry multiple-D^- centres found for the other rare-earth ions. The laser selective excitation spectroscopy to be described links these lines with the set of lines near 797 nm in the $^3H_4$ multiplet spectra.

In the higher D^- concentration spectra, another set of lines appears near the C_{3v} lines around 695 nm in the $^3F_3$ spectra and near 803 nm in the $^3H_4$ spectra. It would be tempting to associate this set of lines with the modifications of the C_{3v} centre which have been observed in the case of CaF_2:Er^{3+} [17]. Unfortunately, the C_{3v} centre lines of the $^3F_3$ multiplet represent the extreme lower-energy limit of the Rhodamine 640 dye laser, so it was not possible to perform laser-selective excitation experiments on this set of D^--compensated centres to confirm this association.

It was possible to pump the set of D^--centre lines near the $^3F_3$ C_{4v} centre lines. However, it was not possible to record a broadband excitation spectrum of these lines, due to the very weak fluorescence efficiency of these D^--compensated centres compared to the C_{4v} and C_{3v} F^- centres. It was found that the D^- centre lines

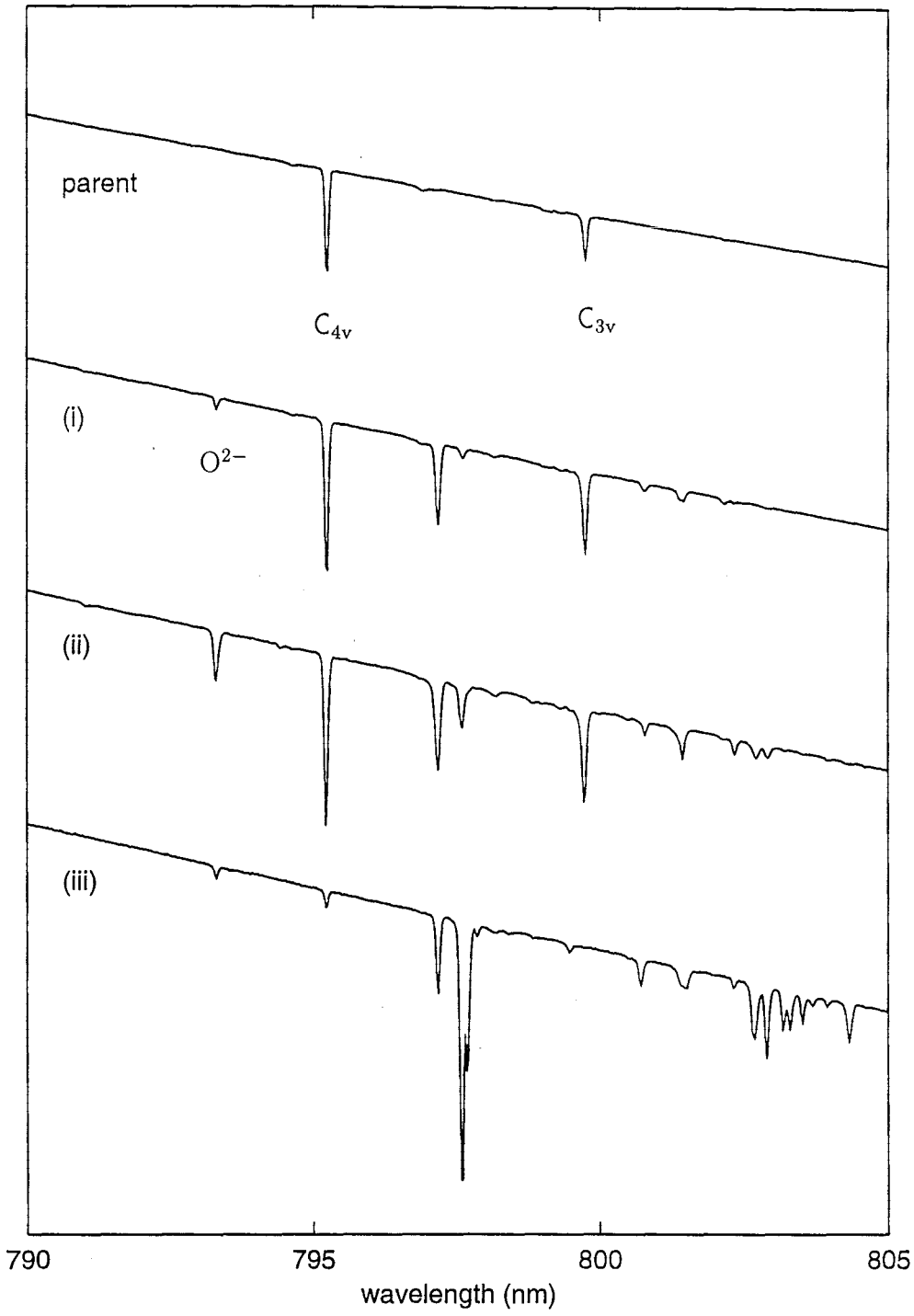

Figure 4.59 : $^3H_4$ multiplet absorption spectra series for the parent CaF_2:0.05%Tm^{3+} crystal and (i),(ii),(iii) samples with increasing D^- concentration. Lines associated with the C_{4v} and C_{3v} F^- centres are labelled in the parent-crystal spectrum and a line assigned to a centre charge-compensated by an O^{2-} ion is also labelled.

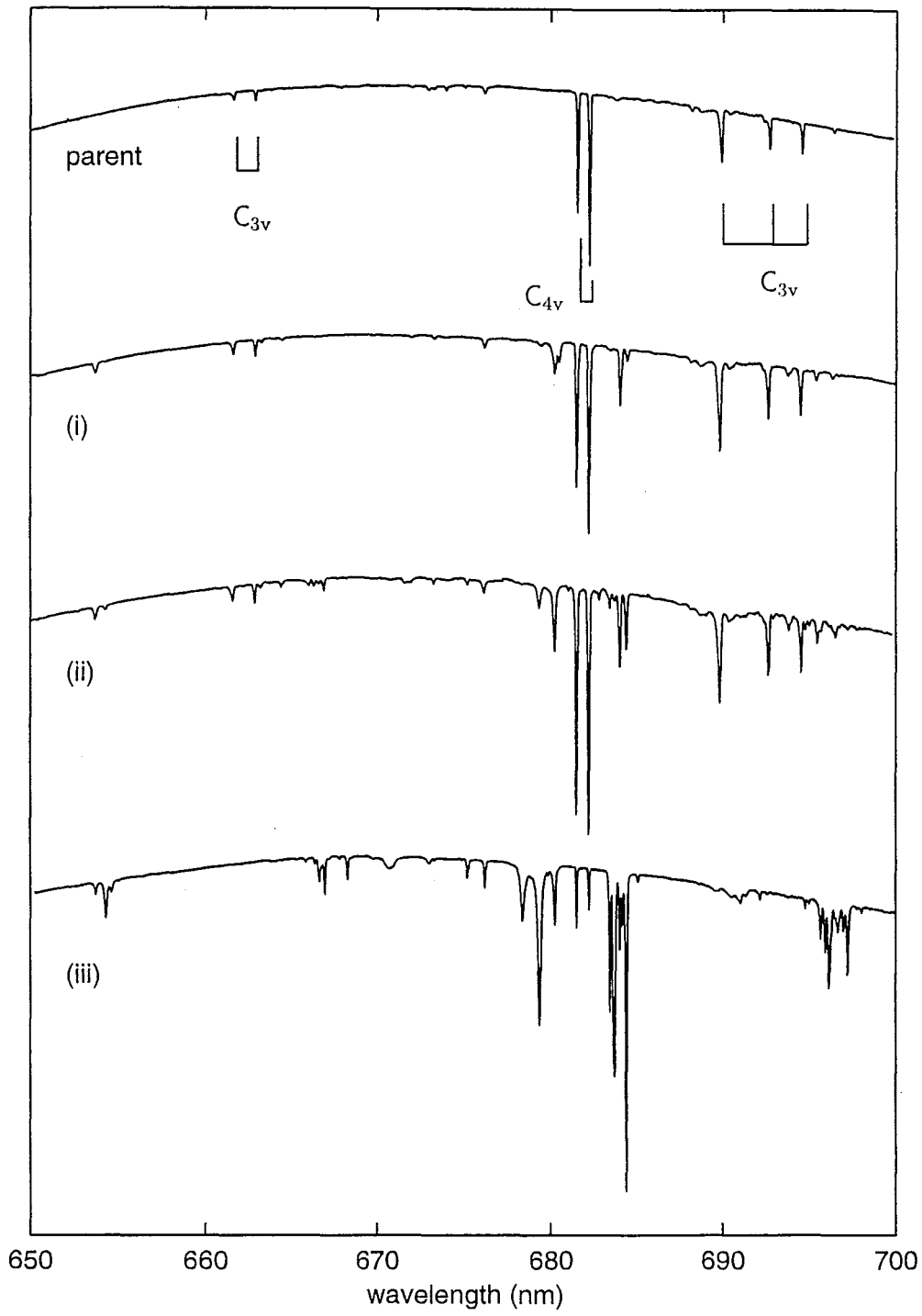

Figure 4.60 : $^3F_3$ (675–700 nm) and $^3F_2$ (650–675 nm) multiplet absorption spectra series for the parent CaF_2:0.05%Tm^{3+} crystal and (i),(ii),(iii) samples with increasing D^- concentration. Lines associated with the C_{4v} and C_{3v} F^- centres are labelled in the parent-crystal spectrum.

could not be identified above the background of the other centres, and in some cases actually appeared as absorption dips in this background.

Coupling of the electronic transitions to vibrational modes of the host-crystal lattice can give a non-zero absorption background of vibronics when the excitation frequency is slightly off resonance with the electronic transition. The transition probability for such an event would depend on the Bose-Einstein phonon density of states at the energy of the mismatch and the phonon occupation number. Even at absolute zero, it is possible to excite a centre by pumping at slightly higher energy than a resonant transition since phonon creation is involved. On the other hand, pumping at lower energy than the resonant transition requires phonon annihilation and the probability for this tends to zero as the temperature tends to zero. Thus at the cryogenic temperatures of the crystal sample, vibronic-absorption would be essentially zero for energies lower than the lowest electronic transition of a multiplet, but non-zero for higher energies.

This has implications for rare-earth ions in the latter part of the lanthanide series, since these ions form in C_{3v} as well as C_{4v} centres. For each multiplet, the energy levels of the C_{3v} centre in CaF_2:Tm^{3+} are typically at lower energy than for the C_{4v} centre. While the D^--compensated centre lines are at lower energy than the F^- C_{4v} centre, they are still higher than the F^- C_{3v} centre. It therefore becomes inevitable that, when pumping the D^- centre excitation lines, some cross pumping of the C_{3v} F^- centre occurs, and the fluorescence from this centre can swamp the relatively weak D^--centre fluorescences.

In the case of CaF_2:Tm^{3+}, the strong absorption of the $^3F_3$ multiplet lines provides an alternative to broadband excitation spectra. Figure 4.61 shows part of the absorption spectrum of the $^3F_3$ multiplet obtained by recording the transmitted laser signal. This differs from the regular absorption spectra, such as in figure 4.60, only in that the wavelength discrimination comes from the tunability of the laser rather than dispersion of a white-light source, and the higher power densities available. It is remarkable to note that, for the 1 cm sample length used, some of these lines exhibit close to 100% absorption of the 100 mW laser.

This method of using the laser absorption effectively took the place of broadband excitation spectra in tuning the laser to peaks before performing site-selective spec-

troscopy, as described in section 3.6.

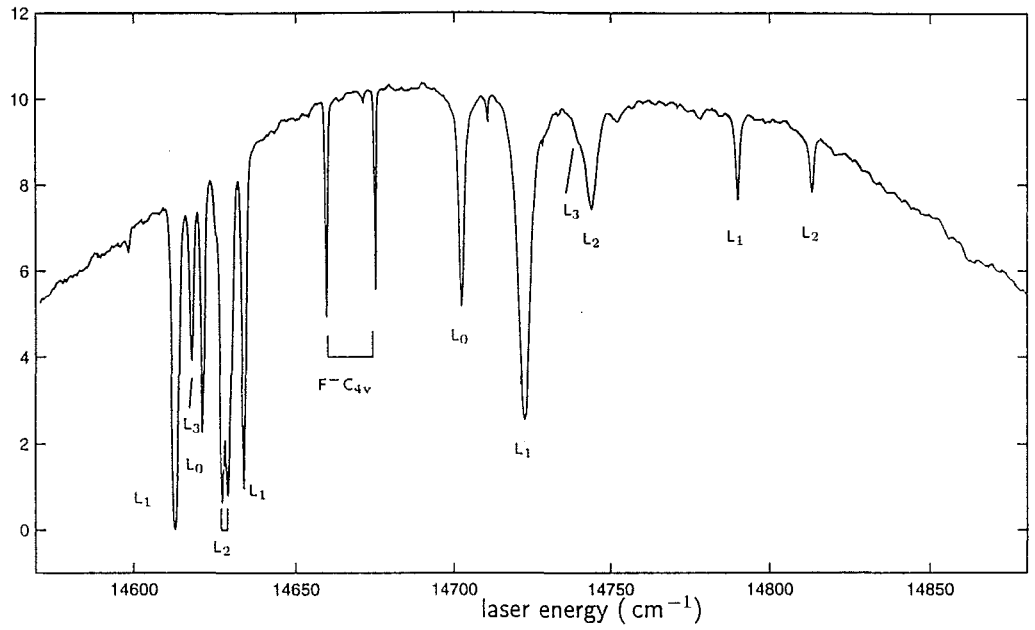

Figure 4.61 : Absorption of continuously-tuned laser radiation by $^3F_3$ multiplet absorption lines for deuterated CaF_2:0.05%Tm^{3+}. Lines assigned to the F^-C_{4v} and L_i centres are labelled.

4.6.2 Laser-Selective Excitation and Fluorescence of D^- Centres

By performing site-selective laser spectroscopy on the absorption lines of figure 4.61, four distinct D^--compensated centres were identified, and these have been arbitrarily labelled L_0, L_1, L_2 and L_3. Because of the weak fluorescence of these centres, and their spectroscopic similarity, it was in many cases not possible to obtain isolated spectra of a single centre. However, by pumping and monitoring different combinations of lines, those features which appear to correspond to the appropriate centres could be identified.

The $^3F_3$ multiplet excitation spectra of these four centres appear in figure 4.62, and the corresponding $^3H_4 \rightarrow {}^3H_6$ fluorescence spectra in figure 4.63. The transition marked with an "o" in each spectrum indicates the line which was pumped/monitored

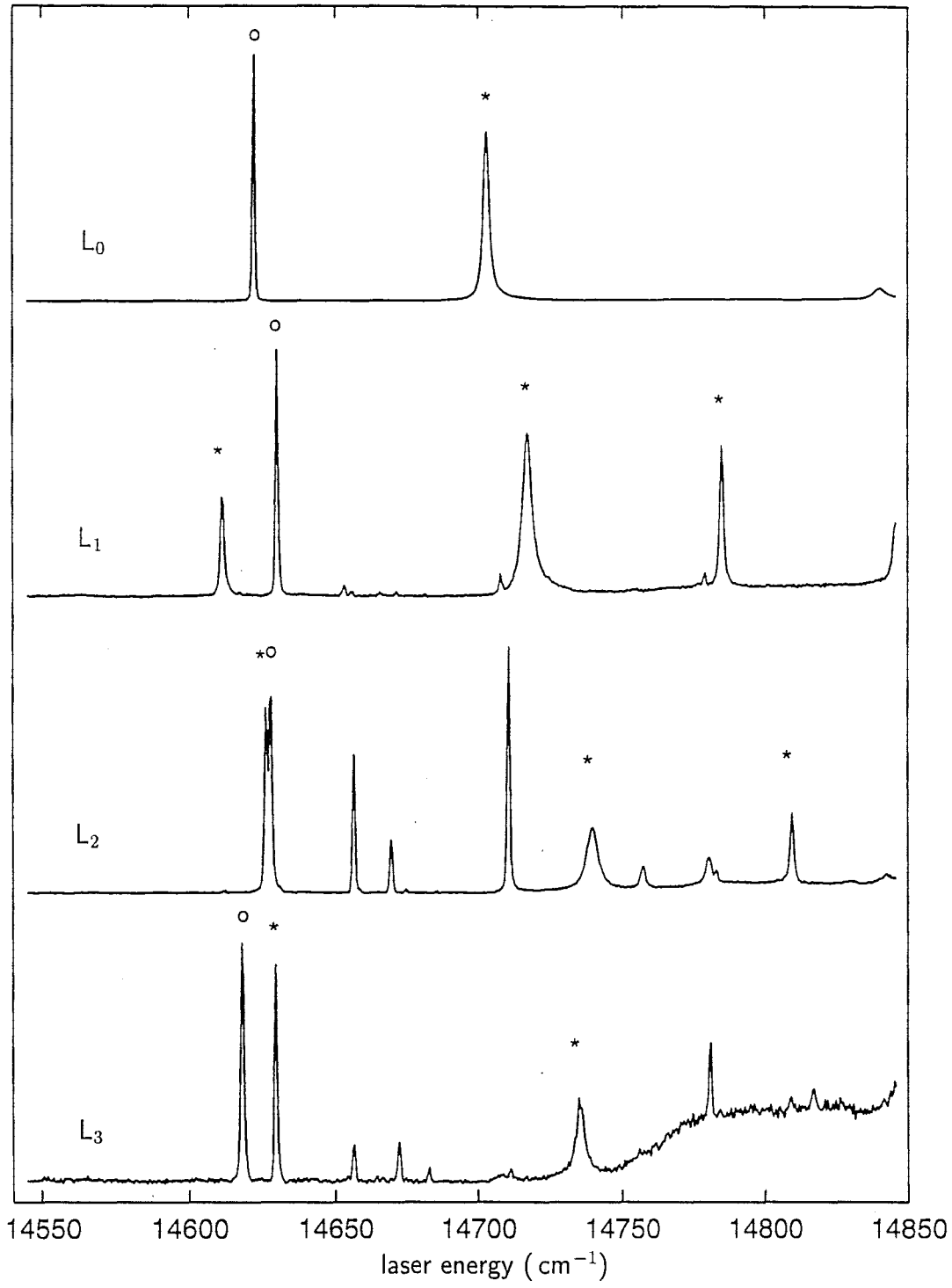

Figure 4.62 : Site-selective excitation spectra of the $^3F_3$ multiplet of the L_i D^--compensated centres in CaF_2:Tm^{3+}:D^-. ∘ indicates the excitation transition pumped to produce the corresponding fluorescence spectrum in figure 4.63, while ⋆ indicates other excitation transitions which arise from that centre.

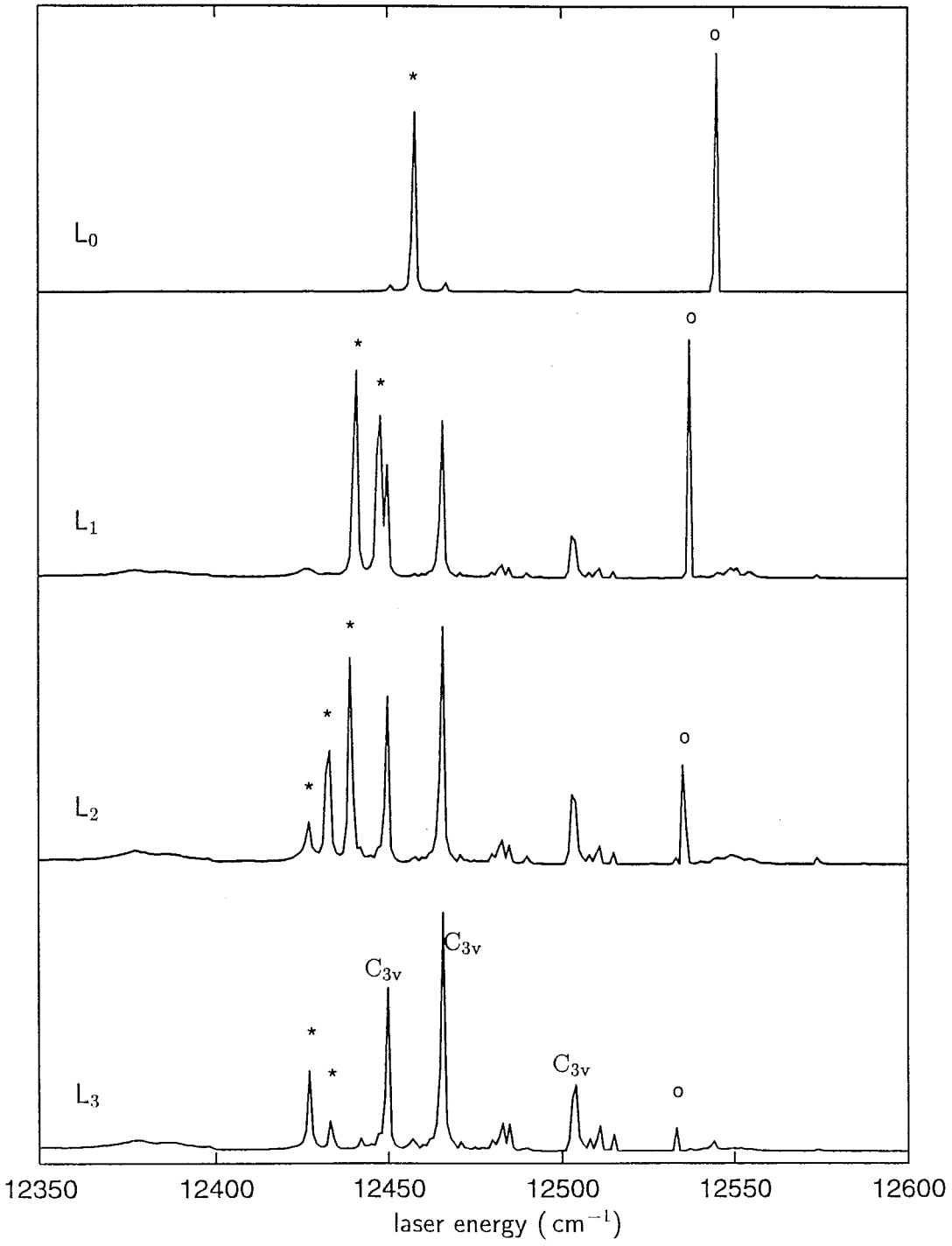

Figure 4.63 : $^3H_4 \rightarrow {}^3H_6$ fluorescence spectra of the L_i D^--compensated centres in $CaF_2:Tm^{3+}:D^-$. o indicates the fluorescence transition monitored to produce the corresponding excitation spectrum in figure 4.62, while $\star$ indicates other fluorescence transitions which arise from that centre. Lines assigned to the F^- C_{3v} centre are labelled in the L_3 spectrum, but are present in all.

to produce the corresponding fluorescence/excitation spectrum for that centre. Transitions marked "$\star$" are other lines which appear to belong with the centre. Cross-pumping of sites was generally unavoidable, and several other lines appear in the spectra. The fluorescence lines of the F^- C_{3v} centre appear in all the fluorescence spectra and are labelled "B" in the L_0 spectrum. The excitation and fluorescence energies of the marked transitions are listed in table 4.34.

Centre	Excitation transition energies (cm^{-1})	Fluorescence transition energies (cm^{-1})
L_0	14620.3, 14701.4	12454.0, 12541.4
L_1	14610.7, 14632.2, 14720.6, 14788.5	12439.2, 12446.1, 12535.6
L_2	14625.6, 14627.1, 14739.4, 14810.1	12425.3, 12431.0, 12437.5, 12533.9
L_3	14616.4, 14627.8, 14789.5	12425.4, 12431.7, 12531.4

Table 4.34 : Transition energies of the L_i centre $^3F_3$ excitation lines and $^3H_4 \rightarrow {}^3H_6$ fluorescence lines.

As an additional complication, fluorescence from "photoproduct" centres (spectroscopically distinct centres produced by non-reversible bleaching of the pumped centre) might also be produced intrinsically in these spectra. This is because the emitting multiplet ($^3H_4$) is not the pumped multiplet ($^3F_3$). The 2000 cm^{-1} gap between the pumped and emitting multiplets is bridged almost entirely by non-radiative decay by creation of phonons. The D^- local-mode phonons have higher energies than the lattice phonons, so the gap can be bridged more easily than by lattice phonons alone. Since it is the creation of these D^- localised vibrations that leads to the D^- ion migration and hence bleaching, it is possible that a certain fraction of the excited centres may have bleached before they fluoresce. The result would be some fluorescence lines of the photoproduct centres of the original centre being pumped.

The solution to this problem would be to pump the same multiplet that is emitting. For the $^3H_4$ multiplet of Tm^{3+}, this can be achieved with a Ti:sapphire laser, which was not available until the final stages of this work. However, the $^3H_4$ absorption lines of the C_{4v}-derived Tm^{3+}-D^- centres all have very similar energies, so that site-selectivity in spectroscopy of bleaching could not always be attained. This similarity

in energies of the $^3H_4$ absorption line between these centres (see figure 4.59) can be understood by the nature of the corresponding transition in the F^- C_{4v} centre. This is a transition between two γ_3 singlets which are both well isolated from other energy levels. As such, their wavefunctions and transition energies would not change greatly in the presence of a lower-symmetry field. In contrast, the lowest energy level of the $^3F_3$ multiplet is a γ_5 doublet and is separated from the nearest state by only $15\,cm^{-1}$. The effect of a perturbing crystal-field would be to split the γ_5 state and this splitting would be relatively sensitive to the strength of the perturbation. This argument would apply also to the C_{4v} centres of $CaF_2:Pr^{3+}$ and $SrF_2:Pr^{3+}$, for which it is the ground state which is a γ_5 doublet which splits under the perturbation.

It appears that the four Tm^{3+}-D^- centres are perturbed C_{4v}-type centres and should be able to be associated with some of the six Pr^{3+}-D^- centres depicted in figure 4.58. In the case of Pr^{3+}, the nature of the centres was distinguished by several features: the order in which they are preferentially formed; their relative fluorescence efficiencies; the vibronic sidebands; and their bleaching behaviour.

When the D^--compensated centres form, those centres involving fewer D^- ions would form first. From the concentration series of figure 4.60, the L_0 centre forms first, then the L_1 centre. It would then follow that these two centres are the counterparts to the C_{4v} and CS(1) centres of $CaF_2:Pr^{3+}:D^-$ and $SrF_2:Pr^{3+}:D^-$ as depicted in figure 4.58, since these are the only two centres involving only one and two D^- ions, respectively. The L_2 and L_3 centres are likely to correspond to two of the remaining configurations—of these, the CS(2) and CS(4) centres seem most likely since these involve only three D^- ions.

This assignment is consistent with the observed fluorescence efficiencies. Centres involving more D^- ions have a greater number of non-radiative channels for bridging large energy gaps by multiple-phonon creation, and are therefore expected to have weaker fluorescence efficiencies. The L_0 centre has a fluorescence intensity nearly an order of magnitude larger than that of the L_1 centre, which in turn is several times larger than those of either the L_2 or L_3 centres. In the fluorescence spectra of figure 4.63, these relative intensities can be gauged approximately by comparing the strengths of the simultaneously-present F^- C_{3v} centre fluorescence lines with those of each D^- centre. The intensities in these spectra should be used only as

a guide because the continuous laser illumination required to record fluorescence spectra tends to bleach the D^- centres thus reducing their recorded line strengths over time.

4.6.3 Bleaching Behaviour of D^- Centres

Introduction

The phenomenon of polarised bleaching has been observed in multi-hydrogenic centres of all of the CaF_2:RE^{3+}:H^- systems studied previously, with all the isotopes of hydrogen tried (H^-, D^- and T^-) producing essentially the same qualitative results. For analogous H^-, D^- and T^- centres, the lighter isotope versions always bleach more easily due to their higher energy vibrational modes. Consequently, they also have lower fluorescence efficiencies and the most detailed experiments have therefore tended to be performed using the D^- isotope. The bleaching behaviour has been divided into two types, centre reorientation and photoproduct-centre formation. In both cases, the final effect is that the interstitial D^- ion has moved to one of the other adjacent interstitial positions in the lattice, thus reorienting the RE^{3+}-centre axis. It appears that the motion of the interstitial ion is not direct, but rather involves one of the adjacent substitutional D^- ions moving out of its position into the new interstitial site and the existing interstitial ion then moving into the substitutional site. This mechanism, termed the interstitialcy mechanism by Catlow *et al* [15], is confirmed by the absence of any bleaching phenomena for any of the D^- C_{4v} centres, for which no substitutional D^- ions are present, associated with any of the rare earths. In some cases, depending on the configuration of the substitutional D^- ion(s), not all four possible vacant interstitial sites may be accessible, since the substitutional ion which moves must be adjacent to both the old and new orientations. The interstitialcy mechanism of bleaching is depicted in figure 4.64 for the CS(2)-type configuration of CaF_2:Pr^{3+}:D^- and SrF_2:Pr^{3+}:D^-.

Whether a centre reorients or produces a photoproduct centre depends on the configuration of the centre. For centre reorientation, the new centre formed is identical to the old one, except that it is now oriented in a different direction. This would not produce any observable effect, but for the fact that the laser may be polarised

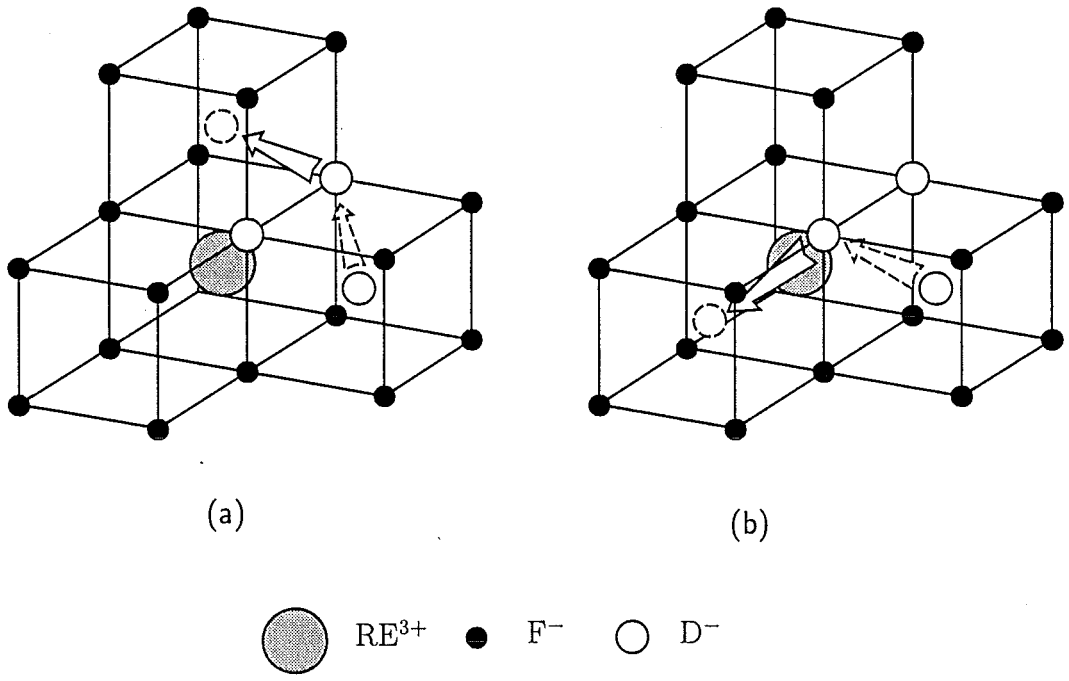

Figure 4.64 : Proposed interstitialcy mechanism for bleaching of the CS(2) centre of CaF_2:Pr^{3+}:D^- and SrF_2:Pr^{3+}:D^- producing (a) centre reorientation, and (b) photoproduct-centre formation. Atomic sizes are not represented to scale.

in such a way as to preferentially excite one of these orientations. Because these centres are perturbations of the C_{4v} centre, the polarisation dependence of the C_{4v} parent is preserved to a good degree, and the different orientations in a $\langle 100 \rangle$ oriented crystal can be accessed almost independently. Such a mechanism gives rise to the reversible bleaching whereby the populations of two different orientations can be fed back and forth from one another by changing the laser polarisation.

For some configurations, the reoriented centre may have an inequivalent configuration from its original form. This photoproduct centre would then have different absorption energies, and the fluorescence level cannot be recovered simply by changing the laser polarisation. If the broadband excitation spectrum is recorded before and after such a bleaching process, it may be possible to identify new lines corresponding to the photoproduct centre. Pumping these new lines of the photoproduct centre would then restore population to the originally bleached centres.

By inspection of the centre configurations of figure 4.58 it is clear that the CS(1) centre should bleach only by centre reorientation, and the CS(3), CS(4) and CS(5) centres only by photoproduct formation.

For the CS(2) centre, both centre reorientation and photoproduct formation occur. Changing the laser polarisation can therefore only partially restore the original population, and repeated switching of the polarisation will lead to a gradual decrease in the fluorescence recovered intensity, while the photoproduct centre population increases.

Bleaching of the CaF_2:Tm^{3+}:D^- L_i Centres

The L_0 centre was not found to bleach at all upon pumping either of its two main excitation lines in figure 4.62. This is consistent with its assignment to the C_{4v} configuration involving a single interstitial D^- ion only.

The other three centres were all observed to bleach. The bleaching curves for the L_1 centre are shown in figure 4.65, for pumping the $14632.2\,cm^{-1}$ transition while monitoring fluorescence at $12535.6\,cm^{-1}$. The fluorescence is bleached to 13% of its original level in both polarisations after two minutes of bleaching at a laser power of 100 mW. After bleaching in the Z polarisation, the Y-polarisation fluorescence recov-

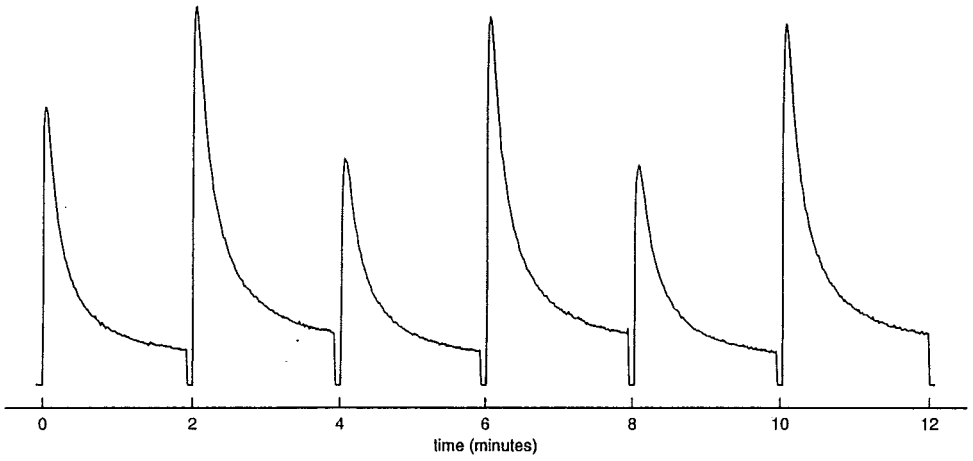

Figure 4.65 : Bleaching curves for the L_1 centre of $CaF_2:Tm^{3+}:D^-$, pumping at $14632.2\,cm^{-1}$ with the laser polarised alternately parallel to the Y and Z laboratory coordinates, and monitoring fluorescence at $12535.6\,cm^{-1}$.

ers to 80% of its original level, and then recovers almost fully to this same level again after the second cycle. The Z-polarisation recovery is almost total after the first cycle. This behaviour of repeated recovery is similar to that observed for the CS(1) centre of $SrF_2:Pr^{3+}:D^-$ [75]. The drop in recovered intensity after the first cycle for the Y polarisation only is not seen for the CS(1) centre of $SrF_2:Pr^{3+}:D^-$, however it is seen for the R site in $CaF_2:Er^{3+}:D^-$ [17]. This behaviour can be explained by the first bleaching processes establishing one of two "bleached-equilibrium" states which are different to the initial state in which all orientations of the centre are equally populated. Reversing the polarisation of the laser transfers the population between the two bleached-equilibrium states, so the initial fluorescence level may not be recovered.

Figure 4.66 shows bleaching curves of the L_2 centre upon pumping the transition at $14743.3\,cm^{-1}$ and monitoring fluorescence at $12533.9\,cm^{-1}$. The bleaching rate for this centre is somewhat faster than for the L_1 centre, for the same laser intensity. This would be consistent with the presence of more D^- ions. The fluorescence intensity appears to reach a non-zero steady-state level, which is the same for both polarisations. The transition being pumped is a broad transition which appears to

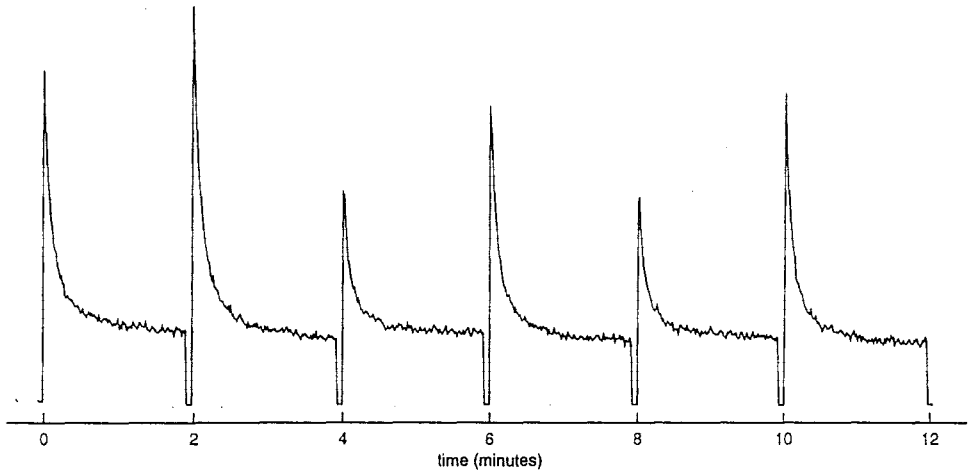

Figure 4.66 : Bleaching curves for the L_2 centre of CaF_2:Tm^{3+}:D^-, pumping at 14743.3 cm^{-1} with the laser polarised alternately parallel to the Y and Z laboratory coordinates, and monitoring fluorescence at 12533.9 cm^{-1}.

lie on a broad background of phonon-absorption features. The steady-state fluorescence could be from the pumping of all orientations equally in phonon-assisted processes, which would prevent further bleaching beyond a certain level. Like the L_1 centre, the Y-polarisation fluorescence recovers only partially after the first cycle, but then recovers back to the same level again after subsequent cycles. Unlike the L_1 centre though, the Z-polarisation fluorescence exhibits a similar behaviour, recovering partially on the first cycle but then fully on subsequent cycles. The explanation put forward for the L_1 centre can also be applied here, with different specific polarisation dependences.

Figure 4.67 shows bleaching curves of the L_3 centre upon pumping the transition at 14616.4 cm^{-1} and monitoring fluorescence at 12531.4 cm^{-1}. The bleaching here is even less complete than for the L_2 centre. The fluorescence recovery follows a similar pattern to the L_2 centre, with the intensity of both polarisations recovering partially on the first cycle, then fully on subsequent cycles. However, the effect is more pronounced for the Y polarisation than the Z polarisation.

The polarisation behaviour displayed for the L_2 and L_3 centres is not consistent with the model configurations of any of the CS(3),CS(4) or CS(5) centres, which

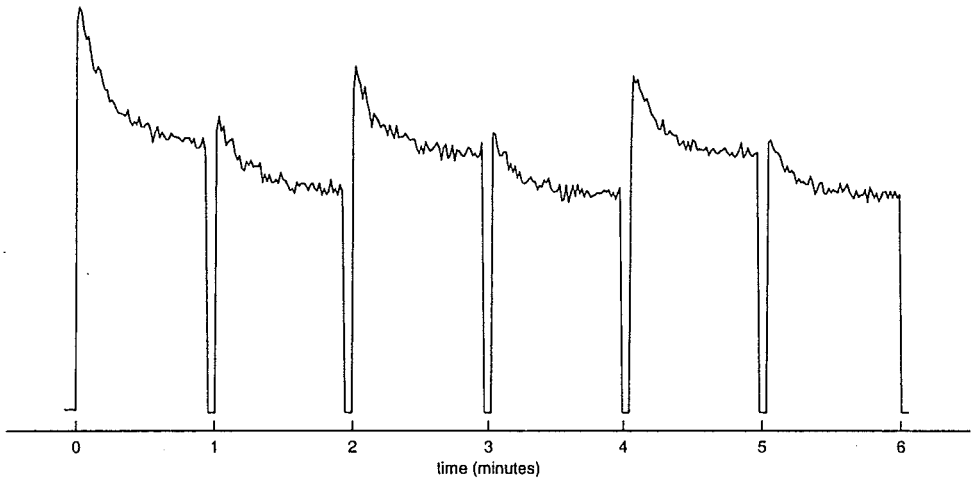

Figure 4.67 : Bleaching curves for the L_3 centre of CaF_2:Tm^{3+}:D^-, pumping at 14616.4 cm^{-1} with the laser polarised alternately parallel to the Y and Z laboratory coordinates, and monitoring fluorescence at 12531.4 cm^{-1}.

do not display any recovery after cycling the laser polarisation. Even the CS(2) centre should continue to recover only partially after each cycle, rather than the full recovery which seems to occur for the second, and presumably subsequent, cycles. In comparison to the CS centres of SrF_2:Pr^{3+} and CaF_2:Pr^{3+}, the sharp excitation lines available for the CaF_2:Tm^{3+} L_i centres are clustered together and can only just be fully resolved. It is possible that the photoproduct centres (which were not observed using the laser absorption method) have energy levels sufficiently close to the parent centres that they lie partially in resonance with the laser while the bleaching of the parent centre is taking place. This would tend to revert some of the population, and lead to a steady state of recovery as observed for the L_2 and L_3 centres.

This is very much a preliminary investigation into the bleachable centres in deuterated CaF_2:Tm^{3+}. In a more comprehensive study, it would be desirable to be able to monitor fluorescence from the same multiplet as was being excited, to avoid the possibility of bleaching occurring before the ion radiates. Therefore, for Tm^{3+}, the $^3H_4$, $^1G_4$ and $^1D_2$ would be better options for pumping than the $^3F_3$ multiplet. With the $^3H_4$ multiplet being in the tuning range of a Ti:sapphire laser, this would be

ideal, however the principle L_i-centre absorption lines are difficult to resolve for this multiplet. The $^1G_4$ multiplet absorption lines are accessible by a coumarin 460 or coumarin 480 dye laser, and this might be a promising area to study. However, the low power output and instability of the blue dyes introduces experimental difficulties. In addition, the absorption lines of the $^1G_4$ multiplet are very weak. The absorption lines of the $^1D_2$ multiplet may just lie within the range of a frequency-doubled Ti:sapphire laser, giving another possible pump region. Again, only low pump powers would be available, but none of the instabilities associated with dyes.

The possibility of upconversion for these centres should also be investigated further, and could be usefully attempted in conjunction with a study of the direct pumping of the $^1G_4$ and/or $^1D_2$ multiplets.

4.7 Summary of the Spectroscopy of CaF_2:Tm^{3+}

The Tm^{3+} ion has several multiplets which can be pumped by tunable dye or Ti:sapphire lasers, and these were utilised to study the CaF_2:Tm^{3+} system for Tm^{3+} concentrations of 0.01%–0.05%.

Excitation and fluorescence spectra upon direct laser-pumping of levels of the $^3H_4$, $^3F_3$, $^3F_2$ and $^1G_4$ multiplets identified two major optically-active Tm^{3+} centres, whose symmetries were determined through polarisation dependences to be tetragonal (C_{4v}) for the dominant centre and trigonal (C_{3v}) for the secondary centre.

These direct laser-pumping results were complemented by the observation of upconversion fluorescence of these single-Tm^{3+}-ion centres upon pumping the $^3F_4 \rightarrow {}^1G_4$ and $^3H_4 \rightarrow {}^1D_2$ excited-state absorption transitions. The broadband upconversion spectrum also revealed at least two other centres which produced more intense upconversion than the C_{4v} and C_{3v} centres. These were not studied in detail, but are presumed to be minor cluster centres which would have enhanced upconversion efficiencies from energy-transfer processes.

From the spectroscopy of the C_{4v} centre, using both direct-pumped and upconversion fluorescence, 31 energy levels were determined. The irrep labels of these levels were identified using polarisation ratios and the few anomalies arising from these polarisation ratios could be explained by magnetic-dipole contributions to σ-allowed transitions. A crystal-field fit to these 31 levels labelled by irreps produced a good fit giving a standard deviation of $8.3\,cm^{-1}$ for varying ten parameters (five crystal-field, three electrostatic, one spin-orbit and a uniform shift). The fitted crystal-field parameters are similar to those obtained for other rare-earths in C_{4v} centres in CaF_2, indicating that these centres have the same physical configuration.

The spectroscopy of the C_{3v} centre yielded 30 energy levels. Polarisation ratios are less clear for C_{3v} centres than for C_{4v} centres because the four possible orientations of the centre are not mutually orthogonal, and because $\gamma_3 \rightarrow \gamma_3$ transitions are both π and σ allowed. The measured polarisation ratios were ambiguous, and a single set of irrep assignments could not be found which was consistent with these, even within the known limitations. A crystal-field fit was attempted without using any irrep assignments, and produced a reasonable standard deviation of $10.2\,cm^{-1}$ for

the 30 levels, for varying eleven parameters (six crystal-field, three electrostatic, one spin-orbit and a uniform shift). However, the irrep assignments taken from this resulting fit were not consistent with some polarisation ratios and Zeeman splittings, indicating that further information is required before a fit can be considered definitive.

A cubic-symmetry centre was also identified by an absorption transition to the $^3H_5$ multiplet. Electric-dipole transitions within a configuration are strictly forbidden for an ion which is located at a site with an inversion centre, and as such the Tm^{3+} cubic centre is not expected to be detected in optical spectroscopy. It was demonstrated, using estimated crystal-field analysis, that only one magnetic-dipole allowed absorption transition is expected for the cubic centre in CaF_2:Tm^{3+}, corresponding to the observed $^3H_6 \rightarrow {}^3H_5$ transition. Zeeman splittings for magnetic fields parallel to the $\langle 100 \rangle$ crystal axis agreed quantitatively with the calculated splitting, and future measurement of the Zeeman splittings for magnetic fields applied along a different axis, such as $\langle 111 \rangle$, should confirm the assignment of this line to the cubic centre.

Comparison of the linestrengths of the cubic-centre absorption transition and a magnetic-dipole allowed transition of the C_{4v} centre showed that the ratio of the concentrations of these two centres in CaF_2:0.01%Tm^{3+} is

$$\frac{N(C_{4v})}{N(\text{cubic})} = 2.7$$

which is similar to the results previously deduced for CaF_2:Er^{3+} by Moore [62].

Deuteration treatment of CaF_2:Tm^{3+} samples produced several new centres due to substitution of D^- ions for interstitial or lattice F^- ions. Four centres were studied by laser-selective excitation and fluorescence spectroscopy and by their bleaching behaviour, pumping levels of the $^3F_3$ multiplet. The strongest of these four centres did not bleach, consistent with being assigned to the D^--compensated C_{4v} centre. The other three appeared spectroscopically similar to this centre but do undergo reversible polarised bleaching and are likely to correspond to the first three CS(i) centres of CaF_2:Pr^{3+}:D^-.

Chapter 5

Sequential-Absorption Upconversion Processes in RE^{3+}-doped CaF_2

The desire to produce cheap, compact lasers operating at visible wavelengths has stimulated much interest in upconversion processes which produce emission at shorter wavelengths than that of an optical pump source. Of particular interest are systems which can be pumped by near-infrared semiconductor-diode lasers, which are themselves compact and relatively inexpensive. While upconversion effects have traditionally been the domain of highly-doped systems or dual pumping schemes, this chapter presents some novel single pump-laser upconversion effects in the single-RE^{3+}-ion centres of low-doped (0.01%) CaF_2.

5.1 Upconversion Mechanisms

Recently, Lenth and Macfarlane [53] and Cockroft [18] have reviewed the major upconversion processes as summarised here, with particular emphasis on the application to upconversion lasers.

Upconversion, being the production of fluorescence of smaller wavelength (higher photon energy) than that of the exciting source, requires the combination of the energy of two photons to promote an optically active ion into a highly excited state. This can be achieved, under appropriate conditions, in a number of different ways. Broadly, the most common mechanisms are energy-transfer, sequential-absorption, photon-avalanche and two-photon absorption.

Energy-Transfer Upconversion

The most common upconversion mechanism is energy-transfer upconversion (ETU). ETU involves at least two ions in close proximity both being pumped to excited states. This can be achieved readily with a single laser if the two ions are identical and situated at equivalent sites. If the energy level scheme is favourable, then one of the predominant relaxation pathways of this combined state may be a radiationless cross-relaxation process with one ion transferring all or part of its energy to the other, putting it into a higher energy state than was achievable by the single-photon process. This process is illustrated in figure 5.1. Ions A and B, having both been pumped to a common metastable intermediate state 3, subsequently undergo a cross-relaxation process. Ion A decays to state 2 transferring some of its energy to ion B, which is raised to state 4. The energy mismatch between E_3-E_2 and E_4-E_3 can be bridged by the creation or annihilation of lattice phonons.

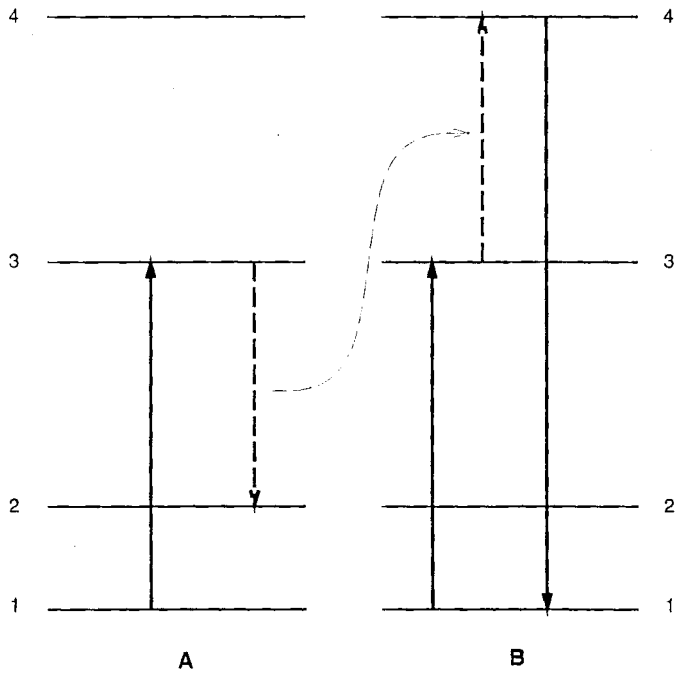

Figure 5.1 : Production of upconversion fluorescence by the energy-transfer mechanism. Solid arrows indicate radiative transitions and dashed arrows indicate phonon-assisted energy-transfer steps.

By the nature of the energy-transfer mechanism, one requires either a high concentration of the optically-active ions, or a host crystal which preferentially forms dopant clusters. $CsCdBr_3$ is an example of a host crystal in which dopant trivalent rare-earth ions preferentially form dimer centres to satisfy charge compensation [59] requirements. Strong upconversion fluorescence has been observed for these crystals doped at relatively low concentrations (around 0.1%) for several of the rare earths, including Er^{3+} [20], Nd^{3+} [10] and Ho^{3+} [65]. In most crystals, however, single-ion centres are predominant at low concentrations, and energy-transfer processes are the domain of higher RE^{3+} concentrations. In CaF_2, clustering is known to be important by 0.1%, and cluster centres are dominant by 0.5% [84].

Sequential-Absorption Upconversion

In the absence of significant clustering, upconversion may still proceed via sequential-absorption upconversion (SAU) processes. This single ion process involves the initial population of an intermediate metastable excited state, followed by a second absorption from that intermediate state to a higher excited state. This process is illustrated in figure 5.2. The long-lifetime intermediate state, 2, is populated by a ground-state absorption (GSA) transition either directly into state 2, or initially into state 3 followed by a relaxation process to state 2. The ion is then promoted directly from the metastable state, 2, into the higher excited state, 4, by an excited-state absorption (ESA) transition.

Such a process is readily achievable if two pump lasers are available to pump the ion at the two wavelengths corresponding to the GSA and ESA transitions, with the only special requirement being the existence of an appropriate long-lived intermediate state. Upconversion laser action using the SAU mechanism has been reported for several rare-earth ions doped into various crystals and glasses. The pumping schemes of several upconversion lasers which have relevance to the upconversion processes investigated in this chapter for Er^{3+}, Tm^{3+}, Ho^{3+} and Nd^{3+}. Some specific examples are now described and are illustrated in figure 5.3.

The first-reported cw upconversion laser used a SAU scheme in $YAlO_3$:Er^{3+} [81]. Green lasing action for the $^4S_{3/2} \rightarrow {}^4I_{15/2}$ transition at 550 nm was obtained upon pumping both a GSA transition, $^4I_{15/2} \rightarrow {}^4I_{9/2}$, at 792 nm and an ESA transition,

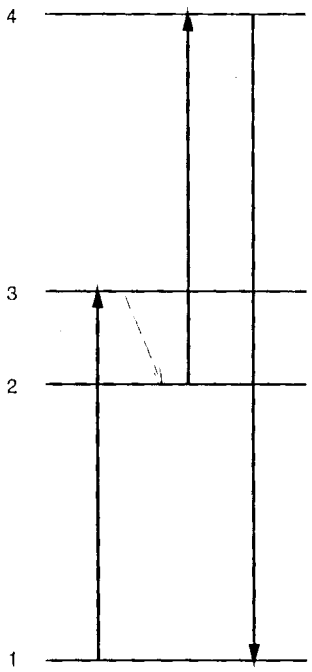

Figure 5.2 : Production of upconversion fluorescence by the sequential absorption of photons. Solid arrows indicate radiative transitions and the dashed arrow indicates phonon-assisted non-radiative decay.

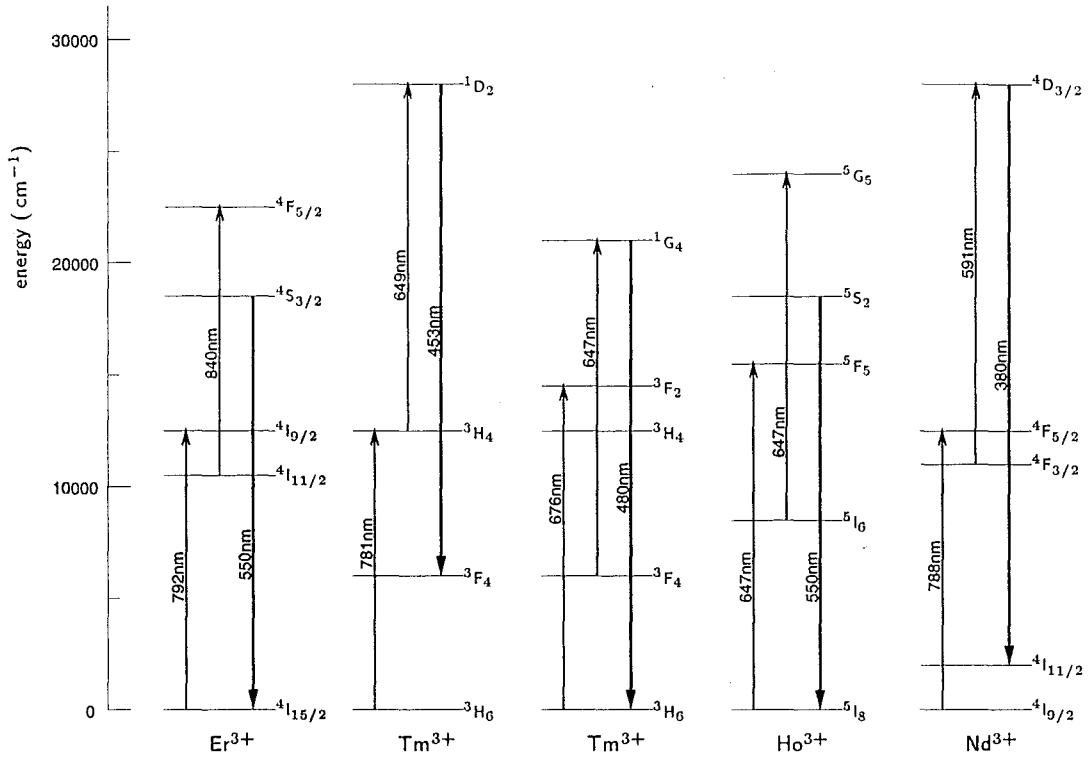

Figure 5.3 : Sequential-absorption processes which have demonstrated upconversion-laser action for Er^{3+} [81], Tm^{3+} [70, 3], Ho^{3+} [4] and Nd^{3+} [58].

$^4I_{11/2} \rightarrow {}^4F_{5/2}$, at 840 nm.

Blue-violet upconversion lasing for the $^1D_2 \rightarrow {}^3F_4$ transition at 453 nm has been achieved in $YLiF_4:Tm^{3+}$ [70] at 75 K upon pumping the GSA transition $^3H_6 \rightarrow {}^3H_4$ at 781 nm and the ESA transition $^3H_4 \rightarrow {}^1D_2$ at 649 nm. This material was subsequently found also to lase at room temperature [71]. Blue lasing at 480 nm for the $^1G_4 \rightarrow {}^3H_6$ transition was reported in a $YLiF_4:Tm^{3+}$ fibre [3], using the 676.4 nm and 647.1 nm lines of a single, multiline krypton-ion laser to pump the $^3H_6 \rightarrow {}^3F_2$ GSA and $^3F_4 \rightarrow {}^1G_4$ ESA transitions respectively.

Tunable, cw green upconversion lasing has been obtained from Ho^{3+}-doped fluorozirconate glass fibre at room temperature, with a single pump laser [4]. A krypton-ion laser at 647.1 nm pumped both GSA and ESA transitions, and the resulting lasing wavelength could be tuned between 540–553 nm by use of an intracavity dispersive prism.

Deep-violet upconversion lasing at 380 nm has been achieved for the $^4D_{3/2} \rightarrow {}^4I_{11/2}$ transition of $LaF_3:Nd^{3+}$ [58] upon pumping the GSA transition $^4I_{9/2} \rightarrow {}^4F_{5/2}$ at 788 nm and the ESA transition $^4F_{3/2} \rightarrow {}^4D_{3/2}$ at 591 nm.

Photon-Avalanche Upconversion

The photon-avalanche process involves a combination of energy-transfer and excited-state absorption processes, as illustrated in figure 5.4. The single pump laser is tuned to match an ESA transition in a wavelength region that has a very low GSA probability. One ion that has been excited to the metastable state, 2 (by the low-probability GSA), can undergo the selected ESA transition. Once in the higher excited state, the ion decays non-radiatively back to the intermediate state, including a partial energy transfer to a nearby similar ion. Both of the ions are then left in the metastable excited state, able to undergo further ESA transitions.

High dopant concentrations are required to allow each donor ion to transfer energy to several possible nearby acceptors, and for each of these to be able to transfer energy in turn to others, thus diffusing the excitation through the crystal. Once the metastable state gains some population, each photon absorbed can leave an extra ion (in addition to the ion in which it was absorbed) populated in this intermediate state.

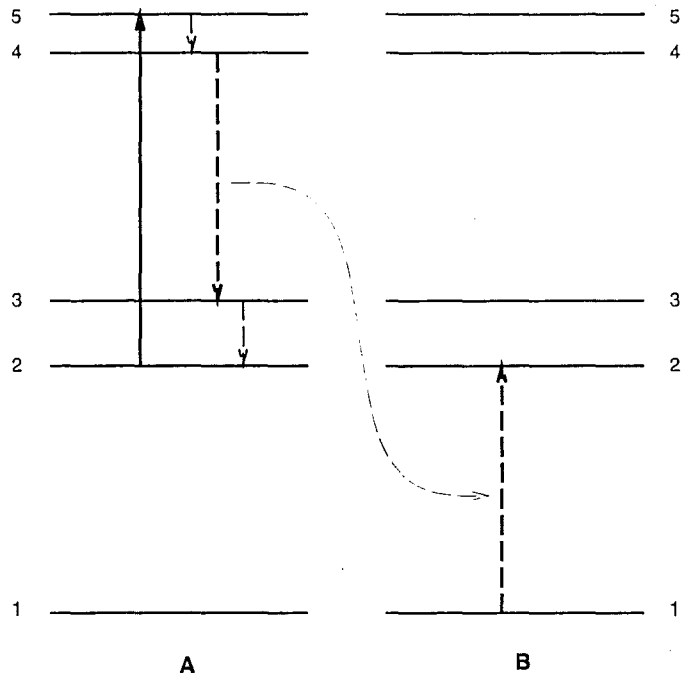

Figure 5.4 : Population of a high-energy state by photon avalanche. The solid arrow indicates the pump transition and dashed arrows indicate a non-radiative phonon-assisted energy-transfer.

As long as the pump power is sufficiently high that the ESA process dominates over radiative relaxation of the metastable state, the population being cycled between the excited states can build up until the lasing threshold is reached.

$YLiF_4$:1.8%Tm^{3+} has demonstrated lasing action for the $^1G_4 \rightarrow {}^3H_6$ transition by a double-relaxation photon-avalanche mechanism with a single krypton pump laser at either 628.6 nm or 647.9 nm [35]. The laser transition is resonant with the $^3F_4 \rightarrow {}^1G_4$ ESA transition. An ion which has been excited to the $^1G_4$ highly-excited state cross-relaxes first to the $^3F_2$ multiplet, and then to the $^3F_4$ multiplet, transferring energy to other Tm^{3+} ions with each step, promoting them into the $^3F_4$ multiplet. Thus a three-for-one population build-up of the $^3F_4$ multiplet is achieved.

Two-Photon Absorption

Two-photon absorption processes are less important as upconversion mechanisms because of their very much weaker transition rates. In these processes, the single pump laser is not resonant with either a GSA or ESA transition, but instead is tuned to exactly half the energy of a GSA transition. The energy of two photons is combined to induce the transition. While the two-photon process is electric-dipole allowed for intra-$4f^n$ transitions, it is a second order process summing over intermediate "virtual" states. Parity requirements mean that the states of the $4f^{n-1}5d$ configuration provide the predominant contribution, and the large energy separation between configurations leads to a low transition rate. The two-photon process is typically many orders of magnitude weaker than the other processes outlined above [18].

5.1.1 Upconversion in Single RE^{3+}-Ion Centres in CaF_2

The systems investigated here all involve rare-earth ions doped into CaF_2 at relatively low concentrations (0.01%) to ensure that isolated single-ion centres are predominant. In using the site-selective laser excitation techniques, it can be further assured that only the known single-ion centres are involved. ETU processes should therefore not be important, and only SAU processes are expected.

However, some caution is required here in assuming that the single-ion centres are

indeed unable to participate in energy-transfer processes. Yellow-to-blue upconversion for the C_{4v} centre of $CaF_2:Pr^{3+}$ has previously been reported for pumping the $^3H_4 \rightarrow {}^1D_2$ GSA transitions [54, 77]. Although the C_{4v} centre is nominally a single-ion centre, the upconversion was determined to be due to an ETU process between distant pairs of C_{4v} centres. This was confirmed by the observation of upconversion under 1 ns pulsed excitation [77]. It appeared that the optimum pump frequency for upconversion was shifted by $0.25\,cm^{-1}$ from that for normal fluorescence, consistent with only a specific subset of the centres (those with a nearby Pr^{3+} ion) undergoing upconversion.

5.2 Upconversion in $CaF_2:Er^{3+}$

Jouart and Oomen [47] have observed green $^4S_{3/2} \rightarrow {}^4I_{15/2}$ upconversion fluorescence for CaF_2:0.5%Er^{3+} upon pumping in the 800 nm region with a Ti:sapphire laser. The results in their work, all performed at room temperature, indicated that the mechanism consisted of a combination of energy transfers and excited-state absorptions. Similar conclusions were made for SrF_2:1.3%Er^{3+} and BaF_2:1.1%Er^{3+}. With the high Er^{3+} concentrations used, and with all observations being at room temperature, no site-selective spectroscopy was performed in that work.

Cockroft *et al* [21] have previously reported weak green $^4S_{3/2} \rightarrow {}^4I_{15/2}$ upconversion fluorescence of the C_{4v} centre of CaF_2:0.05%Er^{3+} upon pumping the $^4I_{15/2} \rightarrow {}^4F_{9/2}$ GSA transitions. It was postulated that the mechanism for this upconversion was a sequential-absorption process, although the possibility of an energy-transfer between remote C_{4v} centres, such as that found for $CaF_2:Pr^{3+}$ [54, 77], was not ruled out.

5.2.1 Red-to-Green Upconversion of the C_{4v} Centre of $CaF_2:Er^{3+}$

For a sample of CaF_2:0.01%Er^{3+}, the results of Cockroft *et al* [21] have been reproduced here. However, in addition to the GSA-pumped upconversion, another series of upconversion peaks was observed with the laser frequency approximately $300\,cm^{-1}$ higher in energy. The upconversion excitation spectrum, monitoring green $^4S_{3/2} \rightarrow {}^4I_{15/2}$ upconverted fluorescence of the C_{4v} centre at $18522\,cm^{-1}$, is presented in figure 5.5.

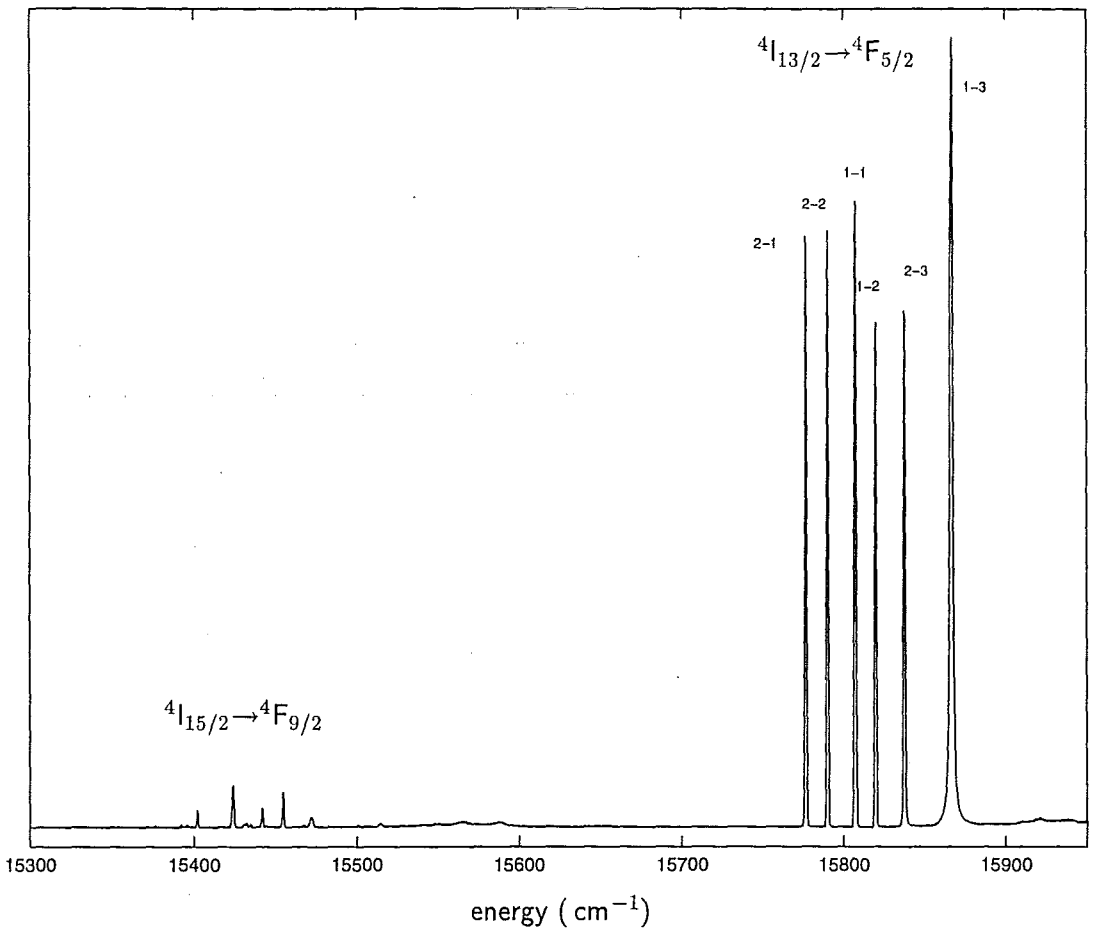

Figure 5.5 : Red-to-green upconversion excitation spectrum of the C_{4v} centre of CaF_2:0.01%Er^{3+}, monitoring green fluorescence at 18522 cm^{-1}. The $^4I_{13/2} \rightarrow {}^4F_{5/2}$ ESA transitions are labelled by their lower and upper crystal-field levels.

The group of peaks labelled Z–D are the upconversion peaks for GSA pumping observed by Cockroft *et al* [21]. The second set, labelled Y–H and with energies given in table 5.1, are an order of magnitude more intense than the Z–D lines and have not previously been reported. Pumping these lines produces the fluorescence spectrum characteristic of the C_{4v} centre, so they are not due to cross pumping. They have been assigned to ESA transitions between the two lowest levels of the $^4I_{13/2}$ multiplet and the three levels of the $^4F_{5/2}$ multiplets. The upconversion-excitation energies measured here and presented in table 5.1 are consistent with transition energies derived (and converted to cm^{-1} in air) from the $^4I_{13/2}$ and $^4F_{5/2}$ crystal-field energies reported by Tallant and Wright [85]. The measured energies have not been calibrated against a standard wavelength source, so may include a uniform shift of about $1\,cm^{-1}$.

ESA transition	measured energy (cm^{-1})	from ref. [85] (cm^{-1})
$Y_1 \rightarrow H_1$	15805.5	15806.6
$Y_1 \rightarrow H_2$	15818.0	15819.1
$Y_1 \rightarrow H_3$	15867.2	15867.2
$Y_2 \rightarrow H_1$	15776.6	15777.5
$Y_2 \rightarrow H_2$	15789.0	15790.0
$Y_2 \rightarrow H_3$	15838.1	15838.1

Table 5.1 : Measured transition energies of $^4I_{13/2} \rightarrow {}^4F_{5/2}$ excitation lines which produce green upconversion-fluorescence for the C_{4v} centre of CaF_2:0.01%Er^{3+}.

The SAU mechanisms for the two groups of lines are illustrated in figure 5.6.

The large difference in upconversion efficiency between the two mechanisms can be understood by considering the mismatch of energy between the incident laser photons and the non-resonant absorption transition. For $CaF_2:Er^{3+}$, the $^4I_{13/2} \rightarrow {}^4F_{5/2}$ ESA transitions have energies approximately $350\,cm^{-1}$ greater than the $^4I_{15/2} \rightarrow {}^4F_{9/2}$ GSA transitions. Thus, when the laser is in resonance with an ESA transition, the photon energy is greater than that of the GSA transitions and so the GSA transition can also proceed into the phonon side-band, even near absolute zero, with the additional creation of a single lattice phonon. In the converse process with the

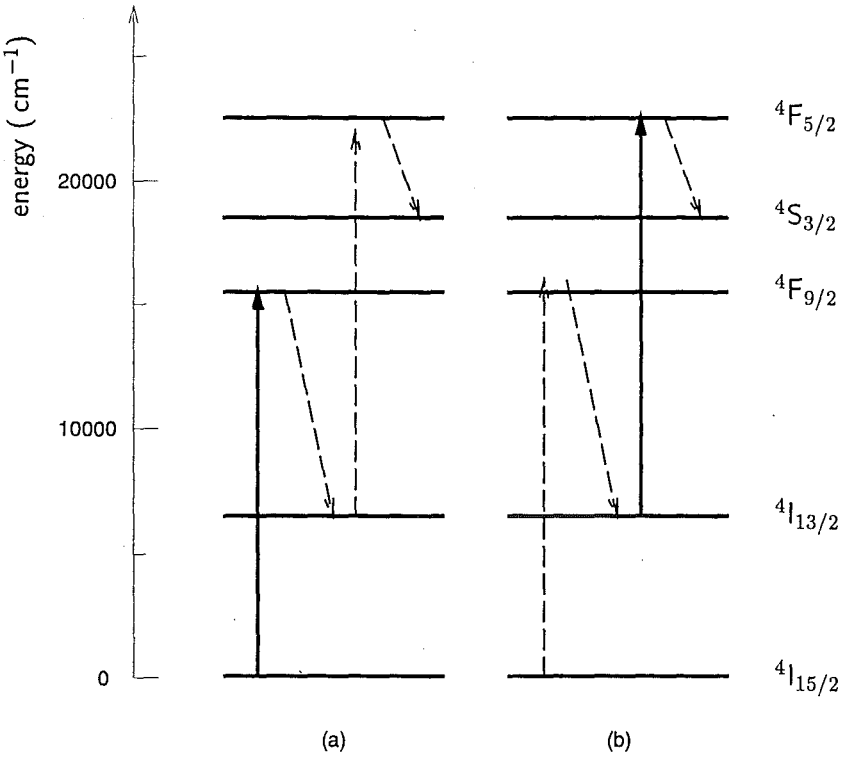

Figure 5.6 : Sequential-absorption processes of CaF_2:Er^{3+} which produce red-to-green upconverted fluorescence from the $^4S_{3/2}$ multiplet, upon pumping (a) the GSA transition, or (b) the ESA transition. The solid lines indicate resonant transitions; the dashed lines indicate phonon-assisted absorption transitions and decay pathways.

laser in resonance with a GSA transition, the photon energy is then less than the ESA transitions and so phonon annihilation would be required for the transition to proceed. Since the phonon occupation number drops to zero at zero temperature, the probability for this process is low. This difference is illustrated in figure 5.7. The two electronic transitions, E_1 and E_2, which correspond to the two steps of a SAU process have associated phonon sidebands, P_1 and P_2. At low temperatures, the situation is asymmetric, with the exothermic phonon-creation sidebands on the high energy side being very much more intense than the endothermic phonon-annihilation sidebands on the low energy side of each electronic transition. When pumping with a single laser frequency, the strength of the upconversion will depend on the product of the two transition strengths at that frequency. Clearly, pumping the higher-energy transition E_1 gives greater upconversion efficiency than pumping E_2, due to the presence of the P_2 phonon sideband near the frequency of the E_1 transition.

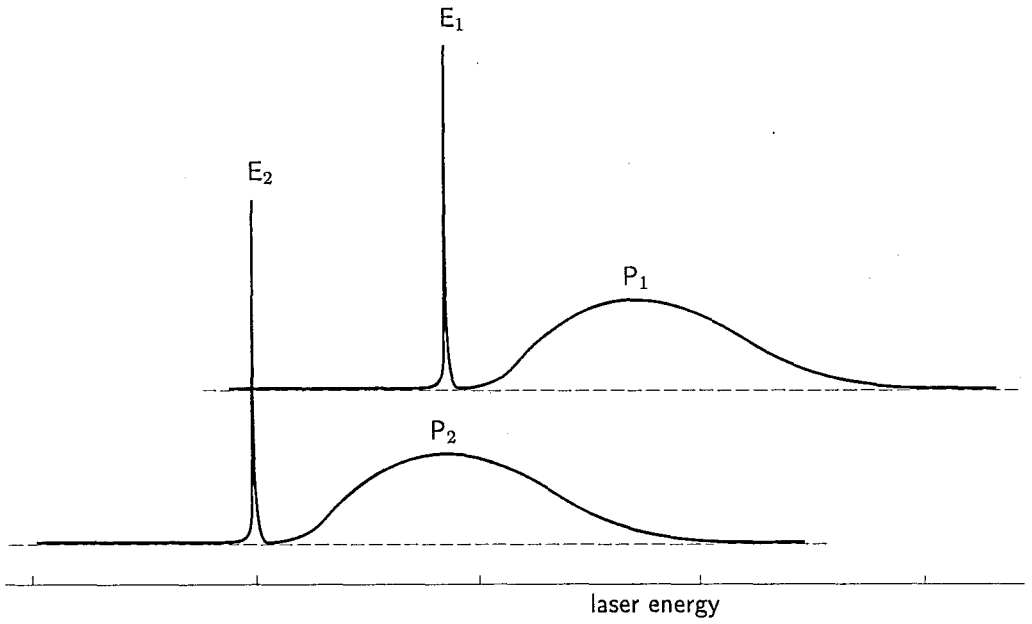

Figure 5.7 : Depiction of the phonon sidebands, P_1 and P_2, associated with the two electronic transitions, E_1 and E_2, of a sequential-absorption process at low temperatures. More efficient upconversion is achieved with the laser tuned to E_1 than E_2, since the phonon sideband P_2 corresponds to this energy.

It would be interesting to compare the relative upconversion strengths of these two mechanisms as a function of temperature. Unfortunately, this cannot be done for the GSA transitions, since the upconversion intensity of other centres (presumably clusters, which upconvert by the more efficient energy-transfer mechanism) is an order of magnitude greater than for the C_{4v} centre in this region. Since all spectral lines broaden with increasing temperature, it would quickly become impossible to discriminate the C_{4v} centre lines from those of other centres. However, upconversion in the ESA region is dominated by the C_{4v} centre since cluster centres have no particular advantage when pumping at these energies. Hence the temperature dependence of the ESA lines of the C_{4v} centre was able to be measured.

Figure 5.8 shows the $^4I_{13/2} \rightarrow {}^4F_{5/2}$ ESA upconversion excitation spectrum as a function of temperature, from 15 K to room temperature. These spectra are not site-selected, but rather were recorded using zero-order detection on the Spex 1700 single monochromator, with a broad bandpass green filter to eliminate any laser scatter and non-upconverted fluorescence. This mode of detection was chosen to eliminate apparent fluorescence diminution due to broadening of the fluorescence lines. If a narrow bandpass of, for example, $1\,cm^{-1}$ were to be employed, then the fraction of total fluorescence which fell within that bandpass would rapidly decrease as the fluorescence lineshapes broadened and the Stark-level populations changed. Detection of all of the upconverted fluorescence provides a more physical indication of the upconversion efficiency.

As the temperature is raised from 15 K to room temperature, the excitation lines broaden considerably as expected. The relative peak intensities of the lines are determined primarily by the relative thermal populations of the Y_1 and Y_2 levels, while the intensity variation of the phonon sidebands associated with the GSA transition would also have some effect. It is remarkable that the overall peak intensities do not vary greatly with temperature, and the total area under the excitation lines therefore increases significantly. An estimate of this increase can be obtained by numerically integrating each of the spectra in figure 5.8. These values have been plotted as a function of temperature in figure 5.9. The reference signal is assumed to be at the level of the 15 K spectrum well away from any excitation lines, and has been subtracted.

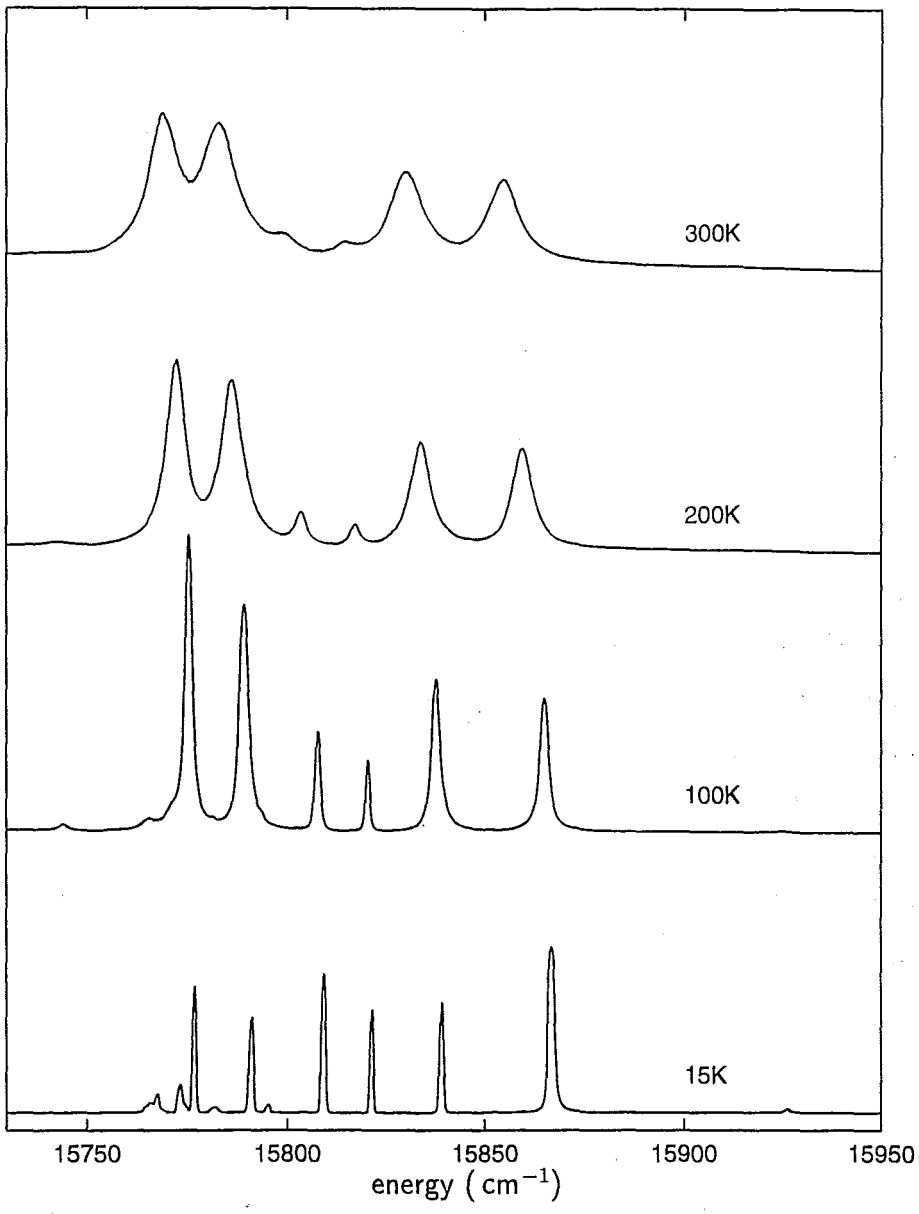

Figure 5.8 : Temperature dependence of the red-to-green upconversion excitation spectrum of the ESA lines of the C_{4v} centre of CaF_2:0.01%Er^{3+}, monitoring broadband green fluorescence centred at 540 nm.

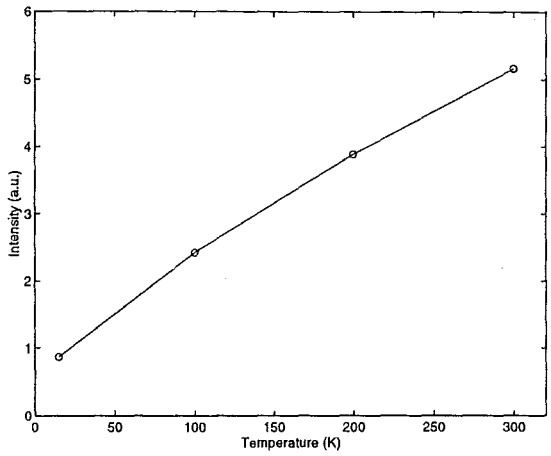

Figure 5.9 : Temperature dependence of the integrated upconversion-excitation intensity of the CaF_2:0.01%Er^{3+} C_{4v} centre ESA transitions of figure 5.8.

This plot indicates how the upconversion intensity might be expected to increase with temperature if the upconversion were to be pumped by a high-power broadband source, rather than a narrow linewidth laser.

Because the spectra of figure 5.8 were recorded without sharp fluorescence wavelength discrimination, there are certainly contributions to the integrated intensities from other than C_{4v} centre ESA upconversion—for example a series of weak lines at the low energy end of the 15 K spectrum. However, by inspection of the spectra, it is apparent that the major contribution to the integrated intensities is from these ESA lines.

5.2.2 Infrared-to-Green Upconversion of the C_{4v} Centre of CaF_2:Er^{3+}

Green upconversion-fluorescence has also been observed in the same sample of CaF_2:0.01%Er^{3+} upon excitation around 800 nm with the Ti:sapphire laser. Again, at this concentration the influence of energy transfers should be considerably less than that determined by Jouart and Oomen [47]. The upconversion-excitation spectrum is shown in figure 5.10. The top spectrum is the broadband (non-selective) upconversion-excitation spectrum, including excitation lines from all upconverting centres. The other three spectra are the site-selective upconversion-excitation spec-

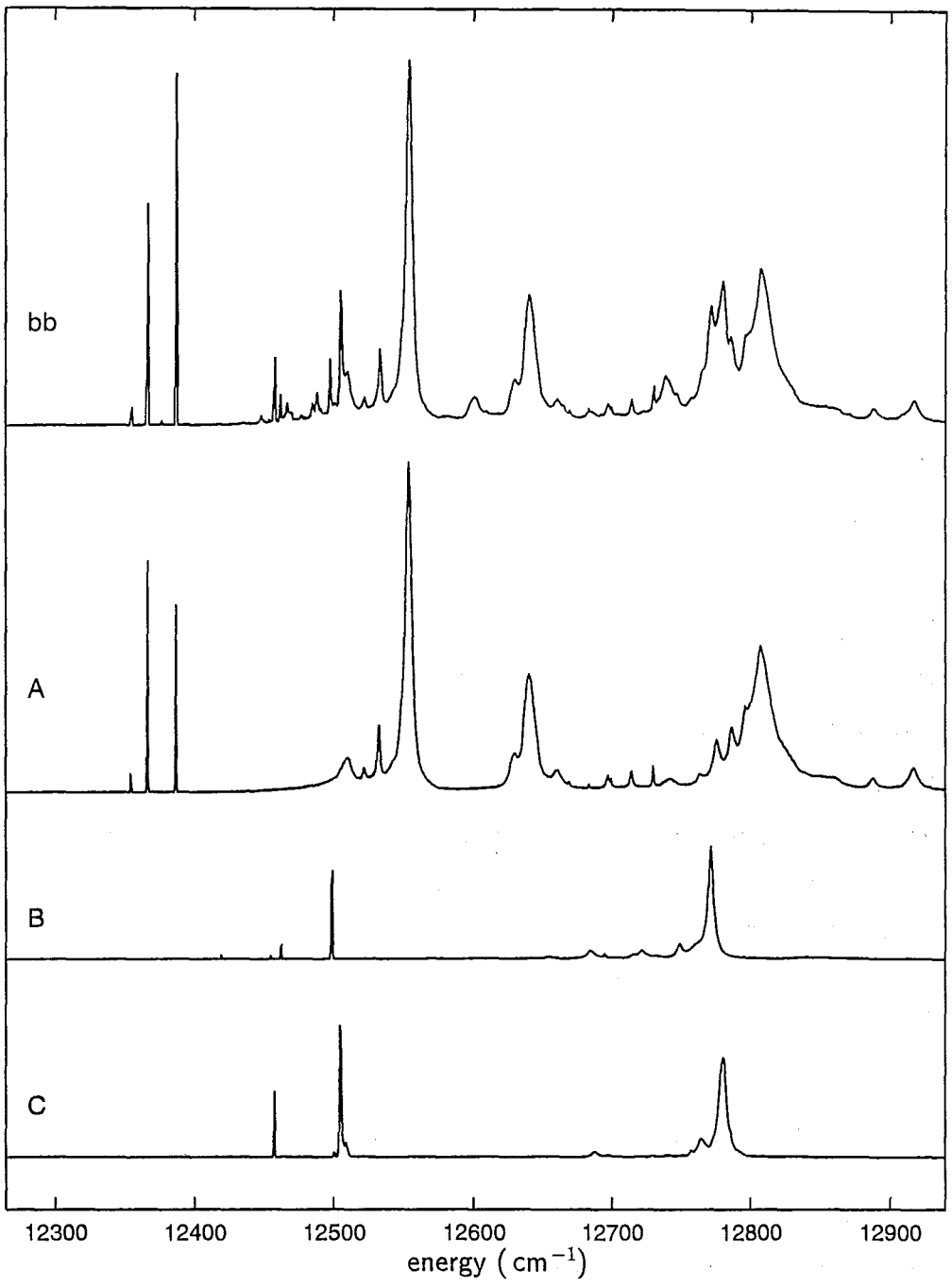

Figure 5.10 : Infrared upconversion excitation spectra of CaF_2:0.01%Er^{3+}, monitoring broadband green emission at 540 nm (bb) and site-selective emission of the A (C_{4v}), B (C_{3v}) and C (dimer) centres at 18549 cm^{-1}, 18615 cm^{-1} and 18627 cm^{-1}, respectively.

tra for monitoring fluorescence of the A (C_{4v}), B (C_{3v}) and C (dimer [85]) centres. The upconversion is dominated by the C_{4v} centre, with the C_{3v} and dimer centres also present.

Assuming an SAU mechanism for the upconversion of the C_{4v} centre, the exact route (GSA or ESA and the intermediate states) should be determinable by examination of the energy levels. The relevant transitions are illustrated in figure 5.11. Pumping in

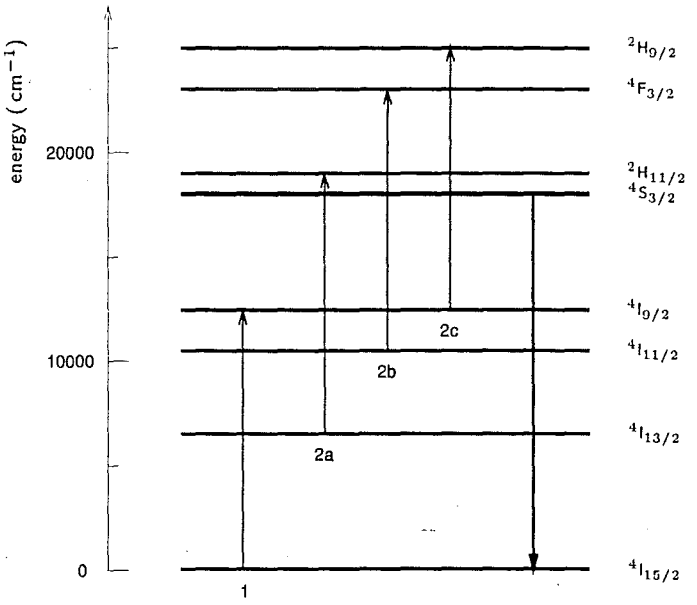

Figure 5.11 : Possible infrared-to-green SAU mechanisms in Er^{3+}. (1) The GSA step and (2a),(2b),(2c) candidates for the ESA step.

the region of the $^4I_{15/2} \rightarrow {}^4I_{9/2}$ GSA transitions, three possibilities are available for an ESA transition, namely the $^4I_{13/2} \rightarrow {}^2H_{11/2}$, $^4I_{11/2} \rightarrow {}^4F_{3/2}$ and $^4I_{9/2} \rightarrow {}^2H_{9/2}$ transitions. Many of the energy levels of these multiplets have previously been measured [85, 30], however some have not. Those energies which have not previously been reported were measured from the absorption spectrum of CaF_2:0.01%Er^{3+}. In particular, of the $^4I_{9/2}$ multiplet C_{4v} crystal-field levels, only one level has been previously reported, at 12801 cm^{-1} [74]. This was assigned to the $Z_1 \rightarrow B_1$ transition. However, such an assignment would indicate that many of the strong upconversion transitions seen in the figure 5.10 would have to correspond to ESA transitions with lower

energies than the GSA transition. It has already been pointed out that upconversion is necessarily very weak under such conditions, at low temperatures. There is a transition at 12801 cm^{-1} which would correspond to the reported absorption line but it is very broad, which is unexpected for a 1→1 transition.

In fact, there are four groups of transitions in the spectrum, near 12370 cm^{-1}, 12540 cm^{-1}, 12650 cm^{-1} and 12800 cm^{-1} which display the same ground-state splitting pattern of 0, 21, 33 cm^{-1}. This suggests that all of these are in fact GSA transitions and the previous assignment of the 12801 cm^{-1} level to the lowest of $^4I_{9/2}$ is incorrect, and it is instead an excited state of that multiplet. This was confirmed by comparison with the absorption spectrum of the $^4I_{9/2}$ multiplet. Figure 5.12 shows this absorption spectrum, along with the C_{4v} centre upconversion-excitation spectrum. The previously reported 12801 cm^{-1} absorption line is the strongest, but again is clearly too broad to correspond to the $Z_1 \rightarrow B_1$ transition. Absorption lines are clearly seen matching the strongest peaks in each of the four groups of three lines mentioned above. The GSA transitions from $Z_{1,2,3}$ to each of four $^4I_{9/2}$ levels are indicated (labelled Z-B).

Table 5.2 lists the state and transition energies of the GSA and ESA transitions which may contribute to the SAU mechanism for infrared-to-green upconversion for the C_{4v} centre of CaF_2:Er^{3+}. The $^4I_{9/2}$ levels determined here are included and denoted with †. Also included and denoted with † are energies of the $^2H_{9/2}$ multiplet which were measured from the absorption spectrum without any site discrimination. Some of these levels may not be associated with the C_{4v} centre and are only included to provide an indication of the range of energies for the $^4I_{9/2} \rightarrow {}^2H_{9/2}$ transitions.

These transition energies confirm that SAU processes for pumping the GSA transitions should indeed be favourable since the $^4I_{9/2} \rightarrow {}^2H_{9/2}$ ESA transitions could be bridged by phonon creation when pumping the lowest GSA transitions. For pumping the higher GSA transitions, these transitions have higher energies than the $^4I_{11/2} \rightarrow {}^4F_{3/2}$ and $^4I_{9/2} \rightarrow {}^2H_{9/2}$ ESA transitions, providing several possible intermediate states for the upconversion. The $^4I_{13/2} \rightarrow {}^2H_{11/2}$ and $^4I_{11/2} \rightarrow {}^4F_{3/2}$ ESA transitions are higher than the lowest GSA transitions so pumping these should also produce upconversion. These transitions are seen in figure 5.12 and are labelled "Y-F" and "A-I" respectively.

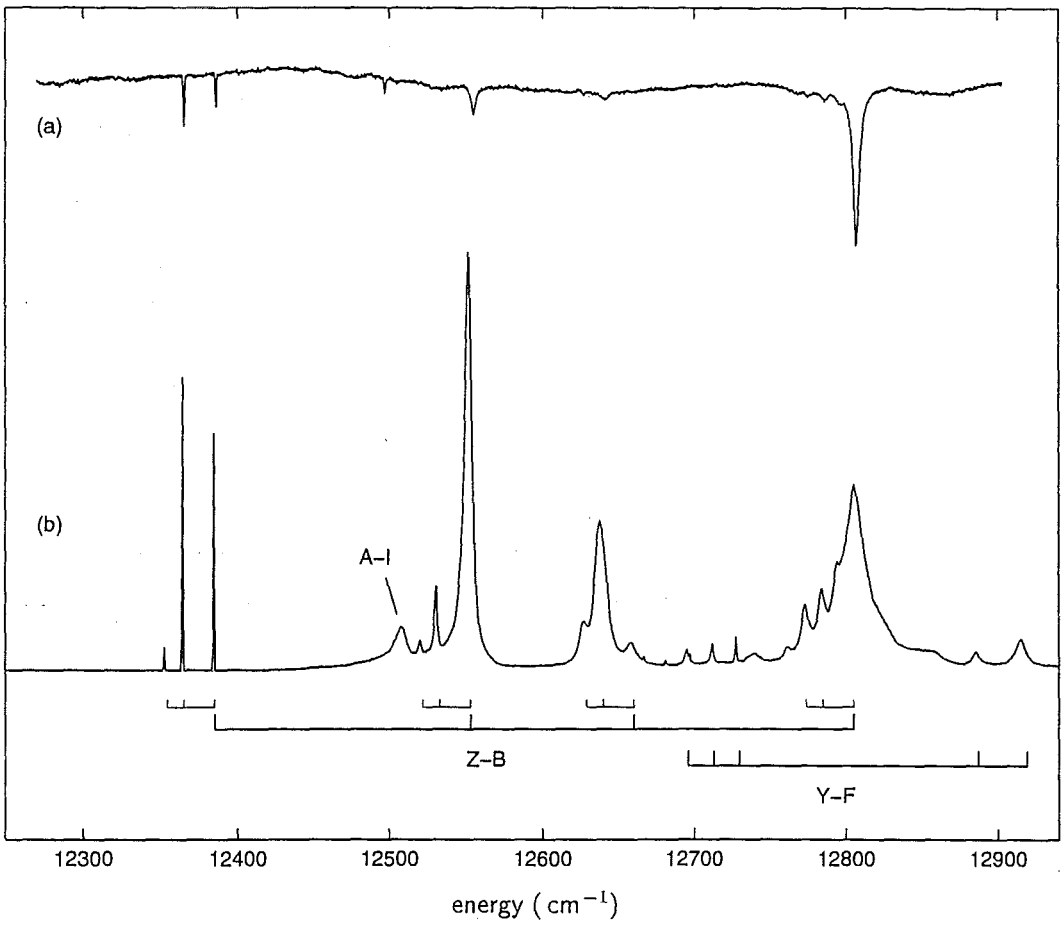

Figure 5.12 : (a) Absorption spectrum of the $^4I_{9/2}$ multiplet of CaF_2:0.01%Er^{3+}. (b) Infrared-to-green upconversion excitation spectrum of the C_{4v} centre in CaF_2:0.01%Er^{3+}. The assigned $^4I_{15/2}\rightarrow{}^4I_{9/2}$ (Z-B) GSA and $^4I_{13/2}\rightarrow{}^2H_{11/2}$ (Y-F) and $^4I_{11/2}\rightarrow{}^4F_{3/2}$ ESA transitions are identified.

Initial states (cm^{-1})		Final states (cm^{-1})		Transition energies (cm^{-1})
$^4I_{15/2}$	0.0, 21.1, 33.1	$^4I_{9/2}$	12383.0†	12383.0, 12361.9, 12349.7
			12551.6†	12551.6, 12530.5, 12518.3
			12658.1†	12658.1, 12637.0, 12624.8
			12803.6†	12803.6, 12782.5, 12770.3
$^4I_{13/2}$	6574.1	$^2H_{11/2}$	19272.0	12697.9
			19287.2	12713.1
			19302.3	12728.2
			19457.2	12883.1
			19486.0	12911.9
$^4I_{11/2}$	10291.5	$^4F_{3/2}$	22794.1	12502.6
$^4I_{9/2}$	12383.0†	$^2H_{9/2}$	24559†	12176
			24581†	12198
			24658†	12275
			24662†	12279
			24679†	12296

Table 5.2 : Energies of the states and transitions which may contribute to infrared-to-green upconversion in the C_{4v} centre of $CaF_2:Er^{3+}$. Energy levels are taken as previously reported [85, 30], except † measured from the non-selective absorption spectrum of CaF_2:0.01%Er^{3+}.

The $^4I_{9/2} \rightarrow {}^2H_{9/2}$ ESA transitions do not appear in the spectrum at 15 K, which is as expected since these transitions are all lower in energy than the related GSA transitions. The temperature sequence to room temperature of the C_{4v} upconversion-excitation spectrum is shown in figure 5.13. New features amongst the $^4I_{13/2} \rightarrow {}^2H_{11/2}$ ESA transition group are transitions from the thermally populated levels of the $^4I_{13/2}$ multiplet. A new, broad line also appears at the low end of the spectrum, at 12320 cm^{-1}. This could be associated with the $^4I_{9/2} \rightarrow {}^2H_{9/2}$ ESA upconversion, which would become favourable as the increasing temperature enhances the intensity of the phonon side-bands below the GSA transition energies.

The intensities in figure 5.13 have been normalised, since they were obtained using high-resolution monitoring which reduces the fluorescence detection at high temperatures. The temperature dependence of the upconversion fluorescence upon pumping the peak of the $Z_2 \rightarrow B_1$ transition, which is the dominant feature at high temperatures, is plotted in figure 5.14. In this case, broadband fluorescence detection at 540 nm was employed to allow for broadening of the fluorescence lines. The increase of this line may be enhanced somewhat by the increase and broadening of the $^4I_{9/2} \rightarrow {}^2H_{9/2}$ ESA transition providing some coincidence between the GSA and ESA steps of the SAU process.

5.3 Upconversion in CaF_2:Tm^{3+}

Jouart *et al* [46] have reported 77 K red-to-blue upconversion fluorescence from the $^1G_4$ and $^1D_2$ multiplets of Tm^{3+} doped into CaF_2, SrF_2, BaF_2 and CdF_2. The pumping wavelengths used to obtain upconversion fluorescence in the C_{4v} centre of CaF_2:Tm^{3+} were similar to those found in chapter 4 of this thesis, while the C_{3v} centre was not reported by them. However, in the work of Jouart *et al*, Tm^{3+} concentrations of up to 2% were used and energy-transfer processes were found to be intrinsic to their observation of upconversion fluorescence. Very slow build-up times of the upconversion fluorescence, of the order of 300 ms, were observed immediately after turning on the laser, supporting a photon-avalanche mechanism.

In contrast, the upconversion results as presented in chapter 4 showed that upconversion in CaF_2:Tm^{3+} was still important for concentrations as low as 0.01%. The

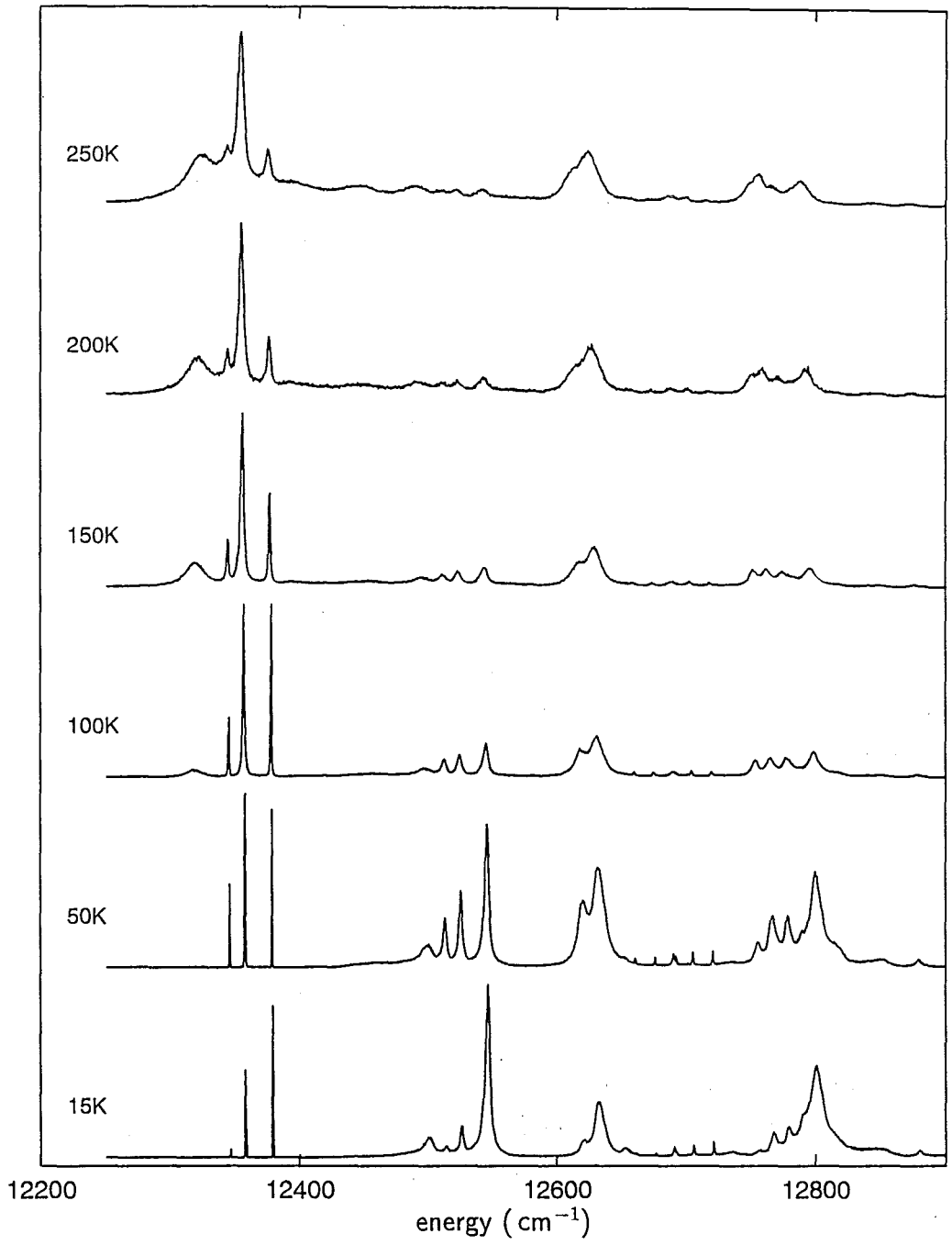

Figure 5.13 : Temperature dependence of the infrared-to-green upconversion-excitation spectrum of the C_{4v} centre in CaF_2:0.01%Er^{3+} for a pump power of 1 W. The fluorescence is monitored at 18548 cm^{-1} and the gain has been adjusted arbitrarily (but see figure 5.14).

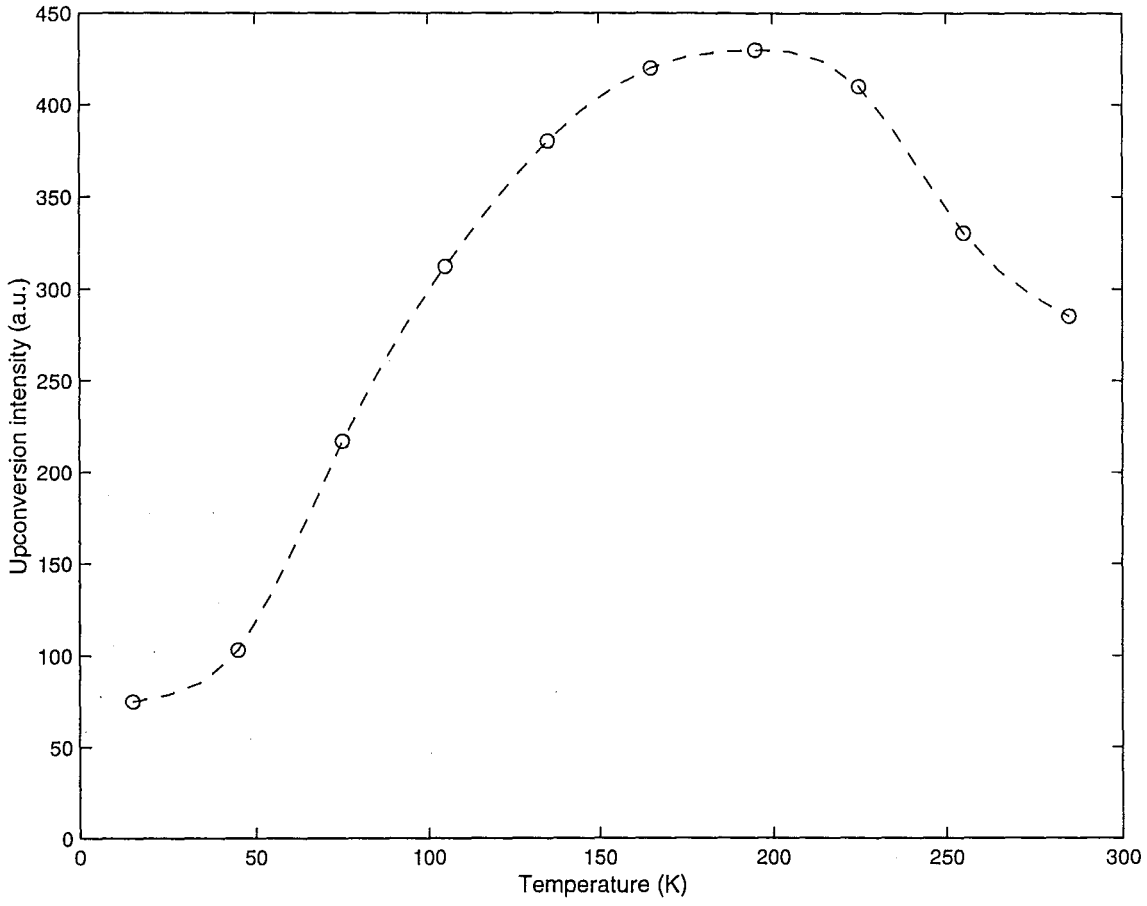

Figure 5.14 : Temperature dependence of the infrared-to-green upconversion-excitation of the C_{4v} centre in CaF_2:0.01%Er^{3+} upon pumping the peak of the $Z_2 \rightarrow B_1$ GSA transition near 12362 cm^{-1} and monitoring broadband green fluorescence at 540 nm. The dashed line is a guide to the eye only.

results presented here indicate that energy-transfer processes are not essential at such low concentrations. Instead, the simple SAU mechanism is able to explain all of the observations for low Tm^{3+} concentrations. With only a single pump laser operating in resonance with the ESA transition, the GSA strength is low but still non-zero, thus allowing the three SAU schemes depicted in figure 5.15 to operate with a single laser. Mechanisms (a) and (b), produced upon pumping with the rhodamine 640 red dye-laser, were observed for both the C_{4v} and C_{3v} centres (as well as several other minority centres), while mechanism (c), pumped with the near-infrared Ti:sapphire laser, was observed for the C_{3v} centre only.

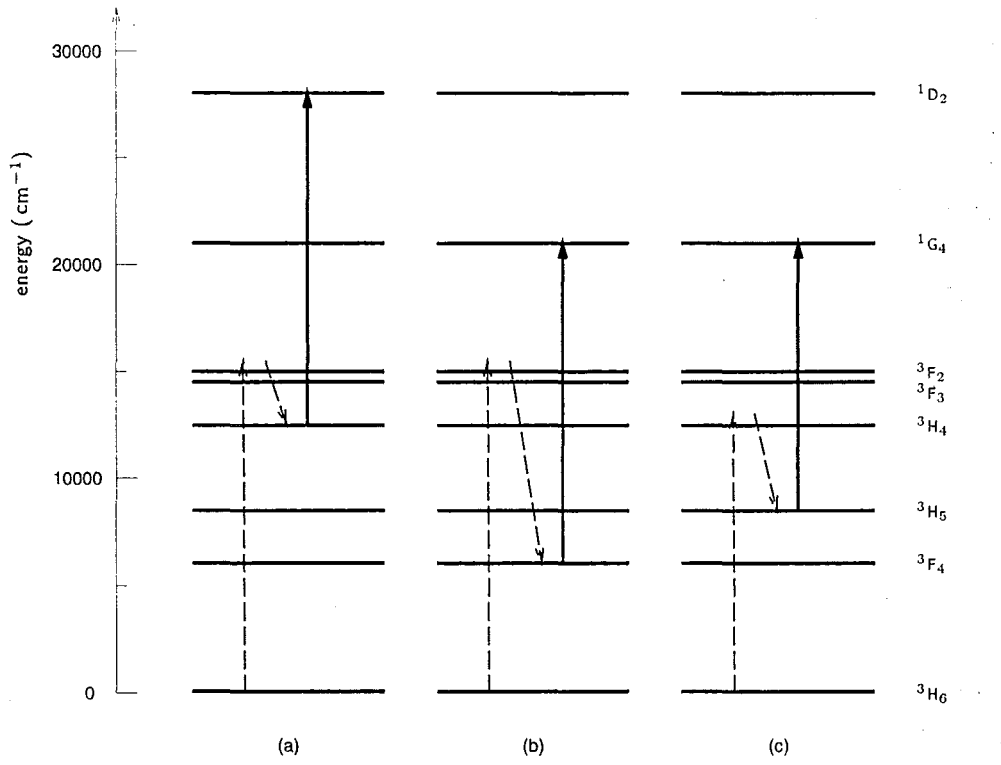

Figure 5.15 : Sequential-absorption processes in CaF_2:Tm^{3+} producing (a) UV and violet upconversion from the $^1D_2$ multiplet, and (b) and (c) blue upconversion from the $^1G_4$ multiplet. The solid lines indicate strong resonant transitions; dashed lines indicate phonon-assisted off-resonance transitions.

5.3.1 Red-to-Blue and Red-to-Violet Upconversion of the C_{4v} and C_{3v} Centres of CaF_2:Tm^{3+}

With only one exception, no upconversion fluorescence from either the $^1G_4$ or $^1D_2$ multiplets was observed upon pumping the GSA transitions to the $^3H_4$, $^3F_3$ or $^3F_2$ multiplets. The exception is the $Z_1 \rightarrow C_2$ transition of the C_{4v} centre which can be seen as a weak feature in the $^3F_4 \rightarrow {}^1G_4$ upconversion-excitation spectrum (figure 4.23 in section 4.3.2).

The lack of upconversion when pumping at the GSA energies can be explained in the same way as for the CaF_2:Er^{3+} case above. Both sets of ESA transitions, $^3F_4 \rightarrow {}^1G_4$ and $^3H_4 \rightarrow {}^1D_2$, have transition energies which are higher than the nearby GSA transition energies. Thus for GSA resonant upconversion, the ESA transition would have to be bridged by phonon annihilation, with vanishing probability at low temperatures. In contrast, for ESA resonant upconversion the GSA transition can be bridged by phonon creation at any temperature.

For the C_{4v} centre, the $Z_1 \rightarrow C_2$ transition actually lies at $20\,cm^{-1}$ higher energy than the $Y_1 \rightarrow D_1$ transition, and so GSA upconversion is seen at the frequency of this transition. For the C_{3v} centre, all of the $Z_1 \rightarrow C_i$ transitions have lower energy than the $Y_1 \rightarrow D_1$ transition, so GSA upconversion necessarily has a much lower efficiency, rendering any GSA upconversion fluorescence unobservable with the techniques employed here.

As described in sections 4.3.4 and 4.4.4, two-laser experiments have been performed on the CaF_2:Tm^{3+} system. Using a cw dye laser and pulsed dye laser together, coincident in the sample, pulsed upconversion could be obtained by tuning one laser to the GSA transition and the other to the ESA transition. With the cw laser tuned to the GSA transition and the pulsed laser tuned on the ESA transition, pulsed upconversion was obtained which had a simple decay transient characteristic of the lifetime of the upper state (either $^1G_4$ or $^1D_2$). When either laser was turned off, or detuned from the transition energy, no upconversion fluorescence could be detected.

When the two lasers were reversed in function, with the cw laser tuned on the ESA transition and the pulsed laser tuned on the GSA transition, pulsed upconversion was again observed. The decay transient in this case included a rise and decay time.

A simple rate equation analysis for a three-level (ground, intermediate and upper state) system under these pumping conditions shows that the rise and decay times are functions of the intermediate and upper state lifetimes, as well as the pump power. While upconversion fluorescence is still observed when the pulsed laser is switched off, an increase of several orders of magnitude is achieved with it on. No upconversion fluorescence was observed with the cw laser blocked and the pulsed laser tuned to the ESA transition.

These results show, not unexpectedly, that the SAU mechanism is the dominant process producing upconversion when both the GSA and ESA transitions are in resonance with a pump laser. This does not discount the possibility that an energy transfer process could be contributing in the single-pump-laser upconversion fluorescence case.

Figures 5.16 and 5.17 are excitation spectra, scanning the laser frequency across the $^3H_4 \rightarrow {}^1D_2$ upconversion transitions, for the C_{4v} and C_{3v} centres respectively. In each case, spectrum (a) shows the excitation spectrum for site-selective monitoring of the violet ($^1D_2 \rightarrow {}^3F_4$) upconversion, while spectrum (b) shows the spectrum for monitoring infrared emission from the $^3H_4$ multiplet. The generation of $^3H_4 \rightarrow {}^3H_6$ fluorescence for pumping at any frequency in this region demonstrates that the first step in the upconversion process, the GSA process, is weak but non-zero at the upconversion wavelengths.

Distinct holes in the infrared emission-detected spectra, figures 5.16(b) and 5.17(b), occur at laser frequencies corresponding to the ESA transition energies, demonstrated by comparison with the upconversion-excitation spectra, figures 5.16(a) and 5.17(a). These holes could have been attributable to a depletion of the pump-laser intensity due to excited-state absorption. However, this explanation is highly improbable, since this would imply that 50% absorption of the pump beam results from tuning onto one of the C_{3v} centre ESA transitions. Inspection of the transmitted laser beam indicated that, in fact, very little extra light was absorbed as the laser was tuned onto the ESA transition.

An alternative explanation is that the $^3H_4$ multiplet branching ratios are changed due to the addition of an alternative decay pathway, viz the $^3H_4 \rightarrow {}^1D_2$ ESA transition. The depletion of the normal fluorescence is a measure of the relative strengths of

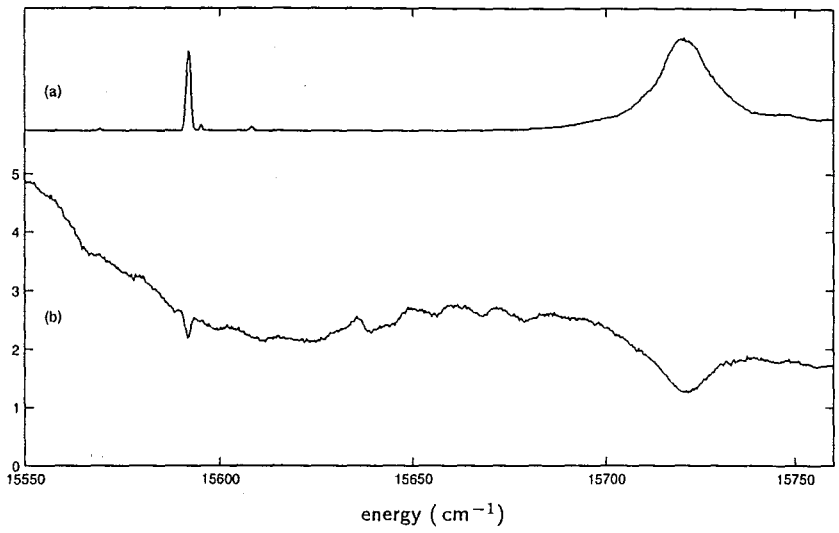

Figure 5.16 : Excitation spectra showing depletion of $^3H_4$ fluorescence at ESA wavelengths of the CaF_2:0.02%Tm^{3+} C_{4v} centre, (a) monitoring $^1D_2 \rightarrow {}^3F_4$ upconversion fluorescence of the C_{4v} centre, (b) monitoring normal $^3H_4 \rightarrow {}^3H_6$ fluorescence of the C_{4v} centre.

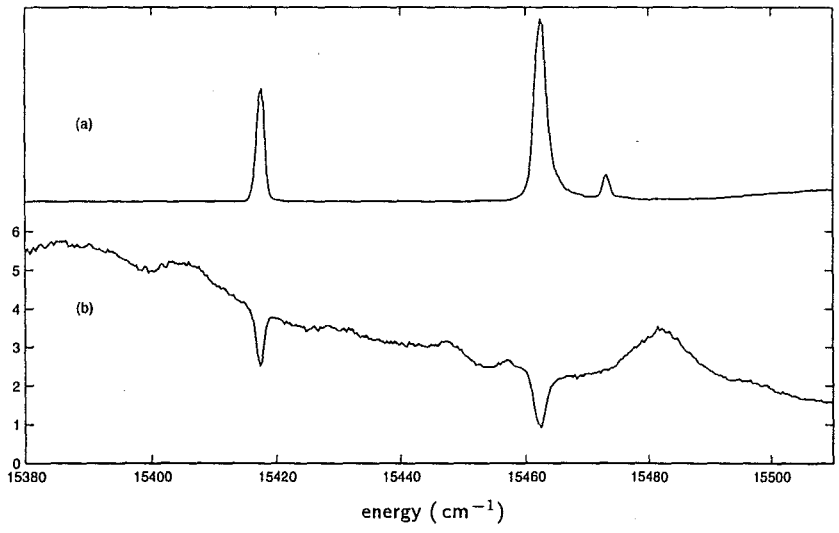

Figure 5.17 : Excitation spectra showing depletion of $^3H_4$ fluorescence at ESA wavelengths of the CaF_2:0.02%Tm^{3+} C_{3v} centre, (a) monitoring $^1D_2 \rightarrow {}^3F_4$ upconversion fluorescence of the C_{3v} centre, (b) monitoring normal $^3H_4 \rightarrow {}^3H_6$ fluorescence of the C_{3v} centre.

the $^3H_4 \rightarrow {}^3H_6$ spontaneous emission and the competing $^3H_4 \rightarrow {}^1D_2$ ESA upconversion process, which will be dependent on the pump-beam intensity. This explanation is a far more likely one than that of the absorbed pump-beam intensity. Given the relatively long lifetime of the $^3H_4$ multiplet (3.3 ms and 3.1 ms for the C_{4v} and C_{3v} centres, respectively—see sections 4.3.4 and 4.4.4), it seems reasonable that a large fraction of the Tm^{3+} ions which get populated to this multiplet would then undergo excited-state absorption before decaying spontaneously to the ground state.

This explanation is supported by the site-selective and transition-selective nature of the fluorescence-depletion holes. Holes are observed only at the ESA wavelengths of the particular centre whose $^3H_4 \rightarrow {}^3H_6$ transition is being monitored. The C_{4v}-centre holes are not seen when monitoring C_{3v} fluorescence, nor vice-versa, nor are the strong upconversion features due to minority centres, as seen in the broadband upconversion excitation spectrum (figure 4.22), evident as holes in either case. In addition, only wavelengths corresponding to $^3H_4 \rightarrow {}^1D_2$ ESA transitions produce holes; those corresponding to $^3F_4 \rightarrow {}^1G_4$ ESA transitions do not. This is consistent with the explanation presented here, since $^3F_4 \rightarrow {}^1G_4$ excited-state absorptions do not deplete population from the $^3H_4$ multiplet. Indeed, if the branching ratio $^1G_4 \rightarrow {}^3H_4$ were significant, then these excited-state absorptions would enhance $^3H_4 \rightarrow {}^3H_6$ fluorescence by feeding back population which had decayed by the other available pathways.

The C_{3v} centre has a greater degree of $^3H_4$-multiplet fluorescence depletion from upconversion than the C_{4v} centre, an indication that the $^3H_4 \rightarrow {}^1D_2$ transitions are stronger for this centre than for the C_{4v} centre. The peak at 15474 cm^{-1} in the C_{3v} centre upconversion-excitation spectrum has been determined to belong to a different centre (section 4.4.2), and this is confirmed by the absence of a corresponding fluorescence-depletion hole at that frequency.

Temperature Dependence

The C_{4v}-centre upconversion-fluorescence intensity has been observed to increase dramatically as the sample is warmed up from 15 K. As with the $CaF_2:Er^{3+}$ case, the temperature dependences of upconversion efficiencies were measured using a broadband filter selecting blue-violet wavelengths and zero-order setting on the Spex 1700 single monochromator. As explained earlier, this is done to allow for the

changing profile of the fluorescence spectrum.

The temperature dependence of the $^3F_4 \rightarrow {}^1G_4$ upconversion fluorescence of the C_{4v} centre, plotted in figure 4.23, has a most remarkable behaviour. This red-to-blue upconversion fluorescence intensity continues increasing as the sample is heated up to room temperature, and appears to level off near room temperature. The upconversion fluorescence efficiency at room temperature shows an increase of a factor of up to 100 over the efficiency at 15 K, depending on the polarisation of the laser.

This increase can be shown to be due to the broadening of the $^3H_6 \rightarrow {}^3F_2$ ground-state absorption lines. For the C_{4v} centre, the $Z_1 \rightarrow C_2$ transition is at 15365 cm^{-1}, only 21 cm^{-1} higher than the $Y_1 \rightarrow D_1$ ESA transition at 15344 cm^{-1}, while the $Z_2 \rightarrow C_2$ transition is at 15281 cm^{-1}, 63 cm^{-1} lower than this ESA transition. Figure 5.19 shows the temperature dependence of the broadband excitation spectrum of these two transitions. As the temperature increases both lines broaden, eventually overlapping the energy region of the $Y_1 \rightarrow D_1$ ESA transition, indicated by the vertical dashed line. The broadband detection used for these spectra allowed for both infrared and blue detection, so that the upconversion-excitation line can be seen, increasing with temperature, on the shoulder of the $Z_1 \rightarrow C_2$ line.

The increase with temperature of the $^3H_4 \rightarrow {}^3H_6$ normal fluorescence upon pumping with the laser at the $Y_1 \rightarrow D_1$ frequency is shown in figure 5.20. The graph shown here is for a $\langle 111 \rangle$ oriented sample, but the graph for a $\langle 100 \rangle$ oriented sample is similar. The shape of this graph is qualitatively similar to the temperature dependence of the red-to-blue upconversion in figure 5.18, which therefore pinpoints this as the dominant factor in determining the upconversion efficiency. The lifetime of the $^3F_4$ intermediate state would also be a determining factor in the upconversion-fluorescence efficiency since a change in this would affect the branching ratio between decay and the ESA processes. However, the infrared fluorescence from this multiplet could not be detected with the available spectrometer so its lifetime could not be measured.

The temperature dependence of the $^1G_4$ multiplet upconversion-fluorescence intensity shows different behaviour for the laser polarised parallel to either the $\langle 100 \rangle$ or the $\langle 111 \rangle$ crystallographic direction. Since the ground-state absorption has es-

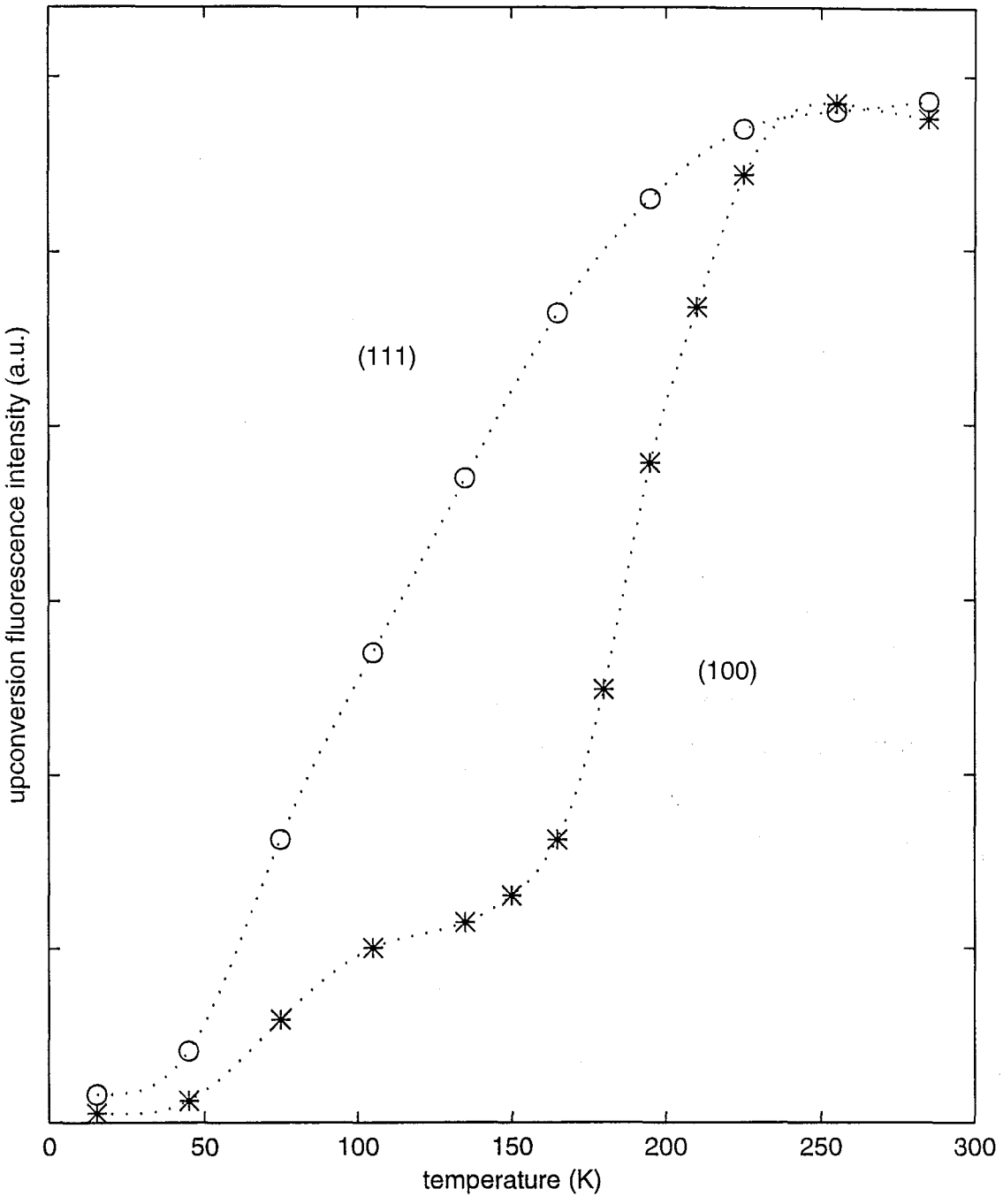

Figure 5.18 : Temperature dependence of red-to-blue upconversion intensity in ⟨100⟩ and ⟨111⟩ oriented CaF_2:0.02%Tm^{3+} pumping the $Y_1 \rightarrow D_1$ ESA transition at 15344 cm^{-1} and monitoring broadband blue fluorescence. The dotted lines are a guide to the eye only.

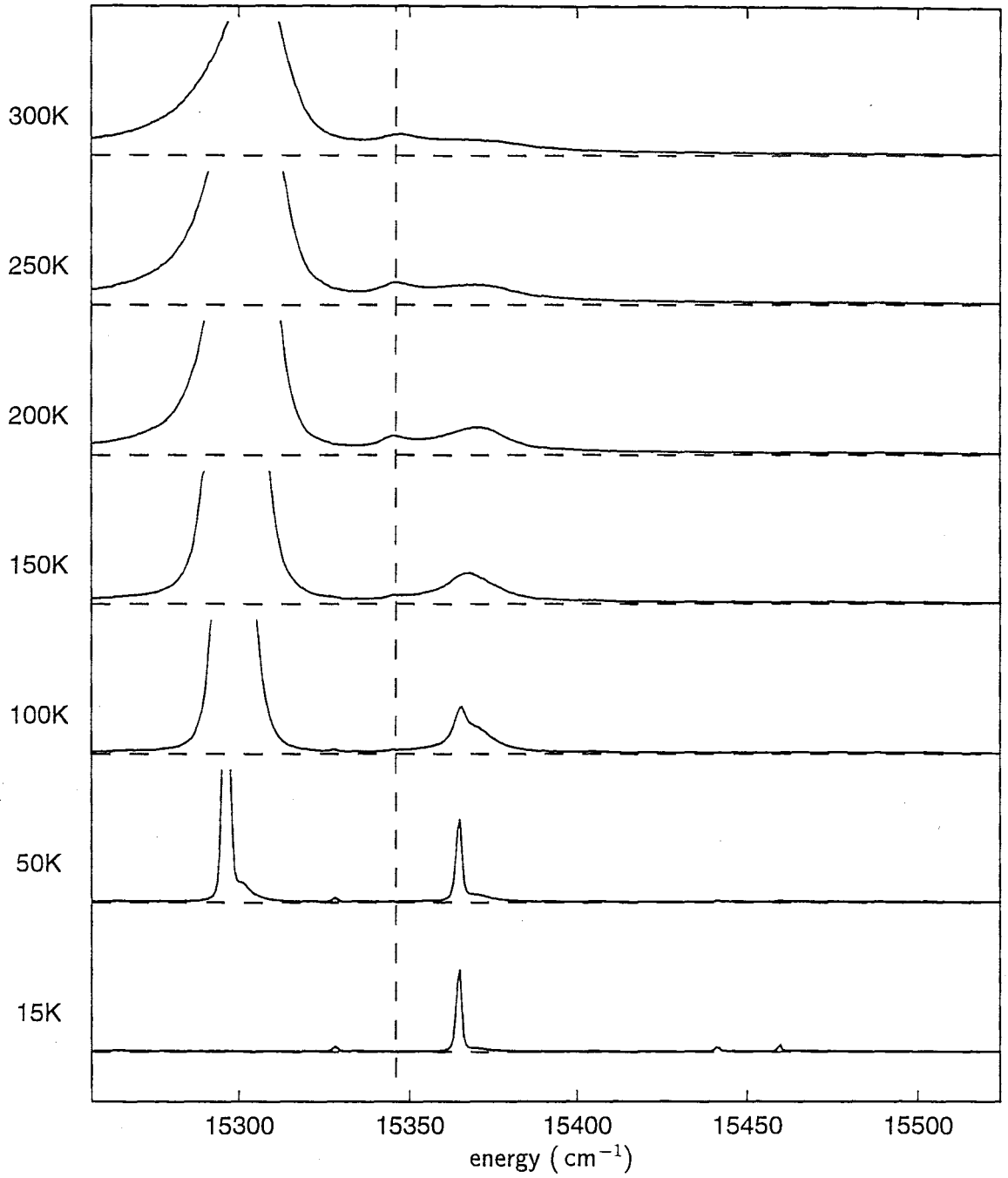

Figure 5.19 : Temperature dependence of the broadband excitation spectrum in the region of the red-to-blue upconversion transitions of CaF_2:0.05%Tm^{3+}, showing the broadening of the $^3H_6 \rightarrow {}^3F_2$ absorption lines across the $Y_1 \rightarrow D_1$ ESA transition energy at 15344 cm^{-1}.

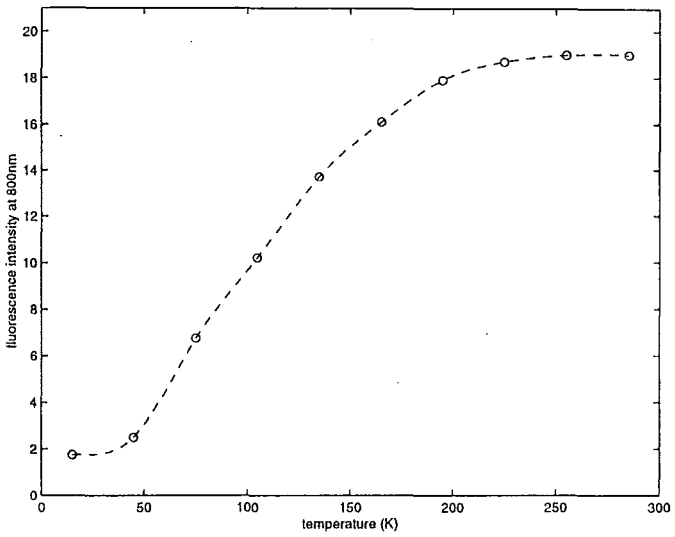

Figure 5.20 : Temperature dependence of the $^3H_4 \rightarrow {}^3H_6$ at 800 nm fluorescence upon pumping at 15344 cm^{-1},the frequency of the $Y_1 \rightarrow D_1$ ESA transition of the C_{4v} centre of $\langle 111 \rangle$-oriented CaF_2:0.05%Tm^{3+}. The dashed line is a guide to the eye only.

sentially the same temperature dependence for both of these configurations, the different upconversion efficiencies must be due to the second step—the ESA process. For $\langle 100 \rangle$ laser polarisation, all Tm^{3+} C_{4v} centres are oriented either parallel or perpendicular to the incident laser polarisation direction and their transition intensities are dependent on the specific centre orientation. As the ESA absorption is a π-allowed transition and π- and σ-transitions excite differently oriented C_{4v} centres independently, only overlap by GSA transitions of π-polarisation will contribute to assisting the ESA upconversion fluorescence. With change in temperature, the set of nearby GSA levels will contribute a varying combination of σ and π transitions, which determines the upconversion fluorescence level.

For $\langle 111 \rangle$ polarisation, all C_{4v} centres are equally inclined at $\cos^{-1}\left(\frac{1}{\sqrt{3}}\right) = 54.7°$ to the incident laser polarisation direction and the combined sequential absorption intensity is from equally inclined centres with no strong polarisation dependence expected.

For temperatures above 160 K the interstitial F^- ions become mobile, so that the C_{4v} centres are able to reorientate freely and any spectral polarisation effects wash

out [41]. Hence, the temperature dependence of the upconversion becomes independent of the laser polarisation at higher temperatures.

The temperature dependence of the $^3H_4 \rightarrow {}^1D_2$ upconversion fluorescence of the C_{4v} centre is plotted in figure 4.24. The upconversion efficiency increases by a factor of 2.4 in heating from 15 K to 60 K, peaks at 60 K, and then decreases to less than 1% of its 15 K level at room temperature. When pumping at the frequency of the $A_1 \rightarrow E_1$ transition, the $^3H_4 \rightarrow {}^3H_6$ fluorescence intensity in the spectra of figure 5.19 increases at a steady rate, with a total increase of a factor of 4 in heating from 15 K to room temperature. The temperature dependence of the $^1D_2$ upconversion-fluorescence intensity clearly depends on other factors. Again, the lifetime of the intermediate state would be expected to be crucial, but it was found in section 4.3.4 that the lifetime of the $^3H_4$ multiplet was essentially independent of the sample temperature, up to room temperature. The effect of the centre orientations with respect to the laser polarisation discussed for the $^3F_4 \rightarrow {}^1G_4$ upconversion above, would not account for the temperature dependence of figure 5.21, since these orientational effects should disappear at elevated temperatures.

The temperature dependence of the $^1D_2$ multiplet lifetime, which was not measured here, remains the other major factor which could influence the efficiency of upconversion-fluorescence production.

5.3.2 Red-to-Blue Upconversion of a Deuterium-Compensated Tm^{3+} Centre

Unexpectedly, new upconverting centres were observed in a sample containing deuterium. Figure 5.22 shows a part of the broadband upconversion-excitation spectrum for the parent CaF_2:0.05%Tm^{3+} crystal and for a crystal which had been deuterated for 48 hours. A new strong upconversion line appears at 15540 cm^{-1} in the spectrum of the sample after deuteration treatment, along with several other weaker lines between 15520–15540 cm^{-1}. These new lines are presumably due to new Tm^{3+} centres formed by the addition of D^- ions to the lattice. When pumping the strong line at 15540 cm^{-1} and monitoring fluorescence at 22140 cm^{-1}, a strong polarisation ratio of 70:1 was measured between the (YY):(YX) configurations. This dependence is characteristic of a π transition of a C_{4v}-symmetry centre, which would be consistent

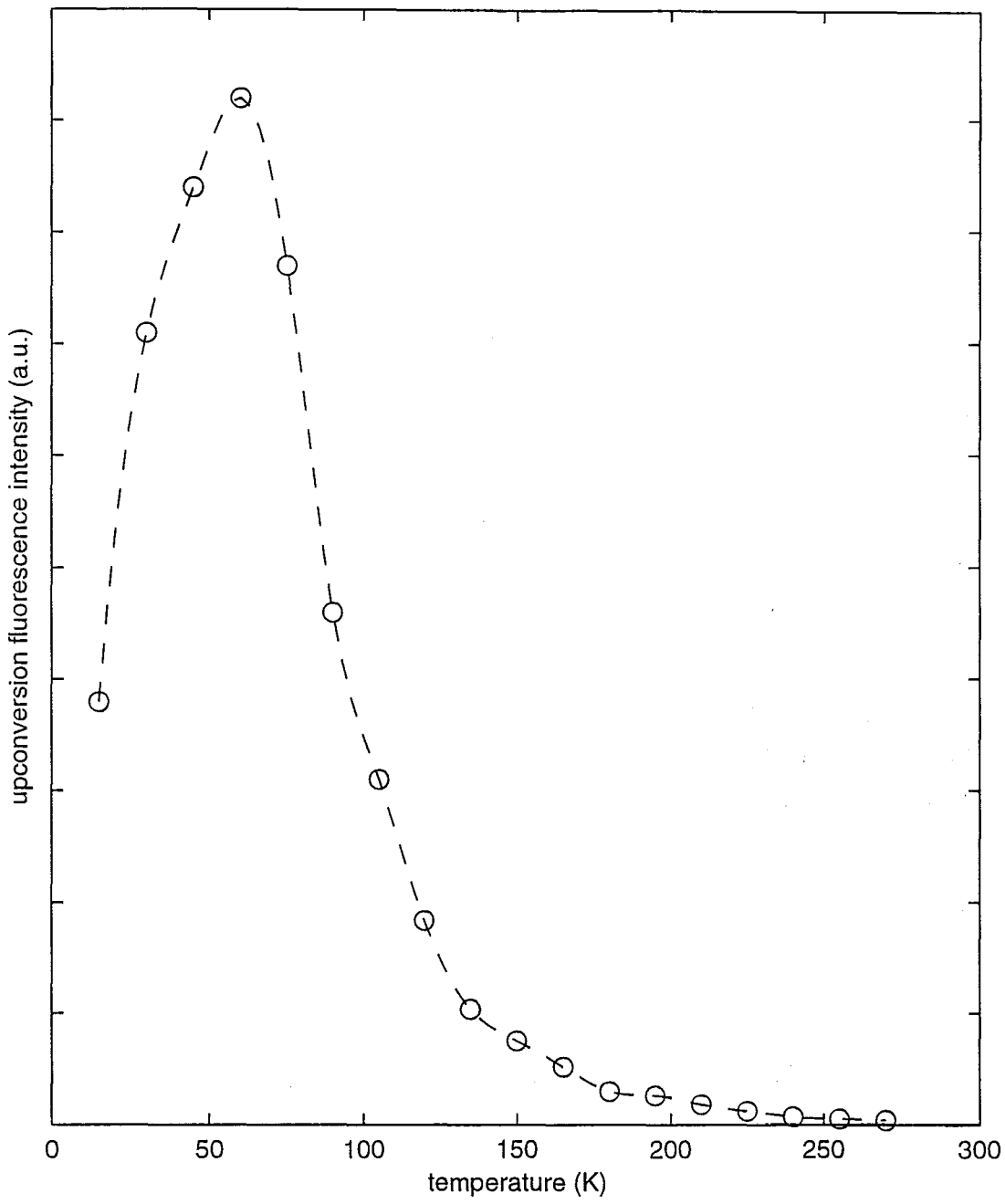

Figure 5.21 : Temperature dependence of red-to-violet upconversion intensity of CaF_2:0.02%Tm^{3+}, pumping the $A_1 \rightarrow E_1$ ESA transition at 15520 cm^{-1} and monitoring broadband blue/violet fluorescence centred at 450 nm. The dashed line is a guide to the eye only.

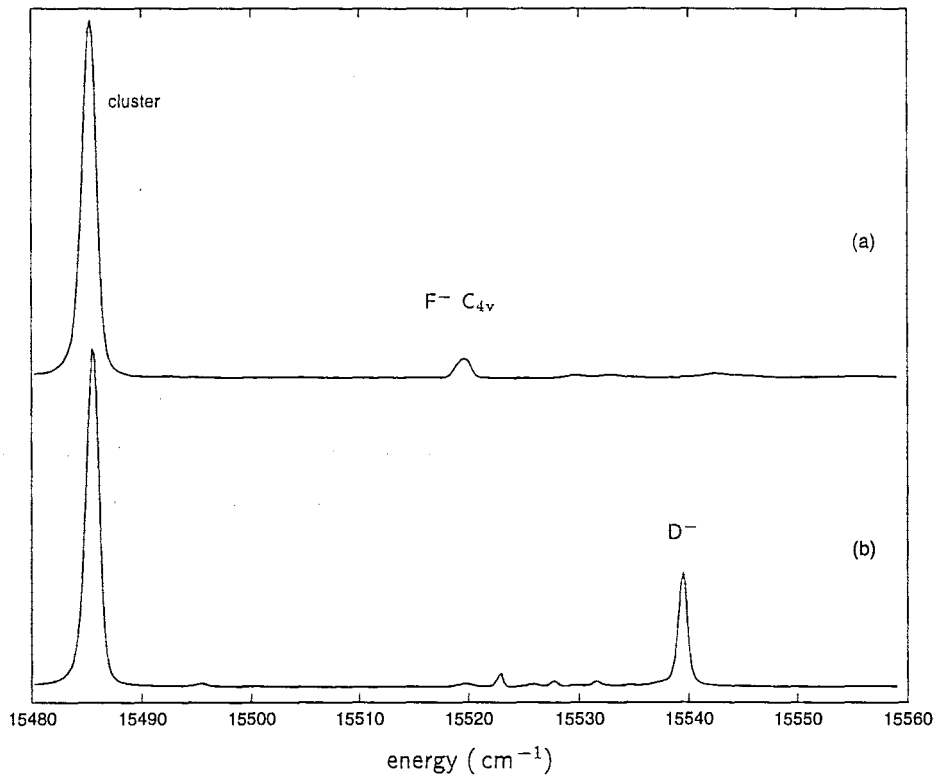

Figure 5.22 : Broadband upconversion-excitation spectrum of CaF_2:0.05%Tm^{3+}, monitoring broadband blue fluorescence. (a) Parent crystal, (b) after 48-hour deuteration treatment. The strong transition at 15485 cm^{-1}, present in both spectra, is thought to be due to a cluster centre (section 4.3).

with the centre being the D^- analogue of the F^--compensated C_{4v} centre (see section 4.6), and rules out the possibility of the centre being the C_{3v} O^{2-}-compensated centre.

In section 4.6, it was found that the $^3H_4 \rightarrow {}^3H_6$ fluorescence of the Tm^{3+} ion was strongly quenched by the presence of D^- ions. This implies a greatly reduced lifetime of the $^3H_4$ multiplet for the D^- C_{4v} centre relative to the F^--compensated centres. Since the efficiency of sequential-absorption processes is expected to be strongly dependent on the lifetime of the intermediate state, the observation of upconversion fluorescence from the $^1D_2$ multiplet, at a greater intensity than the F^- C_{4v}-centre, is quite unexpected. However the high local-mode phonon energies, around 700 cm^{-1}, would provide increased efficiency for the phonon-sideband GSA transition. This extra ground-state absorption may outweigh the effect of the decreased intermediate-state lifetime.

No further spectroscopic evidence has been obtained that these new lines are due to D^--compensated centres. It is possible that other centres may have formed due to the thermal cycling during the deuteration treatment. However, the polarisation behaviour observed for the strongest line is strongly suggestive of a C_{4v}-symmetry centre. This would arise from the proposed charge compensation along a $\langle 100 \rangle$ direction by an interstitial D^- ion.

5.3.3 Infrared-to-Blue Upconversion of the C_{3v} Centre of CaF_2:Tm^{3+}

A cursory search was made for upconversion fluorescence in CaF_2:0.02%Tm^{3+} upon excitation in the region of 12000–13000 cm^{-1} with a Ti:sapphire laser. The excitation spectrum for monitoring broadband upconversion-fluorescence at 475 nm, shown in figure 5.23 is dominated by a single peak, corresponding to the $X_1 \rightarrow D_2$ transition of the C_{3v} centre. The fluorescence spectrum obtained upon pumping this transition was identical to that obtained for excitation of the $^1G_4$ multiplet by direct pumping or by $^3F_4 \rightarrow {}^1G_4$ excited-state absorption. The absence of a strong ESA transition for the C_{4v} centre may be due to low transition strengths, since the $X_1 \rightarrow D_1$ transition is both electric-dipole and magnetic-dipole forbidden. The $X_1 \rightarrow D_2$ transition is 300 cm^{-1} higher than this, and may form part of the broad feature near 12960 cm^{-1}.

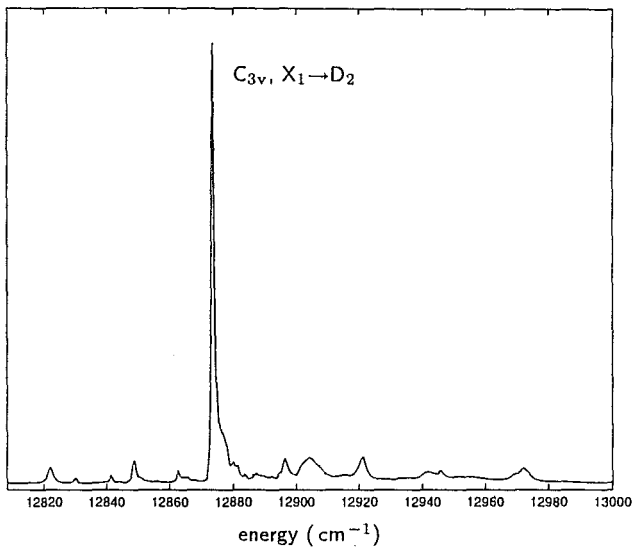

Figure 5.23 : Broadband upconversion-excitation spectrum of CaF_2:0.02%Tm^{3+}, pumping the $^3H_5 \rightarrow {}^1G_4$ ESA transitions, monitoring broadband blue fluorescence at 480 nm.

As with the red-to-blue/violet upconversion, no upconversion fluorescence was detected upon pumping the ground-state absorption transitions. This can be understood in the same way as discussed previously, with the ESA transitions having higher energy than the GSA transitions and transition-bridging by phonon creation being much more favourable than by phonon annihilation, at low temperatures.

5.4 Upconversion in CaF_2:Ho^{3+}

Mujaji *et al* [64] have reported a thorough investigation of the spectroscopy of the CaF_2:Ho^{3+} C_{4v} and C_{3v} centres. At 15 K, very weak $^5S_2 \rightarrow {}^5I_8$ upconversion fluorescence was observed upon pumping the $^5I_8 \rightarrow {}^5F_5$ GSA transitions.

Zhang *et al* [94] have reported red-to-green upconversion in CaF_2:0.1%Ho^{3+} at 77 K. They were able to correlate many of their excitation and fluorescence transition peaks with the energy level schemes of the C_{4v} and C_{3v} centres of Mujaji *et al* [64] and the dimer centre of Seelbinder and Wright [80]. For the dimer centre, energy transfer was determined to be the dominant upconversion mechanism, while for the C_{4v} and C_{3v} single-Ho^{3+} ion centres, the dominant upconversion mechanism

was determined to be the sequential-absorption (SAU) mechanism. Upconversion-excitation transitions for these two centres were assigned to either GSA or ESA resonant pumping. These were distinguished by comparison with the excitation spectrum for monitoring red fluorescence from the $^5F_5$ multiplet, which contained only GSA transitions.

In figure 5.24, the red-to-green upconversion-excitation spectrum of CaF_2:0.01%Ho^{3+} is shown at temperatures of 15, 100, 200 and 300 K. Fluorescence was monitored at 540 nm in broadband mode, so as to capture all upconverted fluorescence. The intensity scales of these spectra are all the same, so that line intensities can be compared between spectra. The peak intensity does not change greatly, although the principal frequencies do change. With the broadening at high temperatures, the integrated intensity increases by an order of magnitude going from 15 K to room temperature.

Figure 5.25 shows the 15 K excitation spectrum for monitoring either broadband $^5F_5 \rightarrow {}^5I_8$ normal fluorescence, spectrum (a), or broadband $^5S_2 \rightarrow {}^5I_8$ upconversion fluorescence, spectrum (b). Spectrum (a) has a large background noise level from the presence of scattered light from the pump laser. All of the major lines in spectrum (a) have been correlated with either the A (C_{4v}) or B (C_{3v}) centre $^5F_5$ multiplet energy levels found by Mujaji *et al* [64]. All of the major peaks in the upconversion-excitation spectrum match peaks in the "down-conversion" excitation spectrum, demonstrating that the GSA transitions dominate the upconversion spectrum at 15 K. The relative intensities of the lines changes for spectra (a) and (b) due to the changing strength of the phonon-assisted excited-state absorption strength across this pumping range.

Referring to the energy-level scheme of Mujaji *et al* [64], the dominance of GSA-resonant upconversion at 15 K is again consistent with the picture of phonon-assisted absorption for the off-resonant transition in the SAU process illustrated in figure 5.26. For the C_{3v} centre, the $^5I_7 \rightarrow {}^5F_3$ transitions lie between 15512–15598 cm^{-1}, just lower than the lowest $^5I_8 \rightarrow {}^5F_5$ GSA transition at 15604 cm^{-1}. At 15 K, the phonon-creation process is the GSA-resonant mechanism, while the much weaker phonon-annihilation process would be the ESA-resonant mechanism. The near match between the highest ESA transition and lowest GSA transition shows up

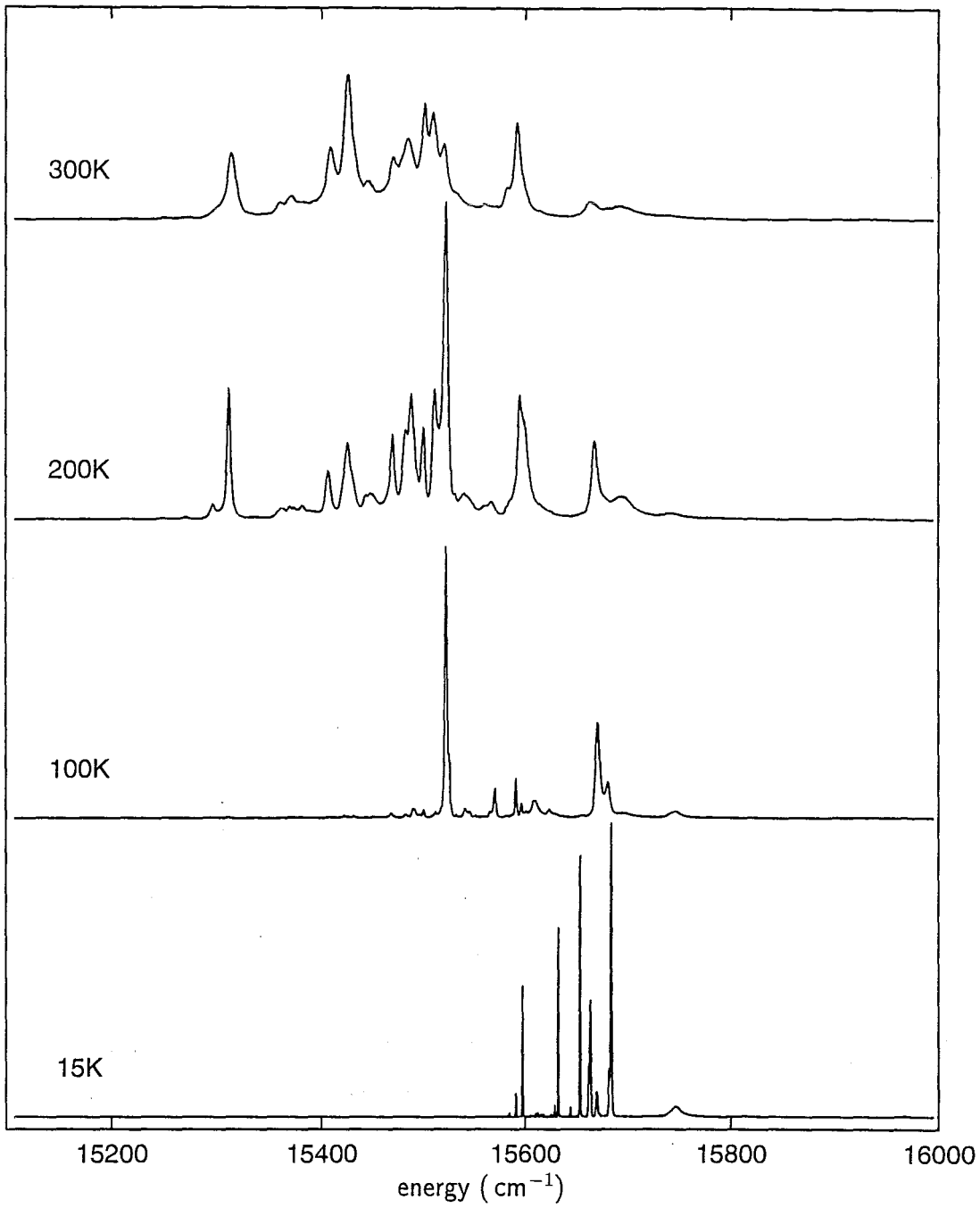

Figure 5.24 : Temperature dependence of the broadband red-to-green upconversion-excitation spectrum of CaF_2:0.01%Ho^{3+}, monitoring broadband green fluorescence at 540 nm. The intensities have not been adjusted.

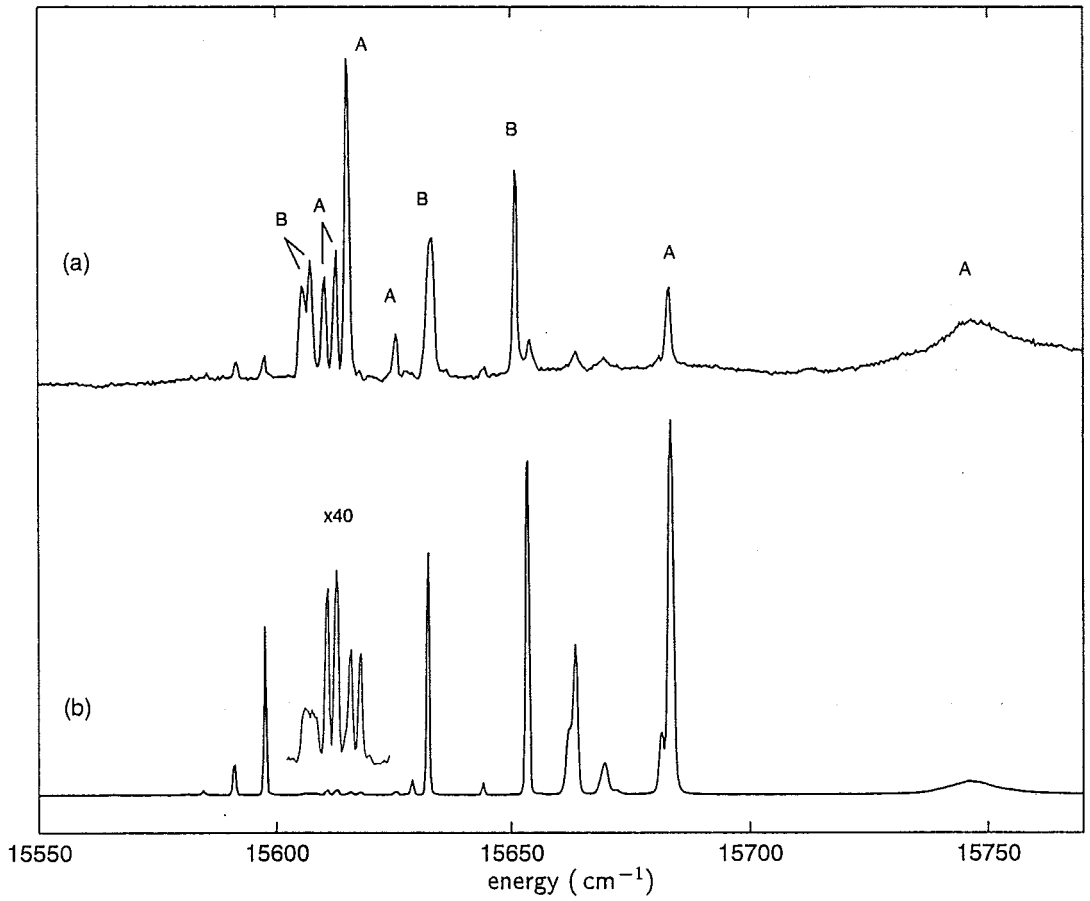

Figure 5.25 : Excitation spectrum of CaF_2:0.01%Ho^{3+} at 15 K, (a) monitoring red fluorescence at 640 nm, and (b) monitoring green upconversion-fluorescence at 540 nm. A and B indicate lines assigned by Mujaji [64] to the C_{4v} and C_{3v} centres, respectively.

as a large peak at 15600 cm^{-1} in the high temperature spectra of figure 5.24 as these two transitions broaden and overlap.

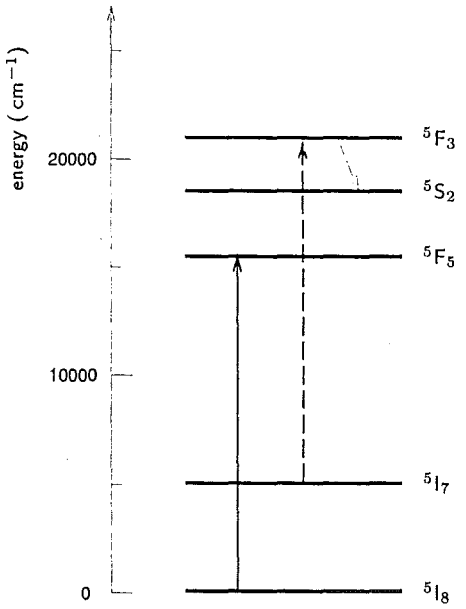

Figure 5.26 : Red-to-green sequential-absorption upconversion mechanism for CaF_2:Ho^{3+}. At 15 K, the dominant mechanism is for the laser to be resonant with a GSA transition.

For the C_{4v} centre, one of the ESA transitions is predicted to be at higher energy than the lowest GSA transition at 15 K. The $Y_1 \rightarrow F_5$ transition should have an energy of 15668 cm^{-1}. A weak line is seen here in spectrum (b) of figure 5.25, although it also matches a weak unassigned transition in spectrum (a), making its assignment uncertain.

At higher temperatures, upconversion for pumping ESA transitions are expected with the phonon-annihilation processes becoming favourable, and lower-energy GSA transitions appearing due to thermal population of the ground-multiplet levels. This would then be consistent with the findings of Zhang *et al* [94] at 77 K. Nevertheless, the two strong new transitions at 15523 cm^{-1} and 15669 cm^{-1} in the upconversion-excitation spectrum at 100 K correspond to GSA transitions from the thermally populated Z_3 level of the C_{4v} centre, rather than to ESA transitions.

5.5 Upconversion in CaF_2:Nd^{3+}

Han *et al* [33] found that pumping the $^4I_{9/2} \rightarrow (^4G_{5/2}, ^2G_{7/2})$ GSA transitions of CaF_2:0.05%Nd^{3+} produced upconversion fluorescence from the $^4D_{3/2}$ and $^2P_{3/2}$ multiplets, while pumping the $^4I_{9/2} \rightarrow {}^2H_{11/2}$ GSA transitions gave no measurable upconversion. In addition, a very weak upconversion-excitation feature [32] was observed corresponding to the $^4F_{3/2} \rightarrow {}^4D_{3/2}$ ESA transition. This observation, together with the lack of observed upconversion fluorescence upon pulsed excitation, suggested that the upconversion mechanism was a sequential-absorption process.

The observation of upconversion upon pumping either GSA or ESA transitions with a rhodamine 6G dye laser was confirmed here. Figure 5.27 is the upconversion-excitation spectrum of the $^4F_{3/2} \rightarrow {}^4D_{3/2}$ ESA transition in CaF_2:0.01%Nd^{3+}, obtained here with a higher signal-to-noise ratio than previously seen [32]. The laser pump power was 250 mW. The upconversion mechanism, illustrated in figure 5.28(a),

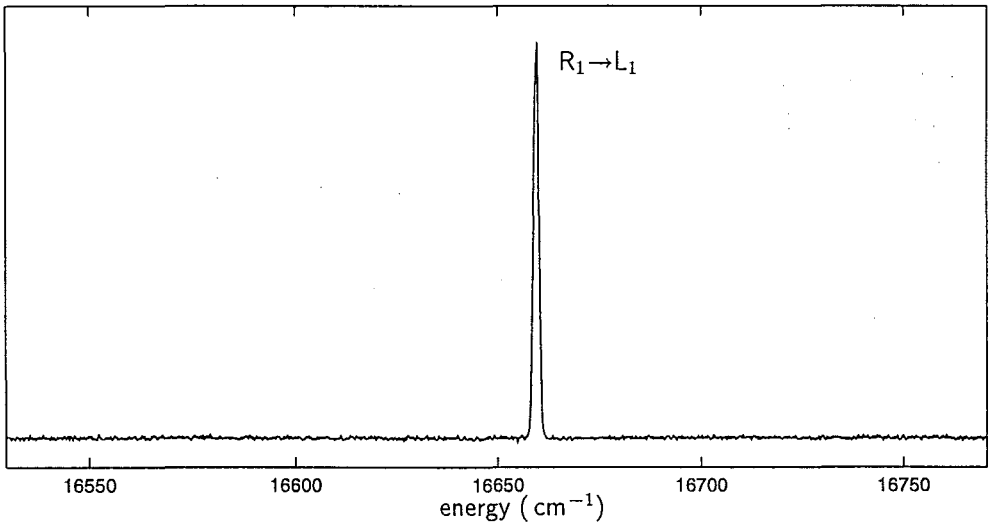

Figure 5.27 : Upconversion-excitation spectrum of the $^4F_{3/2} \rightarrow {}^4D_{3/2}$ ESA transition in CaF_2:0.01%Nd^{3+}, monitoring upconverted $^4D_{3/2} \rightarrow {}^4I_{13/2}$ fluorescence at 24150 cm^{-1}.

shows how both sets of excitation lines are observed. The $^4I_{9/2} \rightarrow {}^2H_{11/2}$ GSA transitions are at higher energy than the $^4F_{3/2} \rightarrow {}^4D_{3/2}$ ESA transition, so pumping these would be expected to produce upconversion fluorescence. Pumping the ESA tran-

sitions at lower energy would normally be very much less efficient. However, in this case, another multiplet exists just below this region. The highest levels of the $^2H_{11/2}$ multiplet are only 400 cm^{-1} lower than the ESA transition, and the upconversion can therefore proceed by a single phonon-creation process.

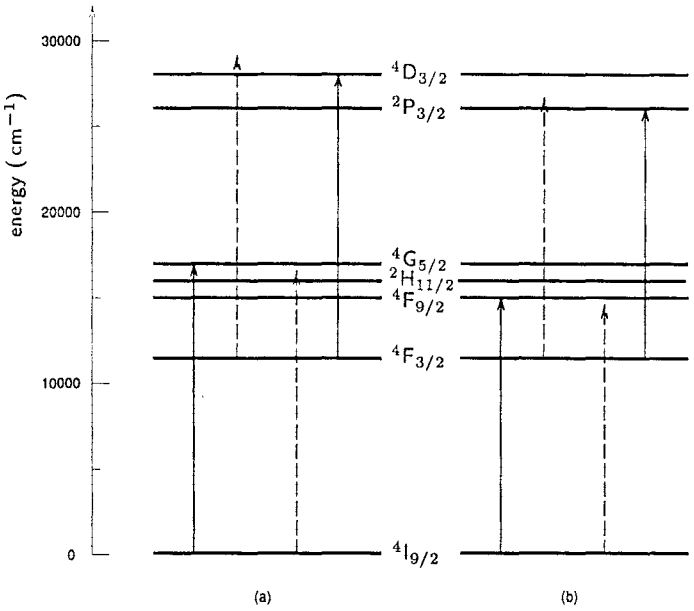

Figure 5.28 : SAU upconversion mechanisms observed for CaF_2:Nd^{3+}. (a) Pumping with rhodamine 6G dye, and (b) pumping with rhodamine 640 dye.

In figure 5.29, as the temperature is increased from 15 K the ESA upconversion increases sharply until about 50 K, and then drops away. At the peak, the upconversion is a factor of 4 greater than at 15 K. The shape of the temperature-dependence curve is most likely due to increased phonon creation which would give rise to stronger phonon-coupling to the off-resonant electronic transition, but also to increased non-radiative decay processes. Competition between these two effects would change with the sample temperature, giving a qualitative explanation for the observed curve.

Upconversion has also been observed here upon pumping with rhodamine 640 dye. The upconversion-excitation spectrum for CaF_2:0.01%Nd^{3+} is shown in figure 5.30 for temperatures of 15, 50 and 100 K. At 15 K, only the $^4I_{9/2} \rightarrow {}^4F_{9/2}$ GSA transitions are seen, while at 100 K new transitions at lower energy are seen. These new transitions do not match the expected GSA transitions from thermally-populated

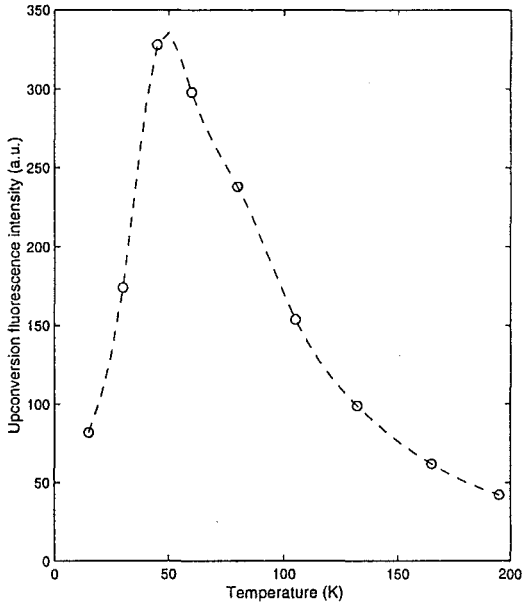

Figure 5.29 : Temperature dependence of ESA upconversion in CaF_2:0.01%Nd^{3+}, pumping the $^4F_{3/2} \rightarrow {}^4D_{3/2}$ transition at 16659 cm^{-1} and monitoring broadband upconversion fluorescence.

ground-multiplet states, but could be the $^4F_{3/2} \rightarrow {}^2P_{3/2}$ ESA transitions. The lower of these two lines matches the $R_1 \rightarrow K_1$ transition energy from the energy level scheme of Han *et al* [33]. The K_2 level had not been found and could be the second new transition seen at 100 K.

The appearance of these two lines at elevated temperatures is expected. The GSA transitions are at slightly higher energy, so that when pumping these the ESA transitions can be bridged by phonon creation. At higher temperatures, the phonon-annihilation process increases, giving the ESA upconversion.

5.6 Sequential-Absorption Processes for Other Rare-Earth Ions in CaF_2

Upconversion in CaF_2:Eu^{3+}

A study of SAU upconversion processes in CaF_2:Eu^{3+}, SrF_2:Eu^{3+} and BaF_2:Eu^{3+} has been carried out by Wells and Reeves [90]. The lifetime of the $^5D_0$ state for the predominant single ion centre in these hosts is 11.8 ms, 13.4 ms and 14.6 ms, respectively, giving a long-lived intermediate state. A high density of electronic states around 35000 cm^{-1}, double the $^5D_0$ multiplet energy, provides a high probability of sequential absorption. Upconversion upon pumping both GSA and ESA transitions were observed in all three hosts. The GSA upconversion was found to increase with temperature, to a maximum at 80 K. In addition, warming the crystal to around 200 K populates the $^5D_1$ states allowing GSA upconversion upon pumping the $^5D_1 \rightarrow {}^7F_0$ transitions.

Universality of Sequential-Absorption in Rare-Earth Ions

The results described in this chapter indicate that sequential-absorption may be a universal phenomenon amongst the lanthanide ions, requiring only a reasonably long-lived intermediate state and a pair of GSA and ESA transitions within several hundred cm^{-1} of each other. Many such instances can be identified by inspection of the energy-multiplet schemes of each of the rare-earths, and only a few have been described in this chapter. Many of course are not accessible at sufficiently high

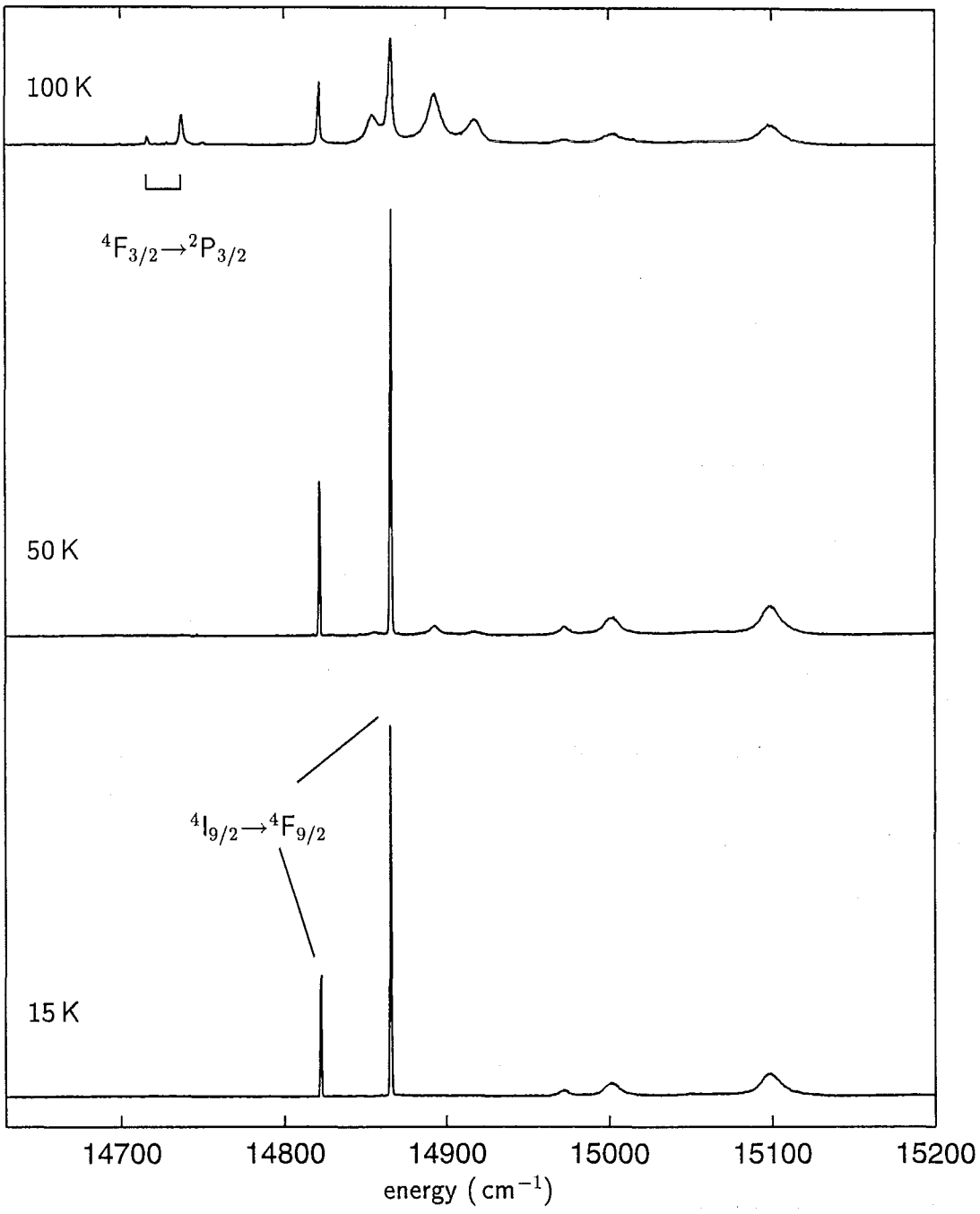

Figure 5.30 : Upconversion-excitation spectrum of the $^4I_{9/2} \rightarrow {}^4F_{9/2}$ GSA and proposed $^4F_{3/2} \rightarrow {}^2P_{3/2}$ ESA transitions of the C_{4v} centre of CaF_2:0.01%Nd^{3+} at 15 K, 50 K and 100 K.

pump powers by currently-available tunable lasers, and there are also some instances where high energy states are almost certainly populated by sequential absorption, but then decay non-radiatively.

The observed yellow-to-blue upconversion in CaF_2:Pr^{3+} [54, 77] has been determined to be due to an energy-transfer process, rather than sequential absorption. This is reasonable since the main candidates for metastable intermediate states, $^1D_2$ and $^1G_4$, do not have matching upper states at the appropriate energy for an ESA process, for the pump laser near 17000 cm^{-1}. However, it may be possible to obtain sequential-absorption upconversion upon pumping in the region of the $^1G_4$ multiplet, with this multiplet acting as the intermediate state, since the $^3P_0$ multiplet lies at slightly more than double the $^1G_4$ energy. This pumping region should be accessible with the long-wavelength optics of the Ti:sapphire laser.

CaF_2:Sm^{3+} has a favourable intermediate multiplet, $^4G_{5/2}$, with a lifetime of 10.4 ms for the C_{4v} centre [88]. Like CaF_2:Eu^{3+}, it also has a high density of electronic states at twice the energy of this multiplet. However, despite an exhaustive search, no measurable upconversion fluorescence was observed upon pumping at, or around the $^4G_{5/2}$ multiplet energies [88]. It is believed that sequential absorption does take place in this system, but that any upconverted fluorescence has been quenched by non-radiative relaxation processes back down to the $^4G_{5/2}$ multiplet.

Tb^{3+} and Dy^{3+} both also have long-lived intermediate states, $^5D_4$ and $^4F_{9/2}$ respectively. However, these both require pumping in the blue region. Blue dye lasers have lower power output than their yellow–red counterparts, making a search for upconversion in these systems difficult. In addition, Dy^{3+} may suffer from a similar problem to Sm^{3+} with low quantum efficiencies for the higher states. The $^5D_3$ higher multiplet of Tb^{3+}, on the other hand, should be a strong emitting state. Violet upconversion fluorescence was seen from CaF_2:0.01%Tb^{3+} at room temperature upon pumping with the 488.0 nm line of an argon-ion laser. However, without a sufficiently high-powered tunable laser source, it has not yet been determined whether this was from a single-ion centre or a cluster, nor what mechanism was involved.

5.7 Summary of Sequential-Absorption Upconversion Processes in CaF_2:RE^{3+}

It has been demonstrated that sequential-absorption upconversion (SAU) processes pumped by a single, moderately high-powered ($\sim$ 100 mW), laser are unexpectedly common for rare-earth ions doped into CaF_2 at concentrations of around 0.01%. The requirements for SAU to proceed are the existence of a pair of ground-state absorption (GSA) and excited-state absorption (ESA) transitions within several hundred cm^{-1} of each other, with the lower state of the ESA transition being a metastable state which becomes populated by radiative or non-radiative decay following the GSA transition. With these conditions met, and the laser tuned to the higher energy of the GSA and ESA transitions, the phonon-sidebands of the other (GSA or ESA) transition are also pumped, giving the possibility of sequential absorption.

Also unexpected was the discovery that many of the SAU processes investigated had upconversion efficiencies which remained constant, or increased by up to two orders of magnitude, when the sample was raised from 15 K to room temperature.

A number of SAU processes have been identified for pumping with infrared, red or yellow tunable lasers. In CaF_2:0.01%Er^{3+}, red-to-green upconversion fluorescence at 540 nm has been observed upon pumping either the $^4I_{15/2}\rightarrow{}^4F_{9/2}$ GSA transitions or the $^4I_{13/2}\rightarrow{}^4F_{5/2}$ ESA transitions of the C_{4v} centre, near 650 nm. The latter, ESA, set of excitation transitions have not previously been reported and produce upconversion fluorescence with an order of magnitude greater efficiency than the former, GSA, set of excitation transitions. When the sample temperature was raised to room temperature, the ESA set of excitation transitions broadened, but maintained their peak intensities.

Also in CaF_2:0.01%Er^{3+}, infrared-to-green upconversion fluorescence at 540 nm has been observed for the C_{4v} and C_{3v} single-ion centres and the "C" cluster centre identified by Tallant and Wright [85]. For the dominant C_{4v} centre the strongest upconversion-excitation transitions were found to be for pumping the $^4I_{15/2}\rightarrow{}^4I_{9/2}$ GSA transitions, while pumping $^4I_{13/2}\rightarrow{}^2H_{11/2}$ or $^4I_{11/2}\rightarrow{}^4F_{3/2}$ ESA transitions also produced upconversion at 15 K. As the sample was heated, one of the GSA-pumped upconversion-excitation lines increased by a factor of 8 before decreasing a little at

room-temperature. A new transition appeared adjacent to this line which could be due to another ESA transition, $^4I_{9/2} \rightarrow {}^2H_{9/2}$. The proximity of the energy of this broad ESA transition to the lowest energy GSA transitions provides some overlap of the two transitions for the enhanced upconversion efficiency at elevated temperatures.

For both the C_{4v} and C_{3v} centres in CaF_2:0.02%Tm^{3+}, 480 nm upconversion fluorescence from the $^1G_4$ multiplet was observed upon pumping the $^3F_4 \rightarrow {}^1G_4$ ESA transitions near 650 nm and 350 nm and 450 nm upconversion fluorescence from the $^1D_2$ multiplet was observed upon pumping the $^3H_4 \rightarrow {}^1D_2$ ESA transitions, also near 650 nm . The red-to-blue upconversion fluorescence from the $^1G_4$ multiplet of the C_{4v} centre was observed to increase by two orders of magnitude when the sample was heated to room temperature. This unusual effect was due to a GSA transition being only 20 cm^{-1} less in energy than the ESA transition being pumped. When the sample was heated, this GSA transition broadened, overlapping the pump-transition energy. Directly pumping two electronic transitions gave a huge increase in efficiency over relying on phonon sidebands to bridge one of the transitions. The red-to-violet/UV upconversion fluorescence from the $^1D_2$ multiplet was observed to increase by a factor of 2.4 upon heating to 60 K, but peaked at 60 K and decreased at higher temperatures. For the C_{3v} centre, all the observed upconversion transitions decreased when the temperature was increased from 15 K.

New upconversion-excitation transitions were observed in CaF_2:0.05%Tm^{3+} after deuteration treatment. The strongest of these gave upconversion fluorescence from the $^1D_2$ multiplet, indicating that the $^3H_4$ multiplet was the intermediate state in the SAU, and polarisation dependence of the fluorescence showed that this new centre had C_{4v} symmetry. The indications are that the centre is the D^--compensated C_{4v} centre known to exist in the crystal (section refcftD). This result was unexpected, since the lifetime of the $^3H_4$ multiplet in this centre would be strongly reduced by non-radiative processes involving D^- local-mode phonons. However, it is proposed that these local-mode phonons aid the cause by providing strong sidebands for the GSA transition.

Infrared-to-blue upconversion fluorescence from the $^1G_4$ multiplet was observed for the C_{3v} centre in CaF_2:0.02%Tm^{3+} upon pumping the $^3H_5 \rightarrow {}^1G_4$ ESA transitions

around 780 nm. Similar upconversion fluorescence was not observed for the C_{4v} centre, proposed to be because of the absence of strong $^3H_5 \rightarrow {}^1G_4$ transitions for this centre.

Red-to-green upconversion fluorescence at 540 nm was observed in CaF_2:0.01%Ho^{3+} for pumping around 640 nm. At 15 K, most of the observed upconversion-excitation lines could be assigned to GSA transitions of the C_{4v} and C_{3v} centres reported by Mujaji *et al* [64]. When the sample was heated to room temperature, the transitions observed at 15 K decreased in intensity, and new transitions appeared for pumping at lower energies. Some of these correspond to the $^5I_7 \rightarrow {}^5F_3$ ESA transitions reported by Zhang *et al* [94] at 77 K, while others could be assigned to GSA transitions from thermally populated levels of the ground multiplet. The overall peak upconversion intensity remained approximately constant between 15 K and room temperature.

CaF_2:0.01%Nd^{3+} gave upconversion fluorescence upon being pumped either around 590 nm or around 670 nm. Both mechanisms involved the $^4F_{3/2}$ intermediate state. As previously reported by Han *et al* [33], upconversion fluorescence was observed from the $^4D_{3/2}$ multiplet at 28000 cm^{-1} when either the $^4I_{9/2} \rightarrow ({}^4G_{5/2}, {}^4G_{7/2})$ GSA transitions or the $^4F_{3/2} \rightarrow {}^4I_{9/2}$ ESA transition were pumped. The ESA-pumped upconversion fluorescence increased by a factor of four when the sample temperature was raised to 50 K, but then decreased again beyond this. Upconversion fluorescence from the $^2P_{3/2}$ multiplet was observed at 15 K upon pumping the $^4I_{9/2} \rightarrow {}^4F_{9/2}$ GSA transitions near 670 nm. No upconversion-excitation lines were observed corresponding to the $^4F_{3/2} \rightarrow {}^2P_{3/2}$ transitions at 15 K, but two lines which match these transition energies appeared when the sample was warmed to 100 K.

When pumping sequential-absorption upconversion with a single pump laser, one or other of the GSA and ESA transitions must be chosen to tune the laser to. In each of the cases studied here, there was a clear preference for choosing one of these two at temperatures around 15 K. In general, more efficient upconversion was achieved when the higher in energy of the two was chosen. This is readily explained by considering the means for pumping the other, off-resonance transition. When the higher-energy transition is pumped, then the lower transition can be bridged by exothermic phonon-creation processes which are always available, even when approaching zero temperature. On the other hand if the lower-energy transition were to

be pumped, then the laser energy is at lower energy than the non-resonant transition and would require phonon-annihilation processes to proceed. The probabilities for these endothermic processes become vanishingly small near zero temperature. The upconversion efficiencies of each of the systems studied here have been accounted for qualitatively by this explanation.

Chapter 6

H^- Local Modes in Hydrogenated RE^{3+}-doped CaF_2 and SrF_2

H^- ions introduced into the CaF_2 or SrF_2 lattice might either substitute for the F^- ions or enter into interstitial positions in vacant F^- cubes [27]. For undoped crystals an H^- ion in an interstitial site would be left with a charge imbalance; these sites have not been observed in pure CaF_2 or SrF_2. Instead, it is observed that the H^- ions substitute solely into lattice F^- sites. If the H^- ion is well isolated from other impurities then this substitutional site will have four neighbouring Ca^{2+} or Sr^{2+} ions

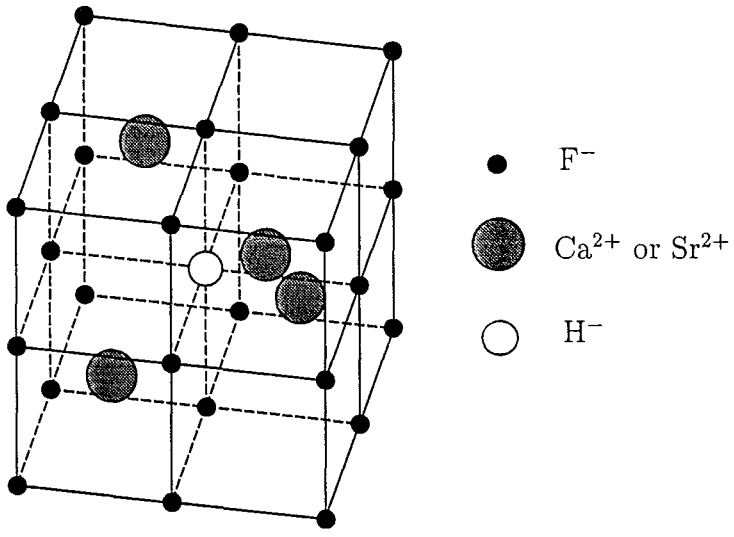

Figure 6.1 : The T_d symmetry substitutional H^- ion site in CaF_2 and SrF_2. Atomic sizes are not represented to scale.

providing the tetrahedral T_d symmetry environment of fig 6.1.

In samples which have been doped with a trivalent rare-earth ion, the H^- ions can provide remote or local charge compensation for the rare-earth ion, as an alternative to the usual charge compensation by F^- ions. One form of charge compensation is for the H^- ion to adopt the interstitial position in a (100) neighbouring cube as in fig 6.2 [44, 24], thus forming a tetragonal C_{4v} symmetry centre analogous to the F^- compensated C_{4v} centre. Remote charge compensation can also take place, producing essentially isolated interstitial H^- ions in cubic O_h symmetry sites.

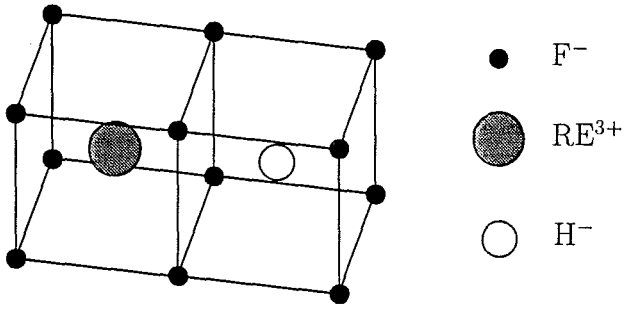

Figure 6.2 : The C_{4v} symmetry H^- compensated RE^{3+} centre in CaF_2 and SrF_2. Atomic sizes are not represented to scale.

For low RE^{3+} concentrations ($< 0.1\%$) the T_d centre is the predominant H^- centre present, while for CaF_2, and in the early part of the RE^{3+} series for SrF_2, the H^- C_{4v} centre is the predominant RE^{3+}-H^- centre formed.

6.1 Local Modes of H^- in CaF_2

Located in the CaF_2 or SrF_2 lattice, the H^- ion experiences approximately the same interionic forces as do the constituent ions of the lattice. However, being much lighter than any of the lattice ions, the H^- ions have much higher vibrational frequencies than the ions of the host lattice. As these high frequency vibrations cannot be propagated by the lattice, they form localised modes about the H^- ion sites.

The H^- vibrational modes in CaF_2 and SrF_2 are seen as sharp infrared absorption

lines in the region of 950–1150 cm^{-1} for CaF_2 and 850–1000 cm^{-1} for SrF_2, with energies depending on the H^--ion site. Elliott *et al* [27] measured the vibration of the H^- ion in the predominant T_d-symmetry site at 20 K as 965 cm^{-1} in CaF_2 and 893 cm^{-1} in SrF_2. The H^- ions in sites associated with rare-earth ions, such as the C_{4v}-symmetry centre, will have energies dependent on the particular rare-earth ion present. The vibrational modes of the H^- ion in the C_{4v} centres have been measured for almost all of the lanthanides in CaF_2 by Jones *et al* [44] and in SrF_2 by Edgar *et al* [24]. The modes for these C_{4v} sites are split into two absorption lines associated with a doubly-degenerate transverse (x-y) vibration and a non-degenerate longitudinal (z) vibration. The infrared-absorption spectrum of CaF_2:0.01%Dy^{3+} hydrogenated for 1.5 hours is shown as an example in figure 6.3. The T_d centre is the dominant H^- centre at this concentration of Dy^{3+}, and the associated absorption line is totally absorbing, with several sidelines due to perturbations of this centre. The two C_{4v}-site absorption lines are the only strong lines at this concentration of Dy^{3+} and H^- which are RE^{3+} dependent.

In the approximation of a single particle moving under a harmonic-oscillator poten-

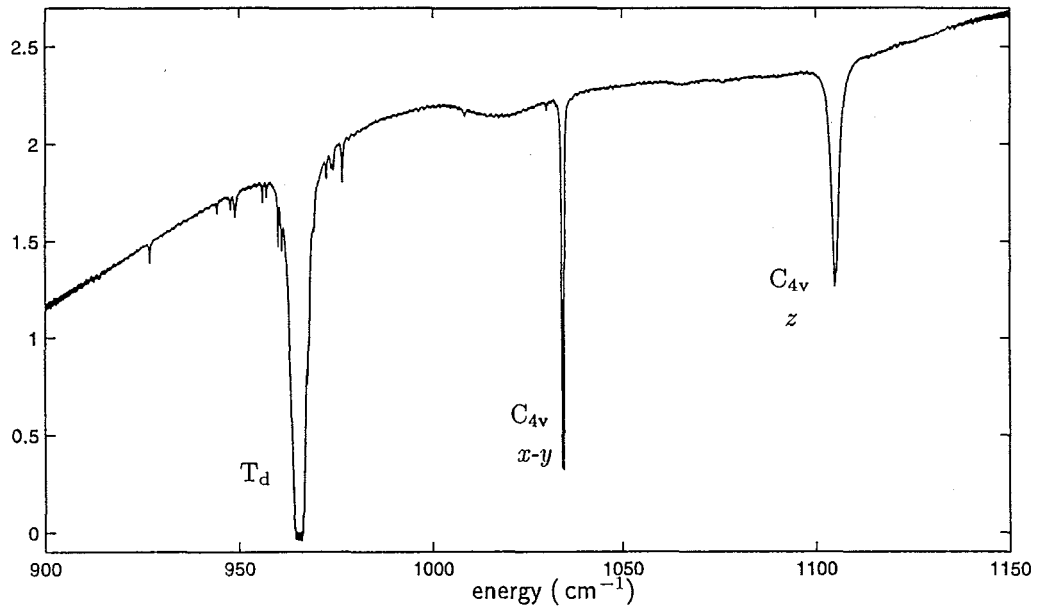

Figure 6.3 : Infrared-absorption spectrum of the H^- vibrational modes in CaF_2:0.01%Dy^{3+}:H^-(1.5 hrs). Absorption lines of the T_d and C_{4v} centres are labelled.

tial, the local-mode vibrations have a $\frac{1}{\sqrt{m}}$ dependence on the mass m of the vibrating particle. Elliott *et al* [27] have found the ratio of the fundamental vibrational frequency for H^- and D^- ions in the T_d site in CaF_2 to be 1.39, only a small deviation from $\sqrt{2}$. Since the harmonic-oscillator potentials of the two sites are expected to be very similar and anharmonic shifts of these vibrational modes are expected to be small, this justifies treating the H^- ion as a single particle moving in a harmonic-oscillator potential well of the almost static neighbouring ions of the host crystal lattice.

The potential-energy term V of a three-dimensional anharmonic oscillator Hamiltonian can be expanded as a power series in the normal coordinates, $x_i (i = 1, 2, 3)$, of the particle; to terms quartic in these coordinates the potential energy is:

$$V = \sum_{i,j} A_{ij} x_i x_j + \sum_{i,j,k} B_{ijk} x_i x_j x_k + \sum_{i,j,k,l} C_{ijkl} x_i x_j x_k x_l$$

For the single-particle local modes of the H^- ion in CaF_2, the normal coordinates are simply x, y and z, the displacements of the ion from its equilibrium position. The exact form of V will depend on the point symmetry at the H^- site, with each term necessarily transforming as the totally symmetric irrep of the H^- site point group (see section 2.3. The potential for T_d symmetry has the form:

$$V = A(x^2 + y^2 + z^2) + Bxyz + C_1(x^4 + y^4 + z^4) + C_2(x^2y^2 + y^2z^2 + z^2x^2)$$

and for C_{4v} symmetry:

$$V = A(x^2+y^2)+Bz^2+Cz^3+Dz(x^2+y^2)+F(x^4+y^4)+Gz^4+Hz^2(x^2+y^2)+Kx^2y^2$$

The work reported in this and the following chapter is concerned primarily with the C_{4v} symmetry H^- centres.

The quadratic terms alone would represent a harmonic-oscillator potential. As these terms are the largest, the H^- ion vibrational wavefunctions and energies are derived from those of a harmonic oscillator, with the higher order anharmonic terms being treated as perturbations.

6.1.1 The Harmonic-Oscillator Approximation

For a vibrating particle of mass m, the coefficients of the second degree terms in the C_{4v} local-mode Hamiltonian are $A = \frac{1}{2}m\omega_x^2$ and $B = \frac{1}{2}m\omega_z^2$ where ω_x and ω_z

are the angular frequencies of the fundamental vibrational modes of the particle, respectively perpendicular (x, y) and parallel (z) to the C_{4v} symmetry axis.

The x, y and z phonon-coordinate operators can be written in terms of the phonon creation and annihilation operators $a^\dagger$ and a:

$$\begin{aligned} x &= \alpha(a_x^\dagger + a_x) \\ y &= \alpha(a_y^\dagger + a_y) \\ z &= \beta(a_z^\dagger + a_z) \end{aligned}$$

$$\text{where } \alpha = \sqrt{\frac{\hbar}{2m\omega_x}} \text{ and } \beta = \sqrt{\frac{\hbar}{2m\omega_z}}.$$

Values of α and β can be estimated from the respective energies of the x-y and z local-modes for each RE^{3+} [44, 24] and are listed in table 6.1.

RE	CaF_2		SrF_2	
	$\alpha\,(\times 10^{-11}\,\mathrm{m})$	$\beta\,(\times 10^{-11}\,\mathrm{m})$	$\alpha\,(\times 10^{-11}\,\mathrm{m})$	$\beta\,(\times 10^{-11}\,\mathrm{m})$
Ce^{3+}	1.300	1.216	1.350	1.323
Pr^{3+}	1.295	1.224	1.347	1.335
Nd^{3+}	1.292	1.222	1.343	1.333
Sm^{3+}	1.285	1.223	1.336	1.336
Gd^{3+}	1.282	1.230	1.334	1.349
Tb^{3+}	1.274	1.225	1.328	1.350
Dy^{3+}	1.272	1.231	1.328	
Ho^{3+}	1.270	1.235	1.329	
Er^{3+}	1.270	1.242		
Tm^{3+}	1.266	1.240		
Yb^{3+}	1.263			

Table 6.1 : Values of α and β for CaF_2:RE^{3+}:H^- and SrF_2:RE^{3+}:H^-

The states of the three-dimensional harmonic oscillator are product states of the three one-dimensional harmonic oscillators $|n_x n_y n_z\rangle = |n_x\rangle|n_y\rangle|n_z\rangle$, where the n_i are the respective phonon-occupation numbers. Each one-dimensional oscillator is

acted upon independently by its own creation and annihilation operators, $a^\dagger$ and a, defined for $i = x, y, z$ by

$$\begin{aligned} a_i^\dagger |n_i\rangle &= \sqrt{n_i + 1}\, |n_i + 1\rangle \\ a_i |n_i\rangle &= \sqrt{n_i}\, |n_i - 1\rangle \end{aligned}$$

The energy eigenvalues of the three-dimensional oscillator in the harmonic approximation are

$$E_{|n_x n_y n_z\rangle} = (n_x + n_y + 1)\hbar\omega_x + (n_z + \tfrac{1}{2})\hbar\omega_z.$$

The corresponding eigenfunctions need to be chosen as appropriate linear combinations of the $|n_x n_y n_z\rangle$ wavefunctions which transform as irreps of the point group, in this case C_{4v}. Such combinations up to $n = n_x + n_y + n_z = 2$, with their C_{4v} irreps and energies, are given in table 6.2.

wavefunction	C_{4v} irrep	energy
$\|000\rangle$	γ_1	0
$\frac{1}{\sqrt{2}}(\,\|100\rangle \pm i\|010\rangle\,)$	$\gamma_5{}^{\pm}$	$\hbar\omega_x$
$\|001\rangle$	γ_1	$\hbar\omega_z$
$\frac{1}{\sqrt{2}}(\,\|200\rangle + \|020\rangle\,)$	γ_1	$2\hbar\omega_x$
$\frac{1}{\sqrt{2}}(\,\|200\rangle - \|020\rangle\,)$	γ_3	$2\hbar\omega_x$
$\|110\rangle$	γ_4	$2\hbar\omega_x$
$\frac{1}{\sqrt{2}}(\,\|101\rangle \pm i\|011\rangle\,)$	$\gamma_5{}^{\pm}$	$\hbar(\omega_x + \omega_z)$
$\|002\rangle$	γ_1	$2\hbar\omega_z$

Table 6.2 : C_{4v} harmonic oscillator wavefunctions

By comparing the classical harmonic oscillator energy $E = \frac{1}{2}m\omega^2 x^2$ and the quantum-mechanical harmonic oscillator energies $E = (n + \frac{1}{2})\hbar\omega$, we can estimate the amplitude of vibration of an H^- ion at the fundamental frequency ($\omega \approx 1000\,\mathrm{cm}^{-1}$) to be $x = \sqrt{\frac{2\hbar}{m\omega}} = 2.6{\times}10^{-11}$ m, or approximately 10% of the RE^{3+}–H^- separation.

6.1.2 Effect of Anharmonic Terms

The higher degree (anharmonic) terms in the Hamiltonian are treated using standard perturbation theory. The third degree (cubic) terms give no first order contribution,

but do have second order contributions, whereas the fourth degree (quartic) terms do contribute first order effects. These two effects are of similar magnitude and must both be considered.

The perturbations have the effect of shifting the energies of the harmonic-oscillator wavefunctions $|n_x n_y n_z\rangle$ and mixing wavefunctions belonging to the same C_{4v} irrep. Thus the three degenerate $|n_x + n_y = 2, n_z = 0\rangle$ second harmonic levels, which have zero-order energy $2\hbar\omega_x$ and irreps γ_1, γ_3 and γ_4, will be split apart by the order of $10\,\mathrm{cm}^{-1}$. However, only the γ_1 level will be observable since the electric dipole selection rules (section 2.3) allow only γ_1 and γ_5 levels to be observed by absorption from the γ_1 ground state.

In addition, since the electric-dipole operator is a rank 1 tensor operator, only $\Delta n = 1$ (fundamental) transitions should be observed. In this case, however, the second order mixing of states of different n makes transitions to higher harmonics weakly allowed.

The original listing of the perturbed energies and eigenfunctions of the C_{4v} anharmonic oscillator by Maradudin and Peretti [60] contains some errors; the corrected perturbed wavefunctions and energies have been listed by Reeves [75]. In the following we deal only with the $n = 1$ fundamental vibrations, and the zero-order harmonic-oscillator wavefunctions (100), (010) and (001) are an adequate approximation.

6.2 Interaction with Electronic States of a Neighbouring RE^{3+} Ion

Thus far, the RE^{3+} electronic and H^- vibrational systems have been treated separately. However combined vibronic transitions, in which both systems undergo a transition, can interact with a single photon. For these it becomes necessary to consider coupling between these systems. In the Born-Oppenheimer approximation, the electronic motion is considered to be much faster than the vibrational motion so that the electronic state of the RE^{3+} is determined by the crystal field due to the instantaneous location of the vibrating ion(s). Thus the displacement from equilibrium of the H^- ion necessitates an adjustment to the crystal field Hamiltonian of

the RE^{3+}; the difference between the static crystal field and the new dynamic field is known as the electron–local-mode-phonon interaction (henceforth often referred to simply as the electron-phonon interaction), V_{ep}. In this approximation, the zero-order coupled vibrational-electronic, or "vibronic", states can then be written as product states, $|\psi\rangle|n_x n_y n_z\rangle$, and the corresponding energies are simply the sum of the two combined energies, as depicted in fig 6.4.

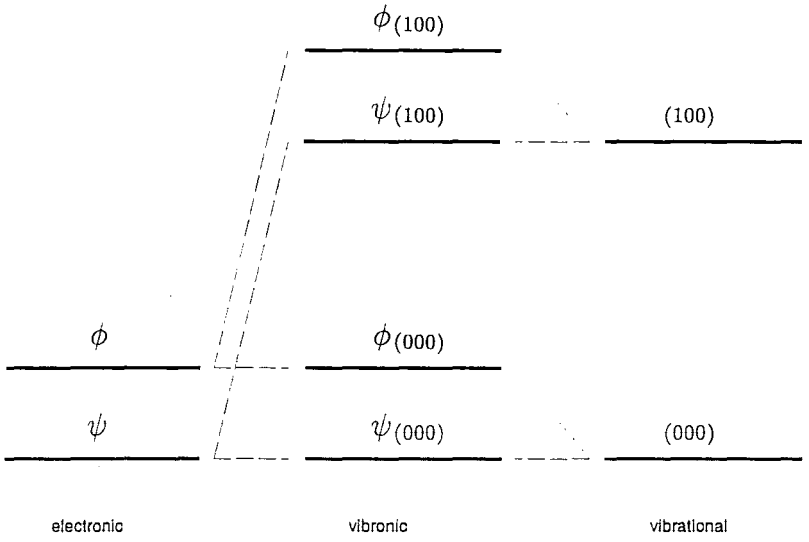

Figure 6.4 : Coupling of vibrational and electronic states

In the cases being studied here we investigate the coupling of the rare-earth electronic ground state with the hydride ion's (100),(010) x-y fundamental vibrational mode. Of particular interest are cases where the RE^{3+} ground state is doubly degenerate, since this will produce four vibronic product states when coupled to the doubly-degenerate x-y vibrational state. The irreps of the product states can be obtained by considering the Kronecker product of the electronic and vibrational state irreps. For C_{4v} symmetry, the possible doublet irreps for the rare-earth electronic states are γ_5 for the even-electron (non-Kramers) ions and γ_6 or γ_7 for the odd-electron (Kramers) ions. Coupled with the γ_5 irrep of the x-y vibrational state, these give the following product state irrep decompositions:

$$\begin{aligned} \gamma_5 \times \gamma_5 &= \gamma_1 + \gamma_2 + \gamma_3 + \gamma_4 \\ \gamma_6 \times \gamma_5 &= \gamma_6 + \gamma_7 \end{aligned}$$

$$\gamma_7 \times \gamma_5 \;=\; \gamma_6 + \gamma_7$$

Thus these x-y vibronic states need not remain degenerate and small splittings of the order of $1\,\mathrm{cm}^{-1}$ may appear, through the electron-phonon interaction, $\mathrm{V_{ep}}$. These splittings were first observed for the Ce^{3+}-H^- and Pr^{3+}-H^- centres in CaF_2 and SrF_2 by Jacobs [39, 40]. The remainder of this chapter, and the following chapter, deal with comparing calculations and measurements of this so-called x-y-splitting and the further shifts and splittings arising upon application of an external magnetic field.

The dynamic crystal-field potential incorporating the vibrational motion of an H^- ion can be written as a Taylor expansion in the H^- ion displacements $[\mathrm{X}_i] = (x', y', z')$:

$$\begin{aligned} \mathrm{V} &= \mathrm{V_o} + \sum_i \frac{\partial \mathrm{V_o}}{\partial \mathrm{X}_i}\,\mathrm{X}_i + \tfrac{1}{2}\sum_{i,j} \frac{\partial^2 \mathrm{V_o}}{\partial \mathrm{X}_i \partial \mathrm{X}_j}\,\mathrm{X}_i \mathrm{X}_j + \ldots \\ &= \mathrm{V_o} + \mathrm{V_{ep}} \end{aligned} \tag{6.1}$$

where $\mathrm{V_o}$ is the static crystal-field potential, given by equation 2.2 for C_{4v} symmetry, and the remaining terms constitute the electron-phonon interaction, $\mathrm{V_{ep}}$.

The differentiation of the static potential with respect to the H^- ion displacements requires the assumption of some sort of model in order to gain the functional form of the B_q^k coefficients of the crystal field. The simplest of these is the point charge model in which the ions are taken to be point charges at their ideal lattice positions; other models include effects due to the non-linear polarisation of the H^- ion and the induced polarisation of the lattice fluorines. In all of these cases, since the electronic wavefunctions are known in JM-basis (spherical harmonic) form, it is convenient to express the potential in terms of spherical harmonics, which makes it advantageous to differentiate with respect to $\mathrm{X}_\pm = \frac{1}{\sqrt{2}}(\mathrm{X} \pm i\mathrm{Y})$ in place of X and Y. This also allows us to determine the zero order coupled wavefunctions more easily by using the C_4 subgroup of C_{4v}, for which $\mathrm{X}_\pm$ are separate irrep bases. Using this basis, the electron-phonon interaction Hamiltonian to second order is:

$$\begin{aligned} \mathrm{V_{ep}} \;=\; & \frac{\partial \mathrm{V_o}}{\partial \mathrm{X}_+}\,\mathrm{X}_+ + \frac{\partial \mathrm{V_o}}{\partial \mathrm{X}_-}\,\mathrm{X}_- + \frac{\partial \mathrm{V_o}}{\partial \mathrm{Z}}\,\mathrm{Z} \\ & + \frac{1}{4}\left(\frac{\partial^2 \mathrm{V_o}}{\partial \mathrm{X}_+^2} + \frac{\partial^2 \mathrm{V_o}}{\partial \mathrm{X}_-^2}\right)\left(\mathrm{X}_+^2 + \mathrm{X}_-^2\right) + \frac{1}{4}\left(\frac{\partial^2 \mathrm{V_o}}{\partial \mathrm{X}_+^2} - \frac{\partial^2 \mathrm{V_o}}{\partial \mathrm{X}_-^2}\right)\left(\mathrm{X}_+^2 - \mathrm{X}_-^2\right) \end{aligned}$$

$$+\frac{\partial^2 V_o}{\partial X_+ \partial X_-}X_+X_- + \frac{1}{2}\frac{\partial^2 V_o}{\partial Z^2}Z^2 + \frac{\partial^2 V_o}{\partial X_+ \partial Z}X_+Z + \frac{\partial^2 V_o}{\partial X_- \partial Z}X_-Z \qquad (6.2)$$

$$= f_-X_+ + f_+X_- + f_zZ + g_{X_+^2+X_-^2}\left(X_+^2 + X_-^2\right) + g_{X_+^2-X_-^2}\left(X_+^2 - X_-^2\right)$$
$$+ g_{[+-]}X_+X_- + g_{Z^2}Z^2 + g_{Z[-]}X_+Z + g_{Z[+]}X_-Z \qquad (6.3)$$

The X_i functions operate on the vibrational part of the wavefunctions, while the f and g functions operate on the electronic part of the wavefunctions. Note that, while the $X_\pm$ notation is more convenient for obtaining the form of the f and g functions, the standard Cartesian coordinates X and Y are more convenient for the vibrational operators. Conversions for the second-degree terms are:

$$\begin{aligned} X_+X_- &= \tfrac{1}{2}\left(X^2 + Y^2\right) \\ X_+^2 + X_-^2 &= X^2 - Y^2 \\ X_+^2 - X_-^2 &= 2iXY \end{aligned}$$

The second-degree terms have been grouped in such a way that the electronic and vibrational parts to each transform as irrep partners of the $C_{\infty v}$ point group of the electron-phonon interaction. The f and g electronic operators must transform as the conjugate irreps to their respective vibrational terms and, in general, can be written as sums of the Racah tensor operators which transform appropriately:

$$f_- = D_1^n C_{-1}^{(n)} \qquad (6.4)$$
$$f_+ = -D_1^n C_1^{(n)} \qquad (6.5)$$
$$f_z = D_0^n C_0^{(n)} \qquad (6.6)$$
$$g_{X_+^2+X_-^2} = E_1^n \left(C_{-2}^{(n)} + C_2^{(n)}\right) \qquad (6.7)$$
$$g_{X_+^2-X_-^2} = E_1^n \left(C_{-2}^{(n)} - C_2^{(n)}\right) \qquad (6.8)$$
$$g_{[+-]} = E_0^n C_0^{(n)} \qquad (6.9)$$
$$g_{Z^2} = F_0^n C_0^{(n)} \qquad (6.10)$$
$$g_{Z[-]} = -F_1^n C_{-1}^{(n)} \qquad (6.11)$$
$$g_{Z[+]} = F_1^n C_1^{(n)} \qquad (6.12)$$

where summations on $n = 2, 4, 6$ are implied.

The D, E and F coefficients would follow by identifying the f and g terms with the derivatives of the crystal-field potential in equation 6.3. However, only the angular

dependence of the static crystal-field Hamiltonian is known, so these derivatives cannot be evaluated without recourse to a model for the form of the radial dependence of the Hamiltonian.

6.3 Estimating Derivatives of the Crystal-Field Potential

6.3.1 Derivatives of the Solid Harmonics

Differentiation of the crystal field potential is most easily facilitated by using solid harmonics defined as:

$$\begin{aligned} \mathrm{R}_m^n(\boldsymbol{r}) &= r^n \mathrm{C}_m^{(n)}(\theta,\phi) && (6.13)\\ &= (-1)^m \sqrt{\tfrac{(n-m)!}{(n+m)!}}\, r^n \mathrm{P}_n^m(\cos\theta) e^{im\phi} && (6.14) \end{aligned}$$

where P_n^m is the associated Legendre polynomial with the conventional phase as defined (for example) in Edmonds [26].

Using this definition, we can differentiate with respect to $\mathrm{X}_\pm = \frac{1}{\sqrt{2}}(x \pm iy)$:

$$\frac{\partial}{\partial \mathrm{X}_\pm} = \frac{1}{\sqrt{2}}\left(\frac{\partial}{\partial x} \mp i\frac{\partial}{\partial y}\right)$$

An outline of the derivation is given in appendix A, with the results:

$$\begin{aligned} \frac{\partial \mathrm{R}_m^n}{\partial \mathrm{X}_\pm} &= \mp\sqrt{\frac{(n\pm m)(n\pm m-1)}{2}}\, \mathrm{R}_{m\mp 1}^{n-1} && (6.15)\\ \frac{\partial \mathrm{R}_m^n}{\partial z} &= \sqrt{(n-m)(n+m)}\, \mathrm{R}_m^{n-1} && (6.16) \end{aligned}$$

and

$$\begin{aligned} \frac{\partial}{\partial \mathrm{X}_\pm}\left(\frac{\mathrm{R}_m^n}{r^{2n+1}}\right) &= \mp\sqrt{\frac{(n\mp m+1)(n\mp m+2)}{2}}\left(\frac{\mathrm{R}_{m\mp 1}^{n+1}}{r^{2n+3}}\right) && (6.17)\\ \frac{\partial}{\partial z}\left(\frac{\mathrm{R}_m^n}{r^{2n+1}}\right) &= -\sqrt{(n-m+1)(n+m+1)}\left(\frac{\mathrm{R}_m^{n+1}}{r^{2n+3}}\right) && (6.18) \end{aligned}$$

Previously, Zdansky *et al* [93] (and subsequently Jacobs *et al* [40, 39], Edgar [23] and Reeves [75]) have defined solid harmonics as:

$$\begin{aligned} \mathrm{T}_{n,x}^m &= r^n \mathrm{P}_n^m(\cos\theta)\cos m\phi \\ \mathrm{T}_{n,y}^m &= r^n \mathrm{P}_n^m(\cos\theta)\sin m\phi && (6.19) \end{aligned}$$

and made use of these to derive relations equivalent to equations (6.15) and (6.16)[1].

6.3.2 A Simple Model—The Point Charge Model

We assume the H^- ion to be a point charge, q, and seek the electrostatic potential energy of the RE^{3+} electron of effective charge σ at coordinates $\boldsymbol{r} = (r, \theta, \phi)$ due to the hydride ion at position $\boldsymbol{r}' = (r', \theta', \phi')$:

$$V(\boldsymbol{r}) = k\frac{q\sigma}{|\boldsymbol{r} - \boldsymbol{r}'|} \tag{6.20}$$

$$= \frac{kq\sigma}{r'}\left(1 - 2\cos\omega\left(\frac{r}{r'}\right) + \left(\frac{r}{r'}\right)^2\right)^{-\frac{1}{2}} \tag{6.21}$$

$$= \frac{kq\sigma}{r'}\sum_{n=0}^{\infty}\left(\frac{r}{r'}\right)^n \mathrm{P}_n(\cos\omega) \tag{6.22}$$

$$= kq\sigma\sum_{n=0}^{\infty}\sum_{m=-n}^{n}\frac{r^n}{(r')^{n+1}}(-1)^m\,\mathrm{C}^{(n)}_{-m}(\theta', \phi')\,\mathrm{C}^{(n)}_{m}(\theta, \phi) \tag{6.23}$$

$$= kq\sigma\sum_{n=0}^{\infty}\sum_{m=-n}^{n}(-1)^m\frac{\mathrm{R}^n_{-m}(\boldsymbol{r}')}{(r')^{2n+1}}\,\mathrm{R}^n_m(\boldsymbol{r}) \tag{6.24}$$

where $k = \frac{1}{4\pi\epsilon}$ and ω is the angle between the vectors $\boldsymbol{r}$ and $\boldsymbol{r}'$. Equation (6.22) has used the generating function for the Legendre polynomials:

$$(1 - 2xh + h^2)^{-1/2} = \sum_{n=0}^{\infty} h^n\,\mathrm{P}_n(x)$$

and equation (6.23) has used the spherical harmonic addition theorem:

$$\mathrm{P}_n(\cos\omega) = \sum_{m=-n}^{n}(-1)^m\,\mathrm{C}^{(n)}_{-m}(\theta', \phi')\,\mathrm{C}^{(n)}_{m}(\theta, \phi)$$

In the form of equation (6.24), the electrostatic potential can be differentiated to any required order with respect to the hydride ion coordinates $\boldsymbol{r}' = (r', \theta', \phi')$ by successive application of equations (6.17) and/or (6.18).

First and second derivatives of the electrostatic potential, with summation on m and n implied, are:

[1]Note, however, that the previous analyses have had an extra phase factor $(-1)^m$ (misprinted as $(-1)^n$ in [93] and [75]) included in the definition of the associated Legendre polynomial, which would introduce a sign change in (6.15), for example, but not in (6.16).

$$\frac{\partial V}{\partial X'_+} = -(-1)^m kq\sigma\sqrt{\tfrac{(n+m+1)(n+m+2)}{2}}\,\frac{R^{n+1}_{-m-1}(\boldsymbol{r}')}{(r')^{2n+3}}\,R^n_m(\boldsymbol{r}) \tag{6.25}$$

$$\frac{\partial V}{\partial X'_-} = (-1)^m kq\sigma\sqrt{\tfrac{(n-m+1)(n-m+2)}{2}}\,\frac{R^{n+1}_{-m+1}(\boldsymbol{r}')}{(r')^{2n+3}}\,R^n_m(\boldsymbol{r}) \tag{6.26}$$

$$\frac{\partial V}{\partial z'} = -(-1)^m kq\sigma\sqrt{(n+m+1)(n-m+1)}\,\frac{R^{n+1}_{-m}(\boldsymbol{r}')}{(r')^{2n+3}}\,R^n_m(\boldsymbol{r}) \tag{6.27}$$

$$\frac{\partial^2 V}{\partial X'^{\,2}_+} = (-1)^m\frac{kq\sigma}{2}\sqrt{\tfrac{(n+m+4)!}{(n+m)!}}\,\frac{R^{n+2}_{-m-2}(\boldsymbol{r}')}{(r')^{2n+5}}\,R^n_m(\boldsymbol{r}) \tag{6.28}$$

$$\frac{\partial^2 V}{\partial X'^{\,2}_-} = (-1)^m\frac{kq\sigma}{2}\sqrt{\tfrac{(n-m+4)!}{(n-m)!}}\,\frac{R^{n+2}_{-m+2}(\boldsymbol{r}')}{(r')^{2n+5}}\,R^n_m(\boldsymbol{r}) \tag{6.29}$$

$$\frac{\partial^2 V}{\partial z'^2} = (-1)^m kq\sigma\sqrt{\tfrac{(n-m+2)!(n+m+2)!}{(n-m)!(n+m)!}}\,\frac{R^{n+2}_{-m}(\boldsymbol{r}')}{(r')^{2n+5}}\,R^n_m(\boldsymbol{r}) \tag{6.30}$$

$$\frac{\partial^2 V}{\partial X'_+\partial X'_-} = -(-1)^m\frac{kq\sigma}{2}\sqrt{\tfrac{(n-m+2)!(n+m+2)!}{(n-m)!(n+m)!}}\,\frac{R^{n+2}_{-m}(\boldsymbol{r}')}{(r')^{2n+5}}\,R^n_m(\boldsymbol{r}) \tag{6.31}$$

$$\frac{\partial^2 V}{\partial X'_+\partial z'} = (-1)^m kq\sigma\sqrt{\tfrac{(n+m+3)!(n-m+1)}{2(n+m)!}}\,\frac{R^{n+2}_{-m-1}(\boldsymbol{r}')}{(r')^{2n+5}}\,R^n_m(\boldsymbol{r}) \tag{6.32}$$

$$\frac{\partial^2 V}{\partial X'_-\partial z'} = -(-1)^m kq\sigma\sqrt{\tfrac{(n-m+3)!(n+m+1)}{2(n-m)!}}\,\frac{R^{n+2}_{-m+1}(\boldsymbol{r}')}{(r')^{2n+5}}\,R^n_m(\boldsymbol{r}) \tag{6.33}$$

The summation on m can be removed if the light ion displacements are assumed to be small. Then the azimuthal angle θ' is very small so that:

$$C^{(n)}_m(\theta',\phi') \approx \begin{cases} 1 \text{ for } m = 0 \\ 0 \text{ for } m \neq 0 \end{cases}$$

Further, since the $C^{(n)}_m(\theta,\phi)$ operators operate within the $4f^N$ electronic configuration, parity considerations require that $n = 2, 4, 6$. The derivatives all have a dependence on $\frac{r^n}{r'^n}$, so that the $n = 2$ terms usually dominate in the point-charge model.

Putting $r' = D$, half the lattice constant of CaF_2 (or SrF_2), and equating the derivatives with the f and g electronic-coordinate operators of equation (6.3) we find:

$$f_- = \sqrt{\tfrac{n(n+1)}{2}}\,\frac{kq\sigma\, r^n}{D^{n+2}}\,C^{(n)}_{-1} \tag{6.34}$$

$$f_+ = -\sqrt{\tfrac{n(n+1)}{2}}\,\frac{kq\sigma\, r^n}{D^{n+2}}\,C^{(n)}_{1} \tag{6.35}$$

$$f_z = -(n+1)\frac{kq\sigma\, r^n}{D^{n+2}} C_0^{(n)} \tag{6.36}$$

$$g_{x_+^2+x_-^2} = \frac{1}{8}\sqrt{\tfrac{(n+2)!}{(n-2)!}}\frac{kq\sigma\, r^n}{D^{n+3}}(C_{-2}^{(n)} + C_2^{(n)}) \tag{6.37}$$

$$g_{x_+^2-x_-^2} = \frac{1}{8}\sqrt{\tfrac{(n+2)!}{(n-2)!}}\frac{kq\sigma\, r^n}{D^{n+3}}(C_{-2}^{(n)} - C_2^{(n)}) \tag{6.38}$$

$$g_{z^2} = \tfrac{1}{2}(n+1)(n+2)\frac{kq\sigma\, r^n}{D^{n+3}} C_0^{(n)} \tag{6.39}$$

$$g_{[+-]} = -\tfrac{1}{2}(n+1)(n+2)\frac{kq\sigma\, r^n}{D^{n+3}} C_0^{(n)} \tag{6.40}$$

$$g_{z[-]} = -(n+2)\sqrt{\tfrac{n(n+1)}{2}}\frac{kq\sigma\, r^n}{D^{n+3}} C_{-1}^{(n)} \tag{6.41}$$

$$g_{z[+]} = (n+2)\sqrt{\tfrac{n(n+1)}{2}}\frac{kq\sigma\, r^n}{D^{n+3}} C_1^{(n)} \tag{6.42}$$

again with summation on n implied. These operators are in the form required by equations 6.4–6.12.

The constants in these electronic-coordinate operators may be evaluated using the lattice constants $2D = 5.46$Å for CaF_2 and $2D = 5.80$Å for SrF_2 [92], and $\langle r^2 \rangle$ shown in table 6.3 in Bohr radii ($a_o = 0.529$Å) as derived by Freeman and Watson [28] from Hartree-Fock calculations. The effective (screened) charges on the RE^{3+} and H^- ions are taken as $q = \sigma = 0.85e$ for CaF_2 and $q = \sigma = 0.96\,e$ for SrF_2, being values found to fit the point-charge model [40, 24]. Matrix elements of the f and g operators can then be calculated as matrix elements of the Racah tensor operators between wavefunctions obtained from static crystal field analyses.

	$\langle r^2 \rangle$ $(a_o{}^2)$	$\langle r^4 \rangle$ $(a_o{}^4)$	$\langle r^6 \rangle$ $(a_o{}^6)$
Ce^{3+}	1.200	3.455	21.226
Pr^{3+}	1.086	2.822	15.726
Nd^{3+}	1.001	2.401	12.396
Sm^{3+}	0.883	1.897	8.775
Eu^{3+}	0.938	2.273	11.670
Gd^{3+}	0.785	1.515	6.281
Dy^{3+}	0.726	1.322	5.102
Er^{3+}	0.666	1.126	3.978
Yb^{3+}	0.613	0.960	3.104

Table 6.3 : Values of $\langle r^2 \rangle$, $\langle r^4 \rangle$ and $\langle r^6 \rangle$, in Bohr radii [28].

6.4 Splitting of the H^- x-y Vibronic Associated with Kramers Ions

The ground state of any Kramers ions in C_{4v} symmetry is either a γ_6 or γ_7 doublet. When either of these is combined with the γ_5 $\frac{1}{\sqrt{2}}[(100) \pm (010)]$ vibrational doublet, they produce a $\gamma_6 + \gamma_7$ pair of vibronic doublets as described in section 6.2. In order to deduce the form of the zero order vibronic wavefunctions, the group-chain decomposition C_{4v}–C_4 may be considered. The decomposition of C_{4v} to C_4 irreps is described in section 2.3, along with multiplication tables and basis functions.

Notation

The electronic states will be denoted by $\psi^{\pm}$ for γ_6 states and $\phi^{\pm}$ for γ_7 states. Their C_4 decompositions and representative basis functions are as in table 6.4.

electronic state	C_{4v}-C_4irreps	basis states
ψ^+	$\gamma_6\mu_5$	$\|\frac{1}{2}\rangle, \|-\frac{7}{2}\rangle$
ψ^-	$\gamma_6\mu_6$	$\|-\frac{1}{2}\rangle, \|\frac{7}{2}\rangle$
ϕ^+	$\gamma_7\mu_7$	$\|-\frac{3}{2}\rangle, \|\frac{5}{2}\rangle$
ϕ^-	$\gamma_7\mu_8$	$\|\frac{3}{2}\rangle, \|-\frac{5}{2}\rangle$

Table 6.4 : Electronic state notation and bases for Kramers ions.

In the harmonic approximation adopted here, the (100) and (010) vibrational states form one possible basis for the x-y vibrational mode of the C_{4v} oscillator. However, for the C_{4v}–C_4 chain decomposition, the appropriate bases are $\frac{1}{\sqrt{2}}[(100) \pm i(010)]$ as in table 6.5.

notation	C_{4v}-C_4irreps	basis
[+]	$\gamma_5\mu_3$	$\frac{1}{\sqrt{2}}[(100) + i(010)]$
[−]	$\gamma_5\mu_4$	$\frac{1}{\sqrt{2}}[(100) - i(010)]$

Table 6.5 : Vibrational state notation and bases.

Using the C_4 multiplication table (section 2.3), the vibronic states which transform as particular C_{4v}-C_4 irreps can be constructed. The $\pm$ labels again follow from the C_4 irrep as in table 6.4. In the case of a γ_6 electronic ground state, the appropriate vibronic states are:

$$\begin{aligned}
\Psi_6^+ &= \psi_1^-[+] \sim \gamma_6\mu_5 \\
\Psi_6^- &= \psi_1^+[-] \sim \gamma_6\mu_6 \\
\Psi_7^+ &= \psi_1^-[-] \sim \gamma_7\mu_7 \\
\Psi_7^- &= \psi_1^+[+] \sim \gamma_7\mu_8
\end{aligned}$$

and in the case of a γ_7 electronic ground state they are:

$$\begin{aligned}
\Phi_6^+ &= \phi_1^-[-] \sim \gamma_6\mu_5 \\
\Phi_6^- &= \phi_1^+[+] \sim \gamma_6\mu_6 \\
\Phi_7^+ &= \phi_1^-[+] \sim \gamma_7\mu_7 \\
\Phi_7^- &= \phi_1^+[-] \sim \gamma_7\mu_8
\end{aligned}$$

We first consider perturbations of these vibronic states due to the electron-phonon interaction, for the cases where the electronic ground state can be considered to be well separated from other electronic states. The exception to this is CaF_2:Er^{3+}:H^- which will be considered separately in section 6.4.6.

- In first-order perturbation, the first-degree electron-phonon terms $f_\pm X_\mp$ and $f_z X_z$ give zero matrix elements between these four vibronic states, since these first-degree terms can only connect states which differ by exactly one vibrational quantum.

- In first-order perturbation, second-degree electron-phonon terms have diagonal matrix elements only, since the wavefunctions as chosen above transform as different C_4 irreps. Since both the electronic and vibrational parts have well defined C_4 irreps, the only terms to be considered are those in which both the electronic and vibrational parts transform as γ_1, namely $g_{[+-]}\, X_+X_- + g_{z^2}\, Z^2$. However the matrix elements of these are identical for each of the four zero-order vibronic states, resulting only in a uniform shift with no net contribution to any x-y splitting.

- In second-order perturbation, the first-degree electron-phonon term $f_z Z$ will have non-zero matrix elements, but will produce only a uniform shift. The first-degree terms $f_-X_+ + f_+X_-$ have electronic and vibrational parts that transform

as conjugate $\gamma_5\mu_3/\gamma_5\mu_4$ irreps and hence connect the four zero-order states to different intermediate states, producing independent shifts for the γ_6 and γ_7 vibronic states, and thus a net x-y splitting.

The major contribution to the x-y splitting is thus from the $f_-X_+ + f_+X_-$ terms acting in second-order perturbation. To find the required intermediate states, we consider the operation of these terms on the zero-order vibronic states:

$$\begin{aligned}(f_-X_+ + f_+X_-)\,\Psi_6^+ &= (f_-X_+ + f_+X_-)\,\psi^-\tfrac{1}{\sqrt{2}}[(100) + i(010)] \\ &= (f_-\psi^-)\alpha\{i(110) + \tfrac{1}{\sqrt{2}}[(200) - (020)]\} \\ &\quad + (f_+\psi^-)\alpha\{(000) + \tfrac{1}{\sqrt{2}}[(200) + (020)]\} \qquad (6.43)\end{aligned}$$

$$\begin{aligned}(f_-X_+ + f_+X_-)\,\Psi_7^+ &= (f_-X_+ + f_+X_-)\,\psi^-\tfrac{1}{\sqrt{2}}[(100) - i(010)] \\ &= (f_-\psi^-)\alpha\{(000) + \tfrac{1}{\sqrt{2}}[(200) + (020)]\} \\ &\quad + (f_+\psi^-)\alpha\{-i(110) + \tfrac{1}{\sqrt{2}}[(200) - (020)]\} \qquad (6.44)\end{aligned}$$

$$\begin{aligned}(f_-X_+ + f_+X_-)\,\Phi_6^+ &= (f_-X_+ + f_+X_-)\,\phi^-\tfrac{1}{\sqrt{2}}[(100) - i(010)] \\ &= (f_-\phi^-)\alpha\{(000) + \tfrac{1}{\sqrt{2}}[(200) + (020)]\} \\ &\quad + (f_+\phi^-)\alpha\{-i(110) + \tfrac{1}{\sqrt{2}}[(200) - (020)]\} \qquad (6.45)\end{aligned}$$

$$\begin{aligned}(f_-X_+ + f_+X_-)\,\Phi_7^+ &= (f_-X_+ + f_+X_-)\,\phi^-\tfrac{1}{\sqrt{2}}[(100) + i(010)] \\ &= (f_-\phi^-)\alpha\{i(110) + \tfrac{1}{\sqrt{2}}[(200) - (020)]\} \\ &\quad + (f_+\phi^-)\alpha\{(000) + \tfrac{1}{\sqrt{2}}[(200) + (020)]\} \qquad (6.46)\end{aligned}$$

Although we use C_4 irreps as an aid to identifying states, the symmetry is still C_{4v} so conjugate states, for example Ψ_6^+ and Ψ_6^-, must remain degenerate and it is not necessary to consider shifts of these conjugate states separately.

Since the $[(200) \pm (020)]$ states are nearly degenerate (compared to the energy separation from the x-y mode), the intermediate states involving these contribute essentially a uniform shift. We need only consider then the vibronic states involving a (000) or (110) vibrational state. The electronic part of these required intermediate

states can be found by considering the C_4 irreps:

$$\begin{aligned}
f_+\psi^- &\sim \gamma_5\mu_3 \times \gamma_6\mu_6 = \gamma_6\mu_5 \sim \psi^+ \\
f_-\psi^- &\sim \gamma_5\mu_4 \times \gamma_6\mu_6 = \gamma_7\mu_7 \sim \phi^+ \\
f_+\phi^- &\sim \gamma_5\mu_3 \times \gamma_7\mu_8 = \gamma_7\mu_7 \sim \phi^+ \\
f_-\phi^- &\sim \gamma_5\mu_4 \times \gamma_7\mu_8 = \gamma_6\mu_5 \sim \psi^+
\end{aligned}$$

Thus, if the ground state transforms as the γ_6 irrep, the intermediate states for Ψ_6^+ will be $\phi_i^+(110)$ and $\psi_i^+(000)$ and for Ψ_7^+ they will be $\phi_i^+(000)$ and $\psi_i^+(110)$. The energy shifts of the Ψ_6 and Ψ_7 states are therefore:

$$\begin{aligned}
\Delta\mathcal{E}(\Psi_6) &= \sum_{i\neq 1} \frac{\alpha^2 \left|\left\langle \psi_i^+ \middle| f_+ \middle| \psi_1^- \right\rangle\right|^2}{\hbar\omega_x - \mathcal{E}_{\psi_i}} + \sum_i \frac{\alpha^2 \left|\left\langle \phi_i^+ \middle| f_- \middle| \psi_1^- \right\rangle\right|^2}{-\hbar\omega_x - \mathcal{E}_{\phi_i}} \\
\Delta\mathcal{E}(\Psi_7) &= \sum_i \frac{\alpha^2 \left|\left\langle \phi_i^+ \middle| f_- \middle| \psi_1^- \right\rangle\right|^2}{\hbar\omega_x - \mathcal{E}_{\phi_i}} + \sum_{i\neq 1} \frac{\alpha^2 \left|\left\langle \psi_i^+ \middle| f_+ \middle| \psi_1^- \right\rangle\right|^2}{-\hbar\omega_x - \mathcal{E}_{\psi_i}}
\end{aligned}$$

and, since the $n = 2$ leading terms dominate in the expansion of the $f_\pm$ operators, we can put $f_\pm = \mp D_1^2\, C_{\pm 1}^{(2)}$ giving:

$$\Delta\mathcal{E}(\Psi_6) = (\alpha D_1^2)^2 \left(\sum_{i\neq 1} \frac{\left|\left\langle \psi_i^+ \middle| C_1^{(2)} \middle| \psi_1^- \right\rangle\right|^2}{\hbar\omega_x - \mathcal{E}_{\psi_i}} + \sum_i \frac{\left|\left\langle \phi_i^+ \middle| C_{-1}^{(2)} \middle| \psi_1^- \right\rangle\right|^2}{-\hbar\omega_x - \mathcal{E}_{\phi_i}} \right) \tag{6.47}$$

$$\Delta\mathcal{E}(\Psi_7) = (\alpha D_1^2)^2 \left(\sum_i \frac{\left|\left\langle \phi_i^+ \middle| C_{-1}^{(2)} \middle| \psi_1^- \right\rangle\right|^2}{\hbar\omega_x - \mathcal{E}_{\phi_i}} + \sum_{i\neq 1} \frac{\left|\left\langle \psi_i^+ \middle| C_1^{(2)} \middle| \psi_1^- \right\rangle\right|^2}{-\hbar\omega_x - \mathcal{E}_{\psi_i}} \right) \tag{6.48}$$

where $\mathcal{E}_{\psi_i}$ and $\mathcal{E}_{\phi_i}$ are the energies of the pure electronic states and the energy of the (110) vibrational state is assumed to be $2\hbar\omega_x$.

Similarly, if the ground state transforms as the γ_7 irrep, the intermediate states for Φ_6^+ are $\phi_i^+(110)$ and $\psi_i^+(000)$, while the intermediate states for Φ_7^+ are $\phi_i^+(000)$ and $\psi_i^+(110)$. The energy shifts are therefore:

$$\Delta\mathcal{E}(\Phi_6) = (\alpha D_1^2)^2 \left(\sum_i \frac{\left|\left\langle \psi_i^+ \middle| C_{-1}^{(2)} \middle| \phi_1^- \right\rangle\right|^2}{\hbar\omega_x - \mathcal{E}_{\psi_i}} + \sum_{i\neq 1} \frac{\left|\left\langle \phi_i^+ \middle| C_1^{(2)} \middle| \phi_1^- \right\rangle\right|^2}{-\hbar\omega_x - \mathcal{E}_{\phi_i}} \right) \tag{6.49}$$

$$\Delta\mathcal{E}(\Phi_7) = (\alpha D_1^2)^2 \left(\sum_{i\neq 1} \frac{\left|\left\langle \phi_i^+ \middle| C_1^{(2)} \middle| \phi_1^- \right\rangle\right|^2}{\hbar\omega_x - \mathcal{E}_{\phi_i}} + \sum_i \frac{\left|\left\langle \psi_i^+ \middle| C_{-1}^{(2)} \middle| \phi_1^- \right\rangle\right|^2}{-\hbar\omega_x - \mathcal{E}_{\psi_i}} \right) \tag{6.50}$$

6.4.1 $CaF_2:Ce^{3+}:H^-$ and $SrF_2:Ce^{3+}:H^-$

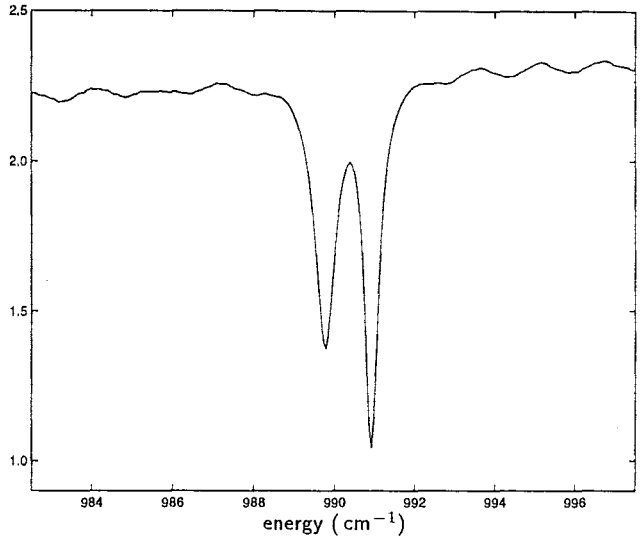

Figure 6.5 : Infrared-absorption spectrum of the x-y splitting in CaF_2:0.01%Ce^{3+}:H^-(2 hrs).

The x-y local-mode absorption line in CaF_2:0.01%:Ce^{3+} hydrogenated for 2 hours is presented in the spectrum of figure 6.5, showing a well-resolved splitting of 1.15 cm^{-1}. In the calculation of the splitting due to the electron-phonon interaction, the major contribution arises from the second-order perturbation, so the vibronic energies and wavefunctions of each of the intermediate states to be considered are required.

Data on the hydrogenic C_{4v} centre in $CaF_2:Ce^{3+}$ appears to be limited only to the ground state g-values obtained by Ashburner *et al* [7] and Kafri *et al* [49]:

$$g_{\parallel} = 3.150 \pm 0.003\ ,\ g_{\perp} = 1.330 \pm 0.001\ .$$

In lieu of further data on this centre, and in light of the fact that the ground state g-values for the F^- C_{4v} centre ($g_{\parallel} = 3.038, g_{\perp} = 1.396$ [9]) are fairly close to those of the H^- centre, the crystal-field energies measured for the F^- C_{4v} centre by Freeth and Jones [29] and the wavefunctions calculated from these (table 6.6) will be adopted. The states of both multiplets, $^2F_{5/2}$ and $^2F_{7/2}$, of the $4f^1$ configuration of Ce^{3+} are considered. The ground state transforms as the γ_7 irrep, so the energy shifts of Φ_6 and Φ_7 are found from equations 6.49 and 6.50. The $C^{(2)}_{\pm 1}$ matrix elements and the

energy (cm^{-1})	wavefunctions
0	$\phi_1^{\pm}(\gamma_7) = 0.907\left\vert\frac{5}{2},\pm\frac{5}{2}\right\rangle + 0.419\left\vert\frac{5}{2},\mp\frac{3}{2}\right\rangle$
516†	$\psi_1^{\pm}(\gamma_6) = 0.993\left\vert\frac{5}{2},\pm\frac{1}{2}\right\rangle \mp 0.117\left\vert\frac{7}{2},\pm\frac{1}{2}\right\rangle$
579	$\phi_2^{\pm}(\gamma_7) = 0.401\left\vert\frac{5}{2},\pm\frac{5}{2}\right\rangle \mp 0.314\left\vert\frac{7}{2},\pm\frac{5}{2}\right\rangle - 0.858\left\vert\frac{5}{2},\mp\frac{3}{2}\right\rangle$
2191	$\psi_2^{\pm}(\gamma_6) = 1.000\left\vert\frac{7}{2},\mp\frac{7}{2}\right\rangle$
2305	$\phi_3^{\pm}(\gamma_7) = 0.518\left\vert\frac{7}{2},\pm\frac{5}{2}\right\rangle + 0.847\left\vert\frac{7}{2},\mp\frac{3}{2}\right\rangle \mp 0.114\left\vert\frac{5}{2},\mp\frac{3}{2}\right\rangle$
2824	$\psi_3^{\pm}(\gamma_6) = 0.993\left\vert\frac{7}{2},\pm\frac{1}{2}\right\rangle \pm 0.117\left\vert\frac{5}{2},\pm\frac{1}{2}\right\rangle$
3562	$\phi_4^{\pm}(\gamma_7) = 0.795\left\vert\frac{7}{2},\pm\frac{5}{2}\right\rangle - 0.526\left\vert\frac{7}{2},\mp\frac{3}{2}\right\rangle \pm 0.123\left\vert\frac{5}{2},\pm\frac{5}{2}\right\rangle \mp 0.274\left\vert\frac{5}{2},\mp\frac{3}{2}\right\rangle$

Table 6.6 : Energy levels of the Ce^{3+} ion in the CaF_2:Ce^{3+} C_{4v} centre [29], and wavefunctions obtained by least-squares fit to this data. † Calculated energy.

intermediate state	vibronic energy relative to Φ (cm^{-1})	$C^{(2)}_{\pm1}$ matrix element	$\Delta\mathcal{E}(\Phi_6^+)\,/\,(\alpha D_1^2)^2$ ($\times10^{-4}\,/\,cm^{-1}$)
$\psi_1^+(000)$	−474	−0.0876	0.162
$\psi_2^+(000)$	1201	−0.1143	−0.109
$\psi_3^+(000)$	1834	0.0339	−0.006
$\phi_2^+(110)$	1569	−0.2935	−0.549
$\phi_3^+(110)$	3295	0.0264	−0.002
$\phi_4^+(110)$	4552	0.1405	−0.043
total shift of Φ_6^+			−0.548

intermediate state	vibronic energy relative to Φ (cm^{-1})	$C^{(2)}_{\pm1}$ matrix element	$\Delta\mathcal{E}(\Phi_7^+)\,/\,(\alpha D_1^2)^2$ ($\times10^{-4}\,/\,cm^{-1}$)
$\phi_2^+(000)$	−411	−0.2935	2.096
$\phi_3^+(000)$	1315	0.0264	−0.005
$\phi_4^+(000)$	2572	0.1405	−0.077
$\psi_1^+(110)$	1506	−0.0876	−0.051
$\psi_2^+(110)$	3181	−0.1143	−0.041
$\psi_3^+(110)$	3814	0.0339	−0.003
total shift of Φ_7^+			+1.919

Table 6.7 : Calculated energy shifts of the Φ_6^+ and Φ_7^+ states for CaF_2:Ce^{3+}:H^-

contribution to the energy shifts due to each of the intermediate states is given in table 6.7.

From table 6.7, the dominant contributions to the x-y splitting come from the intermediate states involving the ϕ_2 electronic state which has a large $C^{(2)}_{\pm 1}$ matrix element with the ϕ_1 state. The $\phi_2(000)$ vibronic state, at lower energy than the x-y vibronic states, transforms as γ_7 and therefore pushes up the Φ_7 doublet, while the $\phi_2(110)$ state is at higher energy and transforms as γ_6, therefore pushing down the Φ_6 doublet.

The total calculated x-y splitting due to the first-degree electron-phonon terms acting in second order can be compared to the measured splitting:

$$\Delta\mathcal{E}_7 - \Delta\mathcal{E}_6 \;=\; 2.467\times10^{-4}\,(\alpha D_1^2)^2 \;=\; 1.15\,\mathrm{cm}^{-1}$$

Therefore, in order to obtain the measured x-y splitting, we would require the αD_1^2 parameter to be:

$$\alpha D_1^2 = 68\,\mathrm{cm}^{-1} \qquad \text{(fitted)}.$$

The D_1^2 parameter contains the radial dependence of the $f_\pm$ operator, and as such its form cannot be determined *a priori*. However, by invoking the point-charge model of section 6.3.2 with appropriate values listed in that section and α from table 6.1, the value of αD_1^2 can be estimated to be:

$$\alpha D_1^2 \;=\; \alpha\sqrt{3}\,\frac{kqe}{D^4}\,\langle r^2\rangle \;=\; 114\,\mathrm{cm}^{-1} \qquad \text{(point-charge model)}.$$

Given the approximations inherent in the point-charge model, this is in quite reasonable agreement with the value determined from the experimental splitting, being a factor of 1.67 greater than that value. This demonstrates that the electron-phonon interaction can produce splittings of a similar size to that observed, and is a probable cause of these splittings.

The infrared absorption spectrum of the x-y mode of SrF_2:0.01%Ce^{3+} hydrogenated for 4.5 hours is given in figure 6.6, showing a splitting which is less than that in the CaF_2:Ce^{3+}:H^- spectrum, but is still well resolved at $0.95\,\mathrm{cm}^{-1}$. Weaker satellite lines which appear at $910.2\,\mathrm{cm}^{-1}$ and $914.8\,\mathrm{cm}^{-1}$ are not associated with the Ce^{3+} ion as they are observed also in other SrF_2 samples which do not contain Ce^{3+}.

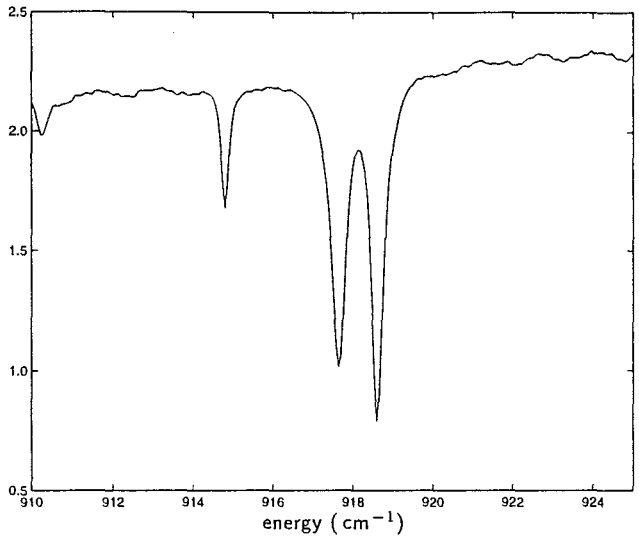

Figure 6.6 : Infrared-absorption spectrum of the x-y splitting in SrF_2:0.01%Ce^{3+}:H^-(4.5 hrs).

No data could be found on the hydrogenic C_{4v} centre in SrF_2:Ce^{3+}, so wavefunctions and energies calculated for the F^- centre (table 6.8) are adopted, as in the CaF_2:Ce^{3+}:H^- case.

The $C^{(2)}_{\pm 1}$ matrix elements and the contribution to the energy shifts due to each of the intermediate states is given in table 6.9, giving a total calculated x-y splitting, to be equated with the measured value, of:

$$\Delta\mathcal{E}_7 - \Delta\mathcal{E}_6 \;=\; 2.686\times10^{-4}\,(\alpha D_1^2)^2 \;=\; 0.95\,\mathrm{cm}^{-1}$$

thus giving the αD_1^2 parameter:

$$\alpha D_1^2 = 59\,\mathrm{cm}^{-1} \qquad \text{(fitted)}.$$

The point charge model, using the constants listed in section 6.3.2 and table 6.1, predicts a value for the D_1^2 parameter for SrF_2:Ce^{3+}:H^- of

$$\alpha D_1^2 \;=\; \alpha\sqrt{3}\,\frac{kqe}{D^4}\,\langle r^2\rangle \;=\; 128\,\mathrm{cm}^{-1} \qquad \text{(point-charge model)}.$$

The discrepancy here is a factor of 2.2, but again this is a reasonable agreement given the model used.

energy (cm^{-1})	wavefunctions
0	$\phi_1^{\pm}(\gamma_7) = 0.890\left\vert\frac{5}{2},\pm\frac{5}{2}\right\rangle + 0.455\left\vert\frac{5}{2},\mp\frac{3}{2}\right\rangle$
445†	$\psi_1^{\pm}(\gamma_6) = 0.996\left\vert\frac{5}{2},\pm\frac{1}{2}\right\rangle$
530†	$\phi_2^{\pm}(\gamma_7) = 0.443\left\vert\frac{5}{2},\pm\frac{5}{2}\right\rangle \mp 0.289\left\vert\frac{7}{2},\pm\frac{5}{2}\right\rangle - 0.847\left\vert\frac{5}{2},\mp\frac{3}{2}\right\rangle$
2212	$\psi_2^{\pm}(\gamma_6) = 0.999\left\vert\frac{7}{2},\mp\frac{7}{2}\right\rangle$
2274	$\phi_3^{\pm}(\gamma_7) = 0.531\left\vert\frac{7}{2},\pm\frac{5}{2}\right\rangle + 0.840\left\vert\frac{7}{2},\mp\frac{3}{2}\right\rangle \mp 0.114\left\vert\frac{5}{2},\mp\frac{3}{2}\right\rangle$
2713	$\psi_3^{\pm}(\gamma_6) = 0.995\left\vert\frac{7}{2},\pm\frac{1}{2}\right\rangle$
3379	$\phi_4^{\pm}(\gamma_7) = 0.796\left\vert\frac{7}{2},\pm\frac{5}{2}\right\rangle - 0.539\left\vert\frac{7}{2},\mp\frac{3}{2}\right\rangle \pm 0.111\left\vert\frac{5}{2},\pm\frac{5}{2}\right\rangle \mp 0.252\left\vert\frac{5}{2},\mp\frac{3}{2}\right\rangle$

Table 6.8 : Energy levels of the Ce^{3+} ion in the SrF_2:Ce^{3+} C_{4v} centre [29], and wavefunctions obtained by least-squares fit to this data. † Calculated energy.

intermediate state	vibronic energy relative to Φ (cm^{-1})	$C^{(2)}_{\pm1}$ matrix element	$\Delta\mathcal{E}(\Phi_6^+)\,/\,(\alpha D_1^2)^2$ ($\times10^{-4}\,/\,cm^{-1}$)
$\psi_1^+(000)$	−473	−0.0853	0.154
$\psi_2^+(000)$	1294	−0.1120	−0.097
$\psi_3^+(000)$	1795	0.0474	−0.013
$\phi_2^+(110)$	1448	−0.2960	−0.605
$\phi_3^+(110)$	3192	0.0248	−0.002
$\phi_4^+(110)$	4297	0.1330	−0.041
total shift of Φ_6^+			−0.604
intermediate state	vibronic energy relative to Φ (cm^{-1})	$C^{(2)}_{\pm1}$ matrix element	$\Delta\mathcal{E}(\Phi_7^+)\,/\,(\alpha D_1^2)^2$ ($\times10^{-4}\,/\,cm^{-1}$)
$\phi_2^+(000)$	−388	−0.2960	2.258
$\phi_3^+(000)$	1356	0.0248	−0.005
$\phi_4^+(000)$	2461	0.1330	−0.072
$\psi_1^+(110)$	1363	−0.0853	−0.053
$\psi_2^+(110)$	3130	−0.1120	−0.040
$\psi_3^+(110)$	3631	0.0474	−0.006
total shift of Φ_7^+			+2.082

Table 6.9 : Calculated energy shifts of the Φ_6^+ and Φ_7^+ states for SrF_2:Ce^{3+}:H^-

6.4.2 CaF_2:Nd^{3+}:H^- and SrF_2:Nd^{3+}:H^-

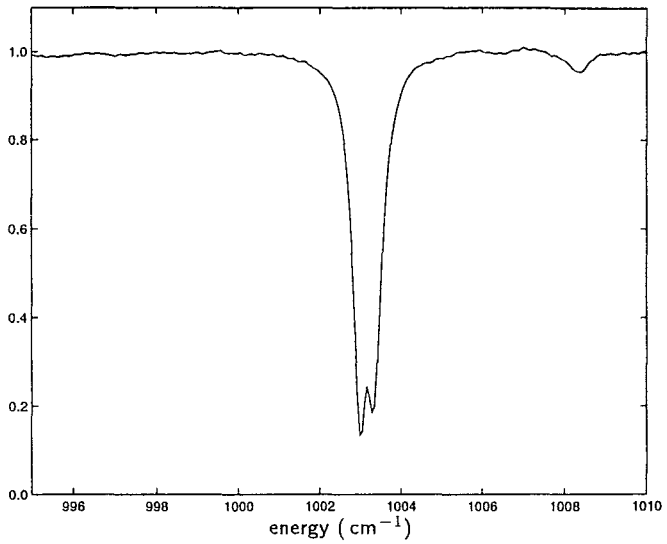

Figure 6.7 : Infrared-absorption spectrum of the x-y splitting in CaF_2:0.01%Nd^{3+}:H^-(1.5 hrs).

Figure 6.7 shows the infrared absorption spectrum of the x-y vibronic lines in CaF_2:0.01%Nd^{3+} hydrogenated for 1.5 hours, with a just-resolved x-y splitting of $0.3\,cm^{-1}$. To calculate an estimate of the x-y splitting, the crystal-field energies and wavefunctions are required.

Data for the deuterated CaF_2:Nd^{3+} and tritiated SrF_2:Nd^{3+} systems have been reported by Han *et al* [33], including crystal field fits to energies of the $^4I_{9/2}$ and $^4I_{11/2}$ multiplets. Since the electronic level differences between the H^-,D^- and T^- compensated centres differ only by a few wavenumbers at most, this data can be assumed for the H^- C_{4v} centres. The $^4I_{9/2}$ multiplet wavefunctions for CaF_2:Nd^{3+}:H^-, calculated from the parameters given in [33], are given in table 6.10. The ground state was found to be a γ_6 state, hence intermediate states for the second-order perturbation calculation are determined from equations 6.49 and 6.50. the intermediate states for the perturbation of the Ψ_6^+ state are $\phi_i^+(110)$ and $\psi_i^+(000)$ while for the Ψ_7^+ state they are $\phi_i^+(000)$ and $\psi_i^+(110)$. The $C_{\pm1}^{(2)}$ matrix elements and the contribution to the energy shifts from each of the intermediate states are given in table 6.11. The total x-y splitting due to the $f_-X_+ + f_+X_-$ terms acting in second

energy (cm^{-1})	wavefunctions
0	$\psi_1^{\pm}(\gamma_6) = -0.884\left\|\frac{9}{2},\pm\frac{9}{2}\right\rangle + 0.436\left\|\frac{9}{2},\pm\frac{1}{2}\right\rangle$
110	$\phi_1^{\pm}(\gamma_7) = 0.924\left\|\frac{9}{2},\pm\frac{5}{2}\right\rangle + 0.366\left\|\frac{9}{2},\mp\frac{3}{2}\right\rangle$
234	$\phi_2^{\pm}(\gamma_7) = -0.376\left\|\frac{9}{2},\pm\frac{5}{2}\right\rangle + 0.905\left\|\frac{9}{2},\mp\frac{3}{2}\right\rangle$
362†	$\psi_2^{\pm}(\gamma_6) = 0.170\left\|\frac{9}{2},\pm\frac{9}{2}\right\rangle + 0.224\left\|\frac{9}{2},\pm\frac{1}{2}\right\rangle - 0.945\left\|\frac{9}{2},\mp\frac{7}{2}\right\rangle$
763	$\psi_3^{\pm}(\gamma_6) = -0.404\left\|\frac{9}{2},\pm\frac{9}{2}\right\rangle - 0.861\left\|\frac{9}{2},\pm\frac{1}{2}\right\rangle - 0.262\left\|\frac{9}{2},\mp\frac{7}{2}\right\rangle$

Table 6.10 : Energy levels of the Nd^{3+} ion in the CaF_2:Nd^{3+} D^- C_{4v} centre [33], and wavefunctions obtained by least-squares fit to this data. † Calculated energy.

intermediate state	vibronic energy relative to Ψ (cm^{-1})	$C_{\pm1}^{(2)}$ matrix element	$\Delta\mathcal{E}(\Psi_6^+)\,/\,(\alpha D_1^2)^2$ ($\times10^{-4}\,/\,cm^{-1}$)
$\psi_2^+(000)$	−641	0.0753	0.0885
$\psi_3^+(000)$	−240	0.0209	0.0182
$\phi_1^+(110)$	1113	0.0057	−0.0003
$\phi_2^+(110)$	1237	0.0142	−0.0016
total shift of Ψ_6^+			+0.1048
intermediate state	vibronic energy relative to Ψ (cm^{-1})	$C_{\pm1}^{(2)}$ matrix element	$\Delta\mathcal{E}(\Psi_7^+)\,/\,(\alpha D_1^2)^2$ ($\times10^{-4}\,/\,cm^{-1}$)
$\phi_1^+(000)$	−893	0.0057	0.0004
$\phi_2^+(000)$	−769	0.0142	0.0026
$\psi_2^+(110)$	1365	0.0753	−0.0416
$\psi_3^+(110)$	1766	0.0209	−0.0025
total shift of Ψ_7^+			−0.0411

Table 6.11 : Calculated energy shifts of the Ψ_6^+ and Ψ_7^+ states for CaF_2:Nd^{3+}:H^-

order is thus calculated to be

$$\Delta\mathcal{E}_6 - \Delta\mathcal{E}_7 \;=\; 0.1459\times10^{-4}\,(\alpha D_1^2)^2 \;=\; 0.3\,\mathrm{cm}^{-1}$$

This gives the αD_1^2 parameter as:

$$\alpha D_1^2 = 140\,\mathrm{cm}^{-1} \qquad \text{(fitted)}.$$

By comparison, the value of this parameter calculated from the point-charge model would be

$$\alpha D_1^2 \;=\; \alpha\sqrt{3}\,\frac{kqe}{D^4}\,\langle r^2\rangle \;=\; 94\,\mathrm{cm}^{-1} \qquad \text{(point-charge model)}.$$

This is again in close agreement, being a factor of 1.5 different, although this time the point-charge-model calculation underestimates, rather than overestimates, the D_1^2 parameter.

The infrared absorption spectrum of the x-y mode of SrF_2:0.01%Nd^{3+} hydrogenated for 2 hours is shown in figure 6.8, showing a small splitting of $0.2\,\mathrm{cm}^{-1}$.

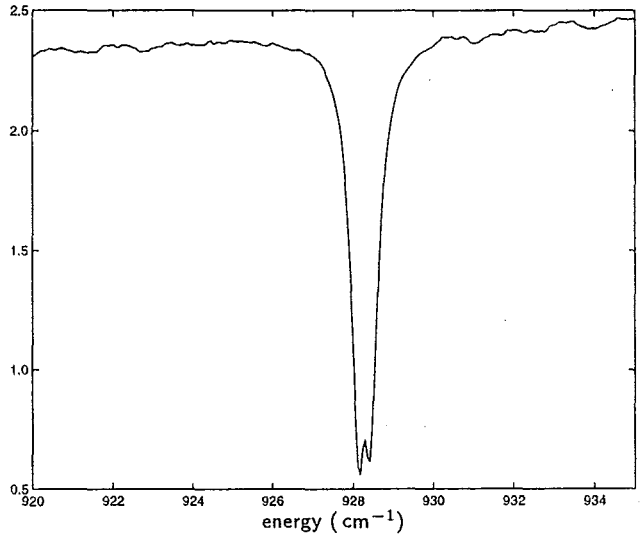

Figure 6.8 : Infrared-absorption spectrum of the x-y splitting in SrF_2:0.01%Nd^{3+}:H^-(2 hrs).

The $^4I_{9/2}$ multiplet wavefunctions for SrF_2:Nd^{3+}:H^-, calculated from the parameters given by Han [33], are given in table 6.12, with the measured energy levels [33]. The

energy (cm^{-1})	wavefunctions
0	$\psi_1^{\pm}(\gamma_6) = -0.867\left\|\frac{9}{2},\pm\frac{9}{2}\right\rangle + 0.470\left\|\frac{9}{2},\pm\frac{1}{2}\right\rangle - 0.102\left\|\frac{9}{2},\mp\frac{7}{2}\right\rangle$
81	$\phi_1^{\pm}(\gamma_7) = 0.950\left\|\frac{9}{2},\pm\frac{5}{2}\right\rangle + 0.301\left\|\frac{9}{2},\mp\frac{3}{2}\right\rangle$
172	$\phi_2^{\pm}(\gamma_7) = -0.308\left\|\frac{9}{2},\pm\frac{5}{2}\right\rangle + 0.935\left\|\frac{9}{2},\mp\frac{3}{2}\right\rangle$
302†	$\psi_2^{\pm}(\gamma_6) = 0.218\left\|\frac{9}{2},\pm\frac{9}{2}\right\rangle + 0.226\left\|\frac{9}{2},\pm\frac{1}{2}\right\rangle - 0.934\left\|\frac{9}{2},\mp\frac{7}{2}\right\rangle$
652	$\psi_3^{\pm}(\gamma_6) = -0.424\left\|\frac{9}{2},\pm\frac{9}{2}\right\rangle - 0.845\left\|\frac{9}{2},\pm\frac{1}{2}\right\rangle - 0.292\left\|\frac{9}{2},\mp\frac{7}{2}\right\rangle$

Table 6.12 : Energy levels of the Nd^{3+} ion in the SrF_2:Nd^{3+} T^- C_{4v} centre [33], and wavefunctions obtained by least-squares fit to this data. † Calculated energy.

matrix elements of $C_{\pm1}^{(2)}$ and the contribution to the second-order electron-phonon-interaction energy shifts from each of the intermediate states are given in table 6.13.

The αD_1^2 parameter is thus fitted by comparing the total calculated x-y splitting due to the $f_-X_+ + f_+X_-$ terms acting in second order with the measured splitting

$$\Delta\mathcal{E}_7 - \Delta\mathcal{E}_6 = 0.1436\times10^{-4}\,(\alpha D_1^2)^2 = 0.2\,cm^{-1}$$

giving

$$\alpha D_1^2 = 120\,cm^{-1} \qquad \text{(fitted)}.$$

The point-charge model would give a calculated value for this parameter of

$$\alpha D_1^2 = \alpha\sqrt{3}\,\frac{kqe}{D^4}\,\langle r^2\rangle = 98\,cm^{-1} \qquad \text{(point-charge model)}.$$

Again a close correspondence with the point-charge-model prediction is found, with a difference in this case of a factor of 1.2.

intermediate state	vibronic energy relative to Ψ (cm^{-1})	$C^{(2)}_{\pm 1}$ matrix element	$\Delta\mathcal{E}(\Psi_6^+)\,/\,(\alpha D_1^2)^2$ ($\times 10^{-4}\,/\,cm^{-1}$)
$\psi_2^+(000)$	-626	0.0753	0.0905
$\psi_3^+(000)$	-276	0.0189	0.0130
$\phi_1^+(110)$	1009	0.0140	-0.0019
$\phi_2^+(110)$	1100	0.0133	-0.0016
total shift of Ψ_6^+			$+0.0999$

intermediate state	vibronic energy relative to Ψ (cm^{-1})	$C^{(2)}_{\pm 1}$ matrix element	$\Delta\mathcal{E}(\Psi_7^+)\,/\,(\alpha D_1^2)^2$ ($\times 10^{-4}\,/\,cm^{-1}$)
$\phi_1^+(000)$	-847	0.0140	0.0023
$\phi_2^+(000)$	-756	0.0133	0.0023
$\psi_2^+(110)$	1230	0.0753	-0.0460
$\psi_3^+(110)$	1580	0.0189	-0.0023
total shift of Ψ_7^+			-0.0437

Table 6.13 : Calculated energy shifts of the Ψ_6^+ and Ψ_7^+ states for SrF_2:Nd^{3+}:H^-

6.4.3 CaF_2:Sm^{3+}:H^- and SrF_2:Sm^{3+}:H^-

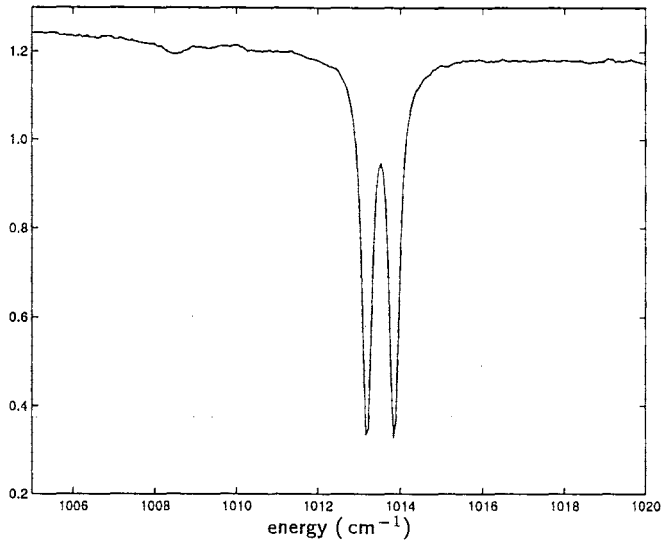

Figure 6.9 : Infrared-absorption spectrum of the x-y splitting in CaF_2:0.01%Sm^{3+}:H^-(2 hrs).

The infrared-absorption spectrum of CaF_2:0.01%Sm^{3+} hydrogenated for 2 hours shows a clear splitting of the x-y vibronic line of 0.67 cm^{-1}, figure 6.9.

Reported data on this system is limited to only the ground state g-values obtained by Ashburner *et al* [7]:

$$g_{\parallel} < 0.1\,, \qquad g_{\perp} = 0.868 \pm 0.001$$

so the energies and wavefunctions adopted are those obtained for the F^- centre by Wells [88]. The g-values of this F^- centre ($g_{\parallel} = 0, g_{\perp} = 0.823$ [7]) are close to those reported for the hydrogenic centre, indicating that these two centres are sufficiently similar that this should be a reasonable approximation. However, while in most cases an energy change of some tens of wavenumbers would not be significant, the ψ_2 state in this scheme is only 28 cm^{-1} from the x-y vibrational energy, and clearly the exact energy of this state would be of vital importance.

The ground state is a γ_6 state, so the calculation proceeds as for Nd^{3+}, using equations 6.47 and 6.48. The $C^{(2)}_{\pm 1}$ matrix elements and the contribution to the energy shifts due to each of the intermediate states is given in table 6.15.

energy (cm^{-1})	wavefunctions
0	$\psi_1^{\pm}(\gamma_6) = 0.985\left\|\frac{5}{2},\pm\frac{1}{2}\right\rangle + 0.102\left\|\frac{9}{2},\mp\frac{7}{2}\right\rangle$
47	$\phi_1^{\pm}(\gamma_7) = 0.397\left\|\frac{5}{2},\pm\frac{5}{2}\right\rangle + 0.871\left\|\frac{5}{2},\mp\frac{3}{2}\right\rangle \mp 0.223\left\|\frac{7}{2},\pm\frac{5}{2}\right\rangle \pm 0.134\left\|\frac{7}{2},\mp\frac{3}{2}\right\rangle$
341†	$\phi_2^{\pm}(\gamma_7) = 0.911\left\|\frac{5}{2},\pm\frac{5}{2}\right\rangle - 0.404\left\|\frac{5}{2},\mp\frac{3}{2}\right\rangle$
985	$\psi_2^{\pm}(\gamma_6) = 0.963\left\|\frac{7}{2},\pm\frac{1}{2}\right\rangle + 0.179\left\|\frac{7}{2},\mp\frac{7}{2}\right\rangle$
1160	$\phi_3^{\pm}(\gamma_7) = 0.908\left\|\frac{7}{2},\pm\frac{5}{2}\right\rangle - 0.315\left\|\frac{7}{2},\mp\frac{3}{2}\right\rangle \pm 0.256\left\|\frac{5}{2},\mp\frac{3}{2}\right\rangle$
1323	$\phi_4^{\pm}(\gamma_7) = 0.330\left\|\frac{7}{2},\pm\frac{5}{2}\right\rangle + 0.924\left\|\frac{7}{2},\mp\frac{3}{2}\right\rangle \mp 0.124\left\|\frac{9}{2},\pm\frac{5}{2}\right\rangle \pm 0.129\left\|\frac{9}{2},\mp\frac{3}{2}\right\rangle$
1353	$\psi_3^{\pm}(\gamma_6) = -0.196\left\|\frac{7}{2},\pm\frac{1}{2}\right\rangle + 0.971\left\|\frac{7}{2},\mp\frac{7}{2}\right\rangle$
2215	$\psi_4^{\pm}(\gamma_6) = 0.961\left\|\frac{9}{2},\pm\frac{1}{2}\right\rangle + 0.177\left\|\frac{9}{2},\pm\frac{9}{2}\right\rangle$
2376	$\psi_5^{\pm}(\gamma_6) = 0.980\left\|\frac{9}{2},\mp\frac{7}{2}\right\rangle$
2403	$\phi_5^{\pm}(\gamma_7) = -0.448\left\|\frac{9}{2},\pm\frac{5}{2}\right\rangle + 0.863\left\|\frac{9}{2},\mp\frac{3}{2}\right\rangle \mp 0.101\left\|\frac{7}{2},\pm\frac{5}{2}\right\rangle \mp 0.141\left\|\frac{7}{2},\mp\frac{3}{2}\right\rangle$
2537	$\phi_6^{\pm}(\gamma_7) = 0.872\left\|\frac{9}{2},\pm\frac{5}{2}\right\rangle + 0.452\left\|\frac{9}{2},\mp\frac{3}{2}\right\rangle \mp 0.113\left\|\frac{11}{2},\pm\frac{5}{2}\right\rangle \pm 0.116\left\|\frac{11}{2},\mp\frac{3}{2}\right\rangle$
2567	$\psi_6^{\pm}(\gamma_6) = 0.975\left\|\frac{9}{2},\pm\frac{9}{2}\right\rangle - 0.187\left\|\frac{9}{2},\pm\frac{1}{2}\right\rangle$

Table 6.14 : Energies of the Sm^{3+} ion in the CaF_2:Sm^{3+} C_{4v} centre, and JM-basis wavefunctions obtained by least-squares fit to the data of Wells [88]. †Calculated energy.

intermediate state	vibronic energy relative to Ψ (cm^{-1})	$C^{(2)}_{\pm 1}$ matrix element	$\Delta\mathcal{E}(\Psi_6^+)\,/\,(\alpha D_1^2)^2$ ($\times 10^{-4}\,/\,cm^{-1}$)
$\psi_2^+(000)$	-28	-0.1160	4.807
$\psi_3^+(000)$	340	-0.0236	-0.016
$\psi_4^+(000)$	1202	-0.0369	-0.011
$\psi_5^+(000)$	1363	-0.0000	-0.000
$\psi_6^+(000)$	1554	0.0072	-0.000
$\phi_1^+(110)$	1060	-0.1145	-0.124
$\phi_2^+(110)$	1354	0.0572	-0.024
$\phi_3^+(110)$	2173	0.0573	-0.015
$\phi_4^+(110)$	2336	-0.0677	-0.020
$\phi_5^+(110)$	3416	0.0312	-0.003
$\phi_6^+(110)$	3550	-0.0213	-0.001
total shift of Ψ_6^+			+4.593

intermediate state	vibronic energy relative to Ψ (cm^{-1})	$C^{(2)}_{\pm 1}$ matrix element	$\Delta\mathcal{E}(\Psi_7^+)\,/\,(\alpha D_1^2)^2$ ($\times 10^{-4}\,/\,cm^{-1}$)
$\phi_1^+(000)$	-966	-0.1145	0.136
$\phi_2^+(000)$	-672	0.0572	0.049
$\phi_3^+(000)$	147	0.0573	-0.224
$\phi_4^+(000)$	310	-0.0677	-0.148
$\phi_5^+(000)$	1390	0.0312	-0.007
$\phi_6^+(000)$	1524	-0.0213	-0.003
$\psi_2^+(110)$	1998	-0.1160	-0.067
$\psi_3^+(110)$	2366	-0.0236	-0.002
$\psi_4^+(110)$	3228	-0.0369	-0.004
$\psi_5^+(110)$	3389	-0.0000	-0.000
$\psi_6^+(110)$	3580	0.0072	-0.000
total shift of Ψ_7^+			-0.271

Table 6.15 : Calculated energy shifts of the Ψ_6^+ and Ψ_7^+ states for CaF_2:Sm^{3+}:H^-

The total x-y splitting in CaF_2:Sm^{3+}:H^- as calculated from the $f_-X_+ + f_+X_-$ terms acting in second order is equated to the measured splitting

$$\Delta\mathcal{E}_7 - \Delta\mathcal{E}_6 \;=\; 4.864\times10^{-4}\,(\alpha D_1^2)^2 \;=\; 0.67\,\mathrm{cm}^{-1}$$

To give the value for the αD_1^2 parameter:

$$\alpha D_1^2 = 37\,\mathrm{cm}^{-1} \qquad \text{(fitted)}.$$

The point-charge model gives a calculated value for this parameter of

$$\alpha D_1^2 \;=\; \alpha\sqrt{3}\,\frac{kqe}{D^4}\,\langle r^2\rangle \;=\; 83\,\mathrm{cm}^{-1} \qquad \text{(point-charge model)}.$$

For CaF_2:Sm^{3+}:H^- then the point-charge-model calculation gives a value 2.2 times larger than that deduced from the measured splitting and the F^- centre energies and wavefunctions.

Almost the entire contribution to the second-order x-y splitting comes from the $\psi_2^+(000)$ intermediate state. This is due to both the large matrix element between the ψ_1^- and ψ_2^+ electronic states and the proximity of this state to the x-y mode. Being only $28\,\mathrm{cm}^{-1}$ away, the contributed shift is large, and also very sensitive to the exact energy difference. While wavefunctions, and hence matrix elements, wouldn't be expected to change much in going from the F^- centre to the H^- centre, changes in the energies might be expected and a downwards shift of this state of $30\,\mathrm{cm}^{-1}$, for example, would halve the calculated x-y splitting due to the $\psi_2^+(000)$ state. This would in turn double the fitted value of αD_1^2, thus accounting for most of the above discrepancy. Therefore, this value must be considered to be very approximate until an energy level scheme for the H^- C_{4v} centre of CaF_2:Sm^{3+}:H^- has been established.

The infrared absorption spectrum of the x-y mode of SrF_2:0.01%Sm^{3+} hydrogenated for 2 hours is shown in figure 6.10, with a splitting of $0.38\,\mathrm{cm}^{-1}$. The spectrum also shows the longitudinal z-mode, the Sm^{3+} ion being the cross-over point of the rare-earth series for the x-y and z-mode energies in the SrF_2 host. Edgar *et al* [24] assigned these two lines on the basis of relative intensities, with the x-y mode at lower energy. However the splitting of the higher energy line when observed at the higher resolution available here indicates that this is in fact the x-y mode. This assignment is confirmed by the Zeeman splittings reported in chapter 7.

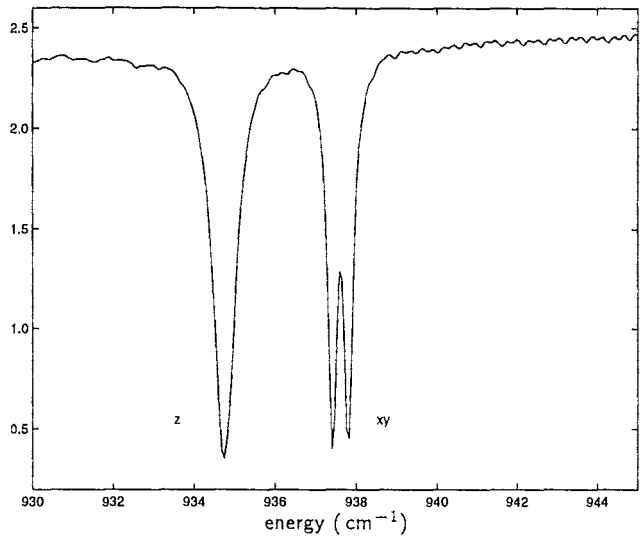

Figure 6.10 : Infrared-absorption spectrum of the x-y splitting in SrF_2:0.01%Sm^{3+}:H^-(2 hrs).

Again, in lieu of data on the H^- C_{4v} centre, the energies of the F^- C_{4v} centre found by Wells [88], and the wavefunctions calculated from these, have been adopted (table 6.16). The $C^{(2)}_{\pm 1}$ matrix elements and the contribution to the energy shifts due to each of the intermediate states is given in table 6.17. The total calculated x-y splitting is compared with the measured value,

$$\Delta\mathcal{E}_7 - \Delta\mathcal{E}_6 \;=\; 2.461\times10^{-4}\,(\alpha D_1^2)^2 \;=\; 0.38\,\mathrm{cm}^{-1}$$

To give a value for αD_1^2 of

$$\alpha D_1^2 = 39\,\mathrm{cm}^{-1} \qquad \text{(fitted)}$$

while the point-charge model would give a calculated value for this parameter of

$$\alpha D_1^2 \;=\; \alpha\sqrt{3}\,\frac{kqe}{D^4}\,\langle r^2\rangle \;=\; 86\,\mathrm{cm}^{-1} \qquad \text{(point-charge model).}$$

These two values have a discrepancy of a factor of 2.2, with the point-charge model predicting too large a value.

The calculation for the SrF_2:Sm^{3+}:H^- x-y mode shows an interesting effect. Although the electronic energies and wavefunctions remain similar to the CaF_2:Sm^{3+}:H^-

energy (cm^{-1})	wavefunctions
0	$\psi_1^{\pm}(\gamma_6) = 0.989\left\|\frac{5}{2},\pm\frac{1}{2}\right\rangle + 0.100\left\|\frac{9}{2},\mp\frac{7}{2}\right\rangle$
35	$\phi_1^{\pm}(\gamma_7) = 0.446\left\|\frac{5}{2},\pm\frac{5}{2}\right\rangle + 0.857\left\|\frac{5}{2},\mp\frac{3}{2}\right\rangle \mp 0.197\left\|\frac{7}{2},\pm\frac{5}{2}\right\rangle \pm 0.124\left\|\frac{7}{2},\mp\frac{3}{2}\right\rangle$
260†	$\phi_2^{\pm}(\gamma_7) = 0.890\left\|\frac{5}{2},\pm\frac{5}{2}\right\rangle - 0.435\left\|\frac{5}{2},\mp\frac{3}{2}\right\rangle \pm 0.104\left\|\frac{7}{2},\pm\frac{5}{2}\right\rangle$
990	$\psi_2^{\pm}(\gamma_6) = 0.935\left\|\frac{7}{2},\pm\frac{1}{2}\right\rangle + 0.309\left\|\frac{7}{2},\mp\frac{7}{2}\right\rangle$
1108	$\phi_3^{\pm}(\gamma_7) = 0.867\left\|\frac{7}{2},\pm\frac{5}{2}\right\rangle - 0.418\left\|\frac{7}{2},\mp\frac{3}{2}\right\rangle \pm 0.261\left\|\frac{5}{2},\mp\frac{3}{2}\right\rangle$
1283	$\phi_4^{\pm}(\gamma_7) = 0.431\left\|\frac{7}{2},\pm\frac{5}{2}\right\rangle + 0.886\left\|\frac{7}{2},\mp\frac{3}{2}\right\rangle \mp 0.107\left\|\frac{9}{2},\pm\frac{5}{2}\right\rangle \pm 0.121\left\|\frac{9}{2},\mp\frac{3}{2}\right\rangle$
1309	$\psi_3^{\pm}(\gamma_6) = -0.315\left\|\frac{7}{2},\pm\frac{1}{2}\right\rangle + 0.943\left\|\frac{7}{2},\mp\frac{7}{2}\right\rangle$
2216	$\psi_4^{\pm}(\gamma_6) = 0.939\left\|\frac{9}{2},\pm\frac{1}{2}\right\rangle + 0.292\left\|\frac{9}{2},\pm\frac{9}{2}\right\rangle$
2330	$\psi_5^{\pm}(\gamma_6) = 0.986\left\|\frac{9}{2},\mp\frac{7}{2}\right\rangle - 0.100\left\|\frac{5}{2},\pm\frac{1}{2}\right\rangle$
2345	$\phi_5^{\pm}(\gamma_7) = -0.566\left\|\frac{9}{2},\pm\frac{5}{2}\right\rangle + 0.797\left\|\frac{9}{2},\mp\frac{3}{2}\right\rangle \mp 0.134\left\|\frac{7}{2},\mp\frac{3}{2}\right\rangle$
2486	$\phi_6^{\pm}(\gamma_7) = 0.805\left\|\frac{9}{2},\pm\frac{5}{2}\right\rangle + 0.568\left\|\frac{9}{2},\mp\frac{3}{2}\right\rangle \mp 0.112\left\|\frac{11}{2},\pm\frac{5}{2}\right\rangle \pm 0.109\left\|\frac{11}{2},\mp\frac{3}{2}\right\rangle$
2527	$\psi_6^{\pm}(\gamma_6) = 0.949\left\|\frac{9}{2},\pm\frac{9}{2}\right\rangle - 0.295\left\|\frac{9}{2},\pm\frac{1}{2}\right\rangle$

Table 6.16 : Energies of the Sm^{3+} ion in the SrF_2:Sm^{3+} C_{4v} centre, and JM-basis wavefunctions obtained by least-squares fit to the data of Wells [88]. †Calculated energy.

intermediate state	vibronic energy relative to Ψ (cm^{-1})	$C^{(2)}_{\pm 1}$ matrix element	$\Delta\mathcal{E}(\Psi_6^+) / (\alpha D_1^2)^2$ ($\times 10^{-4} / cm^{-1}$)
$\psi_2^+(000)$	52	−0.1132	−2.463
$\psi_3^+(000)$	371	−0.0381	−0.039
$\psi_4^+(000)$	1278	−0.0363	−0.010
$\psi_5^+(000)$	1392	−0.0000	−0.000
$\psi_6^+(000)$	1589	0.0114	−0.001
$\phi_1^+(110)$	973	−0.1137	−0.133
$\phi_2^+(110)$	1198	0.0620	−0.032
$\phi_3^+(110)$	2046	0.0652	−0.021
$\phi_4^+(110)$	2221	0.0651	−0.019
$\phi_5^+(110)$	3283	0.0287	−0.003
$\phi_6^+(110)$	3424	−0.0269	−0.002
total shift of Ψ_6^+			−2.722

intermediate state	vibronic energy relative to Ψ (cm^{-1})	$C^{(2)}_{\pm 1}$ matrix element	$\Delta\mathcal{E}(\Psi_7^+) / (\alpha D_1^2)^2$ ($\times 10^{-4} / cm^{-1}$)
$\phi_1^+(000)$	−903	−0.1137	0.143
$\phi_2^+(000)$	−678	0.0620	0.057
$\phi_3^+(000)$	170	0.0652	−0.250
$\phi_4^+(000)$	345	0.0651	−0.123
$\phi_5^+(000)$	1407	0.0287	−0.006
$\phi_6^+(000)$	1548	−0.0269	−0.005
$\psi_2^+(110)$	1928	−0.1132	−0.066
$\psi_3^+(110)$	2247	−0.0381	−0.006
$\psi_4^+(110)$	3154	−0.0363	−0.004
$\psi_5^+(110)$	3268	−0.0000	−0.000
$\psi_6^+(110)$	3465	0.0114	−0.000
total shift of Ψ_7^+			−0.261

Table 6.17 : Calculated energy shifts of the Ψ_6^+ and Ψ_7^+ states for SrF_2:Sm^{3+}:H^-

ones, the energy of the x-y vibration has shifted to the lower energy side of the ψ_2 electronic state, at 938 cm^{-1}. This state now pushes the Ψ_6 vibronic down in energy rather than up. Again the shift due to this intermediate state is the dominant factor, so the order of the two doublet vibronic states is the reverse of the CaF_2:Sm^{3+}:H^- case. In addition, this intermediate state is now further from the adopted position of the ψ_2 state, and so the x-y splitting should be less sensitive to the exact energies than it was for CaF_2:Sm^{3+}:H^-.

6.4.4 CaF_2:Dy^{3+}:H^-

The infrared absorption spectrum of the x-y mode in CaF_2:0.01%Dy^{3+} hydrogenated for 7 hours is shown in figure 6.11, showing a measured splitting of 0.42 cm^{-1}.

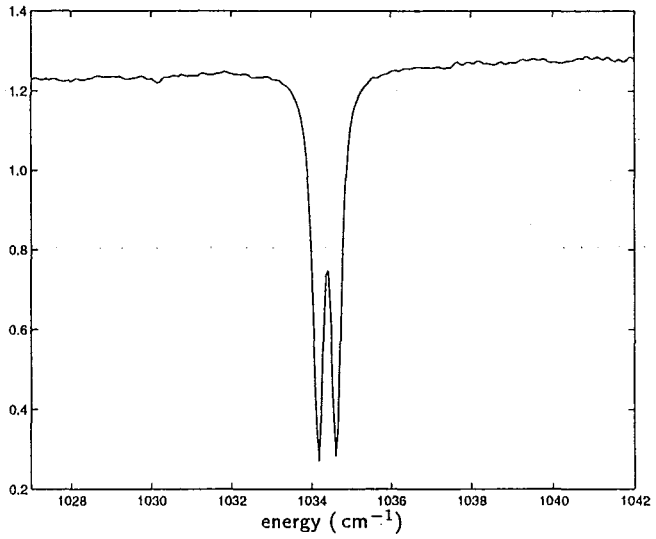

Figure 6.11 : Infrared-absorption spectrum of the x-y splitting in CaF_2:0.01%Dy^{3+}:H^-(7 hrs).

No data has been reported on the CaF_2:Dy^{3+}:H^- system, and furthermore, very little reliable data on the parent CaF_2:Dy^{3+} system seems to exist. Bierig and Weber [11] have reported the EPR spectrum of a tetragonal centre in CaF_2:Dy^{3+} with g-values of $g_{\parallel} = 1.78$ and $g_{\perp} = 2.84$, while several authors [55, 68, 5, 82] have reported optical spectroscopy of tetragonal centres. However, there is much disagreement on the

assignment of centres, and none of the proposed energy-level schemes yield crystal field parameters consistent with the EPR g-values or with parameters obtained for other CaF_2:RE^{3+} C_{4v} centres. Antipin *et al* [5] reported that no resonances could be found in CaF_2:Dy^{3+} which could correspond to a tetragonal centre, and noted that the g-values reported by Bierig and Weber [11] could correspond to a tetragonal Nd^{3+}–Na^+ centre previously reported by McLaughlan [61].

With this in mind, crystal field parameters are here estimated by interpolation from the F^- compensated C_{4v} centre fits for terbium [66] and holmium [64] (see table 4.11). In varying the parameters between these two extremes, the $^6H_{15/2}$ energies and wavefunctions did not change greatly; those obtained using the mid-point parameters of table 6.18, are given in table 6.19.

parameter	value (cm^{-1})	parameter	value (cm^{-1})
B_C^4	−1208	B_A^2	746
B_C^6	591	B_A^4	430
		B_A^6	432

Table 6.18 : Crystal-field parameters used to calculate CaF_2:Dy^{3+} C_{4v} centre energies and wavefunctions, interpolated from the parameters reported for CaF_2:Tb^{3+} [66] and CaF_2:Ho^{3+} [64].

The wavefunctions in table 6.19 have been truncated at terms with coefficients of less than 0.1. The full calculated ground-state wavefunction gives the g-values as

$$g_{\parallel} = 17.12 \ , \ g_{\perp} = 0.036$$

which agree well with the wavefunction obtained by Antipin *et al* [5], despite the fact that the $^6H_{15/2}$ energy levels are quite different.

The form of the ground-state wavefunction in table 6.19 also explains the absence of an observed EPR resonance for this centre. The transition to be measured in an EPR experiment, $\phi_1^- \leftrightarrow \phi_1^+$, cannot proceed by an electric-dipole or magnetic-dipole-operator matrix element, since the rank 1 operator can only connect states with $\Delta m = 0, \pm 1$. This is related to the small value of $g_{\perp}$, since the Zeeman operator has the same form as the magnetic-dipole operator. In fact, the wavefunction does

energy (cm^{-1})	wavefunctions
0	$\phi_1^{\pm}(\gamma_7) = 0.992\left\|\pm\frac{13}{2}\right\rangle + 0.107\left\|\pm\frac{5}{2}\right\rangle$
104	$\phi_2^{\pm}(\gamma_7) = 0.996\left\|\mp\frac{11}{2}\right\rangle$
148	$\psi_1^{\pm}(\gamma_6) = 0.224\left\|\pm\frac{9}{2}\right\rangle - 0.291\left\|\pm\frac{1}{2}\right\rangle + 0.411\left\|\mp\frac{7}{2}\right\rangle + 0.833\left\|\mp\frac{15}{2}\right\rangle$
199	$\psi_2^{\pm}(\gamma_6) = 0.724\left\|\pm\frac{9}{2}\right\rangle - 0.445\left\|\pm\frac{1}{2}\right\rangle + 0.239\left\|\mp\frac{7}{2}\right\rangle - 0.467\left\|\mp\frac{15}{2}\right\rangle$
233	$\phi_3^{\pm}(\gamma_7) = 0.107\left\|\pm\frac{13}{2}\right\rangle - 0.708\left\|\pm\frac{5}{2}\right\rangle + 0.692\left\|\mp\frac{3}{2}\right\rangle$
295	$\psi_3^{\pm}(\gamma_6) = 0.609\left\|\pm\frac{9}{2}\right\rangle + 0.355\left\|\pm\frac{1}{2}\right\rangle - 0.646\left\|\mp\frac{7}{2}\right\rangle + 0.279\left\|\mp\frac{15}{2}\right\rangle$
569	$\psi_4^{\pm}(\gamma_6) = 0.221\left\|\pm\frac{9}{2}\right\rangle + 0.767\left\|\pm\frac{1}{2}\right\rangle + 0.592\left\|\mp\frac{7}{2}\right\rangle$
613	$\phi_4^{\pm}(\gamma_7) = 0.694\left\|\pm\frac{5}{2}\right\rangle + 0.714\left\|\mp\frac{3}{2}\right\rangle$

Table 6.19 : $^6H_{15/2}$-multiplet energies and wavefunctions of the Dy^{3+} ion in the CaF_2:Dy^{3+} C_{4v} centre, calculated using the interpolated crystal-field parameters of table 6.18.

have small (< 0.1) $\left|\mp\frac{3}{2}\right\rangle$ and $\left|\mp\frac{11}{2}\right\rangle$ components giving a non-zero matrix element. The parallel Zeeman effect, on the other hand, gains its splitting from diagonal matrix elements, and the dominance of a component with large m gives the large value of $g_{\|}$.

The $C_{\pm1}^{(2)}$ matrix elements of the intermediate vibronic states with the x-y vibronic states and the calculated second order shift due to each of these intermediate states is given in table 6.20.

The αD_1^2 parameter is fitted by equating the total combined calculated x-y splitting from table 6.20 with the measured splitting

$$\Delta\mathcal{E}_7 - \Delta\mathcal{E}_6 = 0.278\times10^{-4}\,(\alpha D_1^2)^2 = 0.42\,cm^{-1}$$

giving the value for αD_1^2:

$$\alpha D_1^2 = 123\,cm^{-1} \qquad \text{(fitted)}.$$

The point-charge model would give a calculated value for this parameter of

$$\alpha D_1^2 = \alpha\sqrt{3}\,\frac{kqe}{D^4}\,\langle r^2\rangle = 67\,cm^{-1} \qquad \text{(point-charge model)}.$$

intermediate state	vibronic energy relative to Φ (cm^{-1})	$C^{(2)}_{\pm 1}$ matrix element	$\Delta\mathcal{E}(\Phi_6^+) / (\alpha D_1^2)^2$ ($\times 10^{-4} / cm^{-1}$)
$\psi_1^+(000)$	-886	0.1783	0.359
$\psi_2^+(000)$	-835	-0.0913	0.100
$\psi_3^+(000)$	-739	0.0455	0.028
$\psi_4^+(000)$	-465	0.0108	0.002
$\phi_2^+(110)$	1138	0.2391	-0.502
$\phi_3^+(110)$	1267	0.0088	-0.001
$\phi_4^+(110)$	1647	0.0091	-0.000
total shift of Φ_6^+			-0.014
intermediate state	vibronic energy relative to Φ (cm^{-1})	$C^{(2)}_{\pm 1}$ matrix element	$\Delta\mathcal{E}(\Phi_7^+) / (\alpha D_1^2)^2$ ($\times 10^{-4} / cm^{-1}$)
$\phi_2^+(000)$	-930	0.2391	0.614
$\phi_3^+(000)$	-801	0.0088	0.001
$\phi_4^+(000)$	-421	0.0091	0.002
$\psi_1^+(110)$	1182	0.1783	-0.269
$\psi_2^+(110)$	1233	-0.0913	-0.068
$\psi_3^+(110)$	1329	0.0455	-0.016
$\psi_4^+(110)$	1603	0.0108	-0.001
total shift of Φ_7^+			0.265

Table 6.20 : Calculated energy shifts of the Φ_6^+ and Φ_7^+ states for CaF_2:Dy^{3+}:H^-

giving a discrepancy of a factor of 1.8 between these two. This discrepancy is still reasonable, especially given the lack of definitive data on the CaF_2:Dy^{3+}:H^- system and the estimated energies and wavefunctions which had to be assumed because of this.

6.4.5 CaF_2:Yb^{3+}:H^-

The Yb^{3+} ion has a tendency to be reduced to the Yb^{2+} form, especially in the hydrogenation process where the aluminium metal acts as a reducing agent. Because of this, the Yb^{3+}-H^- C_{4v} centre is difficult to produce in the same concentrations as for the other lanthanides, and the vibrational modes associated with the H^- ion in this site were not included in the work by Jones *et al* [44]. A pattern of four H^- vibrational lines were observed at 1043.4, 1049.8, 1074.6 and 1100.7 cm^{-1} at 80 K by Chambers and Newman [16] and attributed to the Yb^{3+}-H^- C_{4v} centre. The pair at 1043.4 and 1074.6 cm^{-1} were found to increase at the expense of the other two as the temperature was lowered to 4.2 K, suggesting the possibility of a low-lying electronic state.

In the infrared-absorption spectrum of CaF_2:0.01%Yb^{3+}:H^- hydrogenated for 30 hours obtained in the current work, figure 6.12, only one of these four lines, centred at 1049.0 cm^{-1}, was observed at 10 K. This is about the energy expected for the x-y absorption line, if the data for the other lanthanides [44] is extrapolated. When measured in the higher resolution now available, this line displayed the splitting characteristic of the C_{4v} x-y vibronics, in this case a splitting of 0.70 cm^{-1}(figure 6.13). The behaviour of this doublet in a magnetic field, as described in chapter 7, is also entirely consistent with being the x-y line of the Yb^{3+}-H^- C_{4v} centre. However, the absence from the spectrum of figure 6.12 of an obvious candidate for the z-mode absorption is anomalous. No sharp lines appear on the high energy side of the x-y-mode, in the region where the z-mode absorption line would be expected to be found [44]. The number of lines on the low energy side of the x-y line is greater than seen for the other lanthanides, but this is expected since a much higher concentration of H^- ions is present. It is possible that one of these lines could be the z-mode absorption, the best candidate being at 1031.4 cm^{-1}, but this would be against the trend set by the other lanthanides [44].

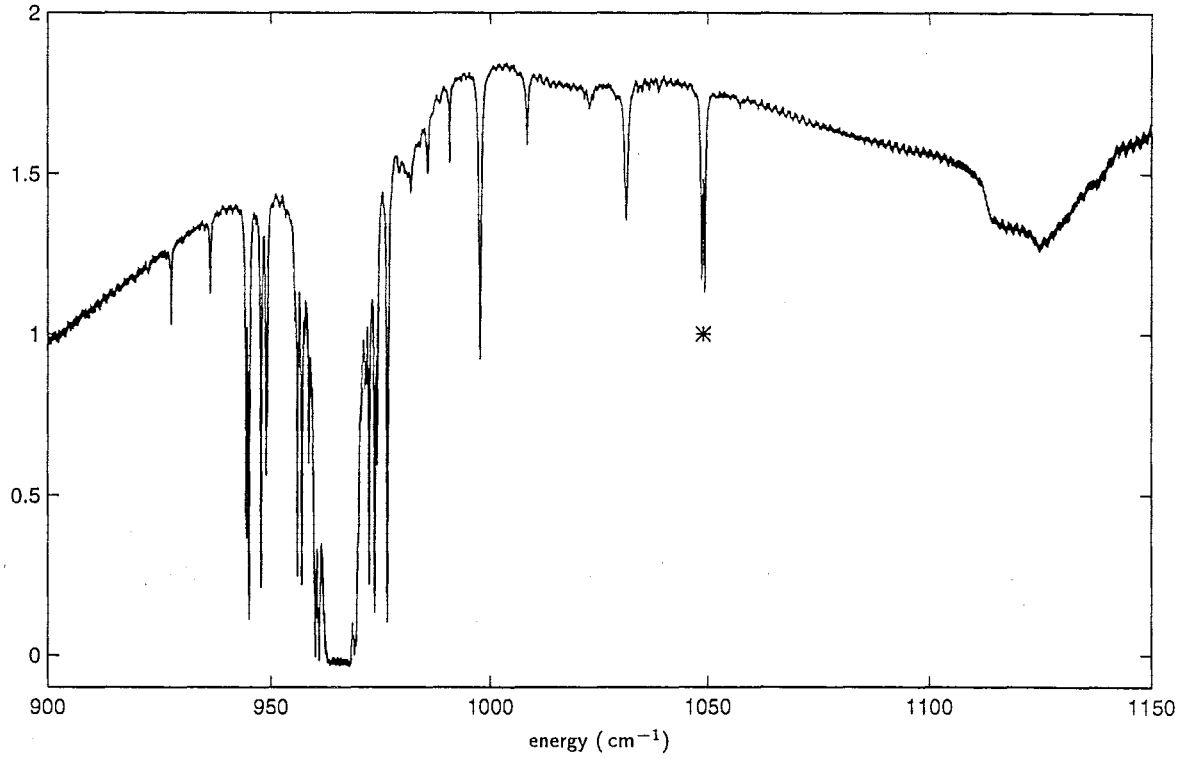

Figure 6.12 : Infrared-absorption spectrum of CaF_2:0.01%Yb^{3+}:H^-(30 hrs). The line labelled * is assigned to the x-y vibrational mode of the Yb^{3+}-H^- C_{4v} centre; the other lines reported by Chambers and Newman [16] are not present.

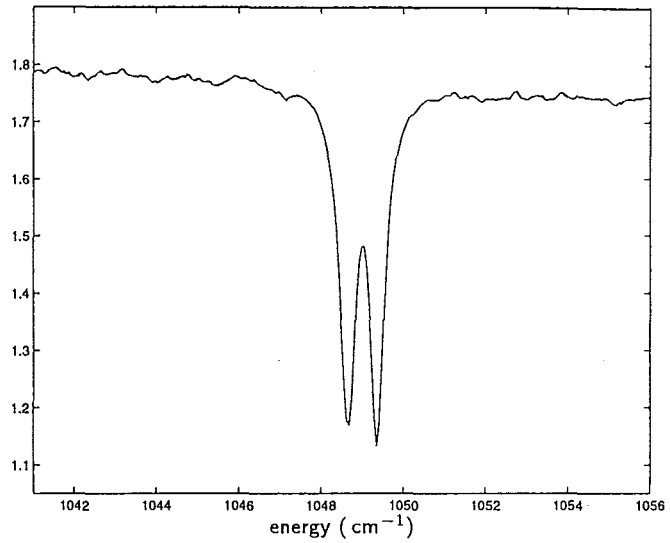

Figure 6.13 : Infrared-absorption spectrum of the x-y splitting in CaF_2:0.01%Yb^{3+}:H^-(30 hrs).

Despite this anomaly, the fact that this doublet is magnetically active indicates that it is associated with a trivalent Yb^{3+} ion, since Yb^{2+} has a full $4f$ shell and should not have a magnetic ground state, and the C_{4v} centre would be expected to be the dominant such centre involving H^- ions.

Calculations of the x-y splitting for CaF_2:Yb^{3+}:H^- can only be rather tentative, since the only relevant data on the electronic states of either the H^- of F^- compensated C_{4v} centres arises from the EPR [50] and ENDOR [8] resonances of the ground state in the F^- C_{4v} centre.

The ENDOR of the CaF_2:Yb^{3+} F^- compensated C_{4v} centre has been reported by Baker and Blake [8], including an estimate of the crystal field parameters. A crystal field calculation using these parameters yields the $^2F_{7/2}$ energies and wavefunctions listed in table 6.21, which are tentatively adopted here for the H^- compensated centre.

The ground state is calculated to be a γ_7 state. Matrix elements and the contribution to the energy shifts from each of the intermediate states is given in table 6.22, with

energy (cm^{-1})	wavefunctions
0	$\phi_1^{\pm}(\gamma_7) = -0.737\left\|\frac{7}{2},\pm\frac{5}{2}\right\rangle + 0.675\left\|\frac{7}{2},\mp\frac{3}{2}\right\rangle$
197	$\psi_1^{\pm}(\gamma_6) = 0.992\left\|\frac{7}{2},\pm\frac{1}{2}\right\rangle + 0.127\left\|\frac{7}{2},\mp\frac{7}{2}\right\rangle$
413	$\phi_2^{\pm}(\gamma_7) = 0.675\left\|\frac{7}{2},\pm\frac{5}{2}\right\rangle + 0.737\left\|\frac{7}{2},\mp\frac{3}{2}\right\rangle$
431	$\psi_2^{\pm}(\gamma_6) = 0.127\left\|\frac{7}{2},\pm\frac{1}{2}\right\rangle - 0.992\left\|\frac{7}{2},\mp\frac{7}{2}\right\rangle$

Table 6.21 : Calculated energies and wavefunctions of the Yb^{3+} ion in the CaF_2:Yb^{3+} C_{4v} centre, from the parameters of Baker and Blake [8].

intermediate state	vibronic energy relative to Φ (cm^{-1})	$C_{\pm1}^{(2)}$ matrix element	$\Delta\mathcal{E}(\Phi_6^+)\,/\,(\alpha D_1^2)^2$ ($\times10^{-4}\,/\,cm^{-1}$)
$\psi_1^+(000)$	-852	0.1298	0.198
$\psi_2^+(000)$	-618	-0.2128	0.733
$\phi_2^+(110)$	1462	0.2694	-0.496
total shift of Φ_6^+			0.434
intermediate state	vibronic energy relative to Φ (cm^{-1})	$C_{\pm1}^{(2)}$ matrix element	$\Delta\mathcal{E}(\Phi_7^+)\,/\,(\alpha D_1^2)^2$ ($\times10^{-4}\,/\,cm^{-1}$)
$\phi_2^+(000)$	-636	0.2694	1.141
$\psi_1^+(110)$	1246	0.1298	-0.135
$\psi_2^+(110)$	1480	-0.2128	-0.306
total shift of Φ_7^+			0.700

Table 6.22 : Calculated energy shifts of the Φ_6^+ and Φ_7^+ states for CaF_2:Yb^{3+}:H^-

the comparison between the total calculated splitting and the measured splitting:

$$\Delta\mathcal{E}_7 - \Delta\mathcal{E}_6 \;=\; 0.265{\times}10^{-4}\,(\alpha D_1^2)^2 \;=\; 0.70\,\mathrm{cm}^{-1}$$

giving a fitted value for αD_1^2 of

$$\alpha D_1^2 = 163\,\mathrm{cm}^{-1} \qquad \text{(fitted)}.$$

The point-charge model gives a calculated value for this parameter of

$$\alpha D_1^2 \;=\; \alpha\sqrt{3}\,\frac{kqe}{D^4}\,\langle r^2\rangle \;=\; 56\,\mathrm{cm}^{-1} \qquad \text{(point-charge model)}$$

which is a factor of 2.9 less than the fitted value. This is a large mismatch, however the crystal-field wavefunctions and energies are very tentative in this case. These calculations should be repeated when a more reliable crystal-field parametrisation is available.

6.4.6 CaF_2:Er^{3+}:H^-

As mentioned previously, the splitting of the x-y vibronic lines of CaF_2:Er^{3+}:H^- is complicated by the presence of a low-lying first excited state at $4.5\,\mathrm{cm}^{-1}$. At the temperatures at which these measurements were carried out, the first excited state will have a significant population and local-mode absorption lines associated with both the ground state and the first excited state are seen in the infrared-absorption spectrum of CaF_2:0.01%Er^{3+} hydrogenated for 7 hours (figure 6.14). These two local modes are separated by $1.47\,\mathrm{cm}^{-1}$, with temperature dependences showing that the lower-energy one is associated with the Z_1 electronic state and the higher with the Z_2 electronic state. The Z_1 x-y line has a splitting of $0.42\,\mathrm{cm}^{-1}$ while the splitting of the Z_2 x-y line is not resolved at the $0.1\,\mathrm{cm}^{-1}$ resolution available. Since purely vibrational transitions are very much stronger than vibronic transitions which involve a change in both electronic and vibrational states, the two "cross" transitions, at $1033.6\,\mathrm{cm}^{-1}$ and $1043.8\,\mathrm{cm}^{-1}$ and indicated by * in figure 6.14, are weak. The intensity of these two transitions is enhanced by admixtures between the Ψ and Φ states from the first-order perturbation matrix of the electron-phonon interaction.

With this low-lying electronic state present, extra contributions to the splittings arise in both first and second order. Because these extra contributions are parametrised

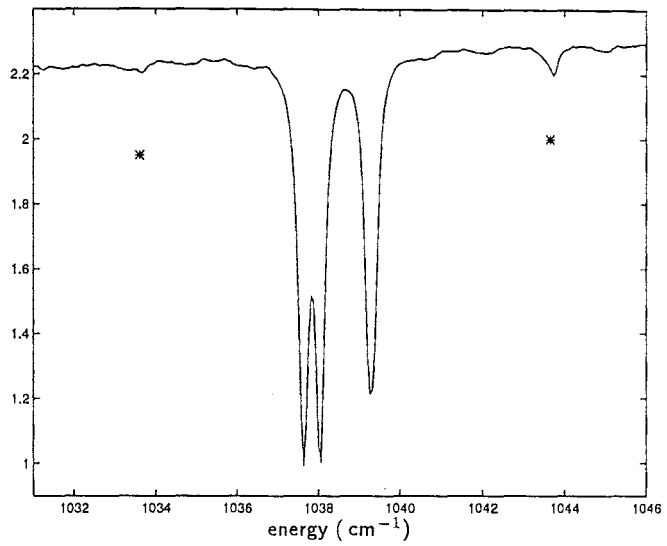

Figure 6.14 : Infrared-absorption spectrum of the x-y splitting in CaF_2:0.01%Er^{3+}:H^-(7 hrs). The weak vibronic transitions between states with different electronic wavefunctions are indicated by *.

by different coefficients of the electron-phonon interaction Hamiltonian, it will not be possible to determine each of these parameters independently, as could be done with the single parameter for the isolated-ground-state cases. Instead, the calculations are presented here with the point-charge model values assumed for these parameters, and this full calculation is then compared with the measured splittings.

The g-values for the ground state and first excited state have been reported by Edgar *et al* [25], and detailed optical and laser spectroscopy of this centre has been carried out by Cockroft *et al* [21], including a crystal field fit of the $^4I_{15/2}$(Z) and $^4I_{13/2}$(Y) multiplets. $^4I_{15/2}$ wavefunctions calculated using the reported parameters are given in table 6.23. The ground state was found to transform as γ_7 and the first excited state as γ_6.

Some of the contributions to the perturbations of the x-y vibronic states gave uniform shifts for the other Kramers ions and were therefore neglected. However for Er^{3+}, the shift may be different for the Φ and Ψ states and must therefore be considered. We thus have contributions in first as well as second order.

energy (cm^{-1})	wavefunctions
0	$\phi_1^{\pm}(\gamma_7) = -0.7165\left\|\pm\frac{13}{2}\right\rangle - 0.5026\left\|\pm\frac{5}{2}\right\rangle + 0.4090\left\|\mp\frac{3}{2}\right\rangle + 0.2562\left\|\mp\frac{11}{2}\right\rangle$
4.5	$\psi_1^{\pm}(\gamma_6) = 0.2301\left\|\pm\frac{9}{2}\right\rangle + 0.9710\left\|\pm\frac{1}{2}\right\rangle$
25.8	$\phi_2^{\pm}(\gamma_7) = 0.4208\left\|\pm\frac{13}{2}\right\rangle + 0.2388\left\|\pm\frac{5}{2}\right\rangle + 0.7169\left\|\mp\frac{3}{2}\right\rangle + 0.5005\left\|\mp\frac{11}{2}\right\rangle$
279.1	$\psi_2^{\pm}(\gamma_6) = 0.7446\left\|\mp\frac{7}{2}\right\rangle + 0.6646\left\|\mp\frac{15}{2}\right\rangle$
376.5	$\phi_3^{\pm}(\gamma_7) = 0.1418\left\|\pm\frac{13}{2}\right\rangle - 0.1752\left\|\pm\frac{5}{2}\right\rangle + 0.5408\left\|\mp\frac{3}{2}\right\rangle - 0.8103\left\|\mp\frac{11}{2}\right\rangle$
423.0	$\phi_4^{\pm}(\gamma_7) = 0.5369\left\|\pm\frac{13}{2}\right\rangle - 0.8117\left\|\pm\frac{5}{2}\right\rangle - 0.1589\left\|\mp\frac{3}{2}\right\rangle + 0.1635\left\|\mp\frac{11}{2}\right\rangle$
426.5	$\psi_3^{\pm}(\gamma_6) = 0.9722\left\|\pm\frac{9}{2}\right\rangle - 0.2313\left\|\pm\frac{1}{2}\right\rangle$
590†	$\psi_4^{\pm}(\gamma_6) = 0.6650\left\|\mp\frac{7}{2}\right\rangle - 0.7457\left\|\mp\frac{15}{2}\right\rangle$

Table 6.23 : Energies and wavefunctions of the Er^{3+} ion in the CaF_2:Er^{3+}:H^- C_{4v} centre, obtained by least-squares fit to the data of Cockroft *et al* [21]. † Calculated energy.

First-Order Perturbations by Second-Degree Terms of the Electron-Phonon Interaction

The matrix formed between these states will contribute a first order perturbation. The diagonal matrix elements will be different for the Φ and Ψ states, giving a shift between the two local-mode energies, and there will be off diagonal matrix elements connecting states with the same C_4 irrep label. The matrix is

	$\phi_1^-[+]$	$\phi_1^+[-]$	$\phi_1^-[-]$	$\phi_1^+[+]$	$\psi_1^-[+]$	$\psi_1^+[-]$	$\psi_1^-[-]$	$\psi_1^+[+]$
$\phi_1^-[+]$	$-\Delta+E_1$						$A-B$	
$\phi_1^+[-]$		$-\Delta+E_1$						$A-B$
$\phi_1^-[-]$			$-\Delta+E_1$		$A+B$			
$\phi_1^+[+]$				$-\Delta+E_1$		$A+B$		
$\psi_1^-[+]$			$A+B$		$\Delta+E_2$			
$\psi_1^+[-]$				$A+B$		$\Delta+E_2$		
$\psi_1^-[-]$	$A-B$						$\Delta+E_2$	
$\psi_1^+[+]$		$A-B$						$\Delta+E_2$

where 2Δ is the splitting between the electronic states ($4.5\,cm^{-1}$), and

$$E_1 = (2\alpha^2-\beta^2)\left\langle\phi_1^+\right|g_{[\pm]}\left|\phi_1^+\right\rangle = (2\alpha^2-\beta^2)E_0^2\left\langle\phi_1^+\right|C_0^{(2)}\left|\phi_1^+\right\rangle$$
$$E_2 = (2\alpha^2-\beta^2)\left\langle\psi_1^+\right|g_{[\pm]}\left|\psi_1^+\right\rangle = (2\alpha^2-\beta^2)E_0^2\left\langle\psi_1^+\right|C_0^{(2)}\left|\psi_1^+\right\rangle$$

$$\begin{aligned} A &= 2\alpha^2\left\langle\psi_1^+\right| g_{X_+{}^2+X_-{}^2} \left|\phi_1^+\right\rangle = 2\alpha^2 E_1^2\left\langle\psi_1^+\right|C_{-2}^{(2)} + C_2^{(2)}\left|\phi_1^+\right\rangle \\ B &= -2\alpha^2\left\langle\psi_1^+\right| g_{X_+{}^2-X_-{}^2} \left|\phi_1^+\right\rangle = 2\alpha^2 E_1^2\left\langle\psi_1^+\right|C_{-2}^{(2)} - C_2^{(2)}\left|\phi_1^+\right\rangle \end{aligned}$$

where we have inserted vibrational matrix elements

$$\begin{aligned} \langle[\pm]|X_+X_-|[\pm]\rangle &= 2\alpha^2 \\ \langle[\pm]|Z^2|[\pm]\rangle &= \beta^2 \\ \langle[\mp]|(X_+{}^2 + X_-{}^2)|[\pm]\rangle &= 2\alpha^2 \\ \langle[\mp]|(X_+{}^2 - X_-{}^2)|[\pm]\rangle &= \mp 2\alpha^2 \end{aligned}$$

and we have used the relation $g_{[\pm]} = -g_{z^2}$ which necessarily follows from Laplace's equation, $\nabla^2 V = 0$, for a point-charge model.

Using the calculated wavefunctions and point-charge model values for the constants in the g coefficients, we insert values

$$\begin{aligned} E_1 &= -0.18\,\mathrm{cm}^{-1} \\ E_2 &= 0.83\,\mathrm{cm}^{-1} \\ A &= 0.054\,\mathrm{cm}^{-1} \\ B &= 0.182\,\mathrm{cm}^{-1} \end{aligned}$$

yielding energy eigenvalues of -2.440, -2.433, 3.083, $3.090\,\mathrm{cm}^{-1}$. With these matrix element values the wavefunctions remain better than 99% pure.

Second-Order Perturbations by First-Degree Terms of the Electron-Phonon Interaction

Second-order perturbations due to the first-degree electron-phonon interaction terms connecting to intermediate states involving (000) and (110) vibrational states arise as with the Ce^{3+} and Sm^{3+} cases. In addition, there are contributions which for Ce^{3+} and Sm^{3+} shifted all the states uniformly and could therefore be ignored. In the case of Er^{3+} however, these will produce different shifts for the Φ and Ψ states and hence must be included. These extra shifts arise from the f_zZ term acting on $(101)\pm i(011)$ intermediate states, and the $f_+X_- + f_-X_+$ terms acting on $(200)\pm(020)$ intermediate states.

The calculated second order shifts due to these terms are listed in tables 6.24 and 6.25.

In addition, the ϕ_2 state at $25.8\,cm^{-1}$ is sufficiently low in energy that second-order effects due to the second-degree Hamiltonian connecting with the $\phi_2[\pm]$ vibronics are significant.

For the $\Phi_{6/7}$ vibronics, these second degree shifts are identical and take the form

$$\begin{aligned}\Delta\mathcal{E}(\Phi_{6/7}) &= \frac{\left|\left\langle\phi_2^-[-]\right|\, g_{[+-]}\, X_+X_- + g_{Z^2}\, Z^2\left|\phi_1^-[-]\right\rangle\right|^2}{\mathcal{E}_{\phi_1}-\mathcal{E}_{\phi_2}} \\ &= \frac{(2\alpha^2-\beta^2)^2(E_0^2)^2\left|\left\langle\phi_2^-\left|C_0^{(2)}\right|\phi_1^-\right\rangle\right|^2}{\mathcal{E}_{\phi_1}-\mathcal{E}_{\phi_2}}\end{aligned}$$

For the Ψ_6 vibronics, the shift is given by

$$\begin{aligned}\Delta\mathcal{E}(\Psi_6) &= \frac{\left|\left\langle\phi_2^-[-]\right|\, g_{X_+^2+X_-^2}(X_+^2+X_-^2) + g_{X_+^2-X_-^2}(X_+^2-X_-^2)\left|\psi_1^-[+]\right\rangle\right|^2}{\mathcal{E}_{\psi_1}-\mathcal{E}_{\phi_2}} \\ &= \frac{16\alpha^4(E_1^2)^2\left|\left\langle\phi_2^-\left|C_2^{(2)}\right|\psi_1^-\right\rangle\right|^2}{\mathcal{E}_{\psi_1}-\mathcal{E}_{\phi_2}}\end{aligned}$$

while for the Ψ_7 vibronics it is

$$\begin{aligned}\Delta\mathcal{E}(\Psi_6) &= \frac{\left|\left\langle\phi_2^-[+]\right|\, g_{X_+^2+X_-^2}(X_+^2+X_-^2) + g_{X_+^2-X_-^2}(X_+^2-X_-^2)\left|\psi_1^-[-]\right\rangle\right|^2}{\mathcal{E}_{\psi_1}-\mathcal{E}_{\phi_2}} \\ &= \frac{16\alpha^4(E_1^2)^2\left|\left\langle\phi_2^-\left|C_{-2}^{(2)}\right|\psi_1^-\right\rangle\right|^2}{\mathcal{E}_{\psi_1}-\mathcal{E}_{\phi_2}}\end{aligned}$$

With the point-charge model values of the E_0^2 and E_1^2 coefficients, these terms shift the Φ_6, Φ_7, Ψ_6 and Ψ_7 states by -0.036, -0.036, 0.077 and $0.029\,cm^{-1}$ respectively.

The total calculated energy shifts are summarised in table 6.26. The larger splitting between the Ψ and Φ vibronics appears to be in reasonable agreement with experiment. However the calculated splitting of the lower of these two pairs is too small by a factor of 30 to account for the $0.4\,cm^{-1}$ splitting observed in figure 6.14. Further, the splitting of the Ψ doublet is calculated to be larger than that of the Φ doublet, when the spectrum indicates the reverse to be true. Thus it would be necessary to scale each of the contributions differently in order to achieve the appropriate

intermediate state	vibronic energy relative to Φ (cm^{-1})	matrix element (cm^{-1})	energy shift of Φ_6^+ (cm^{-1})
$\psi_1^+(000)$	−1034	1.07	.0011
$\psi_2^+(000)$	−759	4.22	.0234
$\psi_3^+(000)$	−612	1.50	.0037
$\psi_4^+(000)$	−448	1.39	.0043
$\phi_2^+(110)$	1064	4.46	−.0187
$\phi_3^+(110)$	1415	2.79	−.0055
$\phi_4^+(110)$	1461	0.35	−.0001
$\psi_1^+\frac{1}{\sqrt{2}}[(200)+(020)]$	1043	1.07	−.0011
$\psi_2^+\frac{1}{\sqrt{2}}[(200)+(020)]$	1317	4.22	−.0135
$\psi_3^+\frac{1}{\sqrt{2}}[(200)+(020)]$	1465	1.50	−.0015
$\psi_4^+\frac{1}{\sqrt{2}}[(200)+(020)]$	1628	1.39	−.0019
$\phi_2^+\frac{1}{\sqrt{2}}[(200)-(020)]$	1064	4.46	−.0187
$\phi_3^+\frac{1}{\sqrt{2}}[(200)-(020)]$	1415	2.79	−.0055
$\phi_4^+\frac{1}{\sqrt{2}}[(200)-(020)]$	1461	0.35	−.0001
$\phi_2^-\frac{1}{\sqrt{2}}[(101)-i(011)]$	1064	2.71	−.0066
$\phi_3^-\frac{1}{\sqrt{2}}[(101)-i(011)]$	1415	4.11	−.0116
$\phi_4^-\frac{1}{\sqrt{2}}[(101)-i(011)]$	1461	5.17	−.0177
total second order shift of Φ_6^+			−0.0700

intermediate state	vibronic energy relative to Φ (cm^{-1})	matrix element (cm^{-1})	energy shift of Φ_7^+ (cm^{-1})
$\phi_2^+(000)$	−1012	4.46	.0196
$\phi_3^+(000)$	−662	2.79	.0117
$\phi_4^+(000)$	−615	0.35	.0002
$\psi_1^+(110)$	1043	1.07	−.0011
$\psi_2^+(110)$	1317	4.22	−.0135
$\psi_3^+(110)$	1465	1.50	−.0015
$\psi_4^+(110)$	1628	1.39	−.0012
$\phi_2^+\frac{1}{\sqrt{2}}[(200)+(020)]$	1064	4.46	−.0187
$\phi_3^+\frac{1}{\sqrt{2}}[(200)+(020)]$	1415	2.79	−.0055
$\phi_4^+\frac{1}{\sqrt{2}}[(200)+(020)]$	1461	0.35	−.0002
$\psi_1^+\frac{1}{\sqrt{2}}[(200)-(020)]$	1043	1.07	−.0011
$\psi_2^+\frac{1}{\sqrt{2}}[(200)-(020)]$	1317	4.22	−.0135
$\psi_3^+\frac{1}{\sqrt{2}}[(200)-(020)]$	1465	1.50	−.0015
$\psi_4^+\frac{1}{\sqrt{2}}[(200)-(020)]$	1628	1.39	−.0012
$\phi_2^-\frac{1}{\sqrt{2}}[(101)+i(011)]$	1064	2.71	−.0066
$\phi_3^-\frac{1}{\sqrt{2}}[(101)+i(011)]$	1415	4.11	−.0116
$\phi_4^-\frac{1}{\sqrt{2}}[(101)+i(011)]$	1461	5.17	−.0177
total second order shift of Φ_7^+			−0.0634

Table 6.24 : Calculated energy shifts of the Φ_6^+ and Φ_7^+ states for CaF_2:Er^{3+}:H^-

intermediate state	vibronic energy relative to Ψ (cm^{-1})	matrix element (cm^{-1})	energy shift of Ψ_6^+ (cm^{-1})
$\psi_2^+(000)$	−764	0.97	.0012
$\psi_3^+(000)$	−617	0.00	.0000
$\psi_4^+(000)$	−453	0.85	.0016
$\phi_1^+(110)$	1033	1.06	−.0011
$\phi_2^+(110)$	1059	1.83	−.0031
$\phi_3^+(110)$	1410	0.34	−.0001
$\phi_4^+(110)$	1456	0.00	−.0000
$\psi_2^+\frac{1}{\sqrt{2}}[(200)+(020)]$	1312	0.97	−.0007
$\psi_3^+\frac{1}{\sqrt{2}}[(200)+(020)]$	1460	0.00	−.0000
$\psi_4^+\frac{1}{\sqrt{2}}[(200)+(020)]$	1623	0.85	−.0004
$\phi_1^+\frac{1}{\sqrt{2}}[(200)-(020)]$	1033	1.06	−.0011
$\phi_2^+\frac{1}{\sqrt{2}}[(200)-(020)]$	1059	1.83	−.0031
$\phi_3^+\frac{1}{\sqrt{2}}[(200)-(020)]$	1410	0.34	−.0001
$\phi_4^+\frac{1}{\sqrt{2}}[(200)-(020)]$	1456	0.00	−.0000
$\psi_2^-\frac{1}{\sqrt{2}}[(101)+i(011)]$	1312	0.00	−.0000
$\psi_3^-\frac{1}{\sqrt{2}}[(101)+i(011)]$	1460	1.88	−0.0023
$\psi_4^-\frac{1}{\sqrt{2}}[(101)+i(011)]$	1423	0.00	−.0000
total second order shift of Ψ_6^+			−0.0092

intermediate state	vibronic energy relative to Ψ (cm^{-1})	matrix element (cm^{-1})	energy shift of Ψ_7^+ (cm^{-1})
$\phi_1^+(000)$	−1043	1.06	.0011
$\phi_2^+(000)$	−1017	1.83	.0033
$\phi_3^+(000)$	−667	0.34	.0002
$\phi_4^+(000)$	−620	0.00	.0000
$\psi_2^+(110)$	1312	0.97	−.0007
$\psi_3^+(110)$	1460	0.00	−.0000
$\psi_4^+(110)$	1623	0.85	−.0004
$\phi_1^+\frac{1}{\sqrt{2}}[(200)+(020)]$	1033	1.06	−.0011
$\phi_2^+\frac{1}{\sqrt{2}}[(200)+(020)]$	1059	1.83	−.0031
$\phi_3^+\frac{1}{\sqrt{2}}[(200)+(020)]$	1410	0.34	−.0001
$\phi_4^+\frac{1}{\sqrt{2}}[(200)+(020)]$	1456	0.00	−.0000
$\psi_2^+\frac{1}{\sqrt{2}}[(200)-(020)]$	1312	0.97	−.0007
$\psi_3^+\frac{1}{\sqrt{2}}[(200)-(020)]$	1460	0.00	−.0000
$\psi_4^+\frac{1}{\sqrt{2}}[(200)-(020)]$	1623	0.85	−.0004
$\psi_2^-\frac{1}{\sqrt{2}}[(101)-i(011)]$	1312	0.00	−.0000
$\psi_3^-\frac{1}{\sqrt{2}}[(101)-i(011)]$	1460	1.88	−0.0023
$\psi_4^-\frac{1}{\sqrt{2}}[(101)-i(011)]$	1423	0.00	−.0000
total second order shift of Ψ_7^+			−0.0042

Table 6.25 : Calculated energy shifts of the Ψ_6^+ and Ψ_7^+ states for CaF_2:Er^{3+}:H^-

state	first order (cm^{-1})	second order (first degree) (cm^{-1})	second order (second degree) (cm^{-1})	total shift (cm^{-1})	experimental ($\pm 0.10\,cm^{-1}$)
$\Phi_6^{\pm}$	−0.190	−0.070	−0.036	−0.296	−0.61
$\Phi_7^{\pm}$	−0.183	−0.064	−0.036	−0.283	−0.19
$\Psi_6^{\pm}$	0.840	−0.009	0.077	0.908	0.98
$\Psi_7^{\pm}$	0.833	−0.004	0.029	0.820	0.98

Table 6.26 : Measured and first and second order calculated shifts of the Ψ_6^+ and Ψ_7^+ states for CaF_2:Er^{3+}:H^-. The contributions from the static-crystal-field Hamiltonian have been subtracted.

splittings. For example, scaling up the contribution of the second-order perturbations from the first-degree Hamiltonian terms would decrease the Ψ splitting while increasing the Φ splitting.

The case of CaF_2:Er^{3+}:H^- remains anomalous in that the extent of the required scaling is very much greater than was required for any of the other Kramers ions.

6.5 Splitting of the H^- x-y Vibronic Associated with Non-Kramers Ions

In the case of a non-Kramers ion, the only doublet irrep in C_{4v} symmetry is γ_5, and the electronic ground state need not necessarily be a doublet. For the H^- C_{4v} centres, only Pr^{3+} has a γ_5 doublet ground state.

Both Ho^{3+} and Tb^{3+} are known to have pseudo-degenerate ground states in the F^- C_{4v} centre. It has been shown by crystal field analysis that this should be fairly independent of the strength of the C_{4v} perturbation [78], and thus is expected to apply also to the hydrogenic centres which should have a similar cubic component of the crystal field. The splittings observed in these two cases are not x-y splittings as such, but instead are independent shifts of the x-y vibronic associated with the two singlet electronic states. In addition hyperfine effects appear to play an important role, especially in the case of CaF_2:Ho^{3+}:H^-, in both the zero-field pattern and the Zeeman effect. As this is beyond the scope of this analysis, the emphasis here is on the doublet ground-state case of Pr^{3+}.

6.5.1 CaF_2:Pr^{3+}:H^- and SrF_2:Pr^{3+}:H^-

When the γ_5 electronic ground state is coupled to the γ_5 x-y vibration, the vibronic states then transform as the product irrep $\gamma_5 \times \gamma_5 = \gamma_1 + \gamma_2 + \gamma_3 + \gamma_4$, as described in section 6.2. Thus, we might expect to see a total lifting of the degeneracy to four lines, instead of just two as in the case of the Kramers ions.

The splitting of the x-y mode of the H^- ion in CaF_2:Pr^{3+}:H^- and SrF_2:Pr^{3+}:H^- was first observed by Jacobs [39]. With a resolution of $0.3\,cm^{-1}$, the line was seen to split into two in both cases, but with a 1:3 intensity ratio. With improved resolution and signal-to-noise ratio available now, the spectra of the x-y modes in CaF_2:0.01%Pr^{3+} hydrogenated for 1.5 hours and in SrF_2:0.01%Pr^{3+} hydrogenated for 2 hours are shown in figures 6.15 and 6.16, respectively. The splittings calculated from the point-charge model in the following analysis are also indicated below these spectra.

The lower, more intense line is still only partially resolved in both of these spectra, with the SrF_2 case showing the clearer splitting. The linewidths are somewhat

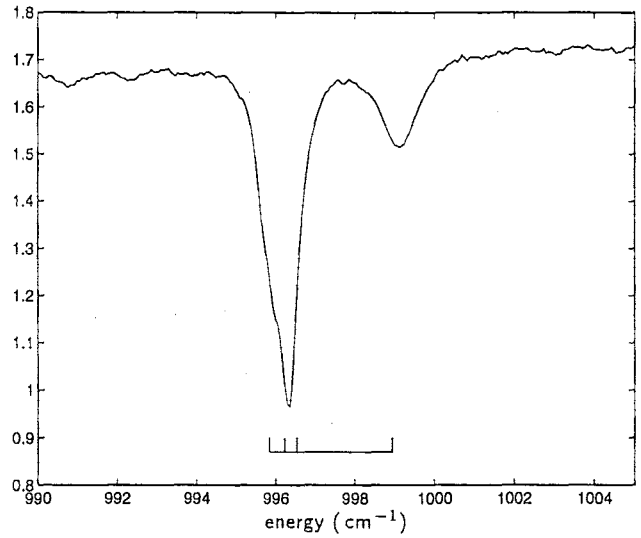

Figure 6.15 : Infrared-absorption spectrum of the x-y splitting in CaF_2:0.01%Pr^{3+}:H^-(1.5 hrs). The splittings calculated using the point-charge model are indicated below the spectrum.

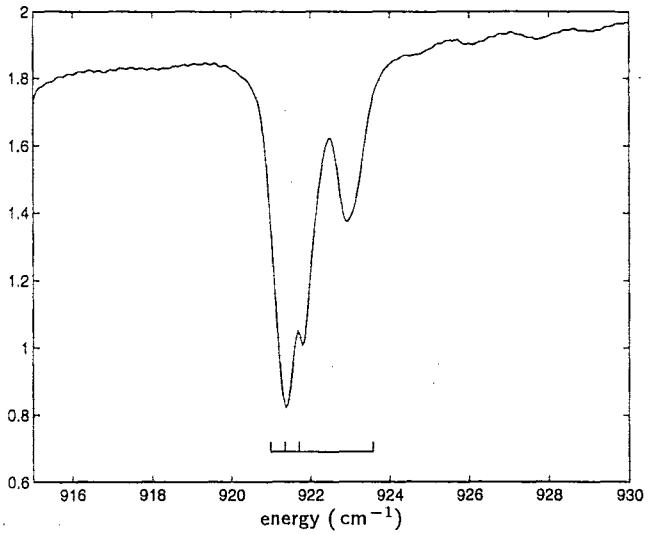

Figure 6.16 : Infrared-absorption spectrum of the x-y splitting in SrF_2:0.01%Pr^{3+}:H^-(2 hrs). The splittings calculated using the point-charge model are indicated below the spectrum.

larger than appeared for most of the Kramers ions, for the same sample treatment conditions, and it may be that the resolution is limited to that observed here by incipient hyperfine splittings (see discussions in section 7.2).

An attempt by Jacobs [39] to calculate the x-y splittings gave a calculated value 5 times greater than measured. This may have been due in part to insufficient knowledge of the Pr^{3+} $^3H_4$ electronic-state energies, however comparison with subsequent calculations suggest other errors may have occurred. Reeves [75] repeated this calculation with better success, however it appears that the eigenvalues of his first-order perturbation matrix include an extra factor of two, and are assigned to different eigenstates than those found in this section.

In the following calculations, the contributions from first and second-order perturbation theory give shifts of similar magnitudes. Because these two contributions are effectively parametrised by different coefficients from the electron-phonon interaction Hamiltonian—E_1^2 for first-order and D_1^2 for second-order effects—and because the measured splitting is not fully resolved, these two parameters cannot be determined independently. Instead, the calculation is presented with the point-charge model values assumed for these parameters, and this full calculation is then compared with the measured spectrum.

Extensive experimental data on the crystal field levels of the D^- compensated centres (which would be expected to yield very similar energies to the H^- centres) has been reported by Reeves *et al* [77]. The experimental g-values are reported as $g_{\|} = 4.13$ for CaF_2 and $g_{\|} = 3.94$ for SrF_2 with $g_{\perp} = 0$ in both cases as expected for non-Kramers ions (section 2.4). The reported $^3H_4$ energies and irreps are reproduced in table 6.27.

Since crystal field analyses have not been very successful, cubic-approximation wavefunctions have been adopted. A $J = 4$ multiplet decomposes to $2\gamma_1 + \gamma_2 + \gamma_3 + \gamma_4 + 2\gamma_5$ and if crystal field mixing between multiplets is neglected then the γ_2, γ_3 and γ_4 states will remain pure, while the two γ_1 states, and likewise the two γ_5 states, will mix. The calculated ground state $g_{\|}$ is 4.03 when the intermediate coupling scheme and cubic wavefunctions are used; this compares well with the experimental values hence would seem to be a reasonable approximation. Again C_4 irreps will be used, though these do not immediately lead to the zero order vibronic wavefunctions as

Cubic wavefunction			energies (cm^{-1})	
			CaF_2	SrF_2
$\psi^{\pm}(\gamma_5)$	=	$\sqrt{\frac{1}{8}}\|4,\pm1\rangle - \sqrt{\frac{7}{8}}\|4,\mp3\rangle$	0	0
$Z_2(\gamma_4)$	=	$\frac{1}{\sqrt{2}}(\|4,2\rangle - \|4,-2\rangle)$	195	108
$Z_3(\gamma_1)$	=	$\sqrt{\frac{7}{24}}(\|4,4\rangle + \|4,-4\rangle) - \sqrt{\frac{10}{24}}\|4,0\rangle$	463	373
$Z_4(\gamma_2)$	=	$\frac{1}{\sqrt{2}}(\|4,4\rangle - \|4,-4\rangle)$	500†	400†
$Z_5(\gamma_1)$	=	$\sqrt{\frac{5}{24}}(\|4,4\rangle + \|4,-4\rangle) + \sqrt{\frac{14}{24}}\|4,0\rangle$	559	461
$Z_6^{\pm}(\gamma_5)$	=	$\sqrt{\frac{7}{8}}\|4,\pm1\rangle + \sqrt{\frac{1}{8}}\|4,\mp3\rangle$	559	490
$Z_7(\gamma_3)$	=	$\frac{1}{\sqrt{2}}(\|4,2\rangle + \|4,-2\rangle)$	834	726

Table 6.27 : Energies [77] and cubic-approximation wavefunctions of the Pr^{3+} ion in the C_{4v} centres of CaF_2:Pr^{3+}:H^- and SrF_2:Pr^{3+}:H^-. †Estimated from crystal field analyses

in the case of Kramers ions. The $\pm$ superscript on the γ_5 wavefunctions follows the notation of the [$\pm$] vibrational states, as in table 6.28. Using the C_4 multiplication

notation	C_{4v}-C_4irrep	basis
ψ^+	$\gamma_5\mu_3$	$\|1\rangle, \|-3\rangle$
ψ^-	$\gamma_5\mu_4$	$\|-1\rangle, \|3\rangle$

Table 6.28 : Electronic state notation and bases for non-Kramers ions.

table (section 2.3), we construct vibronic states:

$$\begin{aligned}
\psi^+[-] &\sim (\gamma_1/\gamma_2)\mu_1 \\
\psi^-[+] &\sim (\gamma_1/\gamma_2)\mu_1 \\
\psi^+[+] &\sim (\gamma_3/\gamma_4)\mu_2 \\
\psi^-[-] &\sim (\gamma_3/\gamma_4)\mu_2
\end{aligned}$$

Because γ_1 and γ_2 irreps decompose to the same μ_1 C_4 irrep, and similarly γ_3 and γ_4 to the same μ_2 C_4 irrep, it is not immediately obvious what the zero order wavefunctions are. For example, at this stage we know only that the γ_1 vibronic state is some linear combination of the two μ_1 states given above.

Because the (orthogonalised) zero-order wavefunctions will involve a combination of

the above wavefunctions, the second-degree electron-phonon terms

$$g_{X_+^2+X_-^2}\left(X_+^2+X_-^2\right)+\ g_{X_+^2-X_-^2}\left(X_+^2-X_-^2\right)$$

will give a first-order contribution to the x-y splitting, in addition to the second-order contributions from the $f_-X_+ + f_+X_-$ terms. The appropriate zero-order wavefunctions are determined from the first-order perturbation matrix.

First-Order Perturbations by Second-Degree Terms of the Electron-Phonon Interaction

The first-order perturbation matrix (neglecting uniform shift contributions) constructed from the above wavefunctions is

	$\psi^+[-]$	$\psi^-[+]$	$\psi^+[+]$	$\psi^-[-]$
$\psi^+[-]$	0	$A+B$	0	0
$\psi^-[+]$	$A+B$	0	0	0
$\psi^+[+]$	0	0	0	$A-B$
$\psi^-[-]$	0	0	$A-B$	0

where

$$\begin{aligned} A &= 2\alpha^2\langle\psi^-|\ g_{X_+^2+X_-^2}\ |\psi^+\rangle \equiv 2\alpha^2\langle\psi^+|\ g_{X_+^2+X_-^2}\ |\psi^-\rangle \\ &= 2\alpha^2 E_1^2\,\langle\psi^-|C_{-2}^{(2)}+C_2^{(2)}|\psi^+\rangle \\ B &= 2\alpha^2\langle\psi^-|\ g_{X_+^2-X_-^2}\ |\psi^+\rangle \equiv -2\alpha^2\langle\psi^+|\ g_{X_+^2-X_-^2}\ |\psi^-\rangle \\ &= 2\alpha^2 E_1^2\,\langle\psi^-|C_{-2}^{(2)}-C_2^{(2)}|\psi^+\rangle \end{aligned}$$

with vibrational matrix elements

$$\begin{aligned} \langle[\mp]|(X_+^2+X_-^2)|[\pm]\rangle &= 2\alpha^2 \\ \langle[\mp]|(X_+^2-X_-^2)|[\pm]\rangle &= \mp 2\alpha^2 \end{aligned}$$

Diagonalising this matrix yields the orthogonalised zero-order wavefunctions and first-order energies given in table 6.29. In order to deduce which irrep each of the combinations transforms as, one can consult the coupling coefficients of Koster [51].

Irrep	Vibronic State	Eigenvalue	CaF_2	SrF_2
γ_1	$\Psi_1 = \frac{1}{\sqrt{2}}(\psi^+[-] - \psi^-[+])$	$-A - B$	$0.215\,cm^{-1}$	$0.220\,cm^{-1}$
γ_2	$\Psi_2 = \frac{1}{\sqrt{2}}(\psi^+[-] + \psi^-[+])$	$A + B$	$-0.215\,cm^{-1}$	$-0.220\,cm^{-1}$
γ_3	$\Psi_3 = \frac{1}{\sqrt{2}}(\psi^+[+] - \psi^-[-])$	$-A + B$	$-0.905\,cm^{-1}$	$-0.926\,cm^{-1}$
γ_4	$\Psi_4 = \frac{1}{\sqrt{2}}(\psi^+[+] + \psi^-[-])$	$A - B$	$0.905\,cm^{-1}$	$0.926\,cm^{-1}$

Table 6.29 : Calculated x-y vibronic wavefunctions and first-order energies for CaF_2:Pr^{3+}:H^- and SrF_2:Pr^{3+}:H^-

However care must be taken over the phases of both electronic and vibrational wavefunctions. The $\psi^{\pm}$ electronic wavefunctions, with phase as given in table 6.27, transform as the spherical harmonics $Y_{1\,\pm1}$, i.e. as $\mp(x \pm iy)$, whereas the $[\pm]$ vibrational states defined here transform simply as $(x \pm iy)$.

Alternatively, matrix elements of $f_-X_+ + f_+X_-$ with $Z_i(000)$ intermediate states can be considered. For example the γ_1 vibronic state should have zero matrix elements with all such intermediate states where Z_i transforms as γ_2, γ_3 or γ_4, but non-zero where Z_i transforms as γ_1.

The A and B matrix elements are evaluated using intermediate coupled $C^{(2)}_{\pm2}$ matrix elements:

$$\begin{aligned} \langle\psi^-|C^{(2)}_2|\psi^+\rangle &= 0.1316 \\ \langle\psi^-|C^{(2)}_{-2}|\psi^+\rangle &= -0.0313 \end{aligned}$$

and the point charge model value of E^2_1 from section 6.3.2 to give $A = 0.3447\,cm^{-1}$ and $B = -0.5599\,cm^{-1}$ for CaF_2:Pr^{3+}:H^- and $A = 0.3527\,cm^{-1}$ and $B = -0.5728\,cm^{-1}$ for SrF_2:Pr^{3+}:H^- and hence the first order energies of table 6.29.

Second-Order Perturbations by First-Degree Terms of the Electron-Phonon Interaction

As with the Kramers ions, the contributing intermediate states are the product states of $^3H_4$ electronic states and the (000) and (110) vibrational states. Again, only intermediate states which transform as the same irrep as the vibronic state

under consideration contribute an energy shift to that state. The energy shifts due to these states are listed in tables 6.30 and 6.31. Intermediate states formed from the $^3H_5$ and higher states give shifts of less than $0.01\,cm^{-1}$, so are neglected. The total calculated energy shifts, depicted in figures 6.17 and 6.18, are as given in the first column of table 6.33.

In each case, the first and second order effects are similar in size, with the second order shift of Ψ_3 due to the nearby $Z_7\gamma_3$ state giving the largest contribution. The infrared-absorption spectra of the x-y splittings, figures 6.15 and 6.16, include a plot of the calculated splittings from table 6.33. The spectra are consistent with the theoretical result that the Ψ_3 state is shifted well away from the other levels which remain unresolved in the case of CaF_2:Pr^{3+}:H^- and partially resolved in the case of SrF_2:Pr^{3+}:H^-, and agree well with the extent of this overall splitting.

In the analysis of section 7.2, it will be shown that, for CaF_2, the order of the three partially resolved states must be changed in order to account for the Zeeman splittings of these lines, with the Ψ_4 state at lowest energy. Since the second-order calculations give the lowest energy for this state, the new order could be accounted for if the second-order perturbations (parametrised by D_1^2) were scaled up relative to the first-order effects (parametrised by E_1^2). For SrF_2, the ordering of states is correct, but the Ψ_4 and Ψ_2 states should be closer together, with the Ψ_1 line resolvable from these. This could also be achieved with a scaling-up of the second-order perturbations relative to the first-order.

If the two parameters, D_1^2 and E_1^2, are allowed to vary freely, then the calculated splitting can be made to match closely the experimental values inferred from the Zeeman splittings. In table 6.32, these fitted parameters are compared to the point-charge model values used in the preceding calculations.

Table 6.33 shows the splitting of the x-y vibronic states for CaF_2:Pr^{3+}:H^- and SrF_2:Pr^{3+}:H^- as calculated using the two sets of parameters from table 6.32 and as determined from the Zeeman splittings of section 7.2. While the fitted parameters do give a much better match to these splittings, the predominant effect of one level being split away from the other three is also predicted by the point-charge model. The comparison between the point-charge and fitted parameters is good, with the second-order perturbation parameter D_1^2, which causes this state to split away requiring a

γ_1 int. states	rel. energy (cm^{-1})	matrix element (cm^{-1})	shift of Ψ_1(cm^{-1})
$Z_3(000)$	−535	16.32	.498
$Z_5(000)$	−439	17.55	.702
$Z_2(110)$	1193	16.70	−.234
		second order shift of Ψ_1	0.966

γ_2 int. states	rel. energy (cm^{-1})	matrix element (cm^{-1})	shift of Ψ_2(cm^{-1})
$Z_4(000)$	−498	23.80	1.138
$Z_7(110)$	1832	28.27	−0.436
		second order shift of Ψ_2	0.701

γ_3 int. states	rel. energy (cm^{-1})	matrix element (cm^{-1})	shift of Ψ_3(cm^{-1})
$Z_7(000)$	−164	28.27	4.873
$Z_4(110)$	1498	23.80	−0.378
		second order shift of Ψ_3	4.495

γ_4 int. states	rel. energy (cm^{-1})	matrix element (cm^{-1})	shift of Ψ_4(cm^{-1})
$Z_2(000)$	−803	16.70	0.347
$Z_3(110)$	1461	16.32	−0.182
$Z_5(110)$	1557	17.55	−0.198
		second order shift of Ψ_4	−0.033

Table 6.30 : Calculated second-order energy shifts of the x-y vibronic states for CaF_2:Pr^{3+}:H^-.

γ_1 int. states	rel. energy (cm^{-1})	matrix element (cm^{-1})	shift of Ψ_1(cm^{-1})
$Z_3(000)$	−536	17.04	.542
$Z_5(000)$	−456	18.33	.737
$Z_2(110)$	1060	17.44	−.287
		second order shift of Ψ_1	0.992

γ_2 int. states	rel. energy (cm^{-1})	matrix element (cm^{-1})	shift of Ψ_2(cm^{-1})
$Z_4(000)$	−502	24.85	1.230
$Z_7(110)$	1651	29.51	−0.528
		second order shift of Ψ_2	0.702

γ_3 int. states	rel. energy (cm^{-1})	matrix element (cm^{-1})	shift of Ψ_3(cm^{-1})
$Z_7(000)$	−193	29.51	4.514
$Z_4(110)$	1342	24.85	−0.460
		second order shift of Ψ_3	4.053

γ_4 int. states	rel. energy (cm^{-1})	matrix element (cm^{-1})	shift of Ψ_4(cm^{-1})
$Z_2(000)$	−784	17.44	0.388
$Z_3(110)$	1308	17.04	−0.222
$Z_5(110)$	1388	18.33	−0.242
		second order shift of Ψ_4	−0.076

Table 6.31 : Calculated second-order energy shifts of the x-y vibronic states for SrF_2:Pr^{3+}:H^-.

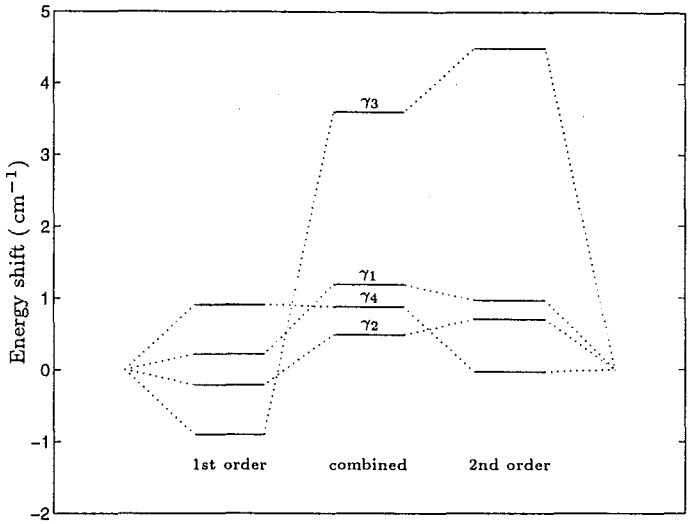

Figure 6.17 : Calculated first and second order contributions to the CaF_2:Pr^{3+}:H^- x-y splitting.

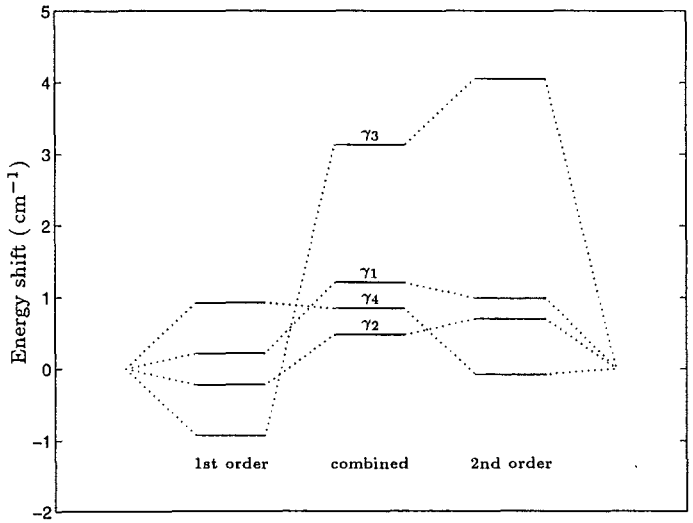

Figure 6.18 : Calculated first and second order contributions to the SrF_2:Pr^{3+}:H^- x-y splitting.

		$\alpha D_1^2(\,cm^{-1})$	$\alpha^2 E_1^2(\,cm^{-1})$
CaF_2	Point-charge model	102	1.72
	Fitted to experimental	92	0.50
SrF_2	Point-charge model	103	1.63
	Fitted to experimental	76	0.78

Table 6.32 : Values of the coefficients of the electron-phonon Hamiltonian as calculated from the point-charge model, and as fitted to the experimental splittings.

scaling factor of less than 1.5 in both cases. The first-order perturbation parameter, E_1^2, is not quite as good being out by a factor of 3.4 for CaF_2:Pr^{3+}:H^- and 2.1 for SrF_2:Pr^{3+}:H^-.

	CaF_2 shifts (cm^{-1})		
	Point-charge model	Fitted	Experimental ($\pm 0.10\,cm^{-1}$)
Ψ_1	1.18	1.13	0.90
Ψ_2	0.49	0.79	0.90
Ψ_3	3.59	3.67	3.70
Ψ_4	0.87	0.51	0.60
	SrF_2 shifts (cm^{-1})		
	Point-charge model	Fitted	Experimental ($\pm 0.10\,cm^{-1}$)
Ψ_1	1.21	1.30	1.40
Ψ_2	0.48	0.93	0.90
Ψ_3	3.13	2.42	2.40
Ψ_4	0.85	1.05	1.00

Table 6.33 : Shifts of the x-y vibronic states for CaF_2:Pr^{3+}:H^- and SrF_2:Pr^{3+}:H^-, calculated from parameters determined from the point-charge model and by fitting to the experimental data, and determined from the experimental Zeeman splittings.

6.6 Summary of the x-y Vibronic Splittings in CaF_2:RE^{3+}:H^- and SrF_2:RE^{3+}:H^-

H^- ions diffused into rare-earth-doped CaF_2 and SrF_2 crystals can enter into interstitial sites adjacent to the rare-earth ion, forming a tetragonal, C_{4v} symmetry centre. The sharp infrared-absorption lines of the doubly-degenerate x-y vibrational mode of the H^- ion in these sites may be split by up to a few wavenumbers, and these splittings have been measured for each of the lanthanides in CaF_2 and for the lanthanides up to Sm^{3+} in SrF_2. An x-y splitting is only observed in cases where the RE^{3+} ion has a doubly-degenerate electronic ground state, and the magnitudes of these splittings are listed in table 6.34. It has previously been demonstrated [40, 39] that this splitting can arise from the electron-phonon interaction acting on the coupled RE^{3+}-H^- vibronic states.

The theoretical ground work for calculating the perturbations due to the electron-phonon interaction has been outlined, with the point-charge-model form of the co-

rare earth	x-y splitting in CaF_2 (cm^{-1})	x-y splitting in SrF_2 (cm^{-1})
Ce^{3+}	1.15	0.95
Pr^{3+}	0.3,0,2.8	0.1,0.4,1.0
Nd^{3+}	0.3	0.2
Sm^{3+}	0.67	0.38
Dy^{3+}	0.42	
Er^{3+}	0.42,1.25,0	
Yb^{3+}	0.70	

Table 6.34 : Measured splittings of the H^- x-y vibronic line of the RE^{3+}–H^- C_{4v} centres in CaF_2 and SrF_2.

efficients being derived using a modified form of Zdansky's solid harmonics [93]. By using the $(x \pm iy)$ basis in place of the usual Cartesian basis for the transverse vibration, a group-chain decomposition approach allowed the coupled vibronic states to be constructed in such a way that the set of intermediate states perturbing each of the four x-y vibronic states could be determined by combining the irreps of the electronic and vibrational parts.

For Kramers ions with well isolated ground states, the main contribution to the x-y splitting comes about as second-order perturbations from first-degree terms of the electron-phonon interaction Hamiltonian. These first-degree terms are parametrised by the $\alpha^n D_1^n$ parameters, and if all but the leading $n = 2$ term are neglected then the entire x-y splitting is proportional to the square of this single $\alpha^2 D_1^2$ parameter. Therefore, by measuring the x-y splitting and calculating the matrix elements for the second-order perturbations, the appropriate value of D_1^2 required to give the splitting can be calculated. These fitted values of $\alpha^2 D_1^2$ are listed in table 6.35, along with the values calculated from the point-charge model.

Also listed in table 6.35 is Pr^{3+}. For the non-Kramers ion with a doublet ground state, first-order perturbations from second-degree terms of the electron-phonon interaction give energy-shift contributions comparable to the second-order perturbations. These first-order perturbations are parametrised by the E_1^2 parameter, again

rare earth	CaF_2 αD_1^2 (cm^{-1})		SrF_2 αD_1^2 (cm^{-1})	
	point-charge	fitted	point-charge	fitted
Ce^{3+}	114	68	128	60
Pr^{3+}	102	92	103	76
Nd^{3+}	94	140	98	120
Sm^{3+}	83	37	86	39
Dy^{3+}	67	123		
Yb^{3+}	56	163		

Table 6.35 : Values of the αD_1^2 electron-phonon interaction parameter as obtained from the point-charge model and by fitting to the experimental x-y splittings in the C_{4v} centres of CaF_2:RE^{3+}:H^- and SrF_2:RE^{3+}:H^-.

with all but the leading $n = 2$ term neglected. Therefore, the four-way x-y splittings for Pr^{3+} can be parametrised by the E_1^2 and D_1^2 coefficients. While these x-y splittings were not fully resolved for either CaF_2:Pr^{3+}:H^- or SrF_2:Pr^{3+}:H^-, they can be inferred from the Zeeman splittings of chapter 7, thus allowing the E_1^2 and D_1^2 parameters to be fitted.

The case of CaF_2:Er^{3+}:H^- is complicated by the presence of a low-lying electronic states at $4.5\,cm^{-1}$ and $25.8\,cm^{-1}$ above the ground state. The electron-phonon interaction contributes first-order perturbations parametrised by the E_0^n and E_1^n coefficients and second-order perturbations parametrised by the D_1^n coefficients. Calculations were done using values for these parameters from the point-charge model which were only partially successful in giving appropriate splittings, with the calculated splitting of the x-y vibronic associated with the Z_1 ground state more than an order of magnitude smaller than the measured splitting.

For those ions for which the D_1^2 parameter could be fitted, table 6.35 shows that the point-charge model predicts values which range from a factor of 2.2 too large to 2.9 too small. While it is acknowledged that the point-charge model should only be considered as a very crude approximation to reality, the order-of-magnitude agreement achieved here indicates that the electron-phonon interaction is a likely cause of the observed x-y splittings.

Further Work

In most cases, the x-y splittings have been sufficiently well resolved to measure the magnitude of the effect. However, cases such as $CaF_2:Nd^{3+}:H^-$, $SrF_2:Nd^{3+}:H^-$ and in particular $CaF_2:Er^{3+}:H^-$, may benefit from measurements using a higher resolution instrument. The cases of $CaF_2:Pr^{3+}:H^-$ and $SrF_2:Pr^{3+}:H^-$ are not fully resolved and should also be reinvestigated at higher resolution, however the limiting linewidth appears to already have been reached unless the Pr^{3+} hyperfine structure itself can be resolved.

Future calculations must refine the methods used to analyse the electron–local-mode-phonon interaction. Other models, which include such effects as the polarisation of the H^- ion itself and of the adjacent lattice F^- ions have been proposed [40]. The polarisation of the H^- ion appears to be an important factor and may give contributions comparable to the point-charge model. Covalency effects have not previously been considered, but may be important, and a treatment involving these could return much insight.

Even within the point-charge model as used here, it has been assumed that the $n = 4$ and $n = 6$ terms in the expansion of the derivatives of the static crystal-field potential can be neglected. This approach has allowed the D_1^2 parameter in the remaining $n = 2$ term to be determined by comparison with the experimental splitting. However, future investigations of the splittings due to the electron-phonon interaction will need to include these $n = 4$ and $n = 6$ terms, as calculated by the chosen models, to be compared with the experimental splitting. Because these three terms are to be combined before the matrix element is squared to calculate the second-order perturbation, the effects are not necessarily additive and may account for the splittings calculated here being either too large or too small.

Chapter 7

Zeeman Spectroscopy of H^- Local Modes in Hydrogenated RE^{3+}-doped CaF_2 and SrF_2

The calculations in the previous chapter were successful in demonstrating that the electron–local-mode-phonon interaction could account quantitatively for the observed splittings of the H^- x-y vibrational mode of CaF_2:RE^{3+}:H^- C_{4v} centres. In this chapter the application of an external magnetic field is used to further confirm the assignment of this x-y vibrational mode and the mechanism of its splitting.

Two magnetic-field geometries were employed. Firstly, with the field along the $\langle 100 \rangle$ cube axis, two distinct magnetic sub-centres are created from the C_{4v} centre; a C_4 symmetry centre with the magnetic field along its symmetry axis, and a C_s symmetry centre with the magnetic field perpendicular to this axis. The absorption spectra of these two sub-centres are superimposed, often leading to complex splitting patterns. To counter these complexities, the second option of applying the magnetic field along a $\langle 111 \rangle$ body diagonal axis is employed. Here the symmetry is lowered to C_1, but the field is equally inclined to all three cubic-crystal axes so that only one magnetic subsite is present.

The magnetic field does not act on the H^- vibrational states, and any shifts or splittings are due only to the Zeeman Hamiltonian acting on the electronic part of the total vibronic wavefunction. The method for calculating the Zeeman splittings is to form the first-order matrix of the unperturbed vibronic wavefunctions, as constructed in chapter 6. The zero-field electron-phonon splittings are a second-order perturbation effect which do not significantly alter the vibronic wavefunctions, and can be included in the matrix as phenomenological parameters. The Zeeman-

Hamiltonian matrix elements are then included between those wavefunctions having identical vibrational components. For the exceptional case of CaF_2:Er^{3+}:H^-, the first-order Zeeman matrix must include also vibronic states corresponding to the low-lying Z_2 electronic state, and further electron-phonon interaction terms between the Z_1 and Z_2 states must be included in the total matrix.

This first-order matrix approach has been outlined by Jones [42] and Jones and Strickland [45] and successfully provides a quantitative prediction of the observed magnetic-field splitting patterns.

A large variation in intensities of the observed absorption lines which have been split by the Zeeman effect arises from two factors. The first is that purely vibrational transitions are much stronger than combined vibrational and electronic transitions. For example, the transition $\psi^+(000) \rightarrow \psi^+(100)$, in which the electronic part of the wavefunction is unchanged, is much stronger than the transition $\psi^+(000) \rightarrow \psi^-(100)$, in which the electronic wavefunctions are different. As the vibrational transitions $(000) \rightarrow (100)$ and $(000) \rightarrow (010)$ have the same strength, the vibronic-transition intensity can be modelled simply by considering the extent of the mixing between the vibronic states.

The second factor in determining linestrengths is the relative thermal populations of the ground state sublevels. The populations follow a Maxwell-Boltzmann distribution with the relative populations, n_1 and n_2, of two levels with an energy separation of Δ being given by:

$$\frac{n_2}{n_1} = \exp\left\{-\frac{\Delta}{kT}\right\}$$

7.1 Calculating the Zeeman Splittings for H^- x-y Vibronics of Kramers Ions

We consider first the cases where the electronic ground state is well isolated. The only example for which this is not so is the case of CaF_2:Er^{3+}:H^-. Kramers ions have an odd number of electrons and for C_{4v} symmetry the electronic states transform as either the γ_6 or γ_7 irreps. The Zeeman analysis for the x-y vibronics for Kramers ions is independent of the irrep of the electronic ground state, so we adopt here the notation of $\psi^{\pm}$ for either a γ_6 or a γ_7 ground state.

In the absence of the external magnetic field, we have energies $-\Delta$ for the $\Psi_6^{\pm}$ and $+\Delta$ for the $\Psi_7^{\pm}$ vibronic states. This zero-field x-y splitting of 2Δ is predominantly a second order effect and is included as an experimentally determined parameter. The sign of Δ could be inferred from the calculations of section 6.4, however the splitting pattern is symmetrical and the sign of Δ is not relevant (in as much as we can neglect second-order Zeeman interactions with nearby states). When the external magnetic field is applied, the additional parallel and perpendicular Zeeman terms P and S must be included between states having the same vibrational components. The general Zeeman matrix for Kramers ions is:

	$\psi^-[+]$	$\psi^+[-]$	$\psi^-[-]$	$\psi^+[+]$
$\psi^-[+]$	$-\Delta - \mathrm{P}$			S^*
$\psi^+[-]$		$-\Delta + \mathrm{P}$	S	
$\psi^-[-]$		S^*	$\Delta - \mathrm{P}$	
$\psi^+[+]$	S			$\Delta + \mathrm{P}$

(7.1)

where the Zeeman terms are given by

$$\begin{aligned} \mathrm{P} &= \mu_B \mathrm{B}_z \langle \psi^+ | \mathrm{M}_0^{(1)} | \psi^+ \rangle = \tfrac{1}{2} \mu_B g_{\parallel} \mathrm{B}_z \\ \mathrm{S} &= -\tfrac{1}{\sqrt{2}} \mu_B (\mathrm{B}_x - i\mathrm{B}_y) \langle \psi^+ | \mathrm{M}_1^{(1)} | \psi^- \rangle = \tfrac{1}{2} \mu_B g_{\perp} (\mathrm{B}_x - i\mathrm{B}_y) \end{aligned}$$

where the $\mathrm{M}_q^{(1)}$ are standard tensor-operator components [26] of $\mathbf{M} = \mathbf{L} + 2\mathbf{S}$.

The Zeeman matrix for the splitting of the vibronic ground-state, $\psi^{\pm}(000)$, involves the same Zeeman terms:

	$\psi^-(000)$	$\psi^+(000)$
$\psi^-(000)$	$-\mathrm{P}$	S^*
$\psi^+(000)$	S	P

(7.2)

giving a linear Zeeman splitting for the Kramers-degenerate ground state. The x-y local-mode transition energies follow as the differences of the energy eigenvalues of these two matrices.

7.1.1 Zeeman Splittings of the x-y Vibronics in CaF_2:Ce^{3+}:H^- and SrF_2:Ce^{3+}:H^-

The Zeeman splittings of the H^- x-y vibronic lines of CaF_2:Ce^{3+}:H^- were measured twice for both $\langle 100 \rangle$ and $\langle 111 \rangle$ orientations. This was done because of the complex

observed splitting pattern, and the need to measure low-doped samples for improved resolution and highly-doped samples to obtain sufficient intensity to measure the weak, vibronic transitions. The ⟨100⟩ spectra were measured on a 2.2 mm thick sample containing 0.01% Ce^{3+} which had been hydrogenated for 2 hours and on a 3.5 mm thick sample containing 0.03% Ce^{3+} which had been hydrogenated for 5 hours. The series of Zeeman spectra of the x-y vibronics for the latter sample is displayed in figure 7.1.

For the ⟨111⟩ magnetic-field orientation, the samples used were a 2.0 mm slice containing 0.01%Ce^{3+} which had been hydrogenated for 2 hours and a 2.0 mm slice containing 0.03%Ce^{3+} which had been hydrogenated for 9 hours. The series of Zeeman spectra of the x-y vibronics for the latter sample is displayed in figure 7.2.

The EPR spectrum of the H^- C_{4v} centre in CaF_2:Ce^{3+}:H^- has been measured by Ashburner *et al* [7], yielding the g-values

$$g_{\parallel} = 3.150 \pm 0.003\ , \quad g_{\perp} = 1.330 \pm 0.001.$$

Using the measured zero-field electron-phonon splitting of 1.15 cm^{-1} (section 6.4) and these g-values in matrix 7.1 yields splittings of the vibronic states as illustrated in figure 7.3 for a ⟨100⟩ magnetic field and in figure 7.4 for a ⟨111⟩ magnetic field.

The absorption spectrum in a ⟨100⟩ field is a superposition of the spectra of the C_4 and C_s magnetic subsites which have the magnetic field parallel and perpendicular to the parent C_{4v}-symmetry axis, respectively. The energy splittings of these two subsites are displayed separately in figure 7.3.

For the C_4 subsite, the two pairs of zero-field vibronic states do not mix, and the Zeeman splittings are linear and identical to the ground-state splitting. Eight transitions should be present. However, because the wavefunctions remain pure, those transitions for which the electronic wavefunction differs from initial to final state will be very weak. Since the Zeeman splitting depends only on the electronic wavefunction component of the vibronic state, the "outside" transitions (1→2 and 2→1) of each set are not observed, and the only transitions which are observed are those for which the initial and final states have the same magnetic-field dependence, hence producing no observed shifts or splittings.

For the C_s subsite the vibronic states do not each split in the field, however they

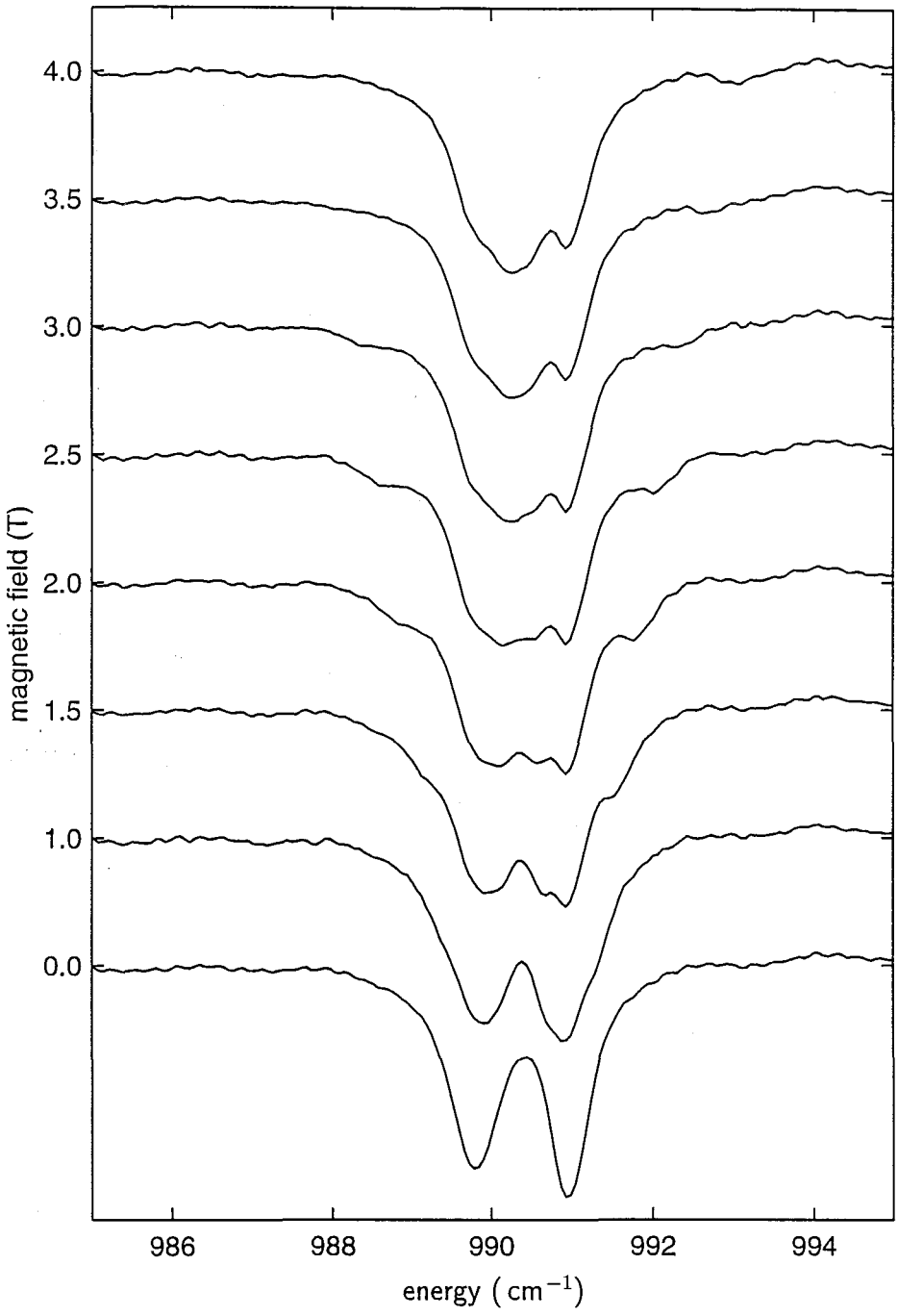

Figure 7.1 : 10 K infrared-absorption spectra of the x-y vibronics in a 3.5 mm slice of CaF_2:0.03%Ce^{3+}:H^-(5 hr) in applied magnetic fields parallel to the $\langle 100 \rangle$ crystal axes. The zero-field spectrum has a maximum absorption of 91%.

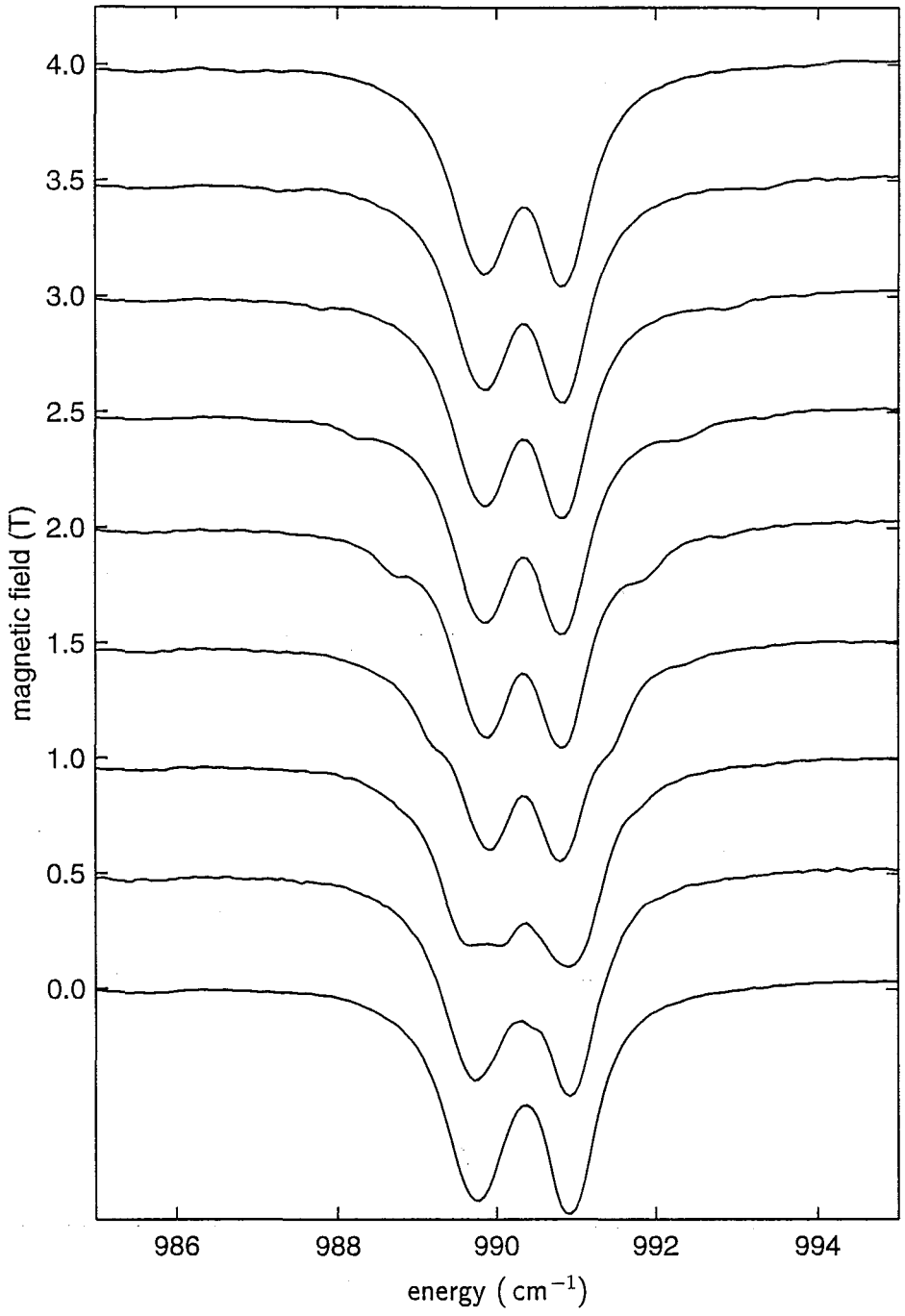

Figure 7.2 : 10 K infrared-absorption spectra of the x-y vibronics in a 2.0 mm slice of CaF_2:0.03%Ce^{3+}:H^-(9 hr) in applied magnetic fields parallel to the ⟨111⟩ crystal axes. The zero-field spectrum has a maximum absorption of 98%.

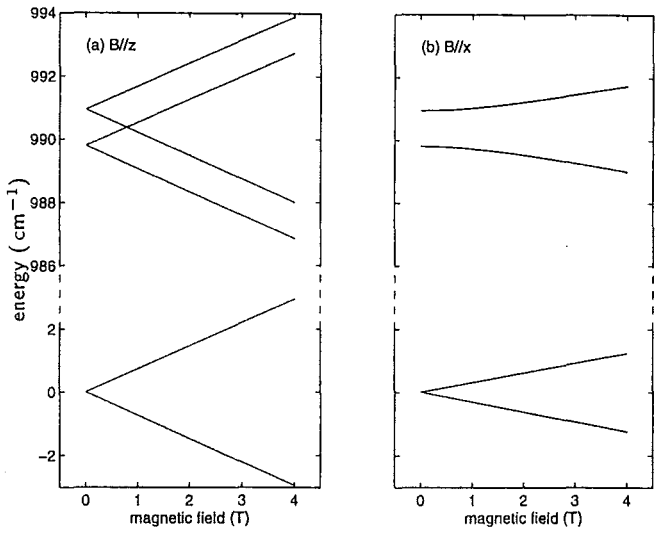

Figure 7.3 : Calculated energies of the ground state and x-y vibronic states of CaF_2:Ce^{3+}:H^- as a function of magnetic field strength, for fields applied (a) parallel to the C_{4v} axis, producing a C_4 symmetry subsite, and (b) perpendicular to this axis, producing a C_s symmetry subsite.

do mix, so that there is an, initially quadratic, "repulsion" between the two. In the limit of a high magnetic field, this separation becomes the identical to the linear splitting displayed by the ground state. All four transitions of the C_s subsite are observed, with intensities that change as the mixing between the vibronic states changes.

In the case of a magnetic field in the $\langle 111 \rangle$ direction only one subsite exists, with C_1 symmetry. The calculated energy splittings in this case are illustrated in figure 7.4. The vibronic states split, initially with the same linear splitting as the ground state, and then becoming non-linear as the states mix. The inner pair of lines mix and exhibit a strong anti-crossing, while the outer pair have a less pronounced repulsion. All transitions are allowed, giving a complex pattern of eight lines.

The transition energies are the differences in the vibronic and ground-state energies. In figure 7.5, the peak energies determined from the $\langle 100 \rangle$ and $\langle 111 \rangle$ Zeeman spectra are plotted against the magnetic field, along with the calculated transition energies. For the $\langle 100 \rangle$ splittings, the calculated splittings of both the C_4 and C_s subsites are

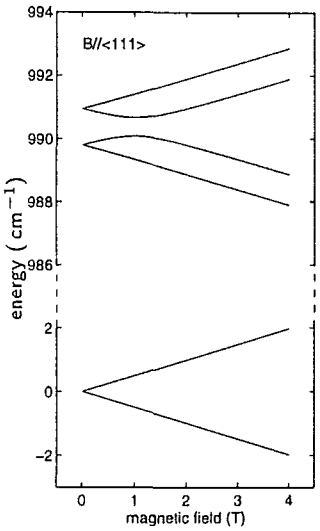

Figure 7.4 : Calculated energies of the ground state and x-y vibronic states of CaF_2:Ce^{3+}:H^- as a function of magnetic field strength, for a field applied along a $\langle 111 \rangle$ crystal axis.

plotted, but with the weak cross transitions of the C_4 subsite omitted.

The experimental points in this plot are in very good agreement with the calculated values, for both $\langle 100 \rangle$ and $\langle 111 \rangle$ magnetic fields. This shows that the first-order perturbation analysis, using no undetermined parameters, is successful in predicting the non-linear splittings of the x-y vibronic lines.

The Zeeman splittings of the x-y vibronic lines in SrF_2:Ce^{3+}:H^- were measured using parent crystals doped at 0.01% of Ce^{3+}. For a $\langle 100 \rangle$ magnetic field a 2.3 mm slice which had been hydrogenated for 3 hours was used, giving the series of spectra shown in figure 7.6. The absorption line near 915 cm^{-1} is a minor hydrogenic centre which is not associated with Ce^{3+} ions, and therefore is unaffected by the magnetic field.

For measurement of the splittings for a magnetic field along the $\langle 111 \rangle$ crystal axis, a 2.0 mm slice of the same boule was hydrogenated for 4.5 hours. The Zeeman spectra of this orientation are given in figure 7.7.

For SrF_2:Ce^{3+}, g-values of the H^- C_{4v} centre have not been reported. However the g-values for the F^- and H^- C_{4v} centres in CaF_2:Ce^{3+} differ only by 4% [7], indicating

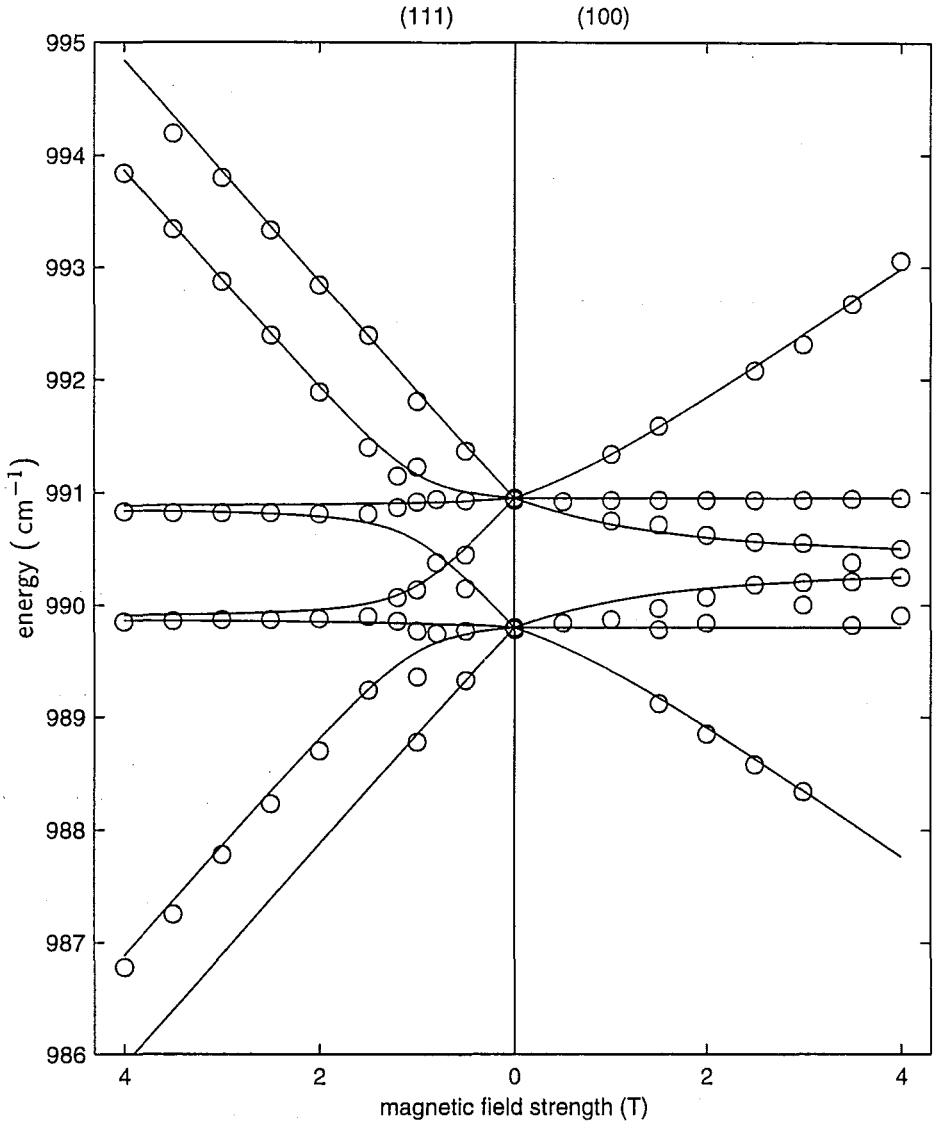

Figure 7.5 : Experimental and calculated Zeeman splitting patterns of the x-y vibronics in CaF_2:0.01%Ce^{3+}:H^-, for magnetic fields parallel to the $\langle 100 \rangle$ and $\langle 111 \rangle$ crystal axes.

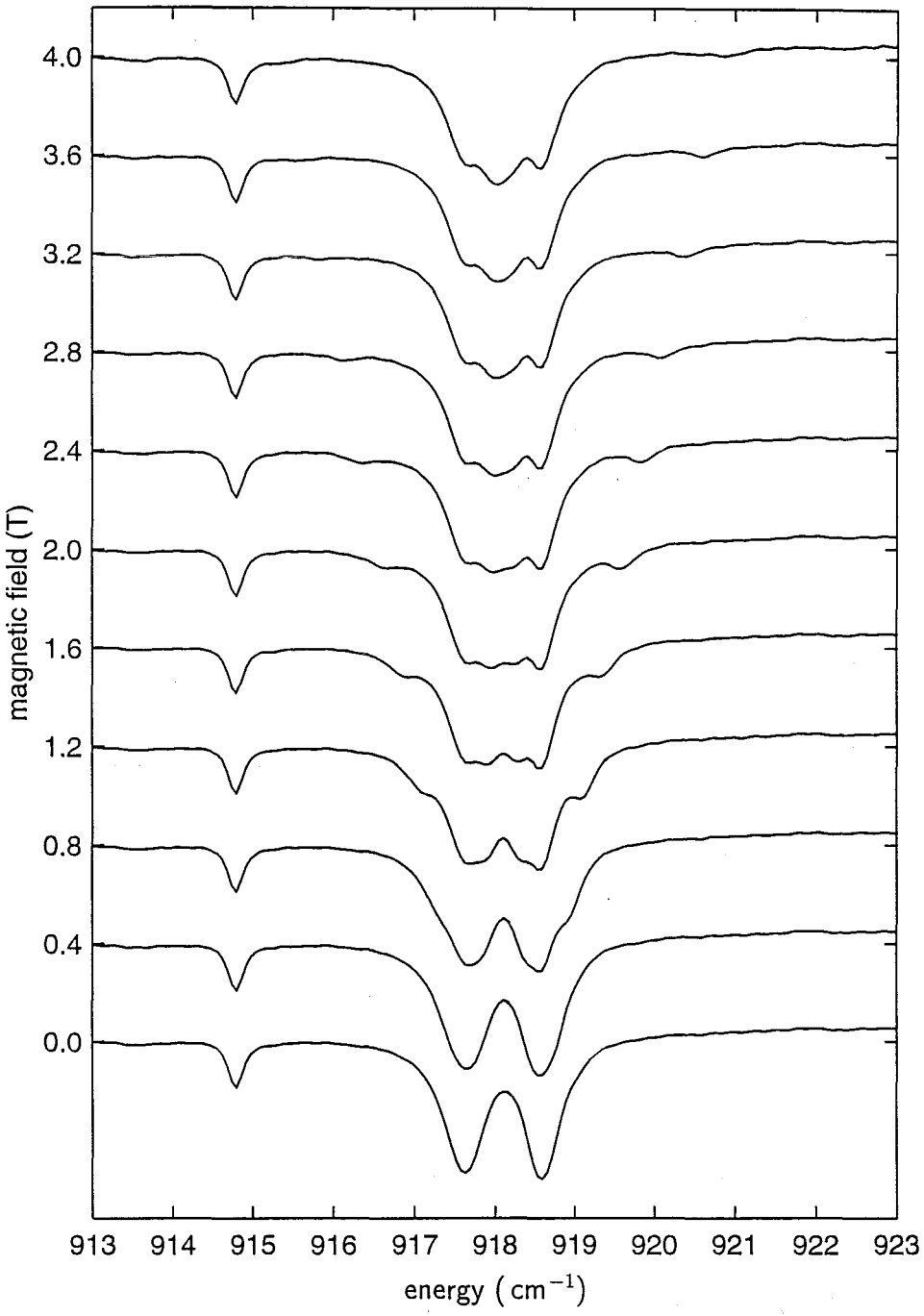

Figure 7.6 : 10 K infrared-absorption spectra of the x-y vibronics in a 2.3 mm slice of SrF_2:0.01%Ce^{3+}:H^-(3 hrs) in applied magnetic fields parallel to the ⟨100⟩ crystal axes. The zero-field spectrum has a maximum absorption of 94%. The line at 914.8 cm^{-1} is associated with a different centre.

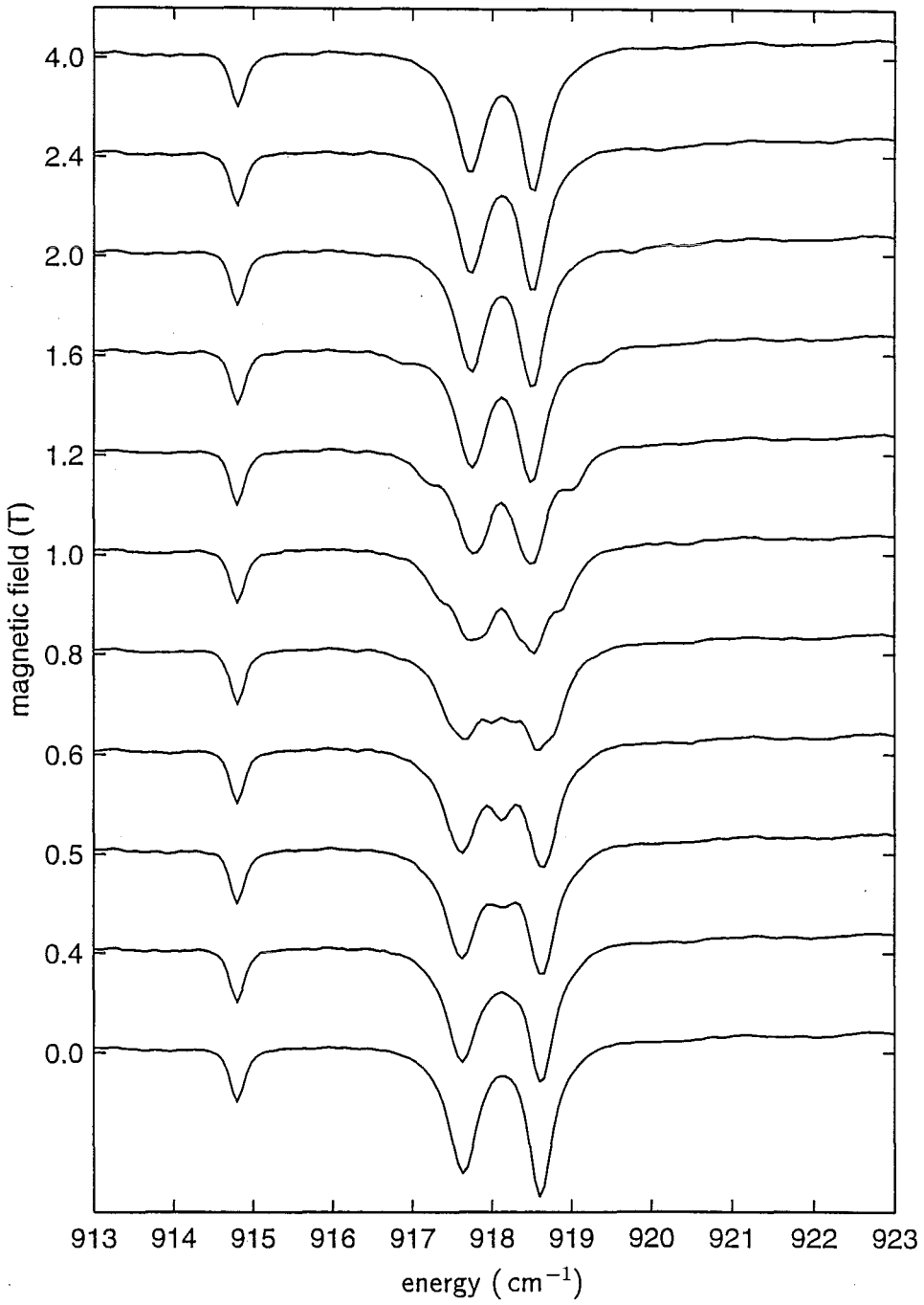

Figure 7.7 : 10 K infrared-absorption spectra of the x-y vibronics in a 2.0 mm slice of SrF_2:0.01%Ce^{3+}:H^-(4.5 hrs) in applied magnetic fields parallel to the ⟨111⟩ crystal axes. The zero-field spectrum has a maximum absorption of 65%. The line at 914.8 cm^{-1} is associated with a different centre.

that these two centres should be sufficiently similar to justify adopting the g-values of the F^- centre in the SrF_2:Ce^{3+}:H^- case. The EPR spectrum of SrF_2:Ce^{3+} has been measured by Brown *et al* [12] and Antipin *et al* [6], giving g-values for the C_{4v} centre as

$$g_{\parallel} = 2.854 \pm 0.003\,, \quad g_{\perp} = 1.472 \pm 0.002.$$

The calculated splitting of the vibronic lines using these g-values and the measured zero-field splitting of $0.95\,\mathrm{cm}^{-1}$ is qualitatively similar to those for CaF_2:Ce^{3+}:H^-, displayed in figures 7.3 and 7.4. The transition energies which follow from these are plotted in figure 7.8 with the experimentally measured transition energies, for both the $\langle 100 \rangle$ and $\langle 111 \rangle$ orientations.

Again, the calculated splittings are in very good agreement with the measured energies, where there was sufficient intensity to measure these. The highest and lowest energy transitions of the $\langle 111 \rangle$ spectra were too weak to be measured. As with CaF_2:Ce^{3+}:H^-, increasing the Ce^{3+} and H^- concentrations would aid in identifying and tracking these weak outer transitions, at the cost of increasing all of the transition linewidths.

Intensity Analysis of the CaF_2:Ce^{3+}:H^- and SrF_2:Ce^{3+}:H^- x-y-Vibronic Zeeman Splittings

The splitting diagrams of figures 7.5 and 7.8 clearly do not represent fully all of the information in the absorption spectra. The large variation in intensities is a feature which can also be analysed by way of the first-order Zeeman matrix 7.1. Pure local-mode vibrational transitions, for which the electronic wavefunctions are unaltered, are electric-dipole allowed transitions which are very much stronger than full vibronic transitions in which both the vibrational and electronic parts change.

For C_{4v} symmetry the vibrational transitions from the ground state, (000), to any linear combination of the (100) and (010) fundamental x-y modes will have the same intensity, thus it remains only to consider the transition in the electronic states. In a general magnetic field, the electronic component of both the ground and vibronic states will be linear combinations of the two Kramers-conjugate ground-state wavefunctions, ψ^+ and ψ^-. The strength of the transition is determined by

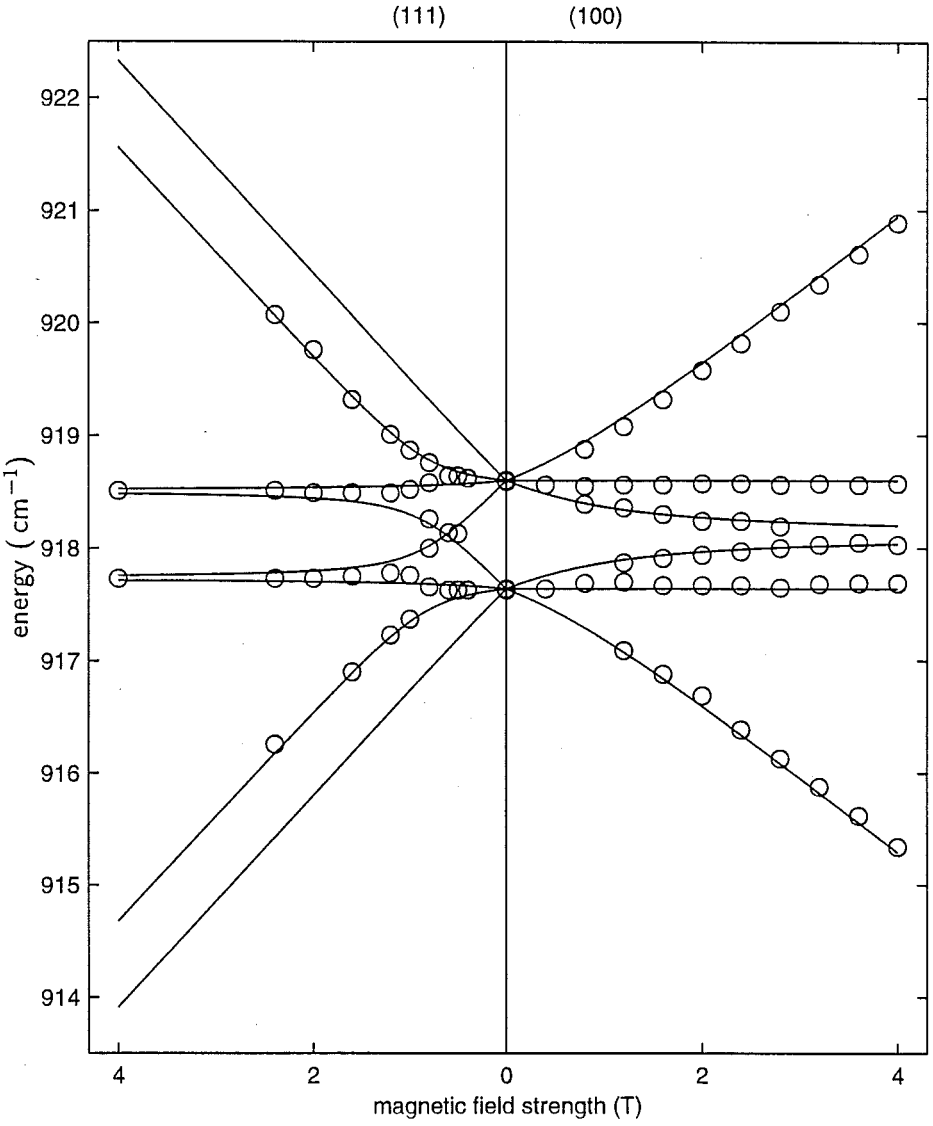

Figure 7.8 : Experimental and calculated Zeeman splitting patterns of the x-y vibronics in SrF_2:0.01%Ce^{3+}:H^-, for magnetic fields parallel to the $\langle 100 \rangle$ and $\langle 111 \rangle$ crystal axes.

these linear combinations, obtained as the eigenfunctions of the Zeeman matrix. Taking the limiting case in this analysis, the transition strengths of $\psi^+ \rightarrow \psi^+$ and $\psi^- \rightarrow \psi^-$ (which must be equal) have been set to unity, while the "cross' transitions $\psi^+ \leftrightarrow \psi^-$ have been set to zero intensity. As an example, the transition

$$a_1\,\psi^+(000) + a_2\,\psi^-(000) \longrightarrow b_1\,\psi^+[\pm] + b_2\,\psi^-[\pm]$$

would have an intensity of $I = |a_1 b_1|^2 + |a_2 b_2|^2$. In addition, the transition strengths are weighted by the Boltzmann factors of their respective ground states, although this has much less effect than the mixing of the wavefunctions.

For a $\langle 100 \rangle$ field, the relative weightings of the C_4 and C_s subsites adds another parameter, since the relative strengths of π and σ components of the transition moment are not known. For a $\langle 111 \rangle$ field, this correction does not arise.

Series of simulated spectra for CaF_2:Ce^{3+}:H^- and for SrF_2:Ce^{3+}:H^- in applied $\langle 111 \rangle$ magnetic fields are shown in figures 7.9 and 7.10, along with the measured spectra for comparison. The absorption coefficient lineshapes for each component line, $\alpha(\sigma)$, were approximated by Lorentzian lineshapes with FWHM linewidths of $0.4\,\mathrm{cm}^{-1}$ for the CaF_2:Ce^{3+}:H^- spectra and $0.3\,\mathrm{cm}^{-1}$ for the SrF_2:Ce^{3+}:H^- spectra. The line strengths were weighted by the transition intensities and Boltzmann factors, and the spectrum converted to transmission intensity by Beer's law:

$$I = \exp\{-\alpha\, x\}$$

where the crystal thickness/concentration parameter, x, was chosen to match the minimum transmittance at zero magnetic field.

The excellent correspondence between the experimental and simulated spectra shows that the first-order perturbation Zeeman analysis incorporating the experimental zero-field splitting and EPR g-values can be used to quantitatively predict not only the energy splittings, but also relative transition intensities.

An unusual feature of the CaF_2:Ce^{3+}:H^- and SrF_2:Ce^{3+}:H^- x-y mode absorption lines is that the lower of the two lines is broadened so that it has a lower peak absorption than the higher component. This behaviour does not occur to this extent for any of the other lanthanide Kramers ions for which an x-y splitting is well resolved, including CaF_2:Sm^{3+}:H^- and SrF_2:Sm^{3+}:H^-, and is not predicted in any way

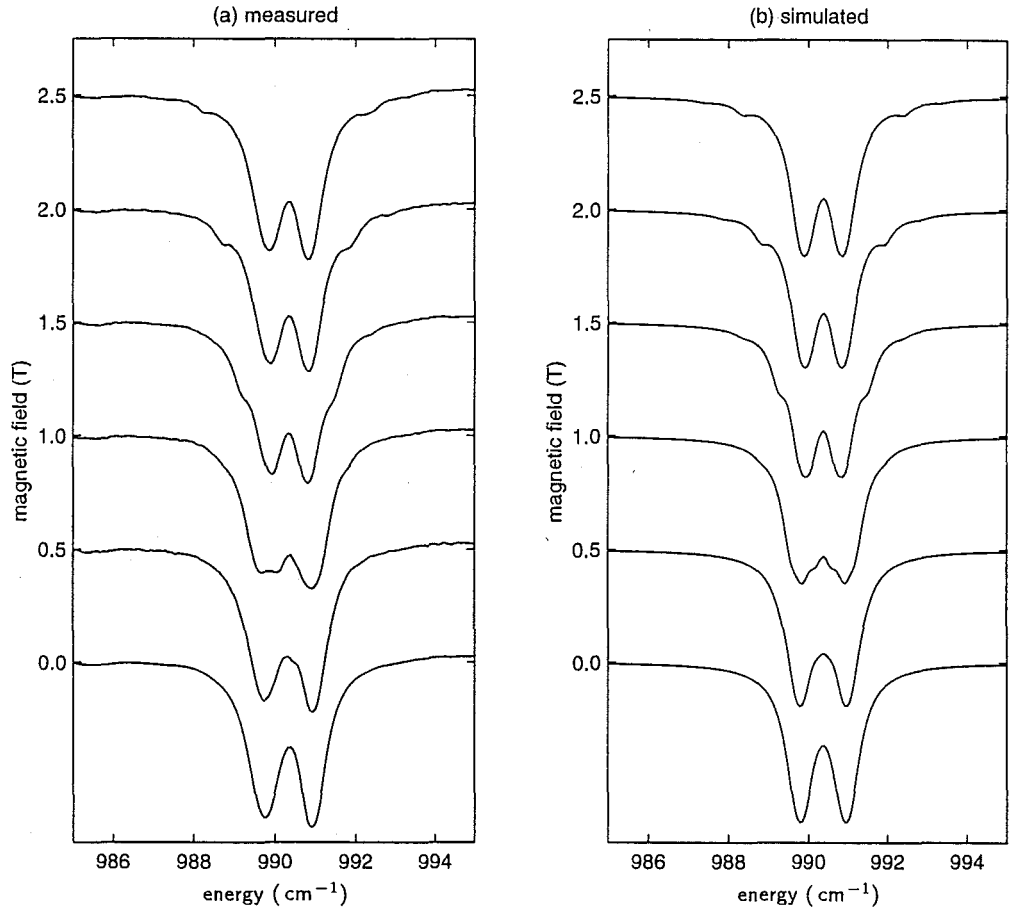

Figure 7.9 : (a) 10 K experimental and (b) simulated infrared-absorption spectra of the x-y vibronics in 2.0 mm-thick CaF_2:0.01%Ce^{3+}:H^-(2 hrs), for magnetic fields parallel to the $\langle 111 \rangle$ crystal axes.

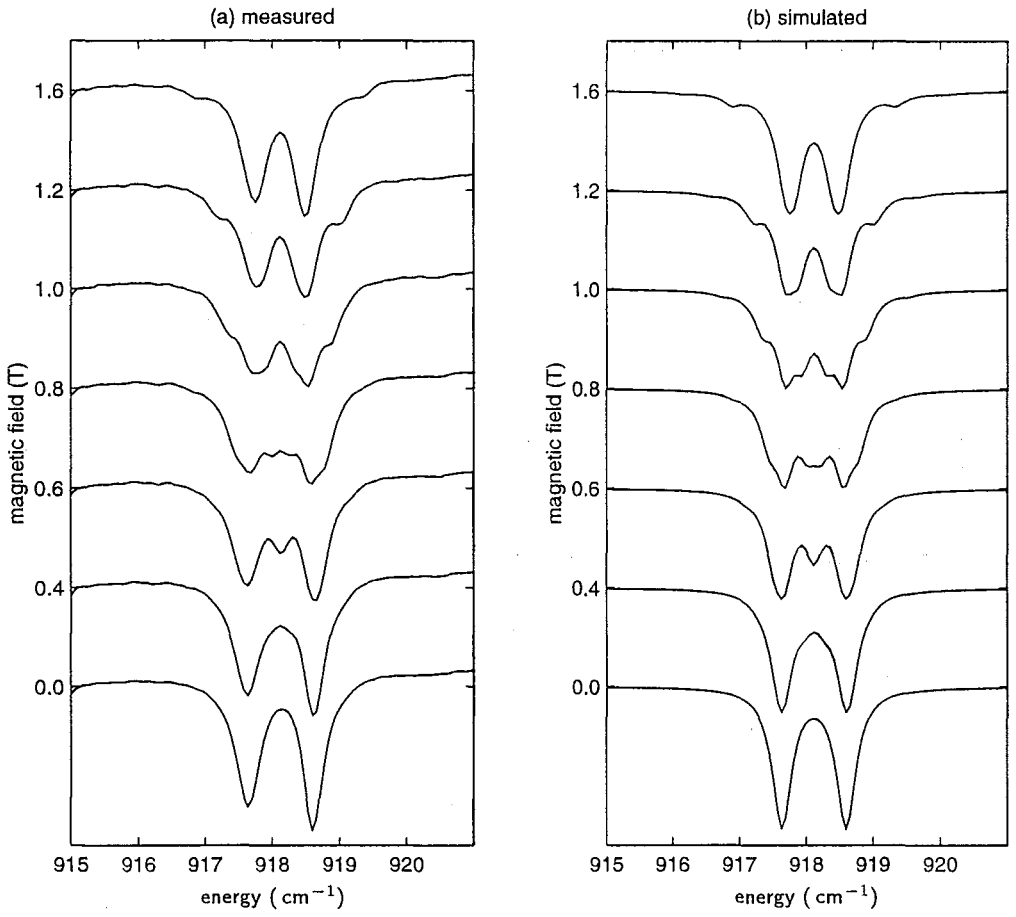

Figure 7.10 : (a) 10 K experimental and (b) simulated infrared-absorption spectra of the x-y vibronics in 2.0 mm-thick SrF_2:0.01%Ce^{3+}:H^-(4.5 hrs), for magnetic fields parallel to the $\langle 111 \rangle$ crystal axes.

by the Zeeman analysis above. It may be that unequal inhomogeneous broadening could arise for these two components. The shifts of the two lines are second-order perturbations due to the electron-phonon interaction, with different intermediate states contributing to each. Since the inhomogeneous broadening would be related to the magnitude of the shift, this broadening may be different for the two lines. However, in section 6.4, the major part of the splitting was shown to be due to the $\phi_2^+(000)$ intermediate state pushing the $\Psi_7^{\pm}$ vibronic states up. Thus any statistical inhomogeneous broadening would be expected to affect the higher-energy vibronic line more than the lower, contrary to observation.

7.1.2 Zeeman Splittings of the x-y Vibronics in CaF_2:Sm^{3+}:H^- and SrF_2:Sm^{3+}:H^-

The Zeeman spectra for the H^- x-y lines of CaF_2:Sm^{3+}:H^- were measured using samples of CaF_2:0.01%Sm^{3+} for both $\langle 100 \rangle$ and $\langle 111 \rangle$ orientations. For the $\langle 100 \rangle$ magnetic field orientation, a 2.1 mm slice hydrogenated for 2 hours was used, while for the $\langle 111 \rangle$ field a 2.2 mm slice hydrogenated for 8 hours was used. The magnetic-field series of spectra for each of these is displayed in figures 7.11 and 7.12. Sm^{3+} is readily reduced to the divalent Sm^{2+} form during crystal growth, and this effect is enhanced by the hydrogenation process, producing bright-green samples from a pale-green parent crystal. This reduction of the samarium ions did not hamper the spectroscopy but the concentration of Sm^{3+} in the samples will be lower than that stated.

Ashburner *et al* [7] have reported the EPR spectroscopy of the H^- compensated Sm^{3+} C_{4v} centre in CaF_2, and found the g-values for this centre to be

$$g_{\parallel} < 0.1 \ , \quad g_{\perp} = 0.868 \pm 0.001.$$

The low value of $g_{\parallel}$ greatly simplifies the $\langle 111 \rangle$ spectra. The splitting in a $\langle 111 \rangle$ magnetic field of the two x-y vibronic states predicted in the case of Ce^{3+} (figure 7.4) was due entirely to the perpendicular component of the field, with the parallel component only contributing quadratic energy shifts. Using the reported value of $g_{\perp}$ and the measured zero-field splitting of 0.67 cm^{-1}, the calculated energy shifts of the vibronic states and splitting of the ground state is shown in figure 7.13, for the

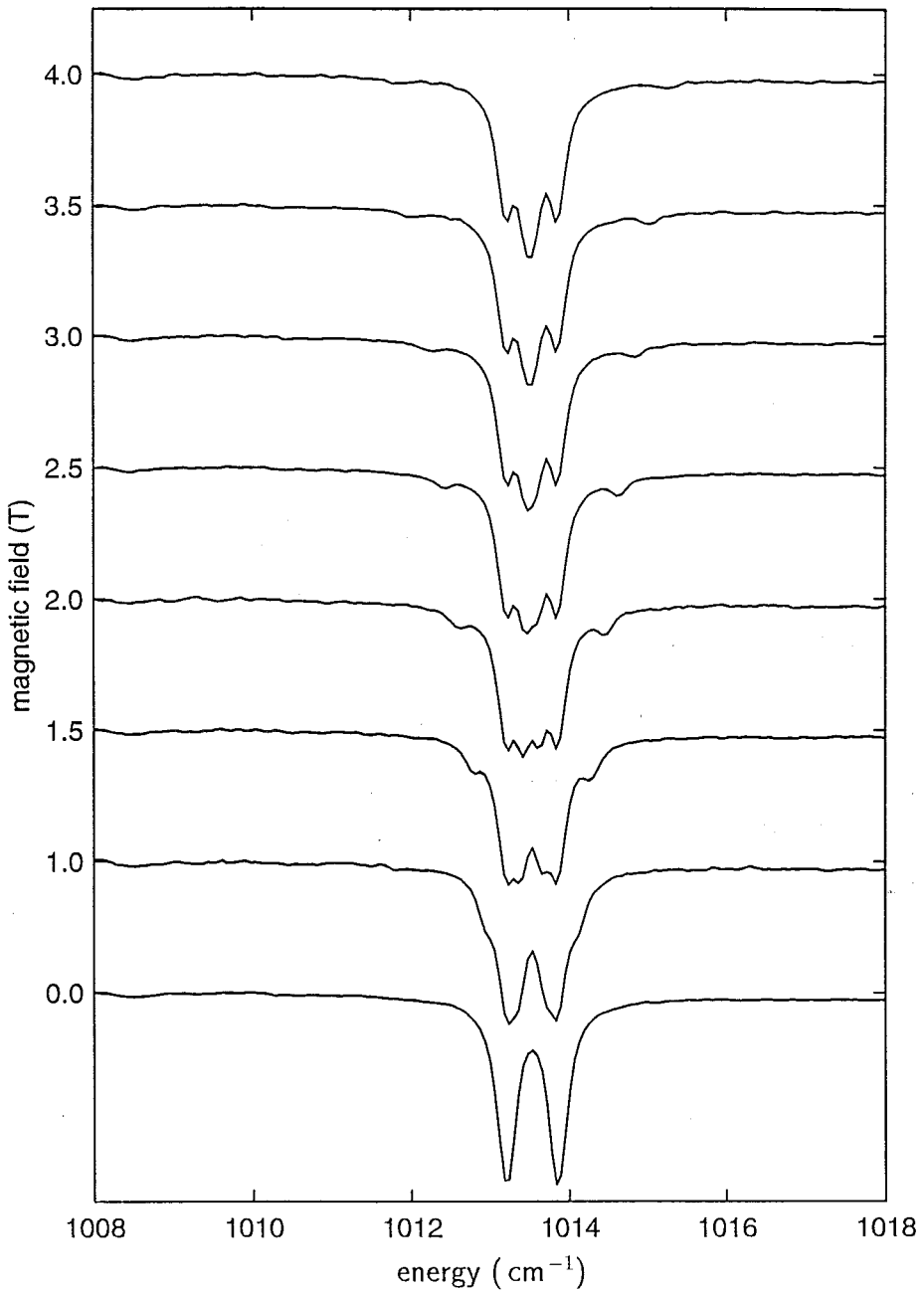

Figure 7.11 : 10 K infrared-absorption spectra of the x-y vibronics in a 2.1 mm slice of CaF_2:0.01%Sm^{3+}:H^-(2 hrs) in applied magnetic fields parallel to the ⟨100⟩ crystal axes. The zero-field spectrum has a maximum absorption of 73%.

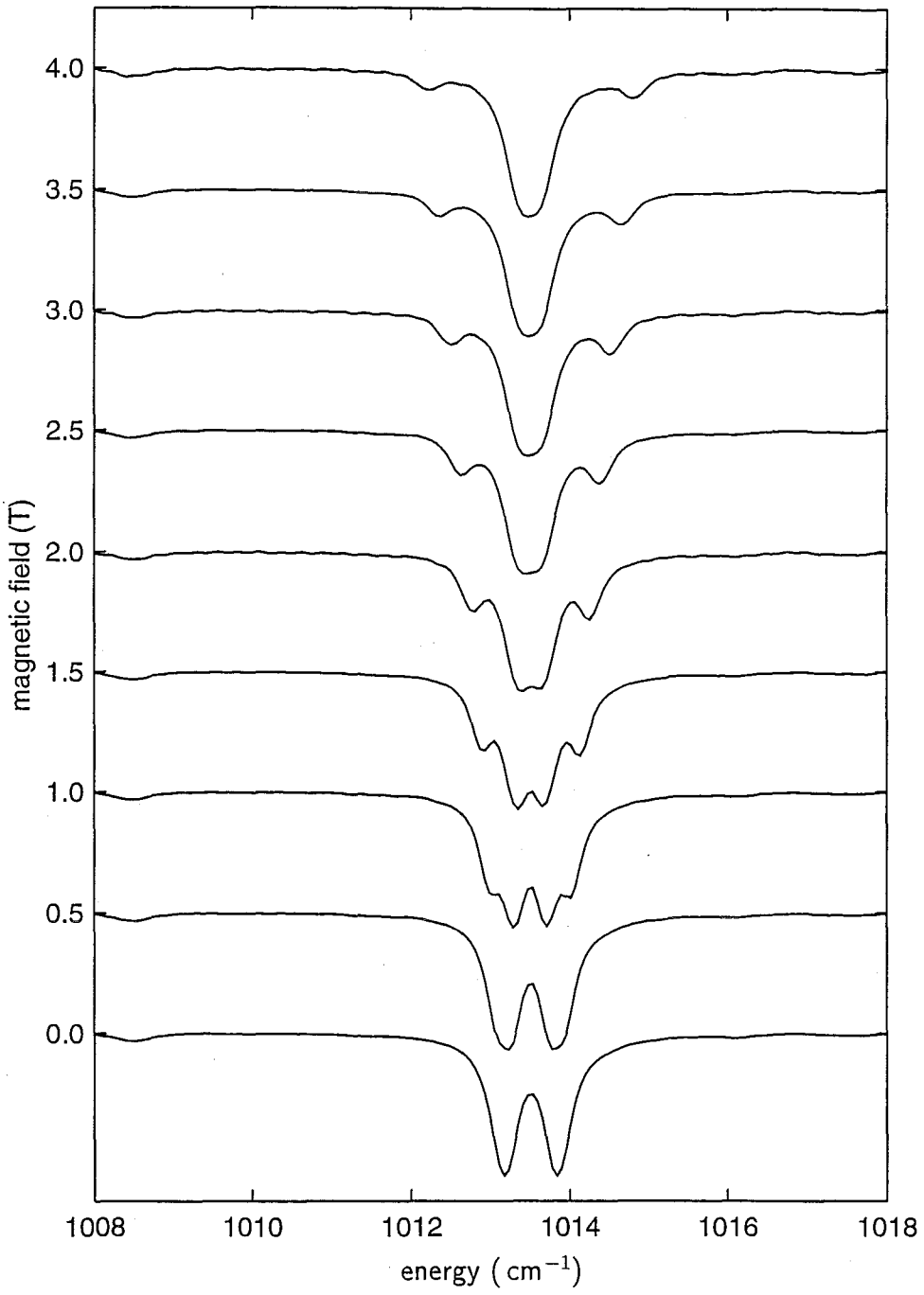

Figure 7.12 : 10 K infrared-absorption spectra of the x-y vibronics in a 2.2 mm slice of CaF_2:0.01%Sm^{3+}:H^-(8 hrs) in applied magnetic fields parallel to the ⟨111⟩ crystal axes. The zero-field spectrum has a maximum absorption of 92%.

C_s subsite.

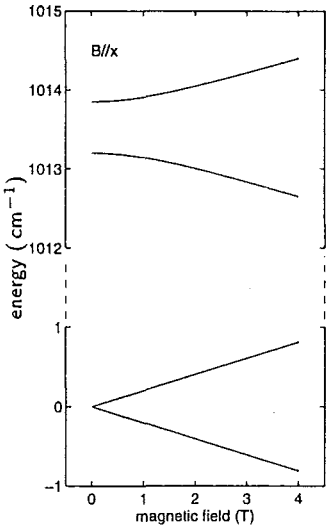

Figure 7.13 : Calculated energies of the ground state and x-y vibronic states of CaF_2:Sm^{3+}:H^- as a function of magnetic field strength, for a field applied perpendicular to the C_{4v} symmetry axis.

If we assume $g_{\|} = 0$ in the Zeeman matrix, the $\langle 111 \rangle$ splittings are identical to those for the C_s subsite of the $\langle 100 \rangle$ orientation, but with the magnetic field scaled by $1/\sqrt{3}$.

The combined C_4/C_s splitting diagram for the $\langle 100 \rangle$ orientation is not affected by the value of $g_{\|}$, since the only transitions observed for the C_4 subsite are unshifted in energy anyway, and so this splitting pattern is qualitatively similar to the Ce^{3+} case.

The calculated transition energies are plotted in figure 7.14 along with the experimental peaks, for both $\langle 111 \rangle$ and $\langle 100 \rangle$ magnetic-field orientations. A $g_{\|}$ value of 0 was used in the calculation, since any splitting for a $g_{\|}$ of up to 0.1 would not be resolved with the available 0.1 cm^{-1} spectral resolution. The correspondence between the experimental and calculated splitting patterns is again very close, but with a suggestion that the outer pair of lines in the $\langle 111 \rangle$ orientation may have a smaller splitting than that calculated. A similar result was found for SrF_2:Sm^{3+}:H^- (figure 7.17). However, in both cases the outer pair of lines in the $\langle 100 \rangle$ splitting

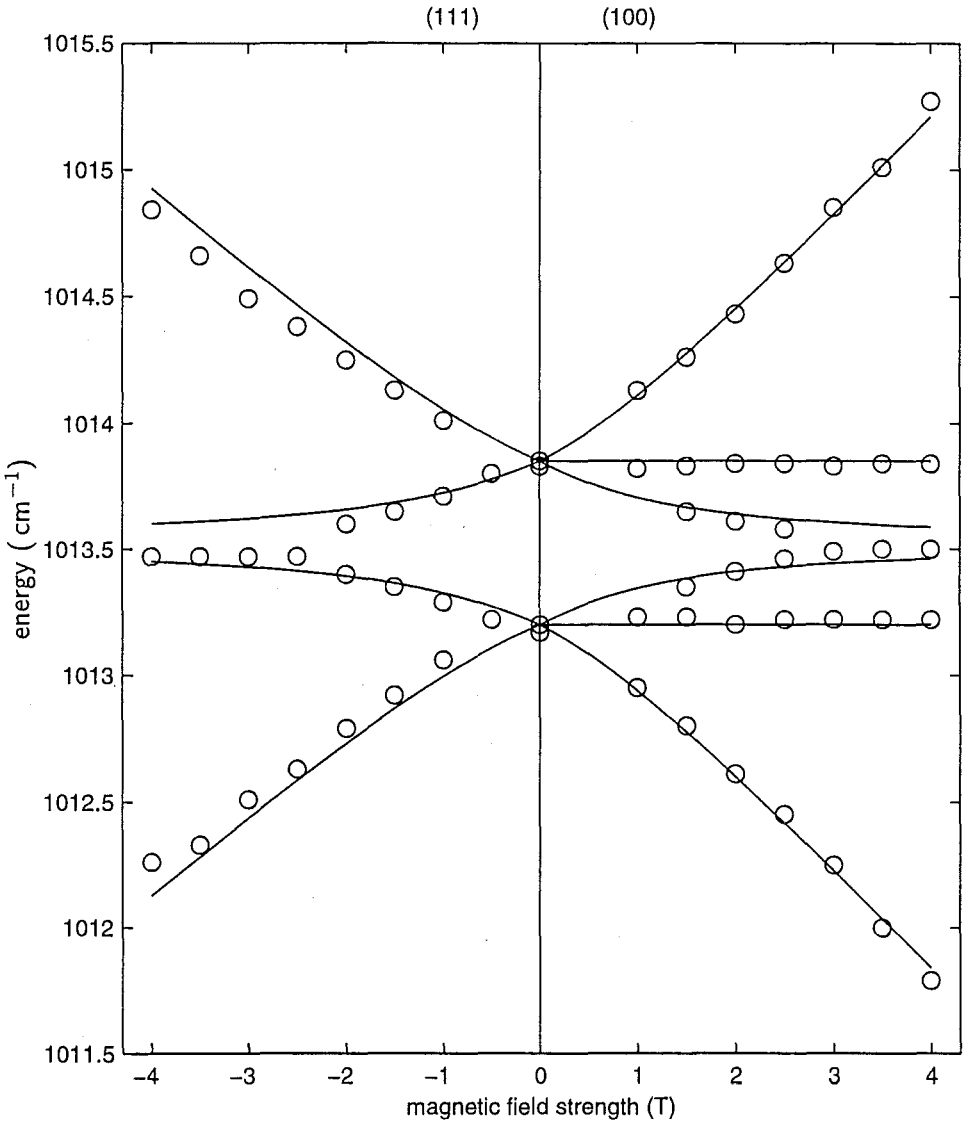

Figure 7.14 : Experimental and calculated Zeeman splitting patterns of the x-y vibronics in CaF_2:0.01%Sm^{3+}:H^-, for magnetic fields parallel to the $\langle 100 \rangle$ and $\langle 111 \rangle$ crystal axes.

matches well with the calculated value, indicating that the value of $g_\perp$ used is correct. Altering $g_\parallel$ can only increase the splitting, so this discrepancy remains anomalous. As it is, the discrepancy is less than the spectral linewidths, but does appear to be consistent for the larger fields.

The Zeeman spectra of SrF_2:Sm^{3+}:H^- were measured using two crystals. For the $\langle 100 \rangle$-orientation of the magnetic field, a 2.4 mm slice of SrF_2:0.01%Sm^{3+} was hydrogenated for 2 hours while for the $\langle 111 \rangle$ orientation, spectra were measured on a 2.0 mm slice of SrF_2:0.02%Sm^{3+}, hydrogenated for 4 hours. The spectra for the $\langle 100 \rangle$ fields are presented in figure 7.15, with those for the $\langle 111 \rangle$ fields in figure 7.16.

The longitudinal z-mode vibronic is also present in these spectra. The z-mode vibronic does not mix to any significant extent with the x-y vibronics in the magnetic field, so has a linear splitting identical to that of the ground state. As for the x-y mode in the C_4 subsite, the "outer" transitions would be expected to be very much weaker than the transitions between like electronic states, which move together in the field producing no splitting. The Zeeman splitting confirms the assignment of the x-y mode to the higher energy pair, as suggested in section 6.4.

The EPR spectroscopy of the H^- C_{4v} centre in SrF_2:Sm^{3+}:H^- has been reported by Newman and Woodward [69], with similar g-values to CaF_2:Sm^{3+}:H^-:

$$g_\parallel < 0.1 \ , \quad g_\perp = 0.862 \pm 0.003.$$

The difference between the spectra for CaF_2:Sm^{3+}:H^- and SrF_2:Sm^{3+}:H^- is thus due mainly to the different zero-field splitting. Assuming $g_\parallel = 0$ and using the zero-field splitting of 0.38 cm^{-1}, the calculated and measured Zeeman splittings are plotted, for both orientations in figure 7.17, showing good agreement between between calculation and measurement, apart from the slightly smaller splitting in the outer lines of the $\langle 111 \rangle$ diagram as discussed above.

Intensity Analysis of the CaF_2:Sm^{3+}:H^- and SrF_2:Sm^{3+}:H^- x-y-Vibronic Zeeman Splittings

An intensity analysis can be carried out for the $\langle 111 \rangle$ Zeeman spectra of CaF_2:Sm^{3+}:H^- and SrF_2:Sm^{3+}:H^- in the same way as was performed for those of CaF_2:Ce^{3+}:H^-

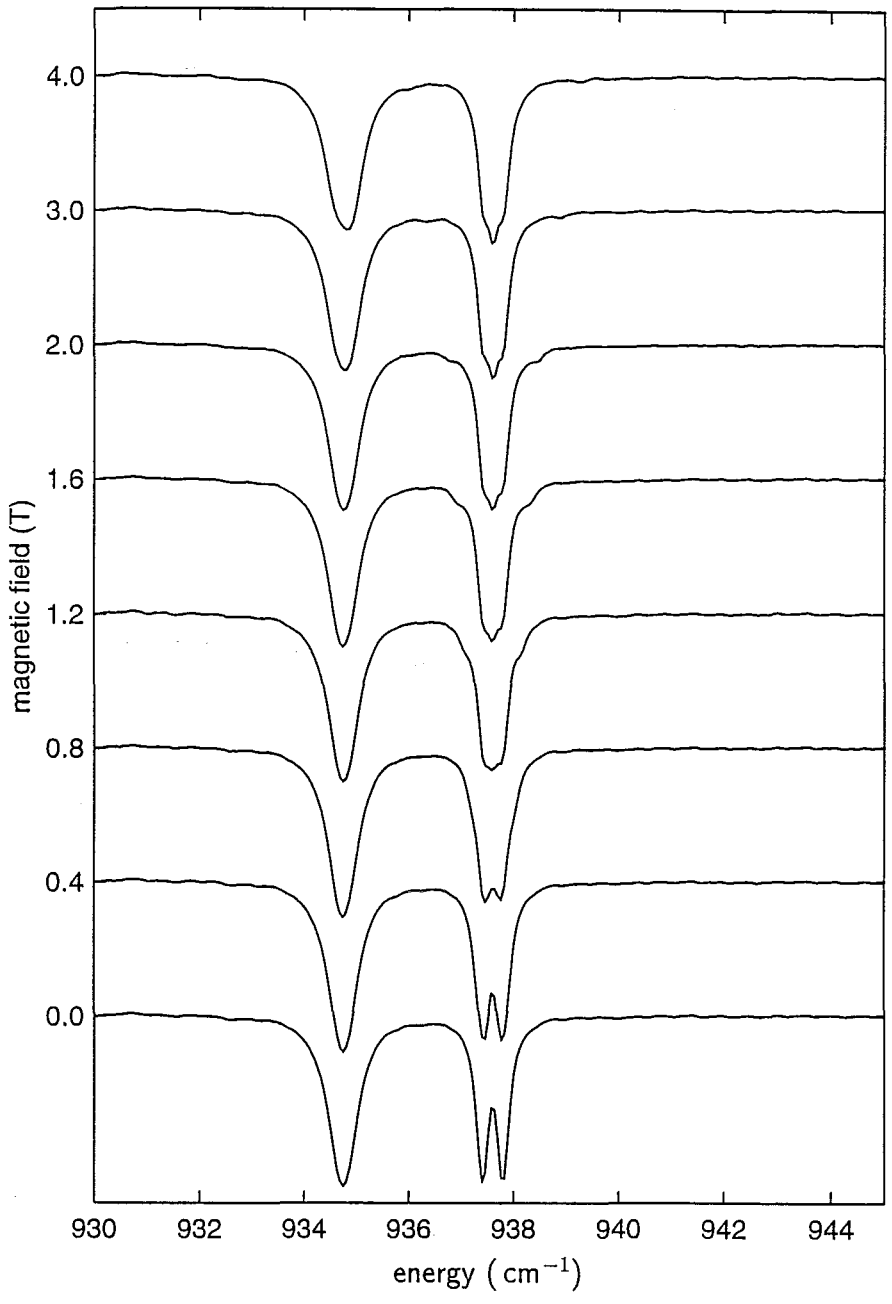

Figure 7.15 : 10 K infrared-absorption spectra of the x-y vibronics in a 2.4 mm slice of SrF_2:0.01%Sm^{3+}:H^-(2 hrs) in applied magnetic fields parallel to the ⟨100⟩ crystal axes. The zero-field spectrum has a maximum absorption of 85%.

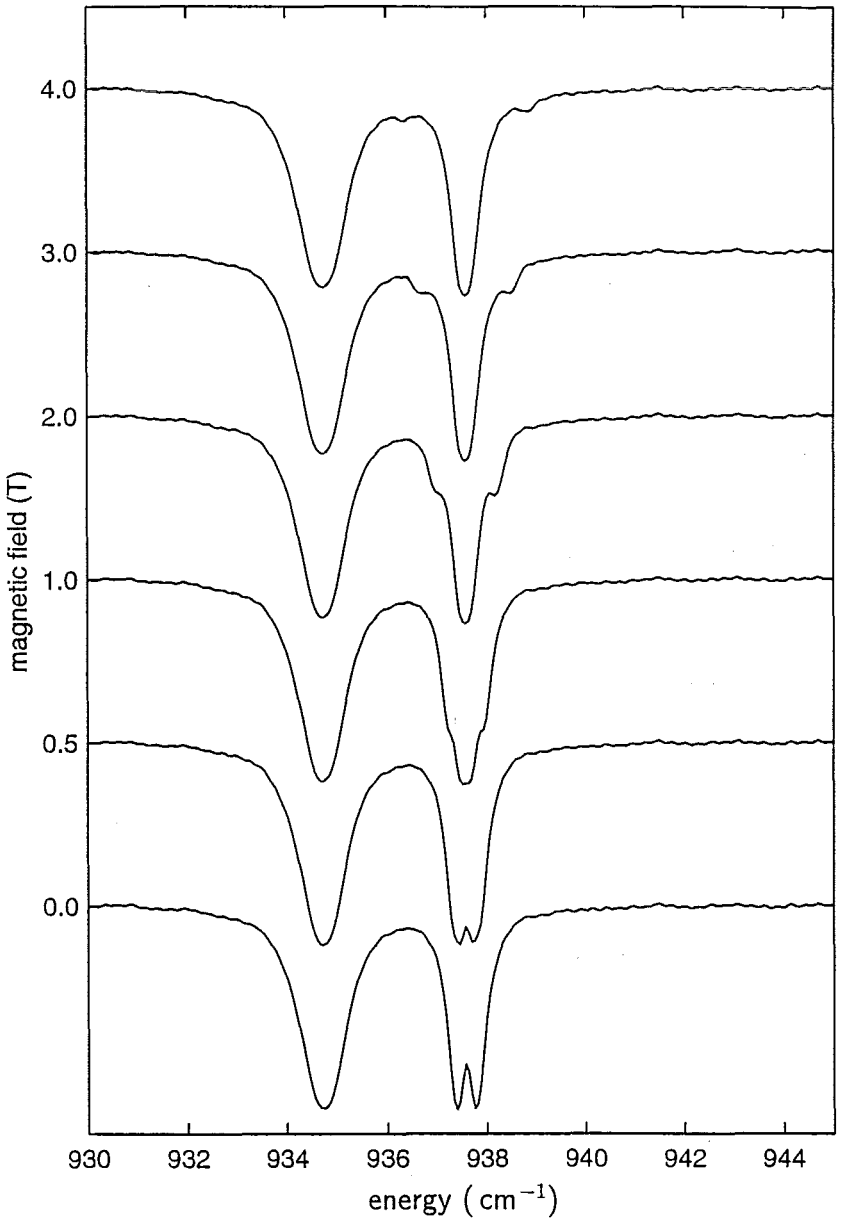

Figure 7.16 : 10 K infrared-absorption spectra of the x-y vibronics in a 2.0 mm slice of SrF_2:0.01%Sm^{3+}:H^-(4 hrs) in applied magnetic fields parallel to the ⟨111⟩ crystal axes. The zero-field spectrum has a maximum absorption of 96%.

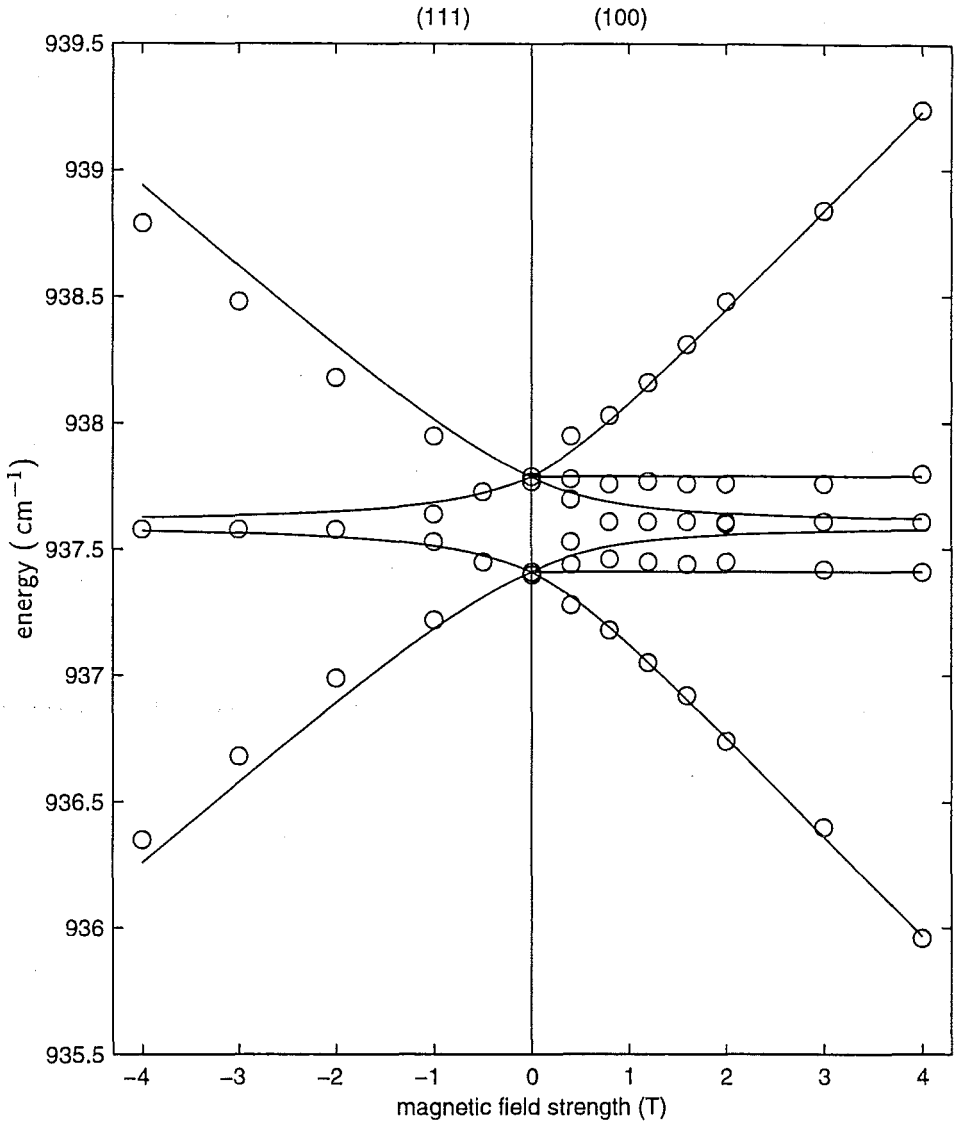

Figure 7.17 : Experimental and calculated Zeeman splitting patterns of the x-y vibronics in SrF_2:0.01%Sm^{3+}:H^-, for magnetic fields parallel to the $\langle 100 \rangle$ and $\langle 111 \rangle$ crystal axes.

and SrF_2:Ce^{3+}:H^-, with the measured and simulated spectra displayed together in figures 7.18 and 7.19.

The absorption-coefficient linewidths were set at $0.28\,cm^{-1}$ (FWHM) for the x-y lines in both cases and $0.70\,cm^{-1}$ (FWHM) for the z line in SrF_2:Sm^{3+}:H^-. Again, the transition strengths of the "cross" transitions, $\psi^+ \leftrightarrow \psi^-$, were set to zero. This produces a good comparison between the measured and simulated spectra for both CaF_2:Sm^{3+}:H^- and SrF_2:Sm^{3+}:H^-.

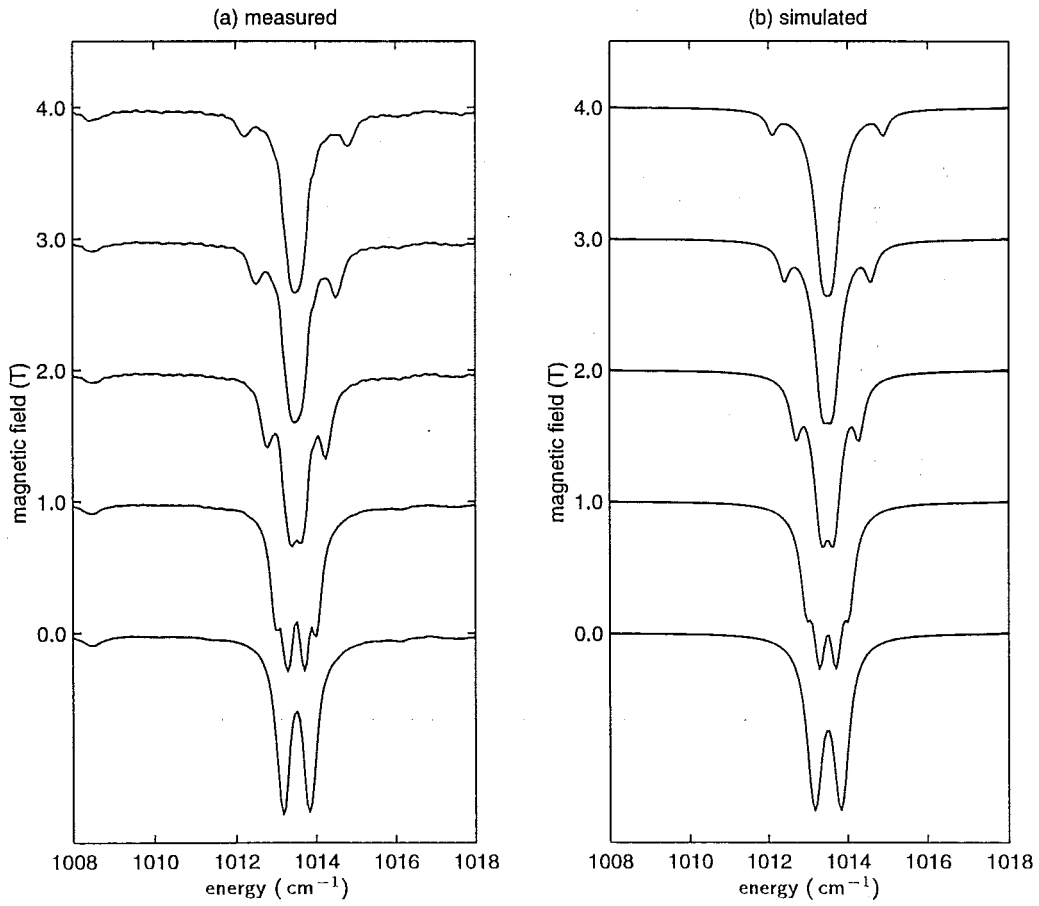

Figure 7.18 : (a) 10 K experimental and (b) simulated infrared-absorption spectra of the x-y vibronics in 2.2 mm-thick CaF_2:0.01%Sm^{3+}:H^-(8 hrs), for magnetic fields parallel to the $\langle 111 \rangle$ crystal axes.

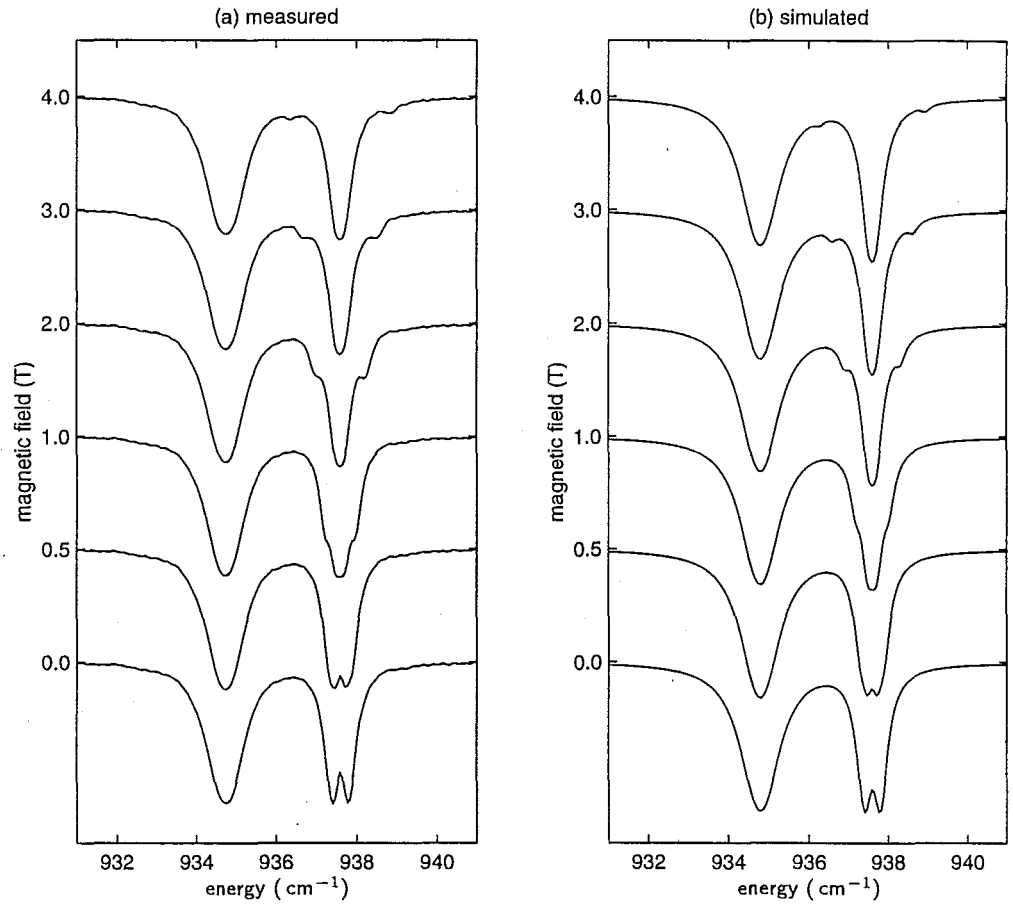

Figure 7.19 : (a) 10 K experimental and (b) simulated infrared-absorption spectra of the x-y vibronics in 2.0 mm-thick SrF_2:0.02%Sm^{3+}:H^-(4 hrs), for magnetic fields parallel to the $\langle 111 \rangle$ crystal axes. The broader, unsplit line at lower energy is the z-mode line.

7.1.3 Zeeman Splittings of the x-y Vibronics in CaF_2:Yb^{3+}:H^-

Like Sm^{3+}, the Yb^{3+} ion is easily reduced to the divalent Yb^{2+} state. In the case of Yb^{3+}, the enhancement of the reduction in the hydrogenation process drastically reduces the concentration of Yb^{3+}, to the extent that the H^- x-y modes of the C_{4v} centre had not previously been identified. After much longer periods of hydrogenation than were required for the other lanthanides, these lines were identified (section 6.4).

The $\langle 100 \rangle$ Zeeman spectra were obtained on a 2 mm slice of CaF_2:0.05%Yb^{3+} which was hydrogenated for 40 hours. These spectra are shown in figure 7.20.

The $\langle 111 \rangle$ Zeeman spectra, shown in figure 7.21, were obtained on a 2 mm slice of CaF_2:0.01%Yb^{3+}, hydrogenated for 30 hours.

With no previous EPR or optical data available on this Yb^{3+}–H^- centre, g-values obtained for the F^- C_{4v} centre by the EPR experiments of Kirton and McLaughlan [50] and ENDOR experiments of Baker and Blake [8] have been adopted:

$$g_{\parallel} = 2.412 \pm 0.003\,, \quad g_{\perp} = 3.802 \pm 0.005.$$

Inserting these g-values and the measured zero-field splitting of $0.70\,cm^{-1}$ into the Zeeman Hamiltonian matrix, the calculated transition energies are plotted in figure 7.22, along with experimental points, for the $\langle 111 \rangle$ and $\langle 100 \rangle$ orientations of the magnetic field.

A poorer signal-to-noise ratio and larger linewidth was obtained in the spectra of CaF_2:Yb^{3+}:H^-, reflecting the difficulty in producing reasonable concentrations of the C_{4v} Yb^{3+}-H^- centre. This has made it very difficult to identify and resolve all of the lines in the spectra. Those lines which have been identified match well with the calculated transition energies in figure 7.22. In the $\langle 100 \rangle$ orientation, the invariant lines of the C_4 subsite could not be resolved from the central peak, with the broadened lineshape of this peak being no more than suggestive of the presence of these two lines. Similar effects are encountered for the $\langle 111 \rangle$-orientation spectra.

The following intensity analysis demonstrates that the large (compared to Ce^{3+} and Sm^{3+}) value of $g_{\perp}$ causes the intensity in the outer transitions to drop very rapidly once the magnetic field is applied.

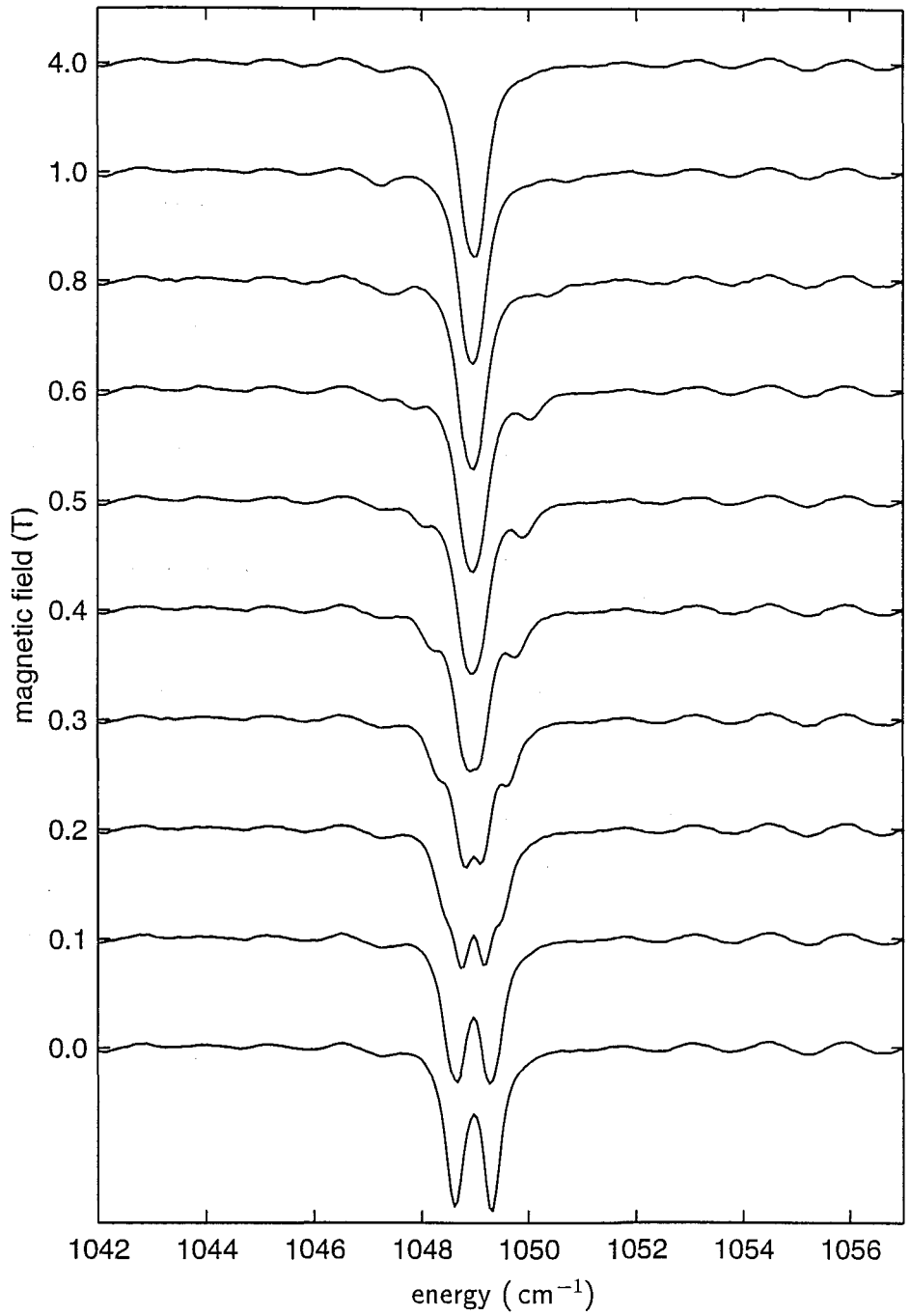

Figure 7.20 : 10 K infrared-absorption spectra of the x-y vibronics in a 2 mm slice of CaF_2:0.05%Yb^{3+}:H^-(40 hrs), in applied magnetic fields parallel to the ⟨100⟩ crystal axes. The zero-field spectrum has a maximum absorption of 59%. A residual background ripple remains in these spectra which could not be removed by dividing out a simple periodic function.

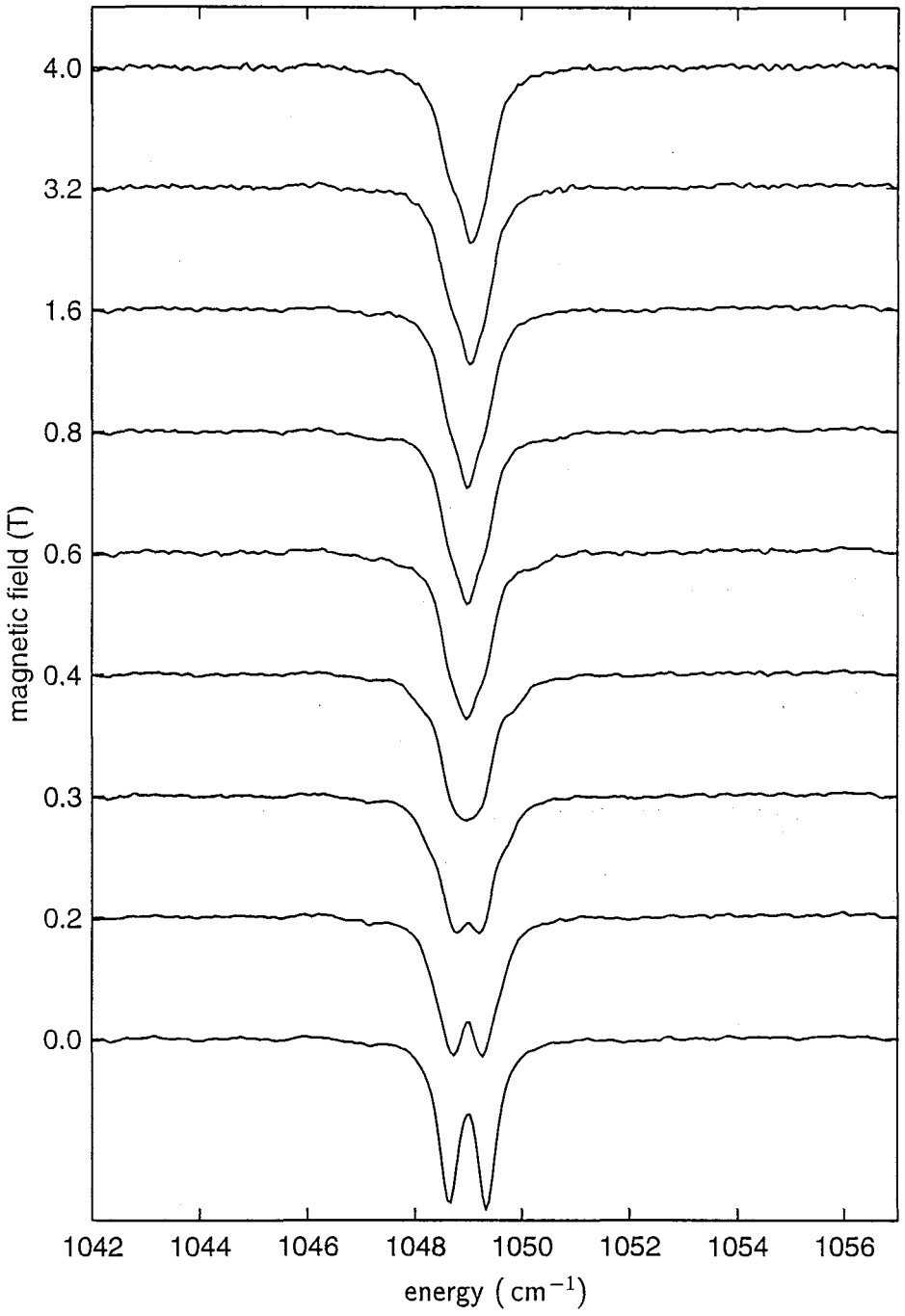

Figure 7.21 : 10 K infrared-absorption spectra of the x-y vibronics in a 2 mm slice of CaF_2:0.05%Yb^{3+}:H^-(30 hrs), in applied magnetic fields parallel to the ⟨111⟩ crystal axes. The zero-field spectrum has a maximum absorption of 35%.

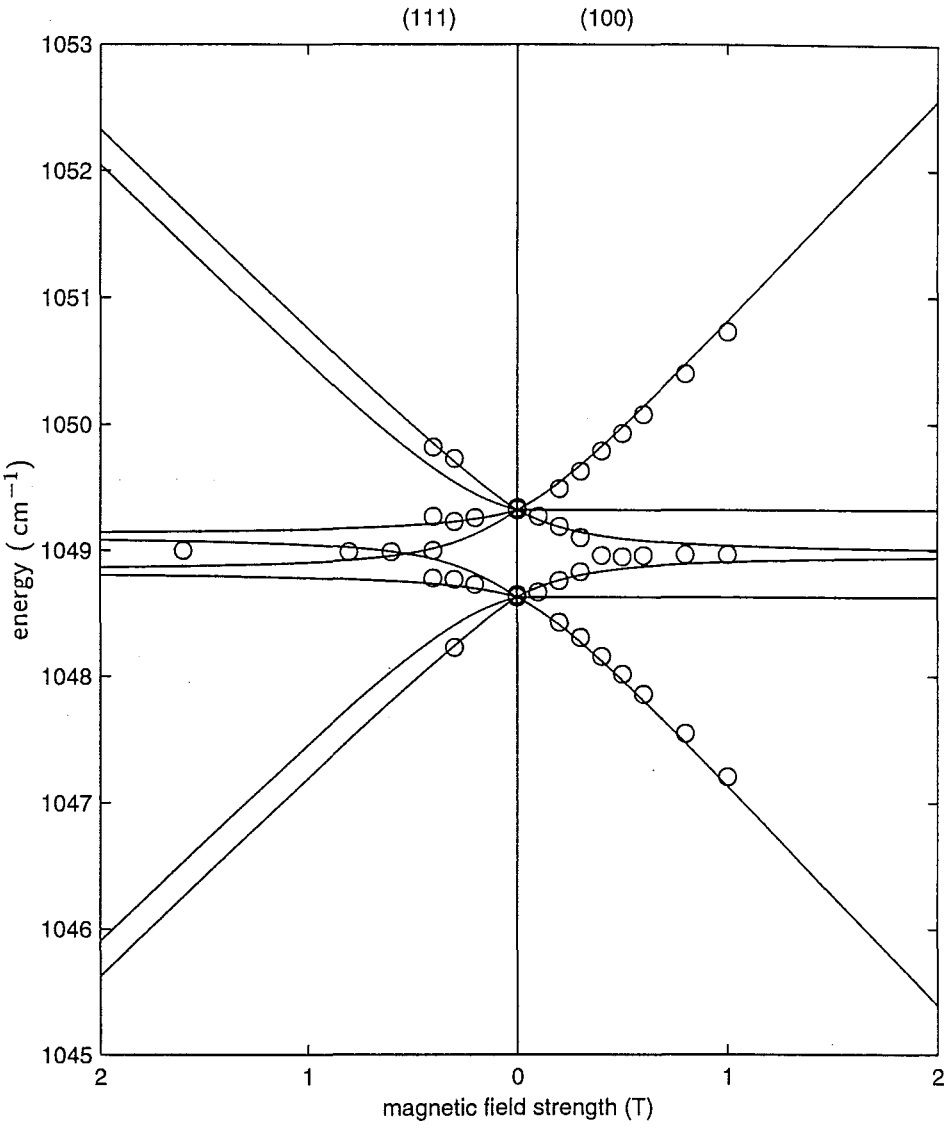

Figure 7.22 : Experimental and calculated Zeeman splitting patterns of the x-y vibronics in CaF_2:0.05%Yb^{3+}:H^-, for magnetic fields parallel to the $\langle 100 \rangle$ and $\langle 111 \rangle$ crystal axes.

Intensity Analysis of the CaF_2:Yb^{3+}:H^- x-y-Vibronic Zeeman Splittings

An intensity analysis can be carried out for the ⟨111⟩ Zeeman spectra of CaF_2:Yb^{3+}:H^- in the same way as with the previous cases, again giving a good agreement between the simulated and experimental spectra in figure 7.23. The linewidths were set at $0.45\,cm^{-1}$ (FWHM), reflecting a long hydrogenation period which would produce a high concentration of H^- ions on nearby substitutional sites, thus increasing inhomogeneous broadening. Again, the strength of the $\psi^+ \leftrightarrow \psi^-$ cross transitions was set to zero.

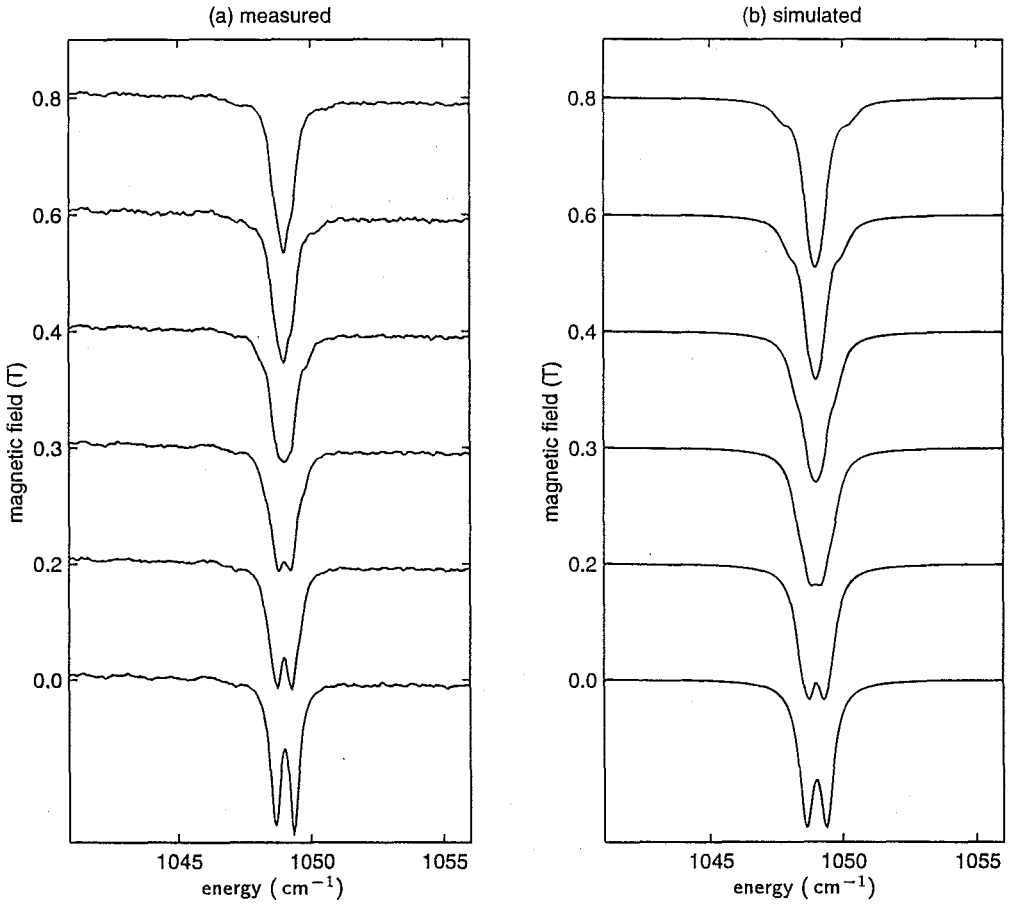

Figure 7.23 : (a) experimental and (b) simulated infrared-absorption spectra of the x-y vibronics in CaF_2:0.01%Yb^{3+}:H^-, for magnetic fields parallel to the ⟨111⟩ crystal axes.

7.1.4 Low Lying Excited States: CaF_2:Er^{3+}:H^-

As discussed in section 6.4, the CaF_2:Er^{3+}:H^- system has a first excited electronic state at 4.5 cm^{-1} above the ground state which will also be significantly populated at 10 K . This state had to be included in the first-order electron-phonon matrix, thus introducing additional first-order contributions to the zero-field electron-phonon interaction splitting. The presence of this nearby state produces far more complex Zeeman splittings than were observed or calculated for any of the other Kramers ions.

The Zeeman spectra for a ⟨111⟩-oriented magnetic field displayed in figure 7.24 were obtained on a 1.8 mm slice of CaF_2:0.01%Er^{3+} which had been hydrogenated for 2 hours.

In calculating the Zeeman effect of these vibronic states, the first-order electron-phonon interaction matrix is extended to include the Zeeman interaction. Using the wavefunction notation already used in section 6.4 with $\phi^{\pm}$ for the $Z_1\gamma_7$ electronic ground state and $\psi^{\pm}$ for the $Z_2\gamma_6$ first excited electronic state at 4.5 cm^{-1}, the full interaction matrix for the eight vibronic states is:

	$\phi^-[+]$	$\phi^+[-]$	$\phi^-[-]$	$\phi^+[+]$	$\psi^-[+]$	$\psi^+[-]$	$\psi^-[-]$	$\psi^+[+]$
$\phi^-[+]$	$E_1 - P_1$			S_1^*			$A - B$	S_3
$\phi^+[-]$		$E_1 + P_1$	S_1				S_3^*	$A - B$
$\phi^-[-]$		S_1^*	$E_2 - P_1$		$A + B$	S_3		
$\phi^+[+]$	S_1			$E_2 + P_1$	S_3^*	$A + B$		
$\psi^-[+]$			$A + B$	S_3	$E_3 - P_2$			S_2^*
$\psi^+[-]$			S_3^*	$A + B$		$E_3 + P_2$	S_2	
$\psi^-[-]$	$A - B$	S_3				S_2^*	$E_4 - P_2$	
$\psi^+[+]$	S_3^*	$A - B$			S_2			$E_4 + P_2$

(7.3)

where A±B are electron-phonon interaction terms, the E_i terms incorporate both crystal-field splitting and electron-phonon interaction parts and the Zeeman terms are:

$$P_1 = \mu_B B_z \langle \phi^+ | M_0^{(1)} | \phi^+ \rangle = \tfrac{1}{2} \mu_B g_{\parallel}^{\phi} B_z$$

$$P_2 = \mu_B B_z \langle \psi^+ | M_0^{(1)} | \psi^+ \rangle = \tfrac{1}{2} \mu_B g_{\parallel}^{\psi} B_z$$

$$S_1 = -\mu_B \tfrac{1}{\sqrt{2}} (B_x - iB_y) \langle \phi^+ | M_1^{(1)} | \phi^- \rangle = -\tfrac{1}{2} \mu_B g_{\perp}^{\phi} (B_x - iB_y)$$

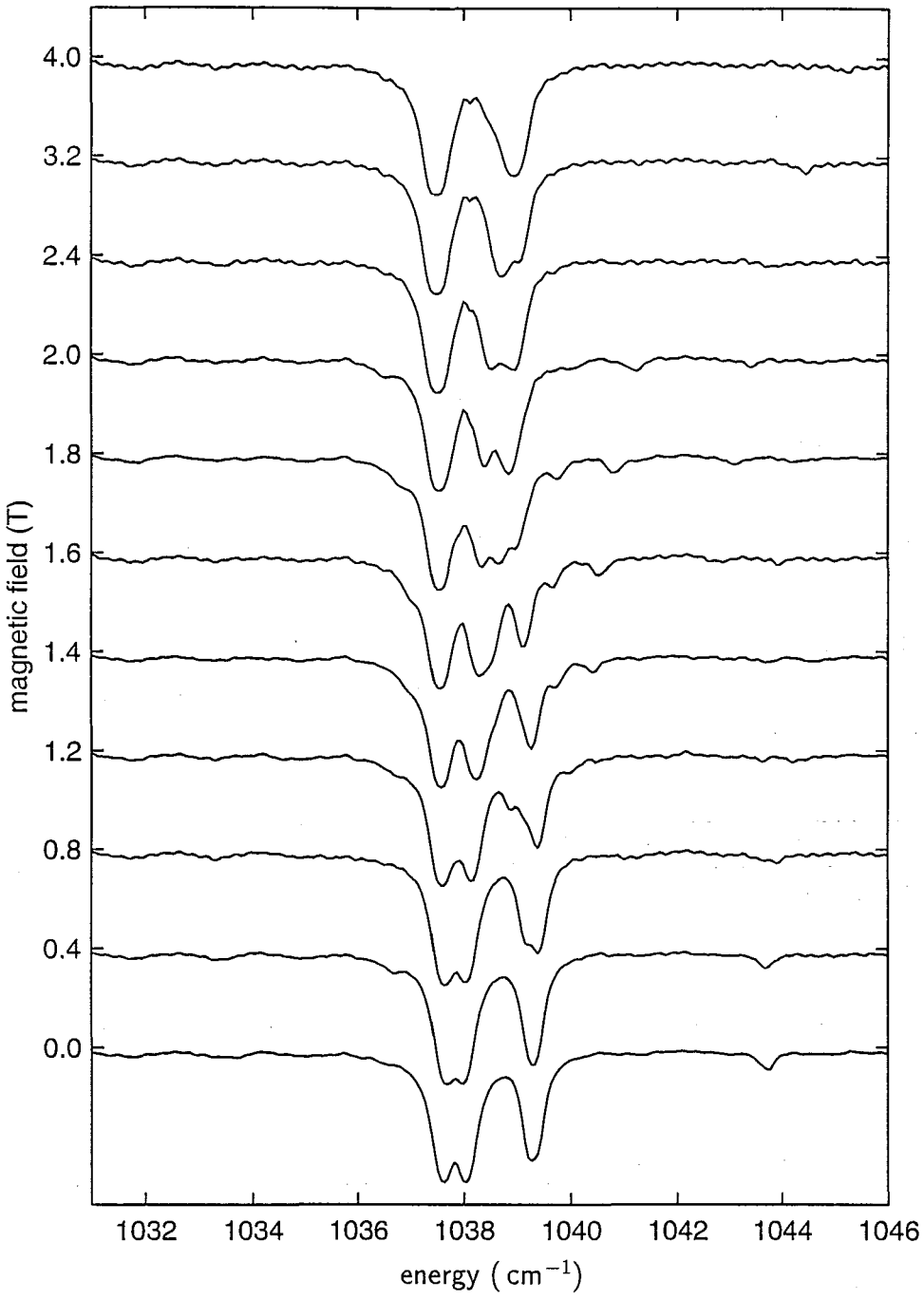

Figure 7.24 : 10 K infrared-absorption spectra of the x-y vibronics in a 1.8 mm slice of CaF_2:0.01%Er^{3+}:H^-(2 hrs) in applied magnetic fields parallel to the ⟨111⟩ crystal axes. The zero-field spectrum has a maximum absorption of 61%.

$$S_2 = -\mu_B \tfrac{1}{\sqrt{2}}(B_x - iB_y)\langle\psi^+|M_1^{(1)}|\psi^-\rangle = +\tfrac{1}{2}\mu_B g_\perp^\psi (B_x - iB_y)$$
$$S_3 = -\mu_B \tfrac{1}{\sqrt{2}}(B_x - iB_y)\langle\psi^-|M_1^{(1)}|\phi^+\rangle = -\tfrac{1}{2}\mu_B g_\perp^\times (B_x - iB_y)$$

with $\mathbf{M} = \mathbf{L} + 2\mathbf{S}$. The EPR g-values have been reported by Edgar *et al* [25] as

$$g_\parallel^\phi = 7.465 \pm 0.01 \qquad g_\perp^\phi = 6.1 \pm 0.1$$
$$g_\parallel^\psi = 1.683 \pm 0.001 \qquad g_\perp^\psi = 9.09 \pm 0.05$$

while the S_3 term was estimated from the calculated wavefunctions.

Again, the electron-phonon terms are introduced as parameters, the E_i's absorbing the second-order shifts. While the A±B electron-phonon interaction parameters (section 6.4.6) could be absorbed into the E_i terms at zero field, they play a large part in determining the mixing of states in a magnetic field and must be included in the Zeeman analysis.

The matrix for the ground states includes the same Zeeman terms and the ground state splitting, E_0:

	$\phi^-(000)$	$\phi^+(000)$	$\psi^-(000)$	$\psi^+(000)$
$\phi^-(000)$	$-P_1$	S_1^*		S_3
$\phi^+(000)$	S_1	P_1	S_3^*	
$\psi^-(000)$		S_3	$E_0 - P_2$	S_2^*
$\psi^+(000)$	S_3^*		S_2	$E_0 + P_2$

(7.4)

It was found in section 6.4 that the second-degree electron-phonon interaction terms estimated from the point-charge model were far too small to account for the zero-field x-y splitting. The A±B parameters in this Zeeman matrix are thus truly parameters in the sense that they are not determined simply by the zero-field splitting. In obtaining the calculated Zeeman splitting diagrams here, the ratio of A/B was held at the value given by the point-charge model, but their magnitudes were scaled together to give the splittings which best approximated the experimental data. Varying these off-diagonal matrix elements gave significant changes to the splitting diagram at moderate and high magnetic fields. The E_i crystal-field/electron-phonon interaction parameters were adjusted, after selecting the value of the scaling factor of A and B, to give the experimental zero-field energies.

Calculation of the transition energies by diagonalisation of these two matrices gives 32 possible transitions. The splitting diagram of these transitions will clearly be

far more complicated than can possibly be resolved using the available $0.1\,cm^{-1}$ resolution. An indication of which transitions are expected to dominate the splitting diagram can be obtained by calculating intensities in a similar way as with the previous cases of Ce^{3+}, Sm^{3+} and Yb^{3+}.

However, attempts to produce full simulated spectra for the $\langle 111 \rangle$ Zeeman splittings of the CaF_2:Er^{3+}:H^- x-y vibronics have not been successful thus far. The presence of the extra electron-phonon terms in the Zeeman matrix introduces parameters which cannot be measured directly, and whose values can only be deduced by trial and error to produce the best possible simulated spectra. While the splitting diagram of figure 7.25 demonstrates that the Zeeman/electron-phonon matrix produces an appropriate pattern, the mismatches are still significant. Because there is no provision for identifying transitions with lines in the simulated spectra of such complex cases, even small mismatches can lead to a very different simulated and experimental spectra.

The experimental and calculated splitting diagrams are plotted in the splitting diagram of figure 7.25, with additional data points from Zeeman spectra obtained by Dr Glynn Jones on CaF_2:0.05%Er^{3+}:H^- [42]. As an intermediate stage to full-blown simulation of the spectra, those transitions which are calculated to have high intensities have been plotted as bold lines.

The calculated intensities depended, as previously, on the admixtures of the wavefunctions, and on the Boltzmann populations of the ground states. The criteria for inclusion of calculated lines as "high intensity" were adjusted to match the presence of experimental data points as closely as possible. In figure 7.25, a transition was plotted as a bold line if the magnitude of the inner product of the normalised electronic wavefunctions was greater than 0.1 and if the initial state had a thermal population of greater than 14%.

This splitting diagram demonstrates that, even for the more complex 32-state case of CaF_2:Er^{3+}:H^-, analysis of the first-order perturbation matrix can give a reasonable estimate of the Zeeman transition energies, and an indication of their relative intensities.

The Zeeman splitting of the CaF_2:Er^{3+}:H^- vibronics for a $\langle 100 \rangle$ field is more complicated, due to the superposition of spectra of the C_4 and C_s subsites. The spectra

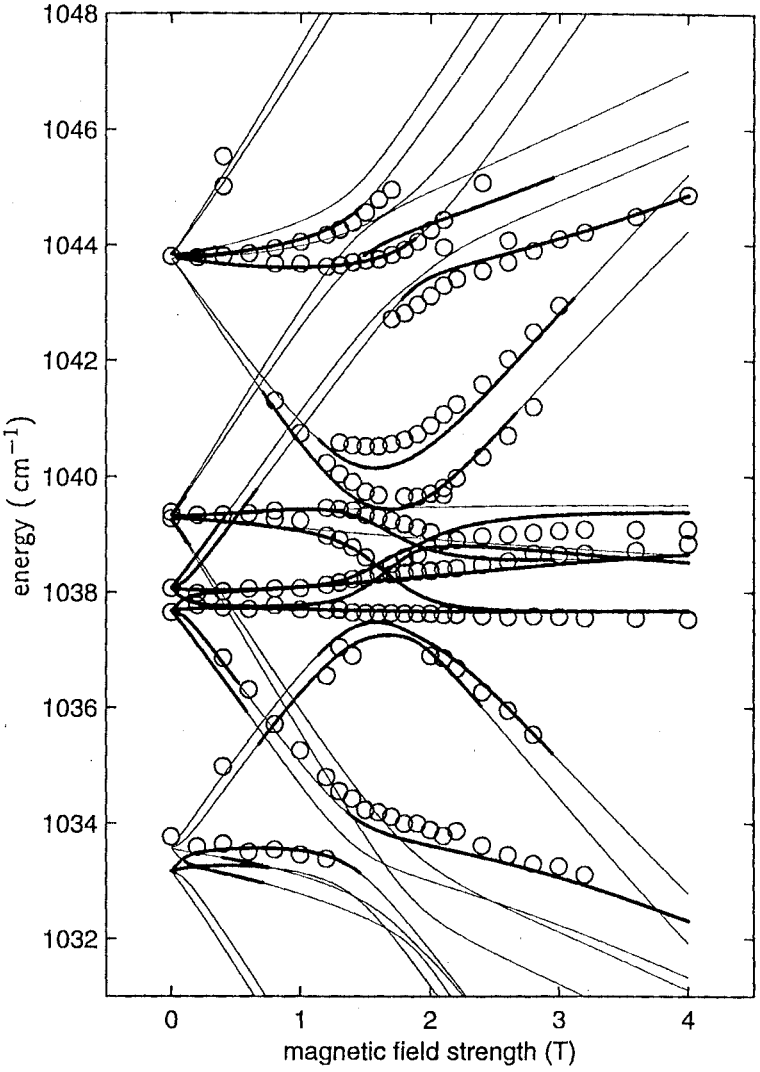

Figure 7.25 : 10 K experimental and calculated Zeeman splitting patterns of the x-y vibronics in CaF_2:0.05%Er^{3+}:H^-, for magnetic fields parallel to the $\langle 111 \rangle$ crystal axis.

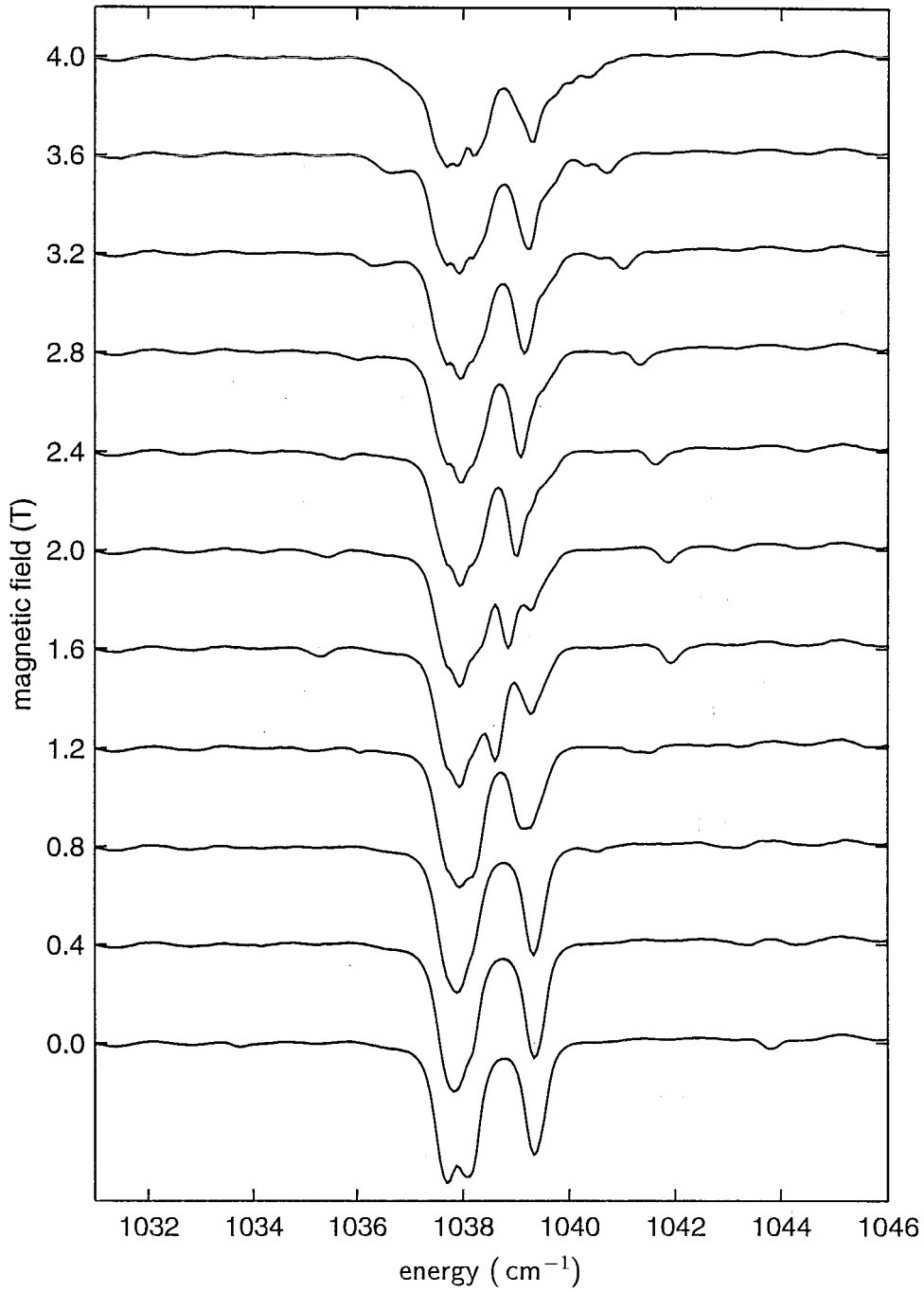

Figure 7.26 : 10 K infrared-absorption spectra of the x-y vibronics in a 3.3 mm slice of CaF_2:0.01%Er^{3+}:H^-(6 hrs) in applied magnetic fields parallel to the ⟨100⟩ crystal axes. The zero-field spectrum has a maximum absorption of 88%.

obtained on a 3.3 mm slice of CaF_2:0.01%Er^{3+}, hydrogenated for 6 hours, are shown in figure 7.26.

The peaks measured from these spectra are plotted in figure 7.27 against the calculated splittings for the two magnetic subsites, C_4 for B$\|$ z and C_s for B$\perp$ z. The calculated energies have been plotted as bold lines for high intensity transitions, following the same criteria as adopted for the $\langle 111 \rangle$ case.

The intensity criteria used here do not accurately quantitatively predict the observed transitions, and attempts at finding a significantly better set of criteria have not been successful. However, the plots do account for the energies of those transitions which were observed. It appears that the C_4 subsite dominates over the C_s subsite for transitions which have split away from the zero-field energies. This is consistent with the mixing between states being less for the C_4 subsite, which is only mixed by the electron-phonon interaction terms whereas for the C_s subsite mixing is effected also by the Zeeman interaction itself.

7.1.5 Zeeman Splittings of the x-y Vibronics in CaF_2:Nd^{3+}:H^- and SrF_2:Nd^{3+}:H^-—Null Effect

The zero-field x-y splittings for CaF_2:Nd^{3+}:H^- and SrF_2:Nd^{3+}:H^- were measured in section 6.4 to be 0.3 cm^{-1} and 0.2 cm^{-1}, respectively. In both cases, the absorption spectrum is not significantly changed when magnetic fields of up to 4 T are applied along the $\langle 111 \rangle$ crystal axes. The Zeeman spectra of the x-y splittings in a 2.1 mm slice of CaF_2:0.01%Nd^{3+}:H^- hydrogenated for 2 hours is shown in figure 7.28, along with a series of simulated spectra for the same magnetic fields.

The lack of any further observed splitting for magnetic fields along the $\langle 111 \rangle$ axis is consistent with the behaviour shown by the simulated spectra, and is due to the low value of $g_\perp$ in this site. The g-values have been reported by Ashburner *et al* [7] as:

$$g_\| = 4.79 \pm 0.01 \, , \; g_\perp = 0.981 \pm 0.001 \, .$$

In this centre the Zeeman splitting is dominated by the parallel effect, which does not mix the C_{4v}–C_4 basis wavefunctions, with only a relatively small perpendicular effect to provide any mixing. With the low level of mixing, the transitions which

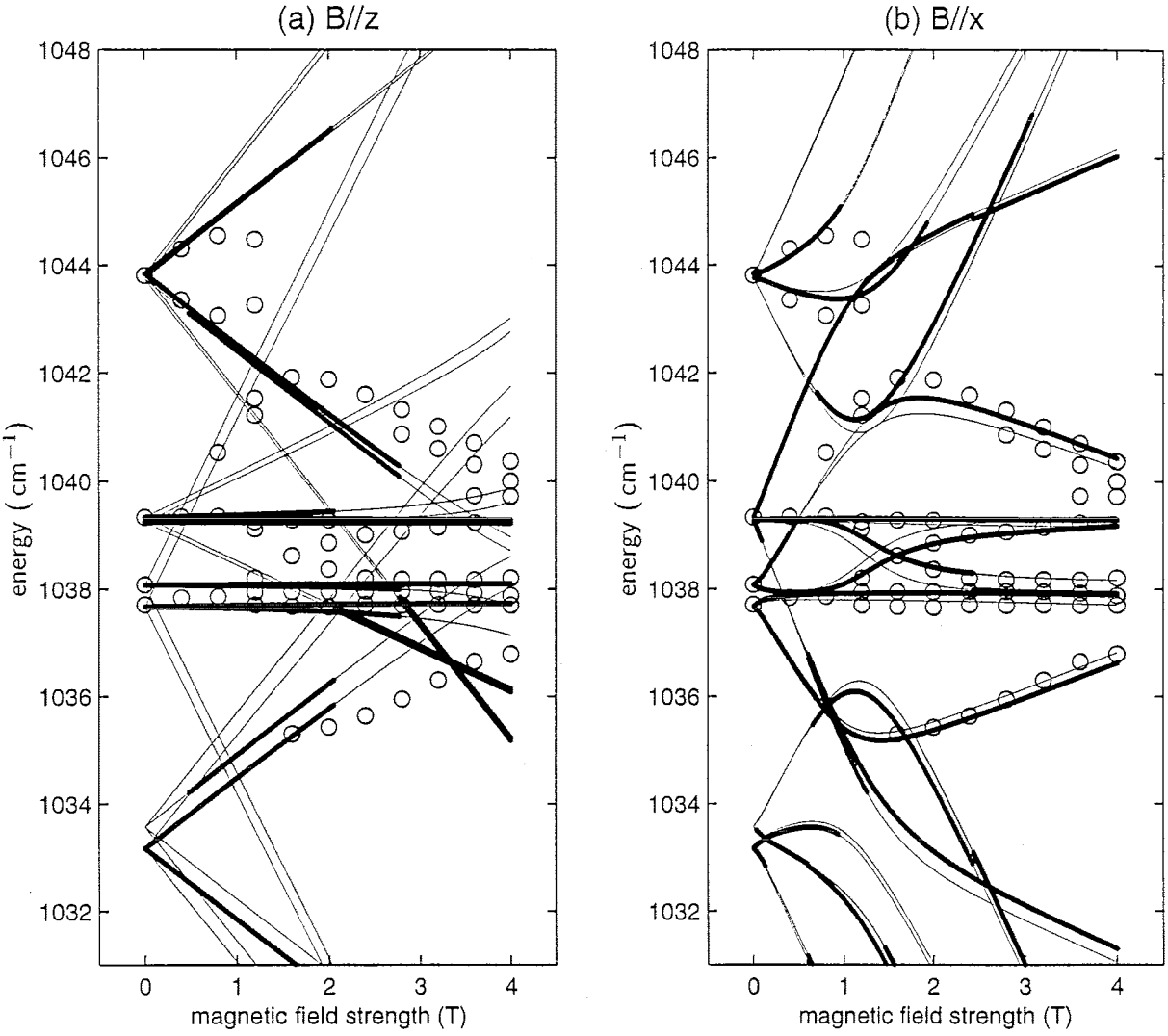

Figure 7.27 : Calculated Zeeman splitting patterns of the x-y vibronics in CaF_2:0.01%Er^{3+}:H^-, for magnetic fields (a) parallel to the C_4 symmetry axis, and (b) perpendicular to this axis, with the experimental data superimposed on both patterns.

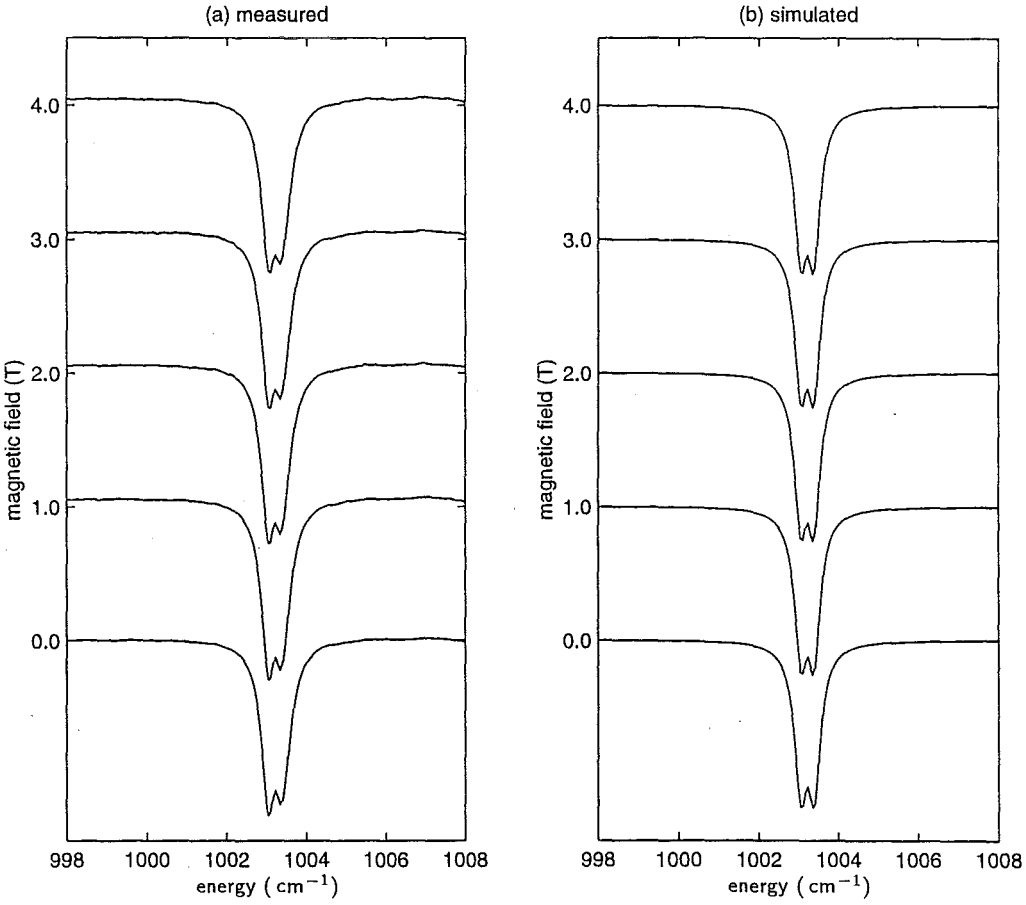

Figure 7.28 : (a) 10 K experimental and (b) simulated infrared-absorption spectra of the x-y vibronics in 2.1 mm-thick CaF_2:0.01%Nd^{3+}:H^-(2 hrs), for magnetic fields parallel to the ⟨111⟩ crystal axes. The measured zero-field spectrum has a maximum absorption of 87%.

split away from the zero-field energies have very low intensities.

A similar null result was found also for a 1.6 mm slice of SrF_2:0.01%Nd^{3+}:H^- hydrogenated for 2 hours, with the same reason for the lack of further splitting applying.

7.1.6 Zeeman Splittings of the x-y Vibronics in CaF_2:Gd^{3+}:H^-—Null Effect

No resolvable x-y splittings were observed for CaF_2:Gd^{3+}:H^-, which is expected since Gd^{3+} has only a very small zero-field splitting for its $^8S_{7/2}$ ground multiplet which arises from second-order mixing with the $^6P_{7/2}$ and higher multiplets above 30000 cm^{-1}. This immediately puts any Zeeman effects which would produce splittings of the order of the experimental linewidth into the high-field regime (compared to the zero-field splitting), where any transitions away from the zero-field energy have very low intensity.

Zeeman spectra were measured for magnetic fields applied along the $\langle 111 \rangle$ axis of a 1.8 mm slice of CaF_2:0.02%Gd^{3+}:H^- hydrogenated for 2 hours, with no observable effect, as expected.

7.1.7 Zeeman Splittings of the x-y Vibronics in CaF_2:Dy^{3+}:H^-—Null Effect

CaF_2:Dy^{3+}:H^- was found to have a well-resolved zero-field x-y splitting of 0.42 cm^{-1} (section 6.4), which might be expected to show clear Zeeman splittings. However, no further Zeeman splittings were measured. The series of spectra for applied magnetic fields along the $\langle 111 \rangle$ crystal axis of a 1.6 mm slice of CaF_2:0.02%Dy^{3+}:H^- hydrogenated for 2 hours is shown in figure 7.29. Again, the absence of further Zeeman splittings is consistent with the simulated spectra in the same figure.

Zeeman spectra for magnetic fields applied along the $\langle 100 \rangle$ crystal axis were also measured, on a 3.0 mm sample of CaF_2:0.02%Dy^{3+}:H^- hydrogenated for 7 hours, also with no further splittings apparent.

The explanation for the absence of further Zeeman splittings comes from the value of $g_\perp$. EPR resonances have not been observed for either the H^- of F^- compensated

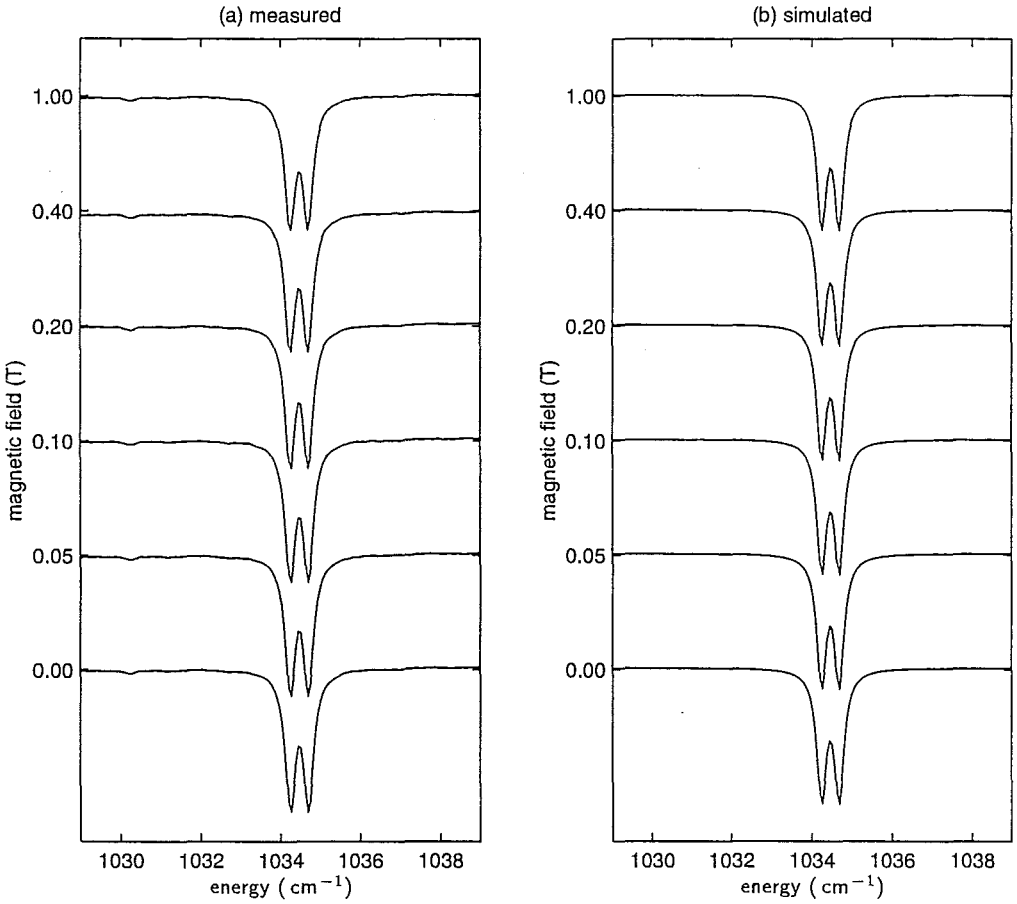

Figure 7.29 : (a) 10 K experimental and (b) simulated infrared-absorption spectra of the x-y vibronics in 1.6 mm-thick CaF_2:0.02%Dy^{3+}:H^-(1.5 hrs), for magnetic fields parallel to the $\langle 111 \rangle$ crystal axes. The measured zero-field spectrum has a maximum absorption of 86%.

C_{4v} centres, and the explanation for this was discussed in section 6.4. The g-values obtained from the crystal-field calculation in that section were:

$$g_{\parallel} = 17.12 \ , \ g_{\perp} = 0.036 \ .$$

With the perpendicular Zeeman effect being negligible, mixing of the C_{4v}–C_4 basis states will be very small, giving very weak transition intensities for the transitions which split away from the zero-field energies.

The negligible perpendicular effect also means that no effect is observed for fields along the $\langle 100 \rangle$ crystal axis, since the C_s sub-site will not have any (significant) splittings and the C_4 subsite retains pure wavefunctions, with very weak "cross' transitions.

7.2 Calculating the Zeeman Splittings for H^- x-y Vibronics of Non-Kramers Ions

The Pr^{3+} ion is the only non-Kramers lanthanide ion which has a degenerate ground state for the C_{4v} symmetry Pr^{3+}-H^- centres in CaF_2 and SrF_2. The zero-order wavefunctions for the x-y vibronic states in these centres were determined in section 6.5 to be:

$$\begin{aligned}
\Psi_1 &= \tfrac{1}{\sqrt{2}}(\psi^+[-] - \psi^-[+]) \\
\Psi_2 &= \tfrac{1}{\sqrt{2}}(\psi^+[-] + \psi^-[+]) \\
\Psi_3 &= \tfrac{1}{\sqrt{2}}(\psi^+[+] - \psi^-[-]) \\
\Psi_4 &= \tfrac{1}{\sqrt{2}}(\psi^+[+] + \psi^-[-])
\end{aligned}$$

which transform as the γ_1, γ_2, γ_3 and γ_4 irreps of the C_{4v} point group, respectively. The perpendicular Zeeman operator, $L_x + 2S_x$, transforms as the γ_5 irrep of the C_{4v} group so does not have matrix elements between any of the vibronic states, giving no perpendicular Zeeman shift to first order. The parallel Zeeman operator, $L_z + 2S_z$, transforms as the γ_2 irrep of the C_{4v} point group so will only provide off-diagonal matrix elements between the $\Psi_1(\gamma_1)$ and $\Psi_2(\gamma_2)$ vibronic states and between the $\Psi_3(\gamma_3)$ and $\Psi_4(\gamma_4)$ states. These terms are simply added to the diagonal matrix containing the zero-field energies as measured (or calculated, since the spectra were not fully resolved) in section 6.5:

	Ψ_1	Ψ_2	Ψ_3	Ψ_4
Ψ_1	E_1	P		
Ψ_2	P	E_2		
Ψ_3			E_3	P
Ψ_4			P	E_4

(7.5)

where the Zeeman term is

$$\begin{aligned}
\mathrm{P} &= \mu_B B_z \langle \Psi_2 | M_0^{(1)} | \Psi_1 \rangle \\
&= \tfrac{1}{2}\mu_B B_z \left(\langle \psi^+ | M_0^{(1)} | \psi^+ \rangle + \langle \psi^- | M_0^{(1)} | \psi^- \rangle \right) \\
&= \mu_B B_z \langle \psi^+ | M_0^{(1)} | \psi^+ \rangle \\
&= \tfrac{1}{2}\mu_B g_{\parallel} B_z
\end{aligned}$$

with $\mathbf{M} = \mathbf{L}+2\mathbf{S}$. The vibronic ground-state, $\psi^{\pm}(000)$ has a linear Zeeman splitting of 2P.

7.2.1 Zeeman Splittings of the x-y Vibronics in CaF_2:Pr^{3+}:H^- and SrF_2:Pr^{3+}:H^-

The Zeeman effect for a magnetic field along the $\langle 100 \rangle$ crystal axis was measured on a 3.5 mm sample of CaF_2:0.01%Pr^{3+} which had been hydrogenated for 10 hours. The resulting spectra are displayed in figure 7.30. For a magnetic field along the $\langle 111 \rangle$ axis, a 3.0 mm thick sample of CaF_2:0.01%Pr^{3+} was hydrogenated for 7 hours, giving the spectra in figure 7.31.

The $g_{\|}$-value of the Pr^{3+}-D^- C_{4v} centre have been reported by Reeves *et al* [77] as 4.13, with $g_{\perp}$ necessarily zero for non-Kramers ions. This value can be adopted for the H^- C_{4v} centre as the wavefunctions do not change significantly between these two centres. With this g-value, the Zeeman matrix for the x-y vibronics of Pr^{3+} produces the energy shifts and splittings plotted in figure 7.32 for a magnetic field along the C_{4v} symmetry axis. The Ψ_1 and Ψ_2 states repel each other and likewise the Ψ_3 and Ψ_4 states, with no interaction between these two pairs. No splittings arise for a field perpendicular to this axis and for a $\langle 111 \rangle$ orientation the magnetic field need only be scaled by a factor of $1/\sqrt{3}$.

The transition energies deduced from this energy splitting are plotted in figure 7.33 for both $\langle 100 \rangle$ and $\langle 111 \rangle$ oriented magnetic fields, along with the experimental transition energies. The zero-field energies to be entered into the Zeeman matrix as parameters were adjusted to give the best correspondence between the experimental and calculated splittings in this diagram. The electron-phonon interaction calculations of section 6.5 predicted that the Ψ_3 state would be pushed up in energy by the presence of a nearby γ_3 intermediate state of lower energy, while the other three states remained close together. Since only the Ψ_4 state interacts with the Ψ_3 state, this can be identified by its behaviour in the presence of the magnetic field, and its zero-field energy adjusted to match this behaviour.

The Ψ_1 and Ψ_2 states are too close to be resolved in the spectra measured here. In the limit of negligible zero-field splitting, the Zeeman effect dominates, giving

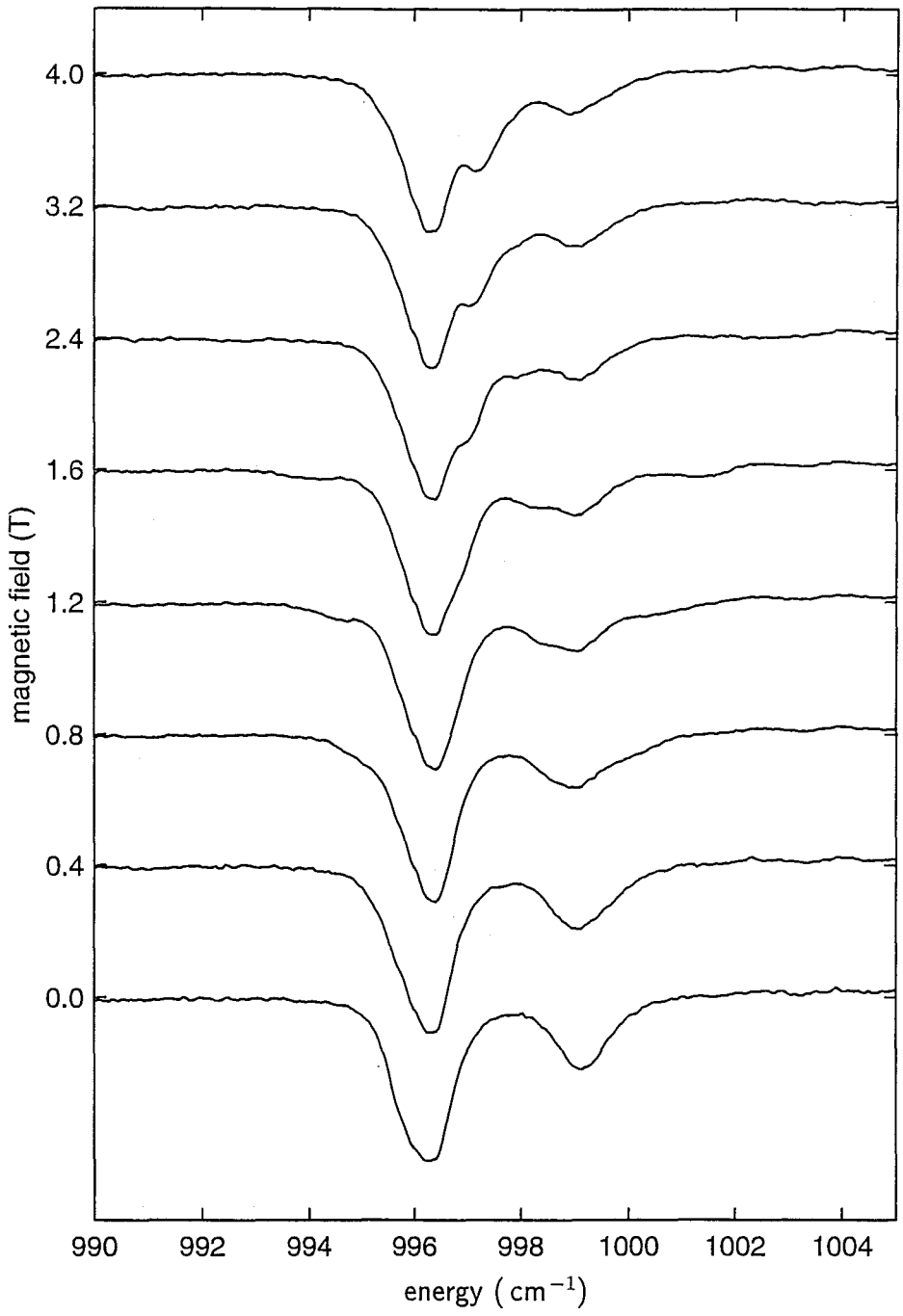

Figure 7.30 : 10 K infrared-absorption spectra of the x-y vibronics in a 3.5 mm slice of CaF_2:0.01%Pr^{3+}:H^-(10 hrs) in applied magnetic fields parallel to the ⟨100⟩ crystal axis. The zero-field spectrum has a maximum absorption of 90%.

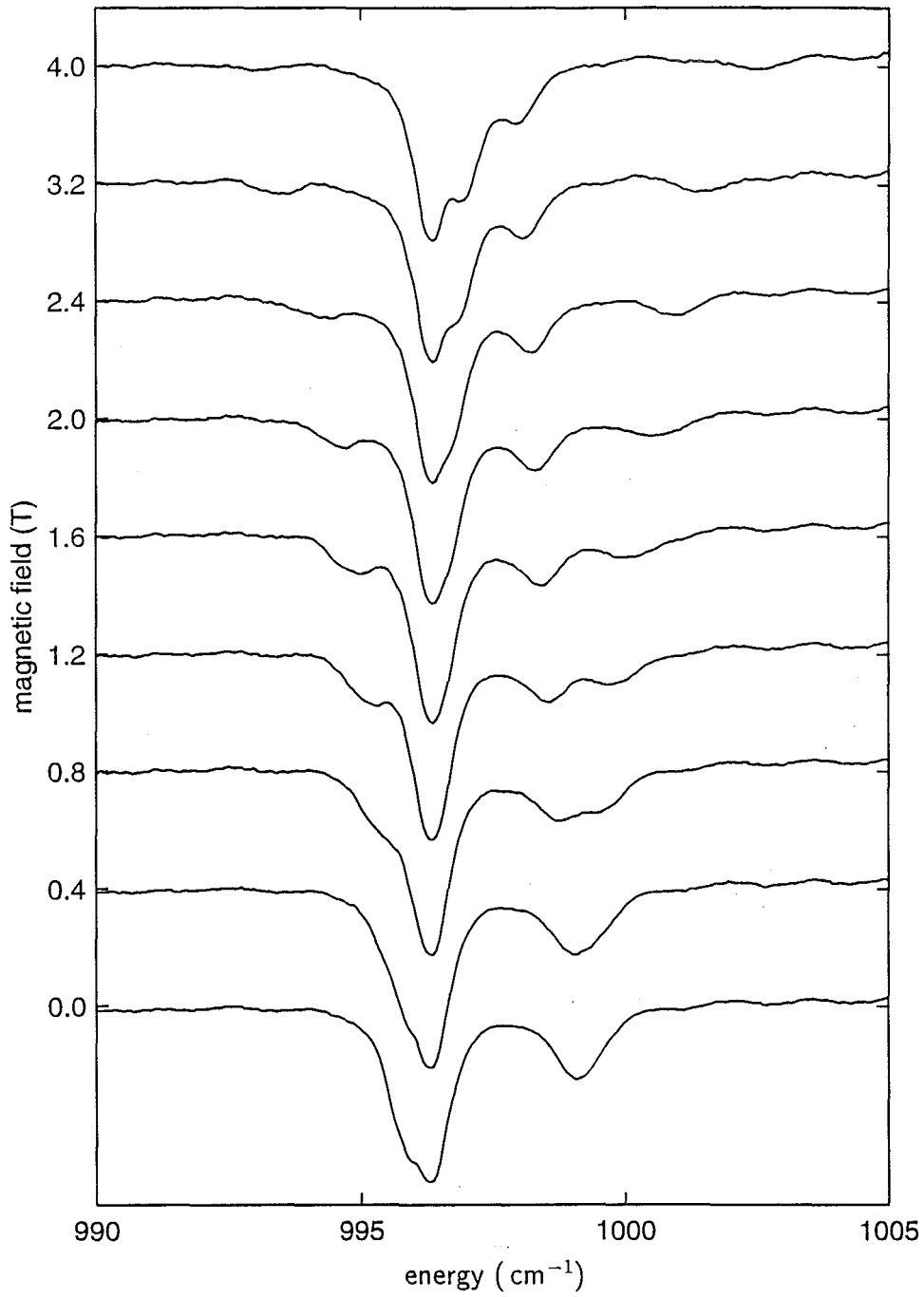

Figure 7.31 : 10 K infrared-absorption spectra of the x-y vibronics in a 3.0 mm slice of CaF_2:0.01%Pr^{3+}:H^-(7 hrs) in applied magnetic fields parallel to the ⟨111⟩ crystal axis. The zero-field spectrum has a maximum absorption of 90%.

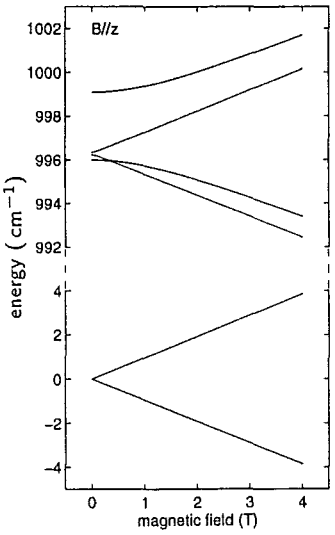

Figure 7.32 : Calculated energies of the ground state and x-y vibronic states of CaF_2:Pr^{3+}:H^- as a function of magnetic field strength, for fields applied parallel to the C_{4v} axis, producing a C_4 symmetry subsite.

a linear splitting. The wavefunctions are then the symmetric and anti-symmetric combinations of Ψ_1 and Ψ_2, i.e. simply $\psi^+[-]$ and $\psi^-[+]$. Since the electronic part of these wavefunctions become essentially the same as those of the corresponding ground state wavefunctions, the transition intensities of the "cross' transitions such as $\psi^+(000) \rightarrow \psi^-[+]$ become very small. This explains the absence of experimental data points on these two transitions in both sets of splitting diagrams.

The zero-field energies which were found to best reproduce the Zeeman splitting pattern are listed in table 7.1, with no measurable zero-field splitting between the Ψ_1 and Ψ_2 states giving their separation $|\delta| < 0.2\,\mathrm{cm}^{-1}$.

These parameters gave a very close correspondence between the calculated and measured Zeeman transition energies, showing that the first-order perturbation approach is as successful for the case of Pr^{3+} as it was for any of the Kramers ions.

The spectra of the x-y vibronics of SrF_2:Pr^{3+}:H^- in a $\langle 100 \rangle$ magnetic field was measured on a 2.5 mm sample of SrF_2:0.01%Pr^{3+} which had been hydrogenated for 4 hours, giving the spectra spectra shown in figure 7.34.

For magnetic fields in the $\langle 111 \rangle$ direction, spectra were measured on a 1.9 mm slice

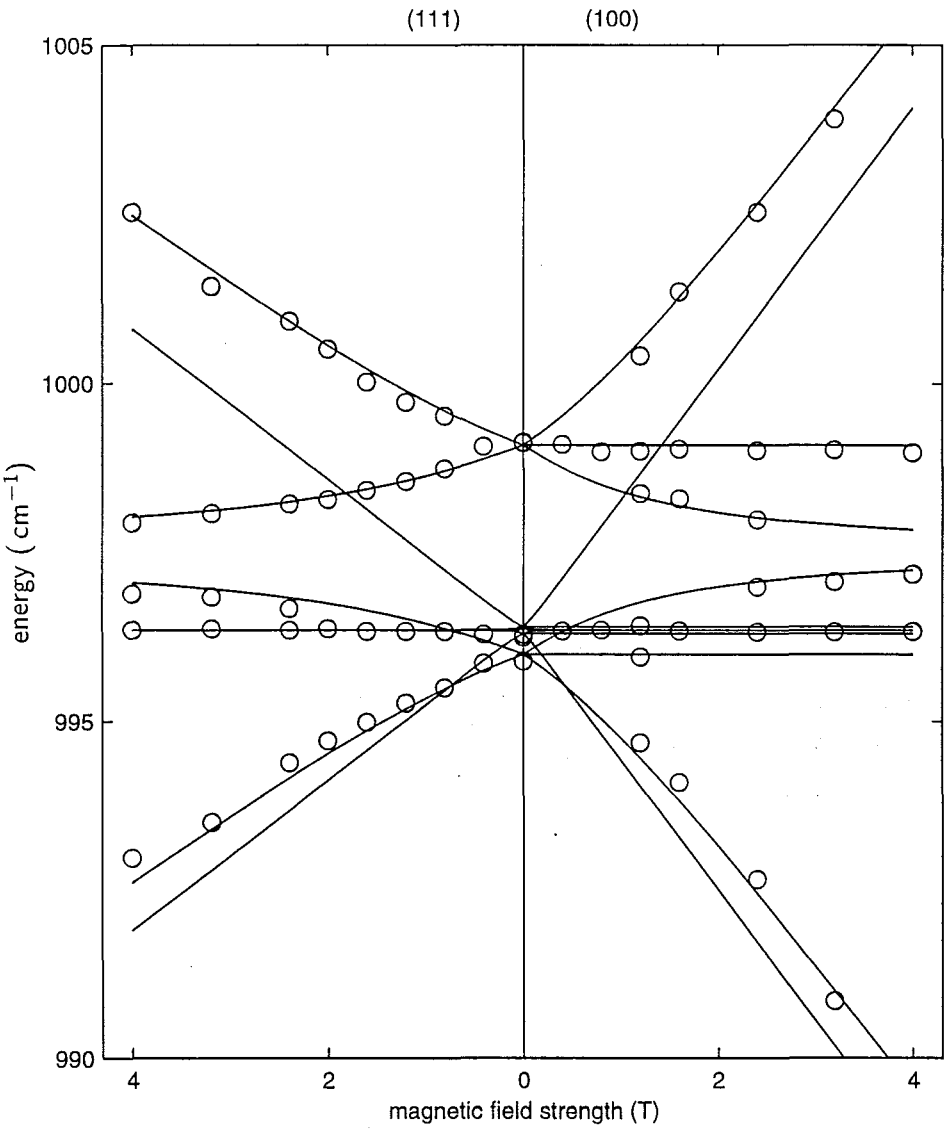

Figure 7.33 : Experimental and calculated Zeeman splitting patterns of the x-y vibronics in CaF_2:0.01%Pr^{3+}:H^-, for magnetic fields parallel to the $\langle 100 \rangle$ and $\langle 111 \rangle$ crystal axes.

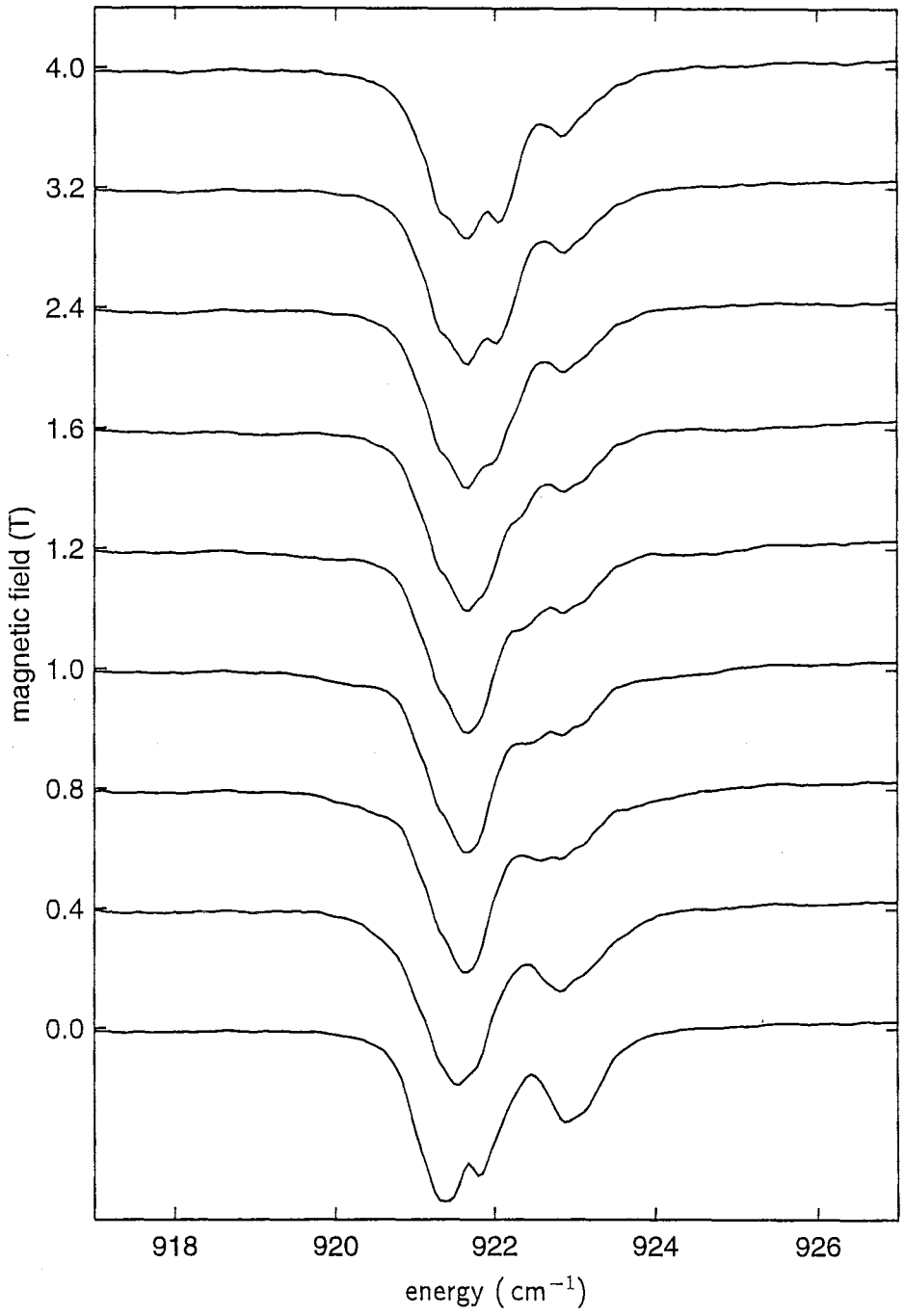

Figure 7.34 : 10 K infrared-absorption spectra of the x-y vibronics in a 2.5 mm slice of SrF_2:0.01%Pr^{3+}:H^-(4 hrs) in applied magnetic fields parallel to the ⟨100⟩ crystal axis.

	CaF_2 energy (cm^{-1})	SrF_2 energy (cm^{-1})
E_1	$996.3 + \delta$	921.9
E_2	$996.3 - \delta$	921.4
E_3	999.1	922.9
E_4	996.0	921.5

Table 7.1 : Zero-field energy eigenvalues for the x-y vibronic states of CaF_2:Pr^{3+}:H^- (with $|\delta| < 0.2\,cm^{-1}$) and SrF_2:Pr^{3+}:H^-, determined from the absorption spectrum and Zeeman splittings.

of SrF_2:0.01%Pr^{3+} hydrogenated for 4 hours, and these are presented in figure 7.35.

Reeves *et al* [77] have reported the $g_{\|}$ value for the Pr^{3+}-D^- C_{4v} centre in SrF_2 as 3.94. Again, this is expected to be very close to the value for the H^--compensated centre and is adopted here. The calculated and experimental Zeeman splittings are plotted in figure 7.36, using this g-value, and the zero-field energies listed in table 7.1, chosen to give the best correspondence between measured and calculated Zeeman energies.

The assignments to the Ψ_3 and Ψ_4 vibronic states are based on the electron-phonon calculation which, like in CaF_2, predicted that the Ψ_3 state was pushed up in energy by the second-order perturbation of the electron-phonon interaction with a nearby γ_3 intermediate state. For Ψ_1 and Ψ_2, the order of these two states does not affect the Zeeman pattern, and these two energies may thus be in the reverse order. The ordering presented here is based on the electron-phonon calculation of section 6.5, and is tentative.

Intensity Analysis of the CaF_2:Pr^{3+}:H^- and SrF_2:Pr^{3+}:H^- x-y-Vibronic Zeeman Splittings

For the calculation of transition intensities, it will be convenient to have the wavefunctions in the simpler form of $\psi^{\pm}[\pm]$, as in the first-order matrix used in section 6.5, rather than in the linear combinations which form the zero-field eigenfunctions, Ψ_i.

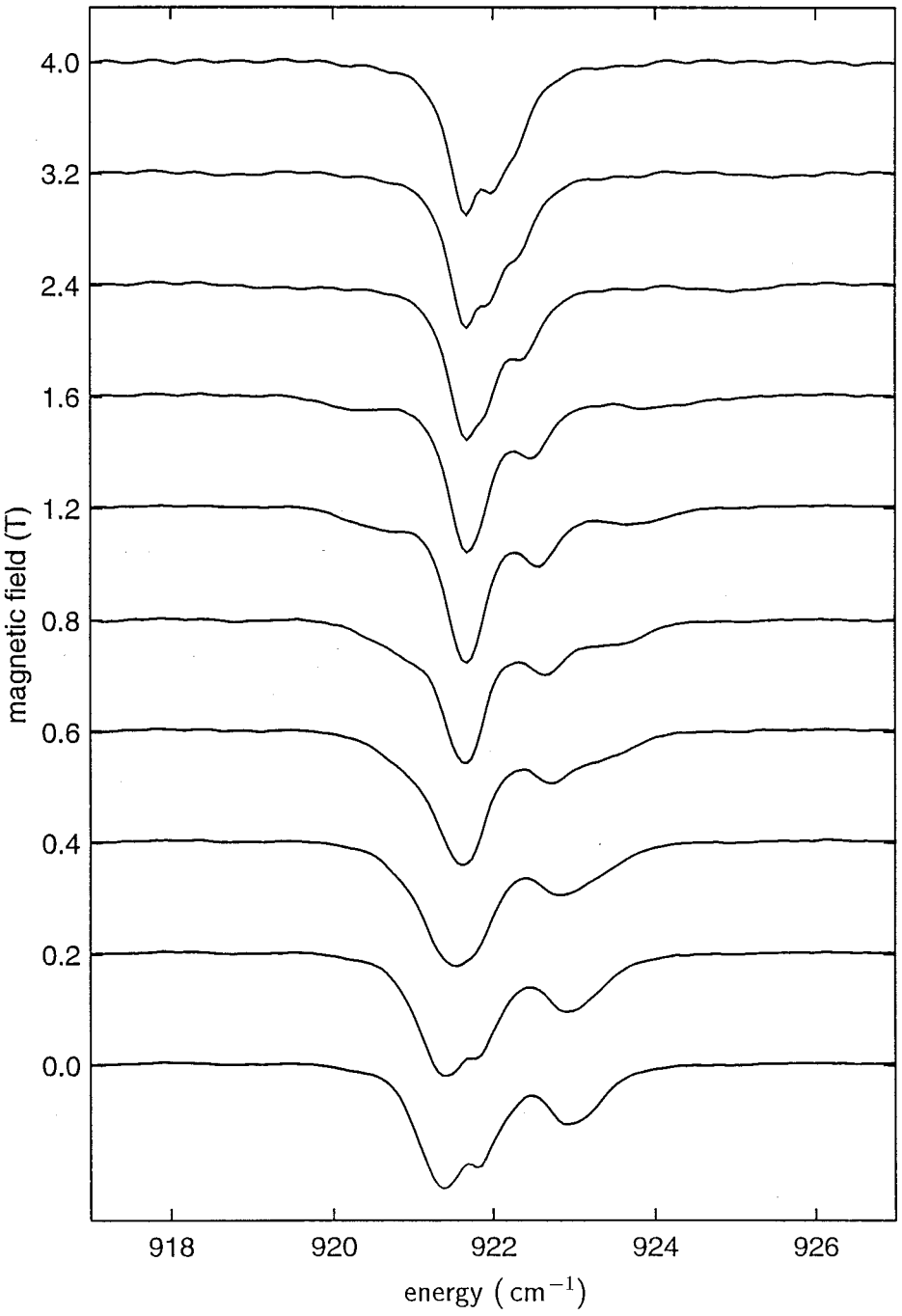

Figure 7.35 : 10 K infrared-absorption spectra of the x-y vibronics in a 1.9 mm slice of SrF_2:0.01%Pr^{3+}:H^-(4 hrs) in applied magnetic fields parallel to the $\langle 111 \rangle$ crystal axis.

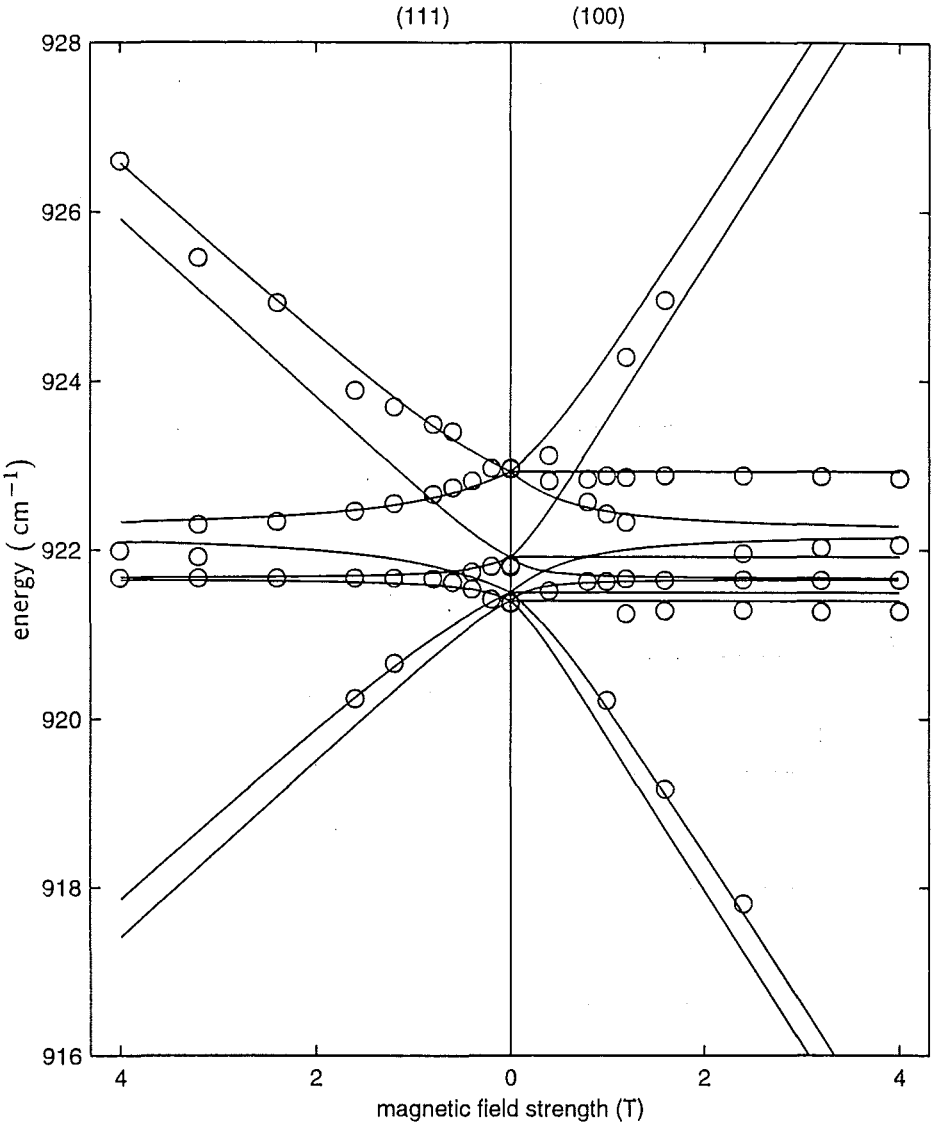

Figure 7.36 : Experimental and calculated Zeeman splitting patterns of the x-y vibronics in SrF_2:0.01%Pr^{3+}:H^-, for magnetic fields parallel to the $\langle 100 \rangle$ and $\langle 111 \rangle$ crystal axes.

This is because it is in this form that the wavefunctions are normalised with respect to vibrational transition intensities. We thus recast the Zeeman matrix in terms of these wavefunctions, but replacing the electron-phonon terms used in section 6.5 with terms deduced from the zero-field energies and known wavefunctions:

	$\psi^+[-]$	$\psi^-[+]$	$\psi^+[+]$	$\psi^-[-]$
$\psi^+[-]$	E_a+P	E_b	0	0
$\psi^-[+]$	E_b	E_a-P	0	0
$\psi^+[+]$	0	0	E_c+P	E_d
$\psi^-[-]$	0	0	E_d	E_c-P

(7.6)

where

$$\begin{aligned} E_a &= \tfrac{1}{2}(E_2 + E_1) \\ E_b &= \tfrac{1}{2}(E_2 - E_1) \\ E_c &= \tfrac{1}{2}(E_4 + E_3) \\ E_d &= \tfrac{1}{2}(E_4 - E_3)\,. \end{aligned}$$

This matrix is related to matrix 7.5 by a unitary transformation and therefore has the same eigenvalues. The new eigenvectors will be in terms of the different basis which allows a direct comparison for intensity calculations, in the same way as was done previously with the Kramers ions.

The argument presented above for having low intensities on some of the transitions is made clearer with this formulation of the Zeeman–electron-phonon matrix. With the Zeeman terms now all on the diagonal it is clear that, in the high magnetic-field limit, the wavefunctions will tend to the $\psi^{\pm}[\pm]$ states of this new basis. Since these contain pure electronic states identical to the electronic part of one or other of the ground state components, the vibronic-transition intensities of transitions in which the electronic state changes (the "cross" transitions) have very low intensity.

Simulated spectra for CaF_2:0.01%Pr^{3+}:H^- have been computed for the $\langle 111 \rangle$ magnetic field cases, and are displayed in figure 7.37 with the measured spectra. Similar assumptions were made here as for the Kramers ions, with zero intensity ascribed to the "cross" transitions. Linewidths of $0.8\,cm^{-1}$ (FWHM) of the absorption coefficient were required to match the measured spectra, considerably larger than

was required for any of the Kramers ions. These linewidths do not appear to reflect inhomogeneous broadening effects, since several samples at zero-field were tried without a significant decrease in linewidth, and the sample preparation was no different to that used for the Kramers ions. It is likely that the extra linewidth is due to unresolved hyperfine splittings, which have not been taken into account in the calculations presented here.

Simulated spectra for SrF_2:0.01%Pr^{3+}:H^- in $\langle 111 \rangle$ magnetic fields are shown in figure 7.38 with the measured spectra. The absorption-coefficient linewidths used in this case were $0.5\,cm^{-1}$ (FWHM). This is less than for the CaF_2 case, but still more than was required for the Kramers ions for similar sample concentrations and

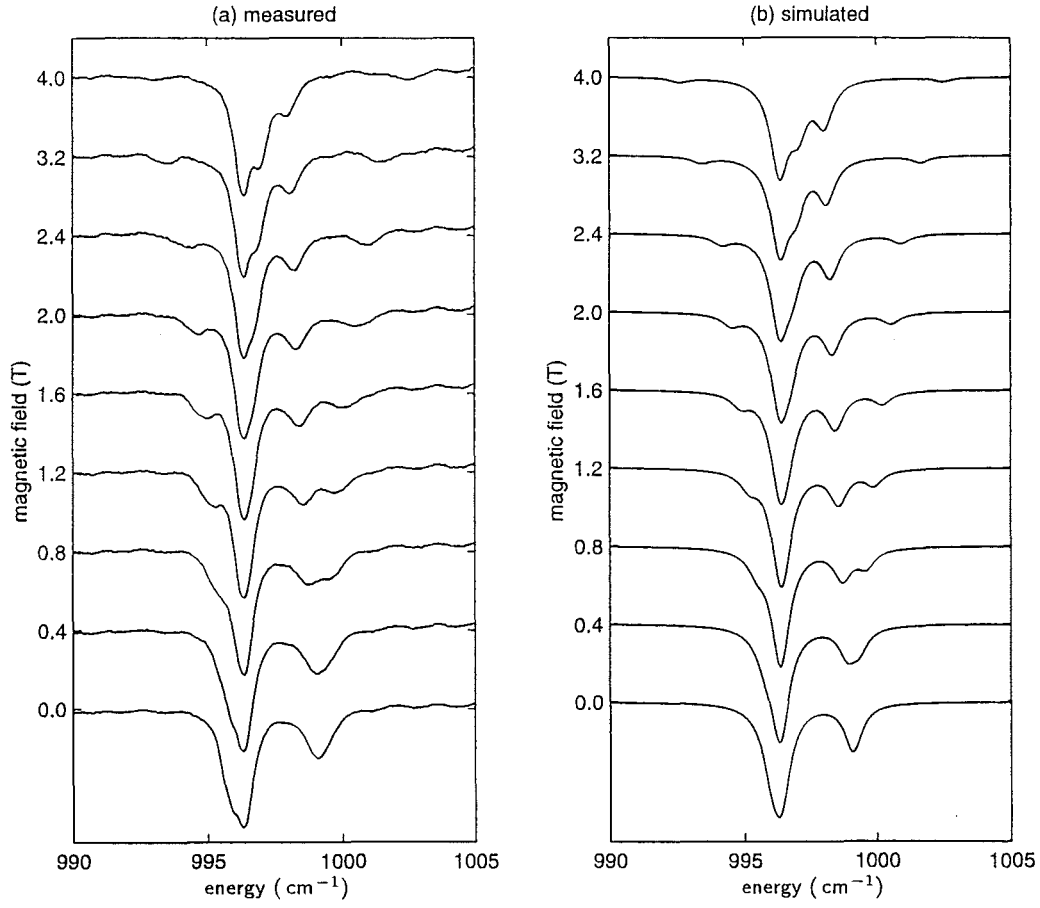

Figure 7.37 : (a) 10 K experimental and (b) simulated infrared-absorption spectra of the x-y vibronics in CaF_2:0.01%Pr^{3+}:H^-, for magnetic fields parallel to the $\langle 111 \rangle$ crystal axes.

preparation conditions, again attributed to unresolved hyperfine structure.

The hyperfine interaction can split each state into six. Reeves *et al* [77] have found that for the CaF_2:Pr^{3+}:D^- C_{4v} centre, the ground state exhibits evenly-spaced hyperfine splittings of 2.82 GHz (0.094 cm^{-1}) between each of the six hyperfine components, giving a total effective homogeneous linewidth of about 14 GHz (0.47 cm^{-1}). In a magnetic field, each Zeeman component would retain the same hyperfine splitting as in zero field, as has been demonstrated by Macfarlane *et al* [57] for the F^- compensated C_{4v} centre.

For the SrF_2:Pr^{3+}:D^- C_{4v} centre, the hyperfine splittings were not fully resolved but

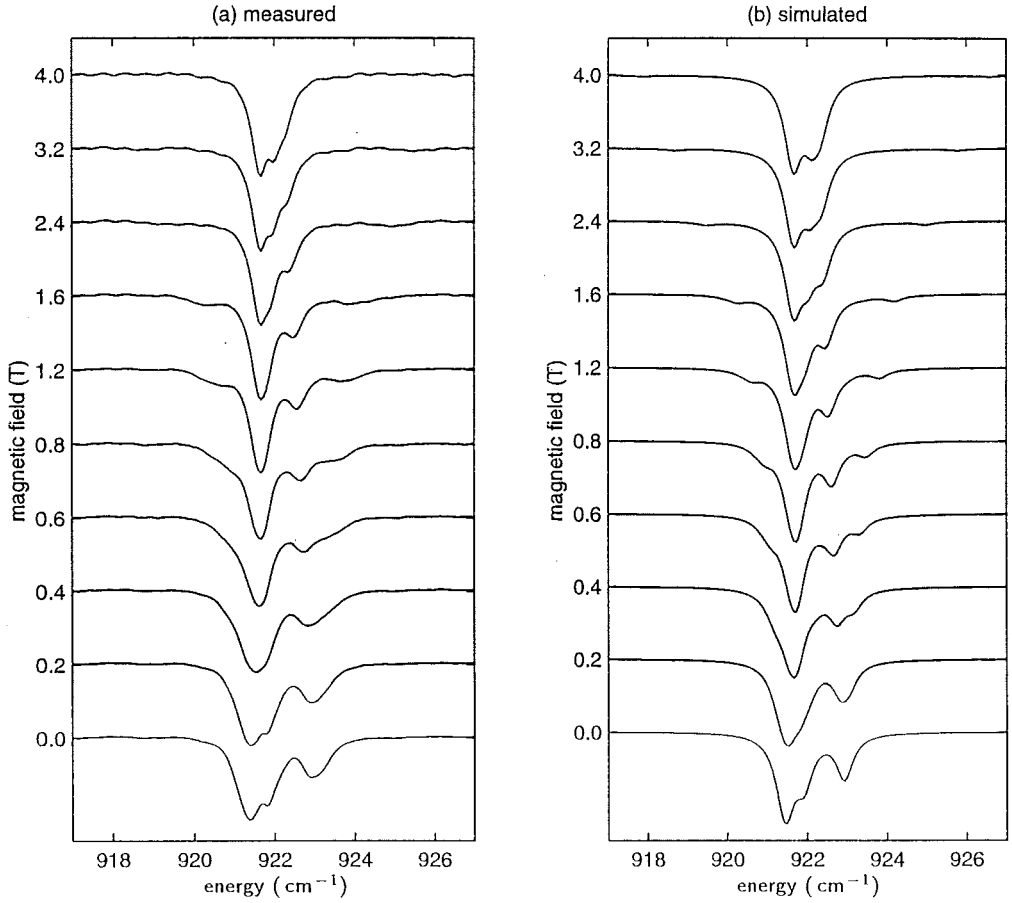

Figure 7.38 : (a) 10 K experimental and (b) simulated infrared-absorption spectra of the x-y vibronics in SrF_2:0.01%Pr^{3+}:H^-, for magnetic fields parallel to the ⟨111⟩ crystal axes.

were estimated at a somewhat smaller value of 2.2 GHz ($0.073\,cm^{-1}$) giving a total effective homogeneous linewidth of 11 GHz ($0.37\,cm^{-1}$).

After adding contributions from inhomogeneous broadening, these values account reasonably well for the broadening of the spectra presented in this section, including the differences in linewidths between the CaF_2 and SrF_2 cases.

Hyperfine mixing will occur between the Ψ_1 and Ψ_2 and between the Ψ_3 and Ψ_4 x-y vibronic states, and will be dependent on the energy splitting between these pairs. The hyperfine-induced line broadening would therefore be expected to vary between the lines and between different magnetic-field strengths. A full calculation of individual linewidths would require inclusion of the hyperfine matrix elements, $AI_z\langle J_z\rangle$, and a separate Zeeman–electron-phonon matrix for each I_z value.

The assumption adopted here of all linewidths being the same is therefore not quite accurate. However the simulated spectra in figures 7.37 and 7.38 still account adequately for the relative intensities in the measured spectra.

7.3 Summary of the Zeeman Effect of the H^- x-y Vibronics

In chapter 6, it was demonstrated that the electron–local-mode-phonon interaction could account for the splitting of the x-y line of the H^- ion in the C_{4v} site adjacent to a rare-earth ion. The zero-order vibronic wavefunctions were constructed by appealing directly to group-theoretical considerations. In cases where the electronic ground state of the rare-earth was well removed from other states, the vibronic wavefunctions thus constructed are unperturbed to first order by the electron-phonon interaction. Therefore, it has been possible to test these wavefunctions using the Zeeman effect.

The hydride ion itself does not have a magnetic moment, so the Zeeman-Hamiltonian matrix elements between vibronic states reduce to matrix elements between the electronic states. These electronic-state matrix elements follow directly from the experimentally determinable g-values of the centre, which in many cases have been reported previously. In the cases where this is not so, the g-values of the closely-related F^- C_{4v} centre can be assumed for the H^- C_{4v} centre. Where even this information was not available, g-values were estimated from crystal-field calculations

using interpolated crystal-field parameters.

With the g-values determined, and the zero-field x-y splitting measured in chapter 6, the first-order Zeeman-Hamiltonian matrix can be constructed without free parameters.

The infrared-absorption spectra of the x-y lines in CaF_2:Ce^{3+}:H^-, SrF_2:Ce^{3+}:H^-, CaF_2:Pr^{3+}:H^-, SrF_2:Pr^{3+}:H^-, CaF_2:Sm^{3+}:H^-, SrF_2:Sm^{3+}:$H^-$and CaF_2:Yb^{3+}:H^- were measured for magnetic fields of up to 4 T applied along the $\langle 100 \rangle$ and $\langle 111 \rangle$ crystal axes. The energies of the Zeeman components were then compared with the calculated splittings, with a high level of agreement in all of these cases.

Intensity analyses also followed from the first-order Zeeman-Hamiltonian matrix. Vibronic transitions, in which both the vibrational and electronic systems undergo transitions, were shown to have negligible intensity compared to purely vibrational transitions, in which the electronic state is unaltered. Transition intensities could therefore be determined by taking inner products of eigenfunctions of the first-order perturbation matrices for the ground state and x-y vibronic states. Simulated spectra were produced for magnetic fields applied along the $\langle 111 \rangle$ crystal axis for each of the above cases, giving good quantitative agreement with the recorded spectra.

The case of CaF_2:Er^{3+}:H^- represented the only example of low-lying electronic states playing a part in the Zeeman splittings. An extended Zeeman/electron-phonon interaction matrix including the x-y vibronic states associated with the Z_2 electronic level was required. This introduced electron-phonon matrix elements which were not directly calculable from the zero-field splittings and had to be treated as parameters. The best-fit Zeeman splitting pattern for magnetic fields along the $\langle 111 \rangle$ axis gave a reasonable match with the experimental data, using calculated intensities to determine which of the calculated transitions should dominate the spectra.

No Zeeman effects were observed for magnetic fields applied parallel to the $\langle 111 \rangle$ crystal axis for CaF_2:Nd^{3+}:H^-, SrF_2:Nd^{3+}:H^- or CaF_2:Gd^{3+}:H^-, and no effects for either $\langle 100 \rangle$ or $\langle 111 \rangle$ magnetic fields were observed for CaF_2:Dy^{3+}:H^-. The absence of Zeeman splitting in each of these cases was explained by the zero-field splitting or the ground-state g-values, and supported by simulated spectra calculated from the Zeeman-Hamiltonian matrix.

Overall, the Zeeman Hamiltonian, considered in first-order perturbation only, has been very successful in modelling the experimental energy shifts and spectral line intensities.

Further Work

One of the limiting factors in this study has been the spectral resolution. It is not known whether the linewidths measured here represent a value close to the inhomogeneously broadened linewidth, or whether instrumental broadening is playing a significant part. It would be beneficial to measure some of the x-y splittings on a higher resolution instrument, such as the Bomem DA 3 FTIR spectrometer which has been made available at Industrial Research Limited, Lower Hutt. If it transpires that the linewidths are significantly less than those measured on the BioRad FTS-40 instrument here, then the Zeeman results presented here could be repeated at such a resolution. This would be particularly beneficial for the complex case of CaF_2:Er^{3+}:H^-, and the small zero-field splitting cases of CaF_2:Nd^{3+}:H^- and SrF_2:Nd^{3+}:H^-.

In magnetic fields oriented along the $\langle 100 \rangle$ crystal axes, some transitions are π-allowed and are not observable with the current magnet configuration. These transitions would be measurable with a split-solenoid magnet, allowing the light path perpendicular to the applied magnetic field. A 6 T split-solenoid magnet is available, but is too large to fit inside the sample compartment of the FTS-40 spectrometer. An arrangement with the light beam being diverted out of the spectrometer and through the magnet cryostat could overcome this problem. Since the H^- vibrational lines measured here are not in a region affected by atmospheric absorption bands, the external beam path would not pose problems in that respect. However, the 6 T split-solenoid magnet is much larger and heavier than the current 4 T magnet, which would pose some technical problems. In most cases, those transitions which are purely π-allowed are also not expected to shift when the magnetic field is applied. Therefore, there is some advantage in retaining the current configuration for these experiments.

While no polarisation effects are expected for sites in the cubic CaF_2 crystal at zero field, such effects could arise upon application of the magnetic field. It would be of

interest to examine the linear and circular polarisation dependences of the Zeeman sub-transitions, and compare these with the theoretically expected behaviour. This could also aid in assigning transitions in the complex cases, such as CaF_2:Er^{3+}:H^-.

Chapter 8

Conclusions and Suggestions for Further Work

The techniques of laser-selective excitation, infrared absorption and Zeeman spectroscopy have been applied to the investigation of rare-earth and hydride ion centres in CaF_2 and SrF_2 crystals.

Laser-selective excitation spectroscopy has been used to determine the energy-level structure of two single-Tm^{3+}-ion centres in CaF_2:Tm^{3+}, determined from polarisation dependences to have C_{4v} and C_{3v} symmetries respectively. The observation of upconversion fluorescence, due to excited-state absorption, from both of these centres extended the range of levels which could be identified to the $^1D_2$ multiplet near $28000\,cm^{-1}$. 31 and 30 energy levels were determined for the C_{4v} and C_{3v} centres, respectively. Clear polarisation ratios for the C_{4v} centre allowed each of the Tm^{3+} states of this centre to be assigned to a C_{4v} irrep label. A crystal-field fit incorporating these assignments was performed, giving a standard deviation of $8.3\,cm^{-1}$ for the 31 levels for ten freely varied parameters, consisting of five cystal-field, four free-ion and one zero-energy parameter. The crystal-field parameters obtained from this fit were similar to those previously obtained for the C_{4v} centres of other CaF_2:RE^{3+} systems, indicating the same structural configuration, as expected.

The ambiguous polarisation ratios obtained for the C_{3v} centre did not permit a set of C_{3v} irrep labels to be assigned to the Tm^{3+} electronic states. A crystal field fit was attempted without irreps, giving a standard deviation of $10.2\,cm^{-1}$ for the 30 levels for eleven freely-varied parameters (six crystal-field, four free-ion and a zero-energy parameter). While the standard deviation is reasonable, the irreps assigned from this fit were not consistent with all of the polarisation ratios and transition-selection

rules, nor with the $^3H_5$ multiplet Zeeman splittings. Clearly, more information regarding these irrep assignments will be required before a definitive crystal-field fit can be attempted. With a 6 T split-solenoid magnet available, laser-selective excitation spectroscopy on Zeeman-split magnetic sub-sites could provide this information. With the magnetic field applied parralel to a $\langle 111 \rangle$ crystal axis, the C_3 magnetic sub-site could be selectively studied. Any splittings would immediately identify γ_3 doublets, while polarisation ratios would become trivial with the orientational degeneracy removed. These polarisation ratios could distinguish between π and π_{md} transitions, thus identifying γ_1 and γ_2 singlets, and would also distinguish between these and transitions to any unresolved doublets. Because of the dimensions of the magnet dewar, tight focussing would not be possible, and upconversion fluorescence would be difficult to obtain with a single pump laser. However, the possibility of pumping with two tunable lasers, either two rhodamine 640 dye lasers or one such and a Ti:sapphire laser may be realisable in this laboratory in the near future. This would give greater intensity of upconversion fluorescence, plus increased sub-site discrimination for simultaneous selective excition of two transitions.

While it was not observed in the optical regime, a cubic centre was also identified in CaF_2:Tm^{3+} by one magnetic-dipole allowed infrared-absorption transition. It was demonstrated that this was expected to be the only allowed absorption transition for a cubic centre. The Zeeman splitting of this transition for magnetic fields applied along a $\langle 100 \rangle$ crystal axis agreed quantitatively with the predicted g-value derived from a cubic crystal-field calculation. Using the linestrengths of the absorption transition, and a magnetic-dipole-only allowed transition of the C_{4v} centre, the relative concentrations of these two centres was calculated, with the C_{4v} centre being present at 2.7 times the concentration of the cubic centre. Zeeman splittings for cubic centres are expected to be isotropic, therefore measurement of the same Zeeman splitting pattern for magnetic fields applied along the $\langle 111 \rangle$ axis would confirm the site symmetry.

After deuteration treatment of the CaF_2:Tm^{3+} samples, many new absorption lines appeared. Four new Tm^{3+} centres were investigated by laser-selective excitation and were proposed to be the D^--compensated analogue of the C_{4v} centre, and three perturbations of this centre involving at least two D^- ions. The strongest of these centres at low D^- concentration did not bleach, consistent with its assignment as

the C_{4v} centre, while the other three demonstrated the reversible polarised bleaching previously demonstrated for other CaF_2:RE^{3+}:H^- systems. Several other D^- sites which are possibly related to the C_{3v} centre were not studied as their absorption lines in the $^3F_3$ multiplet lay beyond the tuning range pof the rhodamine 640 dye laser. Unexpectedly, several new lines appeared in the upconversion excitation spectrum for the deuterated samples, with the strongest of these producing strongly polarised fluorescence characteristic of C_{4v}-symmetry centres, indicating that it was from the C_{4v} D^- centre.

Upconversion fluorescence has been observed from several single-ion CaF_2:RE^{3+} centres, and was shown to be consistent with arising from a sequential-absorption upconversion (SAU) mechanism for two steps having transition energies within a few hundred cm^{-1} of each other. With only a single pump laser, this had to be tuned to one of the two steps of the process, either the ground-state absorption (GSA) or the excited-state absorption (ESA) transition. The other of these two transitions, not in resonance with the laser, was pumped via lattice-phonon sidebands. At low temperatures ($\sim$ 15 K), more efficient upconversion was achieved if the higher-energy of the two transitions was pumped, since a phonon-creation process could then bridge the non-resonant transition, rather than the low-probability phonon-annihilation process that would be required if the lower-energy transition were pumped. Red-to-green and near-infrared-to-green upconversion fluorescence were observed for the C_{4v} centre in CaF_2:0.01%Er^{3+}, with ESA pumping dominating in the former case and GSA pumping in the second. Red-to-blue, red-to-violet/UV and near-infrared-to-blue upconversion fluorescence was obtained from single-ion centres in CaF_2:0.02%Tm^{3+}, for pumping three sets of ESA transitions. GSA-pumped upconversion was not observed in CaF_2:Tm^{3+}. In CaF_2:0.01%Ho^{3+}, red-to-green upconversion was observed for pumping GSA transitions of the C_{4v} and C_{3v} centres. Yellow-to-UV and red-to-violet upconversion fluorescence were observed in CaF_2:0.01%Nd^{3+}, with the former case, obtained upon pumping either GSA or ESA transitions having been reported previously by Han *et al* [33]. The latter case was dominated by GSA-pumped upconversion.

Several of these specific upconversion mechanisms were undiminished, or even enhanced, as the sample was warmed up from 15 K. The red-to-green and infrared-to-green upconversion fluorescence in CaF_2:Er^{3+} and the red-to-green upconversion

fluorescence in CaF_2:Ho^{3+} all retained their peak intensities to room temperature, despite the transitions broadening considerably. The red-to-blue upconversion fluorecence if the C_{4v} centre in CaF_2:Tm^{3+} was remarkable in increasing in intensity by a factor of 100 when warmed to room temperature. This exceptional behaviour was found to be due to a near coincidence of the energies of a GSA and ESA transition which overlapped when the transitions broadened at elevated temperatures.

It appears that sequential-absorptioon upconversion is a relatively universal phenomenon, requiring only suitably close GSA and ESA transition energies, and a metastable intermediate state. A continuation of this study for other rare-earth ions, other host crystals and other pump-wavelength regions may lead to a more quantitative understanding of the dependence of the upconversion efficiency on sample temperature, the transition-energy mismatch and the available lattice-phonon energies.

The splitting of the H^- x-y vibration infrared-absorption line has been measured for the C_{4v} centres in CaF_2:RE^{3+}:H^- and SrF_2:RE^{3+}:H^-. As has previously been reported, such splittings only occur for these centres where the associated rare-earth ion has a degenerate electronic ground state. Thus a coupling between the RE^{3+} electronic and H^- vibrational systems has been proposed, with the electron–local-mode-phonon able to induce splittings of the x-y vibronic states. The derivation of the electron-phonon interaction for these systems has been outlined. Using different basis states for the transverse vibration than previous works, a simpler form for derivatives of the solid harmonics was derived, and the point-charge model used to calculate radially-dependent coefficients of the electron-phonon interaction Hamiltonian. These coefficients were also found from the measured x-y splittings for comparison. Reasonable agreement has been obtained, given the crudeness of the point-charge model, with discrepancies in the D_1^2 electron-phonon Hamiltonian parameter of up to a factor of 2.9. This order-of-magnitude agreement demonstrated that the electron–local-mode-phonon interaction would be able to produce the observed x-y splittings. Further calculations have been suggested which would involve incorporating higher-degree terms in the expansion of the solid-harmonic derivatives, higher order perturbations and more elaborate models for the interaction.

Assuming the electron-phonon interaction mechanism for the x-y splittings, the

zero-order vibronic wavefunctions were determined by group-representation considerations. From these wavefunctions, the effect of an external applied magnetic field could be calculated from the Zeeman-interaction Hamiltonian. The case of CaF_2:Er^{3+}:H^- required the consideration of a second set of nearby vibronic states associated with a low-lying first-excited electronic state. Extra electron-phonon terms had to be incorporated in this Hamiltonian matrix, thus introducing some undetermined parameters. The best-fit splitting patterns were in reasonable agreement with the experimental data in this case, with intensity calculations indicating which lines of the complex calculated splitting pattern were expected to dominate. For isolated x-y vibronic states, these calculations did not require any further parametrisation beyond the measured zero-field splittings and electronic g-values. The agreement between measured and calculated Zeeman splitting patterns for magnetic field applied parallel to either the $\langle 100 \rangle$ or $\langle 111 \rangle$ crystal axes was excellent in these isolated-state cases. Furthermore, transition intensities were also derived from the first-order Hamiltonian matrix, and simulated spectra for magnetic fields along the $\langle 111 \rangle$ direction were plotted. These gave very good agreement with the experimental spectra, accounting fully for the observed variation in intensities. The measurement of polarisation dependences would be a useful extension of this work, with anisotropic absorption expected for Zeeman sub-transitions. With the zero-order wavefunctions well known, these polarisation effects could be compared with expected polarisations. If successful, this would be an aid to assignment of transitions in the complex CaF_2:Er^{3+}:H^- case. In addition, those transitions which are only π allowed are not observable with the current configuration of the optical path parallel to the direction of the applied magnetic field. This would be remedied by the use of a split-solenoid magnet, allowing the optical path to be perpendicular to the magnetic-field direction.

The rare-earth-doped CaF_2 system is in many respects a model system for spectroscopy. At low rare-earth concentrations, several different centres are formed, each having a high symmetry, while lower-symmetry cluster centres are formed at moderate concentrations. Light hydride and deuteride ions can be diffused into the crystal, and form centres by themselves or associated with dopant rare-earth ions. The isotropy of the host crystal leads to orientational degeneracy for axial centres which, while giving complicated polarisation dependences, leads to interesting

bleaching and re-orientation effects. The use of the various spectroscopic techniques in this thesis have demonstrated some interesting, and indeed surprising, physics even in a well-studied and supposedly "simple" crystal system.

References

[1] Abragam A and Bleaney B (1986) *Electron Paramagnetic Resonance of Transition Ions.* (Dover Publications, Inc).

[2] Aizenberg I B, Malkin B Z and Stolov A L (1971) *Cubic centers of the Er^{3+} ion in crystals of the fluorite type.* Sov Phys Sol St **13** 2155.

[3] Allain J Y, Monerie M and Poignant H (1990) *Blue upconversion fluorozirconate fibre laser.* Electron Lett **26** 166.

[4] Allain J Y, Monerie M and Poignant H (1990) *Room temperature cw tunable green upconversion holmium fibre laser.* Electron Lett **26** 261.

[5] Antipin A A, Davydova M P, Eremin M V, Luks R K and Stolov A L (1971) *Crystalline field in anisotropic activator Dy^{3+} centers in fluorite single crystals.* Opt Spectrosc **33** 372.

[6] Antipin A A, Kurkin I N, Chirkin G K and Shekun L Ya (1965) *Electron paramagnetic resonance of Ce^{3+} ions in SrF_2 and BaF_2 single crystals.* Sov Phys Solid State **6** 1590.

[7] Ashburner I J, Newman R C and McLaughlan S D (1968) *Charge commpensation of trivalent rare earth by interstitial hydrogen ions in calcium fluoride.* Phys Lett **27A** 212.

[8] Baker J M and Blake W B J (1970) *Endor of $^{173}Yb^{3+}$ on tetragonal sites in calcium fluoride: determination of the crystal field parameters.* Proc Roy Soc Lond A **316** 63.

[9] Baker J M, Hayes W and Jones D A (1959) *Paramagnetic resonance of impurities in CaF_2.* Proc Phys Soc **73** 942.

[10] Barthem R B, Buisson R and Cone R L (1989) *Spectroscopic analysis of Nd^{3+} pairs in $CsCdBr_3$.* J Chem Phys **91** 627.

[11] Bierig R W and Weber M J (1963) *Paramagnetic resonance of dysprosium in cubic and axial fields in CaF_2.* Phys Rev **132** 164.

[12] Brown M R, Thomas H, Whiting J S S and Shand W A (1969) *Experiments on Er^{3+} in SrF_2. I. Fluorescence quantum efficiencies and lifetimes.* J Chem Phys **50** 881.

[13] Butler P H (1981) *Point Group Symmetry Applications.* (Plenum Press).

[14] Carnall W T, Goodman G L, Rajnka K and Rana R S February (1988) *A systematic analysis of the spectra of the lanthanides doped into single crystal LaF_3.* Technical Report ANL-88-8 (Argonne National Laboratory).

[15] Catlow C R A (1976) *The defect properties of anion-excess alkaline-earth fluorides: I. Low defect concentrations.* J Phys C **9** 1845.

[16] Chambers D N and Newman R C (1969) *Compensation of trivalent europium and ytterbium ions in calcium fluoride by interstitial hydride ions.* Phys Stat Sol **35** 685.

[17] Cockroft N J (1987) *Laser Selective Excitation of Erbium Ions in Crystalline Solids.* (PhD thesis, University of Canterbury).

[18] Cockroft N J (1994) *Application of energy upconversion spectroscopy to novel laser and phosphor design.* Journal of Alloys and Compounds **207/208** 33.

[19] Cockroft N J, Han T P J, Reeves R J, Jones G D and Syme R W G (1987) *Reversible polarized bleaching in hydrogenated rare-earth-doped fluorides.* Opt Lett **12** 36.

[20] Cockroft N J, Jones G D and Syme R W G (1989) *Upconversion fluorescence spectroscopy of Er^{3+} pairs in $CsCdBr_3$.* J Chem Phys **86** 521.

[21] Cockroft N J, Thompson D, Jones G D and Syme R W G (1987) *Site-selective spectroscopy of hydrogenic sites in CaF_2:Er^{3+} crystals.* J Chem Phys **86** 521.

[22] Dieke G H (1968) *Spectra and Energy Levels of Rare Earth Ions in Crystals.* (John Wiley & Sons, Inc).

[23] Edgar A (1974) *Solid State Spectroscopy: The Electron Paramagnetic Resonance Spectra of Gadolinium and Erbium Ions in Hydrogenated Alkaline Earth Fluoride Crystals.* (PhD thesis, University of Canterbury).

[24] Edgar A, Freeth C A and Jones G D (1977) *Infrared and electron-paramagnetic-resonance spectra of trivalent rare-earth ions in hydrogenated strontium-fluoride crystals.* Phys Rev B **15** 5023.

[25] Edgar A, Jones G D and Presland M R (1979) *Optical and EPR spectra of hydrogenated and deuterated crystals of calcium fluoride containing erbium.* J Phys C: Solid State Phys **12** 1569.

[26] Edmonds A R (1957) *Angular Momentum in Quantum Mechanics.* (Princeton University Press).

[27] Elliott R J, Hayes W, Jones G D, Macdonald H and Sennett C T (1965) *Localized vibrations of H^- and D^- ions in the alkaline earth fluorides.* Proc Roy Soc (London) **A289** 1.

[28] Freeman A J and Watson R E (1962) *Theoretical investigation of some magnetic and spectroscopic properties of rare-earth ions.* Phys rev **127** 2058.

[29] Freeth C A and Jones G D (1982) *Zeeman infrared spectra of calcium and strontium fluoride crystals containing cerium and neodymium.* J Phys C: Solid State Phys **15** 6833.

[30] Freeth C A, Jones G D and Syme R W G (1982) *The transverse Zeeman effect in calcium fluoride crystals containing erbium.* J Phys C: Solid State Phys **15** 5667.

[31] Hall J L and Schumacher R T (1962) *Electron Spin Resonance of hydrogen atoms in CaF_2.* Phys Rev B **127** 1892.

[32] Han T P J (1988) *Solid State Spectroscopy: Laser Selective Excitation Studies of Neodymium.* (PhD thesis, University of Canterbury).

[33] Han T P J, Jones G D and Syme R W G (1993) *Site-selective spectroscopy of Nd^{3+} centers in CaF_2:Nd^{3+} and SrF_2:Nd^{3+}.* Phys Rev B **47** 14706.

[34] Hayes W and Twidell J W (1961) *Paramagnetic resonance of X-irradiated CaF_2:Tm and of CaF_2:Yb.* J Chem Phys **35** 1521.

[35] Hebert T, Wannemacher R, Macfarlane R M and Lenth W (1992) *Blue continuously pumped upconversion lasing in Tm^{3+}:$YLiF_4$.* Appl Phys Lett **60** 2592.

[36] Hildebrand F B (1976) *Advanced Calculus for Applications.* (Prentice-Hall, Inc).

[37] Hodby J W (1974) *Electronic Properties.* in Hayes W (ed.) *Crystals with the Fluorite Structure.* (Oxford University Press).

[38] Hüfner S (1978) *Optical Spectra of Transparent Rare Earth Compounds.* (Academic Press, Inc).

[39] Jacobs I T (1971) *Solid State Spectroscopy: Rare Earth - Hydride Centres in the Alkaline Earth Fluorides.* (PhD thesis, University of Canterbury).

[40] Jacobs I T, Jones G D, Zdansky K and A Satten R (1971) *Electron-phonon interaction effects in the spectra of hydrogenated, Deuterated, and tritiated crystals of calcium and strontium fluoride containing cerium.* Phys Rev B **3** 2888.

[41] Jamison S P and Reeves R J (1995) *Optical depolarization in CaF_2:RE^{3+} and SrF_2:RE^{3+} C_{4v} centers due to dipole reorientation.* J Lumin **66&67** 169.

[42] Jones G D (1994) *Zeeman spectroscopy of H^- local modes in rare-earth doped CaF_2.* J Lumin **58** 20.

[43] Jones G D and Murdoch K M (1994) *Laser site-selective spectroscopy of Tb^{3+} ions in CaF_2 and SrF_2.* J Lumin **60&61** 131.

[44] Jones G D, Peled S, Rosenwaks S and Yatsiv S (1969) *Spectra of hydrogenated calcium fluoride containing rare-earth ions.* Phys Rev **183** 353.

[45] Jones G D and Strickland N M (1995) *Zeeman spectroscopy of local modes of the C_{4v} H^- centre in CaF_2:Er^{3+}.* J Lumin **66&67** 253.

[46] Jouart J P, Bouffard M, Klein G and Mary G (1994) *Red-to-blue up-conversion spectroscopy of Tm^{3+} in SrF_2, CaF_2, BaF_2 and CdF_2.* J Lumin **60&61** 93.

[47] Jouart J P and Oomen E W J (1992) *Upconversion in Er^{3+}-doped fluorite-type crystals excited at 800nm.* Phys stat sol (b) **172** 461.

[48] Judd B R (1962) *Optical absorption intensities of rare-earth ions.* Phys Rev **127** 750.

[49] Kafri A, Kiro D, Yatsiv S and Low W (1968) *ESR spectra of trivalent rare earth ions in CaF_2 containing H^- ions.* Solid St Commun **6** 573.

[50] Kirton J and McLaughlan S D (1967) *Correlation of electron paramagnetic resonance and optical absorption spectra of CaF_2:Yb^{3+}.* Phys Rev **155** 279.

[51] Koster G F, Dimmock J O, Wheeler R G and Statz H (1963) *Properties of the Thirty-two Point Groups.* (MIT Press).

[52] Lea K R, Leask M J M and Wolf W P (1962) *The raising of angular momentum degeneracy of f-electron terms by cubic crystal fields.* J Chem Phys Solids **23** 1381.

[53] Lenth W and Macfarlane R M (1990) *Excitation mechanisms for upconversion lasers.* J Lumin **45** 346.

[54] Lezama A, Oria M and de Araujo C B (1986) *Site-selective spectroscopy via energy upconversion in CaF_2:Pr^{3+}.* Phys Rev B **33** 4493.

[55] Luks R K, Saitkulov I G and Stolov A L (1969) *Optical spectra of CaF_2 single crystals activated by Dy^{3+}.* Sov Phys - Solid State **11** 210.

[56] Macfarlane R M (1993) *Spectral holeburning in the trivalent thulium ion.* Opt Lett **18** 829.

[57] Macfarlane R M, Burum D P and Shelby R M (1993) *Hyperfine structure and nuclear and electronic Zeeman effect of the $^1D_2 \leftrightarrow {}^3H_4$ transition of Pr^{3+}:CaF_2.* Phys Rev B **29** 2390.

[58] Macfarlane R M, Tong F, Silversmith A J and Lenth W (1988) *Violet cw neodymium upconversion laser.* Appl Phys Lett **52** 1300.

[59] Macpherson G L and Henling L M (1977) *EPR spectrum of coupled pairs of Gd^{3+} ions in single crystals of $CsCdBr_3$.* Sov Phys - Solid State **11** 210.

[60] Maradudin A A and Peretti J (1967) *Impurity-induced second-harmonic infrared absorption and raman scattering by U-center localized modes in alkali-halide crystals.* Phys rev **161** 852.

[61] McLaughlan S D (1967) *Electron paramagnetic resonance of trivalent-rare-earth-monovalent-alkaline-earth ion pairs in CaF_2.* Phys Rev **160** 287.

[62] Moore D S (1980) *Laser spectroscopic and EPR studies of defect equilibria in rare earth doped fluorite structure crystals.* (PhD thesis, University of Wisconsin).

[63] Mujaji M (1992) *Solid State Spectroscopy: Laser Selective Excitation of Holmium Ions in Crystalline Solids.* (PhD thesis, University of Canterbury).

[64] Mujaji M, Jones G D and Syme R W G (1992) *Polarization study and crystal-field analysis of the laser-selective excitation spectra of Ho^{3+} ions in CaF_2 and SrF_2 crystals.* Phys Rev B **46** 14398.

[65] Mujaji M, Jones G D and Syme R W G (1992) *Upconversion fluorescence spectroscopy of Ho^{3+} dimer pairs in $CsCdBr_3$.* J Lumin **53** 473.

[66] Murdoch K M (1993) *Laser Spectroscopy, Energy Transfer and Bleaching Processes in Crystalline Rare-Earth Centres.* (PhD thesis, University of Canterbury).

[67] Muto K (1972) *Absorption soectra and Zeeman effects of Tm^{3+} in CaF_2.* J Phys Chem Solids **34** 2029.

[68] Nara H and Schlesinger M (1972) *Analysis of the optical spectra of Dy^{3+} doped calcium fluoride.* J Phys C **5** 606.

[69] Newman R C and Woodward R J (1974) *An EPR analysis of Yb, Er and Sm centres in strontium fluoride.* J Phys C: Solid State Phys **7** L432.

[70] Nguyen D C, Faulkner G E and Dulick M (1989) *Blue-green (450-nm) upconversion Tm^{3+}:YLF laser.* Applied Optics **28** 3553.

[71] Nguyen D C, Faulkner G E, Weber M E and Dulick M (1990) Proc SPIE, Solid State Lasers **1223** 54.

[72] Nielson C W and Koster G F (1963) *Spectroscopic coefficients for the p^n, d^n and f^n configurations.* (MIT Press).

[73] Ofelt G S (1962) *Intensities of crystal spectra of rare-earth ions.* J Chem Phys **37** 511.

[74] Rector C W, Pandey B C and Moos H W (1966) *Electron paramagnetic resonance and optical Zeeman spectra of type II CaF_2:Er^{3+}.* J Chem Phys **45** 171.

[75] Reeves R J (1987) *Laser Selective Excitation Spectroscopy of Praseodymium Ions in Hydrogenated Fluorite Crystals.* (PhD thesis, University of Canterbury).

[76] Reeves R J, Jones G D and Syme R W G (1989) *Spectroscopy of reversible bleaching centers in hydrogenated SrF_2:Pr^{3+} and CaF_2:Pr^{3+} crystals.* Phys Rev B **40** 6475.

[77] Reeves R J, Jones G D and Syme R W G (1992) *Site-slelctive spectroscopy of Pr^{3+} C_{4v} symmetry centres in hydrogenated CaF_2:Pr^{3+} and SrF_2:Pr^{3+} crystals.* Phys Rev B **46** 5939.

[78] Reid M F and Butler P H (1982) *The point group crystal field and the superposition model for RE^{3+} ions in CaF_2 and SrF_2.* J Phys C **15** 4103.

[79] Rotenberg M, Metropolis N, Bivins R and Wooten Jr. J K (1959) *The 3-j and 6-j symbols.* (MIT Press).

[80] Seelbinder M B and Wright J C (1979) *Site-selective spectroscopy of CaF_2:Ho^{3+}.* Phys Rev B **20** 4308.

[81] Silversmith A J, Lenth W and Macfarlane R M (1987) *Green infrared-pumped erbium upconversion laser.* Appl Phys Lett **51** 1977.

[82] Sivaram A, Jagannath H, Ramachandra Rao D and Venkateswarlu Putcha (1979) *Steady state and transient fluorescence studies of CaF_2:Dy^{3+} single crystals.* Phys Chem Solids **40** 1007.

[83] Stevens K W H (1952) *Matrix elements and operator equivalents connected with the magnetic properties of rare earth ions.* Proc Phys Soc **A65** 209.

[84] Tallant D R, Moore D S and Wright J C (1977) *Defect equilibria in fluorite structure crystals.* J Chem Phys **67** 2897.

[85] Tallant D R and Wright J C (1975) *Selective laser excitation of charge compensated sites in CaF_2:Er^{3+}.* J Chem Phys **63** 2074.

[86] Tanabe Y and Sugano S (1954) *On the absorption spectra of complex ions. I and II.* J Phys Soc Jap **9** 753, 766.

[87] Ward R W and Whippey P W (1974) *Vibronic Sideband of Er^{3+} in CaF_2.* Can J Phys **52** 1185.

[88] Wells J P R. Private Communication.

[89] Wells J P R (1993) *Infrared Zeeman Spectroscopy of Rare-Earth Ions in Alkaline Earth Fluoride Crystals.* (MSc thesis, University of Canterbury).

[90] Wells J-P R and Reeves R J (1995) *Up-conversion fluorescence of Eu^{3+} doped alkaline earth fluoride crystals.* J Lumin **66&67** 219.

[91] Wybourne B G (1965) *Spectroscopic Properties of Rare Earths.* (John Wiley & Sons, Inc).

[92] Wyckoff R W G (1964) *Crystal Structures.* 2 edn vol. 1 (John Wiley & Sons, Inc).

[93] Zdansky K and Edgar A (1971) *Electron spin resonance of gadolinium-hydride and gadolinium-deuteride ion pairs in calcium fluoride crystals.* Phys Rev B **3** 2133.

[94] Zhang X, Jouart J P, Bouffard M and Mary G (1994) *Site-selective upconversion luminescence of Ho^{3+}-doped CaF_2 crystals.* Phys Stat Sol **184** 559.

Appendix A

Differentiation of Solid Harmonics

The following recurrence relations, quoted from Edmonds [26], are satisfied by the associated Legendre polynomials and are central to this derivation:

$$(n-m+1)\mathrm{P}_{n+1}^{m}(\zeta) - (2n+1)\zeta\mathrm{P}_{n}^{m}(\zeta) + (n+m)\mathrm{P}_{n-1}^{m}(\zeta) = 0 \tag{A.1}$$

$$\zeta\mathrm{P}_{n}^{m}(\zeta) - (n-m+1)(1-\zeta^2)^{\frac{1}{2}}\mathrm{P}_{n}^{m-1}(\zeta) - \mathrm{P}_{n-1}^{m}(\zeta) = 0 \tag{A.2}$$

$$\mathrm{P}_{n+1}^{m}(\zeta) - \zeta\mathrm{P}_{n}^{m}(\zeta) - (n+m)(1-\zeta^2)^{\frac{1}{2}}\mathrm{P}_{n}^{m-1}(\zeta) = 0 \tag{A.3}$$

$$(n-m+1)\mathrm{P}_{n+1}^{m}(\zeta) + (1-\zeta^2)^{\frac{1}{2}}\mathrm{P}_{n}^{m+1}(\zeta) - (n+m+1)\zeta\mathrm{P}_{n}^{m}(\zeta) = 0 \tag{A.4}$$

$$(1-\zeta^2)^{\frac{1}{2}}\mathrm{P}_{n}^{m+1}(\zeta) - 2m\zeta\mathrm{P}_{n}^{m}(\zeta) + (n+m)(n-m+1)(1-\zeta^2)^{\frac{1}{2}}\mathrm{P}_{n}^{m-1}(\zeta) = 0 \tag{A.5}$$

$$\begin{aligned}(1-\zeta^2)\frac{\partial}{\partial\zeta}\mathrm{P}_{n}^{m}(\zeta) &= (n+1)\zeta\mathrm{P}_{n}^{m}(\zeta) - (n-m+1)\mathrm{P}_{n+1}^{m}(\zeta) \\ &= (n+m)\mathrm{P}_{n-1}^{m}(\zeta) - n\zeta\mathrm{P}_{n}^{m}(\zeta)\end{aligned} \tag{A.6}$$

The derivation is most easily facilitated by using solid harmonics defined as:

$$\begin{aligned}\mathrm{R}_{m}^{n}(\boldsymbol{r}) &= r^n\mathrm{C}_{m}^{(n)}(\theta,\phi) \\ &= (-1)^m\sqrt{\tfrac{(n-m)!}{(n+m)!}}\, r^n\mathrm{P}_{n}^{m}(\cos\theta)e^{im\phi}\end{aligned} \tag{A.7}$$

where the associated Legendre polynomials P_{n}^{m} are taken to be

$$\mathrm{P}_{n}^{m}(\zeta) = \frac{(1-\zeta^2)^{\frac{m}{2}}}{2^n n!}\frac{d^{n+m}}{d\zeta^{n+m}}(\zeta^2-1)^n$$

as defined, for example, by Edmonds [26], and $\zeta = \cos\theta = \frac{z}{r}$, so that $(1-\zeta^2)^{\frac{1}{2}} = \sin\theta$.

Using this definition, we can differentiate with respect to $\mathrm{X}_\pm = \frac{1}{\sqrt{2}}(x \pm iy)$ by converting to derivatives with respect to spherical coordinates (see for example Hildebrand [36], and note $\frac{\partial}{\partial\theta} = \frac{\partial\cos\theta}{\partial\theta}\frac{\partial}{\partial\cos\theta} = -\sin\theta\frac{\partial}{\partial\zeta}$).

$$\begin{aligned}
\frac{\partial}{\partial \mathrm{X}_\pm} &= \frac{1}{\sqrt{2}}\left(\frac{\partial}{\partial x} \mp i\frac{\partial}{\partial y}\right) \\
&= \frac{1}{\sqrt{2}}(\cos\phi \mp i\sin\phi)\left(\sin\theta\frac{\partial}{\partial r} + \frac{\cos\theta}{r}\frac{\partial}{\partial\theta} \mp \frac{i}{r\sin\theta}\frac{\partial}{\partial\phi}\right) \\
&= \frac{1}{\sqrt{2}}e^{\mp i\phi}\left(\sin\theta\frac{\partial}{\partial r} - \frac{\cos\theta\sin\theta}{r}\frac{\partial}{\partial\zeta} \mp \frac{i}{r\sin\theta}\frac{\partial}{\partial\phi}\right) \qquad \text{(A.8)}
\end{aligned}$$

Since the solid harmonics are well defined in terms of the spherical coordinates, the differentiation of these follows as:

$$\begin{aligned}
\frac{\partial \mathrm{R}_m^n}{\partial \mathrm{X}_\pm} &= (-1)^m\sqrt{\tfrac{(n-m)!}{(n+m)!}}\tfrac{1}{\sqrt{2}}e^{\mp i\phi}\left(\sin\theta\frac{\partial r^n}{\partial r}\mathrm{P}_n^m e^{im\phi}\right. \\
&\qquad \left. - \frac{\cos\theta\sin\theta}{r}r^n\frac{\partial \mathrm{P}_n^m}{\partial\zeta}e^{im\phi} \mp \frac{i}{r\sin\theta}r^n\mathrm{P}_n^m\frac{\partial e^{im\phi}}{\partial\phi}\right) \\
&= (-1)^m\sqrt{\tfrac{(n-m)!}{(n+m)!}}\tfrac{1}{\sqrt{2}}r^{n-1}e^{i(m\mp1)\phi} \\
&\qquad \times\left(\frac{n\sin^2\theta \pm m}{\sin\theta}\mathrm{P}_n^m - \cos\theta\sin\theta\frac{\partial \mathrm{P}_n^m}{\partial\zeta}\right) \qquad \text{(A.9)}
\end{aligned}$$

Combining (A.3) and (A.4) we have, for $m \neq 0$:

$$\mathrm{P}_n^m(\zeta) = \frac{(n+m-1)(n+m)}{2m}\sin\theta\mathrm{P}_{n-1}^{m-1}(\zeta) + \frac{\sin\theta}{2m}\mathrm{P}_{n-1}^{m+1}(\zeta) \qquad \text{(A.10)}$$

and then combining (A.10), (A.5) and (A.6):

$$\begin{aligned}
\frac{\partial \mathrm{P}_n^m(\zeta)}{\partial\zeta} &= \left(\frac{n\sin^2\theta + m}{2m\cos\theta\sin\theta}\right)\mathrm{P}_{n-1}^{m+1}(\zeta) \\
&\quad + \left(\frac{(n+m)(n+m-1)(n\sin^2\theta - m)}{2m\cos\theta\sin\theta}\right)\mathrm{P}_{n-1}^{m-1}(\zeta) \qquad \text{(A.11)}
\end{aligned}$$

We can then substitute (A.10) and (A.11) into (A.9):

$$\begin{aligned}
\frac{\partial \mathrm{R}_m^n}{\partial \mathrm{X}_\pm} &= (-1)^m\sqrt{\tfrac{(n-m)!}{(n+m)!}}\frac{r^{n-1}}{\sqrt{8}\,m}e^{i(m\mp1)\phi} \times \\
&\quad \left((\pm m - m)\mathrm{P}_{n-1}^{m+1} + (\pm m + m)(n+m-1)(n+m)\mathrm{P}_{n-1}^{m-1}\right) \qquad \text{(A.12)}
\end{aligned}$$

and treating the X_+ and X_- cases separately leads to the simple combined equation:

$$\frac{\partial \mathrm{R}_m^n}{\partial \mathrm{X}_\pm} = \mp\sqrt{\tfrac{(n\pm m)(n\pm m-1)}{2}}\ \mathrm{R}_{m\mp1}^{n-1} \quad \text{, for } m \neq 0. \qquad \text{(A.13)}$$

For the $m = 0$ case, $\mathrm{R}_0^n = r^n \mathrm{P}_n(\cos\theta)$, so:

$$\frac{\partial \mathrm{R}_0^n}{\partial \mathrm{X}_\pm} = \tfrac{1}{\sqrt{2}} e^{\mp i\phi} \left(\sin\theta n r^{n-1} \mathrm{P}_n - \frac{\cos\theta \sin\theta}{r} r^n \frac{\partial \mathrm{P}_n}{\partial \zeta} \right) \tag{A.14}$$

From the definition of the associated Legendre polynomial for $m = 1$:

$$\begin{aligned} \mathrm{P}_n^m(\zeta) &= (1-\zeta^2)^{m/2} \frac{\partial^m \mathrm{P}_n(\zeta)}{\partial \zeta^m} \\ \mathrm{P}_n^1(\zeta) &= (1-\zeta^2)^{1/2} \frac{\partial \mathrm{P}_n(\zeta)}{\partial \zeta} \\ &= \sin\theta \frac{\partial \mathrm{P}_n(\zeta)}{\partial \zeta} \end{aligned} \tag{A.15}$$

then using (A.15) and (A.2) in (A.14) we obtain:

$$\begin{aligned} \frac{\partial \mathrm{R}_0^n}{\partial \mathrm{X}_\pm} &= \tfrac{1}{\sqrt{2}} e^{\mp i\phi} \left(n \sin\theta r^{n-1} \mathrm{P}_n - \frac{\cos\theta \sin\theta}{r} r^n \left[\frac{n \mathrm{P}_n}{\cos\theta} + \frac{\mathrm{P}_{n-1}^1}{\cos\theta \sin\theta} \right] \right) \\ &= -\tfrac{1}{\sqrt{2}} r^{n-1} \mathrm{P}_{n-1}^1 e^{\mp i\phi} \\ &= \mp \frac{\sqrt{n(n-1)}}{2} \mathrm{R}_{\mp 1}^{n-1} \end{aligned} \tag{A.16}$$

which is equation (A.13) for the $m = 0$ case. Hence we have in general:

$$\boxed{\frac{\partial \mathrm{R}_m^n}{\partial \mathrm{X}_\pm} = \mp \sqrt{\frac{(n \pm m)(n \pm m - 1)}{2}} \mathrm{R}_{m \mp 1}^{n-1} \qquad \text{for } -n \le m \le n.} \tag{A.17}$$

Differentiation with respect to z again requires conversion to spherical coordinates:

$$\begin{aligned} \frac{\partial}{\partial z} &= \cos\theta \frac{\partial}{\partial r} - \frac{\sin\theta}{r} \frac{\partial}{\partial \theta} \\ &= \cos\theta \frac{\partial}{\partial r} + \frac{\sin^2\theta}{r} \frac{\partial}{\partial \zeta} \end{aligned} \tag{A.18}$$

Then, again making use of (A.6):

$$\begin{aligned} \frac{\partial \mathrm{R}_m^n}{\partial z} &= (-1)^m \sqrt{\tfrac{(n-m)!}{(n+m)!}} \left(\cos\theta \frac{\partial r^n}{\partial r} \mathrm{P}_n^m + \frac{\sin^2\theta}{r} r^n \frac{\partial \mathrm{P}_n^m(\zeta)}{\partial \zeta} \right) e^{im\phi} \\ &= (-1)^m \sqrt{\tfrac{(n-m)!}{(n+m)!}} \, r^{n-1} (n+m) \mathrm{P}_{n-1}^m(\zeta) e^{im\phi} \end{aligned} \tag{A.19}$$

$$\boxed{\frac{\partial \mathrm{R}_m^n}{\partial z} = \sqrt{(n-m)(n+m)}\,\mathrm{R}_m^{n-1} \qquad \text{for } -n \le m \le n.} \tag{A.20}$$

It will be useful to have derivatives of the quantities $\frac{\mathrm{R}_m^n}{r^{2n+1}}$, so:

$$\begin{aligned}\frac{\partial}{\partial \mathrm{X}_\pm}\left(\frac{\mathrm{R}_m^n}{r^{2n+1}}\right) &= -(2n+1)\frac{1}{r^{2n+2}}\frac{\mathrm{X}_\mp}{\sqrt{2}\,r}\mathrm{R}_m^n + \frac{1}{r^{2n+1}}\frac{\partial \mathrm{R}_m^n}{\partial \mathrm{X}_\pm} \\ &= -\frac{2n+1}{\sqrt{2}}\frac{\mathrm{X}_\mp}{r^{2n+3}}\mathrm{R}_m^n \\ &\quad \mp \frac{1}{r^{2n+1}}\sqrt{\tfrac{(n\pm m)(n\pm m-1)}{2}}\,\mathrm{R}_{m\mp 1}^{n-1}\end{aligned} \tag{A.21}$$

Combining (A.1) and (A.4):

$$-(2n+1)\sin\theta \mathrm{P}_n^m + (n+m)(n+m-1)\mathrm{P}_{n-1}^{m-1} - (n-m+1)(n-m+2)\mathrm{P}_{n+1}^{m-1} = 0 \tag{A.22}$$

and combining (A.2) and (A.3):

$$-(2n+1)\sin\theta \mathrm{P}_n^m - \mathrm{P}_{n-1}^{m+1} + \mathrm{P}_{n+1}^{m+1} = 0 \tag{A.23}$$

We can simplify (A.21) by using (A.22) for the X_+ case and (A.23) for the X_- case and obtain:

$$\boxed{\frac{\partial}{\partial \mathrm{X}_\pm}\left(\frac{\mathrm{R}_m^n}{r^{2n+1}}\right) = \mp\sqrt{\frac{(n\mp m+1)(n\mp m+2)}{2}}\left(\frac{\mathrm{R}_{m\mp 1}^{n+1}}{r^{2n+3}}\right) \qquad \text{for } -n \le m \le n.} \tag{A.24}$$

Differentiating with respect to z:

$$\begin{aligned}\frac{\partial}{\partial z}\left(\frac{\mathrm{R}_m^n}{r^{2n+1}}\right) &= -(2n+1)\frac{1}{r^{2n+2}}\frac{z}{r}\mathrm{R}_m^n + \frac{1}{r^{2n+1}}\frac{\partial \mathrm{R}_m^n}{\partial z} \\ &= -(2n+1)\frac{z}{r^{2n+3}}\mathrm{R}_m^n + \frac{1}{r^{2n+1}}\sqrt{(n-m)(n+m)}\mathrm{R}_m^{n-1}\end{aligned} \tag{A.25}$$

and, using (A.1):

$$\boxed{\frac{\partial}{\partial z}\left(\frac{\mathrm{R}_m^n}{r^{2n+1}}\right) = -\sqrt{(n-m+1)(n+m+1)}\left(\frac{\mathrm{R}_m^{n+1}}{r^{2n+3}}\right) \qquad \text{for } -n \le m \le n.} \tag{A.26}$$